THE PHYSICS AND CHEMISTRY OF SOLIDS

AN INTERNATIONAL JOURNAL

VOLUME 17 1960

Editor-in-Chief **HARVEY BROOKS** *Cambridge, Mass.*

Associate Editors
H. B. G. CASIMIR *Eindhoven*
G. J. DIENES *Brookhaven*
JACQUES FRIEDEL *Paris*
E. M. LIFSHITZ *Moscow*

Editorial Advisory Board

U.S.A.

E. N. Adams, Pittsburgh
D. Alpert, Illinois
L. Apker, Schenectady
J. Bardeen, Illinois
D. S. Billington, Oak Ridge
R. G. Breckenridge, Cleveland
Leo Brewer, Berkeley, Calif.
E. Burstein, Penn.
J. A. Burton, New Jersey
N. Cabrera, Virginia
G. C. Danielson, Iowa
I. Estermann, Washington, D.C.
J. C. Fisher, Schenectady
F. Herman, Princeton
Conyers Herring, New Jersey
A. R. von Hippel, Cambridge, Mass
J. H. Hollomon, Schenectady
W. V. Houston, Houston
H. B. Huntington, Troy
H. M. James, Purdue
C. Kittel, Berkeley, Calif.
W. Kohn, Pittsburgh
J. A. Krumhansl, Cleveland
A. W. Lawson, Chicago
H. W. Leverenz, Princeton
O. T. Marzke, Pittsburgh
B. T. Matthias, New Jersey
L. R. Maxwell, Silver Spring
Joseph E. Mayer, Chicago
E. W. Montroll, Maryland
David Pines, Princeton
George T. Rado, Washington, D.C.
H. Reiss, New Jersey
J. R. Reitz, Cleveland
A. Rose, Princeton
O. C. Simpson, Argonne
R. Smoluchowski, Pittsburgh
F. H. Spedding, Iowa
D. Turnbull, Schenectady
J. H. Van Vleck, Harvard
B. E. Warren, Cambridge, Mass.
Eugene P. Wigner, Princeton
B. H. Zimm, Schenectady

Canada

R. E. Burgess, Vancouver
D. K. C. MacDonald, Ottawa
W. B. Pearson, Ottawa

United Kingdom

A. Charlesby, Shrivenham, Berks.
W. J. Dunning, Bristol
F. C. Frank, Bristol
H. K. Henisch, Reading
H. Jones, London
J. W. Mitchell, Bristol
A. B. Pippard, Cambridge
M. H. L. Pryce, Bristol
R. A. Smith, Malvern
K. W. H. Stevens, Nottingham
F. C. Tompkins, London

France

E. F. Bertaut, Grenoble
A. Guinier, Orsay
Louis Néel, Grenoble
Louis Weil, Grenoble

Germany

M. Born, Bad Pyrmont
Ulrich Dehlinger, Stuttgart
R. Hilsch, Göttingen
G. Leibfried, Aachen
E. Mollwo, Erlangen
H. Pick, Stuttgart
M. von Laue, Berlin
H. Welker, Erlangen

Italy

F. G. Fumi, Pavia

Czechoslovakia

J. Tauc, Praha

Japan

Toshinosuke Muto, Tokyo

The Netherlands

A. Michels, Amsterdam
G. W. Rathenau, Amsterdam

Sweden

J. O. Linde, Stockholm
Per-Olov Löwdin, Uppsala

Switzerland

G. Busch, Zurich
P. Scherrer, Zurich

U.S.S.R.

G. S. Zhdanov, Moscow

PERGAMON PRESS **NEW YORK · LONDON · PARIS** **LOS ANGELES**

NOTES FOR CONTRIBUTORS

I. GENERAL

1. Submission of a paper to the *Journal of the Physics and Chemistry of Solids* will be taken to imply that it represents original research not previously published (except in the form of an abstract or preliminary report), that it is not being considered for publication elsewhere, and that if accepted, it will not be published elsewhere in the same form, in any language, without the consent of the editor-in-chief. It should deal with original research work in the field of the physics and chemistry of solids.

2. Papers should be submitted to the appropriate regional editor (all English-language papers to be sent to the U.S. editor).

3. Papers will be published as quickly as possible after acceptance, and, subject to space being available, should appear in the following issue, if this is due for publication not earlier than three months after the acceptance date. Short communications under the heading of "Letters to the Editor" will receive priority for publication, and will be published in the issue following receipt, if accepted not later than the beginning of the month preceding publication.

4. Fifty free reprints of each paper are supplied. Additional copies can be obtained at a reasonable cost if ordered when proofs are returned. A reprint order form will accompany first proofs.

II. SCRIPT REQUIREMENTS

1. Papers submitted should be concise and written in a readily understandable style. Scripts should be typed and double spaced and submitted in duplicate to facilitate refereeing.

It will be appreciated if authors clearly indicate any special characters used. An abstract, not exceeding 200 words, should be provided in the language of the paper. French and German papers should be submitted with English abstract and titles, but if this is not possible the abstract will be translated by the publishers. To conserve space, authors are requested to mark less important parts of the paper, such as details of experimental technique, methods, mathematical derivations, etc. for printing in small type. The technical description of methods should be given in detail only when such methods are new. Authors will receive proofs for correction when their papers are first set; page proofs will be sent only when the amount of alteration makes it advisable.

2. Illustrations should not be included in the typescript of the paper, and legends should be typed on a separate sheet. Line drawings which require redrawing should include all relevant details and clear instructions for the draughtsman. If figures are already well drawn it may be possible to reproduce them direct from the originals, or from good photo-prints if these can be provided. It is not possible to reproduce from prints with weak lines. Illustrations for reproduction should normally be about twice the final size required. The lettering should be sufficiently large and bold to permit this reduction. Photographs should only be included where they are essential.

3. Tables and figures should be so constructed as to be intelligible without reference to the text. Every table and column should be provided with an explanatory heading. Units of measure must always be clearly indicated. The same data should not be published in both tables and figures. The following standard symbols should be used on line drawings since they are easily available to the printers: ○, ●, +, ×, □, ■, △, ▲, ◇, ◆, ▽, ▼.

4. References are indicated in the text by superior numbers in parentheses, and the full reference should be given in a list at the end of the paper in the following form:

1. HILL R., *J. Iron St. Inst* **158**, 177 (1948).
2. PEARSON C., *The Extrusion of Metals*, p. 137. Chapman and Hall, London (1944).

Abbreviations of journal titles should follow those given for *Physics Abstracts*. It is particularly requested that authors' initials, and appropriate volume and page numbers, should be given in every case.

Footnotes, as distinct from literature references should be indicated by the following symbols—*, †, ‡, ‡‡, commencing anew on each page; they should *not* be included in the numbered reference system.

5. Due to the international character of the journal no rigid rules concerning notation and spelling will be observed, but each paper should be consistent within itself as to symbols and units.

Vol. 17
1960

CONTENTS LISTS FOR VOLUME 17, NOS. 1–4

Volume 17 Numbers 1/2

page

J. B. MULLIN and K. F. HULME: Orientation-dependent distribution coefficients in melt-grown InSb crystals 1

S. VAN HOUTEN: Semiconduction in $Li_xNi_{(1-x)}O$ 7

J. GRAHAM: Lattice spacings and colour in the system alumina–chromic oxide 18

P. E. WIGEN and J. A. COWEN: Paramagnetic resonance absorption in several electron-irradiated molecular crystals 26

J. C. WOOLLEY and C. M. GILLETT: Electrical properties of GaSb–InSb alloys 34

R. D. MAURER: Light scattering by neutron irradiated silica 44

J. E. ZIMMERMAN and F. E. HOARE: Low-temperature specific heat of dilute Cu–Mn alloys 52

A. CIMINO and M. MAREZIO: Lattice parameter and defect structure of cadmium oxide containing foreign atoms 57

C. COTTINI, G. FABRI, E. GATTI and E. GERMAGNOLI: Influence of disorder on the lifetime of positrons in anthracene 65

H. KOELMANS: Association and dissociation of centres in luminescent ZnS–In 69

WERNER KÄNZIG: Paramagnetic resonance of the antimorph of the *F*-center 80

WERNER KÄNZIG: Paramagnetic resonance study of radiation damage in lithium fluoride 88

ROBERT C. MILLER: On the origin of Barkhausen pulses in $BaTiO_3$ 93

K. S. IRANI, A. P. B. SINHA and A. B. BISWAS: Crystal distortion in spinels containing Mn^{3+} ions . . 101

GY. GERGELY: Surface recombination and diffusion processes in cathodoluminescence and electron bombardment induced conductivity 112

SIMONE ODIOT et D. SAINT-JAMES: Diffraction paramagnétique des neutrons par les ions de terres rares . . 117

MANUEL CARDONA and WILLIAM PAUL: Pressure dependence of the direct energy gap in germanium . . 138

D. I. BOLEF, N. T. MELAMED and M. MENES: Elastic constants of hexagonal cadmium sulfide . . . 143

K. WEISER: Theory of solubility of interstitial impurities in germanium and silicon 149

Letters to the Editor:

J. C. PHILLIPS: Direct observation of open magnetic orbits 162

R. NITSCHE: The growth of single crystals of binary and ternary chalcogenides by chemical transport reactions 163

P. CAMAGNI, G. CHIAROTTI and A. MANARA: Generation of vacancies during plastic deformation of KCl crystals 165

P. P. CRAIG, D. E. NAGLE and R. D. REISWIG: Resonant absorption of gamma radiation in superconductors 168

A. BLANDIN and J. FRIEDEL: On quadrupolar effects in alloys 170

W. A. HARRISON: Bismuth Fermi surface 171

G. BEMSKI and B. SZYMANSKI: Spin resonance of electrons on donors in *p*-type silicon 173

Book Review:

"Colloque National de Magnétisme Commemoratif de l'oeuvre de PIERRE WEISS" (reviewed by J. E. GOLDMAN) 176

Books received 176

Volume 17 Numbers 3/4

F. J. BLATT: On the metastable γ-phase uranium–molybdenum alloys 177

O. SCHNEPP: The absorption spectra of magnesium and manganese atoms in solid rare gas matrices . . 188

W. G. SPITZER and J. R. LIGENZA: Oxygen exchange between silica and high pressure steam 196

G. J. OGILVIE and A. A. THOMSON: Influence of temperature and bombardment rate on disorientation of silver single crystals by ion bombardment 203

D. KAHN and A. J. GLASS: Photocapacitance effects in additively colored alkali halide crystals 210

page

E. J. Gibson: The effects of gamma radiation on solids. Exo-electron emission from irradiated iron oxide catalysts 220

C. E. Miller: The ionic distribution in the garnets $Gd_3Al_3Fe_2O_{12}$ and $Y_3Al_3Fe_2O_{12}$ 229

F. E. Pretzel and C. C. Rushing: Properties of lithium hydride—II. Optical absorption by color centers . 232

Gaston Fischer and F. T. Hedgcock: Magnetic susceptibility and galvanomagnetic effects in pure and *p*-type tellurium 246

M. Coopersmith and R. Brout: Threshold concentration for the existence of ferromagnetism in dilute alloys 254

P. E. Seiden: The relation of transition parameters for linear processes to measurable parameters in ferrimagnetic resonance 259

M. J. Weber: Nuclear quadrupole spin–lattice relaxation in solids. 267

A. J. Strauss and A. J. Rosenberg: Preparation and properties of $CdSnAs_2$ 278

J. M. Luttinger and P. J. Stiles: Theory of the magnetic susceptibility of holes in germanium . . 284

S. Nikitine, J. B. Grun et M. Sieskind: Etude spectrophotométrique de la série jaune de Cu_2O aux basses températures 292

C. S. Fuller, W. Kaiser and C. D. Thurmond: Donor equilibria in the germanium–oxygen system . . 301

T. Riste: Critical magnetic scattering of neutrons in magnetite 308

T. Riste and A. Wanic: A neutron diffraction study of spin fluctuations in α-Fe_2O_3 318

Letters to the Editor:

J. F. Dewald: On the transition to metallic behavior in zinc oxide 334

G. Bemski and B. Szymanski: Observations of oscillatory magnetoresistance in InAs at microwave frequencies 335

M. Cardona: Optical determination of the conduction band structure of GaSb 336

N. B. Grover and Y. Goldstein: A thermal shutter phenomenon in field-effect measurements. . . 338

A. C. Gossard, A. M. Portis and W. J. Sandle: Nuclear magnetic resonance in ferromagnetic Fe^{57}. . 341

E. M. Conwell: Disturbances of carrier concentration in high electric field 342

Vol. 17
1960

Tôme 17 N^{os} 1/2

J. B. Mullin et K. F. Hulme: Coefficients de distribution dépendants de l'orientation dans les cristaux de InSb obtenus par fusion 1

S. van Houten: Semiconduction dans $Li_xNi_{(1-x)}O$ 7

J. Graham: Espacements réticulaires et coloration pour les systèmes alumine–oxyde chromique . . 18

P. E. Wigen et J. A. Cowen: Absorption en résonance paramagnétique par divers cristaux moléculaires irradiés aux électrons 26

J. C. Woolley et C. M. Gillett: Propriétés électriques des alliages GaSb–InSb 34

R. D. Maurer: Diffusion de la lumière par la silice irradiée aux neutrons 44

J. E. Zimmerman et F. E. Hoare: Chaleur spécifique à basse température des alliages Cu–Mn dilués . 52

A. Cimino et M. Marezio: Paramètre de réseau et défaut de structure de l'oxyde de cadmium contenant des atomes étrangers 57

C. Cottini, G. Fabri, E. Gatti et E. Germagnoli: Influence du désordre sur la durée de vie du positron dans l'anthracène 65

H. Koelmans: Association et dissociation de centres dans ZnS–In luminescent 69

W. Känzig: Résonance paramagnétique d'un trou piégé par une lacune. 80

W. Känzig: Etude par résonance paramagnétique des défauts d'irradiation dans le fluorure de lithium. . 88

R. C. Miller: Sur l'origine des signaux Backhausen dans $BaTiO_3$ 93

K. S. Irani, A. P. B. Sinha et A. P. B. Biswas: Distorsion des cristaux de spinelles contenant des ions Mn^{3+} 101

Gy Gergely: Recombinaison de surface et processus de diffusion dans la luminescence cathodique et dans la conduction induite par bombardement électronique 112

page

T. Riste et A. Wanic: Etude par diffraction de neutrons de fluctuations de spin dans α-Fe_2O_3 . . . 318

Lettres au Rédacteur:

J. F. Dewald: Sur le passage au comportement métallique dans l'oxyde de zinc 334

G. Bemski et B. Szymanski: Observation de résistances magnétiques oscillantes en InAs dans les fréquences micro-ondes 335

M. Cardona: Détermination optique de la structure de la bande de conduction de GaSb. 336

N. B. Grover et Y. Goldstein: Phénomène thermique intervenant dans les mesures d'effet de champ . 338

A. C. Gossard, A. M. Portis et W. J. Sandle: Résonnances nucléo-magnétiques dans du Fe^{57} ferromagnétique 341

E. M. Conwell: Perturbations des concentrations de courants porteurs dans les hauts champs électriques 342

Band 17 Nr. 1/2

J. B. Mullin und K. F. Hulme: Orientierungsabhängige Verteilungskoeffizienten in aus der Schmelze gezüchteten InSb-Kristallen 1

S. van Houten: Halbleitereigenschaften in $Li_zNi_{(1-z)}O$ 7

J. Graham: Gitterkonstanten und Farbe im System Aluminiumoxyd–Chromoxyd 18

P. Wigen und J. A. Cowen: Paramagnetische Resonanzabsorption in verschiedenen elektronenbestrahlten Molekülkristallen 26

J. C. Woolley und C. M. Gillett: Elektrische Eigenschaften von GaSb–InSb Legierungen 34

R. D. Maurer: Lichtstreuung in neutronenbestrahltem Quarz 44

J. E. Zimmerman und F. E. Hoare: Spezifische Wärme von verdünnten Cu–Mn Legierungen bei tiefen Temperaturen 52

A. Cimino und M. Marezio: Gitterkonstante und Fehlstellenstruktur bei Cadmiumoxyd welches Fremdatome enthält 57

C. Cottini, G. Fabri, E. Gatti und E. Germagnoli: Der Einfluss der Ordnung in Anthracen au die Lebenszeit von Positronen. 65

H. Koelmans: Assoziation und Dissoziation der Zentren in lumineszierendem ZnS–In 69

W. Känzig: Paramagnetische Resonanz der zum F-Zentrum antimorphen Fehlstelle. 80

W. Känzig: Paramagnetische Resonanzstudien der Strahlenschädigung in Lithiumfluorid 88

R. C. Miller: Über den Ursprung der Barkhausensprünge in $BaTiO_3$ 93

K. S. Irani, A. P. B. Sinha und A. B. Biswas: Kristallverzerrungen in Spinellen mit Mn^{3+}-Ionen . . 101

Gy. Gergely: Oberflächenrekombination und Diffusionsprozesse bei der Kathodenlumineszenz und der durch Elektronenbestrahlung hervorgerufenen Leitfähigkeit 112

Simone Odiot und D. Saint-James: Paramagnetische Neutronenstreuung durch die Ionen der seltenen Erden 117

M. Cardona und W. Paul: Druckabhängigkeit der Energielücke in Germanium 138

D. I. Bolef, N. T. Melamed und M. Menes: Elastische Konstanten von hexagonalem Cadmiumsulfid . 143

K. Weiser: Theorie der Löslichkeit von Zwischengitterverunreinigungen in Germanium und Silizium. . 149

Briefe an den Herausgeber:

J. C. Phillips: Direkte Beobachtung offener magnetischer Bahnen 162

R. Nitsche: Das Wachsen von Einkristallen binärer und ternärer Verbindungen der Erdalkaliabkömmlinge durch chemische Transportreaktionen. 163

P. Camagni, G. Chiarotti und A. Manara: Die Bildung von Leerstellen während der plastischen Verformung von KCl-Kristallen 165

P. P. Craig, D. E. Nagle und R. D. Reiswig: Resonanzabsorption von Gammastrahlung in Supraleitern 168

A. Blandin und J. Friedel: Über Quadrupoleffekte in Legierungen 170

page

S. ODIOT et D. SAINT-JAMES: Diffraction paramagnétique des neutrons par les ions de terres rares . . 117

M. CARDONA et W. PAUL: Dépendance en pression de l'écart en énergie pour les transitions directes dans le germanium 138

D. I. BOLEF, N. T. MELAMED et M. MENES: Constantes élastiques du sulfure de Cadmium hexagonal . 143

K. WEISER: Théorie de la solubilité des impuretés interstitielles dans le Germanium et le Silicium. . . 149

Lettres au Rédacteur:

J. C. PHILLIPS: Observation directe d'orbites magnétiques ouvertes 162

R. NITSCHE: La croissance de monocristaux de chalcogenides binaires et ternaires par des réactions de transport chimique 163

P. CAMAGNI, G. CHIAROTTI et A. MANARA: Création de lacunes au cours de la déformation plastique de cristaux de KCl 165

P. P. CRAIG, D. E. NAGLE et R. D. REISWIG: Absorption résonante de rayons gamma dans les supraconducteurs 168

A. BLANDIN et J. FRIEDEL: Sur l'effet quadrupolaire dans les alliages 170

W. A. HARRISON: La surface de Fermi du Bismuth 171

G. BEMSKI et B. SZYMANSKI: Résonance de spin des électrons liés à des centres donneurs dans le silicium de type *p* 173

Revue de Livre:

"Colloque National de Magnetisme Commemoratif de l'oeuvre de PIERRE WEISS" (revu par J. E. GOLDMAN) 176

Ouvrages reçus 176

Vol. 17
1960

Tôme 17 Nos 3/4

F. J. BLATT: La phase γ métastable des alliages Uranium–Molybdène 177

O. SCHNEPP: Spectres d'absorption d'atomes de magnésium et de manganèse dans les matrices de gaz rares solidifiés 188

W. J. SPITZER et J. R. LIGENZA: Echange d'oxygène entre la Silice et la vapeur d'eau à haute pression . 196

G. J. OGILVIE et A. A. THOMSON: Influence de la température et du taux de bombardement sur la désorientation de monocristaux d'argent soumis à un bombardement ionique 203

D. KAHN et A. J. GLASS: Effets de la lumière sur la capacité des cristaux d'halogénures alcalins colorés additivement 210

E. J. GIBSON: Effets des rayons gamma sur les solides. Emission d'exo-électrons par de l'oxyde de Fer irradié servant comme catalyseur 220

C. E. MILLER: Distribution des ions dans les grenats $Gd_3Al_3Fe_2O_{12}$ et $Y_3Al_3Fe_2O_{12}$ 229

F. E. PRETZEL et C. C. RUSHING: Propriétés du Lithium–Hydride—II. Absorption de la lumière par points centraux colorés 232

G. FISCHER et F. T. HEDGCOCK: Susceptibilité magnétique et effet galvanomagnétique dans le tellure pur et de type *p* 246

M. COPPERSMITH et R. BROUT: Seuil de concentration pour l'apparition du ferromagnétisme dans les alliages dilués 254

P. E. SEIDEN: Relation en résonance ferrimagnétique entre les paramètres de transition dans les processus linéaires et les paramètres mesurables 259

M. J. WEBER: Relaxation nucléaire quadrupolaire spin-réseau dans les solides 267

A. J. STRAUSS et A. J. ROSENBERG: Préparation et propriétés de $CdSnAs_2$ 278

J. M. LUTTINGER et P. J. STILES: Théorie de la susceptibilité magnétique des trous dans le Germanium . 284

S. NIKITINE, J. B. GRUN et M. SIESKIND: Etude spectrophotométrique de la série jaune de Cu_2O aux basses températures 292

C. S. FULLER, W. KAISER et C. D. THURMOND: Equilibre des donneurs dans le système germanium–oxygène 301

T. RISTE: Diffusion magnétique critique des neutrons dans le magnétite 308

page

W. A. HARRISON: Die Fermifläche von Wismut 171

G. BEMSKI und B. SZYMANSKI: Spinresonanz der Elektronen von Donatoren in Silizium vom *p*-Typ . . 173

Buchbesprechung:

"Colloque National de Magnetisme Commemoratif de l'oeuvre de PIERRE WEISS" (besprochen von J. E. GOLDMAN) 176

Bucher erhalten 176

Band 17 Nr. 3/4

F. J. BLATT: Über die mestastabile γ-Phase von Uran–Molybdän-Legierungen 177

O. SCHNEPP: Die Absorptionsspektren der Magnesium- und Manganatome in der festen Matrix von Edelgasen 188

W. SPITZER und J. R. LIGENZA: Austausch des Sauerstoffs zwischen Quarz und Hochdruckdamp . . 196

G. J. OGILVIE und A. A. THOMSON: Einfluss der Temperatur und der Bestrahlungsdosis auf die Desorientierung von Silbereinkristallen durch Ionenbestrahlung 203

D. KAHN und A. J. GLASS: Photokapazitätseffekte in zusätzlich gefärbten Alkalhalogenidkristallen . . 210

E. J. GIBSON: Der Einfluss der Gammastrahlung auf Festkörper. Exo-Elektronenemission von bestrahlten Eisenoxydkatalysatoren 220

C. E. MILLER: Die Ionenverteilung in den Granaten $Cd_3Al_3Fe_2O_{12}$ und $Y_3Al_3Fe_2O_{12}$ 229

F. E. PRETZEL und C. C. RUSHING: Eigenschaften des Lithiumhydrids—II. Optische Absorption durch Farbzentren 232

G. FISCHER und F. T. HEDGCOCK: Magnetische Suszeptibilität und galvanomagnetische Effekte in reinem Tellur und Tellur vom *p*-Typ 246

M. COOPERSMITH und R. BROUT: Die Grenzkonzentration für das Auftreten des Ferromagnetismus in verdünnten Legierungen 254

P. E. SEIDEN: Die Beziehung zwischen den Parametern der Übergangswahrscheinlichkeit linearer Prozesse und messbaren Parametern bei der ferrimagnetischen Resonanz 259

M. J. WEBER: Kernquadrupol-Spin–Gitter Relaxation in Festkörpern 267

A. J. STRAUSS und A. J. ROSENBERG: Herstellung und Eigenschaften des $CdSnAs_2$ 278

J. M. LUTTINGER und P. J. STILES: Theorie der magnetischen Suszeptibilität von Leerstellen in Germanium 284

S. NIKITINE, J. B. GRUN und M. SIESKIND: Spektrophotometrische Untersuchung der gelben Serie des Cu_2O bei tiefen Temperaturen 292

C. S. FULLER, W. KAISER und C. D. THURMOND: Donator Gleichgewichte im System Germanium–Sauerstoff 301

T. RISTE: Kritische magnetische Streuung von Neutronen in Magnetit 308

T. RISTE und A. WANIC: Eine Untersuchung der Spinschwankungen in α-Fe_2O_3 mit Hilfe der Neutronenbeugung 318

Briefe an den Herausgeber:

J. F. DEWALD: Über den Übergang zu metallischem Verhalten in Zinkoxyd 334

G. BEMSKI und B. SZYMANSKI: Beobachtung einer periodischen magnetischen Widerstandsänderung in InAs bei Mikrowellenfrequenzen 335

M. CARDONA: Die optische Bestimmung der Struktur des Leitfähigkeitsbandes von GaSb 336

N. B. GROVER und Y. GOLDSTEIN: Ein thermisches Störphänomen bei Messungen des Feldeffektes . 338

A. C. GOSSARD, A. M. PORTIS und W. J. SANDLE: Kernmagnetische Resonanz in ferromagnetischem Fe^{57} 341

E. M. CONWELL: Störungen der Trägerstrom-Konzentration im hochelektrischen Feld 342

Tom 17 Ha. 1/2

Ж. Б. Муллин и К. Ф. Хулм: Козффициенты зависящего от ориентации раслределения образованных лри расплавлении кристаллов 1

С. ван Гоутен: Полупроводимость в $Li_xNi_{(1-x)}O$ 7

page

Ж. Грагам: Решетчатые пространства и цвета в системе глинозем-окись хрома . . 18

П. Е. Виген и Ж. А. Коуен: Поглощение парамагнитного резонанса во многих облучённых электронами молекулярных кристаллах 26

Дж. ч. Уулей и Ч. М. Жилет: Электрические свойства GaSb–InSb сплавов . . 34

Р. Д. Маурер: Рассеяние света облучёёного нейтронами кремня 44

Дж. Е. Циммерман и Ф. Е. Гор: Теплоёмкость разбавленных сплавов Cu–Mn при низкой температуре 52

А. Чимино и М. Марезио: Параметр решетки и дефекты структуры CdO, содержащего иосторонние атомы 57

Ч. Коттини, Ж. Фабри, Е. Гатти, и Е. Жерманиоли: Влияние беспорядка на время жизни позитронов в антрацене 65

Г. Гоелманс: Соединения и разделения центров в Люминесцентном Zns–In . . 69

Вернер-Кенциг: Парамагнитный резонанс антиморфа центра ф (“F”) 80

Вернер-Кенциг: Изучение иарамагнитного резонанса иовреждения излучением фтористого лития. 88

Р. Миллер: О происхожденин скачков Баркгаузена в $BaTiO_3$ 93

К. С. Ирани, А. П. Б. Синха и А. Б. Бисуас: Кристаллическое искажение в спинелях содержавших ионы Mn^{3+} 101

Дж. Джержели: Процессы иоверхностной рекомбинации и диффузии в лроводимости индуктированной катодной люминисценцией и электроной бомбардировкой. . 112

Симон Одио и Д. Сан Джемс: Парамагнитная диффракция нейтронов ионами редких земель 117

Мануел Кардона и Уилиам Пол: Зависимость от давления непосредственного разрыва в энергетической кривой германии 138

Д. И. Болеф, Н. Т. Меламед, М. Менес: Урругие константы гексагонального сульфида кадмия 143

К. Вайзер: Теория растворимости промежуточных загрязнений в германии и в кремнии 149

Письма в редакцию:

Дж. К. Филлипс: Прямое наблюдение открытых магнитных орбит . . . 162

Р. Нитче: Рост одиночных кристаллов бинарных и тройных халькогенидов иереносными химическими реакциами 163

П. Камани, Ж. Киаротти и А. Манара: Порождения вакансий во время пластических деформаций кристаллов KCl 165

П. П. Крейг, Д. Е. Негл, и Р. Д. Рейцвиг: Резонансное иоглощение гамма-излучение в сверхпроводниках 168

А.Бланден и Ж. Фридель: О куардупольных эффектах в сплавах 170

Уа. А. Гаррисон: Поверхность Бисмут-Ферми 171

Г. Бемски, и Б. Шиманский: Спиновый резонанс электронов на донорах в кремнии типа л (*p*) 173

Рецензия На книги:

Национальное совещание о магнетизме, в память труда Пьера Вайс. (рецензент Ж. Е. Голдманом) 176

Полученные книги 176

Vol. 17
1960

Том 17 На. 3/4

page

Ф. Дж. Блат: О метастабильной γ фазе урано-молибденовых славп 177

О. Шнеп: спектры поглощения атомов магния и марганца в твёрдых матрацах для инертных газов 188

В. Г. Шпицер и Ж. Р. Лигенца: обмен кислорода между кремнием и паром высокого давления 196

Г. Дж Огилви и А. А. Томсон: Влияние температуры и скорости бомбардировки на дезориентацию единичных кристаллов серебра посредством бомбардировки ионами 203

Д. Кан, и А. Дж. Глас: Эффекты фотоэлектрической ёмкости в аддитивно- окрашенных щёночных галоидных кристаллах 210

Е. Дж. Гибсон: Воздействия гамма излучения на твёрдые тела. Екзо электронная змиссия из облучённых катализаторов железной окиси 220

Ч. Е. Миллер: Ионное распределение в гранатах $Gd_3Al_3Fe_2O_{12}$ и $Y_3Al_3Fe_2O_{12}$ . . 229

Ф. Е. Претцел, и Ч. Ч. Рашинт: Свойства водородистого лития—II Оптическая абсорбция цветными центрами 232

Гастон Фишер и Ф. Т. Хеджгок: Магнитная чувствительность и галваномагнитные эффекты в чистом теллуре и теллуре типа п 246

М. Куперсмит и Р. Браут: Порог концентрации для наличия ферромагнетизма в разбавленных сплавах 254

П. Е. Эайден: Отношения переходных параметров к измеряемым параметрам для линейных процессов в ферромагнитном резонансе 259

М. Дж. Вебер: Ядерная квадруполь спинрешетчатая релаксация в твёрдых тедах. . 267

А. Дж. Страус и А. Дж. Розенберг: Приготовление и свойства $CdSnAs_2$ . . . 278

Дж. М. Лутингер и П. Дж. Стайлс: Теория магнетической чувствительности отверстий в германии 284

С. Никитин, Дж. Б. Грун и М. Зискинд: Спектрофотометрическое исследование жёлтой серии Cu_2O при низких температурах 292

Ч. С. Фуллер, В. Кайзер и Ч. Д. Турмонд: Равновесие донора в системе германий–кислород 301

Т. Ристе: Критическое магнетическое рассеяние нейтронов в магнетите . . . 308

Т. Ристе и А. Ваник: Исследование спин-колебаний в α-Fe_2O_3 диффракцией нейтрона . 318

Письма в редакцию:

Ж. Ф. Девалд: О переходе к металлическому режиму в окиси цинка. . . . 334

Г. Бемский и Б. Шеманский: Наблюдения колебательного магнитосопротивления в InAs при микроволновых частотах 335

М. Кардона: Оптическое определение структуры полосы проводимости . . 336

Н. Б. Гровер и Я. Гольдштейн: Явление термического затвора в ибмерениях полевого действия 338

А. Ч. Госсард, А. М. Портис и В. Дж. Сандл: Ядерный магнитный резонанс в ферромагнитном Fe^{57} 341

Е. М. Конвел: Нарушения несущей концентрации в электрическом поле высокого напряжения 342

AUTHOR INDEX TO VOLUME 17

(B) denotes book review

Bemski, G. 173, 335
Biswas, A. B. 101
Blandin, A. 170
Blatt, F. J. 177
Bolef, D. I. 143
Brout, R. 254
Camagni, P. 165
Cardona, M. 138, 336
Chiarotti, G. 165
Cimino, A. 57
Conwell, E. M. 342
Coopersmith, M. 254
Cottini, C. 65
Cowen, J. A. 26
Craig, P. P. 168
Dewald, J. F. 334
Fabri, G. 65
Fischer, G. 246
Friedel, J. 170
Fuller, C. S. 301
Gatti, E. 65
Gergely, Gy. 112
Germagnoli, E. 65
Gibson, E. J. 220
Gillett, C. M. 34
Glass, A. J. 210
Goldman, J. E. 176 (B)
Goldstein, Y. 338
Gossard, A. C. 341
Graham, J. 18
Grover, N. B. 338
Grun, J. B. 292
Harrison, W. A. 171
Hedgcock, F. T. 246
Hoare, F. E. 52
van Houten, S. 7
Hulme, K. F. 1
Irani, K. S. 101
Kahn, D. 210
Kaiser, W. 301
Kanzig, W. 80, 88
Koelmans, H. 69
Ligenza, J. R. 196
Luttinger, J. M. 284
Manara, A. 165
Marezio, M. 57
Maurer, R. D. 44
Melamed, N. T. 143
Menes, M. 143
Miller, C. E. 229
Miller, R. C. 93
Mullin, J. B. 1
Nagle, D. E. 168
Nikitine, S. 292
Nitsche, R. 163
Odiot, S. 117
Ogilvie, G. J. 203
Paul, W. 138
Phillips, J. C. 162
Portis, A. M. 341
Pretzel, F. E. 232
Reiswig, R. D. 168
Riste, T. 308, 318
Rosenberg, A. J. 278
Rushing, C. C. 232
Saint-James, D. 117
Sandle, W. J. 341
Schnepp, O. 188
Seiden, P. E. 259
Sieskind, M. 292
Sinha, A. P. B. 101
Spitzer, W. G. 196
Stiles, P. J. 284
Strauss, A. J. 278
Szymanski, B. 173, 335
Thomson, A. A. 203
Thurmond, C. D. 301
Wanic, A. 318
Weber, M. J. 267
Weiser, K. 149
Wigen, P. E. 26
Woolley, J. C. 34
Zimmerman, J. E. 52

Vol. 17
1960

J. Phys. Chem. Solids Pergamon Press 1960. Vol. 17, Nos. 1/2, pp. 1–6. Printed in Great Britain.

ORIENTATION-DEPENDENT DISTRIBUTION COEFFICIENTS IN MELT-GROWN InSb CRYSTALS

J. B. MULLIN and K. F. HULME

Royal Radar Establishment, Ministry of Aviation, Great Malvern, Worcestershire, England

(*Received* 2 *February* 1960)

Abstract—During the growth of indium antimonide crystals from the melt planar crystallographic facets can develop on the solid–liquid interface. At growth rates of 2 cm/hr the distribution coefficients for Te have been shown to be different by a factor of ~ 6 on and off {111} facets—the values being ~ 3 and $\sim 0{\cdot}5$ respectively; a similar effect has been found for a residual donor impurity. The "facet effect" is not due to a solute-enriched boundary layer. The theoretical significance of the results is discussed.

INTRODUCTION

IN CRYSTAL growing or zone-melting distribution coefficients are important parameters; they govern the concentration of the solute in the resultant solid, provided transport in the vapour phase or diffusion in the solid is negligible. The distribution coefficient of a solute is the ratio of the solute concentration in the solid to the solute concentration in the liquid. In the definition of the equilibrium distribution coefficient, k_0, one need not specify either the orientation of the solid–liquid interface across which equilibrium is achieved or exactly where in the solid or the liquid the concentrations are to be measured, provided that regions within a few atom spacings of the interface are excluded in order to obtain concentrations representative of the bulk solid and liquid; the value of k_0 may depend on solute concentration at high concentrations. At a finite rate of growth an impurity boundary layer develops in the liquid near the interface when stirring in the melt is incomplete (TILLER *et al.*[1], BURTON *et al.*[2, 3], WAGNER[4], HULME[5]). Two distribution coefficients k_{eff} and k^* can be distinguished in this situation (see Fig. 1). The effective distribution coefficient, k_{eff}, is the quantity measured experimentally by determining the solute concentration in the solid as a function of mass fraction solidified; it is defined as the concentration in the solid taken immediately behind the interface in a volume small compared with the total volume solidified whilst again excluding the first few atom layers in the solid divided by the concentration in the liquid outside the boundary layer (i.e. at a few multiples of D/R from the interface, where D is the diffusion coefficient of the solute in the liquid and R is the growth rate). The magnitude of k_{eff} can depend on the rate of growth, the interface orientation, the stirring conditions in the liquid and the solute concentration. In the definition of k^*, the concentration in the solid is defined as for k_{eff}, but

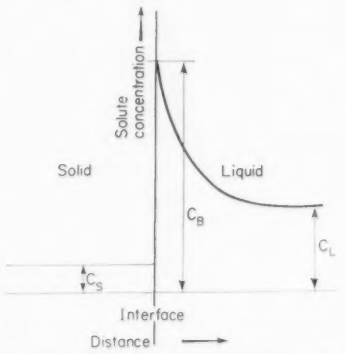

FIG. 1. The solute boundary layer. $k_{eff} = C_S/C_L$
$k^* = C_S/C_B$
Diagram drawn for the case $k^* < 1$.

the concentration in the liquid is taken in a region close to the interface sufficiently narrow to avoid any concentration variation in the boundary layer whilst excluding the first few atom layers in the liquid; k^* may in principle differ from k_0 and may depend on growth rate, interface orientation and solute concentration, but it is by virtue of its definition independent of stirring conditions in the melt. k_{eff} is always nearer to unity than k^*. Under conditions of very good stirring, however, the value of k_{eff} closely approaches that of k^*.

The existence of the impurity boundary layer in the liquid complicates experimental attempts to measure the difference between k_0 and k^*. However, for Sb in Ge at high growth rates ($\sim$20 cm/hr) there have been indications that k^* varied slightly with orientation. BURTON *et al.*[2–3] have developed a theory of the variation of k_{eff} with growth rate and stirring rotation rate; on the basis of this theory and their experimental results they concluded that for Sb in Ge k^* was very close to k_0. Previously HALL[6] had contended that k^* varied with growth rate and orientation. The variation with growth rate was discounted by BURTON *et al.*, but HALL's results may still be taken to indicate that k^* varied with seed orientation ($\sim$5 per cent differences at 10 cm/hr and $\sim$10 per cent differences af 20 cm/hr between seeds orientated along $\langle 100 \rangle$, $\langle 110 \rangle$ and $\langle 111 \rangle$ directions). BURTON *et al.* also obtained evidence, from an autoradiograph of a twinned crystal, of a change (less than 5 per cent) of k^* for Sb in Ge with interface orientation at a growth rate of 18 cm/hr. The present authors have found that the variation with interface orientation of k^* for Te in InSb is remarkably large at low growth rates (2 cm/hr).

Previous work on the distribution coefficient of Te in InSb was based on the apparently reasonable assumption that k^* was close to k_0 and had no orientation-dependence. Te, a donor impurity in InSb, is considered to be an important impurity element in material purified by zone-refining, since its k_{eff} appears to be close to unity. HARMAN[7] estimated k_{eff} to be 0·8 in polycrystalline material. The present authors (HULME and MULLIN[8]) confirmed that in polycrystalline material k_{eff} was just less than unity. From later experiments (MULLIN and HULME[9]) in which electromagnetic stirring of the molten zone was used a value of $\sim$0·9 can be deduced (for k^*). However, one of us (MULLIN[10]) when attempting to measure k_{eff} in single crystals encountered anomalous results from which the only permissible conclusion was that k_{eff} was about unity for crystals oriented close to a $\langle 111 \rangle$ direction. STRAUSS[11], using seed crystals oriented "approximately on the $\langle 111 \rangle$ direction", found k_{eff} to be 0·54 at a growth rate of 1·3 cm/hr and rotation rate of 130 r.p.m. and apparently encountered no anomalies. MULLIN had found that the Te concentrations in the crystal did not vary smoothly with the mass fraction of crystal pulled, but increased and decreased in an irregular manner. It is now possible to understand the cause of these difficulties. A preliminary account has already been given (HULME and MULLIN[12]).

EXPERIMENTAL

Apparatus

InSb crystals were pulled from the melt by the Czochralski technique; the melt temperature was controlled by a servo-system and a resistance heater. The pull rate was 2 cm/hr and the rotation rate 100 r.p.m. In some cases the crystals were pulled under vacuum, in others under one atmosphere pressure of H_2. The seed crystals were oriented close to a $\langle 111 \rangle$ direction except where otherwise stated. Autoradiographs of radioactively doped crystals were taken by placing slices ground flat with 4F carborundum in contact with standard X-ray film for about a week and then developing the film in standard high contrast developer. Where carrier concentrations are quoted they were determined by measuring the Hall constants of rectangular crystal specimens at 77°K in a field of 1950 G.

InSb belongs to the point group $\bar{4}\,3m$, which means that $\{111\}$ and $\{\bar{1}\bar{1}\bar{1}\}$ faces are not equivalent to one another. ALLEN[13] has shown that in DEWALD's[14] notation etch pits only appear on the $\{\bar{1}\bar{1}\bar{1}\}$ faces when etching takes place in CP_4. We used this method to distinguish $\{111\}$ and $\{\bar{1}\bar{1}\bar{1}\}$ faces.

RESULTS

(i) *Appearance of crystals*

Facets. The ends of crystals when parted from the residual melt by a sharp increase in pull rate often showed a planar facet on an otherwise curved

Vol. 17
1960

FIG. 2. Photograph of crystal ends of R6., X × 3½. A, facet; B, rounded surface; C, Spike due to solidified droplet of melt.

FIG. 3. Photograph of crystal ends of R15., X × 3½. A, facet; B, rounded surface; C, Spike due to solidified droplet of melt.

[facing p. 2

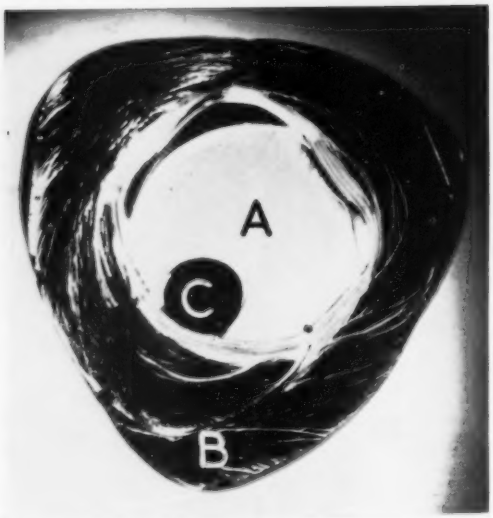

FIG. 4. Photograph of crystal ends of R12., X × 3½. A, facet; B, rounded surface; C, Spike due to solidified droplet of melt.

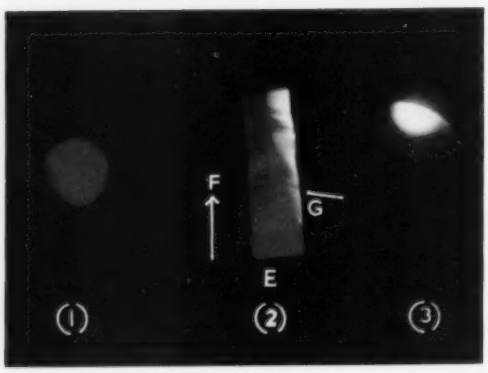

FIG. 5. Autoradiographs of radio-Te doped crystal: Section 1, slice taken from the top of the crystal perpendicular to growth direction; Section 2, slice taken between sections 1 and 3 parallel to the growth direction; Section 3, slice taken near the bottom of the crystal perpendicular to the growth direction; E, seed end; F, growth direction; G, trace of (111) plane; positive prints i.e. white = high Te conc.

surface. Typical examples are shown in Figs. 2, 3 and 4. The spikes and rings are associated with the way the crystal parted from the melt while still rotating. X-ray back reflection Laue photographs showed that the facets were parallel to {111} planes in the crystals.* If the seed orientation was not exactly along a ⟨111⟩ axis the (111) facet was displaced to one side (Figs. 2 and 3). The facet dimensions ranged from 2 mm to 3 cm, the size depending on the amount the seed was off the ⟨111⟩ axis and on the general interface curvature. (The solid surface was convex, at least in the final stages of growth, under the growth conditions used.) The fact that {111} facets are observed on the ends of crystals does not of course prove that the facets are present during growth. However, evidence that they are is often provided by the shapes of the crystals; a (111) facet which intersects the edge of the interface affects the cross-sectional shape of the crystal. This may be seen in Figs. 2 and 3; since the crystal is nearly on a ⟨111⟩ axis one would expect to find threefold symmetry, which is not observed—the crystal tending to draw in where the facet intersects the edge. In favourable cases one can deduce from the shape of the crystal that the facet has been present on the interface during most of the growth.

(*ii*) *Tellurium-doped crystals*

In an attempt to understand the anomalies encountered by MULLIN autoradiographs were taken of a crystal doped with radio-Te. These are shown in Fig. 5. A section perpendicular to the growth direction near the start of growth (section 1) showed a uniform Te distribution. A similar section taken a few mm from the end of growth (section 3) showed that there was a region of enhanced Te concentration at one side of the crystal. The donor concentrations measured in and out of the Te-enhanced region in section 3 were $1{\cdot}5\times10^{19}$/cm^3 and $2{\cdot}4\times10^{18}$/cm^3 respectively, which indicated that the Te was in atomic solution in both regions—the concentration ratio being 6·3. Using the portion of the crystal between these two cross-sections autoradiographs were taken of longitudinal sections (i.e. parallel to the growth direction); one of these is shown in Fig. 5 (section 2). It indicated that the Te-rich region appeared after about a quarter of the crystal had grown and then increased in dimensions. In the longitudinal section straight lines can be seen in the Te-rich region; an X-ray orientation determination showed that these lines were traces of a (111) plane, the seed being ~12° off the [111] direction. The end of the crystal is shown in Fig. 2. The distinctive shape near the end of growth indicated that the Te-enhanced region is associated with the (111) facet. (Compare Fig. 2 with Fig. 5, section 3). The longitudinal section shows the history of the facet development; the straight lines in the Te-enhanced region are attributed to fluctuations of the growth conditions. It is concluded that, at a growth rate of 2 cm/hr, k_{eff} for Te in InSb is about a factor of 6 larger on a {111} facet than on the curved interface adjacent to a {111} facet, at least for high Te concentrations.

Results obtained on another Te-doped crystal (non-active) have allowed us to estimate the value of k_{eff} on a (111) facet. The end of this crystal was completely covered by a (111) facet. The carrier concentration at the top of the crystal (mass fraction ~0) was $1{\cdot}6\times10^{18}$ electrons cm^3; at the bottom of the crystal (mass fraction ~0·75) it was $2{\cdot}2\times10^{16}$ electrons/cm^3. This indicated a k_{eff} of 3·8, which agrees with the value of 3·5 deduced from the carrier concentration on the top slice and the weights of Te and InSb used (it was assumed, as is usual, that each Te atom contributed one conduction electron).

(iii) *Undoped crystals*

A series of undoped crystals (R2–R15) were pulled from high purity indium antimonide melts. The InSb was purified by a method previously described by HULME[15] which produces *n*-type material with ~10^{14} electrons/cm^3 (at 77°K); it is not known whether these electrons arise from dissolved atoms of a residual donor impurity or from lattice defects. The seed orientation of the crystals was within 3° of a [111] axis.

Carrier concentrations in slices (~2mm thick) cut perpendicular to the growth direction were measured; the variation of carrier concentration in a given slice was often unexpectedly large. The ratios of the maximum to minimum carrier concentrations in a number of crystal slices are given in Table 1. The ratio can be as high as 15. A

* (A small (100) facet has been observed on the end of a heavily twinned crystal.)

Table 1. *Uniformity in undoped* InSb *crystals*

Slice from crystal no.	Seed Orientation	Mean carrier conc. $\times 10^{-13}$ (/ cm^3)	Fraction of slice covered by $\langle 111 \rangle$ orientation	Ratio max. min. carrier conc.	No. of twins
R2	111	26	1·0	5·7	0
R3	111	11	0·7	12	1
R4	111	23	0·8	14	1
R6	111	12	1·0	13	0
R7	111	17	—	15	1
R8	111	2·3	$<$ 0·1	2·4	8
R9	111	5·3	0·4	1·7	1
R10	111	3·0	0·2	1·9	4
R11	111	7·9	0·4	3·3	1
R12	111	5·8	0·6	7·7	1
R12	111	7·1	0·4	5·1	1
R13 ∓	111	2·1	0·3	1·8	5
R14 ∓	111	10	0·5	4·9	4
R15 ∓	111	43	1·0	15	0
R26	311	15	0	1·8	0
R31	311	6·6	0	1·3	0
R19	311	23	0	1·33	0

∓ Electromagnetic stirring of the melt.

Vol. 17
1960

feature common to these various (111) slices was that the high carrier concentrations were confined to a patch which was surrounded by a region of lower carrier concentration. This feature applied to the (111) areas of slices from twinned crystals. R12 was an example of this (see Fig. 6). The twin boundary in this case roughly divided the growth face into two equal areas representing approximately [111] and $[\bar{5}\bar{1}\bar{1}]$ growth directions. The [111] area has a patch of high donor density surrounded by a region of lower donor density, whereas the $[\bar{5}\bar{1}\bar{1}]$ area has a uniformly low carrier density. Similar results were found in other twinned crystals. When the whole interface had the $[\bar{5}\bar{1}\bar{1}]$ growth direction the carrier density was uniform. These results suggested that {111} facets

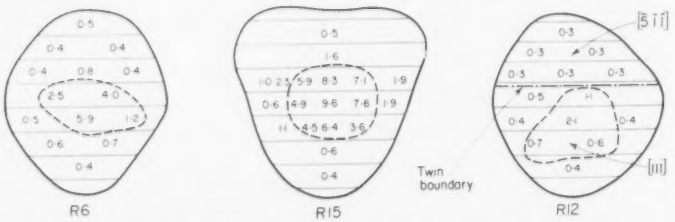

FIG. 6. Number of electrons/cm^3 ($\div 10^{14}$) in slices of crystals (R6, R15 and R12) taken perpendicular to the growth direction. Parallel lines denote edges of HALL constant samples. The decimal points mark the positions of the HALL probes for the carrier concentration measurements. The dotted lines represent approximately the mean carrier density contours; they separate patches of high carrier density from regions of low carrier density.

were influencing the distribution of a residual donor impurity, the effect being similar to that found in tellurium-doped crystals.

A direct indication that {111} facets were responsible for the high donor concentration was found in two crystals, R14 and R15. Slices were taken within 2 or 3 mm of the ends of the crystals on which there were centrally situated facets. The size and position of the facets coincided with the patches of high carrier density found in the slices. For R15 the correlation may be seen by comparing the facet (Fig. 4) with the carrier densities in Fig. 6—(R15). During the growth of R14 and R15 the melts were vigorously swirled, in the opposite direction to the crystal rotation, by means of a 400-cycle rotating magnetic field to increase the stirring in the melt. In fact under normal stirring conditions (100 r.p.m. rotation rate), very uniform crystals have been pulled by growing on a [311] orientation and thus avoiding any large area {111} facets. (See Table 1, R26, R31 and R19.)

DISCUSSION

The results show that there is a difference of k_{eff} on and off a (111) facet for Te and indicate that a residual donor impurity shows the same effect. The question arises whether this difference in k_{eff} is due to a difference in k^* or to a difference in the development of the boundary layer, (i.e. a difference in stirring) on and off a (111) facet. Consider the results on the radio Te-doped crystal. It might be argued that a facet partially covering the interface could interfere with the hydrodynamic flow of the liquid adjacent to the interface causing different boundary layer conditions on and off the facet. However, take the extreme case of an interface containing two regions, A and B, A being completely stirred and B completely unstirred. On A the boundary layer is completely removed and the concentration in the liquid at the interface is the same as that in the bulk liquid; on B the concentration in the liquid at the interface is $1/k^*$ times the concentration in the bulk liquid. Thus the impurity concentrations in the parts of the solid growing behind A and behind B differ by a factor of $1/k^*$; this is the greatest difference which can arise due to differences in stirring. In the radio-tellurium doped crystals a ratio of 6·3 was found. This cannot be reconciled with the previously reported values of the distribution coefficient (0·9, 0·8 or 0·54). It is concluded that a genuine difference in k^* has been observed.

We now consider the numerical values of k_{eff} on and off a (111) facet for which we use the symbols k_{eff} (on 111) and k_{eff} (off 111).† The non-active Te-doped crystal gave us k_{eff} (on 111) $\sim 3{\cdot}5$. From the results of the radio-Te doped crystal, k_{eff} (on 111)/k_{eff} (off 111) $\sim 6{\cdot}3$; thus k_{eff} (off 111) $\sim 0{\cdot}55$. This agrees with the value of 0·54 obtained by STRAUSS[11] under similar growth conditions. Thus, in STRAUSS's crystals (111) facets must have been absent or small—a deduction which does not contradict his statement that his crystals were grown "in approximately the ⟨111⟩ direction". The values of k_{eff} obtained on polycrystalline material (0·8 and 0·9) and the value obtained by MULLIN (~ 1) can now be readily understood; they are average values which depend on the fraction of the interface covered by {111} facets.

Despite some uncertainty about the state of the boundary layer in our experiments it is possible to make some important deductions about the values k^* (on 111) and k^* (off 111) for Te. In fact, we may say k^* (on 111) $> 3{\cdot}5$ and k^* (off 111) $< 0{\cdot}5$, because the effect of boundary layers is always to make k_{eff} closer to unity than k^*. Thus, k^* (on 111)/k^* (off 111) > 6, a deduction which is independent of whether the stirring differs on and off a facet. If the diffusion coefficient of Te in liquid InSb (D_{Te}) is equal to that of Zn, (D_{Zn}) the theory of BURTON *et al.*[3] and the results obtained by STRAUSS[11] on the variation with growth conditions of k_{eff} for Zn allow following conclusions: k^* (on 111) ~ 4, and k^* (off 111) $\sim 0{\cdot}5$. The assumption that D_{Te} and D_{Zn} are equal to one another or nearly so is plausible. If, however, D_{Te} is much smaller than D_{Zn} then k^* (on 111) will be much greater than 4 whereas k^* (off 111) will not be greatly altered from 0·5; this is a consequence of the theory of BURTON *et al.*[3] which predicts that k_{eff} is much more sensitive to stirring conditions if $k^* > 1$ than if $k^* < 1$.

Having established that k^* is different on and off

† It is tacitly assumed in our discussion that the distribution coefficient of Te is not strongly dependent on concentration and that k_{eff} (off 111) does not vary markedly with interface orientation once one is off the (111) orientation. These assumptions are essentially justified by the self-consistency of the picture finally obtained.

a (111) facet for Te, it is reasonable to conclude that the non-uniform carrier concentrations in undoped crystals are due to a residual donor impurity which shows the same effect. The position here is complicated by the possible presence of compensating p-type impurities.† Compensation would increase the ratio of maximum to minimum concentrations in a slice. The facet effect suggests that perhaps the residual donor is Te. However, there are other possibilities. The divergence of the values found by STRAUSS[11] and by MULLIN[10] for the distribution coefficient of Se suggests that Se, also a donor, shows the facet effect. Indications have also been obtained that S (another donor) shows the facet effect.‡

The explanation of the variation of k^* with interface orientation must reside in a variation of the exchange rates of solute atoms between solid and liquid on and off a (111) facet. Two models of the exchange process have been proposed, one by HALL[6] and another by THURMOND[15]. These predict opposite variations of k^* with growth rate; experiments on the variation of k^* on and off a (111) facet with growth rate would be necessary to decide which (if either) is appropriate, and which of the values of k^* we have found for Te is closest to k_0. Any detailed theory must take into account the possibility that the growth processes on and off a (111) facet are different. The existence of {111} facets suggests that growth on a (111) plane is slow, and involves the lateral movement of steps which are created either by two-dimensional nucleation or by virtue of the presence of a screw dislocation. If the interface just off the (111) facet is considered to consist of closely spaced steps their sideways speed will be smaller than on the (111) facet. It may be that the difference in step velocity on and off a (111) facet causes the difference in k^*. A more detailed knowledge of the nature of the solid–liquid interface will probably be needed before an exact atomic description of the "facet effect" can be made.

† Many of the undoped crystals were pulled under vacuum to eliminate volatile p-type impurities (Zn, Cd).

‡ The agreement between the values for Cd and Zn obtained by STRAUSS and by MULLIN suggest that the facet effect is unimportant for these elements, and we have obtained no indications to the contrary in experience of Zn- and Cd-doped crystals. It is also believed that Ge shows no facet effect when used as a doping element.

Acknowledgements—It is a pleasure to acknowledge the experimental contributions of O. JONES and W. H. E. WILGOSS and the assistance of J. WRIGHT, J. ELCOX, M. CROFTS and M. STEVENS. We are grateful to Professor F. C. FRANK of the University of Bristol for the benefit of a valuable discussion.

This paper is published by permission of the Controller, H.B.M., Stationery Office.

REFERENCES

1. TILLER W. A., JACKSON K. A., RUTTER J. W. and CHALMERS B., *Acta Met.* **1,** 428 (1953).
2. BURTON J. A., KOLB E. D., SLICHTER W. P. and STRUTHERS J. D., *J. Chem. Phys.* **21,** 1991 (1953).
3. BURTON J. A., PRIM R. C. and SLICHTER W. P., *J. Chem. Phys.* **21,** 1987 (1953).
4. WAGNER C., *J. Metals, N.Y.* **6,** 154 (1954).
5. HULME K. F., *Proc. Phys. Soc. Lond.* **68B,** 393 (1955).
6. HALL R. N., *J. Phys. Chem.* **57,** 86 (1953).
7. HARMAN T. C., *J. Electrochem. Soc.* **103,** 128 (1956).
8. HULME K. F. and MULLIN J. B., *J. Electronics and Control* **3,** 160 (1957).
9. MULLIN J. B. and HULME K. F., *J. Electronics and Control* **4,** 170 (1958).
10. MULLIN J. B., *J. Electronics and Control* **4,** 358 (1958).
11. STRAUSS A. J., *J. Appl. Phys.* **30,** 559 (1959).
12. HULME K. F. and MULLIN J. B., *Phil. Mag.* **4,** 1286 (1959).
13. ALLEN J. W., *Phil. Mag.* **2,** 1475 (1957).
14. DEWALD J. F., *J. Electrochem. Soc.* **104,** 244 (1957).
15. HULME K. F., *J. Electronics and Control* **6,** 397 (1959).
16. THURMOND C., *Semiconductors,* (edited by HANNAY N. B.) p. 157. Reinhold, New York (1959).

J. Phys. Chem. Solids Pergamon Press 1960. Vol. 17, Nos. 1/2, pp. 7–17. Printed in Great Britain.

SEMICONDUCTION IN $Li_xNi_{(1-x)}O$

S. VAN HOUTEN

Philips Research Laboratories, N. V. Philips' Gloeilampenfabrieken
Eindhoven, Netherlands

(*Received* 23 *April* 1960)

Abstract—NiO is an insulator, which may be made conducting by the addition of lithium oxide. This behaviour can be explained in terms of an energy level scheme consisting of full, localized Ni^{2+} levels with empty Ni^{+} levels approximately 5 eV above them. The consequence of introducing lithium into the lattice is that the Li^{+} ions are compensated by Ni^{3+} ions, giving $Li^{+} \cdot Ni^{2+}$ acceptor levels at approximately 0·03 eV above the Ni^{2+} levels. Electrical conduction, which is always *p*-type, may be described in terms of a thermally activated diffusion of holes from one nickel ion to another. The activation energy is connected with self-trapping by the polarization induced by the hopping hole itself. A detailed account is given of the calculation of the energy levels, starting from the ionization energies of the free ions and combining them with Madelung potentials. Corrections are made for the polarization of the lattice and for differences in crystal field stabilization between the Ni ions of different valencies. Measurements of Seebeck effect and electrical resistance as a function of temperature and lithium concentration are discussed in terms of this model. It is shown that the oxygen band, lying much lower than the Ni^{2+} levels, does not give any contribution to the electrical conduction.

1. INTRODUCTION

PURE, STOICHIOMETRIC NiO is a green compound with rocksalt structure. Below its Néel point $T_N = 523°K$ the lattice is slightly distorted to give a rhombohedral cell with $\alpha = 60°6'$ at room temperature.[1] It is an insulator with a specific resistance $\rho > 5 \times 10^{14}\ \Omega$ c.m.

NiO is antiferromagnetic, the spins in one particular set of succeeding (111) planes being antiparallel.[2,3,4] When the composition of the compound deviates from stoichiometry or when some lithium is built in in the lattice it becomes a semiconductor with specific resistances down to $10^{-1}\ \Omega$ cm at room temperature. Then it is a black substance, the unit cell decreasing slightly with increasing lithium content as a consequence of the difference in ionic radius between Ni^{2+} and Ni^{3+} ions.[5,6] In this paper we restrict ourselves to concentrations smaller than 20 at. per cent lithium.

By the simple energy-band theory NiO should be a conductor as it has an incompletely filled 3*d*-shell. It is found, however, to be an insulator. It was concluded therefore by VERWEY and DE BOER[7,8] and by MOTT[9] that the collective electron treatment as used by BLOCH and WILSON is not a good approximation in this case, but the HEITLER–LONDON approximation, starting from atomic wave functions, should rather be used here.

According to VERWEY and DE BOER[7,8] it is a necessary condition for conduction to take place that there are ions of the same element but of different valency at crystallographically equivalent lattice points. In pure stoichiometric NiO this can be achieved by the reaction $2Ni^{2+} \rightarrow Ni^{+} + Ni^{3+}$. This needs, however, a large energy, so that at normal temperatures such an exicted state does not occur. Therefore NiO is an insulator. It is also possible to get Ni^{3+} ions in the lattice by making Ni vacancies or adding some Li_2O to the substance. Each singly charged lithium ion is then compensated by a Ni^{3+} ion ("controlled valency"[5]). In this model, a certain activation energy is necessary for conduction, as the positive holes are attracted to the Li^{+} ions, which have an effective negative charge. As soon as the hole is freed, no activation energy was thought to be necessary for the transport. This assumption is not, however, in agreement with the experiments, as will be discussed in this paper.

We will show that the idea of HEIKES and JOHNSTON[10] that conduction should be considered as a thermally activated diffusion process is correct. According to these authors the activation energy is a consequence of the self-trapping of the moving hole by its own polarization field. It is, however, important to realize that in general the activation energy is built up from two parts, viz. loosening energy and a transport term. The former depends on the distance between the transport level and the acceptor levels, the latter is determined by the self-trapping. The former is small when the acceptor distance is small, the latter is small when the charge carriers move fast.

In this paper the conduction process will be discussed in terms of an electronic energy level scheme (Fig. 7), as has also been used by MORIN[11,12] and by JONKER[13]. As will be discussed later in this paper, the mobilities μ of the charge carriers are very low and increase exponentially with temperature. Besides it follows from measurements of the Seebeck effect that the effective number of available states equals the number of ionic sites, viz. $5{\cdot}5\times10^{22}$ cm^{-3}. Therefore a description of the conduction in terms of bands does not apply. Essentially we have here localized full Ni^{2+} levels and empty Ni^{+} levels. A localized energy level is one in which the wave functions of the cations overlap so little that a certain energy is required for a hole (or an electron) to jump from one level to another. $Li^{+}\cdot N^{2+}$ acceptor levels are lying at a distance E_a above the Ni^{2+} levels. The distances in this energy level scheme will be calculated or experimentally determined.

MORIN[12] has previously suggested that the acceptor is not a Li^{2+} ion but a Ni^{3+} ion next to a Li^{+} ion. This author assumes, however, that the Li^{+} ions are not compensated by Ni^{3+} ions only but to some extent also by O^{-} ions, that is to say he assumes the oxygen band to be not far below the Ni^{2+} levels so that there are some holes in this band also, at least at low lithium concentrations. As the mobility in the oxygen band is assumed to be high (10–100 cm^2/V sec) with respect to that in the Ni^{2+} levels, a small number of holes in this band would suffice to explain the conduction. We will show, however, in this paper that conduction in an oxygen band does not take place.

Though many measurements on NiO have been reported, it seemed worth while to remeasure the conductivity and Seebeck effect as a function of temperature and of lithium concentration, since much of the older work is either incomplete or made on ill defined samples. The thermal conductivity λ has also been measured, since it was suggested[14] that the system $Li_xNi_{(1-x)}O$ should be a good material to use in a thermoelectric generator at high temperatures. The efficiency of such a generator depends on the figure of merit

$$Z = \theta^2\sigma/\lambda$$

of the material used, where θ is the Seebeck coefficient, σ the specific electrical conductivity and λ the thermal conductivity. The measurements of the thermal conductivity are reported elsewhere.[15] It was found that λ decreases sharply with the first per cent lithium added to the NiO and then gradually levels off. A linear relationship is found between the mean Li–Li distance in the lattice and the mean free path of the phonons L_2 for phonon-impurity scattering. As it is to be expected that L_2 is independent of temperature λ for large Li concentrations will not follow a $1/T$ law. When, however, it is assumed that λ does follow such a law an upper limit for Z can be calculated. It is shown[15] that for a lithium concentration of 15 per cent $Z < 3\times10^{-4}$ at a temperature of 1100°C. At this temperature, however, Li evaporates from the substance at a considerable rate. Therefore $Li_xNi_{(1-x)}O$ is not such a very useful material for thermo-electric generation.

2. EXPERIMENTAL

2.1 *Preparation*

$Li_xNi_{(1-x)}O$ was prepared by firing an intimate mixture of Li_2CO_3 and $NiCO_3$ at 900°C. After milling the product obtained, it was pressed into bars or discs and fired at 1200°C for 3 hr in air in a covered platinum crucible. The density of our samples varied from 75–95 per cent of the theoretical value. Best results were obtained with hydrostatically pressed samples. Using no binder and a pressure of 10 tons/cm^2 the density of the probes after pressing was about 77 per cent of the theoretical value and this could be increased to about 95 per cent by firing in the usual way.

Measurements were made on four series of 10 samples each varying in composition from 0·005 per cent to 20 per cent Li. After all the measurements were finished these samples were analysed for Li and Ni^{3+} content. For a few samples the agreement between Li and Ni^{3+}

Vol. 17
1960

content was not satisfactory and the results obtained from these samples were therefore disregarded.

The pure NiO samples were fired at 1550°C, the density varying from 88 per cent to 95 per cent. They were always cooled from temperatures of 800°C in an atmosphere of N_2 to prevent oxidation of the samples at lower temperatures.

2.2 *Seebeck effect*

For the high-temperature measurements of the Seebeck effect bars were placed between two platinum blocks in a furnace with a strong temperature gradient.

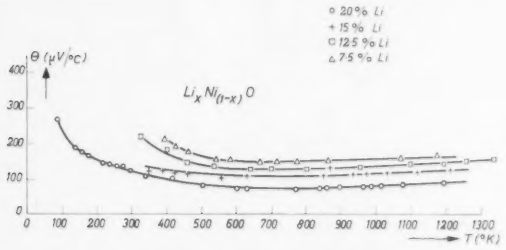

FIG. 1. Seebeck effect as a function of absolute temperature for samples containing different amounts of lithium.

Pt–PtRh thermocouples were welded in the Pt blocks. The Seebeck effect was measured between the Pt wires. For the low-temperature measurements copper blocks were used, which were placed in a glass tube cooled with liquid nitrogen.

The thermo e.m.f. was measured with a Philips pH meter with an internal resistance of $10^{13}\Omega$ when the resistance R of the bars was very high, and with a bridge circuit when R was low.

In Fig. 1 is plotted the Seebeck coefficient θ in $\mu V/°C$ as a function of absolute temperature for samples with different lithium concentrations. As a consequence of the high resistances of the samples the Seebeck effect at low temperatures could be measured only of samples with high lithium concentrations. The concentration dependence of θ at room temperature is shown in Fig. 2.

2.3 *Specific resistance*

The specific resistance was measured in most instances using the potential-probe method, sometimes with and a.c.-bridge method or directly with d.c. when

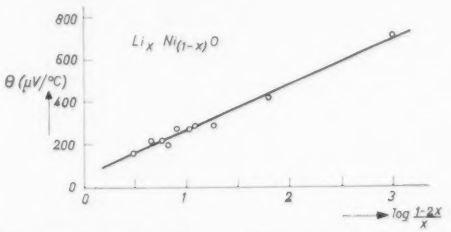

FIG. 2. Seebeck effect at 40°C as a function of Ni^{3+} concentration x.

the resistance was very high. Graphite or In–Hg amalgam was used as the contact, as VAN UITERT[16] had done in his investigations on ferrites.

In Fig. 3 the temperature dependence of the specific resistance ρ for some of our purest NiO samples is plotted. The temperature dependence of ρ for $Li_xNi_{(1-x)}O$ at several Ni^{3+} concentrations is shown in Fig. 4. The dependence of ρ on the Ni^{3+} concentration at room temperature is given in Fig. 5.

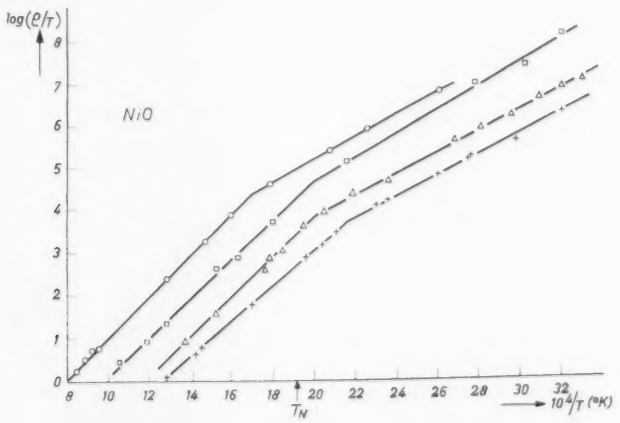

FIG. 3. Temperature dependence of specific resistivity for several samples of pure NiO. T_N is *the* Néel point.

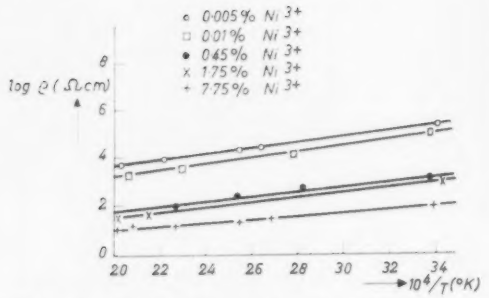

FIG. 4. Specific resistivity as a function of temperature for samples containing different amounts of lithium.

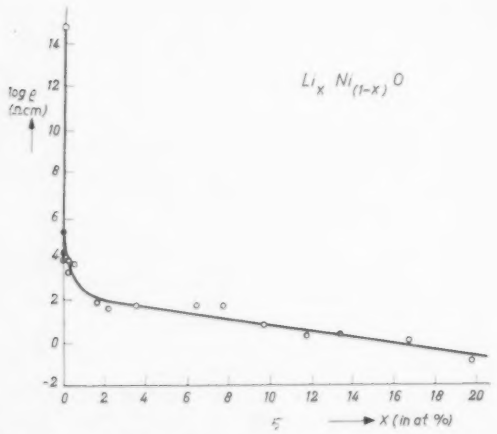

FIG. 5. Specific resistivity at room temperature as a function of the Ni^{3+} concentration x.

3. CALCULATION OF THE ENERGY LEVEL SCHEME

For a discussion of the conduction mechanism in NiO it is important to have some insight in the energy level scheme. Assuming that the lattice is built up from Ni^{2+} and O^{2-} ions, the location of the energy levels has therefore been calculated starting from the ionization energies of the free ions and combining them with the Madelung potential, 24·13 eV. This is shown in Fig. 6(a). For the second and third ionization energies of nickel the values given by FINKELNBURG and HUMBACH[17] are used, viz. 18·15 eV and 36·10 eV respectively; for the electron affinity of oxygen a value of −9·0 eV is used. The lattice constant of NiO is 4·176 Å.

To improve the result a correction should be applied for the polarization of the lattice and a smaller correction for the difference in crystal field stabilization of the Ni ions with different valency state. In Figs. 6(a) and (c) the different energies that contribute to the final positions of the energy levels are plotted. Zero point of the energy scale is taken as the energy of an electron

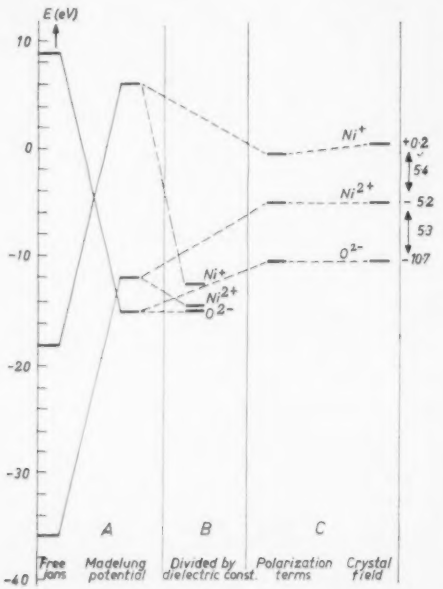

FIG. 6. Calculation of the electronic energy level diagram in NiO. In (a) the ionization potentials are combined with the Madelung potential. In (b) the result of (a) is divided by ϵ and in (c) the result of (a) is corrected for polarization energy and crystal field stabilization.

at rest in vacuum. It will be made clear by means of an example why some contributions are positive and others negative. Let us see how much energy it takes to bring an electron from a filled Ni^{2+} level to infinity, that is consider the reaction $Ni^{2+} \rightarrow Ni^{3+} + e^-$. Naturally this costs the third ionization energy of nickel, but one gets back the Madelung energy because a Ni^{3+} ion is bound much tighter in the lattice than a Ni^{2+} ion. Moreover, polarization energy is gained because the excess charge on the Ni^{3+} ion agrees with an excess charge in a lattice point that polarizes its surroundings. The energy level does not shift as a consequence of differences in crystal field stabilization because

Vol. 17
1960

Ni^{2+} ions happen to be stabilized as much as Ni^{3+} ions.

In an analogous way one can understand the positions of the O^{2-} band and the Ni^{+} levels, by considering the reactions $O^{2-} \rightarrow O^{-}+e^{-}$ and $Ni^{2+}+e^{-} \rightarrow Ni^{+}$.

A very simple method of obtaining a polarization correction was used by MORIN[12] who divided the energy differences obtained from the combination of ionization energies and Madelung potential by the dielectric constant ϵ, using a value $\epsilon = 5$. He points out, however, that a value of $\epsilon = 10$ seems to be more appropriate. Lately[18] a value for the dielectric constant of $\epsilon = 12$ was reported, and as we assume that MORIN would have used this value if he had known it when he made his calculations, the result of his method using this value for ϵ is plotted in Fig. 6(b). The energy difference between the oxygen band and the Ni^{2+} levels and between the Ni^{+} and Ni^{2+} levels is 0·25 eV and 1·75 eV respectively. No matter what value for ϵ is used, however, we do not think that this method can be justified theoretically. Especially the ionization energies, which are specific free-ion properties, should not be divided by ϵ.

We therefore think it better to add correction terms for the polarization of the lattice. A simple way in which a rough idea about this correction can be obtained is given by YOST's method,[19] in which the crystal is considered as a medium of uniform dielectric constant with a cavity in which the excess charge is located. The difficulty in this method is how to make a proper choice of the form and the dimensions of this cavity. When a spherical hole of radius R is chosen, the polarization energy W is given by the equation

$$W = (e^2/2R)(1-1/\epsilon) \qquad (1)$$

Using for R the ionic radius one calculates for W the values given in Table 1. A feature of this method is that the dipole–dipole interaction is implicitly taken into account. As it is not certain that the value of the ionic radius should be used for R, the results obtained with this method were not used.

Table 1. *Polarization energies calculated with* YOST's *method.*

Value of dielectric constant	$\epsilon = 12$[18]	$\epsilon = n^2 = 5{\cdot}4$[18]
Excess charge on nickel	8·4 eV	7·5 eV
Excess charge on oxygen	5·0 eV	4·4 eV

Table 2. *Polarization energies calculated with the method of* MOTT *and* LITTLETON.

	With ionic displacements	Rigid lattice
Excess charge on Ni	6·8 eV	5·0 eV
Excess charge on O	4·4 eV	3·1 eV

A more satisfactory method is that indicated by MOTT and LITTLETON[20]. Here the dipoles μ on all lattice sites induced by an excess charge at a point Q are calculated. As the "0th approximation" the magnitudes of these dipoles are calculated assuming the crystal to be a continuum. In calculating the effect of all these dipoles on the excess charge, however, the crystal is considered as an array of point dipoles at lattice sites. In the first approximation the six nearest neighbours are considered separately. A detailed account of these calculations is given in the appendix. The result is shown in Table 2.

One should realize in considering these values

that, though we believe the method by which they are calculated is essentially correct, the true values may differ somewhat from the values indicated, as a consequence of the fact that the exact values for the polarizabilities are not known. In Fig. 6(c) the effect of these polarization energies on the location of the energy levels is indicated.

Another important point to consider is the difference in crystal field stabilization between Ni^{1+}, Ni^{2+} and Ni^{3+} ions. This stabilization is a consequence of the splitting of the originally five-fold above is valid between the Ni^{2+} and Ni^{3+} ions as between the Ni^{2+} and Ni^{+} ions, though in opposite direction. In this way for Ni^{+} $Dq = 580$ cm^{-1} and for Ni^{3+} $Dq = 1300$ cm^{-1} is obtained.

In order to calculate the stabilization energies it is necessary to know whether the Ni^{3+} ions are in a weak field (high spin state) or in a strong field (low spin state). As may be seen from Table 4, the stabilization in the former case is 8 Dq and in the latter 18 Dq. For Ni^{+} and Ni^{2+} ions there is no difference.

Table 3. Crystal field splitting in octahedral fields for transition metal ions. The values given are Dq in cm^{-1}.

Ion / Valency state	V	Cr	Mn	Fe	Co	Litt.
2	—	1390	1230	1030	840	(23)
3	1860	1720	2100	1350	1920?	
2	1180	1400	750	1000	1000	(24)
3	1800	1760	2100	1400	—	

Table 4. States and energies in octahedral fields.

Valency state	Number of 3d electrons	Weak field		Strong field	
		Configuration	Stabilization	Configuration	Stabilization
Ni^{+}	9	$\epsilon^6\gamma^3$	6 Dq	$\epsilon^6\gamma^3$	6 Dq
Ni^{2+}	8	$\epsilon^6\gamma^2$	12 Dq	$\epsilon^6\gamma^2$	12 Dq
Ni^{3+}	7	$\epsilon^5\gamma^2$	8 Dq	$\epsilon^6\gamma^1$	18 Dq

degenerate 3d levels in three lower $d\epsilon$ levels and two higher $d\gamma$ levels. The value of the splitting of the $d\gamma$ and $d\epsilon$ levels (10 Dq) for Ni^{2+} ions could be obtained from the absorption spectrum of a thin foil of polycrystalline NiO. The result $Dq = 870$ cm^{-1} is in good agreement with values reported in literature.[11,21,22] The value of Dq for Ni^{+} and Ni^{3+} is, however, not known. As may be seen from Table 3 the ratio between Dq values for transition metal ions in the 2 and 3 valency state is approximately 1·5; values for monovalent ions are not known. We suggest that the same ratio as given

TANABE and SUGANO[23] calculated the energy diagrams for transition metal ions. From the diagram for d^7 one can see that the ground state goes from $d\epsilon^5\, d\gamma^2$ to $d\epsilon^6\, d\gamma^1$ at a value of approximately $Dq = 2100$ cm^{-1}. As this value is appreciably larger than the value we suggest for Dq, we assume the Ni^{3+} ions to be in a high spin state.

Now the crystal field stabilization for the three valency states may be calculated as

Ni^{+} 0·4 eV
Ni^{2+} 1·3 eV
Ni^{3+} 1·3 eV

Vol. 17
1960

From these values it is seen that only the Ni^+-level in the energy level diagram shifts upwards over a distance of 0·9 eV as is indicated in Fig. 6(c).

We find as a result of the calculations described in this section that the distance between the Ni^{2+} and the Ni^+ levels is approximately 5·4 eV. A value of 5·3 eV is found for the distance between the O^{2-} band and the Ni^{2+} levels. One should realize that the oxygen band has some width, so that the distance between the top of the O^{2-} band and the Ni^{2+} levels is less than 5·3 eV.

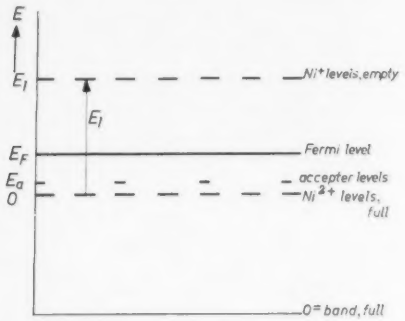

FIG. 7. Energy level scheme at an arbitrary scale.

4. DISCUSSION

4.1 *Discussion of the energy level scheme*

The energy level scheme is redrawn in Fig. 7. The energy of the Ni^{2+} levels is taken as a zero point of the energy scale in this figure. As stated in the introduction the Ni^{2+} levels are localized, as probably are the Ni^+ levels. As no conduction is found in pure NiO as a consequence of the large Ni^+–Ni^{2+} level distance there is no experimental evidence for localization of the Ni^+ levels. Due to differences in Madelung energy a Ni^{3+} ion next to a Li^+ ion gives rise to a $Li^+ \cdot Ni^{2+}$ acceptor level at some distance E_a above the Ni^{2+} levels. It is very difficult, however, to calculate an exact value for E_a. In the next section we will discuss how E_a can be determined from measurements of the Seebeck effect at low temperatures. The position of the Fermi level E_F depends, of course, on the temperature.

4.2 *Discussion of the measurements of the Seebeck effect*

The Seebeck effect θ is given by the equation

$$\theta = (1/eT)(AkT + E_F) \qquad (2)$$

where E_F is the energy of the Fermi level (Fig. 7) and AkT is a term representing the transport of kinetic energy. In oxides AkT is usually of the order of a few kT and may often be neglected, as JONKER[13] showed for the case of cobalt ferrite. E_F is either given by

$$E_F = \tfrac{1}{2}\, kT \ln (p^0/C_a) + \tfrac{1}{2}E_a \qquad (3)$$

or by

$$E_F = kT \ln (p^0/C_a) \qquad (4)$$

where C_a is the number of acceptors per cm^3, p^0 is the number of available states, which is $5{\cdot}5 \times 10^{22} - 2C_a$ per cm^3 for NiO and E_a is the energy difference between the Ni^{2+} levels and the acceptor levels (Fig. 7). Equation (3) holds when

$$|4(C_a/p^0) \exp (E_a/kT)| \gg kT \qquad (5a)$$

i.e. when E_a is large, or when though E_a is small the temperature is very low and the acceptor concentration high. Equation (4) holds when

$$|4(C_a/p^0) \exp (E_a/kT)| \ll kT \qquad (5b)$$

i.e. when $E_a \leqslant kT$ or when $C_a/p^0 \ll 1$.

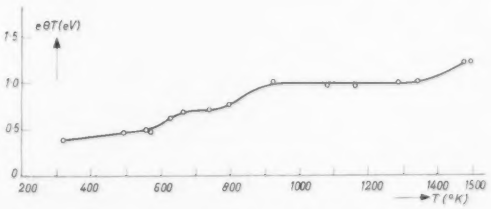

FIG. 8. $e\theta T$ as a function of absolute temperature for pure NiO.

The distance of the Fermi level E_F (Fig. 7) above the conduction level is in general given by $e\theta T = e\pi$, where π is the Peltier coefficient. Therefore a plot of $e\theta T$ as a function of T shows the variation of E_F. At high temperatures E_F may nearly reach the intrinsic value. In that case it depends on the relative values of the mobilities of the holes and electrons whether $e\theta T$ reaches E_F and stays there or whether it goes down to zero at last. The latter is the case when the mobilities of holes and electrons are the same.

Figure 8 gives the variation of $e\theta T$ with T for pure NiO. The horizontal part at 1 eV suggests a considerable level density at 2 eV above the Ni^{2+} levels. MORIN[12] concludes from analogous

measurements up to 1300°K that the distance between the oxygen band and the Ni^{2+} levels is 2 eV. We find, however, that $e\theta T$ rises again at temperatures above 1300°K, indicating that the stationary part of $e\theta T$ is not due to intrinsic properties of NiO but rather to unknown acceptor levels of accidental impurities of other crystal imperfections. We therefore attribute the small conductivity ($10^{-14}\,\Omega^{-1}\,cm^{-1}$) still present in our purest samples to these unknown impurities.

It is seen from Fig. 1 that for Li doped samples θ increases with decreasing temperature in the low temperature region as a consequence of the term $1/2\,E_a$ in equation (3). From this temperature dependence a value for E_a can be calculated as $E_a = 0{\cdot}035$ eV.* It follows from this result that at temperatures only a little above room temperature all acceptors are ionized and the number of holes in the Ni^{2+} levels is $p = C_a$. A similar low value of E_a is found in other oxidic semiconductors.

This result is not in agreement with MORIN's[12] assumption that part of the conduction takes place in the oxygen band. For in that case E_a would be as much larger as the distance between the O^{2-} band and the Ni^{2+} levels, giving a much sharper increase of θ with decreasing temperature. This distance is calculated using MORIN's method as 0·25 eV when a value for the dielectric constant of $\epsilon = 12$ is used. Moreover this same distance would give an extra contribution of approximately $400\mu V/°C$ to the Seebeck effect at normal temperatures (equation 4). It is found, however, (Fig. 2) that the experimental points can be represented by a straight line

$$\theta = 0{\cdot}6\,k/e + 1{\cdot}1(k/e)\ln(p^0/C_a)$$

and this result agrees very well with that expected from equation (3).

As the sign of the Seebeck effect is positive for all concentrations, the conduction is assumed to be p-type, though strict evidence for the sign of the charge carriers can be obtained only from measurements of the Hall effect, which could up to now not be measured.

*After completing these measurements we learned that HEIKES[25] made independently analogous measurements of the Seebeck effect at low temperatures with similar results.

4.3 *Discussion of resistivity measurements*

The resistance as a function of temperature is given by the equation

$$\rho = \rho_0 \exp(q/kT) \tag{6}$$

defining an activation energy q. As HEIKES and JOHNSTON[10] pointed out, however, it is better to use the equation

$$\rho = \rho_0' \, T \exp(q/kT) \tag{6a}$$

the inclusion of T being a consequence of the fact that conduction in NiO may be considered as a diffusion process, as will be discussed later in this section. The equations (6) and (6a) give somewhat different results for q only at high temperatures when used over a large temperature range.

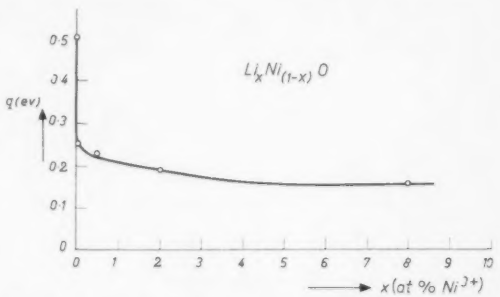

FIG. 9. Activation energy as a function of Ni^{3+} concentration.

From Fig. 3 it is seen that the activation energy at low temperatures is about 0·5 eV and at high temperatures about 1·0 eV in pure NiO. The transition takes place at temperatures near $T_N = 523$°K, the Néel temperature of NiO. It is seen that the transition temperature differs for different samples, probably as a consequence of small differences in heat treatment. Such a transition at about T_N was found also for MnO, CoO and CuO by HEIKES and JOHNSTON[10], who attributed this to a change in elastic properties of the crystal. In the near future we will study the occurence of this and other kinds of anomalous behaviour of the resistivity as a function of temperature in NiO and other oxidic compounds more extensively, as we expect this to give more insight in the conduction process and its relation to the magnetic properties.

The dependence of the activation energy q

Vol. 17
1960

measured in the temperature range 300–500°K on the Ni^{3+} concentration x in $Li_xNi_{(1-x)}O$ is shown in Fig. 9. It is seen that q at first decreases sharply with x and later much more slowly. This behaviour is not in accordance with the original idea of DE BOER and VERWEY[7] that activation energy is loosening the hole from the lithium ion, for then a more gradual decrease of q with x is to be expected and a zero activation energy should be found for $x \approx 10$ per cent, as then each Ni ion has at least two Li neighbours. Moreover, in that case q should be $1/2E_a$, but it is found that q is 0·1–0·2 eV and E_a is only 0·035 eV. Therefore q is assumed to be a mobility factor rather than one of carrier concentration. q is thus connected with the activation of the jumping of a hole between "normal" Ni ions.

HEIKES and JOHNSTON[10] were the first to point out that q is a consequence of self-trapping by the polarization induced by the hopping hole itself. For such a polarization potential to be set up, a hole must reside on a given lattice site for a time τ that is comparable with or larger than the vibrational period τ_0 of the lattice, which is usually of the order of 10^{-13} sec. If this model is right, the wandering of a hole through the lattice can be treated as a thermally activated diffusion process with a mobility

$$\mu = \frac{e\, d^2 \nu_0 \exp(-q/kT)}{kT} \qquad (7)$$

where d is the shortest interatomic distance between two Ni ions and $\nu_0 = 1/\tau_0$. As q as a function of Ni^{3+} concentration x is known, $\mu(x)$ can be calculated when the exact value for ν_0 is known. This value for ν_0 can be obtained, however, by comparing the mobilities $\mu(x)$ obtained from equation (7) with the mobilities calculated from

$$\mu = 1/pe\rho \qquad (8)$$

where $p = C_a$. The specific resistivity ρ as a function of Ni^{3+} concentration x is known (Fig. 5). Combination of the mobilities found from the equations (7) and (8) gives a value for ν_0 of $1{\cdot}1 \times 10^{12}$ sec^{-1} for the whole concentration region. This value is quite satisfactory as compared with the value for the vibrational period of the lattice, which may be calculated from the Debije temperature, 410°K[26], as $\nu_0 = 8{\cdot}5 \times 10^{12}$ sec^{-1}. The mobilities at room temperature calculated in this way vary from 2×10^{-5} to 60×10^{-5} cm^2/V sec. The absence of a measurable Hall effect is also in accordance with these low mobilities found.

Such a behaviour is also found in other oxides. JONKER[13], for instance, found values of ν_0 varying from $6{\cdot}5 \times 10^{12}$ sec^{-1} to $1{\cdot}0 \times 10^{14}$ sec^{-1} in cobalt ferrite.

5. CONCLUSIONS

The important point with transition metal oxides of the NiO type is, that there is no $3d$-band, but localized $3d^x$-levels, where x has a value appropriate for the oxide under discussion. In the case of NiO one has full $3d^8$-levels (Ni^{2+}-levels) and empty $3d^9$-levels (Ni^{+}-levels). As a consequence of the large distance between these levels intrinsic conductivity at normal temperatures is absent. Conduction is a consequence of an electronic transition from the full Ni^{2+}-levels to acceptor levels, e.g. $Li^+ \cdot Ni^{2+}$ levels, when lithium is added to the substance, or $\square \cdot Ni^{2+}$ levels when nickel vacancies are made in the lattice by annealing NiO in oxygen (Fig. 7).

As we have seen, pure NiO is a very poor conductor, the small conductivity still present is probably a consequence of accidental impurities giving acceptor levels at a high distance above the Ni^{2+} levels, e.g. 1–2 eV. This may also explain the large activation energy found for pure NiO and the sharp decrease in the activation energy when some lithium is added to the substance. In pure NiO the activation energy is largely due to the energy needed to ionize the unknown acceptor levels, but as soon as a small number of $Li^+ \cdot Ni^{2+}$ acceptor levels is present, practically no energy is needed to ionize these acceptors and the activation energy actually found is a consequence of the self-trapping of the moving holes.

It is concluded from theoretical as well as from experimental arguments, that MORIN's[12] model, assuming part of the conduction to take place in the oxygen $2p$ band, cannot be right. This author considers two extreme situations: (a) NiO doped with so much lithium that only holes in the Ni^{2+} levels contribute to the conduction, and (b) NiO so pure, that holes in the oxygen $2p$ band predominate in conduction. Now one cannot understand why in the former situation no electrons from the oxygen band can be activated to the

acceptor levels, when in the latter case electrons from this band can be activated to the Ni^{+}-levels. Moreover, intrinsic conduction is highly improbable. As discussed in Section 4·3, conduction in an O^{2-} band should give an extra contribution to the Seebeck effect and this is not found.

Acknowledgements—The author wishes to thank Dr. G. H. JONKER for many stimulating discussions. Thanks are also due to Dr. A. BRIL for making the optical measurements and to Mr. J. VISSER for the chemical analysis.

APPENDIX. CALCULATION OF THE POLARIZATION ENERGY

The polarization $\boldsymbol{P}$ at a distance r from Q is given by

$$\boldsymbol{P} = \frac{\mu_O + \mu_{Ni}}{2a^3} = \frac{e}{4\pi r^2}(1 - 1/\epsilon) \tag{9}$$

where μ_O and μ_{Ni} are the dipole moments on an oxygen ion and a nickel ion respectively, a is the shortest interatomic distance between O and Ni and $\epsilon = 12$ is the dielectric constant.
The dipole moments are given by

$$\begin{aligned} \mu_O &= E_{eff}(\alpha_O + 4e^2/p) \\ \mu_{Ni} &= E_{eff}(\alpha_{Ni} + 4e^2/p) \end{aligned} \tag{10}$$

where E_{eff} is the effective polarizing field and α is the electronic polarizability; p is a repulsive force constant which will be discussed later. The values of α_O and α_{Ni} may be calculated using the equations given by PAULING[27]:

$$\frac{n^2 - 1}{n^2 + 2} = \frac{4\pi}{3} \cdot \frac{4}{a^3}(\alpha_O + \alpha_{Ni}) \tag{11}$$

$$\alpha_O/\alpha_{Ni} = R_O/R_{Ni} \tag{12}$$

where n is the refractive index, taken here to be $\sqrt{5{\cdot}4}$; R is the mole refractivity. For R_O/R_{Ni} a value of 10 was used, being the value found in aqueous solutions.[29] In this way the following values for the electronic polarizabilities were obtained:

$$\alpha_O = 2{\cdot}34 \text{ Å}^3$$

$$\alpha_{Ni} = 0{\cdot}23 \text{ Å}^3$$

MOTT and LITTLETON[20] have shown that the value of the constant p mentioned above is given by

$$p = \frac{2A4e^2}{3a^2}(1/\rho - 2/a) \tag{13}$$

where A is the Madelung constant and ρ the repulsive exponent. Using a value of 960 kcal/mole[28] for the lattice energy to calculate ρ, we obtain $4e^2/p = 1{\cdot}42$ Å^3.

Combination of the equations (9) and (10) gives for the dipole moments

$$\mu_O = M_O e a^3/r^2 \text{ and } \mu_{Ni} = M_{Ni} e a^3/r^2 \tag{14}$$

where

$$M_O = \frac{1}{4\pi}(1 - 1/\epsilon)\frac{\alpha_O + 4e^2/p}{\frac{1}{2}(\alpha_O + \alpha_{Ni}) + 4e^2/p} \tag{15}$$

M_{Ni} being given by an analogous equation.
The potential ϕ_k at the point Q due to a dipole μ_k at a distance r is

$$\phi_k = \mu_k/r^2 \tag{16}$$

The potential energy resulting from the potentials of all the dipoles is given by

$$\begin{aligned} W &= \tfrac{1}{2} e \sum \phi_k \\ &= -\tfrac{1}{2} e^2/a[M_O a^4 \sum_{O} 1/r_O^4 + M_{Ni} a^4 \sum_{Ni} 1/r_{Ni}^4] \end{aligned} \tag{17}$$

where $\sum_{O}$ denotes a sum over all oxygen ions and $\sum_{Ni}$ a sum over all nickel ions. These summations were calculated by JONES and INGHAM[29]. When the excess charge is located at an oxygen ion or at a nickel ion the result is respectively:

$$\begin{aligned} W_O &= -e^2/2a[10{\cdot}1977 M_{Ni} + 6{\cdot}3346\, M_O] \\ W_{Ni} &= -e^2/2a[10{\cdot}1977\, M_0 + 6{\cdot}3346\, M_{Ni}] \end{aligned} \tag{18}$$

These equations for the polarization energy (the "0th approximation") may be improved by considering the six nearest neighbours of the ion in question separately. When the excess charge is located on a nickel ion the dipole moments of the six oxygen ions surrounding it are a consequence of the field resulting from:
(1) the excess charge on the nickel ion, the field being e/a^2
(2) the field of the five other oxygen dipoles,

$$E_O^{I} = -2{\cdot}371\, \mu_O'/a^3 \tag{19}$$

(3) the field of all the other dipoles,

$$E_O^{II} = -e/a^2(0{\cdot}388 M_O + 1{\cdot}965 M_{Ni}) \tag{20}$$

So the dipole moments of the six oxygen ions are

$$\mu_O' = (\alpha_0 + 4e^2/p)(e/a^2 + E_O^{I} + E_O^{II}) \tag{21}$$

Similar equations hold when the excess charge is on an oxygen ion.
In this approximation the polarization energy is given by

$$\begin{aligned} W_O &= -e^2/2a[4{\cdot}1977\, M_{Ni} + 6{\cdot}3346\, M_O] - 3\mu_{Ni}' e/a^2 \\ W_{Ni} &= -e^2/2a[4{\cdot}1977\, M_O + 6{\cdot}3346\, M_{Ni}] - 3\mu_O' e/a \end{aligned} \tag{16}$$

In still higher approximations the same process is carried out for next nearest neighbours and so on. We restrict

Vol. 17
1960

ourselves to the first approximation as the exact values for the polarizabilities are not known. A small extra correction is made, however, for the fact that the radius of a Ni^{3+} ion for instance is 0·06 Å smaller than that of a Ni^{2+} ion.[30] We assumed that as a consequence of this smaller radius the nearest neighbours shift over a distance of 0·03 Å giving a small extra contribution to the polarization energy. The same correction is applied for the fact that a Ni^{+} ion and an O^{-} ion are larger than a Ni^{2+} ion and an O^{2-} ion respectively.

The same calculations were carried out for the simpler case of a rigid lattice, which is of importance for optical processes. In this case one should take $\epsilon = n^2$ and $4e^2/p =$ in the equations given above.

REFERENCES

1. Rooksby H. P., *Acta Cryst., Camb.* **1,** 226 (1948).
2. Shull C. G., *Phys. Rev.* **83**, 333 (1951).
3. Singer J. R., *Phys. Rev.* **104**, 929 (1956).
4. Roth W. L., *Phys. Rev.* **110**, 1333 (1958).
5. Verwey E. J. W., Haaijman P. W., Romeijn F. C. and van Oosterhout G. W., *Philips Res. Rep.* **5,** 173 (1950).
6. Goodenough J. B., *J. Phys. Chem. Solids* **5**, 107 (1958).
7. de Boer J. H. and Verwey E. J. W., *Proc. Phys. Soc. Lond.* extra part, **49**, 59 (1937).
8. Verwey E. J. W., *Semi-conducting Materials*, p. 151. Butterworths, London (1951).
9. Mott N. F., *Proc. Phys. Soc. Lond.* **A62**, 416 (1949).
10. Heikes R. R. and Johnston W. D., *J. Chem Phys.* **26**, 582 (1957).
11. Morin F. J., *Phys. Rev.* **83**, 1005 (1951); **93,** 1005 and 1199 (1954).
12. Morin F. J., *Bell. Syst. Tech. J.* **37**, 1047 (1958).
13. Jonker G. H., *J. Phys. Chem. Solids* **9**, 165 (1959).
14. Schuh R. J. and Tallent R. J., *Appl. and Ind.* **45**, 345 (1959).
15. van Houten S., *Philips Res. Rep.*, to be published.
16. van Uitert L. G., *J. Chem. Phys.* **23**, 1883 (1955).
17. Finkelnburg W. and Humbach W., *Naturwissenschaften* **42**, 35 (1955).
18. Newman R. and Chrenko R. M., *Phys. Rev.* **114**, 1507 (1959).
19. Yost W., *J. Chem. Phys.* **1**, 466 (1933).
20. Mott N. F. and Littleton M. J., *Trans. Faraday Soc.* **34**, 485 (1938).
21. Kröger F. A., Vink H. J. and van den Boomgaard J., *Physica* **18**, 77 (1952).
22. Doyle W. P. and Lonergan G. A., *Disc. Faraday Soc.* **26**, 27 (1958).
23. Tanabe Y. and Sugano S., *J. Phys. Soc. Japan* **9,** 753 (766 (1954).
24. McClure D. S., *J. Phys. Chem. Solids* **3**, 311 (1957).
25. Heikes R. R., private communication.
26. Seltz H., De Witt B. J. and McDonald H. J., *J. Amer. Chem. Soc.* **62**, 88 (1940).
27. Pauling L., *Proc. Roy. Soc.* **A114**, 181 (1927).
28. Landolt Börnstein, *Zahlenwerte und Funktionen*, I Band, 1. Teil s. 402 and 4. Teil s. 542. Springer Verlag, Berlin (1950).
29. Jones J. E. and Ingham A. E., *Proc. Roy. Soc.* **A107,** 636 (1925).
30. Johnston W. D., Miller R. C. and Mazelski R. *J. Phys. Chem.* **63**, 198 (1959).

J. Phys. Chem. Solids Pergamon Press 1960. Vol. 17, Nos. 1/2, pp. 18–25. Printed in Great Britain.

LATTICE SPACINGS AND COLOUR IN THE SYSTEM ALUMINA–CHROMIC OXIDE

J. GRAHAM

Chemical Research Laboratories, Melbourne, Australia

(*Received* 15 *February* 1960; *revised* 3 *May* 1960)

Abstract—Precision lattice spacing determinations have been made on well crystallized specimens throughout the system, and the diffuse reflectivity of the samples measured. There is no anomaly at 8 mol per cent Cr_2O_3 as found by earlier workers, the change in both the colour and the crystal field surrounding the chromium ions being continuous and smooth, though changes in the crystallographic environment of these ions cannot be followed in detail. Atomic parameters have been obtained for pure chromic oxide, revealing that the structure is rather less distorted than the similar structures of α-alumina and α-Fe_2O_3.

INTRODUCTION

AFTER many years of widely dispersed and conflicting experimental activity, it has now been qualitatively established[1] that the colour change from ruby red to chromic oxide green in the solid solution series Al_2O_3–Cr_2O_3 is due to a gradual shift of the absorption band structure with chromium content, brought about by changes in the crystal field in which the chromium ions are placed.[2,3]

The present work originated in a study of lattice spacings designed to determine the composition of the ceramic phase in chromium–alumina cermets; considerable quantitative differences were found between the published lattice spacing data (on which the discussion of colour had been based) and that found experimentally. In view of the importance of ruby in maser techniques, and its possible application as a low-temperature thermometer,[4] it was thought worthwhile to present the new data on lattice spacings, and to correlate it with the absorption structure in the visible region, for the complete system Al_2O_3–Cr_2O_3.

Historically, the optical properties of ruby have been regarded as anomalous. The solution of green Cr_2O_3 in colourless alumina was not expected to be red, and the fact that red solid solutions were turned green reversibly on heating was not understood. A change in oxidation state of the chromium ion to account for the colour change was ruled out by magnetic and other studies, and a connection between the colour change and the antiferromagnetic exchange coupling which occurs in Cr_2O_3 is excluded by the composition at which the colour change occurs—the magnetic change occurs near 100 per cent Cr_2O_3 at room temperature, while the colour change occurs at about 30 per cent Cr_2O_3. Other hypotheses which have been put forward include the colloidal distribution of Cr_2O_3 particles in the alumina, and the existence of two phases in the system, the one red and the other green.[5] The latter was supported by X-ray evidence, and has been quoted as recently as 1951,[6] in spite of considerable evidence that the substitutional solid solution extends from 0–100 per cent.[7,8,9]

SAMPLE PREPARATION

Morgan's pure calcined alumina powder No. 932, and commercial chromic oxide powder supplied by Hopkin and Williams, were used in this investigation; the purity of the alumina was 99·75 per cent, the major impurity being $<0{\cdot}25$ alkalis. The iron content is 0·007. The chromic oxide was 99·3 per cent pure, containing $\sim 0{\cdot}1$ per cent Fe_2O_3 and 0·15 per cent Al_2O_3, with 0·2 per cent water. The accurately weighed

powders were intimately mixed in the desired proportions in a mechanical agate mortar, using toluene as a lubricant. After drying, the powders were pressed at 30,000 p.s.i. in a $\frac{1}{2}''$ steel die to form pellets weighing about 3 g. These were fired four at a time in covered alumina boats in an electric furnace, atmospheres used being air and argon; the firing schedules are given in Fig. 1.

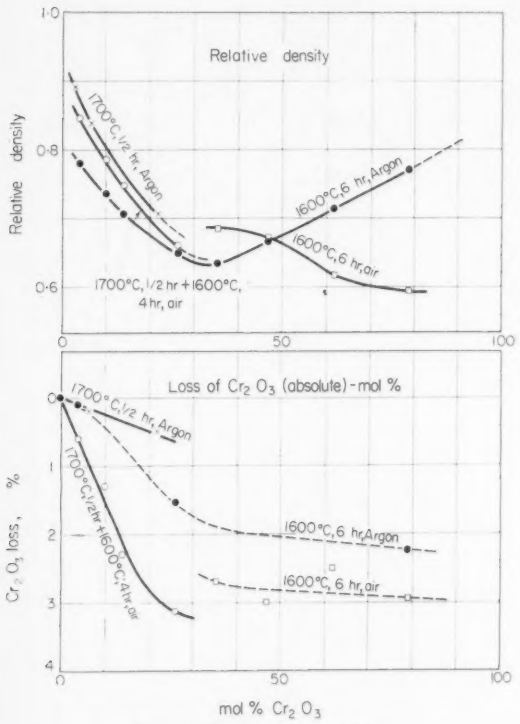

FIG. 1. Fabrication variables.

Since most of the difficulties of the previous workers[9,10] seemed to be centred around inhomogeneity and poor crystallization of the solid solutions, as judged from the scatter of the X-ray results, a portion of each specimen was given a hydrothermal treatment in a simple sealed steel bomb at 800°C and 5000 p.s.i. for 35hr.[11] This resulted in a slight improvement in the X-ray patterns, so these were the samples used in the work.

All specimens were analysed for Cr_2O_3 by the A.S.T.M. method for analysing chrome ores and refractories,[12] except that the initial fusion with Na_2O_2 was carried out in a platinum crucible lined with Na_2CO_3. Thanks are due to Miss B. TERRELL for the analyses.

SINTERING AND PHYSICAL PROPERTIES

The ratio for observed to theoretical density, and the chromic oxide loss by volatilization, are given in Fig. 1 as functions of composition. Although the relative densities were not very high, all the samples produced hard, strong compacts without the use of a flux (cf. WILDE and REES[9]). It will be observed that the chromic oxide loss does not increase in proportion to the amount present, and that the loss is reduced by sintering in argon. The former finding does not accord with the results of WARSHAW and KEITH[13], but the difference is probably due to the fact that our specimens were covered. The relative density attained seems to depend as much on the composition and the furnace atmosphere as on the time and temperature of firing, and there is some

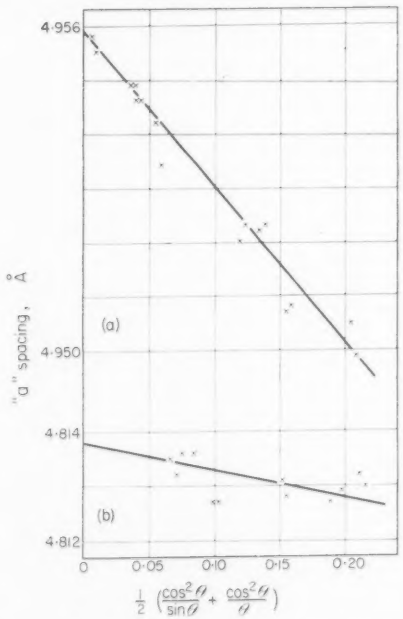

FIG. 2. Representative Nelson–Riley lattice spacing extrapolation curves. The samples are (a) Pure Cr_2O_3 (well crystallized) and (b) 22 mol per cent Cr_2O_3–78 mol per cent Al_2O_3 (poorly crystallized). The extrapolation is weighted according to the angle and the intensity of the reflections.

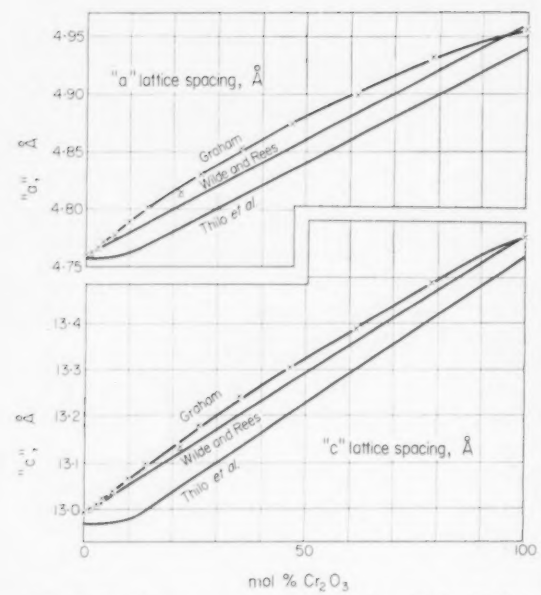

FIG. 3. Lattice parameters a and c for Al_2O_3–Cr_2O_3 solid solutions.

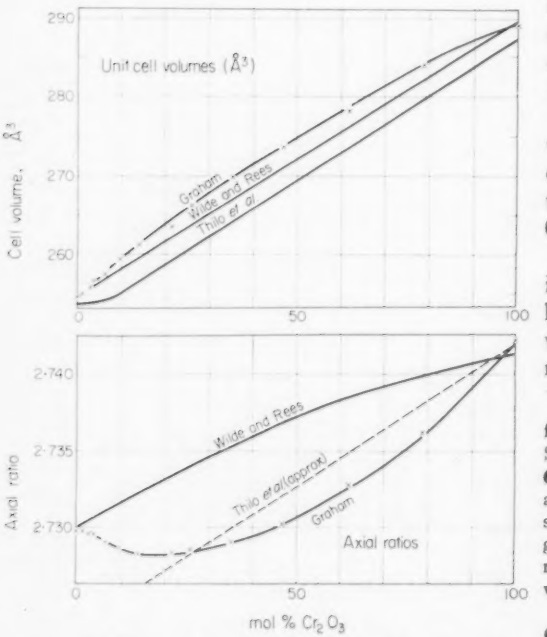

FIG. 4. Unit cell volumes and axial ratios for Al_2O_3–Cr_2O_3 solid solutions.

correlation between the relative density and the chromic oxide loss.

Significantly, the specimens whose compositions lie near the minimum of the relative density curve are those for which the X-ray patterns are least sharp. Diffusion rates must be lower here than near the extremes of the system.

LATTICE SPACINGS

The sintered compacts were broken in a percussion mortar and ground in an alumina mortar; X-ray powder patterns were obtained in a Philips 11·46 cm camera using CuKα radiation, as no longer wavelength tube was available. Measurements were made on eight or nine back-reflection lines (from (3, 1, 10) to (3 3 6)) to reduce the random errors which appear when reliance is placed on only three reflections. The "l" indices varied. from 0 to 15, giving good sensitivity for the trial and error determination of axial ratios. The Nelson–Riley extrapolation function was used, and representative extrapolations are shown in Fig. 2.

With sharp patterns, this procedure results in a precision of about $\pm$ 0·0002 in c/a, $\pm$ 0·0002 Å in a_0, and $\pm$ 0·0015 Å in c_0, if we use hexagonal indices for the rhombohedral lattice. The probable errors for the worst patterns in this study are estimated at $\pm$ 0·0005 in c/a $\pm$ 0·001 Å in a_0, and $\pm$ 0·005 Å in c_0.

All measurements were made at room temperature (25°C $\pm$ 5); since the thermal expansion of alumina at 20°C is 6×10^{-6}/°C, the errors due to temperature fluctuations $\gtrsim$ 0·0001 Å in a_0, or 0·0004 Å in c_0.

The results are plotted in Figs. 3 and 4. It is immediately apparent that the deviations from linearity in both axial directions and in molar volume are positive, and not negative as previously reported.[9,10] This result will be discussed below.*

* After the present manuscript had been prepared for the press, another significant paper appeared, SCHMITZ-DU MONT O. and REINEN D., *Z. Elektrochem.* **63,** (8), 978 (1959). This contains both lattice spacings and absorption curves for chromic oxide–alumina solid solutions. Agreement with the present results is quite good, though the precision of the lattice spacing measurements is lower, and the variation of the absorption wavelength with composition is slightly non-linear.

Precision lattice spacings have been measured for low Cr_2O_3 contents by JAN J. P., STEINEMANN S. and DINICHERT P., *Helv. Phys. Acta* **33,** (2), 123–130 (1960), summarized in *J. Phys. Chem. Solids* **12,** 349 (1960).

Vol. 17
1960

That considerable reliance can be placed on these figures can be seen from the fact that the root mean square deviation from the curve of best fit is 0·04 per cent, as compared with 0·08 per cent for WILDE and REES, and 0·14 per cent for THILO *et al.* If one point at 22 mol per cent is omitted, the r.m.s. deviation falls to 0·02 per cent for the present results. The improvement is brought about by the better crystalization of our ruby solid solutions, which enables the back-reflection doublets to be measured. For example, THILO *et al.*[10] had to rely on reflections below 35° Bragg angle.

The random errors introduced by these inaccurate measurements, however, can hardly account for the different trend of the curves; this is almost certainly due to errors in composition. It seems unlikely that the A.S.T.M. method will over-estimate the chromic oxide content, yet our chromic oxide loss by volatilization at 1600°C and 1700°C is very much lower than that of THILO *et al.* at 1300°C. The order of magnitude of our Cr_2O_3 loss is similar to that of WARSHAW and KEITH[13], so it seems reasonable to question the accuracy of the rather involved analytical method used by THILO *et al.*

The effect of the volatilization of Cr_2O_3 is seen in a difference between the exterior and interior of the sintered compacts—X-ray patterns of filings from the exterior were diffuse (due to grading of composition), whereas the crushed bulk sample gave sharp reflections. An exaggeration of this effect would seem to account for the "two phases" of STILLWELL[5], and provides a possible explanation for the discrepancies between the different sets of results.

COLOUR

The confusion created by the early qualitative observations of colour was resolved by RITSCHL and MÜLLER[1] as mentioned previously. They measured the optical absorption spectrum throughout the system, using the same specimens as THILO *et al.* had used for their X-ray work. They observed only one separate absorption band, in the yellow, the wavelength of which varied with composition. Like the lattice spacings of THILO *et al.*, this curve showed a discontinuity of slope at 8 per cent Cr_2O_3, corresponding with discontinuities in other properties found in the same specimens.

A modified Beckman ratio recording spectrophotometer was used in the present work to obtain diffuse reflectivity curves for flat powdered samples deposited from suspension in water onto glass slides. The incident beam was focussed normally onto the specimen, and the diffuse reflectance measured at an angle of 45°. The reflected intensity was compared with that from a similar sample of pure alumina. The kind of spectrometer trace obtained is shown in Fig. 5.

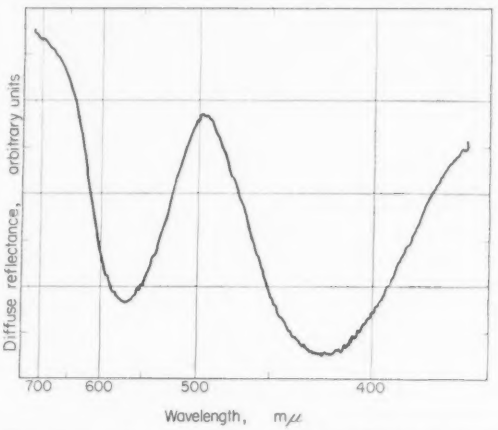

FIG. 5. A typical uncorrected diffuse reflectivity curve for an Al_2O_3–Cr_2O_3 powder sample.

Variations in the thickness and particle size distribution in the specimens caused changes in the reflected intensities, but it was found experimentally that this had little effect on the positions of the reflection minima (absorption maxima), and the band widths. Specimens were made up with extremes of thickness and grain size, and the variations in position and half-width of a sharp reflectance peak were measured. No change in peak position could be observed, even when the specimen was displaced so that some of the incident radiation missed the specimen; half-peak widths showed a probable error of about $\frac{1}{2}$ per cent.

When the instrument was set to measure the absorption of a pure alumina specimen, it was observed that the intensity scale changed with the wavelength, neither the 100 per cent nor the 0 per cent absorption datum lines being constant. To put the measurements on a more reliable

basis, per cent transmission was therefore measured* (giving a constant 0 per cent transmission value), and all curves were corrected to the standard 100 per cent transmission curve of pure alumina. Absorption curves were then obtained by plotting the reciprocal of the transmission on logarithmic paper.

Measurement of the absorption band half-widths presented no difficulties in the alumina-rich end of the system, but as the band-widths increased with addition of Cr_2O_3, considerable overlapping occurred. The bands were separated semi-analytically on the assumption of a symmetrical gaussian shape,[14] and although the assumption is not strictly true, it is felt that the figures obtained for the band half-width will give a fair quantitative measure of the actual half-width. The main change in shape as Cr_2O_3 is added is the formation of a tail on the long wavelength side of the $^4A_{2g} \rightarrow {}^4T_{2g}$ (yellow) absorption band; interference from a strong ultraviolet absorption band also affects the shape of the $^4A_{2g} \rightarrow {}^4T_{1g}$ (blue) band. The results are given in Fig. 6.

It is regretted that the polycrystalline specimens used do not permit differentiation of the ordinary and extraordinary rays.

The widths of the absorption bands in general increase as the amount of chromium increases, and the absorption maxima move to longer wavelengths. This trend is in accord with the theory, that the breadths and positions of the absorption bands both depend on $d(h\nu)/d\Delta$, i.e. the rate of change of energy of the level with crystal field.[15,16]

Except for pure Cr_2O_3, in which antiferromagnetic interactions might be expected to affect the absorption spectrum, the band energy is seen to change, within the limits of accuracy, linearly with composition. Since the band energy also changes approximately linearly with the crystal field,[17] this indicates that the crystal field also changes linearly with composition. If the contrast with the (non-linear) lattice spacing is real (and the spectrographic work may not be sufficiently accurate to decide this), it seems possible that the electronic energy governs the solid solution behaviour; that is, the lattice parameters adapt themselves to give a linear change in the crystal field around the Cr^{+++} ions.

It will be seen that the $^4T_1$ band changes energy more rapidly with composition than does the $^4T_2$ band, in agreement with the energy levels calculated by TANABE and SUGANO for a crystal field value about 2.

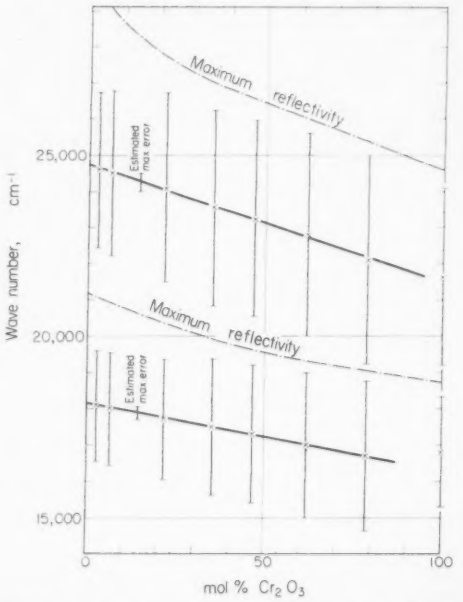

FIG. 6. Variation of wave-number of maxima and minima in diffuse reflectivity with composition. Approximate half-widths of the absorption bands are shown.

The linear energy variation contrasts strongly with the work of RITSCHL and MÜLLER[1], and it seems likely that the anomalies at 8 per cent in all the properties studied by them are introduced through errors of composition. Recent studies on the fine structure of the absorption spectra of rubies throw little light on this subject owing to their extremely limited composition range.

DISCUSSION

THILO *et al.* have shown that the temperature at which the colour change from red to green occurs on heating decreases with increasing chromium content, and it must be assumed that the same mechanism produces the colour change

* The per cent transmission value corresponds to the intensity of the reflected radiation.

Vol. 17
1960

Table 1. *Observed and calculated structure amplitudes for* Cr_2O_3
(*Rhombohedral indices*)

	F calc.	*F* obs.		*F* calc.	*F* obs.
(110)	−32	30	(32$\bar{1}$)	−41	40
(211)	−48·5	51	(420)	63.5	60
(10$\bar{1}$)	52	50	(532)	−54·5	56
(210)	36	35	(400)	−25	20
(200)	−19	17·5	(521)	7	0
(220)	−47·5	48.5	(531)	−13	0
(321)	89	87·5	(41$\bar{1}$)	−44	49·5
(20$\bar{1}$)	− 7	7	(21$\bar{3}$)	47	40
(21$\bar{1}$)|	27*	26	(32$\bar{2}$)	11·5	16
(332)|			(440)	6·5	0
(310)	−56·5	54·5	(541)	−52	51
(2$\bar{1}\bar{1}$)	70	65	(552)|	38*	45·5
(320)	6	0	(644)|		
(422)	0·5	0	(43$\bar{1}$)	51	64
(433)|	51*	65·5	(654)	12	9
(432)|			(622)	−36·5	36
(20$\bar{2}$)	39	35	(33$\bar{2}$)|	37*	60
(411)	27	30	(653)|		
(31$\bar{1}$)	−17	15·5	(30$\bar{3}$)	41	40·5
(431)|	28*	28	(631)	−41	39
(30$\bar{1}$)|			(644)|	47·5*	41·5
(442)	−40	45	(42$\bar{2}$)|		
(444)	24·5	29			

$$\frac{\Sigma\,|(F\text{ obs.}-F\text{ calc.})|}{\Sigma\,F\text{ obs.}} = 0{\cdot}124$$

* $= \sqrt{(P_aF_a^2+P_bF_b^2)}$.

Shortest oxygen–oxygen distance = 2·66 Å. ($v = 0{\cdot}310$).
Shortest metal–oxygen distance = 2·01 and 1·97 Å ($u = 0{\cdot}095$).

both with change of temperature and of composition. As the rhombohedral angle, i.e. shape of the rhombohedral unit cell, is probably unaffected by an increase in temperature,[18] it would appear that the colour change is due to the volume of the cell (determining the strength of the crystal field) rather than to its symmetry, which could also affect the relative positions of the energy levels.

In these oxides, each metal ion is surrounded in roughly octahedral co-ordination by six oxygen ions, which are approximately close packed. A regular octahedron of oxygen ions in contact can easily accommodate an Al^{+++} ion, the radius of the octahedral hole being 0·57Å, whereas the radius of Al^{+++} is 0·51 Å. The Cr^{+++} ion, with radius 0·63 Å, would cause an expansion of the octahedron.

In this connection, it is interesting that the V^{+++} ion, which also forms substitutional solid solutions with Al_2O_3, has a radius of 0·66 Å, and is thus even more strongly compressed than the Cr^{+++} ion. From optical measurements, the trigonal crystal field to which each of these ions is subjected is of the same magnitude.[19]

For pure alumina,[20] the metal–oxygen distances are close to the sum of the ionic radii of aluminium and oxygen, but the shortest oxygen–oxygen distances are only 2·49 Å as against 2·80 Å for the sum of two oxygen radii. This distortion is thought to be due to the mutual repulsion of the Al^{+++} ions within neighbouring octahedra;[21] other factors appear to be operative, however, including covalent bonding; for the molar volume of alumina is more than 14 per cent less than the

volume occupied by a corresponding configuration of close-packed oxygens only.

The complete structure of chromic oxide has not been reported previously; the atomic parameters have now been determined from the powder intensities obtained on a Philips diffractometer. The observed and calculated structure amplitudes are given in Table 1. A small temperature factor correction ($B = 0{\cdot}37$) has been applied, and the reliability quotient is 0·124. Values of u and v given are for Wyckoff's unit cell, which differs from that of the International Tables by a translation of the origin by $(\frac{1}{4}, \frac{1}{4}, \frac{1}{4})$. There are four metal ions in special positions (c) *at uuu*, $\bar{u}\bar{u}\bar{u}$, B.C., and six oxygen ions in special positions (e) at $v\bar{v}0$; $\bar{v}0v$; $0v\bar{v}$; $\frac{1}{2}-v, v+\frac{1}{2}, \frac{1}{2}$; $v+\frac{1}{2}, \frac{1}{2}, \frac{1}{2}-v$; $\frac{1}{2}, \frac{1}{2}-v, v+\frac{1}{2}$. The oxygen arrangement is less distorted than that in alumina, but the cell volume is still very much too low for a purely ionic structure, so that the Cr^{+++} ions, if they exist as such, would be under strong compression throughout the system. The relevant variables for close-packed oxygen ions, Cr_2O_3, V_2O_3, and Al_2O_3 are compared as far as they are known in Table 2.

Table 2. Comparison of parameters for α-Al_2O_3, α-Cr_2O_3, V_2O_3 *and close-packed* O^{--} *ions.*

	α-Al_2O_3	α-Cr_2O_3	V_2O_3	Close-packed O^{--}
a	4·76	4·96	4·94	4·85
c	12·99	13·59	13·99	14·55
a^2c	294·2	333·8	341·7	342·2
c/a	2·73	2·74	2·83	3·00
v	0·303	0·310		0·333
u	0·105	0·095		(0·083)

Now the present lattice spacing results indicate that the total deviation from linearity of the cell volumes in the rhombohedral solid solutions is less than 1 per cent, so that even to determine the variation of the *mean* metal–oxygen distances would require measurement of the metal and oxygen parameters to an order of magnitude better than this accuracy. At present, this is out of the question. Even more difficult is the determination of the precise atomic configuration around a particular chromium ion,[22] and the charge distribution around each ion, which alone would enable a calculation of the crystal field strength at the ion, and indicate the degree of ionic compression and distortion. For example, the closest distances of approach of metal and oxygen ions in pure alumina are 1·89 and 1·93 Å, and in pure Cr_2O_3 are 1·97 and 2·01 Å, a difference of 4 per cent; but this does not allow any conclusion to be reached regarding the Cr^{+++}–O^{--} distances in dilute ruby solutions, and because of this, the energy level changes cannot be directly related to these inter-ion distances.

The positive deviations from linearity which are found in our lattice spacing curves indicate an apparent diameter for the Cr^{+++} ion *greater* than that in Cr_2O_3; the average molar volume increases initially more rapidly than the simple linear law predicts, so that there is no abnorma compression in this region as derived from THILO's curves by ORGEL. There is a smooth and continuous change in both unit cell dimensions and energy level separations throughout the system.

Unfortunately, insufficient points were obtained on the lattice spacing curves at the chromium rich end of the solid solution to decide whether the antiferromagnetic ordering affects these parameters to an observable extent; certainly such effects are infinitesimal compared with the deviations from Vegard's law in the body of the solid solution, and SINGH's introduction of antiferromagnetism to explain the anomaly in THILO's results at 8 mol per cent Cr_2O_3 thus seems rather unrealistic.

Acknowledgement—Thanks are due to Dr. J. FERGUSON for his help with the spectrographic work.

Vol. 17
1960

REFERENCES

1. RITSCHL R. and MÜLLER R., *Z. Phys.* **133,** 237 (1952).
2. ORGEL L. E., *Nature, Lond.* **179,** 1348 (1957).
3. SINGH L., *Nature, Lond.* **181,** 1264–5 (1958).
4. DAUNT J. G. and BRUGGER K., *Z. Phys. Chem.* **16,** 203 (1958).
5. STILLWELL C. W., *J. Phys. Chem.* **30,** 1441 (1926).
6. WEYL W. A., *Coloured Glasses*, The Society of Glass Technology, Sheffield (1951).
7. BUNTING N., *Bur. Stand. J. Res., Wash.* **6,** 947 (1931).
8. THOSAR B. N., *Phil. Mag.* **26,** 380, 878 (1938).
9. WILDE W. T. and REES W. J., *Trans. Brit. Ceram. Soc.* **42,** 123 (1943).
10. THILO E., JANDER J. and SEEMANN H., *Z. anorg. Chem.* **279,** 2 (1955).
11. ROY R. and TUTTLE O. F., *Physics and Chemistry of the Earth*, Vol. I, (edited by AHRENS L. H., RANKAMA K. and RUNCIMAN S. K.). Pergamon Press, London (1956).
12. *Manual of A.S.T.M. Standards on Refractory Materials.* American Society for Testing Materials (1952).
13. WARSHAW I. and KEITH M. L., *J. Amer. Ceram. Soc.* **37,** 161 (1954).
14. GRUM-GRZHIMAILO S. V. and ENIKEEVA M. G., *Soviet Physics, Crystallography* **2,** 180 (1957).
15. ORGEL L. E., *J. Chem. Phys.* **23,** 1824 (1955).
16. MOFFITT W. and BALLHAUSEN C. J., *Ann. Rev. Phys. Chem.* **7,** 107 (1956).
17. TANABE Y. and SUGANO S., *J. Phys. Soc., Japan* **9,** 753, 766 (1954).
18. KLEIN D. J., Atomics International, Metallurgy and Ceramics, U.S.A.E.C. N.A.A.-SR-2542 (1958).
19. MCCLURE D. S., *Advances in Solid State Physics* **9,** 399 (1959).
20. WYCKOFF R. W. G., *Crystal Structures*, Vol. I. Interscience Publishers, New York and London (1948).
21. PAULING L., *The Nature of the Chemical Bond*, 2nd. Ed. Cornell University Press (1940).
22. BORIE B., *Acta Cryst., Camb.* **10,** 89 (1957).

J. Phys. Chem. Solids Pergamon Press 1960. Vol. 17, Nos. 1/2, pp. 26–33. Printed in Great Britain.

PARAMAGNETIC RESONANCE ABSORPTION IN SEVERAL ELECTRON-IRRADIATED MOLECULAR CRYSTALS*†

P. E. WIGEN‡ and J. A. COWEN

Department of Physics, Michigan State University, East Lansing, Michigan

(*Received* 23 *March* 1960)

Abstract—Paramagnetic resonance in a series of hydrated and deuterated molecular crystals irradiated with one MeV electrons at liquid air temperature has been associated with a hole localized on the hydrogen bonded oxygen of the oxyion group. In each case hyperfine structure due to the hydrogen bonding proton has been analyzed with the aid of a Hamiltonian containing an anisotropic term and an isotropic term and the results interpreted to give the relative position of the nucleus and the paramagnetic center.

INTRODUCTION

IT IS WELL known that paramagnetic resonance absorption is an excellent probe of crystalline electric and local magnetic fields. We have made use of this fact to locate and analyze the paramagnetic centers produced in $Li_2SO_4 \cdot H_2O$, $Li_2SO_4 \cdot D_2O$, $CaSO_4 \cdot 2H_2O$ and $Na_2CO_3 \cdot H_2O$ by electron irradiation at liquid air temperature. The crystal structure and the location of the protons in the lithium sulfate and the calcium sulfate have recently[1–5] been redetermined so that in these crystals the position of the nuclei is well known. The anisotropic hyperfine structure of the resonance lines has been used to identify the paramagnetic center and to obtain some information about the wave functions. The analysis has been applied to the sodium carbonate and the positions of some of the protons determined.

EXPERIMENTAL

The single crystals of lithium sulfate and sodium carbonate were grown from saturated aqueous solutions at approximately 50°C usually taking a few days to obtain crystals of suitable size. The monodeuterate was prepared by heating the powdered monohydrate in an open crucible at 200°C overnight, dissolving it in 99·9 per cent D_2O and again growing crystals from the saturated solution. The calcium sulfate (gypsum) was obtained from several different locations in the form of natural single crystals.

The crystals were irradiated at liquid air temperature for two minutes in a one MA beam of one MeV electrons from a General Electric resonant transformer accelerator. The samples were then transferred without warning to the spectrometer and resonance data taken at liquid air temperature for rotation about three mutually orthogonal axes. The orientation was done optically on the external faces of the crystals and was accurate to approximately 2°.

The microwave experiments were done at 9300 mc in a standard magic tee reflection system using 280 c/s magnetic field modulation and derivative detection with presentation on an X–Y recorder. The field was varied automatically by an electronic power supply and calibration points were inserted on each record using a proton resonance probe.

* Supported by the National Science Foundation and by a Michigan State All-University research grant.

† To be submitted by PEW in partial fulfillment of the requirements for the Ph.D. degree at Michigan State University, East Lansing, Michigan.

‡ An Eastman Kodak Fellow in Physics.

THEORY

The spectra consisted of one strong isotropic line occuring at the free electron g value and several anisotropic lines—some strong, some weak. The isotropic line is attributed to an electron trapped at a vacancy or lattice defect while the strong anisotropic lines are associated with a center exhibiting hyperfine structure from a single nucleus. A comparison of the data for rotation about the b axis in lithium sulfate monohydrate and monodeuterate (Figs. 1 and 2) shows that the deuteration has replaced a nucleus of spin $\frac{1}{2}$ with one of spin 1 with a splitting between components which is one-third as large. There is, in addition, a weak line (Fig. 3) showing slight anisotropy which we have not been able to assign to a particular center. The data also shows (particularly in the deuterated case) that the extreme of the g factor variation does not coincide in angle with the extreme of the hyperfine structure. Similar data were obtained for all three crystals.

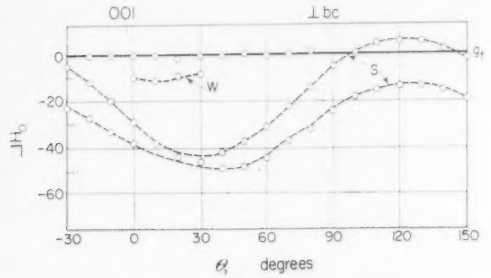

FIG. 1. Angle dependence of the resonance lines in $Li_2SO_4 \cdot H_2O$ for rotation about the (010) axis. The S center corresponds to the strong lines discussed in the article while the W center is the much weaker line that is readily masked by the S lines and the isotropic line.

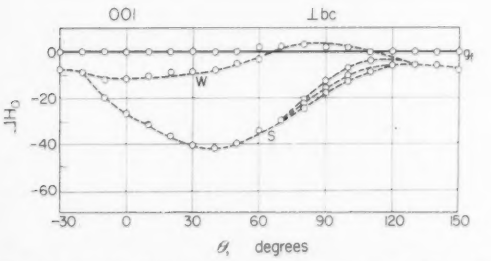

FIG. 2. Angle dependence of the resonance lines in $Li_2SO_4 \cdot D_2O$ for rotation about the (010) axis. The S center corresponds to the strong lines discussed in the article and the W center is the much weaker line.

We have attempted to fit the data with a Hamiltonian which consists of a tensor $\mathbf{g}$ interaction and a tensor hyperfine interaction whose principal axes do not necessarily coincide. The analysis is restricted, for simplicity, to a spin $\frac{1}{2}$ center interacting with a single nucleus of spin $\frac{1}{2}$—this describes the system with which we are dealing quite accurately.

FIG. 3. Resonance spectrum of $Li_2SO_4 \cdot H_2O$ showing the isotropic line, two anisotropic lines and the masking of the weak line.

The Hamiltonian then is

$$\mathcal{H} = \beta \bar{s} \cdot \mathbf{g} \cdot \bar{H} + \bar{S} \cdot \mathbf{A} \cdot \bar{I} \qquad (1)$$

In order to obtain the energy levels we define an effective magnetic field $\bar{H}'$ which is equal in magnitude to $\bar{H}$ but rotated by the tensor operator $\mathbf{g}$

$$g' \bar{H}' = \mathbf{g} \cdot \bar{H} \qquad (2)$$

where g' is a scalar. Thus in a co-ordinate system

in which $\boldsymbol{g}$ is diagonal

$$H' = H\frac{\hat{i}g_{xx}\alpha_1+\hat{j}g_{yy}\alpha_2+\hat{k}g_{zz}\alpha_3}{(g_{xx}^2\alpha_1^2+g_{yy}^2\alpha_2^2+g_{zz}^2\alpha_3^2)^{1/2}} \quad (3)$$

where the α_i are the direction cosines of $\bar{H}$ with respect to the principal axes of $\boldsymbol{g}$. The energy levels are

$$E = \pm\left[\frac{g'\beta H'}{2} \pm \tfrac{1}{4}(A_{xz}^2+A_{yz}^2+A_{zz}^2)^{1/2}\right] \quad (4)$$

where quantization is along $\bar{H}'$.

In order to evaluate the hyperfine term we define $\hat{\eta}'$ a unit vector along $\bar{H}'$, then

$$(A_{xz}^2+A_{yz}^2+A_{zz}^2)^{1/2} = |\hat{\eta}'\cdot\boldsymbol{A}| \quad (5)$$

since the g factor variation is quite small, the angle between $\bar{H}'$ and $\bar{H}$ is small—less than 2° for the variation in g which we observe (2·002 to 2·055). Therefore if $\hat{\eta}$ is a unit vector along $\bar{H}$

$$|\hat{\eta}'\cdot\boldsymbol{A}| \approx |\hat{\eta}\cdot\boldsymbol{A}| \quad (6)$$

and the hyperfine structure term is essentially independent of the g factor variation.

The analysis proceeds by extracting the g factor variation from the three sets of data, diagonalizing the $\boldsymbol{g}$ tensor to determine its principal axes and values, and independently extracting the hyperfine structure data and determining the principal axes and values of the $\boldsymbol{A}$ tensor. The analytical methods[6] of diagonalizing the $\boldsymbol{g}$ tensor are of little use in this case because the roots of the third degree equation in g are practically equal and accuracy is lost in the calculation. A method involving the projection of the three sets of data by means of a stereographic net was used to obtain the principal values and axes of both tensors.

The $\boldsymbol{g}$ tensor was found to have axial symmetry so that in a co-ordinate system in which $\boldsymbol{g}$ is diagonal the usual form is obtained.

$$E = \pm\frac{\beta H}{2}(g_{\parallel}^2\cos^2\theta+g_{\perp}\sin^2\theta)^{1/2} \quad (7a)$$

where θ is the polar angle measured from the symmetry axis of $\boldsymbol{g}$. The $\boldsymbol{A}$ tensor exhibited, in some cases, a small deviation from axial symmetry so that it should be of the form

$$\pm\tfrac{1}{4}(A_{xx}^2\sin^2\theta'\cos^2\phi'+A_{yy}^2\sin^2\theta'\sin^2\phi'+ +A_{zz}^2\cos^2\theta')^{1/2} \quad (7b)$$

where θ' is the polar angle measured from the z direction and ϕ' is the azimuthal angle measured from the x direction. Thus it is $g_{\parallel}$, $g_{\perp}$, A_{xx}, A_{yy} and A_{zz} as well as the polar and azimuthal angles of the unique or symmetry axes of the two tensors which one should obtain from the experimental data. Only the magnitudes, but not the signs of the components of the $\boldsymbol{A}$ tensor can be determined in this manner.

The purpose of the analysis has been to determine the nature and the location of the paramagnetic center and an attempt has been made to express the results in terms of the separation of the proton and the center. Thus for the case of an axially symmetric hyperfine structure interaction, the hyperfine term (equation (7b)) has been further fitted to a Hamiltonian

$$\mathcal{H}_{hfs} = g_e g_n\beta_e\beta_n\left(-\frac{\bar{S}\cdot\bar{I}}{r^3}+\frac{3\,\bar{S}\cdot\bar{r}\,\bar{r}\cdot\bar{I}}{r^5}+ +a\bar{S}\cdot\bar{I}\right) \quad (8)$$

where the first two terms are the dipole–dipole terms and the last term has been added to take account of a possible isotropic interaction.

Equating this to the $\boldsymbol{A}$ tensor and observing that $\bar{r}$ lies along the z axis we have

$$A_{xx} = A_{yy} = g_n\beta_n[-1/r^3+a] \quad (9a)$$

$$A_{zz} = g_n\beta_n[2/r^3+a] \quad (9b)$$

in gauss.

Furthermore

$$A_{zz}-A_{xx} = g_n\beta_n\,3/r^3 \quad (10a)$$

$$A_{zz}+2A_{xx} = g_n\beta_n 3a \quad (10b)$$

It is interesting to note that by adding this further condition that the dipole–dipole plus isotropic terms do represent the hyperfine interaction, the signs of the components of the $\boldsymbol{A}$ tensor can be determined. The right hand side of equation (10a) is positive and if $|A_{xx}|>|A_{zz}|$, A_{xx} will be negative. The sign of A_{zz} will be the same as that of A_{xx} unless the hyperfine lines cross as they do in the calcium sulfate (Fig. 9). Having already obtained the direction of the line of interaction from the orientation of the $\boldsymbol{A}$ tensor, we may now evaluate r, the separation between the proton and the

Vol. 17
1960

center. The orientation of the unique axis of the g tensor gives information about the direction of the crystalline electric field but is not simply related to an interaction vector as is A to $\vec{r}$.

RESULTS AND DISCUSSION

$Li_2SO_4 \cdot H_2O$

Lithium sulfate monohydrate is a monoclinic crystal having a space group C_2^2-$P2_1$. The dimensions of the unit cell, which contains two molecules, are $a = 5{\cdot}43$ Å, $b = 4{\cdot}84$ Å and

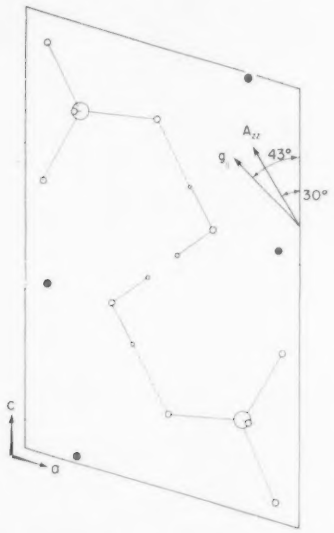

FIG. 4. Projection of the crystal structure of $Li_2SO_4 \cdot H_2O$ onto the (010) plane.
Lithium ⊙ Oxygen ○
Sulfur ◯ Proton ○

$c = 8{\cdot}14$ Å with the angle between the a and c directions $\beta = 107°$. Since, in the monoclinic class there are only two orthogonal axes, an axis perpendicular to the plane containing the b and c axes was chosen as the third one for the purpose of taking data. This was the first crystal which was investigated, and it was by means of the deuteration that the suggestion arose of associating with each molecule of the unit cell a single spin $\frac{1}{2}$ center which interacted with a proton in the water of hydration. The resonance data in conjunction with the crystallographic data made it possible to assign the center to a modified bond localized on that oxygen of the sulfate group which was hydrogen bonded by the water proton. In Figs. 4 and 5 this system is indicated by a dotted line.

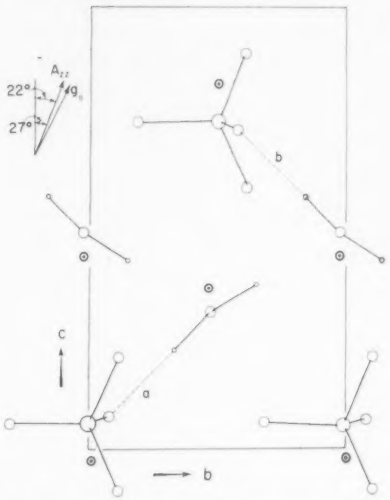

FIG. 5. Projection of the crystal structure of $Li_2SO_4 \cdot H_2O$ on the plane containing the b and c axes. The values given in Table 1 correspond to the "a" center.

Some of the qualitative features of the data (Figs. 1, 2 and 6) may be compared with the crystal structure. It is seen that for the b-axis rotation the two centers are equivalent giving the pair

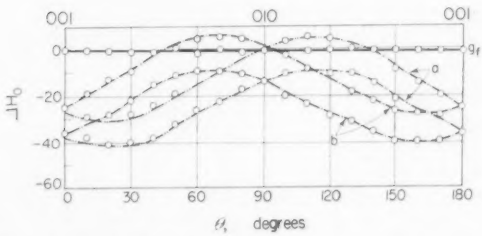

FIG. 6. Angle dependence of the resonance lines in $Li_2SO_4 \cdot H_2O$ for rotation about an axis perpendicular to the plane containing the b and c axes.

of lines of the data, while for the rotation about the axis perpendicular to the bc plane there are two centers for which the maximum or minimum in the hyperfine splitting should be approximately 70° apart; again the data indicates just this.

Crystallographic and nuclear magnetic resonance data give 2·65 Å for the separation of the sulfate oxygen and the water oxygen and 0·98 Å is the accepted value for the proton–water oxygen distance leaving 1·67 Å for the distance between the proton and the sulfate oxygen. The A tensor, from which we must determine r, shows deviations from axial symmetry which can be explained qualitatively as due to an additional hyperfine interaction due to the nearest lithium nucleus.

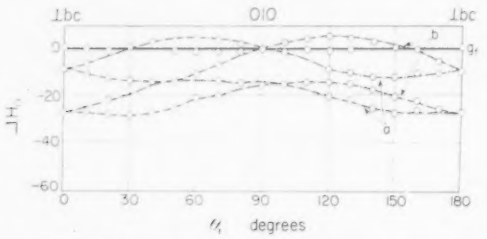

FIG. 7. Angle dependence of the resonance lines in $Li_2SO_4 \cdot H_2O$ for rotation about the (001) axis.

If we consider this to be an independent tensor interaction then its z-axis is approximately perpendicular ($\sim 80°$) to that of the proton interaction so that a correction to the observed data is possible based on the following argument. The unresolved hyperfine structure ($I = 3/2$) causes a shift in the mean value of the observed lines which is approximately one-third the splitting caused by the proton. Since the two interaction tensors lie approximately at right angles, the experimentally observed values of A_{ii} can be considered to be made up of two terms, a proton term having $A_{xx} = A_{yy} = -16$ G and $A_{zz} = +1$ G; and a lithium term with $A_{xx} = A_{yy} = -5$ G and $A_{zz} = 0$ G. Using these numbers one would obtain for the equivalent experimental values $-16-0 = -16$, $-16-5 = -21$ and $1-5 = -4$, which compare very well with the observed values. Similarly a calculation of r using the proton numbers gives $r = 1{\cdot}7 \pm 0{\cdot}1$ Å. One should note that the direction of the z-axis of the proton tensor depends very critically on the presence of this second interaction and that the direction obtained from the stereographic projection is not as accurate in this case as in the other two. Since all of the g values are greater than the free electron value, one attributes the

Table 1. *Results obtained for* $Li_2SO_4 \cdot H_2O$

$g_\parallel = 2{\cdot}040 \pm 0{\cdot}001$
$g_\perp = 2{\cdot}002 \pm 0{\cdot}001$

Polar angle 47° from (001)
Azimuthal angle 61° from (010)
$A_{xx} = -21 \pm 1$ G
$A_{yy} = -16 \pm 1$ G
$A_{zz} = -\ 4 \pm 1$ G

Polar angle 32° from (001)
Azimuthal angle 65° from (010)
$r = 1{\cdot}7$ Å*
$a = 11$ G*

* Corrected for estimated lithium nucleus interaction.

paramagnetism to a hole strongly localized on the sulfate oxygen.

It appears, then, that in the lithium sulfate we are able to assign the strong lines to two centers, one a trapped electron exhibiting a free electron g

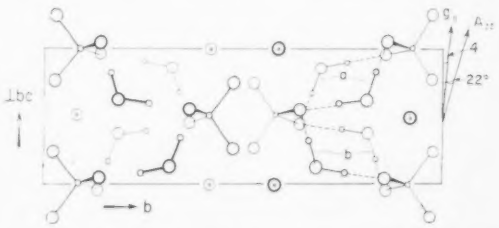

FIG. 8. Projection of the crystal structure of $CaSO_4 \cdot 2H_2O$ onto the [100] plane. The values given in Table 2 correspond to the "a" center.

Calcium ⊙ Oxygen ○
Sulfur ○ Proton ○

value, the other a hole localized on the hydrogen bonded oxygen. The weak line has not been identified in part because the strong lines, which are all about 8 G wide, mask the weak line for certain orientations making the analysis difficult. This line width is probably due to unresolved hyperfine structure from the remaining protons and lithium nuclei.

$CaSO_4 \cdot 2H_2O$ (*gypsum*)

Gypsum is also a monoclinic crystal with space group $C_{2h}^6 - B2/b$ having $a = 5{\cdot}68$ Å $b = 15{\cdot}18$ Å, $c = 6{\cdot}52$ Å and $\beta = 118°$, containing four molecules in the unit cell. This being a dihydrate

Vol. 17
1960

there are four hydrogen bonded oxygens of the type identified in the lithium sulfate, each one bonded to two protons. Fig. 8 indicates that these occur as pairs of essentially equivalent oxygens so that there should be two non-equivalent centers each interacting with two non-equivalent protons. The angle dependence of the resonance lines taken for rotation about the *c* axis (Fig. 9) shows, in

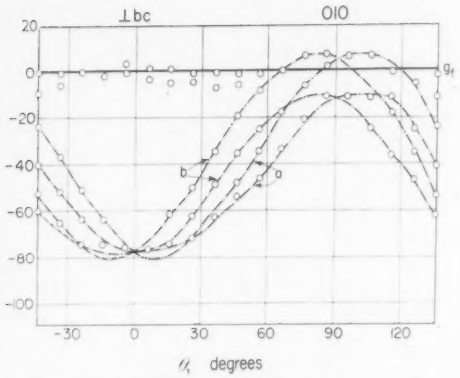

FIG. 9. Angle dependence of the resonance lines in $CaSO_4 \cdot 2H_2O$ for rotation about the (001) axis.

addition to a single isotropic line at the free electron *g* value, that there are two non-equivalent centers each exhibiting a hyperfine structure due to a single proton. Data for the rotation about the other two orthogonal axes indicates the same resonance lines. In addition, all three rotations exhibit a rather poorly resolved group of weak lines all of which are located near the free electron *g* value.

The analysis of the data carried out in a manner similar to the lithium sulfate case gives the computed values of Table 2 for one of the centers—the other is imaged in a mirror plane perpendicular to the *b* axis. The results indicate that for these two centers the paramagnetic entity is a hole with properties very much like those of the center in lithium sulfate and gives strong confirmation to the analysis and identification of the center in that case. There still remains the question of what happened to the other proton which should have given a further hyperfine interaction. There are several possibilities, but we are not prepared to choose between them.

Table 2. Results obtained for $CaSO_4 \cdot 2H_2O$

$g_{\parallel}$	$= 2{\cdot}051 \pm 0{\cdot}001$
$g_{\perp}$	$= 2{\cdot}003 \pm 0{\cdot}001$
Polar angle 10° from (⊥ bc)	
Azimuthal angle 22° from (001)	
A_{xx}	$= -17 \pm 1$ G
A_{yy}	$= -17 \pm 1$ G
A_{zz}	$= 2 \pm 1$ G
Polar angle 28° from (⊥bc)	
Azimuthal angle 26° from (001)	
r	$= 1{\cdot}6$ Å
a	$= 10{\cdot}6$ G

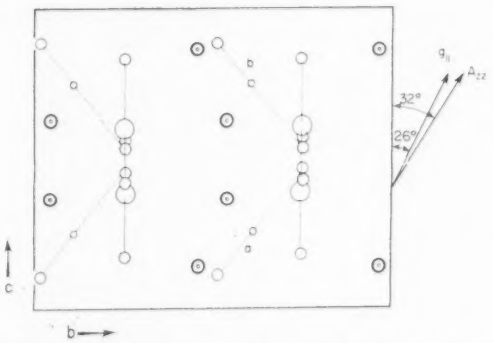

FIG. 10. Projection of the crystal structure of $Na_2CO_3 \cdot H_2O$ onto the [100] plane. The values given in Table 3 correspond to the "*a*" center.

Sodium ⊙ Oxygen ○
Carbon ◯ Proton ○

$Na_2CO_3 \cdot H_2O$

In order to further verify the analysis and, in particular, to apply it to a system in which the proton positions were not so well known, data was taken on sodium carbonate monohydrate. This is a rhombohedral crystal with space group $C_{2v}^5 - P_{ba}$ having $a = 10{\cdot}72$ Å, $b = 6{\cdot}44$ Å and $c = 5{\cdot}24$ Å with four molecules in the unit cell.[7] Figs. 10, 11 and 12 show that pairs of these are equivalent for all rotations so that we should expect two non-equivalent centers. The data (Figs. 13 and 14) indicate that there are two such centers and further that the "isotropic free electron" line is shifted to $g = 2{\cdot}009$ and shows slight

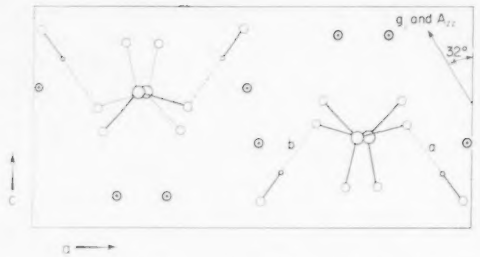

FIG. 11. Projection of the crystal structure of $Na_2CO_3 \cdot H_2O$ onto the [010] plane.

splitting into two components. In this case the position of the protons has not been investigated using either nuclear magnetic resonance or neutron diffraction as in the other two cases but

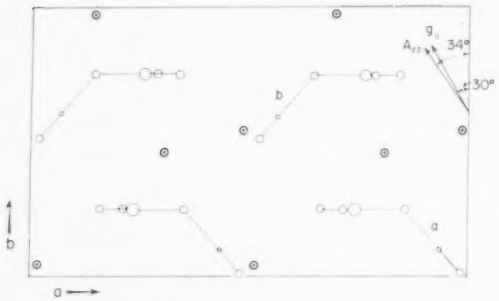

FIG. 12. Projection of the crystal structure of $Na_2CO_3 \cdot H_2O$ onto the [001] plane.

the crystal structure has been accurately determined. The distance from the water oxygen to the nearest neighbor carbonate oxygen is 2·7 Å so that this is probably the hydrogen bonded group.

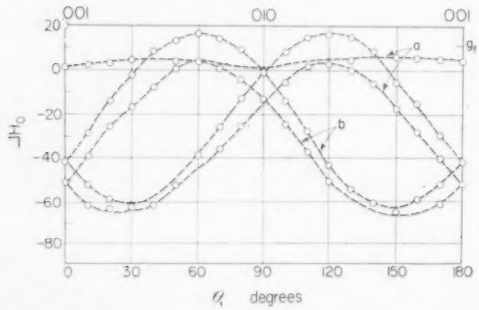

FIG. 13. Angle dependence of the resonance lines in $Na_2CO_3 \cdot H_2O$ for rotation about the (100) axis.

The analysis of our data gives an A tensor having its unique axis along this bond and gives $r = 1{\cdot}6$ Å (Table 3).

Thus here too the center which is described by a hole localized on the hydrogen bonded oxygen of the oxyion group appears. The slight shift and

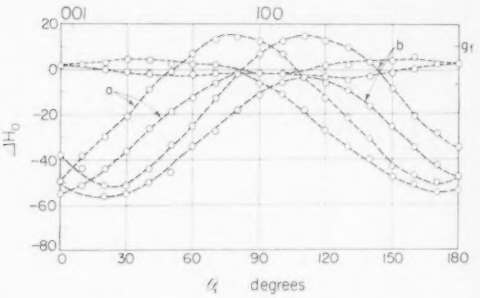

FIG. 14. Angle dependence of the resonance lines in $Na_2CO_3 \cdot H_2O$ for rotation about the (010) axis.

Table 3. Results obtained for $Na_2CO_3 \cdot H_2O$

$g_\parallel = 2{\cdot}055 \pm 0{\cdot}001$
$g_\perp = 2{\cdot}002 \pm 0{\cdot}001$

Polar angle 37° from (001)
Azimuthal angle 28° from (010)

$A_{xx} = -20 \pm 1$ G
$A_{yy} = -20 \pm 1$ G
$A_{zz} = 0 \pm 1$ G

Polar angle 48° from (001)
Azimuthal angle 34° from (010)

$r = 1{\cdot}6$ Å
$a = 13{\cdot}3$ G

splitting of the "isotropic" line probably is due to a trapping of the electrons at a site somewhat different than that in the other two cases—there is no reason for this trap to always show essentially free electron characteristics.

Acknowledgements—We wish to thank the Agricultural Engineering Department for the irradiation, in particular Professors R. NICHOLAS and D. WIANT and Mr. A. STEWART. We would also like to acknowledge many fruitful discussions with Drs. R. D. SPENCE and P. M. PARKER.

Vol. 17
1960

REFERENCES

1. LARSON A. C. and HELMHOLZ L., *J. Chem. Phys.* **22,** 2149 (1954).
2. SOUTIF M., DREYFUS B. and AYANT Y., *C.R. Acad. Sci., Paris* **233,** 395 (1951).
3. PAKE G. E., Thesis, Harvard (1948).
4. HARAHIRA E. and MURAKAMI M., *J. Phys. Soc., Japan.* **2,** 239 (1956).
5. ATOJI M. and RUNDLE R.E., *J. Chem. Phys.* **29,** 1306 (1958).
6. GEUSIC J. E. and BROWN L. C., *Phys. Rev.* **112,** 64 (1958).
7. *Strukturbericht* **4,** 42 (1936).

J. Phys. Chem. Solids Pergamon Press 1960. Vol. 17, Nos. 1/2, pp. 34–43. Printed in Great Britain.

ELECTRICAL PROPERTIES OF GaSb–InSb ALLOYS

J. C. WOOLLEY and C. M. GILLETT

Department of Physics, University of Nottingham, England

(*Received* 12 *April* 1960; *revised* 12 *May* 1960)

Abstract—Reasonably homogeneous, polycrystalline, solid ingots of GaSb–InSb alloys have been produced by slow directional freezing techniques, and have been used to investigate the variation of electrical properties as a function of composition. Values of extrapolated thermal energy gap E_0, electron mobility, and mobility ratio have been determined for some 25 specimens covering the complete composition range. Estimates have been made of the variation of effective mass values and, by comparison with optical energy gap values, of the energy gap temperature coefficient β. From the variation of mobility with temperature, values of mobility temperature exponent x have been obtained.

At the InSb-rich end of the composition range, the results indicate a smooth variation of the various parameters with composition, without any appreciable change in the band structure from that of InSb. The results at the GaSb-rich end of the range are complicated, firstly by the presence in GaSb of two conduction bands of only small energy separation, and secondly by an effect which extends over a considerable range of composition and is thought probably to be due to ordering in the alloys. As a result, correlation of the optical and electrical results is difficult in this range of composition.

Vol. 17
1960

INTRODUCTION

CONSIDERABLE work has been carried out to determine the available composition range of semiconductor alloys produced by solid solution beween two semiconducting compounds each having the zinc blende structure.[1,2,3,4,5] Information is now becoming available on the electrical properties of some of these alloys, but in many cases the data is limited. Electrical measurements have been reported on the following alloy systems: InAs–InP[1] GaAs–InAs,[6] CdTe–ZnTe,[5] CdTe–HgTe,[7] GaAs–Ga_2Se_3,[8] AlSb–GaSb,[9] InSb–In_2Te_3.[10] In a recent paper, IVANOV-OMSKII and KOLOMIETS[11] have reported electrical measurements on the equimolecular alloy of the GaSb–InSb system. The present authors have recently investigated the variation of optical energy gap as a function of composition for alloys of the GaSb–InSb system.[12] The present paper reports an investigation of the electrical properties of these alloys.

PREPARATION OF SPECIMENS AND METHODS OF MEASUREMENT

Each of the two compounds concerned was first prepared separately, by melting together under vacuum the appropriate amounts of the elements. The elements used were all of 99·999 per cent purity, and in the case of InSb the compound was further purified by normal zone refining methods.

The alloys were produced by the slow directional freezing technique described previously,[12] and in order to obtain the required range of composition three ingots were used, these having approximate mean compositions of (A) 70 mol. per cent GaSb, 30 mol. per cent InSb (B) 30 mol. per cent GaSb, 70 mol. per cent InSb and (C) 10 mol. per cent GaSb, 90 mol. per cent InSb respectively. Sections from various points on these ingots provided specimens covering practically the whole range of composition in the alloy system, i.e. from InSb to 94 mol. per cent GaSb, and the degree of homogeneity of these specimens was the same as that of the specimens used previously in the optical work.[12] As indicated in that case, some inhomogeneity still remains however. To cover the range of composition from 94–100 mol. per cent GaSb, ingots of the appropriate compositions were made up and annealed at 520°C for 4 weeks. Some of these were rather less homogeneous than the specimens produced by directional freezing however and only one of them was used in the measurements described below.

For the electrical measurements, specimens were cut from cross sections of the directionally frozen ingot, and for each composition measurements were made to determine the values of Hall coefficient R_H and conductivity σ as a function of temperature in the range

90–850°K. The specimens were cut to the approximate dimensions $7\times1\times1$ mm. and were lightly etched in CP-4 etchant before attaching the electrical contacts. For the measurements below room temperature, the current electrodes and a copper–constantan thermocouple were soldered (using high purity indium solder) to the ends of the specimen, and the potential and Hall probes spot welded to the specimen in the normal positions. In the case of the high temperature measurements, the potential and Hall probes were again spot welded to the specimen but the current connections were made by pressure contacts, and the temperature determined by a Pt/PtRh thermocouple, the hot junction of which was held close to the specimen. Specimen currents of up to 60 mA were used, and all voltages were measured by means of a potentiometer accurate to 1μV. Magnetic fields of up to 6 kOe were provided by an electromagnet. During each set of observations at a given temperature, the temperature was held constant to $\pm$ 1°C.

CALCULATION OF PARAMETER VALUES

As shown below, the large majority of specimens used were p-type in the impurity range, and in the temperature range investigated each of these showed a transition from p-type to n-type behaviour as intrinsic effects began to predominate. Thus the simple single carrier formulae for R_H and σ could not be used and the more accurate equations had to be used to determine the variation of electron and hole densities (n and p) and of electron mobility μ_n as a function of temperature.

When carriers of both signs are present, the standard equations for R_H and σ are

$$R_H = \frac{r}{e}\frac{nb^2-p}{(nb+p)^2} \tag{1}$$

$$\sigma = e\mu_n(n+p/b) \tag{2}$$

where for p-type material

$$p = n+p_e \tag{3}$$

and

$$b = \mu_n/\mu_p,$$

p_e being the resultant hole density due to impurities.

Here the value of the Hall coefficient ratio r has been taken as unity. From equations (1) and (3)

$$n = \frac{1}{2e}\frac{(b-1)}{(b+1)}\frac{1}{R_H} - \frac{p_e}{b+1} \pm \pm \frac{1}{b+1}\left\{\frac{(b-1)^2}{4R_H^2e^2} - \frac{p_eb}{R_He}\right\}^{1/2} \tag{4}$$

If it is assumed that at low temperature the intrinsic contribution is negligible so that

$$R_{H\,\mathrm{ext}} = \frac{1}{p_ee} \tag{5}$$

then it is readily shown that

$$\frac{R_{H\max}}{R_{H\,\mathrm{ext}}} = \frac{(b-1)^2}{4b} \tag{6}$$

where $R_{H\max}$ is the maximum value attained by R_H above the Hall inversion temperature. From equations (4), (5) and (6), the variation of n can be determined as a function of temperature.

Standard theory gives the equation

$$\frac{np}{T^3} = A(m_n^*m_p^*)^{3/2}\exp\left(-\frac{E_g}{kT}\right)$$

and assuming $E_g = E_0+\beta T$ in the temperature range considered, and that m_n^* and m_p^* are independent of T

$$\log_{10}\frac{np}{T^3} = \log_{10}A + \frac{3}{2}\log_{10}(m_n^*m_p^*) - \frac{E_0}{2{\cdot}303\,kT} - \frac{\beta}{2{\cdot}303\,k} \tag{7}$$

Hence the slope of the graph of $\log_{10}np/T^3$ vs. $1/T$ gives E_0. Combining this value of E_0 with the room temperature value of E_g from optical work enables a value of the coefficient b to be estimated. Then assuming parabolic bands so that $A = 4(2\pi k/h^2)^3$, the intercept of the $\log_{10}np/T^3$ vs. $1/T$ graph gives a value for $(m_n^*m_p^*)^{1/2}$. If spherical energy surfaces and lattice scattering are assumed, then

$$b = \frac{\mu_n}{\mu_p} = \left(\frac{m_p^*}{m_n^*}\right)^{5/2} \tag{8}$$

and hence m_n^* and m_p^* can be calculated. Although these assumptions can not be accurately applied to the present materials, the results can be used to give an indication of the probable variation of effective mass values.

Finally from equations (2) and (3)

$$\mu_n = \left\{\sigma\Big/ne\left(1+\frac{1}{b}\right)+\frac{ep_e}{b}\right\} \tag{9}$$

and assuming $\mu_n \propto T^{-x}$, a graph of $\log\mu_n$ vs. $\log T$ enables a value of x to be determined.

RESULTS AND DISCUSSION

(a) *Results of Hall measurements*

The variation of R_H as a function of temperature for various typical specimens is shown (on a log scale) in Fig. 1 and the curves are seen to be those characteristic of materials with predominant p-type impurity. As the temperature is increased from the liquid oxygen temperature, some decrease in R_H and hence increase in p_e occurs, due

to finite activation energy of impurities, but in most cases the curve levels out before the Hall inversion temperature is reached, and in each case the value of R_H in this range has been taken as

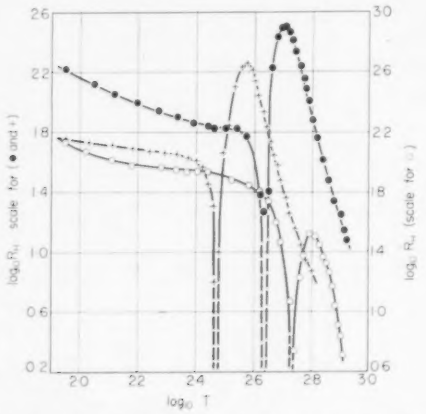

FIG. 1. $\log_{10}R_H$ vs. $\log_{10}T$ for various typical specimens
+ 24 mol. per cent GaSb, 76 mol. per cent InSb
● 76 mol. per cent GaSb, 24 mol. per cent InSb
○ GaSb

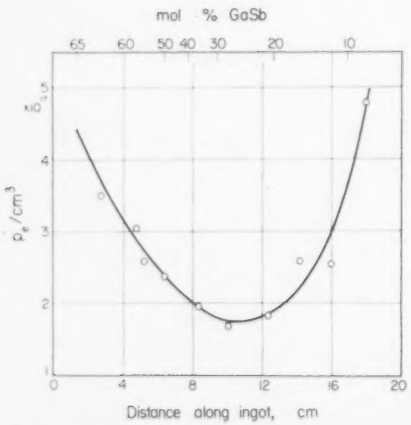

FIG. 2. Variation of p_e with position along ingot B (mean composition 30 mol. per cent GaSb, 70 mol. per cent InSb).

$R_{H\text{ext}}$ required in equations (5) and (6). These extrinsic range values of R_H showed that two of the three directionally frozen ingots, viz. A and B were p-type along the complete length of the ingot, while the third, C, which contained only 10 mol. per cent GaSb mean composition, was n-type along the whole length. The variation of p_e with position along the length of ingot B is shown in Fig. 2, the variation of composition with position also being indicated. It is seen that the value of p_e reaches a minimum of $1{\cdot}7\times10^{17}/\text{cm}^3$ near the centre of the ingot and reaches values between 4 and $5\times10^{17}/\text{cm}^3$ at each end. The form of this curve is of interest as far as the behaviour of GaSb itself is concerned. It has been suggested[13] that the p-type character usually observed with GaSb could be due to non-stoichiometry in the compound, but recently BOLTAKS and GUTOROV[14] have claimed that the results in GaSb are due to the

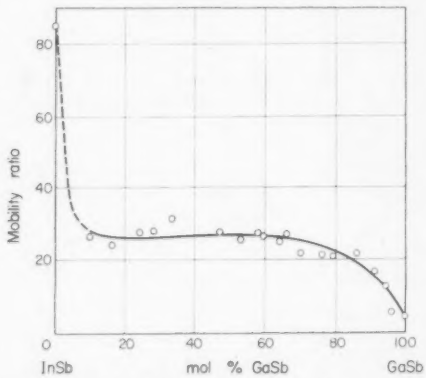

FIG. 3. Variation of mobility ratio b with composition.

presence of both donor and acceptor impurities with slightly different segregation coefficients. From the present results, it is seen that in the latter half of ingot B the value of p_e rises from $1{\cdot}7$ to $4{\cdot}8\times10^{17}/\text{cm}^3$ as the GaSb content falls from 30 to 10 mol. per cent. Since the InSb used for the alloy was n-type with less than 2×10^{16} donors/cm^3 and the GaSb was p-type with approximately 3×10^{17} acceptors/cm^3, it would appear impossible to explain the variation of p_e along ingot B by non-stoichiometric behaviour. A plausible explanation can only be produced by postulating the presence of both p- and n-type impurities having segregation coefficients which are different one from the other and which vary along the length of the ingot as the composition varies. The variation of p_e with position along ingot A and n_e along ingot C further support this suggestion.

Vol. 17
1960

From the results of R_H vs. temperature on the p-type specimens a value of the mobility ratio b can be obtained immediately from equation (6). The use of specimens from ingots A and B thus enabled a value of b to be obtained for all alloy compositions except those in the range 0–10 mol. per cent GaSb where only n-type specimens were obtained. The resulting variation of b with composition is shown in Fig. 3. It is seen that the value drops very rapidly from 85 for InSb, being 27 at 10 mol. per cent GaSb, but then stays reasonably constant up to approximately 75 mol. per cent GaSb after which it falls again to the value of 4·5 for GaSb.

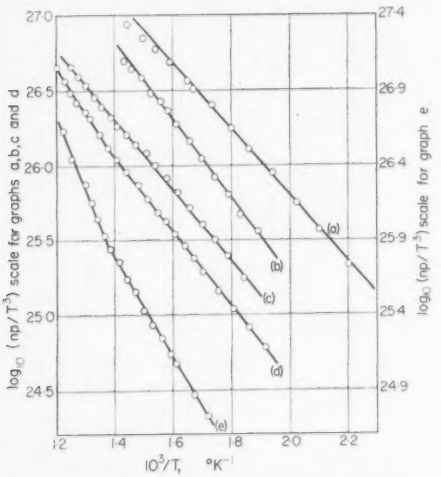

FIG. 4. $\text{Log}_{10} np/T^3$ vs. $10^3/T$ for typical alloy specimens.
(a) 47 mol. per cent GaSb, 53 mol. per cent InSb
(b) 64 mol. per cent GaSb, 36 mol. per cent InSb
(c) 70 mol. per cent GaSb, 30 mol. per cent InSb
(d) 76 mol. per cent GaSb, 24 mol. per cent InSb
(e) 91 mol. per cent GaSb, 9 mol. per cent InSb

Using the data from the Hall effect measurements and equations (4), (5) and (6), values of np/T^3 were calculated for each specimen and graphs of $\log np/T^3$ vs. $1/T$ plotted. Typical examples of these graphs are shown in Fig. 4. From equation (7) these should be straight lines with a slope dependent on E_0 and it is seen that the graphs are linear over a considerable range of temperature. Two points are illustrated by the graphs in Fig. 4. Firstly, graphs (a) and (b) for alloys of high InSb content, show some deviation from the straight line at high temperatures. This is due to the onset of degenerate behaviour, for which case the equations in Section 3 do not apply. Sufficient results are available at lower temperatures for a value of E_0 to be obtained. Secondly, graphs (d) and (e), which represent alloys of high GaSb content, are seen to divide into two parts, each being linear and hence giving a separate value of E_0. Thus for alloys of GaSb content higher than 70 mol. per cent, two values of E_0 were obtained, a low temperature and a high temperature value, and also a transition temperature T_c. The values of E_0 are plotted against composition in Fig. 5 and also the values of T_c over the range of composition where this is observed. On the question of the accuracy with which the two values of E_0 and the value of T_c can be determined, it is clear that whatever the mechanism causing this effect, there will be some transition range around T_c. Hence there will be some uncertainty in the value of T_c, and reasonable values of E_0 will only be obtained from results at temperatures well away from the transition range. From a study of the experimental results, it is estimated that the error in T_c will not be greater than 20°C. The lower value of E_0 (E_{01}) can be obtained with reasonable accuracy (say

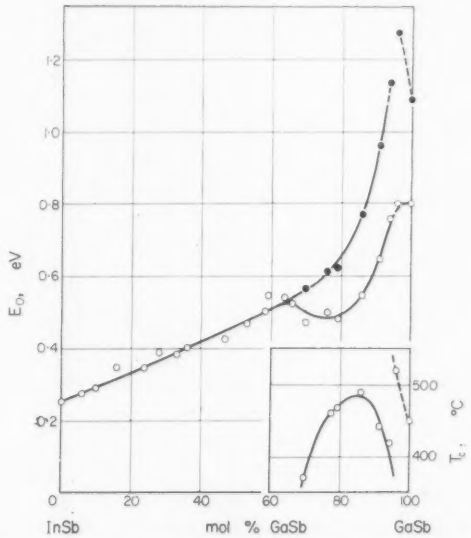

FIG. 5. Variation of extrapolated energy gap E_0 and transition temperature T_c with composition.

$\pm 0{\cdot}02$ eV) as measurements can be made at temperatures well below T_c, but the upper value of $E_0(E_{02})$ will probably be less accurate as a large temperature range above T_c cannot be used owing to the proximity of T_c to the melting point of the alloy. The variation of E_0 given above is to be compared with the corresponding variation of the optical energy gap E_g previously published,[12] but repeated here for convenience in Fig. 6.

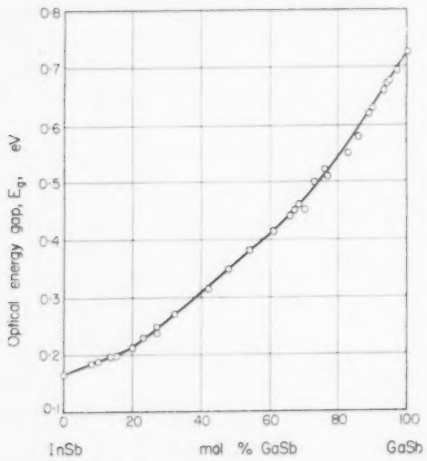

FIG. 6. Variation of room temperature optical energy gap E_g with composition.

If the values of E_{01} (Fig. 5) and the values of E_g (Fig. 6) are compared, estimates of the value of a mean temperature coefficient β for the temperature range from room temperature to approximately 400°C can be made. The variation of β as a function of composition is shown in Fig. 7. Although the experimental scatter is large, it is seen that β has an approximately constant value of -3 to -4×10^{-4} eV/°C except in the composition range 65–95 mol. per cent GaSb where it rapidly changes and takes positive values at some compositions. The value of β obtained in this way will depend on the value assumed for E_g, which in turn depends on the method used to interpret the optical data. For polycrystalline alloys of the type used here, this interpretation is somewhat arbitrary and as indicated previously[12] these particular values of E_g were obtained by determination of the apparent onset of transmission through specimens of about 100 μ thickness. Use of other conventions for interpreting optical data could give slightly different values for E_g, but should not greatly affect the shape of the E_g curve shown

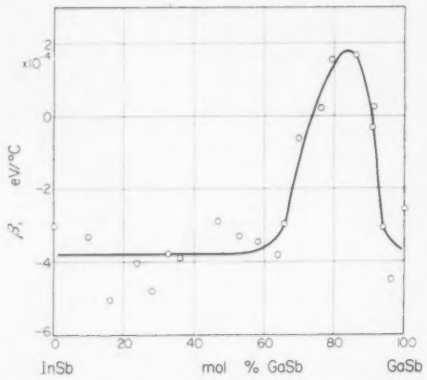

FIG. 7. Variation of energy gap temperature coefficient β with composition.

in Fig. 6. Changes in the form of the E_g curve would result in corresponding changes in the β curve in Fig. 7, but it appears probable that whatever method is used to obtain E_g from the optical

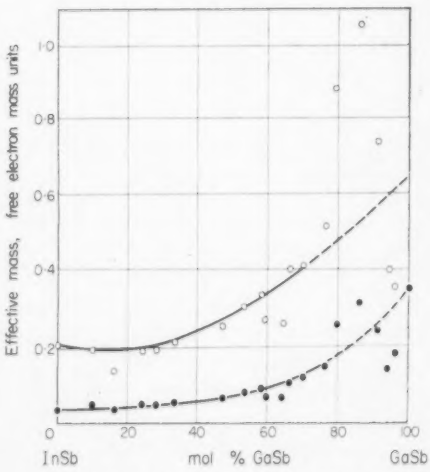

FIG. 8. Variation of m_n^* and m_p^* with composition ● m_n^* ○ m_p^*.

data, the peak in the β curve in the composition range 65–95 mol. per cent GaSb will still occur. It is hoped to carry out a more detailed investigation of the absorption edge of these alloys in the near future.

Vol. 17
1960

As indicated in Section 3, when β is known equations (7) and (8) allow the values of m_n^* and m_p^* to be estimated provided spherical energy surfaces etc. are assumed. While these assumptions may not be accurately true here, it is of interest to observe the form of the variation of these parameters with composition, and these are shown in Fig. 8. Again a continuous trend in the values from InSb to GaSb is observed except for fluctuations in the composition range of anomalous behaviour.

(b) *Discussion of Hall measurement results*

In Fig. 5 the value of E_0 shows a practically linear variation with composition up to approximately 65 mol. per cent GaSb but at this point the graph splits into two parts. From a consideration of the work of SAGAR[15] the two values of E_0 for GaSb itself can be attributed to two different minima in the conduction bands. SAGAR has suggested that at room temperature GaSb has its lowest conduction band minimum at the centre of the Brillouin zone but that a further set of minima occur at a slightly higher energy and along the [111] directions in k space. The energy separation of the minima at room temperature is estimated to be approximately 0·08 eV with a rate of change with temperature of

$$\frac{d}{dt}(\Delta E) \approx -3\times10^{-4}\ \text{eV/°C}.$$

This interpretation is confirmed by the work of KEYES and POLLAK[16]. The present work indicates that the reduction in energy separation with temperature continues at higher temperatures and that the [111] minima fall in energy below the (000) minimum at temperatures above 450°C. Assuming from Fig. 6 a value of 0·72 eV as the room temperature value of E_g for GaSb, the values of E_0 from Fig. 5 can be used to determine the values of the temperature coefficients β for the two types of minima proposed, assuming that the two have the same energy at 450°C. The resulting values of β are -3×10^{-4} eV/°C for the low temperature E_0 and -7×10^{-4} eV/°C for the high temperature E_0, giving a difference ($\Delta\beta \equiv d/dt(\Delta E)$) of -4×10^{-4} eV/°C in reasonable agreement with the value given by SAGAR. The room temperature energy separation of the minima calculated on this basis (0·17 eV) is rather different from SAGAR's value, however.

When comparing these values, it should be borne in mind that in obtaining the value of 0·17 eV, it has been assumed that the variation of energy gap with temperature can be treated as strictly linear over the whole range of temperature from room to 600°C. While it is true that such a linear variation is a valid approximation over a limited range of temperature, e.g. 250°C–450°C, a typical range over which electrical measurements were made to obtain E_0, and hence that the measured E_0 values are truly characteristic of the electrical behaviour in that range of temperature, it is by no means certain that this assumption of linear behaviour can be applied over much larger temperature ranges.[17] This fact, in addition to the inaccuracy in the value of E_{02}, could easily explain the discrepancy in the estimated values for the energy separation of the band minima of GaSb at room temperature.

As a further check that the change in E_0 was not in fact caused by some structural effect such as a phase change, powder photographs were taken of GaSb at 560°C. No change could be detected in the high temperature photographs as compared with similar photographs at room temperature except the usual small change in Bragg angle of the lines due to thermal expansion. This observed change allowed a calculation to be made of the mean linear expansion coefficient of GaSb over this range, and a value of $7\pm1\times10^{-6}$/°C was obtained.

When the GaSb–InSb alloys are considered it is of interest to see whether the two values of E_0 can again be attributed to different conduction band minima as in the case of GaSb. For various reasons this does not appear to possible. One point is that the two E_0 curves appear to coalesce at about 65 mol. per cent GaSb and that for alloys of lower GaSb content only one value of E_0 is observed, a behaviour which would appear very unlikely if two band minima were being observed. A second point comes from the variation of the transition temperature T_c with composition (Fig. 5). It is seen that as InSb is added to GaSb the value of T_c increases to 520°C at 96 mol. per cent GaSb, but at 94 mol. per cent GaSb the observed value of T_c has fallen to 420°C and as further InSb is added it rises to a maximum and then falls

again. Such a variation would seem to indicate that the values of T_c are being determined by more than one process.

Initially, in order to explain the energy gap values, a band change similar to that in the Ge–Si alloys was considered, i.e. a variation of the relative energies of different band minima with composition, so that room temperature values would indicate one band minimum in one composition range and another band minimum at other compositions. This appears to be ruled out, if as seems to be generally accepted,[15,18] the room temperature band structures of GaSb and InSb are of the same type with the lowest minimum in the conduction band occurring at $k = 0$. Moreover, it would not be possible to explain the form of the room temperature optical energy gap results (Fig. 6) in terms of such a band change.

Thus to explain the variation of E_0 and T_c with composition over the alloy range 65–95 mol. per cent GaSb, some effect must be postulated other than the change of lowest band minimum with composition as seen with Ge–Si alloys or the change of lowest band minimum with temperature as shown by GaSb and alloys within a few per cent of this composition, as neither of these effects would appear to be satisfactory over the alloy range 65–95 mol. per cent GaSb. One explanation which is suggested by various experimental results is that of ordering of the gallium and indium atoms in the lattice. In such a case, up to 94 mol. per cent GaSb, the value E_{01} would apply to the minimum band gap in the ordered structure, and the value E_{02} to the minimum band gap in the disordered structure, T_c representing the ordering temperature. The following points can be quoted as supporting this:

(a) The form of the T_c vs. composition curve between 70 and 94 mol. per cent GaSb is typical of the variation of ordering temperature with composition.

(b) The form of the low temperature E_0 curve in this composition range is similar to that observed in systems where ordering occurs.[19]

(c) If the graph of lattice parameter with composition for this alloy system[2] is investigated as accurately as is possible with the present alloys, it is found to show small deviations from the Vegard line, but to intersect that line at an approximate composition of 75 mol. per cent GaSb. It has been shown[20] that such an intersection can indicate the possibility of ordering in the vicinity of that composition.

(d) The form of the solidus of the alloy system[21] indicates that the solid solution is not ideal in the composition range considered.

To check this suggestion, specimens in this range of composition have been annealed at various temperatures above and below the possible ordering temperature given by T_c, and then X-rayed in the normal way. No definite origins of ordering have been observed, although this could be partly due to the poor X-ray photographs obtained, because of some degree of inhomogeneity in the specimens used, which with the present method of preparation cannot be avoided. This inhomogeneity could be important, for because of the low diffusion rates observed in these alloys,[2] the degree of long range order might be relatively small, and so any superlattice lines would be weak and diffuse. It is of interest to note that BRAUNSTEIN *et al.*[22] have postulated a short range ordering in Ge–Si alloys in order to explain optical absorption data. It is hoped to carry out further work on this question of ordering when better alloy specimens are available.

Thus it is seen from the above discussion that if ordering is postulated to explain the electrical results, this can only apply in the approximate composition range 65–94 mol. per cent GaSb, while the results for 96 mol. per cent GaSb and GaSb itself must be explained in terms of a band change. Thus the behaviour in the range 95–100 mol. per cent GaSb could be a more complicated form. Again, production of alloys in this range has proved somewhat difficult, but it is hoped to investigate this range more thoroughly with better alloy specimens.

(c) *Conductivity measurement*

In addition to Hall effect, the variation of conductivity with temperature was also observed for each alloy specimen. Typical curves of log σ against $1/T$ are shown in Fig. 9. These show the usual division into an intrinsic and extrinsic range. In order to compare the values for various alloys of different impurity content, the values of log σ in the intrinsic range have been extrapolated to room temperature to give an effective room temperature intrinsic conductivity. The variation

Vol. 17
1960

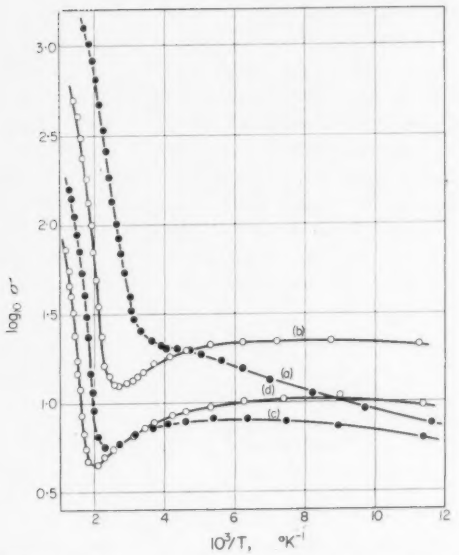

FIG. 9. $\text{Log}_{10}\sigma$ vs. $10^3/T$ for typical alloy specimens
(a) 10 mol. per cent GaSb, 90 mol. per cent InSb
(b) 47 mol. per cent GaSb, 53 mol. per cent InSb
(c) 76 mol. per cent GaSb, 24 mol. per cent InSb
(d) 94 mol. per cent GaSb, 6 mol. per cent InSb

of this value as a function of composition is shown in Fig. 10.

The measured values of σ were used to give the corresponding values of mobility, and in the extrinsic range the simple Hall mobility for one type of carrier $\mu = \sigma R_H$ has been used. As the high InSb content alloys are n-type, the room temperature results for these give μ_n, while with the large majority of the alloys, the extrinsic range results give a room temperature value for μ_p. For comparison purposes, these values of μ_p have been multiplied by the corresponding value of b, and Fig. 11 shows the resultant variation of μ_n with composition, the results from the two types of material being shown differently. It is seen that μ_n falls rapidly from the value for pure InSb, but levels out in the middle of the composition range at a value of the order 10^4 cm²/V sec, and then at high GaSb content falls again

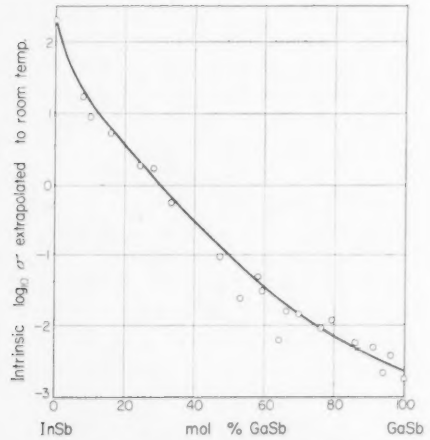

FIG. 10. Variation of intrinsic conductivity (extrapolated to room temperature) with composition.

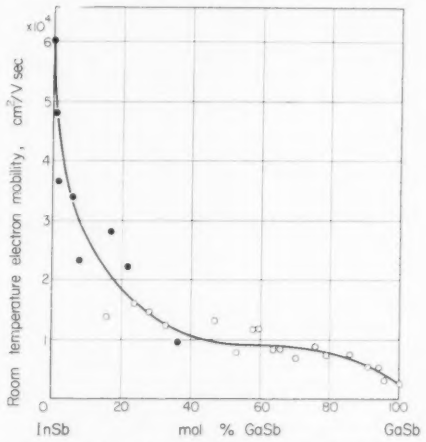

FIG. 11. Variation of room temperature electron mobility with composition ○ from p-type alloys ● from n-type alloys.

to the GaSb value. This form of curve is somewhat different from that which might be expected from simple alloy scattering theory, which would predict a minimum near 50 mol. per cent GaSb. However various other factors will influence the form of this curve, e.g. (i) the increase in effective mass as the GaSb content of the alloys is increased, (ii) the interband scattering which can be expected to occur with GaSb and alloys close to this composition, (iii) the effect on alloy scattering of any possible ordering in the alloys. Thus the simple curve showing a minimum at 50 per cent is not to be expected. For the p-type alloys, p_e lies in the range 8×10^{16} to $4{\cdot}5\times10^{17}/\text{cm}^3$, while the values of R_H for the n-type specimens give values of n_e

in the range 6×10^{15} to 3×10^{16}/cm^3. These latter specimens are probably compensated however, with a total impurity content comparable with that of the p-type material. Thus the mobility values quoted correspond to material of relatively high impurity content. It is probable however that with alloys of this type, the predominant scattering mechanism at room temperature is not impurity scattering but alloy scattering. This is considered further below.

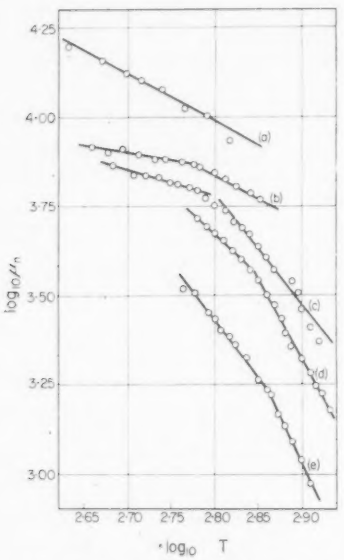

FIG. 12. $\text{Log}_{10}\mu_n$ vs. log T for typical alloy specimens
(a) 10 mol. per cent GaSb, 90 mol. per cent InSb
(b) 47 mol. per cent GaSb, 53 mol. per cent InSb
(c) 70 mol. per cent GaSb, 30 mol. per cent InSb
(d) 86 mol. per cent GaSb, 14 mol. per cent InSb
(e) 91 mol. per cent GaSb, 9 mol. per cent InSb

To obtain values of μ_n for temperatures greater than that corresponding to the peak in the R– vs. T curve, equation (9) has been used, and for each alloy the variation of log μ_n against log T determined. Typical results are shown in Fig. 12. In a large number of cases the log μ_n vs. log T graph divides into two linear sections of different slope with a small transition region between the two. Applying the relation $\mu\propto T^{-x}$ to these results, two values of x can be obtained for each specimen. The low temperature values of x (x_1) are shown plotted against composition in Fig. 13. There is considerable experimental scatter on the points, but a smooth curve can reasonably be drawn through them. This value of x_1 falls from 1·5 for InSb as GaSb is added, but over a range from 20–65 mol. per cent GaSb lies within the limits 0·8 to 1·0. This is to be compared with the values of x between 0·7 and 0·85, obtained by GLICKSMAN[23] for Ge–Si alloys, and the theoretical value of $x = 0{\cdot}5$ for alloy scattering given by NORDHEIM[24] and BROOKS[25]. It appears from this, that as indicated above, at these temperatures and in this range of composition the predominant scattering effect is that for alloy scattering. For alloys of GaSb content greater than 65 mol. per cent the

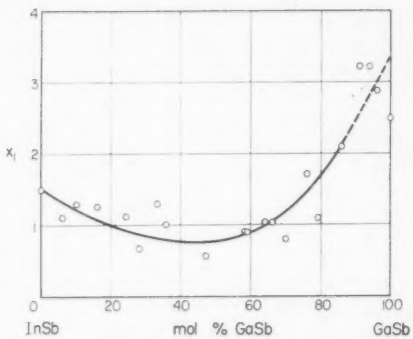

FIG. 13. Variation of mobility temperature exponent x_1 with composition (assuming that $\mu\propto T^{-x_1}$ at lower temperatures).

value of x_1 rises sharply, attaining values of 3·2 in the range 90–95 mol. per cent GaSb. Here the effects discussed previously appear to affect the scattering processes, but insufficient data is available for this to be discussed.

The high temperature values of x (x_2) are less definite, occurring near to the maximum temperature of measurement. Up to 60 mol. per cent GaSb however the value lies between 1·5 and 2·0 and would appear to correspond to a predominence of lattice scattering at the higher temperatures. For compositions with more than 60 mol. per cent GaSb, larger values of x_2 are obtained rising to a peak value of 5·8 between 90 and 95 mol. per cent GaSb. In this range, the scattering processes will be complicated by the effects discussed above, and little can be said about the values of x_2 at this

Vol. 17
1960

stage. The temperature range in which the transition from x_1 to x_2 occurs shows some correlation with the values of T_c given in Fig. 5, but the effect is more complicated than the transition observed in the graphs giving E_0.

Acknowledgements—The authors are indebted to Professor L. F. BATES for the facilities of his laboratory. The work described forms part of an investigation carried out for the Admiralty.

REFERENCES

1. FOLBERTH O. G., *Z. Naturf.* **10a,** 502 (1955).
2. WOOLLEY J. C. and SMITH B. A., *Proc. Phys. Soc. Lond.* **72,** 214 (1958).
3. WOOLLEY J. C. and SMITH B. A., *Proc. Phys. Soc. Lond.* **72,** 867 (1958).
4. HERMAN F., GLICKSMAN M. and PARMENTER R. H., *Progress in Semiconductors* Vol. II p. 17. Heywood, London (1957).
5. KOLOMIETS B. T. and MALKOVA A. A., *Zh. tekh. fiz., Mosk.* **28,** 1162 (1958).
6. ABRAHAMS M. S., BRAUNSTEIN R. and ROSI F. D., *J. Phys. Chem. Solids* **10,** 204 (1959).
7. LAWSON W. D., NIELSEN S., PUTLEY E. H. and YOUNG A. S., *J. Phys. Chem. Solids* **9,** 325 (1959).
8. NASLEDOV D. N. and FELTIN'SH I. A., *Soviet Physics—Solid State* **1,** 510 (1959–60).
9. BURDIYAN I. I. and KOLOMIETS B. T., *Soviet Physics—Solid State* **1,** 1067 (1959–60).
10. WOOLLEY J. C., GILLETT C. M. and EVANS J. A., *J. Phys. Chem. Solids* **16,** 138 (1960).
11. IVANOV-OMSKII V. I. and KOLOMIETS B. T., *Soviet Physics—Solid State* **1,** 512 (1959–60).
12. WOOLLEY J. C., EVANS J. A. and GILLETT C. M., *Proc. Phys. Soc. Lond.* **74,** 244 (1959).
13. DETWILER D. P., *Phys. Rev.* **97,** 1575 (1955).
14. BOLTAKS B. I. and GUTOROV YU. A., *Soviet Physics—Solid State* **1,** 930 (1959–60).
15. SAGAR A., *Phys. Rev.* **117,** 93 (1960).
16. KEYES R. W. and POLLACK M., Westinghouse Research Labs. Scientific Paper, 6–40602–3–P5 (1959).
17. ANTONCIK E., *Czech. J. Phys.* **5,** 449 (1955).
18. KANE E. O., *J. Phys. Chem. Solids* **1,** 249 (1957).
19. WOOLLEY J. C. and RAY B., *J. Phys. Chem. Solids* **15,** 27 (1960).
20. APTEKAR A. I. and FINKELSHTEIN B., *Zh. eksp. teor. fiz.* **21,** 900 (1951).
21. WOOLLEY J. C. and LEES D. G., *J. Less Common Metals* **1,** 192 (1959).
22. BRAUNSTEIN R., MOORE A. R. and HERMAN F., *Phys. Rev.* **109,** 695 (1958).
23. GLICKSMAN M., *Phys. Rev.* **111,** 125 (1958).
24. NORDHEIM L., *Ann. Phys.* **9,** 607 (1931).
25. BROOKS H., *Adv. in Electronics and Electron Physics,* **7,** 85 (1955).

J. Phys. Chem. Solids Pergamon Press 1960. Vol. 17, Nos. 1/2, pp. 44–51. Printed in Great Britain.

LIGHT SCATTERING BY NEUTRON IRRADIATED SILICA

R. D. MAURER

Corning Glass Works, Corning, N.Y.

(*Received* 2 *May* 1960)

Abstract.—The intensity of light scattered by fast neutron irradiated fused silica indicates that the damaged volume per primary struck atom is about (67 Å)³. There is dissymmetry of scattering showing that this small volume is strung out in a long thin, or rodlike, region in order to give interference effects. The angular dependence of scattering for the H_h and V_v components is different and can be accounted for by assuming that strain surrounds the damaged region. Theories of the strain scattering effect are developed to give a quantitative account of the scattering. These indicate how the angular dependence of scattering may be interpreted to discriminate between the effect of strain and the effect of the length of the rodlike regions. The length is found to be approximately 1800 Å.

INTRODUCTION

DESPITE the large amount of work performed with heavy particle damage in solids, little experimental information is available on the spatial distribution of damage resulting from a single primary struck atom. The intensity of scattered light gives information about the volume of these regions, while the angular dependence is a measure of their extent. On the other hand, little can be learned from light scattering about the atomic nature of the damage since imperfections or clusters of imperfections smaller than about a tenth of a wave length scatter in phase and hence appear the same as homogeneous damage within a region of this size. As will be shown, damage from a single primary extends over a distance comparable to the wave length of light and the angular dependence of scattering exhibits unusual interference effects. From macroscopic density changes Primak has estimated the damaged volume from a single primary as about (84 Å)³ in silica.[1] This is comparable to the average value of (67 Å)³ found in this work. In addition, the light scattering indicates that the damaged regions are rod shaped and surrounded by strain resulting from the change in volume that they undergo.

EXPERIMENT

Blocks of Corning fused silica (Code 7940) about $32 \times 38 \times 7{\cdot}5$ mm were irradiated in a graphite reactor at Oak Ridge. The irradiation facility had enriched uranium surrounding it and the neutron spectrum was close to a fission spectrum. Water cooling kept the temperature during irradiation below 40°C. The glass remained substantially colorless. At the highest exposures, the absorption coefficient at 436 mμ did not exceed $0{\cdot}09$ cm^{-1} so that corrections to the scattered intensity were small and corrections to the angular dependence of scattering were negligible. Light scattering measurements were made at 436 mμ in the instrument previously described using benzene as an index fluid.[2] This introduces a small index of refraction difference between the glass and fluid which alters the scattered intensity comparison and the angular distribution of scattering. No correction was made for these effects because they were small compared with other uncertainties. Absolute scattering values with incident unpolarized light were obtained by comparing with filtered benzene and using the value of $48{\cdot}4 \times 10^{-6}$ cm^{-1} for R_u (90) of benzene.* For the measurements with incident

* The symbol R_u (90) designates Rayleigh's ratio perpendicular to the incident beam with incident unpolarized light. It is the scattered power per unit solid angle per unit volume of sample per unit incident intensity.

polarized light, the absolute scattering power was established by measuring $V_v+H_h+2V_h$ from a secondary standard that had previously been compared with benzene using incident unpolarized light.* From this the quantity $V_v+H_h+2V_h$ for benzene was obtained.

RESULTS

Figure 1 shows the scattered intensity as a function of exposure. In addition to these data, an irradiation of 1×10^{15} nV gave no change in scattering within the precision of measurement.

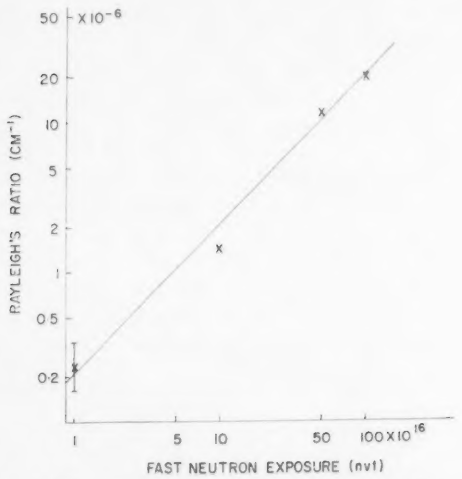

FIG. 1. The scattered light intensity with incident unpolarized light vs. the neutron exposure.

The straight line in the figure is drawn with a slope of unity indicating that the damaged centers are scattering independently. On the basis of these data the scattering will be analyzed by the summation of intensities scattered by individual damaged regions.

An important feature of the scattering is the presence of dissymmetry (I_{45}/I_{135}) showing that the damaged regions are comparable to the wave length of light in extent. With incident unpolarized light the dissymmetry was about 1·4. However, measurements with incident polarized light showed that this dissymmetry is due almost wholly to the V_v component while the H_h component had a dissymmetry less than unity. To make sure the instrument was functioning properly, the polarized components scattered by an optical glass were measured and the dissymmetries for both V_v and H_h were equal and within 3 per cent of unity as expected.[2] In conventional scattering from isotropic centers the two components are expected to show the same interference effects. The opposite angular dependence is therefore highly unusual. However, similar results have been predicted theoretically in the analysis of the effect of strain surrounding the scattering center.[3] Strain scattering shown below can give a satisfactory account of this peculiar scattering. Only the two highest irradiations gave sufficient scattered light intensity to make good measurements of the various polarizations. These results are given in Table 1. The values were corrected for optical absorption of the sample and the variation of scattering volume with angle in order to place them on the same intensity scale.

The polarized scattering components permit an estimate of the contribution of fluorescence to these results since it appears equally in all components V_v, H_h and V_h and is independent of scattering angle. The smallest value of these components therefore represents the maximum amount of fluorescence. With incident unpolarized light it could represent a maximum of 10 per cent of the recorded intensity. In the V_v component it would be a much smaller fraction but the V_h component could be entirely fluorescence since it is the smallest. These estimates are important since the sample's fluorescence appeared to the unaided eye to be much stronger than any scattering could have been. With incident 546 mμ light, the red fluorescence reported previously was observed.[4] At 436 mμ the fluorescence was much less than with the 546 mμ line and would therefore interfere less with the scattering observations. In addition, the receiver was equipped with an interference filter for this wave length so that most of the fluorescent light was eliminated.

DISCUSSION OF THE RESULTS

Gross features of the scattering

The scattered intensity is a gross feature of

* The symbol h or H represents horizontally polarized light and v or V vertically polarized light. The capitals give the polarization of the scattered light under observation with incident light of polarization shown by the subscript. The symbol P_p is used to designate any arbitrary combination of these.

the scattering that can be used to obtain an estimate of the volume of the damaged region. It will be analyzed as if the scattering were from isotropic centers although from what follows later it is clear that the centers are not isotropic. The anisotropy does not alter the magnitude of the intensity sufficiently to be taken into account at this stage. Furthermore, this approximate analysis of the intensity provides a clear indication of the shape of the damaged regions which is necessary to interpret their anisotropy.

Several sizes or types of damaged region may be expected because of the variation of energies of the primary struck atom with its angle of recoil and the spread of incident neutron energies. There are also two types of primary, but silicon and oxygen have almost the same fast neutron cross section and the masses are not greatly disparate. The following analysis treats the centers as identical and therefore represents a type of average. Using 1 MeV as the average neutron energy, the appropriate cross sections for silicon and oxygen are 3·0 barns. From this value and the density of 2·20 g cm^{-3}, the number of damaged regions per unit volume, N, is given by $N = 0{\cdot}20\,E$ where E is the exposure in nV. Rayleigh's ratio, representing the intensity of scattered light, is given by the data of Fig. 1 as $R_u\,(90) = 2{\cdot}04 \times 10^{-23}\,E$ in cm^{-1}. These two values permit an estimate of the volume V of the scattering region through the Rayleigh–Gans–Born approximation for isotropic centers which gives

$$R_u\,(90) = 2N\lambda^{-4}(\pi n \langle \Delta n \rangle V_{\mathrm{av}})^2 i(90) \qquad (1)$$

where n is the index of refraction of the sample (1·46 here), $\langle \Delta n \rangle_{\mathrm{av}}$ is the average variation in refractive index of the damaged volume V, λ is the vacuum wave length of the light, and $i(\theta)$ is an interference function characteristic of the shape and size of the scattering regions. The Rayleigh–Gans–Born approximation assumes that the incident plane wave remains a plane wave throughout the scattering region which is good for small variations in refractive index. The function $i(\theta)$ is approximately equal to unity when the size of the volume is not very large compared to a wave length of light—that is, when the dissymmetry is not far from unity as was observed.

Equation (1) requires a value of $\langle \Delta n \rangle_{\mathrm{av}}$ to yield the volume of the damaged region. The average value of refractive index change over the volume V cannot be greater than the refractive index change in the bulk sample at saturation. This stems from the long wave length of light which means that essentially bulk quantities are appropriate to the scattering equations. On the other hand, $\langle \Delta n \rangle_{\mathrm{av}}$ might be less than the saturation value if the damage were widely distributed. Therefore we will use in equation (1):

$$\langle \Delta n \rangle_{\mathrm{av}} = f \Delta n \qquad (2)$$

where Δn is the variation in refractive index in a bulk sample at saturation and f is the fraction of the volume possessing the equivalent of saturation damage. It is shown below that f is of the order of unity. The combination $f\,\Delta n V$ now appearing in equation (1) is proportional to the polarizability of the damaged volume and expresses the fact that variations in refractive index and the size of the volume are equivalent. Equations (1) and (2) give $fV = (67\ \text{Å})^3$ using the experimental[1] value, $\Delta n = 0{\cdot}01$.

For any value of f, the quantity fV represents the average volume possessing saturation damage per primary and hence must agree with bulk changes in density during the approach to saturation. Primak has analyzed such data and obtained a value of $(84\ \text{Å})^3$ for this quantity.[1] From an exponential approach to saturation as he used, but an average cross section as used here, a value of $(74\ \text{Å})^3$ is obtained. No matter which analysis is employed there is close agreement showing that the preceding interpretation of the light scattering is essentially correct.

An estimate of the value of f can be obtained by studying the possibility of interparticle interference. That is, as the volume concentration of scattering centers is increased the scattering from separate centers interferes so that the intensity no longer increases linearly with concentration and the scattering in the forward direction is reduced preferentially. Such effects do not appear even at the highest exposure as shown by the linear relationship in Fig. 1 and also by the fact that the dissymmetry of scattering does not diminish. Interparticle interference effects appear at various concentrations depending upon the size and shape of the scattering centers, but they are usually detected before ten per cent volume concentration is reached—that is, $NV < 0{\cdot}1$. From

Vol. 17
1960

Table 1. *Scattered light of various polarizations with polarized incident light of* 436 mμ

Sample	Component	Scattered intensity			Dissymmetry
		45°	90°	135°	
5×10^{17} nV	H_h	19·3	2·6	22·9	0·84
	V_v	64·6	39·6	35·4	1·82
	V_h	2·6	1·9	2·3	—
1×10^{18} nV	H_h	29·1	3·5	36·2	0·80
	V_v	112	65·6	62·1	1·80
	V_h	3·6	2·5	3·1	—

These results represent only the increase in scattering due to irradiation. All data have been corrected for the change in scattering volume with angle and are given on the same intensity scale. The sum $H_h+V_v+2V_h$ at 90°, which is proportional to R_u (90), is 200 for benzene on this scale.

above, NfV is about 0·06 at the highest exposure so $f \geqslant 0{\cdot}6$ with the larger values more probable. On this basis a reasonable estimate for the total volume of the scattering region is $V \approx (70\,\text{Å})^3$ and the damage within this region approaches that found in the bulk sample at saturation.

The value of 70 Å represents the approximate linear extent of the damaged region if it were roughly spherical. Such a size is far too small to give the dissymmetry of scattering which was, in fact, observed. Consequently the damaged volume must be strung out in some long rodlike region. The scattering of thermal waves in irradiated sapphire possibly indicates a similar shape.[5] This is not to imply that the damaged region is exactly straight or well defined even though such descriptions will be used for the purpose of calculation below. The dissymmetry of 1·4 indicates a rod length greater than 1000 Å. Therefore the rod must be considered very thin (< 18 Å) compared to its length and, in such a case, the dissymmetry ordinarily can be interpreted in a straightforward way to give the length. However, the different angular variations found for the polarized components show that the results do not represent an ordinary situation. The following theoretical analysis provides an explanation of the polarization effects and shows how they may be interpreted to provide an estimate of the length of these regions.

Detailed features of the scattering

The preceding analysis has assumed an isotropic scattering center which gives good estimates of the quantities that were derived but is inadequate for describing the observations with polarized light. Since the damaged region occupies less volume after damage than before, it is surrounded by a strained region with anisotropic refractive indices resulting from the photoelastic effect. This outer region of altered optical properties contributes to the scattering as well as the damaged region itself. GOLDSTEIN[3] analyzed the problem for spheres and showed that the strained region affects only the angular variation of H_h. From this, the effect of strains on the scattering may be characterized by the dissymmetry ratio D, defined by

$$D = \text{dissymmetry of } H_h/\text{dissymmetry of } V_v$$

For isotropic centers D is unity while for inhomogeneities cooled from high temperatures it can be either more or less than unity.[3] The data in Table 1 give an average value for D of about 0·45. To assess the influence of strain around two different shapes, rods and spheres are analyzed in the appendixes. From (1A) and (6A) with $p = 0{\cdot}197$ and $q = 0{\cdot}088$,[6] the sphere gives a value for D of 0·09 and the rod a value of 0·31. Both are less than unity showing that strains can cause the effect observed; however, the rod shape gives a value closer to the observed value. If the damage along the rod were in fairly widely separated regions, the model of a string of spheres might be appropriate. In Appendix 1 this is shown to give a value of D the same as a single sphere, which is much too low. In other words, damage along the rod is fairly uniform—a conclusion deduced independently above after considering

the absence of interparticle interference effects. This analysis of the polarization of the scattering generally corroborates the deductions made from the analysis of the intensity of scattering.

The length of the rodlike regions can be estimated best from the V_v component since it is least affected by strains. From (6A), a dissymmetry of 1·8 corresponds to a rod 1800 Å long. Using only the first term, which is appropriate in the absence of strains, this dissymmetry corresponds to a rod 1600 Å long. The length must be approximately equal to the range of the primaries which have an average energy of about 200 keV with incident neutrons of 1 MeV. This may be compared with the 950 Å range found for 40 keV argon ions in a silicate glass.[7]

The rodlike regions possess a volume approximately equal to the damaged volume calculated from macroscopic changes so these must comprise a large part of the damage. A rod shape indicates the preservation of momentum. Consequently, a large part of the damage must occur during the initial part of the primary's path before its momentum is lost.

Acknowledgements—The author is indebted to Dr. C. M. NELSON of the Solid State Division, Oak Ridge National Laboratory, for making several helpful comments as well as for carrying out the irradiations. Dr. MARTIN GOLDSTEIN contributed many stimulating suggestions.

APPENDIX 1

Light scattering by a sphere under stress

This appendix shows how GOLDSTEIN'S[3] expressions for scattering by a sphere under stress can be applied to radiation damage for estimating the effect of strain. First, the refractive index increments are expressed in terms of the photoelastic constants so that quantitative estimates for the change in the H_h and V_v components can be made. Second, a development shows that an assemblage of non-interacting spheres exhibits scattering similar to a single sphere.

The expressions for a sphere may be written[3]

$$V_v = V_0(2\pi nV)^2\lambda^{-4}R_0^{-2}[\alpha+(\delta_0/3)]^2$$

$$H_h = H_0(2\pi nV)^2\lambda^{-4}R_0^{-2}[\alpha\cos\theta-(\delta_0/6)(3+\cos\theta)]^2$$

$$V_h = H_v = 0 \qquad (1A)$$

These are in Goldstein's notation, with α the incremental refractive index difference between the sphere and the bulk sample, and δ_0 the difference between the radial and tangential refractive indices due to the strains, evaluated at the surface of the sphere. The scattered intensities for one sphere per unit volume of the sample are V_v and H_h while the incident intensities are V_0 and H_0. R_0 is the distance from the sample to the point of observation, and V is the volume of the sphere.

The three stress–strain equations may be written in the form

$$Ee_i = p_i-\sigma(p_j+p_k)+Ee_0 \qquad (2A)$$

where E is Young's molulus, σ is Poisson's ratio, and e_0 is the strain due to damage alone in the absence of stress. The value of e_0 is constant inside the sphere and zero outside. The strains for the sphere are then[8]

inside the sphere

$$e = \frac{e_0(1+\sigma)}{3(1-\sigma)}$$

outside the sphere

$$e_r = -2e_\phi = -\frac{2e_0(1+\sigma)R^3}{3(1-\sigma)r^3}$$

These are utilized in the three photoelastic equations of the form[9]

$$-\Delta n_i = n^2(qe_i+pe_j+pe_k) \qquad (3A)$$

The change in refractive index due to damage alone can be described closely by the photoelastic constants[6] so (3A) gives

$$\Delta n = -n^2(q+2p)e_0$$

$$\alpha = \frac{\Delta n(1+\sigma)}{3(1-\sigma)}$$

$$\delta_0 = \frac{\Delta n(p-q)(1+\sigma)}{(q+2p)(1-\sigma)}$$

where Δn is the same as in equation (2). Substituting these in (1A) and using the measured values of the photoelastic constants[6] permits calculation of the ratio of the dissymmetry of the H_h component to the dissymmetry of the V_v component.

The above problem can be applied to an assemblage of spheres if they do not interact. The scattered amplitude for any scattered intensity of polarization P_p is given by a summation over all the spheres in the assemblage

$$p_p = p'_p\,(\text{sphere})\sum\exp(i\boldsymbol{ks}\cdot\boldsymbol{r}_j)$$

Assuming that the size of the spheres and their separation are small compared to a wave length, the summation may be replaced by an integral. The result is then multiplied by its complex conjugate and averaged over all orientations to give the scattered intensity. The quantity

Vol. 17
1960

$(p'_p)^2$ is spherically symmetric so the orientation average is only over the form of the assemblage giving

$$P_p = P'_p \text{ (sphere) } n'^2 i(\theta)$$

where P'_p (sphere) is the appropriate expression from (1A), n' is the number of spheres per unit volume in the assemblage, and $i(\theta)$ is the interference function ordinarily associated with the shape of the assemblage. For rods it is given by[10]

$$i_1(ksL) = 2(ksL)^{-2}[\cos ksL - 1 + ksLSi(ksL)] \tag{4A}$$

where

$$Si(X) = \int_0^X \frac{\sin t}{t}\, dt$$

L is the length of the rod and $ks = 4\pi\lambda_m^{-1} \sin(\theta/2)$ with θ the angle of scattering.

From this and (1A), the V_v component exhibits the interference associated with the form of the assemblage while the H_h component exhibits the interference of the form altered by the strains. The ratio of the dissymmetry of the H_h component to the dissymmetry of the V_v component is the same as for a single sphere.

APPENDIX 2

Light-scattering by a rod under stress

This appendix develops expressions for the scattering by a smooth rod under stress with particular emphasis on the problem of radiation damage. The damage consists of long thin regions which are approximated here as sections of an infinite rod under stress. That is, end effects are neglected.

The strain problem can be solved with the form of solution given by PORITSKY[11] and equation (2A). The following boundary conditions are applied. The tangential strains are equal at the rod surface, the radial stresses are equal at the surface, and all the strains vanish at infinity. In addition, there is no axial displacement since all sections of an infinite rod cannot be equivalent if there is. The strains are then inside the rod

$$e_r = e_\phi = \frac{e_0(1+\sigma)}{2(1-\sigma)}, \qquad e_z = 0$$

and outside the rod

$$e_r = -e_\phi = -\frac{e_0(1+\sigma)R^2}{2(1-\sigma)r^2}, \qquad e_z = 0$$

Substituting these in (3A) gives the components of the polarizability tensor, P.

Scattering by a segment of this rod can be calculated following the formalism used by GOLDSTEIN[3] in describing the sphere under stress. First, the contribution of a thin slice of the rod and its surrounding strain field is evaluated. Then the sum of these slices, with proper compensation for phase, represents the scattering by the rod. The center of the disc-like section is chosen as the origin and orientation of the disc is expressed by the angles between a line perpendicular to the disc and $\boldsymbol{s}$. As usual, $\boldsymbol{s} = \boldsymbol{S} - \boldsymbol{S}_0$ where $\boldsymbol{S}$ and $\boldsymbol{S}_0$ are unit vectors in the direction of scattering and in the direction of the incident wave respectively. In the laboratory coordinate system, the incident light beam direction is along X_1 with X_2 vertical. A second coordinate system based on $\boldsymbol{s}$ is formed by rotating this system about X_2 an amount $\theta/2$ so the X_3 direction is along $\boldsymbol{s}$. A third coordinate system is the cylindrical coordinate system of the rod shown in Fig. 2 where X_1 is the r direction, X_2 the ϕ direction and X_3 the z direction.

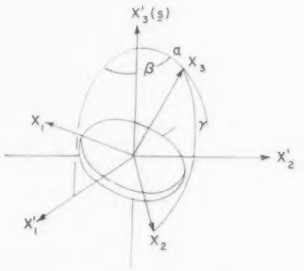

FIG. 2. Relation between the system based on $\boldsymbol{s}$ (primed coordinates) and the system based on the orientation of the rod illustrating the T matrix transformation.

The contribution of a small volume element $dV = r\, dr\, d\phi\, dz$ is given by

$$\boldsymbol{E}_s = 2\pi n\, dV \lambda^{-2} R_0^{-1} \cos(\boldsymbol{kr} \cdot \boldsymbol{s}) MT^{-1}PTM\boldsymbol{E}_0 \tag{5A}$$

where all the terms except the matrices were defined previously. Here the polarizability tensor is expressed in terms of refractive index increments. The matrix M transforms from the laboratory system based on the incident beam to the system based on $\boldsymbol{s}$.

$$M = \begin{vmatrix} \cos(\theta/2) & 0 & \sin(\theta/2) \\ 0 & 1 & 0 \\ -\sin(\theta/2) & 0 & \cos(\theta/2) \end{vmatrix}$$

The matrix T transforms from this system to the coordinate system based on the disc. If we use the notation $(X_i X'_j)$ to designate the cosine of the angle between the X_j axis in the former system and X_i axis in the new system, then

$$T = \begin{vmatrix} (X_1X'_1) & (X_1X'_2) & (X_1X'_3) \\ (X_2X'_1) & (X_2X'_2) & (X_2X'_3) \\ (X_3X'_1) & (X_3X'_2) & (X_3X'_3) \end{vmatrix}$$

where

$$(X_1X'_1) = \cos\gamma\sin\beta - \sin\gamma\cos\beta\cos\alpha$$

$$(X_1X'_2) = -\sin\gamma\sin\beta\cos\alpha - \cos\gamma\cos\beta$$

$$(X_1X'_3) = \sin\alpha\sin\gamma$$

$$(X_2X'_1) = \sin\gamma\sin\beta + \cos\gamma\cos\beta\cos\alpha$$

$$(X_2X'_2) = \cos\gamma\sin\beta\cos\alpha - \sin\gamma\cos\beta$$

$$(X_2X'_3) = -\sin\alpha\cos\gamma$$

$$(X_3X'_1) = \sin\alpha\cos\beta$$

$$(X_3X'_2) = \sin\alpha\sin\beta$$

$$(X_3X'_3) = \cos\alpha$$

The last operation in M transforms to the scattering direction $\boldsymbol{S}$. It leaves the propagation of the scattered beam along $\boldsymbol{S}$ in the X_1 direction so the X_2 component is scattered light of vertical polarization and the X_3 component is horizontal polarization.

From equation (5A) the amplitude of the scattered light of vertical polarization, E_{vs}, and of horizontal polarization, E_{hs}, can be derived. The incident light, $\boldsymbol{E}_0$, has only an X_2 component, v_0, for the former and only an X_3 component, h_0, for the latter. Integrating over all the volume elements comprising the disc-like section of the rod and strain field gives

where

$$c' = \cos(krs\sin\alpha\sin\gamma)$$

$$K = \frac{\pi n\Delta n(1+\sigma)}{\lambda^2 R_0(2p+q)(1-\sigma)}$$

The radius of the rod, R, is taken as very small compared to a wave length. Therefore the integral inside the rod is approximately equal to πR^2 and the integrals outside may be evaluated through the approximation[12]

$$\int_X^\infty \frac{\cos y}{y}\,dy \approx -\log CX$$

where C is a constant. The logarithmic integrals are integrated by parts with the result that

$$E_{vs}(\text{disc}) = 2Kv_0\pi R^2\,dz[p-(p-q)\sin^2\beta\cos^2\alpha]$$

$$E_{hs}(\text{disc}) = Kh_0\pi R^2\,dz\{[(p+q)\cos\theta-(p-q)]+ +(p-q)\cos^2\alpha[(1+\cos\theta)+(1-\cos\theta)\cos^2\beta]\}$$

The amplitude scattered by a rod is the sum of disc-like elements with compensation for phase so the right hand sides of the above equations are multiplied by a factor

$$\int_{-L/2}^{L/2}\cos(ksz\cos\alpha)\,dz = \frac{2\sin(\tfrac{1}{2}ksL\cos\alpha)}{ks\cos\alpha}$$

Vol. 17
1960

$$\frac{E_{vs}(\text{disc})}{dzKv_0} = [(p+q)(\sin^2\beta\cos^2\alpha+\cos^2\beta)+2p\sin^2\alpha\sin^2\beta]\int_0^R\int_0^{2\pi} c'r\,dr\,d\gamma+$$

$$+R^2(p-q)\left[(\cos^2\beta-\sin^2\beta\cos^2\alpha)\int_0^{2\pi}\cos 2\gamma\int_R^\infty c'\frac{dr}{r}d\gamma+\sin 2\beta\cos\alpha\int_0^{2\pi}\sin 2\gamma\int_R^\infty c'\frac{dr}{r}d\gamma\right]$$

$$\frac{E_{hs}(\text{disc})}{dzKh_0} = \left\{(p+q)\left[\cos^2\frac{\theta}{2}\sin^2\alpha-\sin^2\frac{\theta}{2}(\sin^2\beta+\cos^2\beta\cos^2\alpha)\right]+\right.$$

$$\left.+2p\left(\cos^2\frac{\theta}{2}\cos^2\alpha-\sin^2\frac{\theta}{2}\sin^2\alpha\cos^2\beta\right)\right\}\int_0^{2\pi}\int_0^R c'\,r\,dr\,d\gamma+$$

$$+R^2(p-q)\left\{\left[\sin^2\frac{\theta}{2}(\cos^2\beta\cos^2\alpha-\sin^2\beta)-\cos^2\frac{\theta}{2}\sin^2\alpha\right]\int_0^{2\pi}\cos 2\gamma\int_R^\infty c'\frac{dr}{r}d\gamma+\right.$$

$$\left.+\sin^2\frac{\theta}{2}\sin 2\beta\cos\alpha\int_0^{2\pi}\sin 2\gamma\int_R^\infty c'\frac{dr}{r}d\gamma\right\}$$

The resultant expressions are squared and averaged over α and β assuming that the scattering is the sum of intensities scattered by a random arrangement of such rods. Finally,

$$V_v = 4V_0K^2V^2[p^2i_1(ksL) - \tfrac{1}{3}p(p-q)i_2(ksL) + \tfrac{3}{40}(p-q)^2i_3(ksL)]$$

$$H_h = H_0K^2V^2\{[(p+q)\cos\theta - (p-q)]^2i_1(ksL) + \tfrac{1}{3}(p-q)(3+\cos\theta)[(p+q)\cos\theta - (p-q)]i_2(ksL) + \tfrac{1}{40}(p-q)^2(19+10\cos\theta+3\cos^2\theta)i_3(ksL)\} \quad (6A)$$

with $V_h = H_v = 0$ shown in a similar way. Here,

$$i_2(X) = 6X^{-2}(1 - X^{-1}\sin X)$$

$$i_3(X) = \frac{10}{3}X^{-5}(X^3 - 3X^2\sin X - 6X\cos X + 6\sin X)$$

and $i_1(ksL)$ is the same as in equation (4A). The first term in each equation of (6A) contains the interference expression associated with rods in the absence of strain. With V_v this is the dominant term and the strains have only a minor influence on the angular variation. On the other hand, with spheres the strains do not influence the angular variation of V_v at all.[3]

REFERENCES

1. PRIMAK W., *Phys. Rev.* **110,** 1240 (1958).
2. MAURER R. D., *J. Chem. Phys.* **25,** 1206 (1956).
3. GOLDSTEIN M., *J. Appl. Phys.* **30,** 501 (1959); **31,** 1697 (1960).
4. PRIMAK W. and UPHAUS R. A., *J. Chem. Phys.* **29,** 972 (1958).
5. BERMAN R., FOSTER E. L. and ROSENBERG H. M., *Report of the Conference on Defects in Crystalline Solids.* The Physical Society, London (1955).
6. PRIMAK W. and POST D., *J. Appl. Phys.* **30,** 779 (1959).
7. HINES R. L., *J. Appl. Phys.* **28,** 587 (1957).
8. LOVE A. E. H., *The Mathematical Theory of Elasticity.* Cambridge University Press, London (1927).
9. *Handbook of Physics,* (edited by CONDON E. U. and ODISHAW H.). McGraw Hill, New York (1958).
10. NEUGEBAUER T., *Ann. Phys., Lpz.* **42,** 509 (1943).
11. PORITSKY H., *Physics* **5,** 406 (1934).
12. JAHNKE E. and EMDE F., *Tables of Functions.* Dover Publications, New York (1945).

J. Phys. Chem. Solids Pergamon Press 1960. Vol. 17, Nos. 1/2, pp. 52–56. Printed in Great Britain.

LOW-TEMPERATURE SPECIFIC HEAT OF DILUTE Cu–Mn ALLOYS

J. E. ZIMMERMAN

Scientific Laboratory, Ford Motor Company, Dearborn, Michigan

and

F. E. HOARE

Physics Department, The University, Leeds, England

(*Received* 7 *March* 1960)

Abstract—Specific heats of several specimens of copper alloyed with from 0·14 to 10 wt.% manganese were measured at liquid helium temperatures; and for some of the specimens, measurements were extended to 15°K. All exhibit an anomalously large specific heat compared to pure copper, of which the excess is associated with the magnetic transition known to occur in these alloys at low temperatures. The excess entropy associated with the anomaly indicates a spin on the manganese atoms of about 2; but for a number of reasons this spin cannot be established accurately. The shape of the specific heat anomaly is different from any of the well-known theoretical forms, e.g. the Schottky or the λ-point types. At the lowest temperatures the excess specific heat is linear in T and essentially independent of Mn concentration for the entire range of composition studied.

Vol. 17
1960

INTRODUCTION

DILUTE Cu–Mn alloys exhibit anomalous resistivity characteristics at low temperatures,[1,2] and constitute one of a class of dilute alloys which possess a resistance maximum and minimum, in contrast to the normal behavior of a resistance which varies monotonically with temperature. This and other properties of the system have led to extensive investigations of the magnetic behavior, in which it was found that a high-temperature paramagnetism (with positive Curie temperature) gives way at low temperatures to anti-ferromagnetic behavior, with hysteresis effects.[3,4,5] This indication of an ordering process suggested specific heat measurements to probe the nature of the transition and the spectrum of quantum states involved.

The presence of specific heat anomaly associated with the above effects was already indicated several years ago by measurements (unpublished) at hydrogen temperatures and above made by G. L. BOOTH and F. E. HOARE at the University of Leeds. The present measurements were carried out in order to obtain a more complete picture of the specific heat anomaly. Preliminary reports of these results have been presented previously.[6,7]

EXPERIMENTAL METHOD

Two separate calorimeters were used in this work and will be briefly described. The first, shown by the sketch in Fig. 1(B), was designed for use at helium temperatures only, and incorporated a vapor bulb thermometer with vacuum-jacketed down tube. The vapor bulb pressure was read on a mercury manometer by means of a cathetometer with an accuracy of approximately 0·02 mm. For purposes of temperature regulation during thermometer calibration, the pumping rate could be regulated, either manually or automatically, to hold the bath pressure constant to within 0·01 mm Hg. This does not mean, of course, that the bath temperature was held correspondingly constant, owing to superheating effects above the λ-point.

The other calorimeter, shown in Fig. 1(A), was used for helium temperatures and above. It consisted of two concentric copper cans, the inner one carrying a heater winding and a carbon

resistance thermometer, by means of which its temperature could be regulated and held constant by electronic control. The inner can also incorporate a gas thermometer bulb at 75 cm³ capacity with vacuum jacketed down tube of about 0·050 in. i.d.

A Wallace and Tiernan "precision dial manometer" was used to read the gas thermometer pressure, which was adjusted to about 80 mm Hg at 4·2°K. Corrections for the dead volume of about 10 cm³ and for the departure of helium from perfect gas behavior were applied. The gas thermometer was standardized at the triple point of normal hydrogen and was checked at the normal boiling points of hydrogen and of helium. These checks showed the thermometer to be accurate to about $\pm 0{\cdot}02°$.

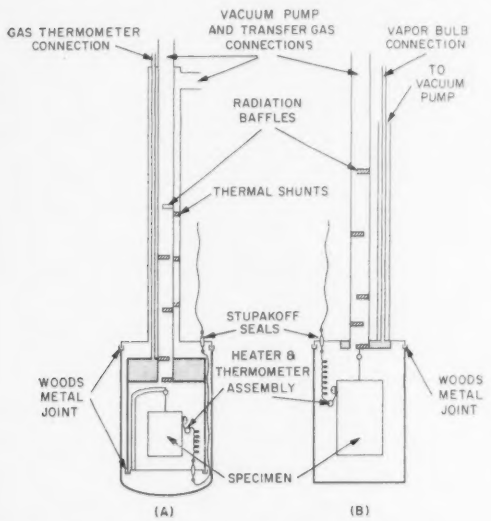

FIG. 1. The colorimeters used for the measurements
(a) from 3 to 16°K
(b) from 1·8 to 4·2°K

A novel feature of these calorimeters was the heater and thermometer assembly attached to the specific heat specimens. This consisted in each case of a handmade 500Ω wire-wound resistor about $\frac{1}{16}$ in. in diameter by $\frac{1}{4}$ in. in length, and a 47 Ω $\frac{1}{10}$ W carbon Allen–Bradley resistor of similar dimensions. The two resistors were cemented into a single copper sleeve, $\frac{1}{10}$ in. o.d. by $\frac{5}{8}$ in. long, with end caps. The copper sleeve was soldered to a thin copper tab, which in turn was held in contact with the specimen by a 3-48 brass screw and nut. Electrical leads between the resistors and the calorimeter walls were of No. 40 manganin and were trimmed to a resistance of 10 Ω per lead. The leads were taken through the calorimeter walls by means of Stupakoff seals, and at this point separate current and potential leads were attached. The method employed here of attaching the addenda to the specimen gave perfectly adequate thermal contact by any test we could devise, and is obviously very simple and convenient since specimens of practically any size or shape can be used. In certain cases where it was desired not to drill a 3-48 clearance hole in the specimen, a copper band in the shape of a miniature hose clamp was used to attach the addenda, again with satisfactory results. The only disadvantage of such a method appeared when specimens of very low thermal diffusivity, e.g. Fe–Mn alloys, were measured and equilibrium times of the order of a minute or more were encountered; however, this difficulty almost certainly arose from the very asymmetrical way in which heat was supplied to the specimen rather than a thermal contact resistance. Even this is not so disadvantageous as might at first be supposed, because if the low diffusivity were caused by a high specific heat, thermal drift rates resulting from extraneous heat input would be correspondingly low, and the net result is but a loss of time rather than accuracy.

Specimens were suspended in the calorimeters by means of a single fine manganin wire, the wire size being chosen more or less according to the weight of the specimen. Some very qualitative evidence indicates that such a suspension gives lower vibrational heating of the specimen than a nylon thread suspension, presumably because of lower internal friction in the wire as compared to thread. Helium transfer gas was used in both calorimeters during calibration of the carbon resistance thermometers. The general experimental procedure was conventional. In the helium-temperature calorimeter the resistance thermometer was calibrated against the vapor pressure thermometer at 12 to 14 points between about 1·8 and 4·2°K, for each run. The R, T data were used to derive (by least squares) an equation of the

form

$$(\log R/T)^{1/2} = A + B \log R + C(\log R)^2,$$

which gave a satisfactory fit, except for a systematic discontinuity at the λ-point of helium of several millidegrees. This small discontinuity was opposite in sense to that which would be predicted on the basis of the small hydrostatic head of helium (about 2 cm) between the vapor bulb and the specimen. In the "high-temperature" calorimeter fifteen or twenty calibration points were obtained between 3 and 20°K and the data were reduced as described above. The quality of the thermometer calibrations is indicated by the scatter of calibration points about the derived curve. For the helium temperature calorimeter this scatter averaged about 0·001° to 0·003°, and for the high-temperature calorimeter 0·01° to 0·02°. These limits on accuracy were determined by instability of the helium bath in the first case, and by backlash and stiction of the Wallace and Tiernan manometer in the second case.

Specific heat measurements were carried out by the usual procedure in non-adiabatic calorimetry. Specimen temperatures were measured at half-minute intervals both before and after heat input, in order to establish drift rates. Heat inputs were adjusted such that the resulting temperature changes were of the order of 5 per cent of the absolute temperature, while corrections for extraneous heat inputs were in general less than 2 per cent of the temperature changes.

SPECIMENS

A total of seven specimens were prepared for this study. Four of these, nominally $\frac{1}{2}$, 1, 2 and 4 per cent Mn, were prepared at the University of Leeds, and the others were prepared by the Metallurgy Department of this Laboratory. Each specimen was vacuum annealed for 16 hr. at about 100°C below the liquidus point. Two of the specimens, for which the specific heat data seemed most significant, were analyzed chemically and spectroscopically. The chemical analysis showed Mn contents of $0{\cdot}135 \pm 0{\cdot}01$ and $0{\cdot}485 \pm 0{\cdot}005$ wt. per cent, respectively, these results being derived from three different analyses on each specimen.

A single crystal of copper of spectroscopic purity was also measured for purposes of comparison. This specimen was furnished by G. A. Alers and J. Neighbours.

RESULTS AND DISCUSSION

The specific heat of pure copper is shown in Fig. 2 along with a straight line representing the equation, $C_v/T = 0{\cdot}690 + 1943\ T^2/344^3$ mJ/mole deg^2, given by Corak *et al.*[8] The specific heats

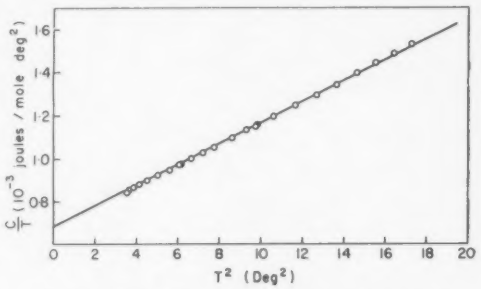

Fig. 2. Specific heat of copper single crystal.

at helium temperatures of specimens containing $\frac{1}{2}$, 1, 4, and 10 per cent Mn are shown in Fig. 3, the line for pure copper being included for comparison. The data for the 2 per cent and the 4 per

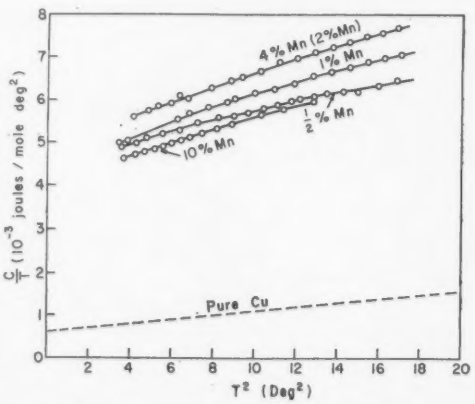

Fig. 3. Specific heats of Cu–Mn alloys at helium temperatures.

cent specimens practically coincide, so the points for the 2 per cent have been omitted for the sake of clarity.

Specific heats at higher temperatures were measured for the specimens of 0·135, $\frac{1}{2}$, and 1 per cent Mn content, and for the copper single

Vol. 17
1960

crystal. Results are shown in Fig. 4, which includes the helium-temperature data for the same specimens.

We have used a plot of C/T vs. T^2 in Fig. 3, as is usual when plotting the specific heats of pure metals at low temperatures. In the present case such a plot has no *a priori* advantage; however the specific heat of each dilute alloy is nearly a straight line in these coordinates, with a large intercept

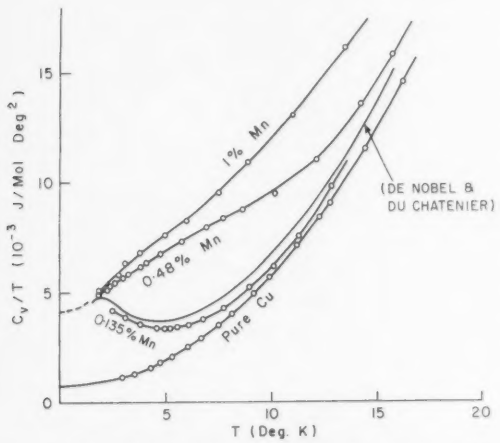

FIG. 4. Specific heats of Cu–Mn alloys up to 16°K. DE NOBEL and DU CHATENIER give 0·13 at. per cent (0·11 wt. per cent) as the Mn concentration of their specimen.

on the vertical axis and a slope somewhat greater than that for pure copper. Thus the anomalous specific heat (specific heat of the alloy minus that of pure copper) at very low temperatures is nearly linear in T, and furthermore, as Fig. 3 shows, is nearly independent of Mn concentrations. These properties of the anomaly are quite unusual and obviously cannot be explained as a simple Schottky or a λ-type anomaly. OVERHAUSER[10] has recently explained those anomalous thermal properties on the basis of a new approach to the antiferromagnetic properties of such alloys. This theory gives quantitative agreement with the results given in Fig. 3. OVERHAUSER's theory has been critized by MARSHALL[11] who has interpreted these results on the basis of well known principles without introducing a new mechanism.

In Fig. 4 C/T vs. T is plotted for the three most dilute alloys, along with the recently published data of DE NOBLE and DU CHATENIER[12] for an alloy containing 0·11 wt. per cent Mn. In these coordinates entropy may be determined by measuring the area under any particular curve. The total entropy S required to disorder an assembly of spins, having spin s is $S = Nk \log (2s+1)$, where N is the number of spins and k is Boltzmann's constant. Thus by determining S for one or more of the alloys represented in Fig. 4, one can calculate s. Obviously the only specimen for which the data are reasonably complete is the one containing 0·48 wt. per cent Mn. The excess entropy of this specimen up to 16°K, using the extrapolation to absolute zero indicated in the figure, is 0·0606 J/mole deg. To this value one must add a number of correction terms in order to obtain the total spin entropy S. First, it is necessary to estimate the entropy remaining under the high-temperature tail of the specific heat curve beyond the range of these measurements. Second, both the lattice and the electronic specific heats of the alloy will in general be different from those of pure copper and will give rise to small entropy corrections. The electronic specific heat change on alloying as estimated from results on other dilute alloys, should be no more than 5 per cent for ½ per cent Mn. An increase of this amount in the electronic specific heat leads to an entropy correction, at 16°K, of −0·0005 j/mole deg, which is practically negligible. The change of lattice heat capacity with alloying has been calculated by WALDORF[9] using measured low-temperature elastic constants, and the entropy correction derived is quite negligible. Since the elastic constant derivation of lattice specific heat applies only to the T^3 region, one cannot definitely assume that the lattice entropy correction at temperatures as high as 10 or 20°K is negligible. Experimental evidence on alloys in this temperature range, from which one might draw conclusions, is lacking. A lower limit for the entropy correction may be obtained by adding a T^5 term (the second order term in the lattice specific heat) to the specific heat of pure copper, with a coefficient chosen to bring the pure Cu curve into coincidence with the alloy curve at about 16°K. This procedure leads to a correction of −0·0064, and a total spin entropy of 0·0542. We cannot place an upper limit on the entropy correction without knowing the shape of the tail of the specific heat anomaly.

If we assume a $1/T^2$ tail above 16°K we get an entropy correction of 0·016 and a total of 0·077. These two values of spin entropy lead to spin values of about 1·1 and 2·1 respectively. The latter is close to the value of 2 derived from magnetic measurements.[3] However, the $1/T^2$ tail assumed for the anomaly does not join smoothly on to the experimental data at 16°K. A smooth fit may be achieved using a $T^{1/2}$ tail, but this leads to an improbably large spin value, and the conclusion is that either the tail of the anomaly is of more complicated form than a simple inverse power of T, or that some combination of lattice heat correction and extrapolation of the tail is required.

For the specimen containing 0·135 per cent Mn, there is considerable uncertainty in the total spin entropy because of the extrapolation to absolute zero. If we assume C/T approaches zero temperature in about the same way as for the other specimens, as indicated by the dashed line in Fig. 4, we get an excess entropy, up to 11°K, of 0·0186, giving a spin of 1·6. Above 11°K the curves for the alloy and for pure copper begin to diverge again, and the general discussion concerning correction terms given in the preceding paragraph is applicable, with similar uncertainty in conclusions. The probable error in the chemical analysis alone leads to an uncertainty in the spin of $\pm$ 0·2. The apparent inconsistency between these results and those of De Nobel and Du Chatenier on an alloy of similar composition, shown in Fig. 4, undoubtedly arises from the different methods of determining composition. Therefore, the data for this specimen also are consistent with the magnetic measurements.

REFERENCES

1. Gerritsen A. N., *Physica* **25,** 489 (1959).
2. Gerritsen A. N., *Physica* **19,** 61 (1953) .
3. Schmitt R. W. and Jacobs I. S., *J. Phys. Chem. Solids* **3,** 324 (1957).
4. Owen J., Browne M., Arp V. and Kip A. F., *J. Phys. Chem. Solids* **2,** 85 (1957).
5. Owen J., Browne M., Knight W. D. and Kittel C. *Phys. Rev.*, **102,** 1051 (1956).
6. Hoare F. E. and Zimmerman J. E., *Bull. Amer. Phys. Soc.* (ser. 2) **3,** 124 (1958).
7. Zimmerman J. E., *Int. Conf. on the Electronic Properties of Metals at Low Temperatures, Geneva, N. Y.*, p. 4 (1958).
8. Corak W. S., Garfunkel M. P., Satterthwaite C. B. and Wexler A., *Phys. Rev.* **98,** 1699 (1955).
9. Waldorf D., *J. Phys. Chem. Solids* **16,** 90 (1960).
10. Overhauser A. W., *Phys. Rev. Letters* **3,** 414 (1959); *J. Phys. Chem. Solids* **13,** 71 (1960).
11. Marshall W., *Phys. Rev.* **118,** 1519 (1960).
12. De Nobel J. and Du Chatenier F. S., *Physica* **25,** 969 (1959).

Vol. 17
1960

J. Phys. Chem. Solids Pergamon Press 1960. Vol. 17, Nos. 1/2, pp. 57–64. Printed in Great Britain.

LATTICE PARAMETER AND DEFECT STRUCTURE OF CADMIUM OXIDE CONTAINING FOREIGN ATOMS

A. CIMINO and M. MAREZIO

Instituto Chimica Gen. e Inorg., e Centro di Chim. Gen. del C.N.R.
Universita di Roma, Rome, Italy

(*Received* 13 *January* 1960; *revised* 27 *February* 1960)

Abstract—The incorporation of additives (In^{3+}, Ag^{1+} or Na^{1+}) into cadmium oxide has been studied by means of precision measurements of the lattice parameter a. It is found that a varies linearly with $N^{1/3}$, where N is the concentration (atoms per cent) of additive. When In is added, a increases. The straight line obtained in the plot of a vs. $N^{1/3}$, however, does not extrapolate to the value of a of the pure oxide, but to a lower value. Initially, therefore, addition of In must decrease the lattice parameter. The result is interpreted as pointing to two distinct mechanisms of incorporation. The first mechanism (i) holds for the first fraction ($\sim 0{\cdot}02$ per cent) of addition, and corresponds to the elimination of interstitial cadmium excess, with consequent decrease of a. The second mechanism (ii) is a controlled valency process, which corresponds to a decrease of valency of cadmium ions, with consequent increase of a. Addition of Ag leads to a contraction of a. The result is explained by a mechanism as in (ii), except that the addition will cause an increase of valency, with consequent decrease of a. The possibility of alternate mechanism is discussed. An excess of cadmium of the order of 0·01 per cent is inferred from the results. A thermal expansion coefficient of $1{\cdot}35 \times 10^{-5}/°C$ is determined from lattice parameter measurements at different temperatures.

THE INVESTIGATION of solid systems containing foreign atoms is of considerable interest for the understanding of the properties of a crystalline solid in terms of its defect structure. Addition of atoms with valency differing from that of the host atoms is particularly important because it provides a means of controlling the type and the concentration of defects. A recent and comprehensive account of the relationship between addition of foreign atoms and type and concentration of defects introduced thereby is given by KRÖGER and VINK[1].

We are here concerned with binary non metallic solids of the type MX. It can be shown that incorporation of foreign atoms can give rise to controlled electronic disorder (as in the system $NiO + Li_2O$) or controlled atomic disorder (as in the system $AgCl + CdCl_2$). The first case is also known as "controlled valency" after VERWEY and coworkers,[2] who were the first to investigate the change in electric properties of this and similar systems. According to these authors, in the example given, some Ni^{2+} ions are substituted by Li^{1+} ions, and there is a variation of an equivalent amount of Ni^{2+} ions to valence $3+$. As noted by KRÖGER, VINK and VAN DEN BOOMGAARD[3], the controlled valency description is not essentially different from the quasi-free carrier description. The controlled valency scheme, however, has the advantage of pointing more explicitly to the effective variation of ion sizes, and its use can therefore be justified when dealing with lattice parameter variations. Thus, the addition of Li_2O to NiO, besides giving rise to marked changes in electrical conductivity, is accompanied by a shrinkage of the lattice, as first observed experimentally by VERWEY and coworkers, due to the passage of some ions from valence $2+$ to $3+$.

A study of the variation of lattice parameters in some semiconducting oxides, namely $NiO + Li^{1+}$, $Fe_2O_3 + Ti^{4+}$, and Mg_2TiO_4 reduced, has been made by BROWNLEE and MITCHELL[4]. In the case of NiO it has been shown that the lattice parameter a varies linearly with $N^{1/3}$, where N is the concentration of Li^{+1} ions. The straight line obtained in the plot of a vs. $N^{1/3}$, however, does

not extrapolate to the value of a corresponding to that of the pure specimen, but to a significantly higher value. From this observation, it could be inferred that the pure oxide is itself defective and contains a certain amount of excess oxygen together with an equivalent amount of Ni^{3+} ions. Extrapolation to zero impurity concentration would in fact give the lattice parameter of ideal stoichiometric oxide. Since in pure NiO cation vacancies are present, initial additions of Li^{1+} tend to increase the lattice parameter due to removal of vacancies and of the corresponding Ni^{3+} ions. Only after all initial vacancies are removed would the lattice contract according to the scheme reported above. The X-ray study would therefore indicate a definite process accompanying the incorporation of foreign atoms, giving useful indications on the behaviour of the solid in terms of its ability to manifest a defective structure.

We thought it desirable to extend the observations to other systems, and CdO was chosen for reasons which will appear later. Cadmium oxide is cubic (NaCl structure) and contains an excess of cadmium. The excess cadmium atoms are believed to be in interstitial positions, since an increase of cadmium excess leads to an expansion of the lattice parameter, as found by FAIVRE[5].

EXPERIMENTAL

Samples. Cadmium hydroxide was precipitated from the nitrate with ammonia, and thoroughly washed. After drying at 110°C, the hydroxide was heated at 300°C in air for 3 hr. The oxide obtained, (hereafter called CdO-300), was reddish brown. "Pure oxide samples" for X-ray analysis were obtained by heating CdO-300 in air at 550°, 750°, 900° or 1000°C, for 3 hr in a platinum crucible and quenching in air. Some measurements of lattice parameter were also carried on CdO prepared in different ways, as discussed below. Specimens of CdO containing additions were prepared by soaking the oxide CdO-300 in 1·5 to 2 volumes of a titrated solution of the nitrate of the foreign atom. The soaked mass was subsequently dried at 110°C for 1 hr, mixed, heated to 500°C for 5 hr, carefully mixed, and finally heated at 900°C for 3 hr. The In^{3+}-doped samples were found to be bluish-brown, while the Ag^{+1} doped ones remained still reddish brown. In the case of Na additions, pelleting was necessary to prevent evaporation of the alkali oxide, and the Na content of the final specimen was always checked by means of flame spectrometry analysis against Cd-containing standard solutions. In the case of In additions, a few checks made with the flame spectrometer indicated that the In present after heat treatment was equal to the theoretical one within experimental errors. Therefore, for both Ga and In, the theoretical amount has always been assumed.

X-ray analysis.[6] All samples were studied by means of a back-reflection symmetrical focusing camera (Charles Supper), 12 cm diameter, using Cu$K\alpha$ radiation. Strictly standardized procedures were adopted and two independent films were taken for each sample. Diffraction lines were measured to an accuracy of 0·005 cm with a Norelco measuring device. Three to five independent readings were made on each film. Because of the positioning marks provided in the camera, checks of shrinkage effects could also be made, but shrinkage was found to be linear. No thermostating was made for the majority of cases, but care was taken to check the temperature continuously during each exposure. Temperature fluctuations were less than $\pm 0{\cdot}4$°C, corresponding to an error of $\pm 0{\cdot}25 \times 10^{-4}$ Å. All lattice parameters were reduced to 21°C by means of the experimentally determined thermal expansion. It should be mentioned that the majority of exposures were taken within ± 3°C from 21°C. Measurements were made on six higher angle lines, the resolved doublets for (600), (531) and (440) reflexions, occurring in the vicinity of 80°, 76°, 68° respectively. The data were analyzed in terms of a graphical extrapolation against $\varphi \tan \varphi$, where $\varphi = \pi/2 - \Theta$. Differences between this method and the analytical one were negligible. A standard error of the order of $0{\cdot}2 \times 10^{-4}$ Å was found in analytical extrapolation. Several reproducibility tests were made on some samples. From these, and from calculated standard deviations, a probable error $\pm 0{\cdot}5 \times 10^{-4}$ Å could be inferred. In assessing the error for individual specimens with regard to the variation of lattice parameter with foreign atom concentration, other factors come in, such as inhomogeneity of the sample, and errors in reproducing the same concentration. The total error in a is of the order of $\pm 1 \times 10^{-4}$ Å. No

Vol. 17
1960

refraction correction has been made. All values are in Angstroms, having assumed the following values for wavelengths: $\lambda_{\alpha 1} = 1{\cdot}54051$ Å, $\lambda_{\alpha 2} = 1{\cdot}54433$ Å.

Experimental results

Values of the lattice parameter a at different temperatures in the vicinity of room temperature are plotted in Fig. 1. From the plot a thermal

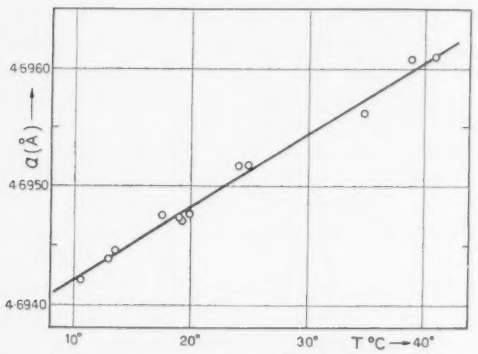

FIG. 1. Lattice parameter a of cadmium oxide as a function of the temperature.

expansion coefficient of $1{\cdot}35 \times 10^{-5}$/°C was determined. This value has been used to refer all data to 21°C. A few checks were made on CdO samples which had been first prepared in oxidation conditions different from the usual hydroxide decomposition in air, namely, Cd metal oxidation, CdO partially reduced with Cd vapor *in vacuo* and CdO from nitrate decomposition. All were subsequently given the usual high temperature treatment in air. Their lattice parameter, within the experimental error, did not differ from the value for CdO obtained from hydroxide. Heating CdO-300 at different temperatures (555°, 750°, 1000°C) did not affect the value of a.

Table 1 lists the values of a of In^{+3}-doped samples, all data being reduced to 21°C. These data have been plotted in Fig. 2 as a function of the cube root of the concentration of In atoms. It can be seen that a good straight line is obtained. It should be noted, however, that the line does not extrapolate for zero In concentration to the value experimentally found for CdO. The intersection of the straight line traced by means of the

Table 1. *Lattice parameters of* CdO *samples containing* In

In (atoms per cent)	a(Å)
0·02	$4{\cdot}69\ 46_6$
0·05	$4{\cdot}69\ 48_1$
0·09	$4{\cdot}69\ 48_2$
0·10	$4{\cdot}69\ 48_3$
0·3	$4{\cdot}69\ 53_7$
0·5	$4{\cdot}69\ 52_8$
0·5	$4{\cdot}69\ 54_7$
0·6	$4{\cdot}69\ 53_8$
0·6	$4{\cdot}69\ 57_2$
0·8	$4{\cdot}69\ 55_9$
1·0	$4{\cdot}69\ 58_2$
1·0	$4{\cdot}69\ 58_2$
1·5	$4{\cdot}69\ 57_9$
2·0	$4{\cdot}69\ 59_9$
3·0	$4{\cdot}69\ 63_8$
3·0	$4{\cdot}69\ 63_9$

method of least squares is 4·69426 Å. The probable error on the extrapolated values is 0·00005 Å, so that the difference from the value of a found for pure CdO is significant, amounting to 0·00063 Å.

Table 2. *Lattice parameters of* CdO *samples containing* Ag

Ag (atoms per cent)	a(Å)
0·1	$4{\cdot}69\ 44_0$
0·2	$4{\cdot}69\ 42_8$
0·2	$4{\cdot}69\ 43_5$
0·5	$4{\cdot}69\ 42_2$
0·8	$4{\cdot}69\ 40_6$
1·0	$4{\cdot}69\ 40_6$
1·5	$4{\cdot}69\ 41_1$
2·0	$4{\cdot}69\ 39_9$
3·0	$4{\cdot}69\ 38_5$
3·0	$4{\cdot}69\ 39_8$

Table 2 reports the data obtained for Ag-containing CdO. The data have been reported in Fig. 2 according to the same plot. Once again, the best straight line does not extrapolate to the value of pure CdO. The difference, however, is less marked. The two extrapolated values, the one determined by In additions, and that determined by Ag addition, do not appear to coincide. In both

cases, each point in the graph represents the average of two films on independently prepared samples.

Some samples containing gallium additions have also been examined. After an initial decrease of the lattice parameter, up to a concentration of 0·3 per cent Ga atoms, it was found that for higher Ga concentrations the lattice parameter did not

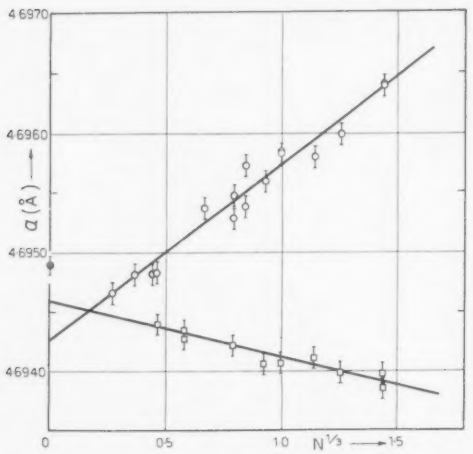

FIG. 2. Lattice parameter a of cadmium oxide containing N atoms per cent of indium (○) or silver (□). $T = 21$°C.

show any significant variation. In view of the dimensional difference between Ga^{+3} ions (r = 0·62 Å) and Cd^{+2} ions (r = 1·03 Å) the result might point to limited solubility of gallium oxide in CdO, with consequent segregation of gallium additions.

DISCUSSION

The incorporation of In_2O_3 or of Ag_2O in CdO should be described according to one of the possible schemes which can be traced when an ion of different charge to that of the host ions is incorporated into an ionic matrix. For a general discussion of the problem reference can be made to the article by KRÖGER and VINK[1]. It is only necessary at this point to recall that either *atomic defects* such as cation vacancies or *electronic defects* such as valency change of In^{+3} or of Cd^{+2}, are introduced by the addition. We shall briefly discuss the possibility of vacancy formation later on.

Addition of indium. Fig. 2 shows that after an initial decrease the lattice parameter increases upon addition of indium. This cannot be caused by a simple ionic size effect since In^{+3} is slightly smaller than Cd^{+3} (r = 0·92 vs. 1·03 Å in Goldschmidt's scale, or 0·81 vs. 0·97 Å in Pauling's scale). We can interpret the above results by means of the following scheme. At the beginning, in the starting material ("pure" CdO), there is an excess of Cd atoms in interstitial position. The hypothesis of oxygen vacancies will be discussed later. It is likely that the interstitial Cd atoms are ionized to Cd^{+1} or Cd^{+2}, but, regardless of the specific degree of ionization, their presence will lead to an expansion of the lattice parameter. In the left hand side of Fig. 3(a), interstitial atoms are represented as Cd^{2+} ions. The corresponding electrons, which are responsible for conduction, (see below), are represented as belonging to lattice ions, but they are not to be thought as permanently trapped. These quasi-free electrons, in our simple scheme, could also be represented as Cd^{1+} ions. As noted in the introduction, the two representations are essentially equivalent for our purpose. The first additions of In_2O_3 must introduce either a variation of atomic disorder or a variation of electronic disorder. The last case is equivalent in our simple ionic model to ionic charge changes ("controlled valency"). However, this possibility should be ruled out, because controlled valency, when an ion of higher charge is introduced, would require the decrease of charge of some ions, thereby leading to an increase of the lattice parameter. As this contradicts the observed decrease of a for low concentrations of In, we must consider only the introduction of atomic disorder. The first additions of In_2O_3 would tend to introduce an equivalent concentration of cation vacancies. These, however, cannot be stable in the presence of a relatively high concentration of interstitials, since thermodynamic equilibrium between interstitials and vacancies must be obeyed, and as a first approximation we can assume that the same equilibrium will hold as in pure CdO. The cation vacancies will therefore be occupied by interstitial atoms, (Fig. 3a) and this process will lead to a relaxation around formerly occupied interstitial sites, and consequently to a decrease of the lattice parameter. When practically all interstitials have disappeared, In_2O_3 will be incorporated in a different

Vol. 17
1960

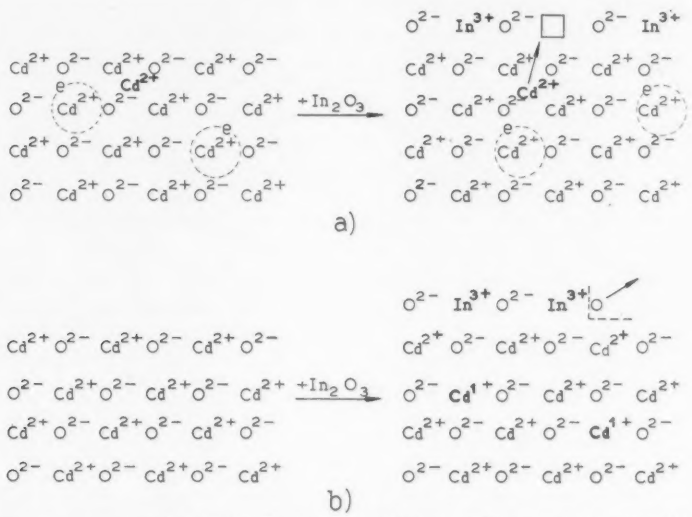

FIG. 3. Incorporation of In_2O_3 (a) first addition, elimination of interstitial cadmium (lattice parameter decreases); (b) controlled valency process (lattice parameter increases).

way, namely according to a controlled valency process. For each addition of indium, an equivalent amount of Cd^{+2} ions will change from $+2$ to $+1$ (Fig. 3b), and as a consequence the lattice parameter will expand because of the larger effective radius of ions with smaller charge. We should like to point out that the present description is schematic and that for instance the problem could equally well be considered in terms of the passage of In ions from a charge $+3$ to $+2$. It must also be noted that we have adopted a strictly ionic model with localized charges, while covalent character is certainly present to a certain extent in these oxides. However, inclusion of these factors would modify only details of our arguments and not change our general conclusions.

The value of a extrapolated for $[In] = 0$ would then correspond to that of an oxide free from defects (interstitials, Cd ions with valency different from $+2$ and In ions).

As the difference between the observed value of the lattice parameter of undoped CdO and the extrapolated one is, in the present hypothesis, due to Cd excess, one can give an estimate of Cd excess present in CdO by a comparison with expansion effects induced by Cd additions. Using FAIVRE's data[5] our observed Δa of $6{\cdot}3 \times 10^{-4}$ Å is found to correspond approximately to an excess of 0·04 per cent Cd.

The present case seems very similar to that outlined by BROWNLEE and MITCHELL[4] who studied additions of Li_2O to NiO, except that in NiO there is a lack of metal, rather than excess. In our case as well, the inversion point in the lattice parameter vs. concentration curve should effectively correspond to the disappearance of all interstitials, that is to say, to a "titration" of Cd excess. Due to the correspondence of 2 In atoms for each Cd atom in interstitial position, if one could determine the inversion point with precision, this would afford a fairly precise means of titration of Cd excess in a way independent from chemical means. The accurate determination of the descending branch of the curve is however experimentally impossible, so that one can only fix an upper limit, this being the lowest concentration used, which appears to be on the straight line. It is also possible to try to calculate and to draw the descending branch of the curve, on the assumption that the contraction is caused by the disappearance of Cd excess, plus the substitution of Cd^{+2} ions with the smaller In^{+3} ions. The first effect can be evaluated by means of FAIVRE's results, while the second effect (which is only a small fraction of the total) can be

estimated by the type of calculation outlined by one of us.[7] The calculation is very rough, and one can only say that the intersection should lie in the vicinity of 0·02 per cent In, which is equivalent to 0·01 per cent Cd, or 4×10^{18} atoms/cm^3. This figure is probably accurate to within a factor of two in giving the metal excess in our CdO. FAIVRE's estimate by chemical titration ($0{\cdot}05\pm0{\cdot}02$ per cent is higher, but it refers to an oxide prepared in conditions different from the present ones (lower decomposition temperature), and moreover, the discrepancy is not too large in view of the errors involved.

It is interesting to recall that electric measurements gave, on different samples, a concentration of free electrons around 3×10^{18}[8] or $1{\cdot}6\times10^{19}$[9] electrons/cm^3. If one assumes that the excess Cd atoms are doubly ionized, and are the source of free electrons at room temperature, one would get a concentration of free carriers of the order of 8×10^{18}, if 0·01 per cent Cd excess is assumed.

It is desirable to examine whether alternate schemes for the incorporation of In additions could in fact be justified by the same observations. We consider the ascending part of the curve of Fig. 2, since we have already shown that the descending one could not be observed with the hypothesis of electronic disorder. If in the ascending line, incorporation of In_2O_3 does not cause a variation of charge, then it must introduce atomic disorder, namely cation vacancies. The effect of a vacancy on the lattice parameter in these oxides has not been the object of either theoretical or experimental investigations. In view of the substantial decrease of ionic character in CdO, as compared to alkali halides, it is questionable whether the theoretically predictable expansion around a vacancy in an ionic crystal[10] would be at all appreciable in the case of CdO. Furthermore, the expansion effect would be lessened by the contraction which would take place because of the introduction of cations with higher charge, in a way similar to that discussed by BASSANI and FUMI[11]. In any event, the possibility of creation of vacancies cannot be ruled out, at least so far. Thus, going back to the hypothesis of cadmium atoms in interstitial position, one could for instance argue that a cadmium excess results from an unbalanced presence of both cation and anion vacancies, and that addition of indium would shift the balance towards a higher concentration of cation vacancies, which would be more effective in the outward displacement of neighbouring atoms. This hypothesis, however, faces the difficulty of explaining the inversion point found with In addition.

Addition of silver. A way of overcoming the difficulties found in assessing a unique meaning to the experimental behaviour of a with In additions is provided by adding univalent atoms. Both sodium and silver are favourable from the point of size; some difficulties, however, were found in the investigation of systems with Na additions. Even though the results are less reproducible, they are in very good qualitative agreement with those obtained with silver. They will be briefly discussed later. Fig. 2 reports the data obtained with Ag additions. It should be pointed out that in both Goldschmidt's and Pauling's scale of ionic radii Ag^{+1} is appreciably larger than Cd^{+2} ($r_{Ag^{+1}} =$ 1·13 or 1·26 A respectively). It is therefore significant that in spite of the difference in radii the introduction of Ag leads to a decrease of the lattice parameter. Unless a controlled valency mechanism is invoked it is difficult to justify such a behaviour. In fact, if one had attributed the observed expansions caused by In additions to vacancy formation, ruling out variations of valency, then in order to be consistent* in the case of Ag additions it would be necessary to assume atomic disorder, such as either the introduction of atoms in interstitial positions which of course would expand the lattice, or the introduction of anion vacancies, which should again be thought of as a process which expands the lattice. In addition, the larger size of Ag^{+1} would increase the expansion effect and furthermore, the electrostatic perturbation introduced by a cation with a lower charge would once more be in the direction of a lattice expansion. In all cases therefore an expansion is expected, contrary to the experimental observation.

We think that the results obtained with Ag are of particular importance, and give support to the formulated mechanism of incorporation. It is of course immaterial in the present formulation to think of a change of valency of Ag^{+1} to Ag^{+2} rather

* It might be argued that the incorporation of Ag_2O is essentially different from that of In_2O_3. While this possibility cannot be ruled out, it appears rather unlikely to us.

Vol. 17
1960

than of a change of valency of cadmium ion.* The effect would always be that of a shrinkage due to the formulation of ions with smaller effective radius. In fact, the same comments apply as those already mentioned in the case of In. Some remarks should be added in considering the value extrapolated by the straight line traced in Fig. 2 for Ag additions. It has been mentioned that this extrapolated value a^0_{Ag}, even though not coincident with the value pertinent to pure CdO, is also different from the value extrapolated for zero In concentration a^0_{In}. It should be noted, in this regard, that Ag_2O could not tend to eliminate interstitial cations, having itself a cation excess. Thus, the "titration" process of interstitial atoms does not take place, and an unknown† amount of interstitial atoms can be left. The extrapolated value would therefore lose a direct meaning. In view of this uncertainty, and of the ambiguity arising from the value of a^0_{Ag}, which is not far, even though significantly different, from either a^0_{In} or a^0, we prefer not to dwell on this point any further, but rather to emphasize once more the qualitative trend shown by this system.

Sodium additions conform with the above view: when pelleting is adopted to prevent evaporation of Na a shrinkage of the lattice parameter is observed, but longer heating times are required, which would be justified by the fact that incorporation is accompanied by an oxidation process, which occurs more easily in unpelletted powder. It is important at this point to recall that incorporation of additions depends on the partial pressure of oxygen in the manner discussed by KRÖGER and VINK[1], so that only as a first approximation is it possible to consider an incorporation scheme valid for all additions of the same valency, with favourable sizes.

As a last point, we would like to recall that the variations of lattice parameters observed are in agreement with a scheme of controlled valency mechanism, as one of us has shown,[7] if volume variations are calculated with the help of elastic theory, and with the simple assumption of considering ions as rigid spheres having fixed radii. In the calculation, ions were given Goldschmidt's ionic radii. It would be easy to show that other consistent sets of radii, such as Pauling's scale, would lead to similar results. In our opinion, even though it is significant that the right order of magnitude is predicted, it would not be meaningful to give too much weight to a distinction between different sets of ionic radii, given the severe assumptions of that calculation and the uncertainty in the radii of ions with anomalous valency. As already pointed out, the observed agreement does not imply that a strictly ionic model must necessarily hold, but simply that ionic radii are a consistent set by which to compute volume variations, in the direction predicted by controlled valency mechanisms. This can be of help in assessing conditions of limited solubility, such as in the quoted case of Ga additions, where large variations of the order of -13×10^{-4} Å, could be expected.[7]

It should be noted that only if randomly dispersed atomic point imperfections are present can we expect the above considerations to hold. Any clustering or precipitation, as for instance along dislocation lines or near the surface of grains, would make it impossible to apply such calculations. It is therefore significant that it has been mentioned[12] that diffuse scattering measurements seem to exclude clustering of added atoms in the system $NiO + Li_2O$, a system for which electrical measurements and lattice parameter variations point to controlled valency processes.

Acknowledgements—We wish to thank Prof. F. G. FUMI for correspondence on the electrostatic effect of impurities, and Dr. A. W. LAWSON for critically reading the manuscript. Financial support by the Comitato Nazionale Ricerche Nucleari for the completion of the work is gratefully acknowledged.

* Changes of valency of O^{2-} to O^-, which would also contract the lattice, are not being considered. They would correspond to quasi-free holes, and there is no evidence of their presence.

† The amount present could in fact be larger than in pure CdO, because of cation excess, which can shift the equilibrium in this direction, or it could also be smaller, if oxidation of Ag-containing CdO could occur more easily, if equilibrium constants regulating the defect concentration in CdO are affected in this way.

REFERENCES

1. KRÖGER F. A. and VINK H. J., *Solid State Physics* Vol. 3, p. 307. (edited by SEITZ F. and TURNBULL D.) Academic Press, New York (1956).
2. VERWEY E. J. W., HAAYMAN P. W., ROMEIJN F. C. and VAN OSTERHOUT G. V., *Philips Res. Rep.* **5**, 173 (1950).

3. KRÖGER F. A., VINK H. J. and VAN DEN BOOMGAARD J., *Z. Phys. Chem.* **203,** 1 (1954).
4. BROWNLEE L. D. and MITCHELL E. W. J., *Proc. Phys. Soc. Lond.* B**65,** 710 (1952).
5. FAIVRE R., *Ann. Chim.* **19,** 11 (1944).
6. With regard to the X-ray techniques adopted, reference can be made to *X-Ray Diffraction by Polycrystalline Materials,* Chapter 15 (edited by PEISER H. S., ROOKSBY H. P. and WILSON A. J. C.) The Institute of Physics, London (1955).
7. CIMINO A., *J. Phys. Chem.* **61,** 1766 (1957).
8. HOGARTH C. A., *Proc. Phys. Soc. Lond.* **64**B, 691 (1951).
9. WRIGHT R. W., *Proc. Phys. Soc. Lond.* **64**B, 350 (1951).
10. MOTT N. F. and LITTLETON M. J., *Trans. Faraday Soc.* **34,** 485 (1938).
11. BASSANI F. and FUMI F. G., *Nuovo Cim.* **11,** 274 (1954).
12. Results of FLINN P. A., quoted by HEIKES R. R. and JOHNSTON W. D., *J. Chem. Phys.* **26,** 582 (1957).

Vol. 17
1960

J. Phys. Chem. Solids Pergamon Press 1960. Vol. 17, Nos. 1/2, pp. 65–68. Printed in Great Britain.

INFLUENCE OF DISORDER ON THE LIFETIME OF POSITRONS IN ANTHRACENE*

C. COTTINI, G. FABRI, E. GATTI† and E. GERMAGNOLI†

Laboratori C.I.S.E., Milano (Italy)

(*Received* 29 *January* 1960; *revised* 24 *March* 1960)

Abstract—The decay features of positrons in anthracene have been experimentally investigated using both single- and poly-crystals at temperatures ranging between −196°C and 295°C. In solid specimens annihilation lifetime was equal to $3{\cdot}7 \times 10^{-10}$ sec independently of the measuring temperature. A very notable effect was however found near the melting point (218°C) a complex decay appearing at about 210°C. Neutron irradiated specimens showed a complex decay even at room temperature.

1. INTRODUCTION

THE features of positron annihilation through a short lifetime ($\tau_1 \sim 10^{-10}$ sec) do not appear to be influenced by temperature in any kind of solid materials; on the other hand it has been pointed out by many authors[1–3] that the long lifetime ($\tau_2 \sim 10^{-9}$ sec) can change both in value and in intensity depending on temperature and state of aggregation of the investigated material. Roughly speaking, temperature effects on positron annihilation have been described only for non-crystalline solids; few exceptions have been reported to date, namely the existence of a rather weak τ_2 component in solid napthalene[3] and the existence of both a τ_2 component and a temperature effect in ice.[2] Undoubtedly considerations involving order–disorder transitions must be of primary importance in explaining such effects.

Available experimental data are very scanty and it seemed convenient to carry out an experimental investigation in the case of another molecular solid, anthracene, using single crystals, molten material, microcrystals of different sizes and radiation damaged monocrystalline specimens.

Anthracene was chosen due to its being available in the shape of big single crystals and owing to its comparatively high melting and boiling points. This fact allowed an accurate search for possible temperature effects both in solid and in liquid states; detailed measurements near melting point have been also carried out.

2. MEASURING TECHNIQUES

The positron source was carrier free ^{22}NaCl. The specimens were two cylindrical single crystals, 10 mm diameter and 5 mm thickness, and the active ^{22}NaCl was deposited directly onto them, so that the source was sandwiched between the crystals.

Freezing baths were used for low temperature measurements; in the intervals 20°C–210°C and 290°–295°C a small furnace kept the temperature constant at ±1°C.

For the investigation of temperature effects near melting point (218°C) a much more accurate control of temperature was required. This was accomplished by immersing the specimens into a boiling naphthalene bath (boiling point 217°C at standard conditions) and carefully controlling the pressure above it. By changing the pressure, the bath temperature was varied between 211°C and 226°C. With this method measurements could be prolonged even up to six hours, the temperature being kept constant at ±0·1°C.

All during the measurements at the above room

* A partial preliminary report about the present research has been published as a letter in *Nuovo Cim.* **14**, 454 (1959).

† Laboratori C.I.S.E., Milano, and Istituto di Fisica del Politecnico, Milano.

temperature anthracene was kept in a purified argon atmosphere.

The delay spectra of annihilation γ-rays with respect to 1·28 meV γ-rays from ^{22}Na were analysed by means of a vernier time sorter,[4] working in connection with two slow channels for energy discrimination. The γ-ray detectors were two plastic scintillators (Pamelon), optically coupled with RCA 6342 photomultipliers.

The resolving time of the apparatus, defined as the full width at half-height of a prompt coincidence curve, was estimated to be $6{\cdot}5 \times 10^{-10}$ sec. Prompt coincidence curves obtained with a ^{60}Co source in the same geometry and with the same pulse energy discrimination were used for the measurements of positron decay.

3. EXPERIMENTAL RESULTS

(a) *Influence of melting*

The experimental results concerning positron lifetime in antracene as a function of temperature are shown in Fig. 1. It is noticed that in the range

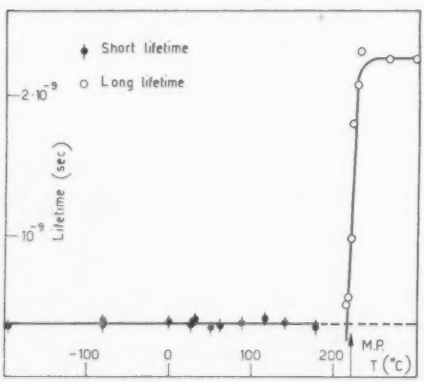

FIG. 1. Positron lifetimes as functions of temperature.

of temperature between −196°C and about +210°C the decay of positrons takes place only through the short lifetime τ_1, its value being fairly constant and equal to $(3{\cdot}7 \pm 0{\cdot}2) \times 10^{-10}$ sec. A few degrees below melting point a complex decay appears; τ_1 remains constant and equal to $3{\cdot}7 \times 10^{-10}$ sec even at temperature much higher than melting point; τ_2 is already equal to $9{\cdot}9 \times 10^{-10}$ sec at 215°C, increases to $2{\cdot}25 \times 10^{-9}$ sec in a temperature range of about 10°C and does not change at higher temperatures. Two typical delay curves are shown in Figs. 2 and 3. Fig. 2 shows also a prompt coincidence curve, which allows a measurement of the over-all resolution time of the apparatus. The described behaviour of anthracene is similar to that reported for naphthalene[3] at high temperature, but differs in the fact that no long-lived component is noticeable below the melting point.

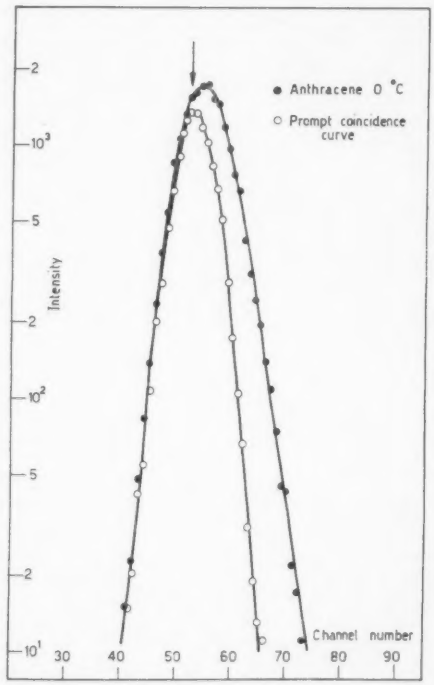

FIG. 2. Prompt coincidence curve showing the resolution of measuring apparatus and typical delay curve of positrons in antracene at room temperature.
1 channel = $1{\cdot}15 \times 10^{-10}$ sec

The lifetime τ_2 shows a sharp temperature effect near the melting point: while the percentage of positrons decaying through a long lifetime τ_2 increases from zero to about 35–40 per cent between 210°C and 215°C and does not change at higher temperature, the lifetime monotonically increases until 225°C.

(b) *Influence of structure*

A new set of measurements was carried out by

Vol. 17
1960

letting the temperature of the anthracene specimens decrease from +295°C to −196°C and analysing the decay features of positrons at some temperatures: the obtained results were equal to the one described in the preceding section. In order to investigate the possible influence of order on the behaviour of positrons in anthracene some measurements were performed at room temperature with specimens of different grain size, the smallest diameter of grains being about 3μ after the anthracene powder had been ground for four days and reduced to a fairly uniform grain size. The decay curves obtained in this case did not show any difference when compared to those which had been obtained with single crystals.

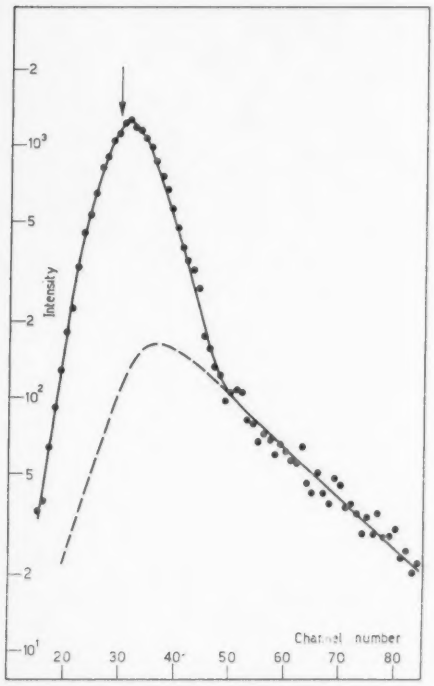

FIG. 3. Delay curve of positrons at 260°C.

Further measurements were carried out with single crystals which had been disordered by being irradiated with ^{60}Co γ-rays and with fast neutrons. After irradiation with an integrated flux of about 4×10^{18} neutrons cm^{-2} the single crystals turned out to be heavily coloured and the decay curves at room temperature were different from those typical of non-irradiated crystals, the difference being not very marked but significantly beyond the experimental uncertainties. Actually the delay curves could be resolved into two distinct mean lives: $\tau_1 = 3{\cdot}8\times10^{-10}$ sec and $\tau_2 \simeq 6\times10^{-10}$ sec, the percentage of positrons decaying through the "long" lifetime being about 30 per cent.

4. DISCUSSION

Two conclusions can be deduced from the results concerning the behaviour of positrons in non-irradiated anthracene specimens: the absence of a long lifetime in the solid, and the close similarity in the decay features of single crystals and thin-grained powder. Concerning the former fact, anthracene differs from napthalene, and this is difficult to explain on the basis of the known properties of the two materials; purely qualitative arguments do not appear sufficient to this end.

Non-formation of positronium in solid anthracene is likely according to the present results: furthermore, the probability of positronium formation increases very sharply in a rather narrow temperature interval at melting point.

The structure of excited bands in the anthracene molecule appears to be so modified on melting that the conditions for the formation of positronium are fulfilled. Alternatively, the formation of positronium in solid anthracene is conceivable provided that a quick triplet–singlet conversion is postulated,[1] but this seems unlikely since the τ_2 component becomes highly probable within a temperature interval which is certainly less than 5°C. This fact, together with the lack of any temperature effect in the fast component both in the solid and in the liquid state, makes it difficult for an effective mechanism of quick triplet–singlet conversion to be postulated.

Evidence has been obtained that formation of positronium is possible in neutron-damaged specimens; though it is reasonably expected that disorder induced by radiation is effective in drastically modifying the band structure of anthracene, a detailed interpretation of the effect is not easy due to the lack of reliable information about the nature of the disorder which is introduced by radiation damage. A few experimental attempts have been made for the purpose of evaluating the percentage of broken molecular bonds and of

investigating the chemical effects due to the fast neutron bombardment: a comparison between the ultra-violet absorption spectra of irradiated and non-irradiated anthracene gave evidence that a non-negligible percentage of molecular bonds had been broken, but a quantitative conclusion appeared to be unreliable. Both thermally induced disorder and radiation damage, though well distinguished in anthracene, are shown by the present work to be effective in introducing a mechanism of slow decay of positrons. Further experiments are planned in order to obtain a more thorough understanding of both radiation damage in anthracene and its influence on the decay of positronium. At present, it is thought that the above described results can provide a valuable additional piece of experimental evidence concerning the interpretation of the behaviour of positronium in solids.

Acknowledgements—We are indebted to Prof. E. LAZZARINI, Istituto di Fisica del Politecnico (Milano) for having performed X-ray and optical analyses of irradiated anthracene specimens. Thanks are also due to Mr. G. SCHIAVINI, of Laboratori C.I.S.E., for his help in the preparation of microcrystalline specimens.

REFERENCES

1. BELL R. E. and GRAHAM R. L., *Phys. Rev.* **90,** 644 (1953).
2. WAGNER R. T. and HEREFORD F. L., *Phys. Rev.* **99,** 593 (1953).
3. LANDES H. S., BERKO S. and ZUCHELLI A. J., *Phys. Rev.* **103,** 828 (1955).
4. COTTINI C. and GATTI E., *Nuovo Cim.* **4,** 1550 (1956); COTTINI C., GATTI E. and VAGHI F., *Nuclear Electronics*, Vol. I, p. 177. I.A.E.A., Vienna (1959); COTTINI C., GATTI E., SVELTO V. and VAGHI F., *Fast-pulse techniques in Nuclear Counting*, p. 49. U.C.R.L.-8706 (1959).

J. Phys. Chem. Solids Pergamon Press 1960. Vol. 17, Nos. 1/2, pp. 69–79. Printed in Great Britain.

ASSOCIATION AND DISSOCIATION OF CENTRES IN LUMINESCENT ZnS–In

H. KOELMANS

Philips Research Laboratories, N. V. Philips' Gloeilampenfabrieken, Eindhoven, Netherlands

(*Received* 24 *September* 1959; *revised* 14 *January* 1960)

Abstract—ZnS–In phosphors, which are efficient upon excitation with $\lambda = 3650$ Å, were prepared by firing in H_2S at 1200°C and quick cooling to room temperature. The emission spectrum depends on the In concentration and consists of three bands at 6200 Å, 5350 Å and 4700 Å. X-ray analysis shows that the maximum amount of In incorporated is about 10^{-2} gram-atoms In per mole ZnS. Refiring the phosphors at 600°C kills the luminescence at room temperature, an effect shown to be due to association. The trivalent In is compensated in the lattice by V_{Zn}''. On the basis of the experimental evidence the 6200 Å band is ascribed to $In_{Zn}^{\cdot}$, the 5350 Å band to the associate $In_{Zn}V_{Zn}'$ and the 4700 Å band to V_{Zn}).*

The low-temperature phosphorescence of the ZnS–In phosphors is strongly stimulated by irradiation into bands at $1{\cdot}8\mu$ and $< 1{\cdot}2\mu$.

1. INTRODUCTION

IN THEIR work on the effect of trivalent substituents on the luminescence of Cu- and Ag-activated ZnS KRÖGER and DIKHOFF[1] found that several of the trivalent substituents introduced new emission bands. In the case of hexagonal ZnS–Ag,In they found a broad extra emission band with a peak at 6500 Å. In hexagonal ZnS–Cu,In the peak of the extra emission was at 6800 Å. From the fact that these bands, in contrast to the blue and green Ag- and Cu-emission, do not move on incorporation of Cd, KRÖGER and DIKHOFF concluded that the long-wave emissions could be ascribed to a characteristic transition in the In^{3+} ion.

KLASENS[2] found the emission peak of In in ZnS–Ag,In at 6100 Å at −183°C and attributed it to the recombination of an electron in the In trap with a hole in the valence band. Because, as HOOGENSTRAATEN[3] has shown, the distance between the trap level and the filled band does not change much on introduction of Cd, the non-characteristic transition proposed by KLASENS also accounts for the fact that the In emission is little affected by Cd substitution.

FROELICH[4], working with ZnS–Cu,In at relatively high In concentrations, found a weak long-wave emission with a peak at about 6700 Å at room temperature. The emission became brighter and shifted towards shorter wavelengths when the phosphor was cooled to −190°C.

Recently APPLE[5] investigated the system ZnS–x (Cu,Ag,Au), y (Ga,In) with y (added) $\geqslant x$. In hexagonal ZnS he found a Cu,In band peaking at 6400 Å, an Ag,In band at 6140 Å and an Au,In band at 7200 Å. The characteristics of these emissions resembled those which appear in ZnS–Cu and ZnS–Ag without added coactivator and at relatively high Cu and Ag concentrations. In a later article APPLE and WILLIAMS[6], assuming a strong association of activator and coactivator, ascribed the long-wave emissions found with In and Ga to a radiative transition from the ground state of the electron-trap to the ground state of the activator. In Section 10 the work of APPLE and of APPLE and WILLIAMS will be discussed in more detail and in relation to the results obtained in this work.

The experiments described in this paper were carried out to get more information about the In emissions in ZnS by studying phosphors activated with In, without other added impurities. As will appear from the following sections ZnS phosphors

* For an explanation of the symbols used see Section 7.

activated with rather high concentrations of In may show a strong luminescence when cooled down quickly from the firing temperature to below 400°C.

2. EXPERIMENTAL PROCEDURE

The samples were made from luminescent grade ZnS (Cl-free, precipitated from $ZnSO_4$).

The concentration of In added ranged from $0{\cdot}2 \times 10^{-2}$ to $2{\cdot}0 \times 10^{-2}$ gram-atoms In per mole ZnS. The In was added to the samples either by adding an In-solution for preparations with low In concentration or by adding the ternary compound

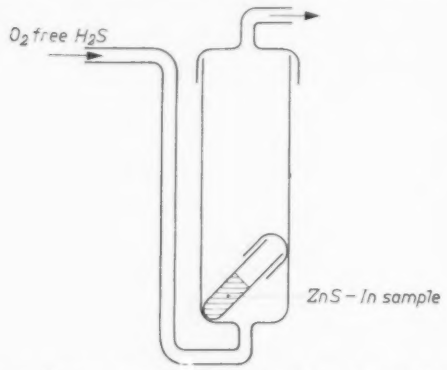

FIG. 1. Quartz apparatus used in firing the ZnS–In phosphors.

$ZnIn_2S_4$ for preparations with high In concentration. It was checked that both ways of adding the In gave the same results. The powders were fired for 30 min at 1200°C in O_2-free H_2S in quartz tubes placed in quartz vessels, as shown in Fig. 1. At 1200°C the In_2S_3 is volatile as appeared from the deposition of In_2S_3 on the cooler parts of the quartz vessel. In order to minimize the evaporation of In_2S_3 the quartz tubes were closed with quartz caps during the firing (Fig. 1). It was established by chemical analysis that after firing, with about 10^{-2} gram-atoms In per mole ZnS added, roughly 50 per cent of the added In remained in the samples. The In concentration found by chemical analysis gives, however, no clue about the amount of In really incorporated into the ZnS lattice. The amount of incorporated In was calculated from the change of the lattice constants of ZnS as is discussed in Section 3. After firing, the samples were quickly cooled to room temperature by taking the quartz vessel from the furnace and dipping it into water. The powders showed a bright luminescence with 3650 Å excitation in a colour ranging from bluish-green at low In concentrations to orange-yellow at high In concentrations. The light output of preparations with medium In concentrations was about 80 per cent of the output of commercial (Zn,Cd)S–Ag phosphors of comparable spectral distribution. The light output drops both at high and at low In concentrations. The light output at room temperature with $0{\cdot}4$, $0{\cdot}6$, $1{\cdot}2$ and $4{\cdot}0 \times 10^{-2}$ In (added) is 40, 80, 100 and 45, respectively (output at $1{\cdot}2 \times 10^{-2}$ In put equal to 100). The phosphors showed only a weak emission on excitation with cathode rays.

The rapid cooling of the powders after firing proved to be an essential part of the procedure. If the powders were allowed to cool slowly almost no luminescence was observed at room temperature. This phenomenon which strongly points to association effects is discussed in some detail in Section 8.

Firing in sulphur vapour and firing in nitrogen gave substantially the same results. Apparently the phosphors are not very sensitive to changes in sulphur pressure.

3. THE AMOUNT OF In INCORPORATED INTO THE ZnS.

High-angle X-ray powder diffraction patterns showed that the introduction of In produced a definite increase of the lattice spacings of ZnS. The results for different In concentrations (added before firing) are shown in Table 1. The c and a values of Table 1 were obtained by averaging values calculated from twelve different reflections. The concentrations of incorporated In as calculated from the increase in lattice spacings of the ZnS are shown in the last column of Table 1. In this calculation only the effect of substituting the bigger In atom for the smaller Zn atom was taken into account. The influence of the vacancies compensating the charge of the In^{3+} was neglected. Comparison with solid solutions of Ga_2S_3 in ZnS, which can be prepared at low temperature, with a wide range of Ga concentrations[7] (so that the concentration of incorporated Ga is known from the preparation) shows that this approximation is not too bad. The Zn–S distance in hexagonal ZnS is 2·35 Å. The In–S distance was taken to be 2·53 Å, this being the In–S distance for In in the

Vol. 17
1960

Table 1. *Lattice constants of* ZnS–In *phosphors*

In conc. added, (gram-atom/mole)	c	a	In conc. incorporated (gram-atom/mole)
$4{\cdot}0 \times 10^{-2}$	$6{\cdot}2641 \pm 0{\cdot}0004$	$3{\cdot}8249 \pm 0{\cdot}0003$	$0{\cdot}8 \times 10^{-2} \pm 0{\cdot}1 \times 10^{-2}$
$1{\cdot}2 \times 10^{-2}$	$6{\cdot}2624 \pm 0{\cdot}0004$	$3{\cdot}8238 \pm 0{\cdot}0003$	$0{\cdot}4 \times 10^{-2} \pm 0{\cdot}1 \times 10^{-2}$
$0{\cdot}4 \times 10^{-2}$	$6{\cdot}2609 \pm 0{\cdot}0004$	$3{\cdot}8229 \pm 0{\cdot}0003$	$0{\cdot}1 \times 10^{-2} \pm 0{\cdot}1 \times 10^{-2}$
zero	$6{\cdot}2606 \pm 0{\cdot}0004$	$3{\cdot}8223 \pm 0{\cdot}0003$	zero

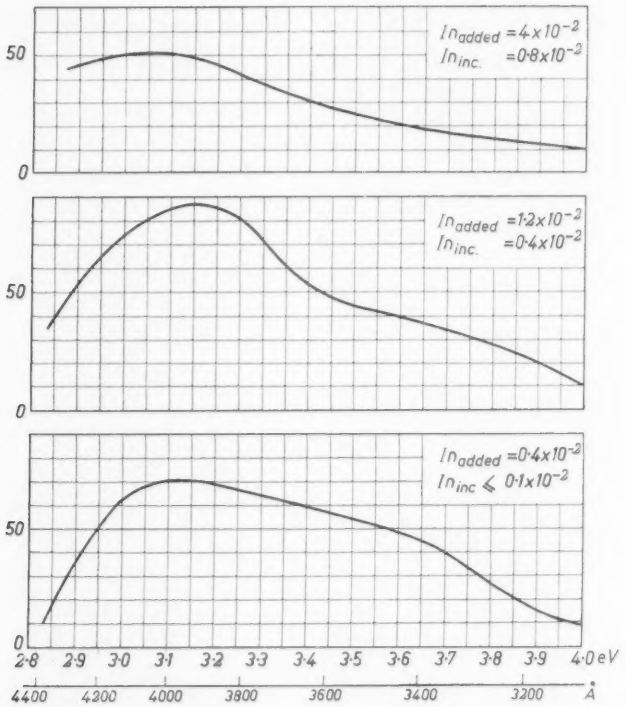

FIG. 2. Excitation spectra of the ZnS–In phosphors with different In concentrations.

tetrahedral arrangement in In_2S_3 as taken from the work of HAHN and KLINGER[8].

4. EXCITATION AND EMISSION SPECTRA

The ZnS–In phosphors, especially those with high In concentrations, show a yellow body colour. The excitation spectra of the luminescence for different In concentrations are given in Fig. 2, the curves showing a maximum at about 4000 Å for low and medium In concentrations. At high In concentration the region of strong excitation extends still further into the visible.

The emission spectra for various In concentrations at room temperature and at $-190°C$ with $\lambda = 3650$ Å excitation are shown in Figs. 3(a) and 3(b). The emission bands are broad and of a composite nature. The maximum of the emission moves to shorter wavelengths with decreasing In

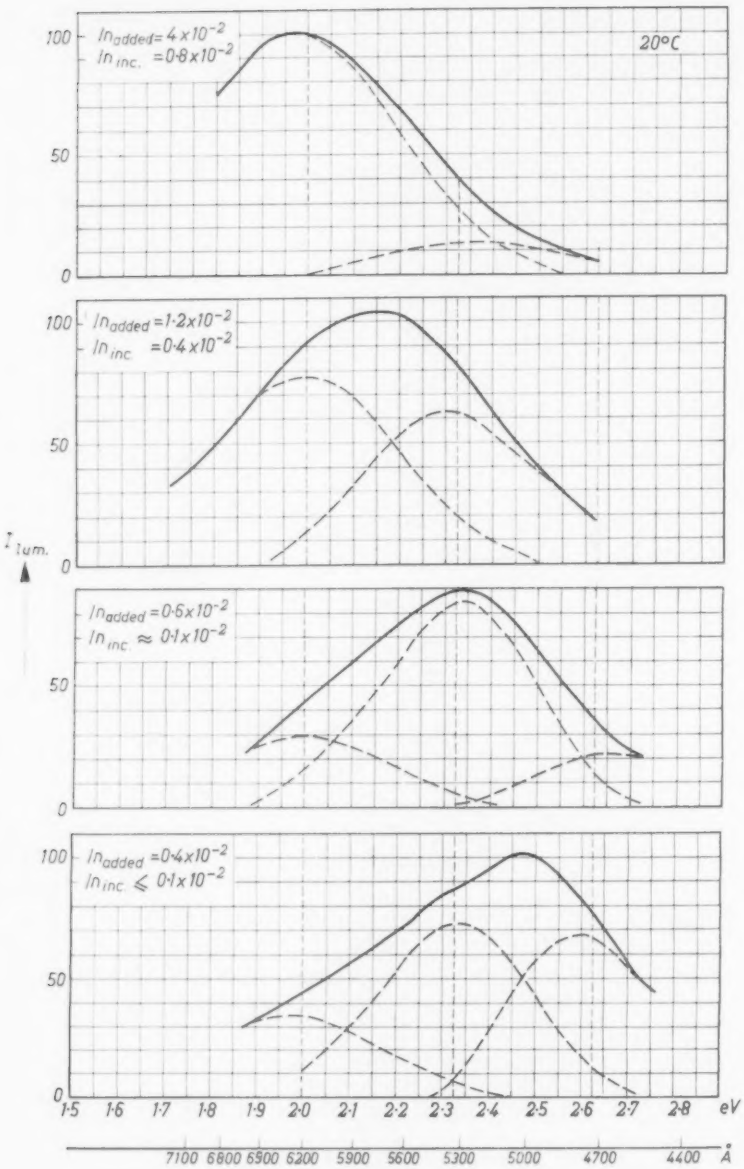

FIG. 3(a)

concentrations and with decreasing temperature. By analysing the emission curves it appeared possible to plot the over-all emission curves, both at room temperature and at −190°C for different In concentrations, as the sum of three normally shaped sub-bands. As is usual in ZnS phosphors the emission (sub-) bands do not move significantly with temperature. The apparent shift of the over-all emission curves with the In concentration and with temperature is entirely accounted for by

Vol. 17
1960

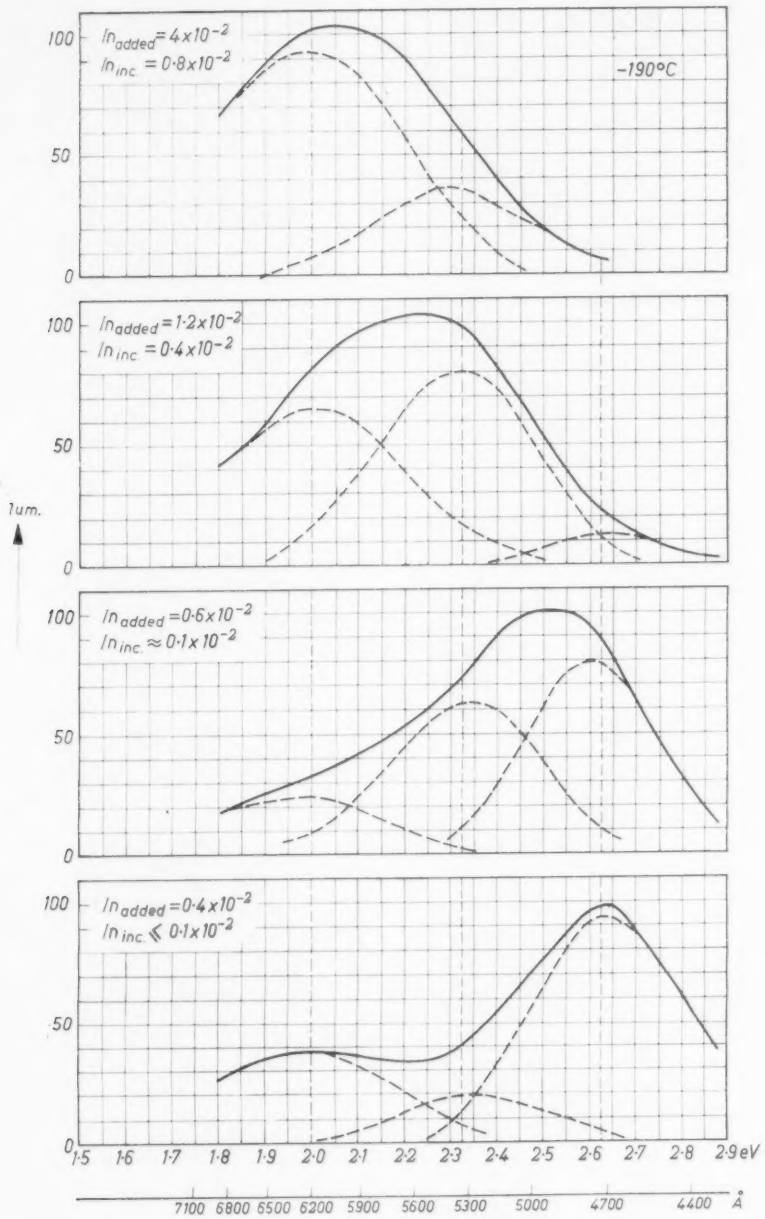
$In_{added} = 4 \times 10^{-2}$
$In_{inc.} = 0{\cdot}8 \times 10^{-2}$
−190°C
$In_{added} = 1{\cdot}2 \times 10^{-2}$
$In_{inc.} = 0{\cdot}4 \times 10^{-2}$
$In_{added} = 0{\cdot}6 \times 10^{-2}$
$In_{inc.} \approx 0{\cdot}1 \times 10^{-2}$
$In_{added} = 0{\cdot}4 \times 10^{-2}$
$In_{inc.} \ll 0{\cdot}1 \times 10^{-2}$
lum.
100
50
0
1·5 1·6 1·7 1·8 1·9 2·0 2·1 2·2 2·3 2·4 2·5 2·6 2·7 2·8 2·9 eV
7100 6800 6500 6200 5900 5600 5300 5000 4700 4400 Å

FIG. 3(b)

FIG. 3. Emission spectra with 3650 Å excitation of the ZnS–In phosphors with different In concentration. (a) At room temperature. (b) At −190°C.

relative changes in the intensity of the sub-bands. The maxima of the sub-bands are at 6200 Å (orange), 5350 Å (green) and 4700 Å (blue), respectively. The room-temperature emission at the highest In concentration is almost purely the orange band, whereas the −190°C emission curve for the lowest In concentration essentially consists of the blue sub-band. Even though the proposed division into sub-bands accounts in a simple and consistent way for the observed emission spectra, such a division might seem somewhat arbitrary if we could not present arguments to support the analysis given. The low-temperature phosphorescence and the glow of the phoshors is of a different colour than the luminescence. This phenomenon is very striking in the sample with the lowest In concentration. The low-temperature luminescence is definitely blue whereas the low-temperature phosphorescence and the glow are in the orange band. The low-temperature phosphorescence can be strongly stimulated with infra-red (cf. Section 5); the emission is then again in the orange band.

Furthermore the orange band at 6200 Å closely corresponds to the orange emission in ZnS–Ag, In[2] whereas the same blue band at 4700 Å is found in ZnS–Ga phosphors.[9]

A discussion of the emission bands and of the possible nature of the centres connected to them will be given in Section 9.

5. INFRA-RED STIMULATION OF THE PHOSPHORESCENCE

The measurements were made with a Perkin Elmer 12C monochromator equipped with a quartz prism. The samples were cooled down to −190°C and excited for 3 sec with 3650 Å radiation. After a waiting period of 70 sec the samples were exposed to the infra-red.

The infra-red stimulation spectrum of the low-temperature phosphorescence (6200 Å band) in a sample with $In_{inc.} = 0{\cdot}8 \times 10^{-2}$ is given in Fig. 4. The stimulated light was detected with an R.C.A. type I.P. 21 photomultiplier tube. The curve of Fig. 4 represents the intensity of the emitted radiation for the same number of quanta at each wavelength and shows a weak band at about 0·7 eV followed by a strong band above 1·1 eV. Owing to measuring difficulties the maximum of this band could not be measured, but it probably extends well into the visible. The spectral distribution of the emitted light was photographed on an Ilford panchromatic F.P. Special film. Excitation in the bands near 0·7 eV and above 1·1 eV only stimulated the orange band.

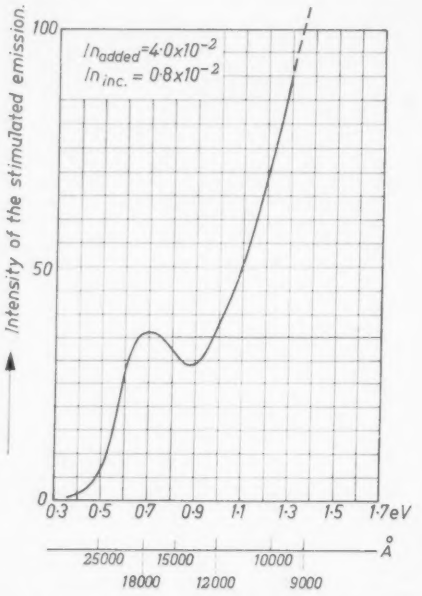

FIG. 4. Infra-red excitation spectra of the low-temperature phosphorescence of ZnS–In phosphors.

6. TEMPERATURE DEPENDENCE OF THE EMISSION: GLOW MEASUREMENTS

Figure 5 gives the temperature dependence of the total emission in a sample with $In_{inc.} = 0{\cdot}4 \times 10^{-2}$. It is seen that already at room temperature the emission is killed by about 40 per cent. Refiring the phosphor at 600°C (Fig. 5) in H_2S causes the curve to shift towards lower temperatures, the room-temperature emission being almost completely quenched in this case (cf. Section 8). In the low-temperature emission of phosphors which were refired at 600°C the blue band was found to be absent. A discussion of this point will be given in Section 9.

The results of the glow measurements (heating rate 2 degrees/sec) are given in Fig. 6.

The glow curve shows two peaks at −75°C and −160°C, respectively, the same peaks being found over the whole range of In concentration which

Vol. 17
1960

was investigated. At both peaks the glow is orange in all cases whereas the luminescence changes from bluish-green at low In concentrations to orange-yellow at high In concentrations.

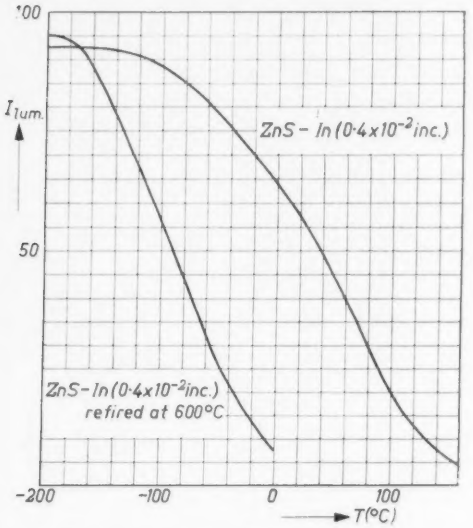

FIG. 5. Temperature dependence of the luminescence of a ZnS–In phosphor fired at 1200°C and quickly cooled, and of the same phosphor refired at 600°C.

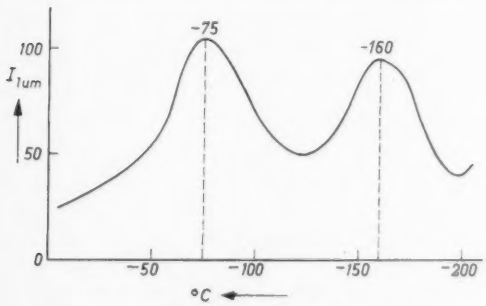

FIG. 6. Glow peaks in ZnS–In phosphors.

7. THE MECHANISM OF INCORPORATION OF In.

In view of the fact that the In atom is bigger than the Zn atom incorporation of In on the interstitial sites of the ZnS lattice is unlikely. So, assuming substitutional incorporation of In, according to KRÖGER and VINK[10], we have in principle the three ways of charge compensation mentioned below.

(a) $[In_{Zn}^{\cdot}] = [n]$
With this way of compensation In and S are incorporated in a 1:1 ratio and it is promoted by reducing conditions (low sulphur pressure).

(b) $[In_{Zn}^{\cdot}] = 2\,[V_{Zn}^{''}]$
With this way of compensation In and S are incorporated in a 2:3 ratio and it is promoted by neutral conditions.

(c) $[In_{Zn}^{\cdot}] = [V_{Zn}^{'}]$
With this way of compensation the In and S are incorporated in a 1:2 ratio and it is promoted by oxidizing conditions (high sulphur pressure).

In the equations above and in the following discussions the atomic notation of KRÖGER and VINK[10] is used, viz;

In_{Zn}^{0} = An In atom which has replaced a Zn atom; effective charge zero, denoted by ^{0}.

$In_{Zn}^{\cdot}$ = An In atom which has replaced a Zn atom; the In atom has lost one electron. Effective charge +1, denoted by $^{\cdot}$.

$V_{Zn}^{''}$ = A Zn atom vacancy which has captured two electrons. This centre corresponds to a Zn ion vacancy in the ionic description. Effective charge −2, denoted by $''$.

$V_{Zn}^{'}$ = A Zn atom vacancy which has captured one electron.
Effective charge −1, denoted by $'$.

$V_{Zn}^{\times}$ = A Zn atom vacancy. Effective charge zero.

n = A free electron.

$[V_{Zn}^{0}]$ = Concentration of Zn atom vacancies etc.

Of the three ways of charge compensation mentioned above mechanism (a) can be ruled out because it would cause the phosphors to show n-conductivity, which is not the case. Mechanism (c) cannot be operating as the main mechanism of charge compensation either, because then one would find free sulphur on dissolving the powders in acids, which is not the case. Even at the highest concentration of incorporated In, viz. about 10^{-2}, no trace of sulphur is found on dissolving the samples in HCl. Thus, at least in the range of In concentrations investigated, only mechanism (b) remains. In the ionic picture this mechanism corresponds to the replacement of 3 Zn^{2+} ions by

2 In^{3+} ions, one Zn ion vacancy being formed. There are several striking examples of this kind of charge compensation in ZnS structures. The ternary compound $ZnAl_2S_4$, for instance, has, according to HAHN and FRANK[11], a ZnS (wurtzite) structure above 1000°C; this means that one quarter of the cation-lattice sites are empty. An even more striking example of this kind is furnished by Ga_2S_3 which, again according to HAHN and FRANK[12], may have a ZnS structure with one third of the cation sites unoccupied.

It seems that in the ZnS-type of structure the close-packed arrangement of the anions is very stable, changes in the number and nature of the cations in the tetrahedral interstices being possible which do not affect the anion sublattice.

8. ASSOCIATION–DISSOCIATION EQUILIBRIA IN ZnS–In

As was already stated in Section 2 the ZnS-In powders in order to show luminescence have to be cooled quickly from the firing temperature to room-temperature. If the phosphors prepared in this way are reheated at 500 to 600°C in H_2S for as short a time as 5 min the room-temperature luminescence disappears almost completely. A refiring at temperatures below 500°C does not affect the luminescence. The killing of the fluorescence due to refiring at 600°C was found to be no function of the sulphur pressure used during refiring. When powders in which the room-temperature luminescence is destroyed by heating at 600°C are reheated at higher temperatures the room-temperature luminescence is gradually restored as the refiring temperature increases. The behaviour described here suggests a gradual association taking place when the samples are slowly cooled from 1200°C to 600°C. Below 500°C the motion of the centres through the lattice is frozen and for this reason quenched samples refired below 500°C do not change their behaviour. X-ray powder diffraction patterns of the powders refired at 600°C show that the lattice spacings, which have increased due to incorporation of In at 1200°C (cf. Section 3) practically drop* to those of pure ZnS in these samples. It thus appears that the high-temperature solution of In_2S_3 in ZnS gets supersaturated on cooling, as a result of which a strong clustering of the dissolved In occurs.

In the foregoing section it was argued that the compensation mechanism was $[In_{Zn}^{\cdot}] = 2[V_{Zn}^{''}]$. It is plausible that the $In_{Zn}^{\cdot}$ and $V_{Zn}^{''}$ centres will attract each other. In the first place these centres have effective charges of differing sign. Further, because the In atoms are bigger than the Zn atoms which they replace, an arrangement in which the $In_{Zn}^{\cdot}$ centres have a $V_{Zn}^{''}$ at a nearest-neighbour site will be energetically more favourable than one in which $In_{Zn}^{\cdot}$ and $V_{Zn}^{''}$ are far apart (volume compensation). The latter effect is certainly one of the effects responsible for In_2S_3 dissolving to a much smaller extent into ZnS than Ga_2S_3 (cf. Section 3), the Ga atom having approximately the same size as the Zn atom.

For the above reasons the onset of association may be represented by the following reactions:

$$In^{\cdot} + V'' \longrightarrow InV' \text{ with } K_1 = \frac{[In^{\cdot}]\ [V'']}{[InV']}$$

and

$$InV' + In^{\cdot} \longrightarrow In_2V^0 \text{ with } K_2 = \frac{[In^{\cdot}]\ [InV']}{[In_2V^0]}$$

For convenience the symbols $In_{Zn}^{\cdot}$, $V_{Zn}^{''}$ etc are written $In^{\cdot}$, V'', etc.

The reaction-constants K_1 and K_2 may be written in terms of association energies E_1 and E_2. (cf. for instance LIDIARD[13]). By choosing reasonable values for E_1 and E_2 the concentrations appearing in (a) and (b) may be calculated as a function of the amount of In incorporated and as a function of temperature. We will not give the calculation because in the forthcoming discussion we only need the general trends, which will be clear without a detailed calculation.

These general trends are:

(1) With increasing concentration of $In_{inc.}$ the concentrations of $In^{\cdot}$ and InV' and especially the concentration of In_2V^0 increase stronger than the concentration of V''.

(2) On slowly cooling down the samples from high temperature the concentration of In_2V^0 increases, whereas the concentrations of the other centres, and especially the concentration of V'', decrease.

* The c and a values of phosphors refired at 600°C are 6·2610 Å and 3·8229 Å, respectively, as compared to 6·2606 Å and 3·8223 Å for the pure ZnS.

Vol. 17
1960

In the next section we will try to correlate the centres $In^{\cdot}$, InV', V'' and In_2V^0 with the three emission bands observed.

9. THE NATURE OF THE CENTRES IN ZnS–In

The emission spectrum of ZnS–In phosphors was found to consist of bands at 6200 Å, 5350 Å and 4700 Å (Section 4). Also the presence of the centres $In^{\cdot}$, InV', V'' and In_2V^0 was made plausible. It is suggested that the following correlation exists between the emission bands and the centres:

(a) The 6200 Å band is due to recombination of electrons in the In traps and holes in the filled band, cf. KLASENS[2].

(b) The 5350 Å band is due to the InV' complexes.

(c) The 4700 Å band is due to the V'' centres.

(d) The In_2V^0 and bigger complexes act as killer centres.

Below, arguments in favour of the assumed correlations will be given. The level scheme proposed for the ZnS–In phosphors is depicted in Fig. 7. On excitation, electrons are brought from

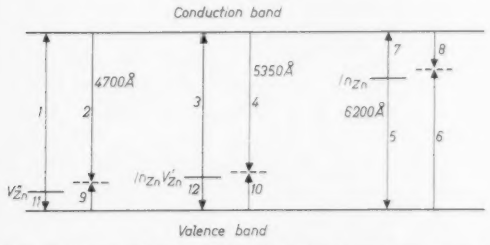

FIG. 7. Level scheme of the ZnS–In phosphors. Levels occupied by an electron are indicated by a fully drawn line, empty levels by a broken line.

the V'' and InV' centres to the conduction band, (processes 1 and 3 of Fig. 7). Some of these electrons drop back into the empty V'' and InV' centres (processes 2 and 4) thus giving rise to the blue and green emission bands, others fill the In traps (process 8). The orange band arises from the recombination of electrons from the In traps with holes in the valence band (process 5) originating from the empty V'' and InV' centres. It is likely that the orange band can also be excited directly (process 6). Without direct excitation the occurrence of a strong orange band (especially at high In concentration (cf. Fig. 3b) at $-190°C$ would be hard to explain, because the escape of holes from the V'' and InV' centres is largely blocked at $-190°C$. The assumption that part of the light emitted in the orange band comes from direct excitation is further supported by the fact that excitation of the phosphor with 4358 Å, instead of with 3650 Å, was found to promote the orange band. The infra-red stimulation of phosphorescence and the glow are attributed to optical and thermal release of holes from the empty V'' and InV' centres (processes 9 and 10 in Fig. 7) towards the valence band followed by recombination with electrons trapped in the In traps, thus giving the orange band. The emptying of the hole traps is already operative at temperatures at which the release of electrons from the In traps (process 7) towards the conduction band is still small. So it is not surprising that in the glow experiments no indication of the well-known deep In trap is found. The position of the levels in Fig. 7 makes it logical to correlate the glow peak at $-75°C$ to the InV' centres and the glow peak at $-160°C$ to the V'' centres. A further argument for this can be obtained from the consideration of the glow behaviour of comparable ZnS–Ga phosphors.[9]

These phosphors also show two glow peaks. One of them is also at $-160°$ (V'') the other at $-105°C$ (GaV'). The infra-red excitation peak of the phosphorescence $> 1{\cdot}1$ eV is probably correlated to the InV' centres and the band at about 0·7 eV to the V'' centres.

The assumption that In_2V^0 and higher complexes act as killers, i.e. as centres which give way to a strong radiationless band–band recombination is corroborated by the fact that both a high In concentration and refiring at 600°C shifts the temperature dependence curve of the phosphors to lower temperature, a phenomenon typical for killer action. The influence of the killers will be the stronger the easier the excited centres release their holes. This means that the green emission and especially the blue emission will be quenched when the concentrations of In_2V^0 and higher complexes rise. The orange emission, however, as far as it is directly excited by process 6 (Fig. 7), will be much less quenched because the electron trap due to In is much deeper than the hole traps of the empty

InV' and V'' centres. The changes in relative importance of the emission bands with increasing In concentration as shown in Figs. 3(a) and 3(b) can now be explained qualitatively as follows:

(a) The contribution of the blue band diminishes with increasing $In_{inc.}$ because the relative concentration of V'' rises less with increasing $In_{inc.}$ than that of the other centres (cf. Section 8), and further because it is more strongly quenched by the increasing concentration of In_2V^0.

(b) The relative importance of the green band first increases with increasing $In_{inc.}$ because the concentration of InV' rises, and then decreases because it is more strongly affected by the increasing In_2V° concentrations than the orange emission.

(c) The relative importance of the orange band increases with increasing $In_{inc.}$ because the orange emission is less quenched by the increasing concentration of In_2V^0 than the green and the blue emissions.

The increased relative importance of the shorter-wavelength emission at low temperature (cf. Fig. 3b) is explained by a decreased migration of holes and consequently a decreased killer action and a decreased transfer of the excitation energy to the centres with a longer-wavelength emission.

As has been stated in Section 6 the low-temperature emission spectra of phosphors which have been refired at 600°C do not show the blue band. This effect is very striking at low In concentrations. At a low temperature the luminescence in these samples without the 600°C treatment is blue whereas the low-temperature luminescence of the samples is yellow after refiring at 600°C. This phenomenon can be explained on the basis of the analysis given. Due to refiring at 600°C the concentration of In_2V^0 and higher complexes rises, whereas especially the concentration of V'' is strongly reduced. Both effects have a quenching influence on the blue emission.

10. CONCLUDING REMARKS

In Section 7 arguments were given for the compensation mechanism $[In_{Zn}^{\cdot}] = 2\,[V_{Zn}^{''}]$ in the ZnS–In phosphors discussed. It might be argued that the luminescence in, e.g. the 4700 Å band, could nevertheless be due to a small concentration of another centre, e.g. $[V_{Zn}']$. However, this is not likely. Firstly the blue band is quite strong; further the concentration of V_{Zn}' in the region of main compensation $[In_{Zn}^{\cdot}] = 2\,[V_{Zn}^{''}]$ is proportional to the square root of the sulphur pressure.

If the blue band were due to V_{Zn}' one might expect variations in intensity of the blue band on changing the sulphur pressure, but, as was already stated in Section 2, the luminescence is not sensitive to changes in sulphur pressure.

There are indications in the literature that the blue bands obtained in ZnS with Cl, Al, Ga or by firing at high temperature may not all be at exactly the same place[14] and may have a different shape.[15] The maxima are found to vary between 4400 Å and 4700 Å.[15] Probably the self-activated blue emission bands are of a composite nature as has also been suggested by other authors.[15] The long-wave part (4700 Å) of the self-activated emission could be due to $V_{Zn}^{''}$ and the short-wave part (4400 Å) to another centre. If this were true, this other centre would probably not be V_{Zn}' because then the Fermi level would be between the levels of $V_{Zn}^{''}$ and V_{Zn}', i.e. close to the valence band. The phosphors of this type should show *p*-conductivity, which has never been observed.

In the level scheme of Fig. 7 the level of the effectively double-charged centre, $V_{Zn}^{''}$, was put at a smaller distance from the valence band than the level of the $In_{Zn}V_{Zn}'$ centre with its single negative charge. If the perturbation potentials due to these centres were of a pure Coulomb nature the relative positions of the levels should be just the reverse.

There are, however, more examples to show that a Coulomb model does not hold. The atoms Ni, Co and O, for instance, which have the same valence as the Zn or S atoms they replace, nevertheless give much deeper electron traps,[3] than Al or Cl which have a valence different from the lattice constituents.

In the present paper the long-wave emission at 6200 Å, found in ZnS–$V_{Zn}^{''}$,In and ZnS–Ag,In, was connected to a radiative transition from the trap level to the valence band. APPLE and WILLIAMS[6] (cf. Section 1), however, ascribed the long-wave bands they found with Ga and In to radiative transitions from the ground state of the trap level to the ground state of the activator. In the model of APPLE and WILLIAMS the characteristics of the long-wave emissions found with a

Vol. 17
1960

Table 2. Long-wave emissions in ZnS *phosphors coactivated with* In.

Phosphor	Author	Maximum of fluorescence	
		at 20°C Å	at −196°C Å
ZnS–*V''*, In	present work	6200	6200
ZnS–Ag, In	present work	6200	6200
ZnS–Ag, In	APPLE and WILLIAMS[6]	6150	6150
ZnS–Cu, In	APPLE and WILLIAMS[6]	6350	6650

given coactivator should depend on the chemical identity of the activator. In the present model this should not be the case.

Table 2 gives a survey of our data about the long-wave emissions obtained with In and those of APPLE and WILLIAMS.

It is seen from Table 2 that, in agreement with our model, the position of the long-wave emission does not depend on the nature of the activator for the combinations *V''*,In and Ag,In. The different location of the peak with Cu,In, however, seems to favour the model of APPLE and WILLIAMS. There are, however, indications (also in APPLE's own work[5]) that at least part of the long-wave emission obtained with Cu,In is due to another centre, which could be identical with the red Cu-centre found by FROELICH[4] in non-coactivated ZnS–Cu phosphors. This might also explain the otherwise somewhat curious shift of the long-wave Cu,In emission to longer wavelengths (cf. Table 2), which occurs at low temperature. In our opinion the different position of the long-wave emission obtained with Cu,In cannot be used as a safe argument in favour of the model of APPLE and WILLIAMS.

Summarizing the present situation one might say that the results with In seem to favour the idea of a long-wave emission characteristic for the coactivator, more work being necessary to elucidate the nature of the long-wave emissions obtained in ZnS activated with Cu alone and in ZnS activated with Cu combined with trivalent coactivators.

Acknowledgements—The author is indebted to Mr. G. MEYER for measuring the infra-red-stimulated phosphorescence and to Dr. A. BRIL under whose supervision the excitation and emission spectra were measured. Thanks are due to Mr. LANGEREIS for measuring the lattice constants of the ZnS–In phosphors. Thanks are also due to Dr. G. DIEMER, Mr. W. VAN GOOL, Dr. W. HOOGENSTRAATEN and Dr. H. A. KLASENS for their helpful criticism.

REFERENCES

1. KRÖGER F. A. and DIKHOFF J., *Physica s'Grav.* **16,** 297 (1950).
2. KLASENS H. A., *J. Electrochem. Soc.* **100,** 72 (1953).
3. HOOGENSTRAATEN W., *J. Electrochem. Soc.* **100,** 356 (1953).
4. FROELICH H., *J. Electrochem. Soc.* **100,** 496 (1953).
5. APPLE E. F., *Enlarged Abstr. Electrochem. Soc.* **32,** 45 (1958).
6. APPLE E. F. and WILLIAMS F. E., *J. Electrochem. Soc.* **106,** 224 (1959).
7. HAHN H. and co-workers, *Z. anorg. Chem.* **279,** 241 (1955).
8. HAHN H. and KLINGER W., *Z. anorg. Chem.* **260,** 97 (1949).
9. KOELMANS H., unpublished results.
10. KRÖGER F. A. and VINK H. J., *Solid State Phys.* **3,** 307 (1956).
11. HAHN H. and FRANK G., *Z. anorg. Chem.* **269,** 227 (1952).
12. HAHN H. and FRANK G., *Z. anorg. Chem.* **278,** 333 (1955).
13. LIDIARD A. B., *Phys. Rev.* **94,** 29 (1954).
14. PRENER J. S. and WEIL D. J., *Enlarged Abstr. Electrochem. Soc.* **32,** 56 (1958).
15. BUBE R. H., *J. Chem. Phys.* **20,** 710 (1952); LEVERENZ H. W., *Luminescence of Solids*, p. 188. John Wiley, New York (1950).

J Phys. Chem. Solids Pergamon Press 1960. Vol. 17, Nos. 1/2, pp. 80–87. Printed in Great Britain.

PARAMAGNETIC RESONANCE OF THE ANTIMORPH OF THE *F*-CENTER

WERNER KÄNZIG

General Electric Research Laboratory, Schenectady, New York, U.S.A.

(*Received* 4 *April* 1960)

Abstract—LiF crystals X-rayed at 77°K and then warmed-up to a temperature between 130°K and 220°K contain a new kind of a trapped-hole center. Its electronic structure was studied by means of paramagnetic resonance. The centre appears to consist of a hole trapped at a Li vacancy, and thus it may be considered as the "antimorph" of the *F*-center. However, the electron deficiency is localized on but two neighboring fluoride ions adjacent to the Li vacancy, so that the symmetry is lower than that of the *F*-center. The new center is closely related to the self-trapped hole, as it can also be described as a F_2^- molecule-ion. However, owing to the vicinity of the Li vacancy the molecular bond is "bent", so that the center has the symmetry of an isosceles triangle lying in a (001) plane with the base along a [110] axis. The thermal stability is higher than that of the self-trapped hole because of the Coulomb field of the vacancy. The main optical absorption band is probably centered at about 3400 Å just as for the self-trapped hole. So far, LiF is the only alkali halide in which a center of this type could be found.

Vol. 17
1960

1. INTRODUCTION

ONE of the most studied imperfections in alkali halides is the *F*-center. Originally, it was defined as the imperfection that gives rise to the optical absorption band that is called the *F*-band. The electronic structure of the *F*-center has been studied very thoroughly in the past, both experimentally and theoretically, and the evidence that it consists of an electron trapped at a halide vacancy is so overwhelming, that this model has become the definition of the *F*-center.

An equally fundamental imperfection should consist of a hole (electron deficiency) trapped at an alkali vacancy. The existence of such a lattice defect was proposed by SEITZ in 1946[1] and later called "the antimorph of the *F*-center".[2] He also speculated that the optical absorption band V_1 might be due to this imperfection.[3] The evidence for this assignment is very uncertain and there are experiments which seem to disagree with it.[4]

The present article describes in some detail the analysis of a paramagnetic resonance spectrum of X-rayed and properly annealed LiF single crystals. The spectrum can be interpreted as arising from a hole trapped at a Li vacancy; i.e. from the antimorph of the *F*-center.* For the sake of brevity, we shall call this center the V_F-center. (The letter *V* is customarily used for the designation of centers involving electron deficiencies, and the subscript *F* shall indicate the structural relationship with the *F*-center.)

The conditions under which the V_F-center is present in LiF are described in another paper.[6] The paramagnetic resonance spectrum was observed at liquid nitrogen temperature with an X-band spectrometer. The optical absorption bands of the V_F-center are expected to overlap considerably with those of other centers, and they have not been isolated as yet.

2. THE QUALITATIVE FEATURES OF THE HYPERFINE SPECTRUM

1. *The over-all symmetry of the V_F-center*

The hyperfine spectrum of the V_F-center is closely related to that of the self-trapped hole.[7,8] The *over-all* symmetry of both centers is orthorhombic with the axes x'//[110], y'//[001] and

* A short preliminary report of this work has been published previously.[5]

$z'//[1\bar{1}0]$. Consequently, there are six equivalent and equally occupied orientations of the orthorhombic axes, so that for a general direction of the d.c. magnetic field, H_0, six "basic spectra" are observed. This number reduces to two for $H_0//[100]$ and $H_0//[111]$, and to three for $H_0//[110]$. Here only these three special orientations will be discussed, although the identification of the basic spectra required a careful study of the spectra for rotation of the crystal about a [001] and a [101] axis. For a given direction of H_0, the basic spectra shall be characterized by the angle θ between H_0 and the orthorhombic axis z'. For H_0 along z' the largest hyperfine splitting is observed.

2. *The detailed symmetry of the V_F-center*

The spread and the anisotropy of the hyperfine spectrum are about the same as for other types of V-centers in LiF[8,9] indicating that the electron deficiency is localized almost full-time on fluoride ions. For general directions of H_0 the basic spectra consist of four lines with roughly equal intensity. This shows that the hole is localized on *two* fluoride ions, which are non-equivalent with respect to an axis along H_0. For special directions of H_0 (e.g. for H_0 in a (110) plane) one of the basic spectra degenerates into a three-line pattern with the intensity sequence 1:2:1, showing that the two fluorine nuclei are *equivalent* with respect to special axes. (Nevertheless, two geometrically equivalent fluorine nuclei can, in special cases, also give rise to a four-line pattern; namely, when the angle θ approaches 90°. This higher order hyperfine effect has been discussed in detail for the self-trapped hole[8].) The main difference between the V_F-center and the self-trapped hole is that in the latter case the two fluorine nuclei are geometrically equivalent for *every* direction of H_0 so that (for θ

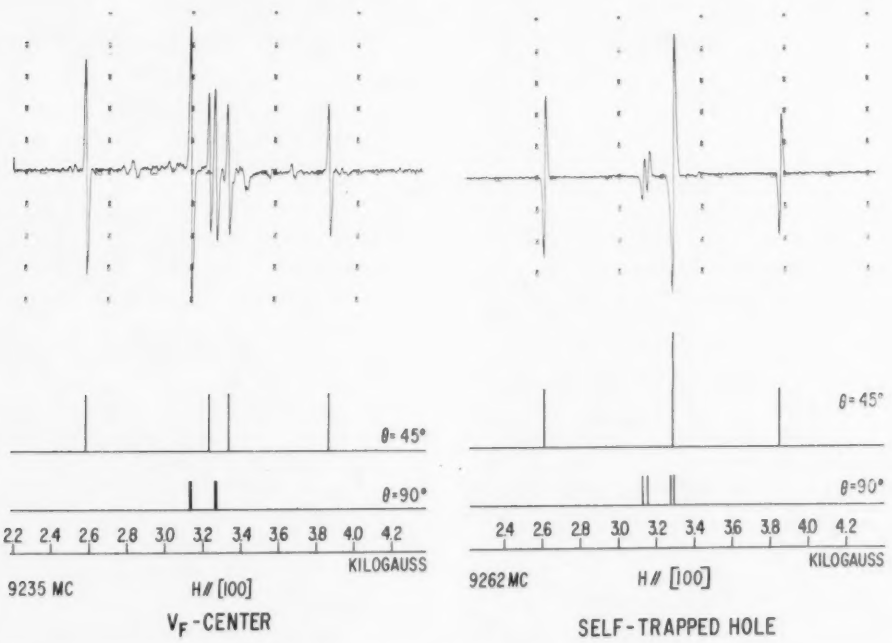

FIG. 1. Paramagnetic resonance spectrum of the V_F-center for $H_0//[100]$ and its decomposition into basic spectra. For comparison the corresponding spectra for the self-trapped hole are reproduced on the right-hand side.

Superposed upon the V_F-center spectrum are a number of much weaker spectra belonging to other, unidentified centers.

Derivative of absorption measured at liquid nitrogen temperature.

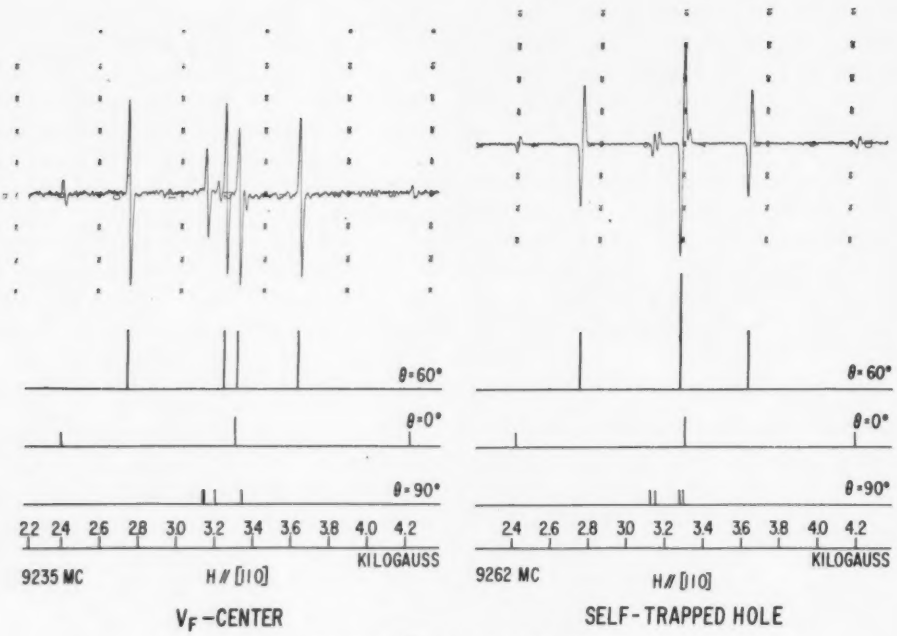

FIG. 2. As Fig. 1, but H_0//[110].

not approaching 90°) a 1:2:1 pattern always results. Figs. 1–3 serve to illustrate these facts: on the left-hand side of each Fig. the paramagnetic resonance spectrum of the V_F-center is reproduced and its decomposition into basic spectra is given. The corresponding data for the self-trapped hole are reproduced on the right-hand side.

Figure 1 shows the data for H_0//[100]. The spectrum of the V_F-center can be derived from the spectrum of the self-trapped hole by splitting the center line of the 45°-spectrum into two about equally intense lines 99 G apart. The position of the outside lines changes relatively little. A small change can be noticed in the 90° spectrum. The first and the second line, which are clearly resolved for the self-trapped hole, merge in the V_F-spectrum. The coincidence can be considered accidental, as it is not connected with the symmetry of the center.

The spectra for H_0//[110] are given in Fig. 2. The 60°-spectrum is a four-line spectrum. The separation of the center lines is smaller than in the 45° spectrum; namely, only 68 G. This indicates that this splitting is not due to a higher order effect (which would increase with increasing θ), but to a real geometrical nonequivalence of the two fluorine nuclei. The 0°-spectrum is a 1:2:1 pattern. The 90° spectrum differs significantly from that for H_0//[100] suggesting that axial symmetry about z' is not as good an approximation as for the self-trapped hole.

The spectra shown in Fig. 3 are obtained with H_0//[111]. The V_F-spectrum for $\theta = 35{\cdot}26°$ is a 1:2:1 pattern. The 90° spectrum is very similar to that for H_0//[110].

From the orientations of H_0 for which the two fluorine nuclei of the V_F-center become geometrically equivalent it can be concluded that the symmetry of the V_F-center is that of an *isosceles triangle* with the base z' and the height x', thus lying in a (001) type plane. (The reasoning is exactly the same as for the V_t-center.[9]) The two fluorine nuclei 1 and 2, on which the hole is localized, are located on the base.*

It is now useful to introduce the tensors $\boldsymbol{T}^{(i)}$

* Note that the paramagnetic resonance experiment does not distinguish whether the apex is on the left-hand side or on the right-hand side of the base. However, this degeneracy could be removed by an externally applied electric field along a [110] axis.

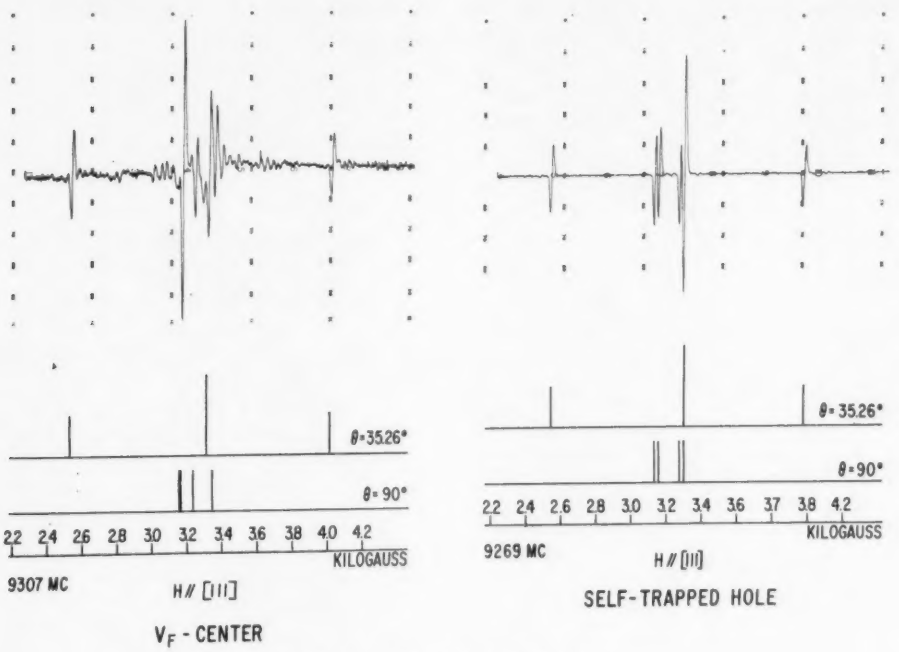

FIG. 3. As Fig. 1, but $H_0 /\!/ [111]$.

which describe the hyperfine interaction with the two fluorine nuclei $i = 1, 2$. The symmetry of the center requires then that these two tensors are equal, but that their principal axes ξ_i, η_i, ζ_i are rotated with respect to the orthorhombic axes x', y' and z'. The axis of rotation is y', and the angles are $+\delta$ and $-\delta$ as is shown in Fig. 4. The self-trapped hole corresponds to the case $\delta = 0$. The following facts indicate that the angle δ for the V_F-center is small:

(a) The separation of the two center lines is small compared to the anisotropy of the hyperfine interaction.

(b) The outside lines are close to those for the self-trapped hole for any orientation of H_0.

3. QUANTITATIVE ANALYSIS OF THE HYPERFINE SPECTRUM

The hyperfine spectrum shall now be analyzed in terms of a spin Hamiltonian of the form

$$\mathcal{H} \simeq g\beta_0 S_z H_z + g_0\beta_0 \boldsymbol{S}\cdot(\boldsymbol{T}^{(1)}\cdot\boldsymbol{I}^{(1)} + \boldsymbol{T}^{(2)}\cdot\boldsymbol{I}^{(2)}), \quad (1)$$

where g_0 is the spectroscopic splitting factor of the free electron and g that of the V_F-center for the direction z of the d.c. magnetic field H_z. The Bohr magneton is designated by β_0, and the spin

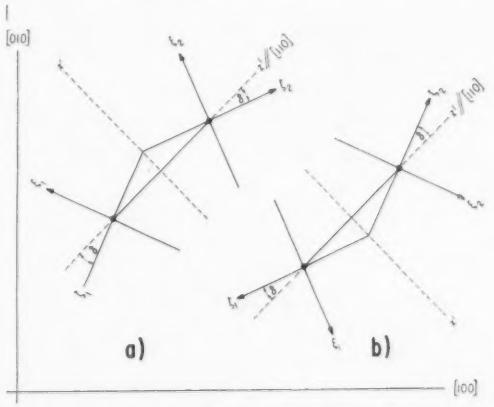

FIG. 4. The symmetry of the V_F-center. The axes x', y', z' are the orthorhombic axes corresponding to the over-all symmetry. For H_0 along z' one observes the largest hyperfine splitting. The axes ξ_i, η_i and ζ_i are the principal axes of the hyperfine tensor $\boldsymbol{T}^{(i)}$.

Note that the paramagnetic resonance spectrum does not distinguish between the situation (a) and the situation (b).

operators of the electron and of the F nuclei by S and I, respectively. To a first-order approximation the hyperfine splitting is the sum of the contributions a_1 and a_2 from the two nuclei 1 and 2. For angles θ not approaching 90° such an approximation is satisfactory but not accurate. Using the

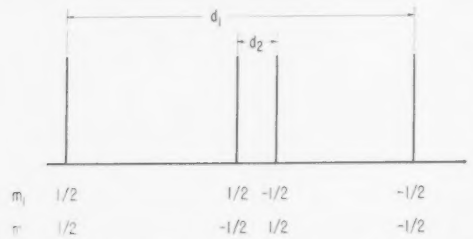

FIG. 5. Assignment of nuclear magnetic quantum numbers to the hyperfine lines of the basic spectra.

assignment of nuclear quantum numbers to the lines of the basic spectra given in Fig. 5, one can write

$$\left.\begin{aligned} d_1 &= a_1+a_2 \\ d_2 &= a_1-a_2 \end{aligned}\right\} \qquad (2)$$

thus eliminating quadratic terms in the nuclear quantum numbers m_i. The a values so obtained are listed in Table 1. These data yield six equations

Table 1. *Contribution of the two nuclei to the hyperfine splitting for special orientations of the d.c. magnetic field* H_0.

Direction of H_0	Angle θ between H_0 and z' (degrees)	a_1 (G)	a_2 (G)
[100]	45	688	589
[111]	35·26	741	741
[110]	0	913	913
[110]	60	483	415

The numbers are derived from the experimental data using equation (2).

for the four unknowns which are the three principal axes of the hyperfine tensors T and the angle of rotation δ. The analysis shows that $T_{\xi\xi}$ and $T_{\eta\eta}$ are small compared to $T_{\zeta\zeta}$ so that the first-order approximation does not permit an accurate determination of $T_{\xi\xi}$ and $T_{\eta\eta}$.* The result of the crude analysis is

$$|T_{\xi\xi}| \ll |T_{\zeta\zeta}|$$
$$|T_{\eta\eta}| \ll |T_{\zeta\zeta}|$$
$$|T_{\zeta\zeta}| = 915 \text{ oersted}$$
$$\delta = 4°.$$

4. INTERPRETATION OF THE HYPERFINE TENSORS

As in earlier work we assume now that the ground-state wave-function of the unpaired electron can be approximated by a linear combination of hybridized atomic wavefunctions centered on the two nuclei.[4,7,9] For a hole on a fluoride ion the wave-function is primarily a $2p$ function. The hyperfine tensors show that the p-functions are oriented along the ζ-axes. Thus the center can be described as a F_2^- molecule-ion with a slightly bent bond. The nonvanishing trace of the hyperfine tensor indicates a considerable isotropic component of the hyperfine interaction, which is due to the admixture of s-function. It is very unlikely that it can be explained by exchange interaction with the core electrons.[9] In order to account for the isotropic part, between 40 per cent and 50 per cent $3s$ character or about 4 per cent $2s$ character has to be admixed to the $2p$ function. In the early work on the halogen$_2^-$ molecule-ions admixture of $(n+1)s$ function to the np function was considered only; however, the normalization of the wave-function suggests that admixture of ns (in the present case $2s$) should rather be considered (e.g. Table 5 of Ref. 4).

It is interesting to note that the hyperfine splitting for the V_F-center is larger than for the self-trapped hole ($T_{\zeta\zeta} = 915$ G compared to $T_{\zeta\zeta} = 887$ G). This indicates that the internuclear distance in the F_2^- molecule-ion is smaller for the V_F-center than for the self-trapped hole. A similar, but considerably larger, difference was encountered in the case of the H-center ($T_{\zeta\zeta} = 956$ G), where the two fluoride ions are pushed together as a consequence of crowding.[4] In fact, the crowding

* In fact, the first-order approximation yields negative values of $T_{\xi\xi}^2$ and $T_{\eta\eta}^2$, both for the V_F-center and for the self-trapped hole. The accurate analysis gave for the self-trapped hole, $T_{\xi\xi} \cong T_{\eta\eta} = 59$ G. Similar values would be expected for the V_F-center. The value of $T_{\zeta\zeta}$ obtained by the first-order approximation is accurate.

Vol. 17
1960

in the H-center leads to additional resolved hyperfine interactions and to a significantly shorter spin-lattice relaxation time. The reduced internuclear distance in the V_F-center must be of another origin. There is no evidence for additional hyperfine interactions in the V_F-center as compared to the self-trapped hole. On the contrary, the line widths, which in both cases are due to unresolved hyperfine interactions with the surrounding ions, appear to be slightly smaller for the

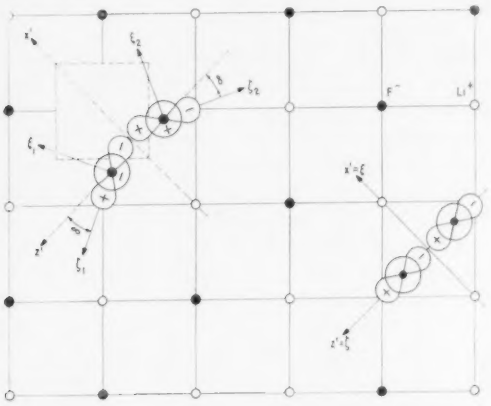

FIG. 6. Very schematic representation of the models for
(a) the V_F-center
(b) the self-trapped hole center.

The p-functions are symbolized by figure eights and the s-admixtures by circles. The relative signs of the p-functions correspond to the antibonding $2p\sigma_u$ level of the F_2^- molecule-ion. The sign of the s-admixture in the V_F-center is suggested by crystalline field considerations. Note that the actual position of the internuclear axis z' of the V_F-center is not known, except for its direction. For example, it may well pass somewhat closer to the center of the I i vacancy than is indicated in the drawing. The angle δ is exaggerated; its actual value is $\delta \cong 4°$.

V_F-center. However, this effect is within experimental errors. The saturation behavior of the V_F-center resonance at 77°K is not significantly different from that of the self-trapped hole. This again suggests a very close relationship between these two centers.

The tilt δ of the hyperfine tensors indicates that the F_2^- molecule-ion in the V_F-center is closely associated with a lattice imperfection. This imperfection has to fulfill the following requirements:

1. It probably has a negative charge. This would explain the higher thermal stability of the V_F-center as compared to the self-trapped hole.

2. It must comply with the detailed symmetry of the center.

3. It must favor a slightly reduced internuclear distance of the F_2^- molecule-ion as compared to the case of the self-trapped hole.

The simplest imperfection that ideally meets all these requirements is a Li vacancy. Thus one arrives at the model for the V_F-center shown very schematically in Fig. 6(a). The smallness of the tilt δ may indicate that the whole F_2^- molecule-ion is displaced towards the Li-vacancy relative to the position it would have in the absence of the Li-vacancy (self-trapped hole, Fig. 6b).

5. THE SPECTROSCOPIC SPLITTING FACTOR AND THE OPTICAL ABSORPTION

A discussion of the level scheme of the halogen$_2^-$ molecule-ion and of its spectroscopic splitting factor was given in the earlier papers on the self-trapped hole and on the H-center,[4,7] and it can be applied to the V_F-center.

The axes of the g-tensor coincide with the axes x', y', z' of the over-all symmetry. The work on the H-center showed that a reduction of the internuclear distance shifts the tensor components $g_{x'}$ and $g_{y'}$ closer to the free electron value, provided that the degree of s-admixture is not reduced. According to the interpretation of the hyperfine splitting, one expects, therefore, that the $g_{x'}$ and $g_{y'}$ values for the V_F-center should be between those for the H-center and those for the self-trapped hole, but closer to the latter ones. Table 2 shows that the difference is within the errors of the experiment. Apparently, the perturbation of the F_2^- molecule ion through the Li vacancy is not significant if one starts out with a self-trapped hole. Consequently, the main optical absorption band of the V_F-center, namely the $\sigma_g - \sigma_u$ transition, is expected to almost coincide with the optical absorption of the self-trapped hole, which is centered at about 3400 Å. It should be possible to isolate the V_F-band by means of the annealing processes described in Ref. 6.

SEITZ proposed that the optical absorption band V_1 in NaCl, KCl and KBr might be due to a hole trapped at an alkali vacancy.[3] So far we have failed to detect in these salts a paramagnetic

Table 2. Principal components of the g-tensors for the V_F-center and for the self-trapped holes measured at 9·3 kMc.

	$g_{x'}$	$g_{y'}$	$g_{z'}$	error
V_F-center	2·023	2·023	2·001	± 0·002
Self-trapped hole (V-center of Refs. 7 and 8)	2·0227	2·0234	2·0031	± 0·001

The principal axes are x', y', and z' as given in Figs. 4 and 6.

resonance spectrum that is connected with the optical V_1-band. In addition, we were unable to detect in these alkali halides a paramagnetic resonance spectrum which could be interpreted as arising from a V_F-center. Therefore, the structure of the center that causes the V_1-band is still an unsolved puzzle.

6. DISCUSSION OF THE MODEL FOR THE V_F-CENTER

We cannot prove, at the present stage, that the model for the V_F-center depicted in Fig. 6 represents the only and unique interpretation of our observations. What we have proved unambiguously, however, is the fact that the center can be described as a F_2^- molecule-ion with a slightly bent bond, so that the symmetry of an isosceles triangle results, which is oriented with respect to the crystal axes as shown in Fig. 4. The position of the isosceles triangle with respect to a translation cannot be unambiguously inferred from the paramagnetic resonance spectra. However, it is important to note that the actual position requires a surrounding with proper symmetry. The proposed model is not only compatible with the present paramagnetic resonance data but also with the greater stability of the V_F-center as compared to the self-trapped hole. In addition, the process of formation of the V_F-center is compatible with the model.[6] Therefore, it has a good chance for being correct.

The difference between the structure of the F-center and of its "antimorph", the V_F-center, is very striking. The F-center in its ground state has cubic symmetry, whereas the symmetry of the V_F-center is lower. The F-center wavefunction is essentially an s-like function, made up from alkali s-functions. Consequently, one does not expect a Jahn–Teller distortion to occur. The situation is different for the V_F-center. The fluorine $2p$ band is the highest filled band, and there the electron is missing. Thus one expects a p-like state for the hole, and, on the basis of the Jahn–Teller theorem, a lower than cubic symmetry. Without a detailed theoretical investigation, one cannot predict what the distorted structure would be. However, the model resulting from the paramagnetic resonance experiments is quite plausible in hindsight. The hole in its ground state certainly has low energy since the electron is missing in the antibonding $2p\sigma_u$ orbital of a "F_2^{2-} molecule-ion". Moreover, the hole in the proposed model can make good use of the electrostatic potential around the Li vacancy so that the energy is further lowered.

According to the proposed model there are twelve equivalent possibilities for the hole to be localized on two of the six fluoride ions adjacent to the Li vacancy. Therefore, the question arises: what is the frequency at which the electron deficiency jumps around the vacancy from one pair of fluoride ions to another? The paramagnetic resonance experiment can distinguish between those six positions of the hole which correspond to nonparallel internuclear axes, because of the anisotropy of the hyperfine interaction and the anisotropy of the g-tensor. At 78°K and at 130°K no broadening of the paramagnetic resonance lines could be observed. Therefore, at these temperatures the jump frequency is at least much smaller than the microwave frequency. DELBECQ *et al.*[11] have shown for the self-trapped hole in KCl that the internuclear axes of the Cl_2^- molecule-ions can be reoriented by inducing the $(\sigma_u-\sigma_g)$-transition

Vol. 17
1960

with properly polarized light. A state can be achieved in which the axes of all Cl_2^- molecule-ions are parallel to the particular [110] -axes of the crystal which are perpendicular to the ***E***-vector of the light. The orientation stays frozen-in at liquid nitrogen temperature. We have verified that the corresponding experiment can also be done with the self-trapped holes in LiF. The close relationship between these and the V_F-centers suggests the possibility of optical reorientation of the V_F-centers. However, experiments carried out at 60°K and above failed to indicate a preferred orientation of the V_F-centers due to polarized light, which should have induced the $(\sigma_u - \sigma_g)$-transition. This failure can be explained by assuming that the hole is "jumping" around the Li vacancy even at 60°K[12] or that the optical orientation is inefficient (compared to the case of the self-trapped hole) because the Li vacancy modifies the level scheme of the whole system.

REFERENCES

1. SEITZ F., *Rev. Mod. Phys.* **18,** 384 (1946).
2. SEITZ F., *Rev. Mod. Phys.* **26,** 7 (1954).
3. SEITZ F., *Phys. Rev.* **79,** 529 (1950).
4. KÄNZIG W. and WOODRUFF T. O., *J. Phys. Chem. Solids* **9,** 70 (1958).
5. KÄNZIG W., *Phys. Rev. Letters* **4,** 117 (1960).
6. KÄNZIG W., *J. Phys. Chem. Solids,* following article.
7. CASTNER T. G. and KÄNZIG W., *J. Phys. Chem. Solids* **3,** 178 (1957).
8. WOODRUFF T. O. and KÄNZIG W., *J. Phys. Chem. Solids* **5,** 268 (1958).
9. COHEN M. H., KÄNZIG W. and WOODRUFF T. O., *J. Phys. Chem. Solids* **11,** 120 (1959).
10. CASTNER T. G., *Phys. Rev.* **115,** 1506 (1959).
11. DELBECQ C. J., SMALLER B. and YUSTER P. H., *Phys. Rev.* **111,** 1235 (1958).
12. DELBECQ C. J., private suggestion.

J. Phys. Chem. Solids Pergamon Press 1960. Vol. 17, Nos. 1/2, pp. 88–92. Printed in Great Britain.

PARAMAGNETIC RESONANCE STUDY OF RADIATION DAMAGE IN LITHIUM FLUORIDE

WERNER KÄNZIG

General Electric Research Laboratory, Schenectady, New York, U.S.A.

(*Received* 4 *April* 1960)

Abstract—The low temperature annealing processes in LiF crystals X-rayed at 77°K have been studied by means of paramagnetic resonance. Four types of hole centers (V-type centers), the structures of which are known from previous work, play an important part; namely, the self-trapped holes, the H-centers, the V_F-centers and the V_4-centers. The relative concentrations of these defects have been measured after X-irradiation at 77°K and after subsequent pulse annealing at successively higher temperatures. Four temperature intervals were found in which the paramagnetic resonance spectra undergo significant changes in intensity. There seems to be a one-to-one correspondence between the annealing processes observed by means of paramagnetic resonance and those detected by other investigators by means of thermoluminescence, conductivity, changes of the optical absorption and of the crystal volume.

Vol. 17
1960

1. INTRODUCTION

THE low temperature annealing of LiF crystals that have been exposed to X-rays at liquid nitrogen temperature has been studied in the past by various techniques. GHORMLEY and LEVY investigated the thermoluminescence peaks.[1] DELBECQ *et al.* measured the optical absorption and its changes upon warming the crystal, the release of trapped charge (conductivity peaks) and the thermoluminescence.[2] Recently, WIEGAND and SMOLUCHOWSKI measured by means of a photoelastic technique the volume changes which LiF crystals undergo during X-irradiation at liquid nitrogen temperature and upon subsequent warming-up, and they tried to correlate these data with the changes in the optical absorption bands.[3]

While these studies permitted some speculations about the nature of the radiation induced damage and about the annealing processes they do not give direct insight into the molecular processes. The present work is complementary to the earlier studies in that the defects were studied on a molecular level; namely, by means of paramagnetic resonance. One of the most serious limitations of this study is, however, that non-paramagnetic defects cannot be observed. Moreover, one is never sure whether there are paramagnetic defects present which may have escaped observation under the conditions of the experiment.

A search for paramagnetic defects was made at various temperatures ranging from 2°K to 130°K, using an X-band spectrometer. The derivatives of the absorption and of the dispersion were recorded using a modulation frequency of the magnetic field of 8 c.p.s. and a modulation amplitude of several oersteds. The microwave power incident on the cavity was varied from μW to mW. About a dozen different paramagnetic defects could be found in X-rayed LiF under these circumstances. The spectra of four defects are predominant, and attention was focused on these. The four centers are all trapped-hole centers (V-type centers). However, the presence of an appreciable number of paramagnetic electron excess centers cannot be excluded, because the conditions of detection may have been unfavorable for these.*

* Assume, for example, an inhomogeneously broadened resonance with a relaxation time, T_1, which is very long and in addition long compared to the spin diffusion time. Such a resonance can escape observation in absorption as well as in dispersion under the conditions of the experiment as outlined above.

2. DESCRIPTION OF THE PARAMAGNETIC DEFECTS

The structures of the four predominant V-type centers have been analyzed in previous papers. Here, only a short description will be given (see Fig. 1).

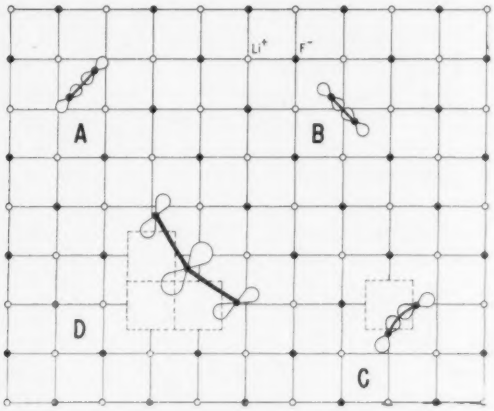

FIG. 1. Schematic representation of the four trapped-hole centers considered in this article. The fluorine nuclei near which the hole is localized are connected with a heavy line. The $2p$-functions forming the main part of the linear combination of atomic orbitals for the hole are symbolized by figure eights. The F-nuclei are represented as full circles and the Li-nuclei as open circles.

(A). Self-trapped hole
(B). H-center
(C). V_F-center
(D). V_t-center

1. *The self-trapped hole*[4,5]

This V-center is an electron deficiency which is not associated with any other imperfection. The hole is localized on two fluoride ions so that a F_2^- molecule-ion results with its axis along a [110]-axis of the crystal (center A in Fig. 1). The paramagnetic resonance absorption was measured at liquid nitrogen temperature. The main optical absorption band is centered around 3400 Å and corresponds to a $p\sigma_u$–$p\sigma_g$ transition.

2. *The H-center*[6]

This center is chemically equivalent to an interstitial F-atom, and it is best described as a F_2^- molecular ion substituting for a F^- ion as shown in Fig. 1 (center B). Its paramagnetic resonance spectrum was measured at liquid nitrogen temperature. The $p\sigma_u$–$p\sigma_g$ optical absorption band is expected to be very close to the corresponding band of the self-trapped hole (3400 Å), but slightly shifted to shorter wavelength. In order to isolate it one has first to find a way to generate H-centers without the presence of self-trapped holes.

3. *The V_F-center*[7]

The V_F-center is believed to be the antimorph of the F-center, since it appears to consist of a hole trapped at a Li vacancy. The hole is again localized on two fluoride ions so that a F_2^- molecule-ion results with a "bent bond" (center C in Fig. 1). The optical absorption band $p\sigma_u$–$p\sigma_g$ is expected to almost coincide with the corresponding band of the self-trapped hole. The paramagnetic resonance absorption was measured at liquid nitrogen temperature.

4. *The V_t-center*[8]

The V_t-center differs in character from the above-mentioned electron deficiency centers, in that it cannot be described as a tightly bound F_2^- molecule-ion. The unpaired electron is localized on three fluoride ions in a $p\pi$-like state as is indicated schematically in Fig. 1 (center D). The paramagnetic resonance cannot be observed at liquid nitrogen temperature, but readily at liquid hydrogen temperature. The optical absorption bands of this center have not been established as yet.

5. *Other paramagnetic centers*

The spectra of the remaining centers are relatively weak. Some of them seem to be related to the spectra of the V-centers described above, others are probably due to impurities.

3. GENERATION AND DECAY OF THE PREDOMINANT HOLE-CENTERS

1. *Crystals X-rayed at* 77°K

The relative concentrations of the four predominant V-type centers was measured by means of paramagnetic resonance after X-raying the crystal at liquid nitrogen temperature and after subsequent pulse annealing for 30 min at successively increasing temperatures. After the annealing pulse the crystal was immediately cooled to 77°K

for the measurement of the spectra of the self-trapped hole, the H-center and V_F-center, and then cooled to 20°K for the investigation of the V_t-center. The saturation behavior of the paramagnetic resonance spectrum was investigated for all four centers in order to account for saturation effects in the determination of the relative concentrations.

In a typical run a slab of Harshaw LiF of 2·6 mm thickness was irradiated in the microwave cavity at liquid nitrogen temperature for about 100 hr.

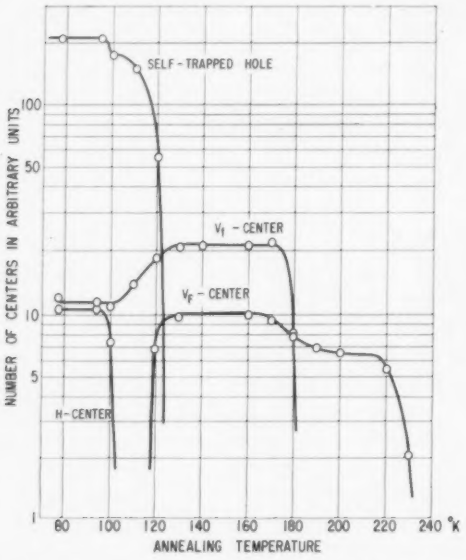

FIG. 2. Concentrations of the four trapped-hole centers in approximately the same units, measured after 30 min annealing pulses at the temperatures given on the abscissa. Note that the ordinate scale is logarithmic. The crystal was X-rayed at liquid nitrogen temperature.

The X-ray source was a General Electric SP–140 tube with tungsten target, operated at 70 kV peak and 8 mA. The sample-to-focus distance was 7·5 cm, and the total filtering corresponded to about 4 mm of aluminum, so that a fairly uniform coloration of the samples was acheived.

It was found that the relative concentration of the four types of hole centres depends upon the batch of the LiF crystals and upon the irradiation time. The production of H-centers and V_t-centers is particularly dependent upon the batch. For the H-centers this is somewhat surprising because in KCl and KBr their production appears to be an intrinsic process which does not depend significantly upon the purity.[6,9]

Fig. 2 summarizes the results obtained in a typical run.

The most abundant paramagnetic hole center is initially (i.e. after X-irradiation at 77°K) the self-trapped hole. The concentration of V_t-centers and of H-centers is about twenty times smaller, and no V_F-centers could be detected.

Between liquid nitrogen temperature and room temperature four temperature intervals were found in which annealing processes occur that affect the four paramagnetic hole centers. These annealing temperatures correspond to the temperatures at which other investigators observed thermoluminescence, conductivity peaks and changes in the optical absorption.[1,2,3] Exact coincidence of the annealing temperatures cannot be expected because the other authors warmed-up their samples continuously, whereas in the present investigation it was necessary to use annealing pulses. As these were of rather long duration (30 min), the "annealing temperatures" indicated by the steep portions of the curves in Fig. 2 are all somewhat lower than those obtained by continuous warming; however, the one-to-one correspondence seems to be unambiguous.

(*a*) *Processes occurring between* 95°K *and* 110°K. The H-centers are the most unstable ones among the centers considered in this paper. They disappear within minutes if the temperature approaches 105°K. The decay of the H-centers is connected with a relatively small drop in the number of self-trapped holes. The drop corresponds roughly to the number of H-centers that have disappeared. This might suggest that the H-center decays by emitting an electron, and thus transforms into a F_2 molecule. The electron in turn annihilates a self-trapped hole. The observed conductivity peak[2] is possibly due to this charge transfer and the thermoluminescence[1,2] to the electron-hole recombination. A decrease in volume of the crystal begins in this temperature range upon warming.[3] However, the "thermal resolving power" of the volume measurements is apparently insufficient to separate the decay of the H-centers from the processes that occur in the next annealing stage and dominate the volume change.

Vol. 17
1960

(*b*) *Processes occurring between* 110°K *and* 130°K. If one disregards the drop of the number of self-trapped holes, which is associated with the decay of the *H*-centers, one finds that the number begins to decrease noticeably at about 110°K, and, with the temperature approaching 130°K, these defects disappear within minutes or even seconds. A preliminary investigation of the kinetics of the destruction of the self-trapped holes seems to indicate the following facts:

(1) The kinetics is predominantly second order.
(2) It is controlled by the diffusion of the self-trapped holes themselves, which jump thermally activated from fluoride pair to fluoride pair.
(3) The diffusion coefficient D of the holes can be approximated by

$$D = D_0 e^{-A/kT}$$

with D_0 of the order of magnitude 0·1 $cm^2 sec^{-1}$ and $A = 0{\cdot}32$ eV.

The decay of the self-trapped holes is intimately connected with an increase in the number of V_t-centers and the formation of V_F-centers. This indicates that some of the migrating holes become trapped at vacancy aggregates and at Li vacancies. However, these two processes account for only about 10 per cent of the vanishing self-trapped holes. An even smaller fraction becomes trapped at more complex imperfections, which leads to the appearance of weak and very complex paramagnetic resonance spectra. No attempt was made to interpret these. The majority of the migrating holes seem to end up in non-paramagnetic states. Probably they recombine with electrons. Intense thermoluminescence[1,2] and a decrease of the optical absorption band attributed to *F*-centers (2425 Å) have been observed.[3] The largest change in the optical absorption is the decrease of the 3400 Å band which is attributed to the self-trapped holes. Although according to the paramagnetic resonance experiments all self-trapped holes disappear at this annealing stage a small fraction of the 3400 Å band remains. This remainder is probably due to the newly created V_F-centers which are expected to have an optical absorption almost coincident with the 3400 Å band.[7]

The decrease of the crystal volume observed by WIEGAND and SMOLUCHOWSKI[3] seems to be connected with the processes described here. At least part of the contraction may be due to the trapping of holes at negatively charged lattice defects such as vacancy aggregates and Li vacancies.

(*c*) *Processes occurring between* 175°K *and* 185°K. In this temperature interval the V_t-centers disappear and the concentration of V_F-centers drops somewhat. Thermoluminescence[1,2] and a conductivity peak[2] have been observed. It is conceivable that the V_t-centers as such are unstable at these temperatures and release the holes, which then recombine with trapped electrons or transform F_2^- molecule ions of V_F-centers into F_2 molecules. However, more complicated processes involving the diffusion of other types of defects cannot be excluded.

(*d*) *Processes occurring between* 220°K *and* 240°K. The V_F-centers anneal out in this temperature interval. It is interesting to note that the V_F-center is more stable than the V_t-center, although in both centers the hole is supposed to be bound to a lattice defect with a single negative charge (see Fig. 1). The electronic structures of the two centers are, however, very different. In the V_F-center the hole is in an antibonding σ_u orbital of a diatomic molecule-ion, whereas in the V_t-center it is in a less stable π-like state.

A thermoluminescence peak[1,2] and a conductivity peak[2] were observed at about 250°K upon continuous warming at a rate of several degrees per minute. Presumably these peaks are connected with the decay of the V_F-centers, and the small discrepancy in the temperature scale is due to the different annealing methods.

2. *Crystals X-rayed at* 20°K

If the LiF crystal is X-rayed at liquid hydrogen temperature instead of at liquid nitrogen temperature the relative abundance of the four trapped hole centers is somewhat different. The self-trapped hole is still the most abundant center; however, the number of V_t-centers is much smaller than in crystals X-rayed at liquid nitrogen temperature. The *H*-centers and the self-trapped holes seem to anneal out as described before. The number of V_t-centers increases and V_F-centers are formed during the decay of the self-trapped hole centers.

Important new paramagnetic centers were not

detected in crystals X-rayed at liquid hydrogen temperature.

3. *Crystals X-rayed at* 195°K

Among the four trapped-hole centers discussed in this paper it is only the V_F-center which "survives" a warming up to dry ice temperature (195°K). The other centers anneal out at lower temperatures, probably because of their own thermal instability. Therefore, after X-irradiation at 195°K one expects no H-centers, V_t-centers or self-trapped holes to be present in the crystal. This is in agreement with the experiment. However, one might expect to find V_F-centers, but none were found. Instead, the paramagnetic resonance spectrum of a new rather complex V-center was detected. An analysis of the very complicated spectrum was not attempted. These results indicate that isolated Li vacancies are either not formed by X-rays at 195°K or they are unstable at this temperature. If such vacancies *were* present they would trap holes, which are known to migrate at this temperature.

REFERENCES

1. Ghormley J. A. and Levy H. A., *J. Phys. Chem.* **56,** 548 (1952).
2. Delbecq C. J., Pringsheim P. and Yuster P. H., *Z. Phys.* **138,** 266 (1954).
3. Wiegand D. A. and Smoluchowski R., *Phys. Rev.* **116,** 1069 (1959).
4. Castner T. G. and Känzig W., *J. Phys. Chem. Solids* **3,** 178 (1957).
5. Woodruff T. O. and Känzig W., *J. Phys. Chem. Solids* **5,** 268 (1958).
6. Känzig W. and Woodruff T. O., *J. Phys. Chem. Solids* **9,** 70 (1958).
7. Känzig W., *Phys. Rev. Letters* **4,** 117 (1960); *J. Phys. Chem. Solids*, preceding article.
8. Cohen M. H., Känzig W. and Woodruff T. O., *J. Phys. Chem. Solids* **11,** 120 (1959).
9. Rabin H. and Klick C. C., *Phys. Rev.* **117,** 1005 (1960).

Vol. 17
1960

J. Phys. Chem. Solids Pergamon Press 1960. Vol. 17, Nos. 1/2, pp. 93–100. Printed in Great Britain.

ON THE ORIGIN OF BARKHAUSEN PULSES IN $BaTiO_3$

ROBERT C. MILLER

Bell Telephone Laboratories, Murray Hill, New Jersey

(*Received* 11 *March* 1960; *revised* 18 *May* 1960)

Abstract—The domain phenomena which give rise to ferroelectric Barkhausen pulses in $BaTiO_3$ have been investigated from an experimental approach. Through direct observation of the domain structure, and simultaneously the Barkhausen pulses, specific domain phenomena have been correlated for the first time with particular Barkhausen pulse shapes. It is found that Barkhausen pulses occur under a variety of different circumstances. Among these are: the nucleation of a reversed domain, the initial growth step of a small reversed domain, the collision of two reversed domains, and the formation of a small backswitched domain which produces a negative Barkhausen pulse. With the average crystal, each of these origins is operative at some point during polarization reversal. It has also been observed with some crystals that Barkhausen pulses continue to occur for times of the order of hours in the absence of an applied field. The duration of the Barkhausen events range from 2 μsec to about 300 μsec and the charge involved during the event is of the order of 10^{-13} C. The theoretical aspects of the problem have not been treated, but several driving forces which may be responsible for the pulses are suggested.

INTRODUCTION

WHEN THE direction of the spontaneous polarization in $BaTiO_3$ is reversed by the application of electric fields which range from several hundred volts per centimeter to several thousand volts per centimeter, small individual current pulses can be observed. This paper, which is experimental in nature, is concerned with the origin of those pulses which are in some manner related to changes in the ferroelectric domain configuration. In keeping with the ferromagnetic analogue, these pulses are termed[1,2] Barkhausen pulses. Those pulses which arise from instantaneous increases in the volume conductivity and from surface effects[3] have not been observed in these experiments; and since they are presumably different in origin from the pulses which arise from changes in the domain configuration, they will not be considered here.

KIBBLEWHITE[2], who was the first one to attempt a comprehensive study of Barkhausen pulses in $BaTiO_3$, suggested that some of the observed Barkhausen pulses might be associated with irregular changes of the ferroelectric domain configuration in a manner similar to the ferromagnetic analogue. Magnetic Barkhausen pulses have been shown[4] to arise from irregularities in the motion of a magnetic domain wall.

In more recent work, CHYNOWETH[5,6] described a very extensive experimental study of the electrical characteristics of Barkhausen pulses observed during polarization reversal in $BaTiO_3$. CHYNOWETH concluded that the Barkhausen pulse could result from the initial rapid growth, immediately after nucleation, of a spike shaped domain. Arguments were presented to demonstrate that this model could account for many of the measured properties of the pulses.

In the course of a study of polarization reversal in $BaTiO_3$ samples which had aqueous LiCl electrodes, the first origin for Barkhausen pulses directly correlated with a specific domain phenomenon was found.[7] In many cases few, but large domains, were observed with the liquid electroded specimens. Simultaneous observations of the switching current $i_s \propto dp/dt$ and the time of occurrence of Barkhausen pulses showed that i_s was quite irregular, and that sharp decreases in i_s were usually accompanied by one or more Barkhausen pulses. (Note that Barkhausen pulses are in general too small and too fast to appear superimposed on the observed i_s.) These observations then led to

the conclusions that one origin for Barkhausen pulses is the rapid polarization reversal of the small volume formed when two growing domains are about to coalesce.

At the time of the investigation mentioned above, it was also noted that Barkhausen pulses sometimes occurred when it was thought that there were no domain "collisions" or nucleations. In particular, Barkhausen pulses were observed when there was a single growing domain.[8] Thus, it appeared that there was more than one origin for Barkhausen pulses. An important limitation encountered in the research just described was the method of observing the antiparallel domain configuration—the etch technique.[9,10] With this method, the sample is etched in certain acids and then examined with a microscope by reflected or transmitted light. This technique suffers from several disadvantages; e.g. the electrodes must be removed from the sample, the $BaTiO_3$ surface is obviously altered by the etch and, most important, it does not permit a continuous viewing of the domain structure during polarization reversal. Through recent advances in experimental techniques,[11] an improved method for observing the domain pattern has been found. Using this method, we have been able to investigate the origin of ferroelectric Barkhausen pulses in $BaTiO_3$ under much better experimental conditions than was heretofore possible. The results of these experiments are described in this paper. It turns out that the Barkhausen effect in $BaTiO_3$ is much more complex than had generally been considered. Much of the data to be described will be left unexplained from a theoretical standpoint; in fact, the data probably raise more theoretical problems than they solve. However, it is felt that the various origins for Barkhausen pulses, and their implications, are of sufficient interest and novel in character to warrant presenting them at this stage of the research.

THE METHOD

The ideal experiment for this investigation is one in which the antiparallel domain pattern, the time of occurrence of Barkhausen pulses and the pulse shapes are all observed simultaneously during polarization reversal. Fortunately, with the introduction of new experimental techniques, this is possible. It has been found that the antiparallel domain configuration can be discerned directly and continuously during polarization reversal.[11] The method is to mount the $BaTiO_3$ sample between crossed polaroids and view through a microscope with transmitted light. The sample must, of course, have transparent or semi-transparent electrodes. Semi-transparent metal electrodes were usually noble metal films, several hundred angstroms thick, on opposite sides of the sample. In some cases, transparent liquid electrodes which consist of a saturated aqueous solution of LiCl have been employed.[7]

A block diagram of the circuitry used to make the electrical measurements is shown in Fig. 1 The circuitry has been described in detail elsewhere[6,7] so that only a brief description of certain aspects of it will be mentioned here. The output of the linear amplifier is fed into a C.R.O.

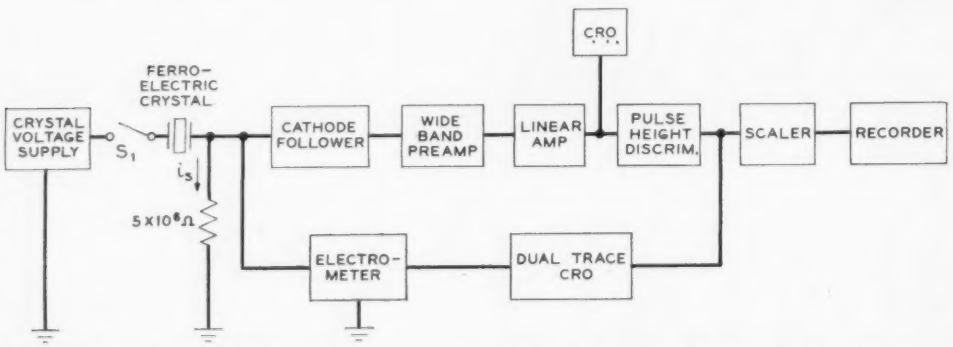

FIG. 1. Block diagram of the circuit used to measure the electrical characteristics of the Barkhausen pulses.

Vol. 17
1960

which is triggered by the Barkhausen pulse and which has a sufficiently fast sweep so that the pulse shape is traced out on the screen. The C.R.O. is equipped with a camera so that the pulses can be recorded. The pulses shown in this paper are reproductions of the photographed oscilloscope traces.

Ideally, the pulses represent plots of charge switched, i.e. the volume of material in which the polarization is reversed during the Barkhausen event, vs. time. In actual fact, these pulses are clipped somewhat by the associated circuitry so that they appear to drop off in amplitude near the end of the Barkhausen event. The duration of the Barkhausen event, called the "rise time" will be loosely defined as the time required for the pulse amplitude to attain its maximum value. This rise time will, of course, be a little less than the actual time duration of the Barkhausen event because of the clipping. The magnitude of the effects of clipping on the pulses has been discussed by CHYNOWETH[5] and will be illustrated when the pulse shapes are described.

The amplitudes of the pulses are converted into units of charge through a straightforward calibration operation described by CHYNOWETH[6].

The direction of the polarization in the sample is generally cycled plus and minus automatically and the measurements are normally made with a step voltage adjusted such that the polarization reverses in times of the order of minutes.

The $BaTiO_3$ *c*-domain samples were obtained from selected "butterfly wings" and prepared as described in an earlier paper.[7]

RESULTS

It is convenient to divide the observed pulses into two broad groups, positive pulses and negative pulses. Positive pulses occur when the Barkhausen events involve spontaneous polarization changes into the direction of the applied field. On the other hand, spontaneous polarization changes into a direction opposite to that of the applied field give rise to negative Barkhasuen pulses. Pulses of both signs have also been observed in other investigations[1,2,12] of Barkhausen pulses in $BaTiO_3$.

The varied circumstances under which the positive pulses are observed will be described first.

(a) *Nucleation pulses.* It is noted that the formation of a small domain in the presence of an applied field is frequently accompanied by a positive pulse. Through the microscope, with crossed polaroids these domains appear as dots, on or near the surface of the crystal, with lateral dimensions of the order of 1μ. These small domains do not usually continue to grow immediately after

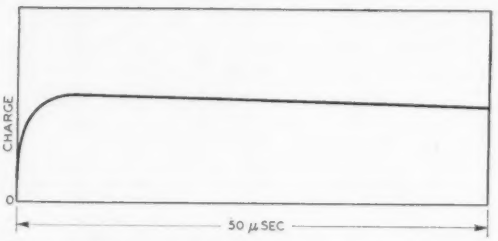

FIG. 2. Barkhausen pulse observed with the nucleation of a domain. The pulse is a plot of charge switched vs. time. The pulse amplitude is 2×10^{-14} C.

the nucleation event; in fact, it may be minutes before they start to grow again. In many cases, the small domains do not grow at all beyond the initial stage, but instead are overrun by other expanding domains. Examination of these small domains by means of the etch technique[9,10] indicates that they extend all the way through the thickness direction of the crystal, and that they are circular in cross section. A reproduction of

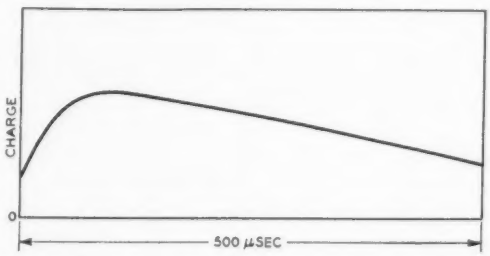

FIG. 3. Barkhausen pulse observed when a small nucleated domain begins to grow after a period of no visible growth. This pulse amplitude is 4×10^{-14} C.

a nucleation pulse which appeared with an applied field of about 450 V/cm is shown in Fig. 2. This rise time is about 5 μsec and the charge switched during the event is 2×10^{-14} C.

(b) *Growth pulses.* When one of the small domains mentioned above starts to grow beyond the initial stage, a single positive Barkhausen

pulse, termed a growth pulse, is frequently observed. One of these pulses observed with a field of 700 V/cm is shown in Fig. 3. The rise time is about 100 μsec and the amplitude 4×10^{-14} C. Most of these pulses are characterized by the long linear rise exhibited by the one shown in the figure.

The effect of clipping on the pulse shape is clearly evident in Fig. 3. The magnitude of this effect is illustrated in Fig. 4 which shows the

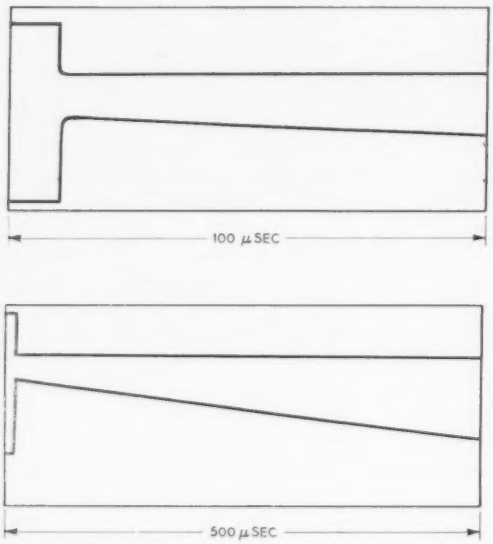

FIG. 4. Illustration of the effect of clipping on square wave forms. In each case the input signal is a minus pulse and the output signal a positive pulse.

output pulse observed when a good square pulse is applied at the input. The input and output pulses are shown as negative and positive pulses, respectively.

(c) *Nucleation plus growth pulses.* When the nucleation and growth events described above are spaced sufficiently close in time, a single pulse with some structure can be observed. These pulses, with the present definition of rise time, can of course have very long rise times. The nucleation plus growth pulse shown in Fig. 5 occurred with a field of 700 V/cm and has a rise time of about 200 μsec and an amplitude of 4×10^{-14} C.

(d) *Collision pulses.* The pulses which occur when two domains come together can have a

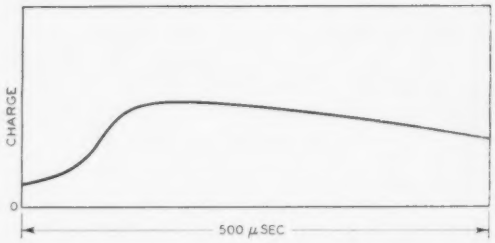

FIG. 5. Barkhausen pulse observed when the nucleation and subsequent growth events take place at almost the same time. The pulse amplitude is 4×10^{-14} C.

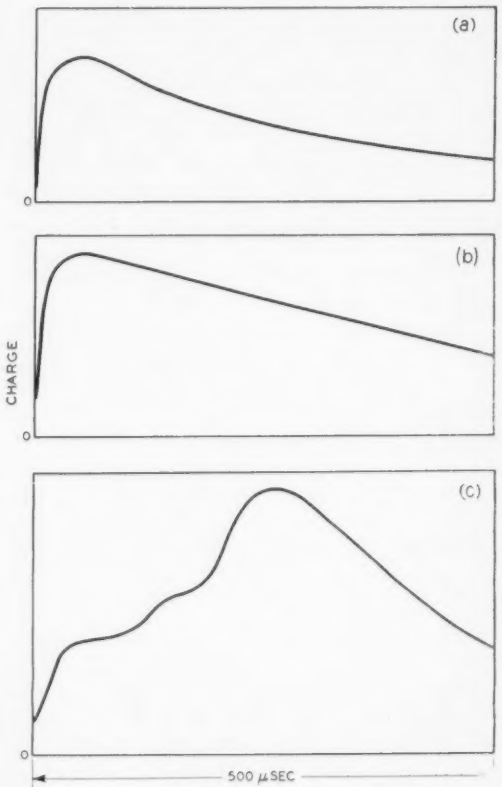

FIG. 6. Three types of Barkhausen pulses which are observed when two domains coalesce. The pulse in (a) occurred when a growing domain overran a small nucleated domain. In (b), a pulse which occurred when two {100} small area 180° domain walls coalesced is shown. The pulse in (c) was observed when two large area {110} 180° domain walls collided. The amplitudes of the pulses in (a), (b), and (c) are 4×10^{-14} C, 3×10^{-14} C and 2×10^{-12} C, respectively.

Vol. 17
1960

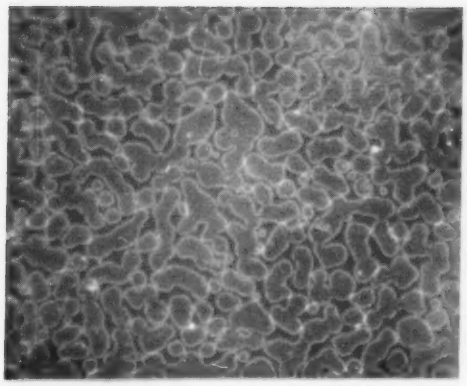

FIG. 7. Photomicrograph showing a portion of the domain configuration of a sample which exhibited positive Barkhausen pulses with no applied field. The lighter areas are the reversed domains. The sample has been etched in acid to make the domain structure visible.

[facing p. 96

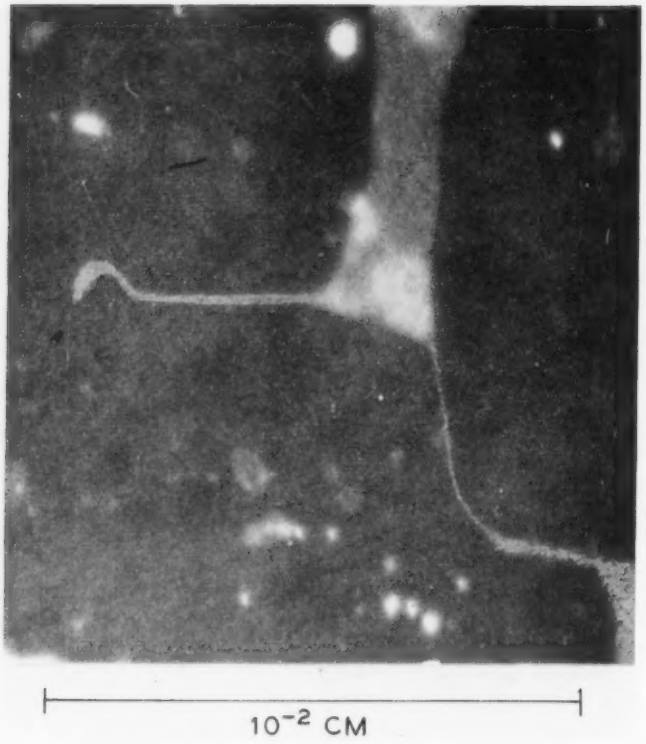

FIG. 9. Photomicrograph of a partially reversed, acid etched, $BaTiO_3$ crystal. The dark areas are the reversed domains. The photomicrograph has been retouched to bring out the narrow unswitched region between the large reversed domains.

variety of shapes and sizes depending on the exact nature of the collision. Three of these pulses are shown in Fig. 6. The first pulse, Fig. 6(a), was observed with a field of 350 V/cm when a growing domain overran a small nucleated domain of the type described in (a). The rise time is 50 μsec and the pulse amplitude 4×10^{-14} C. Fig. 6(b) shows a pulse observed when two domains came together such that two small-area {100} 180° domain walls[7,8] coalesced. This pulse, observed with a field of about 700 V/cm, has a rise time of 50 μsec and an amplitude of 3×10^{-14} C. Finally, in Fig. (6c), a Barkhausen pulse is shown which occurred with a field of 330 V/cm when two large area (each about 10^{-2} cm long) {110} 180° domain walls coalesced. This latter origin of collision pulses can give rise to pulses whose shapes vary from the corner collision type, Fig. 6(b), for small area {110} wall collisions, to the more complicated variety shown in Fig. 6(c) for large area {110} wall collisions. The pulse in Fig. 6(c) is a very large one, 2×10^{-12} C, and has three distinct humps. Pulses with double humps have also been observed when two domains coalesce.

(e) *Other positive pulses.* The positive pulses described up to this point have been correlated with particular domain phenomena through studies of crystals which reversed polarization with relatively few domains. Under these conditions, which are the usual ones, the domains attain sufficient size so that their history is not difficult to follow. In some cases, however, it is not possible to distinguish individual domains. All the evidence indicates that under these conditions, polarization reversal takes place with many small domains and likewise, with many Barkhausen pulses. Of the crystals which behaved in the above manner, a few of these were also found to exhibit positive Barkhausen pulses even with no voltage applied to the specimen. To observe pulses under these circumstances, the sample is partially reversed (perhaps about $\frac{3}{4}$ of the total volume) with a field of several thousand volts per centimeter. Then the field is removed and it is found that pulses of the same sign continue to occur, sometimes even for hours after the removal of the field. These pulses do not all have the same shape. However, most of them are similar to those shown in Fig. 6(b) and a few similar to those given in Figs. 3 and 5. Examination of the domain configuration using the etch technique revealed that at the time the pulses appeared with zero applied field, there were many small domains. A photomicrograph of a portion of this pattern as seen on one side of the sample is shown in Fig. 7. The other side of the sample reflected the pattern shown in Fig. 7, but in addition parts of the interstices between the reversed domains contained small domains which did not extend all the way through the thickness of the crystal. It seems clear from these data that for positive Barkhausen pulses (that is, positive pulses with respect to the last field applied) to occur with zero field, one requires small domains very close together.

It has also been observed that positive pulses occur with the motion of rough, irregular walls. These pulses have many of the characteristics of the collision pulses and are believed to have in effect the same origin as the collision pulses. The visual data on this type of pulse are rather meager, but it appears that part of the advancing wall is temporarily pinned at a certain point. Then, as the remainder of the wall continues to advance, one finally arrives at a situation where the wall wraps around the pinned point and then, in effect, a collision takes place. The pinning points cannot usually be identified with crystalline imperfections. There is some preliminary evidence which indicates that the presence of rough walls during polarization reversal can be influenced by the electroding operation. Rough walls are seldom observed with liquid electroded crystals.

The negative Barkhausen events. It has been observed on occasion that a small region of the crystal behind an advancing domain wall will suddenly reverse its polarization in a direction *opposite* to that of the applied field and hence give rise to a negative Barkhausen pulse and a "backswitched" domain. Fig. 8 shows a negative Barkhausen pulse which was observed with a field of plus 450 V/cm applied to the sample. This same particular pulse was photographed a number of times and the pulse shape was found to be very reproducible. The pulse has a rise time of 50 μsec and an amplitude of 10^{-13} C. The negative pulses frequently have rise times which are somewhat shorter than 50 μsec.

In some cases, negative Barkhausen pulses occur with zero field after a crystal has been partially or completely switched. These pulses

which are about 10^{-13} C in amplitude, can have very short rise times, i.e. several micro seconds. The pulses which arise under these circumstances have the shortest rise times of all those observed.

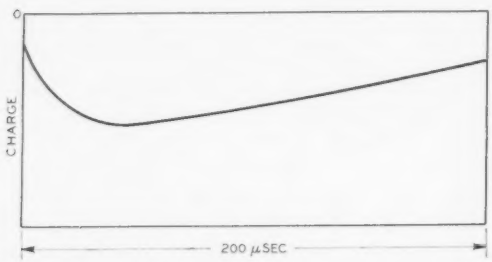

FIG. 8. Negative Barkhausen pulse observed with a field of plus 450 V/cm applied to the sample. The pulse amplitude represents a charge of 10^{-13} C.

DISCUSSION

It is not easy to compare in any detail the present results with those of earlier investigations; however, it is believed that all the pulse shapes described in the earlier studies have also been observed in the course of the present experiments. These pulses include the double and triple hump pulses, the relatively short rise time negative pulses and the "normal" positive pulses.[1,2,5,12] A close comparison between the present data and those of KIBBLEWHITE[2] does not seem warranted since it is known that his crystals contained some domains polarized in a direction perpendicular to the field, i.e. *a*-domains. The presence of *a*-domains complicates the interpretation of the results as electromechanical effects may become important under these conditions.

In view of the quantitative aspects of the extensive data collected by CHYNOWETH[5], it should prove fruitful if these older data could be identified with a particular domain phenomenon. With this goal in mind, a sample was obtained from CHYNOWETH and the domain dynamics of polarization reversal for the specimen was studied. Electrically, that is Barkhausen-wise, this sample behaved in a similar manner to the other samples studied by CHYNOWETH[12]. Direct examination of the domain pattern indicated that this specimen was similar to many others studied during this investigation. In particular, a number of the origins for positive pulses described earlier must have been operative during polarization reversal. On the basis of these and other data,[13] it is concluded that the data obtained by CHYNOWETH cannot be ascribed to a single type of domain phenomenon. We now believe the positive pulses observed by CHYNOWETH were largely made up of growth pulses (Fig. 3) and collision pulses (Figs. 6(a) and 6(b)) along with lesser numbers of nucleation pulses (Fig. 2) and nucleation plus growth pulses (Fig. 5).

What can be said about the details of the domain phenomena and the driving forces which give rise to these pulses? Additional data described below shed some light on this question insofar as collision pulses are concerned. With several crystals whose domains were particularly easy to see directly, it has been noted that when two 180° domain walls are sufficiently close, there appears to be a repulsion between them. This repulsion results in the formation of a very narrow metastable region which then suddenly disappears coincidently with the generation of a positive Barkhausen pulse. The photomicrograph reproduced in Fig. 9 shows a portion of the domain configuration of an etched partially, reversed, crystal. A narrow region, $\approx 1\mu$ wide, between two domains is evident at two places in the figure. Frequently these narrow regions follow tortuous paths that strongly suggest that the walls repel each other. It is believed that the positive pulses which occur with zero applied field result from the collapse of these narrow regions between domains. The photomicrograph shown in Fig. 7 demonstrates that such narrow regions do exist under the conditions where pulses are observed with zero field. In addition, these positive pulses possess shapes which are very similar to those observed when small domains coalesce.

The origin of a repulsive force between 180° domain walls is not known, however, there are two obvious possibilities which will be mentioned. There is considerable evidence[7,14–16] that the 180° walls are not always in the plane of the ferroelectric axis which, if true under the present conditions, would mean that the walls possess a net surface charge density and hence approaching walls could repel each other. Examination of both sides of etched crystals as well as direct observation of the domains do not indicate any slant with respect to the ferroelectric axis for walls similar

Vol. 17
1960

to those shown in Fig. 9. Estimates based on the more accurate of these two methods, the etch technique, give an upper limit of 0·3° for the slant angle. It is, of course, assumed in making the above estimates that the walls do not stabilize during the various operations required by the method of observation. There is also the possibility that a narrow region between two 180° domain walls does not reverse readily due to surface layer effects as described in two recent papers.[17,18]

Consider the magnitude of the crystal volumes involved in the collision Barkhausen event. For two domains coming together along a side 4×10^{-4} cm long, a pulse of 2×10^{-14} C was observed. The charge flowing in the external circuit to the electrodes when the spontaneous polarization P_s is reversed in a volume v is given by[1] $Q = 2P_s v/d$ where d is the crystal thickness. If it is assumed that the volume v has a uniform cross section A and that it extends through the thickness direction of crystal, then $Q = 2P_sA$ so with $Q = 2\times10^{-14}$ C and $P_s = 2{\cdot}6\times10^{-5}$ C/cm², the area A becomes 4×10^{-10} cm². From the size of the two domains involved, the upper limit of the dimension along the walls is 4×10^{-4} cm, so that the minimum average width of the area is 100 Å. With a uniform separation of 100 Å, it is difficult to conceive of a driving force responsible for the pulse. Therefore, it seems unlikely that the Barkhausen event starts with a uniform 100 Å separation of the two domain walls. In qualitative terms, it is believed that the collision type Barkhausen event begins when the two walls coalesce at some point after which surface tension effects due to the wall energy, and perhaps aiding electric fields from charges on slanted walls, come into play and give rise to a high local dp/dt—hence a positive pulse. There are not sufficient data available to construct a single detailed quantitative model for this process. Since these and other relevant data are in principle obtainable with the present state of the art, it would seem advisable to defer a discussion of the several possible models, until these data are available.

The nucleation and growth pulses indicate that the nucleation and growth of domains in $BaTiO_3$ comprises a two-step process. It is found that a given nucleation site may serve as a nucleation center for a given polarity on many successive reversals. Some of these centers can be identified with visible crystalline or electrode imperfections; however, other reproducible centers have not been correlated with any abnormalities of the electroded specimen. In any case, these results show that the nucleation sites are not spatially distributed in a random manner throughout the crystal, but that they are most likely connected with crystalline or electrode imperfections, some of which are not observable.

Once the initial stage of growth is over, the observations show that many of the domains either cease growing or continue to grow at a greatly reduced rate. This phenomenon is difficult to explain if the nucleus extends all the way through the thickness of the crystal as is indicated by the observations of etched crystals. Likewise, it is difficult to explain why a pulse should occur when the small nucleated domains begin to grow at a normal rate after the period of no visible growth. The two-step process would be more plausible if the nucleated domains were, for example, spikes which did not extend all the way through the crystal. For in this case, if the shape and size of the nucleus were such that the depolarizing field was approximately cancelled by the applied field, then growth would slow down and possibly even cease. However, in time, the polarization charges on the slanted 180° walls of the spike could become partly neutralized and permit further growth which might become more rapid (due to reduced depolarizing fields) as the nucleus approached the opposite electrode. This model seems to be ruled out by the etch studies. However, it may be that the etch technique does not give an accurate reproduction of the dynamic domain configuration on the scale of these small domains. In any event, the details of the domain dynamics which give rise to the nucleation and growth pulses remain unknown.

Perhaps the most difficult pulses to explain are the negative pulses. In some cases, they occur at reproducible sites for many reversals, after which the sites may become inoperative. The number of negative Barkhausen pulses which is usually orders of magnitude less than the number of positive pulses, has been observed to increase with *increasing* positive field. Also, the small back-switched domains which arise coincidently with a negative pulse can usually be removed by a

sufficiently long application of the positive field. There is no tendency for the backswitched domains to cluster, in fact, they sometimes appear to repel each other. These data suggest that opposing fields due to surface layers[17,18] coupled with imperfections of some sort may be important factors in causing the negative pulses.

It has been proposed[20,21] that the 180° domain wall in $BaTiO_3$ moves through a nucleation or step mechanism so that one might expect to observe pulses during the motion of a smooth 180° wall. However, experiment shows that no pulses are present under these conditions. Estimates of the volumes and charges consistent with these models for the wall motion are many orders of magnitude smaller than the minimum detectable (5×10^{-15} C) with the present apparatus. Therefore, the absence of pulses during the motion of a smooth wall does not rule out the proposed models for the sidewise motion of 180° domain walls in $BaTiO_3$.

SUMMARY

An investigation of the domain phenomena responsible for Barkhausen pulses in $BaTiO_3$ has shown that these pulses arise under a number of different circumstances. Those pulses whose origin is related to the initial growth of domains indicate that the nucleation and growth of domains is a two step process. Furthermore, the nucleation sites are not randomly distributed over the crystal as has been proposed by other investigators. The characteristics of the pulses which occur when two growing domains coalesce depend on the exact nature of the two colliding walls. It is believed that surface tension effects arising from the domain wall energy, and perhaps enhancing electric fields due to slanted domain walls, may be the driving forces responsible for the collision pulses. The pulses observed during the motion of rough, irregular walls, as well as those which occur with zero applied field, are believed to have origins similar to the collision pulses. When the spontaneous polarization in a small region of the crystal suddenly lines up anti-parallel to the field, a negative Barkhausen pulse is observed. The sites at which this phenomenon occurs are also not randomly distributed through the crystal.

In most cases, it is possible to predict the domain phenomenon giving rise to a particular pulse from an examination of the pulse shape. Therefore, information on the domain dynamics of polarization reversal of a crystal can be obtained from a study of its Barkhausen pulse characteristics. Now that the origins of the various pulses have been correlated with specific domain phenomena, it should prove fruitful to carry on further research aimed at explaining the shapes of the pulses.

Acknowledgements—It is a pleasure to acknowledge numerous stimulating and enlightening discussions with Dr. A. G. CHYNOWETH on the subject of this paper. The author would also like to thank Mr. A. SAVAGE for his help and patience in collecting much of the data, and Mr. R. C. LINARES for the $BaTiO_3$ crystals.

REFERENCES

1. NEWTON R. R., AHEARN A. J. and MCKAY K. G., *Phys. Rev.* **75,** 103 (1949).
2. KIBBLEWHITE A. C., *Proc. Inst. Elect. Engrs.* **102B,** 59 (1955).
3. TOLSTOI N. A., *Zh. tekh. fiz., Mosk.* **20,** 970 (1950).
4. WILLIAMS H. J. and SHOCKLEY W., *Phys. Rev.* **75,** 178 (1949).
5. CHYNOWETH A. G., *Phys. Rev.* **110,** 1316 (1948).
6. CHYNOWETH A. G., *J. Appl. Phys.* **30,** 280 (1959).
7. MILLER R. C., *Phys. Rev.* **111,** 736 (1958).
8. MILLER R. C. and SAVAGE A., *Phys. Rev.* **112,** 755 (1958).
9. HOOTON J. A. and MERZ W. J., *Phys. Rev.* **98,** 409 (1955).
10. PEARSON G. L. and FELDMAN W. L., *J. Phys. Chem. Solids* **9,** 28 (1959).
11. MILLER R. C. and SAVAGE A., *Phys. Rev. Letters* **2,** 523 (1959).
12. CHYNOWETH A. G., private communication.
13. MILLER R. C. and SAVAGE A., unpublished data.
14. MERZ W. J., *Phys. Rev.* **95,** 690 (1954).
15. LITTLE E. A., *Phys. Rev.* **98,** 978 (1955).
16. CAMERON D. P., *I.B.M. J. Res. Developm.* **1,** 2 (1957).
17. DROUGARD M. E. and LANDAUER R., *J. Appl. Phys.* **30,** 1663 (1959).
18. MILLER R. C. and SAVAGE A., *J. Appl. Phys.* **31,** 662 (1960).
19. MERZ W. J., *Phys. Rev.* **91,** 513 (1953).
20. ABE R., *J. Phys. Soc. Japan* **14,** 633 (1959).
21. MILLER R. C. and WEINREICH G., *Phys. Rev.* **117,** 1460 (1960).

J. Phys. Chem. Solids Pergamon Press 1960. Vol. 17, Nos. 1/2, pp. 101–111. Printed in Great Britain.

CRYSTAL DISTORTION IN SPINELS CONTAINING Mn^{3+} IONS*

K. S. IRANI, A. P. B. SINHA and A. B. BISWAS

National Chemical Laboratory, Poona 8, India

(*Received* 28 *October* 1959; *revised* 27 *April* 1960)

Abstract—The effect of chemical composition on tetragonal–cubic spinel transformations in the systems Mn_3O_4–$MgAl_2O_4$ and $MgMn_2O_4$–$MgAl_2O_4$ has been studied by X-ray diffraction. The unit cell dimensions of the various compounds have been determined at room temperature. The c' and a' values do not change linearly with composition but show an abrupt change at a critical composition, beyond which $c' = a'$, and the systems have the cubic spinel structure. The cation distribution has been worked out from an analysis of the X-ray diffraction intensities, and thus a correlation between the actual number of distorting Mn^{3+} ions at the octahedral sites, and the degree of distortion, has been obtained. The critical number of Mn^{3+} ions required at these sites to maintain the tetragonal spinel structure at room temperature has been accurately determined.

INTRODUCTION

A NUMBER of substances are now known which possess the tetragonal spinel structure isomorphous with hausmannite (Mn_3O_4).[1] The tetragonal distortion from the ideal cubic spinel structure is attributed to the presence of certain cations, such as Mn^{3+} or Cu^{2+}, which, when located at the octahedral sites, tend to form dsp^2 square coplanar bonds.[2] Another plausible explanation based on crystal field theory has recently been put forward.[3]

The effect of the removal of these distorting cations on crystal distortion has been studied by FINCH, SINHA and SINHA[4]. They replaced these cations with non-distorting ones through the formation of solid solutions of tetragonal (Mn_3O_4) and cubic (AFe_2O_4) spinels. The conclusions were drawn on the assumption that in the solid solutions all the Mn^{3+} ions occupied the octahedral sites as they did in the parent Mn_3O_4. This assumption is made plausible by the theoretical preference of Mn^{3+} ions for the octahedral sites.[2] It was not possible to confirm this by the X-ray diffraction method because in the systems Mn_3O_4–AFe_2O_4 most of the cations have nearly equal scattering powers for X-rays.

Recently WICKHAM and CROFT[5] studied the systems

$$Zn_xGe_{1-x}Mn_2O_4,\ Zn_xGe_{1-x}Co_{2-2x}Mn_{2x}O_4,$$
$$Zn_xLi_{1-x}Mn_2O_4.$$

However, this study also suffers from the drawback of the assumption that in the solid solutions the cations maintain the same sites which they had in the parent compounds. Furthermore, in the system $Co_{3-x}Mn_xO_4$, the results are inconclusive, as suggested by these authors,[5] because of the likely electron transfer between Mn^{3+} and Co^{3+} ions.

Thus it was considered desirable to study systems where the cation distribution in solid solutions could be experimentaly determined and where any electron exchange between the cations was unlikely and thus the valency states could be checked chemically. The systems Mn_3O_4–$MgAl_2O_4$ and $MgMn_2O_4$–$MgAl_2O_4$ were, therefore, studied by IRANI[6]. Here both the Mg^{2+} and the Al^{3+} ions can be distinguished from the Mn^{3+} ions, because of the appreciable difference in their X-ray scattering factors. Furthermore, the change of valencies of Mg^{2+} and Al^{3+} ions is unlikely.

In what follows the results obtained from solid

* Contribution No. 407 from the National Chemical Laboratory, Poona.

solution studies of the systems Mn_3O_4–$MgAl_2O_4$ and $MgMn_2O_4$–$MgAl_2O_4$ are described, which indicate the minimum number of Mn^{3+} ions required at the octahedral sites for maintaining long range order to produce observable bulk distortion to the related lattice of lower symmetry. These results also reveal the co-operative nature of bulk distortion in tetragonal spinels.

EXPERIMENTAL PROCEDURE

Solid solutions of the spinels Mn_3O_4–$MgAl_2O_4$ and $MgMn_2O_4$–$MgAl_2O_4$ were prepared from mixtures of the individual component spinels. The molar proportions of the components in the solid solution were varied over the whole range from 100 per cent of one component to 100 per cent of the other. The mixtures were intimately ground in an agate mortar under alcohol and the dried mass was kept in a platinum crucible open to air and heated at 1200°C for several hours, in an electric furnace whose temperature could be controlled to ± 5°C. The samples were quenched to room temperature, powdered, and analysed by X-ray diffraction using a 14 cm Debye Scherrer powder camera and Mo $K\alpha$ radiation filtered through Zr. The photographs thus obtained were analysed to check that homogeneous solid solutions had been formed.

Because the samples were heated at elevated temperatures, they can take up or lose oxygen to give a non-stoichiometric compound. This would change the valency of manganese ions present. The average valency was therefore determined chemically by the standard oxalate–permanganate titration. This gave the average valency of manganese ions in excess over the divalent state. This was found to be always slightly higher than the nominal value.

The axial parameters were determined to an accuracy of ± 0·02 Å. The intensities were estimated by comparison with intensity scale strips. The strongest reflexion was arbitrarily assigned the value of 100, and the others the corresponding comparative intensities.

The intensities were calculated for the various possible reflexions, considering different possible structures in a given system using the formula

$$I_{cal} = |F|^2_{hkl} \cdot p \cdot \frac{1+\cos^2 2\theta}{\sin^2\theta \cdot \cos\theta}$$

where the symbols have their usual significance. The correction for the opposing effects of absorption and thermal vibrations of the ions in the lattice were not applied.

Vol. 17
1960

RESULTS

The system Mn_3O_4–$MgAl_2O_4$

The unit cell dimensions for the various compositions studied are given in Table 1. The three tetragonal phases appear isomorphous

Table 1. *Unit cell dimensions for* Mn_3O_4–$MgAl_2O_4$ *systems*

Composition Mn_3O_4–$MgAl_2O_4$	Symmetry *	c' †	a' †	c'/a' †
16 : 0	T	9·37	8·07	1·16
14 : 2	T	9·15	8·02	1·14
12·6 : 3·4	T	9·00	8·08	1·11
11 : 5	C	—	8·34	1·00
10 : 6	C	—	8·29	1·00
9 : 7	C	—	8·29	1·00
8 : 8	C	—	8·26	1·00
3·4 : 12·6	C	—	8·17	1·00
0 : 16	C	—	8·03	1·00

* T = Tetragonal C = Cubic.

† Values refer to the face-centred tetragonal pseudo cell. $c' = c$, $a' = a\sqrt{2}$; where c and a refer to the smaller crystallographic unit cell (space group D^{19}_{4h}).

with hausmannite having the space group $I4_1/amd$–D_{4h}^{19}, and the remaining phases show cubic symmetry and are isomorphous with the spinel structure having the space group $Fd3m-O_h^7$. The space group D_{4h}^{19} for the parent compound, hausmannite, has been well established on the basis of recent neutron diffraction experiments.[7] The possibility that the present tetragonal phases are isomorphous with copper chromite (space group D_{2d}^{12})[8] and not hausmannite (D_{4h}^{19}) is unlikely on the grounds that for the former, reflexions of the type *hko* with $h+k=2n$ should be present whilst for the latter there is an additional limitation that both h and k should be $2n$. The absence of the reflections 110, 310, 330 support the space group D_{4h}^{19} for all the tetragonal phases under study. In the hausmannite structure the metal ions are distributed over the special positions 4(*a*) and 8(*d*), and the oxygen ions occupy the 16(*h*) sites (*oxz* etc.). Thus we have to determine (i) the distribution of the cations over the 4(*a*) and 8(*d*) sites, and (ii) the oxygen ion parameters x and z. The present X-ray diffraction data are not adequate to determine the oxygen ion parameters very accurately. It is, however, possible to determine the cation distribution in these phases, which is required to correlate the distortion with the actual number of Mn^{3+} ions at the octahedral sites. The degree of distortion varies with Mn_{oct}^{3+} ions up to the critical composition only, hence intensity calculations were made for the following compositions:

Mn_3O_4:$MgAl_2O_4$ = 14 : 2, 12·6 : 3·4 and 11 : 5.

The analysed chemical composition is given in column 2 of Table 2. These compounds contain four types of cations viz. Mn^{2+}, Mn^{3+}, Mg^{2+} and Al^{3+}. However, the Mn^{2+} and Mn^{3+} possess nearly identical X-ray scattering powers and may be treated as similar, and designated as "*A*". On the same considerations, the Mg^{2+} and Al^{3+} can be denoted together as "*B*". The analysed chemical compositions reveal that these are metal deficit compounds and may contain vacant cation sites or interstitial oxygen ions. In a close packed structure of oxygen ions the second possibility is unlikely; the unit cell chemical formula for each composition can then be represented as shown in column 3 of Table 2 where □ represents vacant cation sites. The tetragonal unit cell formulae have been

Table 2. Formulae for Mn_3O_4–$MgAl_2O_4$ *systems*

Nominal composition Mn_3O_4–$MgAl_2O_4$	Chemically analysed composition	Unit cell formula $Z=8$ $Mn^{3+}=A$ $Mg^{2+}=Al^{3+}=B$	Cation distribution
14:2	$Mn^{2+}_{0.82}Mn^{3+}_{1.79}Mg^{2+}_{0.12}Al^{3+}_{0.25}O_4^{2-}$	$A_{20.9}B_8\square_{0.1}O_{32}^{2-}$	$A_mB_n\square_{8-p}[A_{20.9-m}B_{3-n}\square_{p-7.9}]O_{32}^{2-}$
12·6:3·4	$Mn^{2+}_{0.72}Mn^{3+}_{1.63}Mg^{2+}_{0.21}Al^{3+}_{0.42}O_4^{2-}$	$A_{18.8}B_8\square_{0.2}O_{32}^{2-}$	$A_mB_n\square_{8-p}[A_{18.8-m}B_{5-n}\square_{p-7.8}]O_{32}^{2-}$
11:5	$Mn^{2+}_{0.55}Mn^{3+}_{1.48}Mg^{2+}_{0.31}Al^{3+}_{0.62}O_4^{2-}$	$A_{16\cdot2_5}B_{7\cdot4_5}\square_{0.3}O_{32}^{2-}$	$A_mB_n\square_{8-p}[A_{16\cdot2_5-m}B_{7\cdot4_5-n}\square_{p-7.7}]O_{32}^{2-}$

doubled for ease of comparison with the larger cubic unit cells. Denoting the number of tetrahedral sites occupied by A ions per unit cell by "m", and those occupied by B ions as "n" (with $m+n=p$) the cation distribution is given in column 4; the cations at the octahedral sites have, by usual convention, been shown enclosed in square brackets.

A preliminary intensity calculation reveals that the concentration of vacant cation sites are too small to affect the X-ray intensities to such a degree as to enable the determination of their distribution. For example, Table 3 gives the values of calculated intensities of a few important reflexions for 11:5 composition (which has the largest value of vacancies in this series).

It was, therefore, decided to neglect the existence of vacancies as far as the X-ray intensities were concerned, and to attempt the determination of m and $z = 0{\cdot}375$ without appreciable loss of accuracy in the determination of the cation distribution. The intensities of the above reflexions were calculated for different values of m at intervals of one.

Having established an approximate cation distribution on the basis of these few reflexion ratios, the theoretical intensities were calculated for all the space group permissible reflexions down to 1·25 Å for the above value of m (= 8) with various values of x and z (with x varying from 0·200 to 0·250 and z from 0·375 to 0·400). The agreement between the observed and calculated intensities were checked with the aid of the disagreement index

$$R = \frac{\sum ||\sqrt{(I_{obs})}| - |\sqrt{(I_{cal})}||}{\sum |\sqrt{(I_{obs})}|}$$

Table 3. Intensities of a few reflexions for the system $Mn_3O_4 : MgAl_2O_4 = 11:5$ *with* ($m = 7$)

$A_7B_{p-7}\square_{8-p}[A_{9\cdot2_5}B_{14\cdot4_5-p}\square_{p-7\cdot7}]O_{32}^{2-}$

hkl	All vacancies at octahedral sites $p = 8$	All vacancies at tetrahedral sites $p = 7{\cdot}7$	Vacancies neglected
220	52	50	52
400	31	32	32
422	15	14	15

only. The scattering factors for the cations at the two types of sites were calculated by taking the average of f_A and f_B in the proportion appropriate to the cation distribution being considered, where f_A is the average of $f_{Mn^{3+}}$ and $2f_{Mn^{2+}}$ and f_B that of $f_{Mg^{2+}}$ and $2f_{Al^{3+}}$. Scattering powers of individual ions were taken from the International Tables.[9] The intensities were then calculated as indicated before.

It was observed that for the first tetragonal phase the reflexions 112, 200, 312, 004, 220 were sensitive to variations in m and thus these are the ones useful for determining the distribution of cations. Furthermore, these reflexions are relatively insensitive to changes in the oxygen ion parameters so that to start with these can be arbitrarily fixed at the ideal value of $x = 0{\cdot}250$ The values of $x = 0{\cdot}210$ and $z = 0{\cdot}395$ give the lowest value of R. Now all the intensities were calculated using these x and z values for different values of m and it was found that $m = 8$ still gave the lowest value of R. The calculated intensities for this model together with the observed values for the various phases are given in Table 4.

The R value is reasonably low and although too much reliance cannot be placed on this because of a small number of reflexions taken, the general agreement is good and it is possible that the neglect of temperature and absorption correction factors does not involve an appreciable error.

Thus the actual formula becomes $A_8[A_{13}B_3]O_{32}$. Out of the 21 A ions 14 are Mn^{3+} while the remainder are Mn^{2+} ions. The distribution of these ions over the tetrahedral and octahedral sites

Vol. 17
1960

Table 4. *Reflexion intensities for* $MnMn_2O_4$: $MgAl_2O_4 = 14{:}2$ $A_mB_{8-m}[A_{21-m}B_{m-5}]O_{32}$ with $m = 8$. *Oxygen parameters* $x = 0{\cdot}210$ $z = 0{\cdot}395$

hkl	I_{cal}	I_{obs}	*R*
101	34	30	7·2%
112	48	50	
200	20	15	
103	69	75	
211	106	100	
202	7	<5	
004	19	20	
220	24	30	
213	0·4	<5	
301	0·1	<5	
204	7	5	
105	34	25	
312	12	15	
303	7	10	
321	46	40	
224	68	75	
215	1·3	<5	
400	28	35	
116	3		
314	0·4	<5	
323	1·1	<5	
411	1·0	<5	
206	4·0		
402	0·2		
305	8	10	
413	16	15	
420	2	<5	

could be deduced by making use of their site preference properties. The Mn^{3+} ions are considered to possess a strong affinity for the octahedral sites.[2,3,10,11] On the other hand, Mn^{2+} ions with d^5 configuration have no such preference for these sites. Thus it is to be concluded that all the 13 *A* ions at the octehadral sites are Mn^{3+} ions. No ambiguity arises regarding the location of Mg^{2+} and Al^{3+} ions, as it is seen that they all occupy the octahedral sites. Thus the unit cell formula is $Mn_7^{2+}Mn^{3+}[Mn_{13}^{3+}Mg^{2+}Al_2^{3+}]O_{32}^{2-}$. If the analysed chemical composition is taken into account, and the extreme case of all vacancies at the octahedral sites is taken, the modified formula becomes $Mn_{6\cdot6}^{2+}Mn_{1\cdot4}^{3+}[Mn_{12\cdot9}^{3+}\square_{0\cdot1}Mg^{2+}Al_2^{3+}]O_{32}^{2-}$ The uncertainty thus introduced is less than the accuracy attempted (*m* has been determined at the intervals of 1 only).

For the second phase the agreement between the observed and calculated intensities is again best for the value of $m = 8$, with $x = 0{\cdot}210$ and $z = 0{\cdot}395$ (Table 5). Proceeding as above we may now write the unit cell formula for this phase as $Mn_{6\cdot3}^{2+}Mn_{1\cdot7}^{3+}[Mn_{10\cdot9}^{3+}Mg_{1\cdot7}^{2+}Al_{3\cdot4}^{3+}O_{32}^{2-}$.

Table 5. *Reflexion intensities for* $MnMn_2O_4$: $MgAl_2O_4 = 12{\cdot}6{:}3{\cdot}4$ $A_mB_{8-m}[A_{18\cdot9-m}B_{m-2\cdot9}]O_{32}$ with $m = 8$. Oxygen parameters $x = 0{\cdot}210$ $z = 0{\cdot}395$

hkl	I_{cal}	I_{obs}	*R*
101	30	40	9·8%
112	55	50	
200	24	20	
103	72	70	
211	115	100	
202	5	<5	
004	19	20	
220	27	35	
213	0·9	<5	
301	0·3	<5	
204	8·5	10	
105	37	20	
312	14	15	
303	7·5	15	
321	53	50	
224	74	75	
215	1·2	<5	
400	31	35	
116	3	10	
314	0·5		
323	0·5		
411	0·9	<5	
402	0·2	<5	
206	4	<5	
305	8·8	10	
413	17	25	
420	3·6	<5	

For the third (cubic) phase, the oxygen ion parameter *u* was first arbitrarily fixed at 0·375 and the intensities were calculated for the reflexions 220, 400 and 422. From the intensity ratios it was found that the agreement was best for $m = 7$. The intensities of all reflexions down to 1·04 Å were then calculated for this *m* with various values of oxygen ion parameter *u*, and the best value was arrived at ($u = 0{\cdot}395$) with the aid of index *R*. With this *u* it was further checked if any change in *m* improved the agreement and it was found that $m = 7$ still gave the best agreement. The

observed and calculated intensities for this composition are given in Table 6. Thus, the formula arrived at is $Mn^{2+}_{.5}Mn^{3+}_{1.5}B_1[Mn^{3+}_{9.5}B_{6.5}]O^{2-}_{32}$.

Table 6. Reflexion intensities for $MnMn_2O_4$: $MgAl_2O_4 = 11:5$ $A_mB_{8-m}[A_{16\cdot5-m}B_{m-0\cdot5}]O_{32}$ with $m = 7$. *Oxygen parameter* $u = 0\cdot395$.

hkl	I_{cal}	I_{obs}	R
111	21·9	20	8·8%
220	52·1	50	
311	123	100	
222	2·7	5	
400	31·8	40	
331	0·9	—	
422	15·2	20	
511	59·8	60	
333	4·7		
440	71·1	75	
531	2·2	—	
442	0·5	—	
620	5·2	10	
533	17	20	
622	6·8		
444	3·9	7	
711	0·1		
551	2·5		
642	11·5	12	
731	10·7	20	
553	13		
800	9·1	10	

The vacancies introduce a maximum uncertainty of 0·3 (Table 2) in the concentration of Mn^{3+} ions at the octahedral sites, so that a mean value of $9\cdot3 \pm 0\cdot2$ can be assigned for the same. In this case there is an ambiguity about the distribution of the Al^{3+} and Mg^{2+} over the two types of sites.

The variation of c', a', and $V^{1/3}$ as a function of the number of Mn^{3+} ions at the octahedral sites is plotted in Fig. 1. It may be mentioned that as observed this value of critical number of Mn^{3+} ions at the octahedral site (9·3 out of 16) is quite different from what one would have got if there had been no exchange of cations at the two sites (11 out of 16). The plot of c'/a' vs. the number of Mn^{3+}_{oct} ions is shown in Fig. 2.

The system $MgMn_2O_4$–$MgAl_2O_4$

Solid solutions of the tetragonal $MgMn_2O_4$ and the cubic $MgAl_2O_4$ were prepared as described

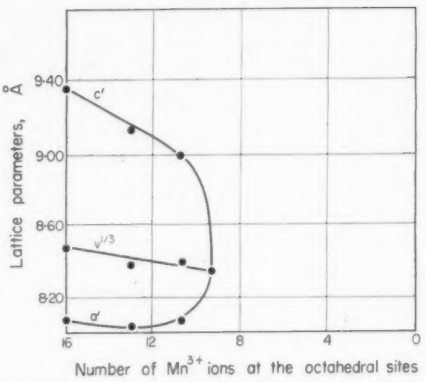

FIG. 1. Cell dimensions for Mn_3O_4–$MgAl_2O_4$ solid solutions against the number of Mn^{3+} ions at the octahedral sites.

before. The observed unit cell dimensions are tabulated in Table 7 for the compositions studied. For reasons mentioned before, the cation distributions were determined for the following three phases only (16:0, 15:1 and 14:2).

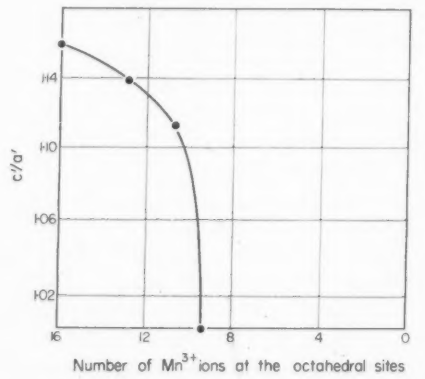

FIG. 2. Cell distortion for Mn_3O_4–$MgAl_2O_4$ solid solutions against the number of Mn^{3+} ions at the octahedral sites.

The analysed chemical compositions reveal that the average valency is higher than the nominal one and this may be attributed to the oxidation of Mn^{3+} to Mn^{4+} because Mg^{2+}, Al^{3+} and O^{2-} are unlikely to change their valencies. The chemical composition thus deduced is given in column 2 of Table 8. The unit cell formula given in column 3 is shown to contain the appropriate amount of

Vol. 17
1960

Table 7. Unit cell dimensions for $MgMn_2O_4$–$MgAl_2O_4$ *systems.*

Composition $MgMn_2O_4$:$MgAl_2O_4$	Symmetry *	c' †	a' †	c'/a' †
16: 0	T	9·32	8·08	1·15
15: 1	T	8·94	8·11	1·10
14: 2	C	—	8·32	1·00
13: 3	C	—	8·33	1·00
12: 4	C	—	8·28	1·00
8: 8	C	—	8·18	1·00
4:12	C	—	8·10	1·00
0:16	C	—	8·03	1·00

* T = Tetragonal C = Cubic

† Values refer to the face-centred tetragonal pseudo cell.

cation vacancies, because the other alternative of interstitial oxygen ion is unlikely. For the calculation of X-ray intensities, since their scattering powers are nearly equal the Mg^{2+} and Al^{3+} ions are identical; so also are the Mn^{3+} and Mn^{4+} ions. Simplified unit cell formulae can therefore be used as are shown in column 4. The structure of pure $MgMn_2O_4$ has been worked out by SINHA, SANJANA and BISWAS[1], and has been found to be "normal".

calculating the intensities for all permissible reflexions using different oxygen parameters (x ranging from 0·200 to 0·250 and z from 0·375 to 0·400) till a minimum disagreement between the observed and calculated intensities was obtained. The refined oyxgen parameter values were then used to determine accurately the cation distribution parameter so that the index R was minimized. The calculated and observed intensities for the final selected models in each phase have been given in

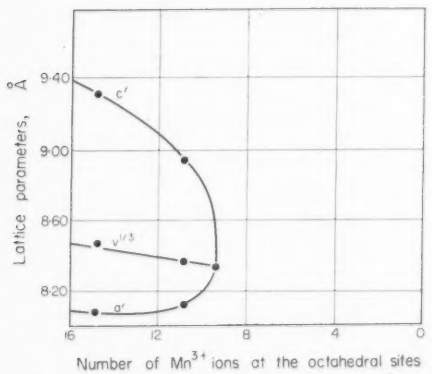

FIG. 3. Cell dimensions for $MgMn_2O_4$–$MgAl_2O_4$ solid solutions against the number of Mn^{3+} ions at the octahedral sites.

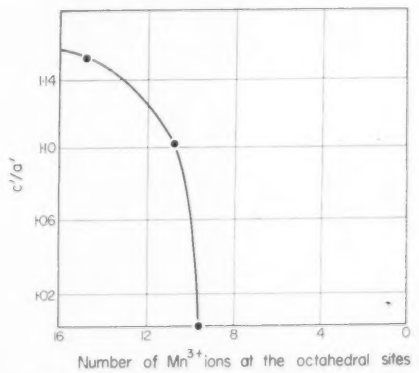

FIG. 4. Cell distortion for $MgMn_2O_4$–$MgAl_2O_4$ solid solutions against the number of Mn^{3+} ions at the octahedral sites.

For the next two phases the oxygen parameters were first arbitrarily assigned the ideal values, and the ratios of cation distribution sensitive reflexions were used for preliminary determination of the cation distribution. This was then used for

Tables 9 and 10 and the respective unit cell formulae become $Mn_4^{3+}B_4[Mn_{11}^{3+}B_5]O_{32}^{2-}$ and $Mn_4^{3+}B_4[Mn_{10}^{3+}B_6]O_{32}^{2-}$. We have now to find as to how many of the A's at the octahedral site are Mn^{3+} ions. The maximum value cannot exceed

Table 8. *Formulae for* $MgMn_2O_4$–$MgAl_2O_4$ *systems.*

Nominal composition $MgMn_2O_4$–$MgAl_2O_4$	Chemically analysed composition	Unit cell formula $Z = 8$	Approximate unit cell formula used for X-ray analysis $Mn^{3+} = Mn^{4+} = A$ $Mg^{2+} = Al^{3+} = B$ $\square$ neglected	Cation distribution determined by X-rays	No. of Mn^{3+} ions at octahedral site
16:0	$Mg^{2+}_{0\cdot99}Mn^{3+}_{1\cdot85}Mn^{4+}_{0\cdot12}O^{2-}_4$	$Mg^{2+}_{7\cdot92}Mn^{3+}_{14\cdot80}Mn^{4+}_{0\cdot96}\square_{0\cdot32}O^{2-}_{32}$	$A_{16}B_8O^{2-}_{32}$ or	$B_8[A_{16}]O^{2-}_{32}$	14·8*–14·7†
			$A_mB_{8-m}[A_{16-m}B_m]O^{2-}_{32}$	$m = 0$	14·8‡
15:1	$Mg^{2+}_{0\cdot99}Mn^{3+}_{1\cdot81}Mn^{4+}_{0\cdot06}Al^{3+}_{0\cdot12}O^{2-}_4$	$Mg^{2+}_{7\cdot92}Mn^{3+}_{14\cdot48}Mn^{4+}_{0\cdot48}Al^{3+}_{0\cdot96}\square_{0\cdot16}O^{2-}_{32}$	$A_{15}B_9O^{2-}_{32}$ or	$A_4B_4[A_{11}B_5]O^{2-}_{32}$	11·0*–10·4†
			$A_mB_{8-m}[A_{15-m}B_{m+1}]O^{2-}_{32}$	$m = 4$	10·7‡
14:2	$Mg^{2+}_{0\cdot99}Mn^{3+}_{1\cdot64}Mn^{4+}_{0\cdot09}Al^{3+}_{0\cdot25}O^{2-}_4$	$Mg^{2+}_{7\cdot92}Mn^{3+}_{13\cdot12}Mn^{4+}_{0\cdot72}Al^{3+}_{2\cdot00}\square_{0\cdot24}O^{2-}_{32}$	$A_{14}B_{10}O^{2-}_{32}$ or	$A_4B_4[A_{10}B_6]O^{2-}_{32}$	10·0*–9·0†
			$A_mB_{8-m}[A_{14-m}B_{m+2}]O^{2-}_{32}$	$m = 4$	9·5‡

* If all Mn^{4+} ions and $\square$ are located at tetrahedral sites.

† If all Mn^{4+} ions and $\square$ are located at octahedral sites.

‡ Assigned values.

that of total Mn^{3+} ions (column 3, Table 8), or the total A at the octahedral site (column 5, Table 8). The minimum Mn^{3+}_{oct} is obtained by placing all the defects (Mn^{4+} ions and □s) at the octahedral site. A major cause of uncertainty ($\sim \pm 0{\cdot}5$) in the number of Mn^{3+}_{oct} is our inability to determine the location of Mn^{4+} ions, which have octahedral site preference comparable to that of Mn^{3+} and hence their distribution cannot be fixed.

Table 9. *Reflexion intensities for* $MgMn_2O_4$: $MgAl_2O_4 = 15{:}1$ $A_mB_{8-m}[A_{15-m}B_{1+m}]O_{32}$ with $m = 4$. *Oxygen parameters* $x = 0{\cdot}250$, $z = 0{\cdot}375$

hkl	I_{cal}	I_{obs}	R
101	53	65	7·4%
112	27·5	30	
200	12	10	
103	65	50	
211	106	100	
202	3	<5	
004	27	30	
220	38	40	
213	2·5	<5	
301	1	<5	
204	9	<5	
105	17	25	
312	10		
303	14·5	15	
321	27	35	
224	74	65	
215	1	<5	
400	32	35	
314	0	<5	
323	1	<5	
116	2·8	<5	
411	1	<5	
402	0	<5	
206	1·9	<5	
305	7	5	
413	14	20	
420	2	<5	

The variation of c', a' and $V^{1/3}$ as a function of the number of distorting cations at the octahedral sites is plotted in Fig. 3, and that of c'/a' against the same parameter in Fig. 4. In this case, the critical number of Mn^{3+} ions at the octahedral sites is 9·5 out of 16, as compared to the value of 14 out of 16 which one would expect if there had been no exchange of cations over the two sites.

Table 10. *Reflexion intensities for* $MgMn_2O_4$: $MgAl_2O_4 = 14{:}2$ $A_mB_{8-m}[A_{14-m}B_{2+m}]O_{32}$ with $m = 4$. *Oxygen parameter* $u = 0{\cdot}389$

hkl	I_{cal}	I_{obs}	R
111	29·4	35	8·4%
220	33·2	35	
311	111·5	100	
222	2·2	<5	
400	41·8	45	
331	<0·1	<5	
422	11·1	15	
511	48	60	
333	5·1		
440	88	75	
531	3·5	5	
442	0·2		
620	4·2	5	
533	14·2	25	
622	5·1		
444	6	7	
711	<0·1		
551	2·8		
642	7·1	5	
731	10·6	25	
553	11·1		
800	9·7	5	

DISCUSSION

The variation of the unit cell dimensions c', a' and c'/a' in the tetragonal region of the solid solutions does not obey Vegard's linearity rule. The nature of the curve is similar to that observed by previous workers in the case of distorted manganites.[4] The tetragonal to cubic transformation takes place in spite of an appreciable fraction of octahedral sites still being occupied by the distorting Mn^{3+} ions. Thus it is established that this transformation is due to the long range disorder of the distorted octahedra formed by these cations. The transformation is confined to a narrow composition region indicative of a co-operative effect. In a pure manganite the Mn^{3+} ions located at the octahedral sites form distorted octahedra with the neighbouring oxygen ions at the corners. Nearly all these octahedra are aligned parallel at room temperature, giving an over-all tetragonal structure. By the introduction of non-distorting cations, through the formation of solid solutions, the distorted octahedra are separated, thereby decreasing the mean interaction energy. The observed values

of x_c compare favourably with those reported for similar systems,[4,5] as is seen in Table 11.

Table 11. Critical composition values (x_c) for solid solutions of spinels containing Mn^{3+} ions.

System	$x_c \times 16$	x_c
$MnMn_2O_4$–$MgAl_2O_4$	9·3	0·58
$MgMn_2O_4$–$MgAl_2O_4$	9·5	0·59
$MnMn_2O_4$–$NiFe_2O_4$	10·0	0·62
$MnMn_2O_4$–$FeFe_2O_4$	9·6	0·60
$MnMn_2O_4$–$CoFe_2O_4$	8·9	0·56
$ZnMn_2O_4$–$GeMn_2O_4$	9·6	0·60
$ZnMn_2O_4$–$LiMn_2O_4$	9·6	0·60
$ZnMn_2O_4$–$GeCo_2O_4$	10·4	0·65

In the systems discussed herein, the locations of the manganese ions have been determined by the X-ray diffraction technique with the assumption (for the first system) that the theoretically determined site preference of the Mn^{3+} ion[2,3,10,11] is valid. However, we have yet to exclude the possibility of an electron transfer of the type.

$$Mn^{3+} + Mn^{3+} \rightarrow Mn^{2+} + Mn^{4+}$$

This is done on the following grounds:

This disproportionation reaction would require an extra energy of the order of 18 eV.[12] and from the known structure of Mn_3O_4 as $Mn^{2+}[Mn^{3+}]_2O_4$ and not $Mn^{2+}[Mn^{4+}Mn^{2+}]O_4$[2] it can be concluded that this reaction cannot take place between any two octahedrally sited Mn^{3+} ions. Also, this transfer is not likely to take place between Mn^{3+}_{tetr} and Mn^{3+}_{oct}. In those tetragonal phases where some Mn^{3+} ions are at the tetrahedral sites this is justified for the following reasons: γMn_2O_3 has the tetragonal spinel structure with $c'/a' = 1{\cdot}16$. The presence of Mn ions of different valencies is ruled out from electrical conductivity measurements.[13] It is thus concluded that all manganese ions at the octahedral and tetrahedral sites are trivalent. The Mn^{3+} ions at the tetrahedral sites will, in the configuration of highest multiplicity, be $(e)^2(t_2)^2$. However, this leads to a Jahn–Teller distortion with $c'/a' < 1$ and the configuration consistent with the observed distortion greater than unity is $(e)^3(t_2)$ for the Mn^{3+} ions at the tetrahedral sites.[14] This is, in fact, in agreement with the total spin values derived from magnetic data.[15] Thus it is to be concluded that in the tetragonal region the manganese ions remain trivalent both at the tetrahedral and octahedral sites.

In the cubic phases the Mn^{3+} ions at the tetrahedral sites, $(e)^3(t_2)$ or $(e)^2(t_2)^2$ or at the octahedral sites $(t_{2g})^3(e_g)$ form a distorted environment which is opposed by the over-all cubic symmetry of the system. Under such circumstances an electron transfer may be favoured which might enable the ions to attain the electronic configuration suitable to the sites in which they are placed. For example, a transfer of an electron from Mn^{3+}_{oct} to Mn^{3+}_{tetr} will create $Mn^{4+}_{oct}(d^3)$ and $Mn^{2+}_{tetr}(d^5)$. The configuration with highest multiplicity for Mn^{2+}_{tetr} is $(e)^2(t_2)^3$, which produces no Jahn–Teller distortion, and is consistent with the cubic symmetry of the tetrahedral site. Similarly the Mn^{4+}_{oct} has the configuration $(t_{2g})^3$ which is stable at the octahedral site without causing a distortion. However the ionization energy required for this process is 18 eV whereas the crystal field stabilization energies are of a much lower order, hence such a transfer is ruled out.

Another interesting observation in these solid solution studies is the strong affinity of Mg^{2+} and Al^{3+} ions for the octahedral sites. The high temperature crystal structure studies on $MgMn_2O_4$[6] have revealed that the preference of the Mg^{2+} for the octahedral sites in the cubic spinel phase is less than that of Mn^{3+} by a small amount of ~ 4 kcal/g atom. However, in the tetragonal $MgMn_2O_4$ this value may be higher because of the crystal field. Thus although at room temperature the Mn^{3+} ions were able to displace all the Mg^{2+} from the octahedral sites, at elevated temperatures a good deal of randomization was observed. In the solid solution, on the other hand, even at room temperature the Mg^{2+} and Al^{3+} ions are able to displace some Mn^{3+} ions from the octahedral sites. It is thus clear that the site preference energy is modified due to the solid solution formation. KRIESSMAN and HARRISON[16] have also observed a similar trend in $Mg_yMn_{1-y}Fe_2O_4$ system. The energy required to transfer the first Mg ion from the octahedral to tetrahedral site decreases with increasing Mn^{2+} ions in the system (see[16] Table 3, variation of θ_0 with y). In $MgMn_{2-x}Al_xO_4$ systems the Mn^{3+} ion is being replaced by a much smaller Al^{3+} ion at the octahedral site. This replacement increases the

Vol. 17
1960

value of u leading to a decrease in the size of the octahedral holes. Such a change increases the Born's repulsive energy at the octahedral sites occupied by the Mn^{3+} ions and thus decreases the net site preference energy. Thus the migration of Mn^{3+} ion to the tetrahedral site in the present system is quite feasible.

REFERENCES

1. Sinha A. P. B., Sanjana N. R. and Biswas A. B., *Acta Cryst., Camb.* **10,** 439 (1957).
2. Goodenough J. B. and Loeb A., *Phys. Rev.* **98,** 391 (1955).
3. Dunitz J. D. and Orgel L. E., *J. Phys. Chem. Solids* **3,** 20 (1957).
4. Finch G. I., Sinha A. P. B. and Sinha K. P., *Proc. Roy. Soc.* **A242,** 28 (1957).
5. Wickham D. G. and Croft W. J., *J. Phys. Chem. Solids* **7,** 351 (1958).
6. Irani K. S., Ph.D. Thesis, Poona University (1958).
7. Kasper J. S., *Bull. Amer. Phys. Soc.* **4,** 178 (1959).
8. Prince E., *Acta Cryst., Camb.* **10,** 554 (1957).
9. *International Tables for the Determination of Crystal Structures,* Vol. II (1935).
10. McClure D. S., *J. Phys. Chem. Solids* **3,** 311 (1957).
11. Miller A. J., *J. Appl. Phys.* **30,** 245 (1959).
12. Romeijn F. C., *Philips Res. Rep.* **8,** 304 (1953).
13. Verwey E. J. W. and De Boer J. H., *Rec. Trav. Chim. Pays-Bas* **55,** 531 (1936).
14. Sinha K. P., *Nature, Lond.* **181,** 835 (1958).
15. Sinha K. P. and Sinha A. P. B., *J. Phys. Chem.* **61,** 758 (1957).
16. Kriessman C. J. and Harrison S. E., *Phys. Rev.* **103,** 857 (1956).

J. Phys. Chem. Solids Pergamon Press 1960. Vol. 17, Nos. 1/2, pp. 112–116. Printed in Great Britain.

SURFACE RECOMBINATION AND DIFFUSION PROCESSES IN CATHODOLUMINESCENCE AND ELECTRON BOMBARDMENT INDUCED CONDUCTIVITY

GY. GERGELY

Research Institute for Telecommunication, Budapest

(*Received* 13 *May* 1960; *revised* 13 *June* 1960)

Abstract—An analysis of the voltage dependence of cathodoluminescence and electron bombardment induced conductivity is given, taking into consideration the surface recombination and diffusion processes. The diffusion equation of DEVORE is combined with YOUNG's and FELDMAN's laws relating to the penetration and energy loss of incident electrons.

A good agreement was obtained between the theoretical and experimental brightness vs. voltage curves. By the analysis of this curve the diffusion length L and the surface recombination velocity S may be determined. It was found that $L = 0{\cdot}05$–$0{\cdot}15$ micron and $S = 5 \times 10^3$–5×10^5 cm/sec for several phosphors.

A THEORETICAL analysis of the shape of photoconductivity spectral distribution was given by DEVORE[1]. Recently, the spectral distribution of photoconductivity was used by BENNY and MORTEN[2] and HARTEN[3] to determine the surface recombination velocity on silicon crystals. A similar problem is encountered in studying the voltage dependence of cathodoluminescence and electron bombardment induced conductivity (denoted as E.B.C. in the following). The penetration depth of electrons is strongly varying with their energy, the voltage dependence of cathodoluminescence or E.B.C. is similar to the spectral response of photoconductivity near the absorption edge.

Plotting the cathodoluminescence brightness $L(V)$ vs. accelerating voltage V for constant bombarding current density i_0 (Fig. 1), gives a curve consisting of a low voltage tail and a linear section. The intercept of this curve with the V axis is called the dead voltage V_d[4–7]. The shape of curve on Fig. 1 is typical for various types of phosphors (ZnS–Ag–Cl, ZnS–Cu, Zn_2SiO_4–Mn etc.), the low voltage tail and the value of V_d however, vary slightly for different phosphors. The voltage dependence of E.B.C. can be represented by a similar curve to that on Fig. 1.[8,9] This behaviour of the brightness curve was explained by assuming the constancy of intrinsic efficiency and the existence of a dead surface layer.[4–6] BROSER proposed an explanation for the dead layer by the surface recombination.[10]

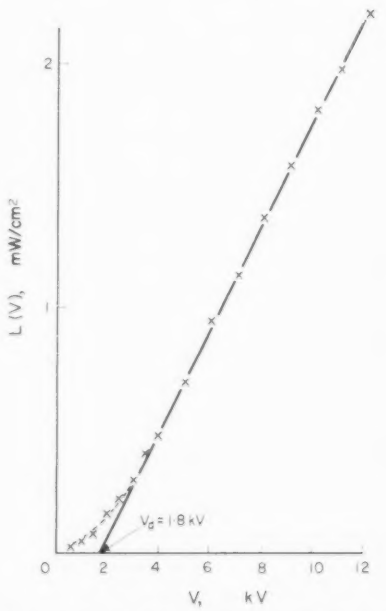

Fig. 1. The cathodoluminescence brightness vs. voltage curve $i_0 = 1\mu A/cm^2$

Vol. 17
1960

ANALYSIS OF THE PROBLEM

In this paper, the voltage dependence of cathodoluminescence and E.B.C. is analysed in a manner similar to that in which it was done by DEVORE, taking into consideration the surface recombination and diffusion processes. In the analysis the following simplifying assumptions were used:

(1) The dimensions of the crystal are essentially larger than the range R of incident electrons and the diffusion length L of released secondaries (electrons and holes).

(2) The penetration, range and energy losses of the incident electron beam follow the type of laws described by YOUNG[11].

(3) The recombination process is linear and its lifetime is τ. Only one type of carrier is taken into consideration.

(4) The effects of traps, space charge induced by electron bombardment and losses of luminescence due to radiationless transitions in the bulk are fully neglected. The surface recombination is radiationless.

The validity of YOUNG's empirical laws was confirmed by several authors[12,13] Range-energy relation for some luminescent films was recently given by FELDMAN[14]. In the present analysis the calculation of the dissipation of beam power and generation of secondaries over the penetration depth was done by using YOUNG's linear approximation. R was calculated according to FELDMAN.

In consequence of assumption (1) the problem can be treated as a one dimensional one. In the calculations the direction of the wide electron beam normally incident on the semi-infinite crystal was taken parallel with the x-axis and the origin of the system was chosen on the crystal surface. The following notations were used:

P_0 = i_0V the incident beam power.

$P(x)$ = the beam power at depth x in the crystal.

$g(x)$ = concentration of carriers generated in the crystal.[11]

$$g(x) = -\frac{1}{\Delta E}\frac{dP(x)}{dx} \tag{1}$$

$$g(x) = \frac{1}{\Delta E}\frac{P_0}{R} \quad \text{if } 0 < x < R \tag{2}$$

and

$$g(x) = 0 \quad \text{if } x > R$$

ΔE = the average work done to create a carrier (electron–hole pair).

The range R is given by:

$$R = KV^b$$

K and b are material constants.[11,14]

$n(x)$ = the concentration of carriers resulting from generation, recombination and diffusion processes.

D = the diffusion coefficient of carriers.

μ = the mobility of carriers.

S = the surface recombination velocity.

E_e = the average energy of emitted photons.

Under steady state conditions a diffusion equation similar to that used by DEVORE may be applied:

$$D\frac{d^2n}{dx^2} = \frac{n}{\tau} - g(x) \tag{3}$$

$$\frac{d^2n}{dx^2} = \beta^2\mu - \gamma \tag{4}$$

$$\beta^2 = \frac{1}{D\tau}, \quad \gamma = \frac{P_0}{\Delta EDR} \quad \text{if } 0 < x < R$$

$$\gamma = 0 \quad \text{if } x > R$$

Solving equation (4):

$$n_1(x) = C_1 \exp\beta x + C_2 \exp -\beta x + \frac{\gamma}{\beta^2} \text{ if } 0 < x < R$$

and

$$n_2(x) = C_3 \exp\beta x + C_4 \exp -\beta x \quad \text{if } x > R$$

The constants $C_1 \ldots C_4$ may be determined by the boundary conditions:

$$Dn'_1(0) = Sn_1(0)$$

$$n_1(R) = n_2(R) \qquad n'_1(R) = n'_2(R)$$

$$n_2(x) = 0 \qquad \text{if } x \to \infty$$

thus:

$$C_1 = -\frac{\gamma}{2\alpha\beta^2} \qquad \alpha = \exp\beta R$$

$$C_2 = \frac{\gamma}{2\alpha\beta^2}\frac{S}{D\beta + S}\left(1 - \frac{D\beta}{S} - 2\alpha\right) \tag{6}$$

$$C_3 = 0$$

$$C_4 = C_2 - \alpha^2 C_1$$

The cathodoluminescence emission is an involved phenomenon resulting from energy transfer, excitation and recombination processes. Disregarding the details to these processes the recombination of a carrier is associated with energy transfer to a luminescent center and the emission of a photon. Under steady state conditions the number of photons emitted is equal to the number of carriers released by incident electrons that recombine. Experimentally no characteristic difference was observed between the brightness curves of sulphide and oxide type (e.g. Zn_2SiO_4–Mn) phosphors. This permits the application of the diffusion equation (3) for both types of phosphors.

The ZnS type phosphors exhibit a power law decay (bimolecular radiative recombination), but by referring equation (3) to holes the linear recombination law may be applied, if the excitation density is low and the number of excited luminescent centers is negligible in comparison to their total number.[15,16] The lifetime τ of holes is determined by the concentration and capture cross section of centers and it may be considered as constant for a given crystal. This is not valid for electrons, but it must be emphasized that several authors have successfully analysed the photoconductivity diffusion processes in CdS using a linear approximation.[17,–20]

The cathodoluminescence brightness $L(V)$ is given by:

$$L(V) = \frac{E_e}{\tau}\left\{\int_0^R n_1(x)\,dx + \int_R^\infty n_2(x)\,dx\right\} \qquad (7)$$

$$L(V) = \eta_0 P_0\left\{1 - Q\frac{1-\exp(-\beta R)}{\beta R}\right\} \qquad (8)$$

$$Q = \frac{S}{D\beta + S}, \qquad \eta_0 = \frac{E_e}{\Delta E}$$

Q is a surface recombination loss parameter.

Equation (8) contains $\beta = 1/L$. The ambipolar diffusion length L is determined by the diffusion of minority carriers (holes).[17,18]

With a slight modification equation (8) may also be employed for the calculation of E.B.C. Assuming a monomolecular recombination mechanism for free electrons (majority carriers) and using suitable higher values for μ and τ, $\sigma(V)$ is given by:

$$\sigma(V) = \mu e\tau\frac{P_0}{\Delta E}\left\{1 - Q\frac{1-\exp(-\beta R)}{\beta R}\right\} \qquad (9)$$

Formula (9) is a linear approximation and the considerations relating to the cathodoluminescence of ZnS are not valid for E.B.C.

THE EVALUATION OF EXPERIMENTAL RESULTS

Comparing the theoretical $L(V)$ curves with the experimental data, β and S may be determined. According to FELDMAN for ZnS:

$$R = 63\,V^{2\cdot4} \qquad (10)$$

R is given in Å when V is expressed in kV. From (10) it follows that:

$$V \sim (\beta R)^{1/2\cdot4}$$

The theoretical $L(V)$ curves are plotted against $(\beta R)^{1/2\cdot4}$ for different values of Q on Fig. 2. These

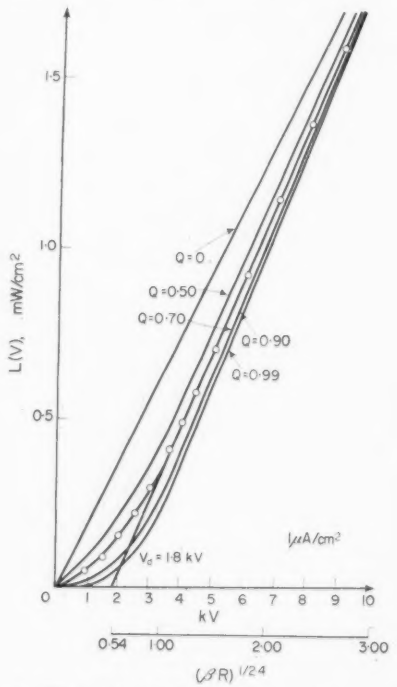

FIG. 2. Theoretical brightness vs. voltage curves for different values of Q. Experimental points denoted by circles (○).

Vol. 17
1960

curves exhibit a low voltage tail and have a linear section the intercept $(\beta R_d)^{1/2\cdot4}$ of which with the horizontal axis corresponds to the dead voltage. By a suitable choice of Q the experimental curve of Fig. 1 can be fitted to a certain curve on Fig. 2. A good agreement was found for $Q = 0{\cdot}7$ and $(\beta R_d)^{1/2\cdot4} = 0{\cdot}54$. Thus:

$$L = \frac{R_d}{0{\cdot}54^{2\cdot4}} = \frac{63\ V_d^{1/2\cdot4}}{0{\cdot}228} \tag{11}$$

and

$$S = \frac{\beta DQ}{1-Q} = \frac{Q}{1-Q}\frac{1}{L}\frac{kT}{e}\mu \tag{12}$$

A detailed study of the voltage dependence of cathodoluminescence was given in a previous paper.[5] Considering the cubic ZnS–Ag–Cl sample discussed in Ref. (5), $V_d = 1{\cdot}8$ kV was found for the microcrystalline sample.

$$L = 1130\ \text{Å} \sim 0{\cdot}1\ \text{micron}$$

The diffusion length is given in the main by the value of V_d, the surface recombination velocity is determined by the low voltage tail of $L(V)$. It is only its order of magnitude that can be estimated, since formula (12) contains D and μ, being an uncertain quantity. The magnitude of the mobility may vary between 1–100 cm²/V sec. Thus:

$$S = 5{\cdot}4\times10^{3}\text{–}5{\cdot}4\times10^{5}\ \text{cm/sec}$$

The latter value is very high, nevertheless not impossible for irregular shaped microcrystals. On the other hand, it is doubtful whether $\mu = 100$ might be used for holes in microcrystals. Unfortunately large single crystals were not at our disposal, but the microcrystals studied fulfilled in practice the conditions of the first assumption of the analysis as to the magnitude of L and R. According to Ref. (5), V_d varied between 1–2 kV for several phosphors, consequently

$$L \simeq 0{\cdot}05\text{–}0{\cdot}15\ \text{micron}$$

From L and μ, the lifetime of holes can be calculated

$$\tau = 5\times10^{-9}\text{–}5\times10^{-11}\ \text{sec},$$

depending on μ.

COMPARISON WITH OTHER AUTHORS' RESULTS

Comparing the results with data published in the literature, the agreement is remarkable with DIEMER's value $L = 0{\cdot}1$ micron for CdS crystal. The latter was determined by the photoelectromagnetic effect.[19] The recent studies of EHRENBERG investigating the penetration of electrons into luminescent crystals[21] confirm the results presented here. The diffusion length of internal secondaries released by β rays was estimated by KALLMAN[22]. The radius of the excitation channel has the magnitude 5×10^{-6}–$1{\cdot}8\times10^{-5}$ cm for ZnO and ZnS type phosphors.

Studying the diffusion of photoconductivity, BROSER[18], AUTH[17] and coworkers have found $L = 1$ resp. 1 to 15 micron for the diffusion length of holes on CdS. It is doubtful, however, whether the resolving power of optical techniques makes it possible to determine $L = 0{\cdot}1$ micron; $L = 1$ micron is probably an estimated upper limit.[18]

On the other hand, $V_d \geqslant 10$ kV was observed by BLEIL[9] and LAPPE[23] for large single crystals of CdS. This allows the supposition that L is essentially larger for high quality single crystals than for microcrystals.

Acknowledgement—The author is indebted to Dr. Z. BODÓ for valuable discussion.

REFERENCES

1. DEVORE H. B., *Phys. Rev.* **102,** 86 (1956).
2. BENNY A. H. and MORTEN F. D., *Proc. Phys. Soc. Lond.* **72,** 1007 (1958).
3. HARTEN H. U., *Philips Res. Rep.* **14,** 346 (1959).
4. DOWLING P. H. and SEWELL J. R., *J. Electrochem. Soc.* **100,** 22 (1953).
5. GERGELY GY., *Z. Phys. Chem.* **211,** 274 (1959).
6. GERGELY GY and HANGOS I., *Symposium on Solid State Physics in Electronics and Telecommunications*, Bruxelles, 1958, Vol. IV. Academic Press London (1960).
7. BRIL A. and KLASENS H. A., *Philips Res. Rep.* **7,** 401 (1952); BRIL A., *Brit. J. Appl. Phys. Suppl.* No. **4,** 10 (1954).
8. PENSAK L., *Phys. Rev.* **75,** 472 (1949).
9. BLEIL C. E., SYNDER D. D. and SIHVONEN Y. T., *Phys. Rev.* **111,** 1522 (1958).
10. BROSER I., private communication.
11. YOUNG J. R., *J. Appl. Phys.* **28,** 524 (1957).
12. LYE R. G. and DEKKER A. J., *Phys. Rev.* **107,** 977 (1957).
13. KANITCHEVA I. R. and BURTSEV V. A., *Fizika Tvordovo Tela* **1,** 1251 (1959).

14. FELDMAN C., *Phys. Rev.* **117,** 455 (1960).
15. SCHÖN M., *Physica* **20,** 930 (1954); *Halbleiterprobleme* Vol. IV, p. 282. Vieweg, Braunschweig (1958).
16. KLASENS H. A., *J. Phys. Chem. Solids* **7,** 175 (1958).
17. AUTH J. and RIDDER R., *Ann. Phys.* **20,** 210 (1957); **2,** 351 (1959).
18. BROSER I. and BROSER–WARMINSKY R., *J. Phys. Chem. Solids* **6,** 386 (1958).
19. DIEMER G., VAN GURP G. J. and HOOGENSTRAATEN W. *Philips Res. Rep.* **13,** 458 (1958); **14,** 11 (1959); *J. Phys. Chem. Solids* **2,** 119 (1957).
20. BALKANSKI M. and BROSER I., *Z. Elektrochem.* **61,** 715 (1957).
21. EHRENBERG W. and FRANKS J., *Proc. Phys. Soc. Lond.* B**66,** 1057 (1953); EHRENBERG W., private communication.
22. KALLMAN H. and DRESSNER J., *Phys. Rev.* **114,** 71 (1959).
23. LAPPE F., *Z. Phys.* **154,** 267 (1959).

Vol. 17
1960

J. Phys. Chem. Solids Pergamon Press 1960. Vol. 17, Nos. 1/2, pp. 117–137. Printed in Great Britain.

DIFFRACTION PARAMAGNETIQUE DES NEUTRONS PAR LES IONS DE TERRES RARES

SIMONE ODIOT* et D. SAINT-JAMES

Centre d'Etudes Nucléaires de Saclay, Gif sur Yvette, France.

(*Received* 27 *January* 1960)

Résumé—Dans cet article on étudie la diffusion paramagnétique des neutrons par les ions de terres rares. Utilisant une méthode due à G. T. TRAMMEL, l'effet du champ cristallin est envisagé. Des résultats qui en découlent, on propose un moyen de déterminer directement les niveaux d'énergie des ions. On discute les expériences réalisées par W. C. KOEHLER et E. O. WOLLAN, et également la validité de la loi $I \simeq \sin^2\beta$ (où β est l'angle entre le vecteur de diffusion et la direction des moments magnétiques).

Abstract—In this paper the paramagnetic scattering of neutrons by rare earth ions is studied. By using a method proposed by G. T. TRAMMEL the crystalline field effects are taken into account. A means of direct determination is then proposed for the level splittings of the ions. Experiments by W. C. KOEHLER and E. O. WOLLAN are discussed, also the validity of the law $I \sim \sin^2\beta$ (where β is the angle between the scattering vector and the magnetic moments) is examined.

1. INTRODUCTION

L'ÉTUDE des terres rares par diffraction des neutrons thermiques a été très poussée au cours de ces dernières années. Parmi ces corps nous relevons le Cérium, le Praséodyme, le Néodyme, l'Erbium et l'Holmium qui paraissent les plus intéressants en raison de leur relativement faible section efficace de capture. L'étude théorique de l'intéraction magnétique des neutrons avec les ions de tels métaux a été réalisée par TRAMMEL[1], tandis que KOEHLER et WOLLAN[2] effectuaient l'étude expérimentale. La première constatation que l'on peut faire est l'existence d'une forte section efficace d'intéraction magnétique (plusieurs barns même pour des vecteurs de diffusion assez importants). Il nous a paru intéressant de reprendre le travail théorique de TRAMMEL en l'étendant aux terres rares non étudiées par cet auteur, (Ce, Pr, Ho) et également d'envisager plus profondément l'influence des "champs cristallins" sur la section efficace.

D'un autre côté nous avons étudié la variation de la section efficace en fonction de l'angle entre le vecteur de diffusion et la direction du moment total de l'ion, lorsque celui-ci peut être considéré comme polarisé ($J_z = J$). La loi obtenue s'écarte notablement de la loi bien connue en $\sin^2\beta$.

2. STRUCTURE ELECTRONIQUE DES TERRES RARES — INFLUENCE DU CHAMP CRISTALLIN

(1) *Ion libre*

Le caractère commun à toutes les terres rares est la présence d'une couche $4f$ incomplète. Cette couche peut contenir quatorze électrons. Il s'ensuit que le nombre quantique orbital l_n de chaque électron peut prendre une des sept valeurs 3, 2, 1, 0, −1, −2, −3. En dessous de sept électrons dans la couche $4f$, on raisonnera sur les électrons, au delà sur les trous.

La règle de HUND oblige à placer électrons et trous avec le spin maximal. En respectant également le principe de PAULI, on pourra définir ainsi un terme spectroscopique par les valeurs de $L = \sum_n \ln$ et $S = \sum_n s_n$ dont la dégénérescence totale est $(2L+1)(2S+1)$.

Dans le cas du Néodyme et de l'Erbium par exemple, qui possèdent respectivement trois électrons et trois trous, le terme spectroscopique

* Actuellement à la faculté des Sciences de Paris.

sera* :

$$(^{+}_{3}\ ^{+}_{2}\ ^{+}_{1})\ \text{c'est-à-dire}\ L = 6 \qquad S = 3/2$$

C'est un terme ^4I de dégénérescence cinquante-deux.

Le deuxième caractère commun aux ions de terres rares, est la présence d'un fort couplage spin orbite, $\lambda \boldsymbol{L} \cdot \boldsymbol{S}$. Dans un ion libre, la dégénérescence du terme spectroscopique est partiellement levée. $\boldsymbol{J} = \boldsymbol{L} + \boldsymbol{S}$ est un bon nombre quantique et les niveaux d'énergie sont repérables par les valeurs de J. Remarquons que l'état fondamental correspond à $J = |\boldsymbol{L}| \mp |\boldsymbol{S}|$ suivant que l'on a affaire à des électrons ou des trous.

Ex : Nd^{+++} $J = 6 - \frac{3}{2} = \frac{9}{2}$ dégénérescence 10

Er^{+++} $J = 6 + \frac{3}{2} = \frac{15}{2}$ „ 16

Les multiplets de J successifs sont très séparés (plusieurs milliers de cm^{-1}) et nous pouvons ne considérer dans ce qui suit que l'état fondamental.

Pour les n électrons de la couche $4f$ on prendra la fonction d'onde sous la forme :

$$\psi_M = \phi_{4f}(\boldsymbol{r}_1, \boldsymbol{r}_2 \ldots, \boldsymbol{r}_n)\Theta_{l,L,S,J,M} \qquad (2.1)$$

où $\Theta_{l,L,S,J,M}$ représente "l'état angulaire" $|JM\rangle$ défini comme précédemment. Pour la fonction radiale on pourra avec TRAMMEL choisir pour chaque électron une fonction hydrogénoïde de la couche $4f$

$$\psi_{4f}(r) \simeq r^3 \exp[-r/2a] \qquad (2.2)$$

Si on se reporte à la définition de ces fonctions on voit que :

$$a = \frac{2a_0}{Z^*} \qquad (2.3)$$

a_0 est le rayon de l'orbite de BOHR (0,529 Å), Z^* la charge effective est de l'ordre de 20.† a est donc de l'ordre de 0,05 Å. La couche $4f$ a donc un rayon très petit.

(2) *Ion dans un solide*

Dans beaucoup de sels de terres rares (en particulier dans les oxides) on peut remarquer qu'il n'existe que peu ou pas d'ordre entre moments magnétiques voisins (sauf peut-être à basse température). Il s'ensuit alors que, pour ces substances, on pourra supposer que pour un ion l'influence de ses voisins sera bien représentée par un "champ cristallin" electrostatique effectif. Sa caractéristique essentielle sera son invariance par un certain groupe de symétrie. Nous allons en envisager les conséquences sur le multiplet J. Des dégénérescences seront levées, certains états $|JM\rangle$ seront mélangés, mais nous remarquerons que le champ est trop faible pour réaliser des mélanges entre J différents.

Dans le langage de la théorie des groupes, le multiplet J correspond à une représentation D^J du groupe des rotations, irréductible dans le cas de l'ion libre. Les fonctions propres $|JM\rangle$ forment une base pour D^J. La symétrie du champ cristallin étant moindre, D^J sera réduite en un certain nombre de représentations irréductibles du groupe de symétrie du champ considéré. Le multiplet J se scindera en un certain nombre de multiplets dont les états propres peuvent servir de base aux représentations irréductibles du groupe.

Par souci de simplification, nous nous sommes bornés pour cette étude à un champ cubique. Dans ce pas D^J sera réduite en μ représentations du groupe du cube: Γ_1, Γ_2, Γ_3, Γ_4, Γ_5 ou du groupe double Γ_6, Γ_7, Γ_8 suivant que J est entier ou 1/2 entier (Cf: BETHE[3], OPECHOWSKI[4] et ABRAGAM[5]):

$$D^J = \sum_{\mu} n_{p_\mu} \Gamma_{p_\mu} \qquad (2.4)$$

Nous donnons pour les terres rares considérées cette réduction dans le tableau 1. Si n_p est différent de l'unité pour certaines représentations, l'énergie des niveaux et leurs fonctions d'onde dépendront explicitement de la forme algébrique de V.

Pour simplifier les calculs ultérieurs nous n'avons retenu que les termes du quatrième degré dans le potentiel celui-ci s'écrit :

$$V_4 = A\sum_n (x_n^4 + y_n^4 + z_n^4 - \tfrac{3}{5}r^4) \qquad (2.5)$$

Le signe de A détermine le niveau le plus bas. D'après KYNCH[6], pour les sulfates de terres rares, A est positif et de l'ordre de 3300 cm^{-1}.

Si ψ_i est la fonction d'onde du niveau Γ_i, l'énergie correspondante sera :

$$E_i = \langle \psi_i | V_4 | \psi_i \rangle$$

* Dans cette notation le chiffre indique la valeur du moment orbital l de l'électron ou du trou, le signe + ou − indique la valeur de son spin ($\pm \frac{1}{2}$).

† Cf : détermination expérimentale de KOEHLER et WOLLAN[2].

Vol. 17
1960

Comme ψ_i est une fonction de base de la représentation Γ_i, on doit avoir également :

$$\langle\psi_i|V_4|\psi_j\rangle = 0$$

et la même énergie E_i pour les fonctions dégénérées correspondant à un même niveau Γ_i.

On voit que l'on obtiendra les niveaux d'énergie de V_4 et les vecteurs propres correspondant en résolvant l'équation séculaire :

$$\det|\langle JM|V_4|JM'\rangle - E\langle JM|JM'\rangle| = 0 \quad (2.6)$$

(3) *Éléments de matrice de* V_4

On pourrait calculer les éléments de matrice de l'équation (2.6) en prenant la forme explicite (2.5) du potentiel et la forme (2.1) pour les états propres $|JM\rangle$. Il est plus élégant de transformer V_4 en une somme d'opérateurs tensoriels irréductibles. Avec RACAH on définira l'opérateur tensoriel $\boldsymbol{T}(k)$ comme un ensemble de $2k+1$ opérateur $T(kq)$ $(q = -k,-k+1,\ldots,k-1,k)$ qui se transforment par rotation comme les harmoniques sphériques* :

$$D(\omega)T(k,q)D(\bar{1}\omega) = \sum_{q'=-k}^{k} T(k,q')\mathscr{D}^k_{q',q}(\omega) \quad (2.7)$$

Il s'ensuit que :

$$[J\pm,T(k,q)] = T(k,q\pm1)[(k\mp q)(k\pm q+1)]^{1/2}$$
$$[J_z,T(k,q)] = qT(k,q) \quad (2.8)$$

Ces opérateurs jouissent d'une propriété fondamentale connue sous le nom de théorème de WIGNER–ECKART :

$$\langle\gamma'J'M'|T(k,q)|\gamma JM\rangle$$
$$= (-)^{J'-M'}\begin{pmatrix} J' & k & J \\ -M' & q & M\end{pmatrix}\langle\gamma'J'||\boldsymbol{T}(k)||\gamma J\rangle \quad (2.9)$$

Ainsi les éléments de matrice d'un opérateur tensoriel sont factorisés en une partie indépendante de M, l'élément de matrice réduit $\langle\gamma'J'||\boldsymbol{T}(k)||\gamma J\rangle$, et en une partie géométrique fournie par le coefficient $3J$ de RACAH :

$$(-)^{J'-M'}\begin{pmatrix} J' & k & J \\ -M' & q & M\end{pmatrix}$$

En regroupant dans (2.5) les termes se transformant comme les harmoniques sphériques, on trouve† :

$$V_4 \simeq \beta A\{J_x^4+J_y^4+J_z^4-\tfrac{3}{5}J^2(J+1)^2+\tfrac{1}{5}J(J+1)\} \quad (2.10)$$

* Cf : EDMONDS[7] et tous les livres de mécanique quantique.

† Cf : STEVENS[8].

le dernier terme de (2.10) vient de la non commutation de J_x, J_y, J_z. On en déduit :

$$\langle JM|V_4|JM\rangle = \beta A\left\{\frac{7}{4}M^4+\frac{M^2}{4}[5-6J(J+1)]+\right.$$
$$\left.+\frac{3}{20}(J-1)J(J+1)(J+2)\right\} \quad (2.11)$$

$$\langle JM\pm4|V_4|JM\rangle = \frac{\beta A}{8}\left[\frac{(J\mp M)!(J\pm M+4)!}{(J\mp M-4)!(J\pm M)!}\right]^{1/2}$$

$$\langle JM'|V_4|JM\rangle = 0 \quad \text{pour } M'\neq M \text{ ou } M'\neq M\pm4$$

β, différent pour chaque terre rare, se détermine aisément si l'on calcule $\langle JJ|V_4|JJ\rangle$ par la méthode directe. Les valeurs ont été données par STEVENS[8], nous les reproduisons dans le tableau 1.

(4) *Résolution de l'equation* (2.6)

La résolution de cette équation de degré $(2J+1)$ peut être effectuée directement par une machine électronique, mais on peut également la factoriser par des méthodes de théorie des groupes. D^J étant réduite selon l'équation (2.4) on sera amené à résoudre μ équations de degrés respectifs n_{p_0} ... n_{p_μ} avec :

$$2J+1 = \sum_{\mu} n_{p_\mu}\, d_{p_\mu}$$

où d_{p_μ} est la dimension de la représentation Γ_{p_μ}. Pour ceci on formera les combinaisons linéaires indépendantes des vecteurs propres $|JM\rangle$ se transformant comme une fonction de base connue f_p^i de Γ_p dans les opérations du groupe.

Soit $\gamma^\alpha_{p,i}$ une telle combinaison il y en aura en tout n_p de linéairement indépendantes et on aura à résoudre l'équation de degré n_p :

$$\det|\langle\gamma^\alpha_{p,i}|V_4|\gamma^\beta_{p,i}\rangle - \langle\lambda\gamma^\alpha_{p,i}|\gamma^\beta_{p,i}\rangle| = 0 \quad (2.12)$$

λ est l'énergie des n_p niveaux correspondant à Γ_p. On poura alors déduire les combinaisons linéaires des $\gamma^\alpha_{p,i}$ qui peuvent servir de base aux divers niveaux.

En opérant sur les d_p-1 partenaires de f_p^i on obtiendra les $n_p(d_p-1)$ fonctions dégénérées d_p à d_p avec les précédentes.

Il reste à former les combinaisons $\gamma^\alpha_{p,i}$.

Tableau 1. *Valeurs pour les différentes terres rares de J, Z*, β et de l'energie des niveaux dans un champ cubique*

Ion	n	Terme	J	Z^*	β	Décomposition	d	Energie
Ce^{+++}	1	^2F	5/2	19,4	$\frac{2}{5\times7\times9}$	Γ_7	2	$-8A/105$
						Γ_8	4	$4A/105$
Pr^{+++}	2	^3H	4	19,7	$\frac{-4}{3^2\times5^2\times11^2}$	Γ_1	1	$-\frac{2^4\times7}{3\times5\times11^2}A$
						Γ_3	2	$\frac{-16}{3\times5\times11^2}A$
						Γ_4	3	$\frac{-8\times7}{3\times5\times11^2}A$
						Γ_5	3	$\frac{8\times13}{3\times5\times11^2}A$
Nd^{+++}	3	^4I	9/2	20	$\frac{-8\times17}{3^3\times11^3\times13}$	Γ_6	2	$\frac{2^3\times3\times7^2}{5}\beta A$
						$\Gamma_8^{(1)}$	4	$(7^2-5\sqrt{7}\sqrt{103})\beta A$
						$\Gamma_8^{(21)}$	4	$(7^2+5\sqrt{7}\sqrt{103})\beta A$
Ho^{+++}	10	^5I	8	22,6	$\frac{-1}{2\times3\times5\times7\times11\times13}$	Γ_1	1	$\frac{-28}{5\times11\times13}A$
						$\Gamma_3^{(1)}$	2	$-0{,}03526\,A$
						$\Gamma_3^{(2)}$	2	$0{,}02967\,A$
						$\Gamma_5^{(1)}$	3	$0{,}002934\,A$
						$\Gamma_5^{(2)}$	3	$0{,}03343\,A$
						$\Gamma_4^{(1)}$	3	$-0{,}03670\,A$
						$\Gamma_4^{(2)}$	3	$0{,}02712\,A$
Er^{+++}	11	^4I	15/2	23	$\frac{2}{3^2\times5\times7\times11\times13}$	Γ_6	2	$0{,}03916\,A$
						Γ_7	2	$-0{,}003463\,A$
						$\Gamma_8^{(1)}$	4	$-0{,}03449\,A$
						$\Gamma_8^{(2)}$	4	$-0{,}01884\,A$
						$\Gamma_8^{(3)}$	4	$+0{,}03548\,A$

Vol. 17
1960

Si $G^p_{(g)}$ est la matrice de transformation des fonctions f_p pour l'élément g du groupe, on aura d'après WIGNER[9].

$$\gamma^{\alpha}_{p,t} = \sum_{g} \sqrt{\frac{d_p}{N}} [G^p_{(g)}]^*_{tt} \, g|JM\rangle \qquad (2.13)$$

N est le nombre d'éléments du groupe, $g|JM\rangle$ le résultat de l'opération g sur le vecteur $|JM\rangle$.

En choisissant toutes les valeurs possibles de M on obtiendra $(2J+1)$ combinaisons $\gamma_{p,t}$ dont seulement n_p sont linéairement indépendantes.

Dans le groupe du cube, les opérations sont des rotations autour d'un axe.* Les angles d'Euler de ces rotations α, β, γ sont égaux à 0, $\pi, \pm\pi/2$ pour le groupe simple et 2π, $3\pi/2$, $5\pi/2$, 3π pour le groupe double.

$$g|JM\rangle = \sum_{M'} \mathscr{D}^J_{M',M}(\omega)|JM'\rangle$$

$$= \sum_{M'} \exp(iM'\alpha/2) \exp(iM\gamma/2) d^J_{M',M}(\beta)|JM'\rangle$$

Les matrices de rotation $d^J_{M',M}(\beta)$ ont des expressions simples pour les angles 0, π, 2π, 3π; pour les angles $\pm\pi/2$, $3\pi/2$, $5\pi/2$ on les déduira des relations de récurence† :

$$-2Md^J_{M',M}(\pi/2)$$

$$= \sqrt{J(J+1)-M'(M'+1)}\, d^J_{M'+1,M}(\pi/2) +$$

$$+ \sqrt{J(J+1)-M'(M'-1)}\, d^J_{M'-1,M}(\pi/2)$$

$$d^J_{M,J}(\pi/2) = (-)^{J-M}\left[\frac{(2J)!}{(J+M)!\,(J-M)!}\right]^{1/2}$$

$$d^J_{M',M}(-\beta) = d^J_{M,M'}(\beta)$$

$$d^J_{M',M}(\pi+\beta) = (-)^{J-M'} d^J_{-M',M}(\beta)$$

Pour déterminer les matrices $G^p_{(g)}$ on prendra les fonctions f_p données par BETHE et VON DER LAGE[10] pour le groupe simple et par ELLIOTT[11] pour le groupe double.

Dans le tableau 2 nous donnons à titre d'exemple les combinaisons $\gamma_{p,t}$ pouvant servir de base aux différents multiplets du Cérium. On pourra se procurer celles relatives aux autres terres rares auprès d'un des auteurs (D.S.J.).

* On ne considère pas l'inversion déjà incluse dans la forme de V_4.

† Cf : EDMONDS p. 53 ff.

Tableau 2. Etats propres des niveaux du cérium dans un champ cubique

Γ_7	$1/\sqrt{(6)}\,\lvert 5/2 \pm 5/2\rangle - \sqrt{(5)}/\sqrt{(6)}\,\lvert 5/2 \mp 3/2\rangle$
Γ_8	$\sqrt{(5)}/\sqrt{(6)}\,\lvert 5/2 \pm 5/2\rangle + 1/\sqrt{(6)}\,\lvert 5/2 \mp 3/2\rangle$ $\lvert 5/2 \pm 1/2\rangle$

3. FORMULES GENERALES DE LA SECTION EFFICACE

Nous allons reprendre dans ce qui suit le traitement de l'article de TRAMMEL un peu trop succint et possédant un assez grand nombre de fautes d'impression qui en rendent la lecture pénible. Nous espérons pouvoir amener un peu de clarté dans un exposé très abstrait.

Nous prendrons dans le Hamiltonien le terme qui décrit l'intéraction des neutrons avec les électrons atomiques sous la forme :

$$H_{\text{int}} = -\frac{e}{c}\sum_n \boldsymbol{\alpha}_n \cdot \boldsymbol{A}_n(\boldsymbol{r}_n - \boldsymbol{r}_N) \qquad (3.1)$$

$\boldsymbol{\alpha}_n$ est l'opérateur vitesse de DIRAC pour le n-ième électron, $\boldsymbol{r}_n$ sa position, $\boldsymbol{r}_N$ est la position du neutron

$$\boldsymbol{A}_n(\boldsymbol{r}) = g_N \boldsymbol{S}_N \times \boldsymbol{r}\, r^{-3}$$

$\boldsymbol{S}_N$ et g_N sont respectivement l'opérateur de spin et le facteur de LANDE du neutron

$$(g_N = -1{,}9e/M_N C)$$

Dans l'approximation de BORN l'onde diffusée par un atome à partir d'un neutron de moment incident $\hbar\boldsymbol{p}_0$ sera :

$$\Psi_s = \sum_f \frac{2iM_N g_N e}{c} \langle \chi_f \psi_f | \boldsymbol{S}_N \cdot \boldsymbol{k} k^{-2} \times$$

$$\times \sum_n \boldsymbol{\alpha} \exp(i\boldsymbol{k}\cdot\boldsymbol{r}_n) | \chi_0 \psi_0 \rangle \times$$

$$\times \frac{\chi_f \psi_f \exp(ip_f r_n)}{r_n} \qquad (3.2)$$

ψ est une fonction propre d'un niveau d'énergie de l'atome, χ représente l'état de spin du neutron, $\boldsymbol{k} = \boldsymbol{p}_0 - \boldsymbol{p}_f$, M_N est la masse du neutron, les indice 0 et f distinguent les quantités avant et après la collision. La somme doit être étendue à

tous les états possibles de l'atome compatibles avec l'équation de conservation de l'énergie :

$$\frac{\hbar^2}{2M_N}(p_0^2-p_f^2) = E_f - E_0 \qquad (3.3)$$

où E est l'énergie de l'atome.

En utilisant l'approximation non relativiste de PAULI, nous écrirons le vecteur courant sous la forme :

$$i\boldsymbol{J}_{f0}(\boldsymbol{k}) = i\frac{e}{c}\langle\psi_f|\sum_n \boldsymbol{\alpha}_n \cdot \exp(i\boldsymbol{k}\cdot\boldsymbol{r}_n)|\psi_0\rangle \simeq$$

$$\simeq \frac{ie}{2mc}\langle\psi_f|\sum_n \boldsymbol{p}_n \exp(i\boldsymbol{k}\cdot\boldsymbol{r}_n) +$$

$$+\sum_n \exp(i\boldsymbol{k}\cdot\boldsymbol{r}_n)\boldsymbol{p}_n + 2i\boldsymbol{k}\times\boldsymbol{s}_n \exp(i\boldsymbol{k}\cdot\boldsymbol{r}_n)|\psi_0\rangle \quad (3.4)$$

Cette formule a été utilisée par HALPERN et JOHNSON[12] dans leur discussion de la diffusion des neutrons par des atomes pour lesquels le terme courant orbital

$$\langle\psi_f|\sum_n \boldsymbol{p}_n \exp(i\boldsymbol{k}\cdot\boldsymbol{r}_n) + \exp(i\boldsymbol{k}\cdot\boldsymbol{r}_n)\boldsymbol{p}_n|\psi_0\rangle$$

est nul.

En utilisant une transformation signalée par TRAMMEL (equations 5 et 6 et appendice) nous écrirons :

$$i\boldsymbol{J}_{f,0}(\boldsymbol{k}) = \frac{e}{2mc}\langle\psi_f|\boldsymbol{k}\times\sum_n\{\tfrac{1}{2}\boldsymbol{l}_n f(\boldsymbol{k}\cdot\boldsymbol{r}_n) +$$

$$+\tfrac{1}{2}f(\boldsymbol{k}\cdot\boldsymbol{r}_n)\boldsymbol{l}n + 2\boldsymbol{s}_n \exp(i\boldsymbol{k}\cdot\boldsymbol{r}_n)\}|\psi_0\rangle$$

$$-\frac{e}{c}\frac{E_f-E_0}{\hbar}\langle\psi_f|\sum_n \boldsymbol{r}_n(i\boldsymbol{k}\cdot\boldsymbol{r}_n)\times$$

$$\times(\exp(i\boldsymbol{k}\cdot\boldsymbol{r}n)-1)|\psi_0\rangle \qquad (3.5a)$$

la deuxième sommation ne contribue pas si $E_f = E_0$ et elle est négligeable pour les neutrons lents ($E \simeq 0{,}1$ eV).

Le vecteur courant deviendra :

$$i\boldsymbol{J}_{f,0}(\boldsymbol{k}) = \boldsymbol{k}\times\frac{e}{2mc}\langle\psi_f|\sum_n\{\tfrac{1}{2}\boldsymbol{l}_n f(\boldsymbol{k}\cdot\boldsymbol{r}_n) +$$

$$+\tfrac{1}{2}f(\boldsymbol{k}\cdot\boldsymbol{r}_n)\boldsymbol{l}_n + 2\boldsymbol{s}_n \exp(i\boldsymbol{k}\cdot\boldsymbol{r}_n\}|\psi_0\rangle \quad (3.5b)$$

avec

$$f(\boldsymbol{k}\cdot\boldsymbol{r}) = 2\sum_{p=0}^{\infty}\frac{(i\boldsymbol{k}\cdot\boldsymbol{r})^p}{(p+2)p!} = \frac{2}{(i\boldsymbol{k}\cdot\boldsymbol{r})^2}\int_0^{i\boldsymbol{k}\cdot\boldsymbol{r}} xe^x\,dx \quad (3.5c)$$

En reportant dans l'équation nous obtenons (3.2) :

$$\psi_s = \frac{Meg_N}{2mc}\sum_f \langle\chi_f\psi_f|S_{N+}P_- +$$

$$+S_{N-}P_+|\chi_0\psi_0\rangle\chi_f\psi_f \exp(ip_f r_n)/r_n$$

avec

$$\boldsymbol{P} = \sum_n\{\tfrac{1}{2}[\boldsymbol{l}_n f(\boldsymbol{k}\cdot\boldsymbol{r}_n) +$$

$$+f(\boldsymbol{k}\cdot\boldsymbol{r}_n)\boldsymbol{l}_n] + 2\boldsymbol{s}_n \exp(i\boldsymbol{k}\cdot\boldsymbol{r}_n)\} \qquad (3.2b)$$

$P_\pm$ et $S_\pm$ sont définis par rapport à la direction de $\boldsymbol{k}$ c'est-à-dire que si $\boldsymbol{k}$ est pris comme axe des z

$$A_\pm = A_x \pm iA_y$$

L'équation (3.2b) exprime le fait que

$$\boldsymbol{S}_N + \sum_n(\boldsymbol{l}_n + \boldsymbol{s}_n)$$

est un invariant de collision dans la direction de $\boldsymbol{k}$.

Si on suppose que les neutrons incidents ne sont pas polarisés, la section efficace différentielle de diffusion sera :

$$\frac{d\sigma}{d\Omega} = \left(\frac{Meg_N}{2mc}\right)^2\sum_f\frac{p_f}{2p_0}\times$$

$$\times\{|\langle\psi_f|P_+|\psi_0\rangle|^2 + |\langle\psi_f|P_-|\psi_0\rangle|^2\} \qquad (3.6)$$

L'equation (3.6) se rapporte à la diffusion par un seul ion d'état initial ψ_0. Dans les substances où l'effet des forces d'échange agissant entre les couches magnétiques des différents ions est faible, il n'y aura pas de corrélation et par conséquent pas de cohérence dans la diffusion magnétique des neutrons. C'est bien ce qui a été observé par KOEHLER et WOLLAN. La section efficace totale sera alors donnée par la sommation statistique sur tous les états initiaux ψ_0 des ions magnétiques.

L'énergie initiale du neutron est suffisamment faible pour ne pas induire de transitions entre multiplets de J différents. Un état de l'atome s'écrira :

$$\psi_i = \sum_M A_m^i|\gamma JM\rangle_1 \qquad (3.7)$$

le nombre quantique additionnel γ spécifie les conditions radiales. Nous indiquons par l'indice 1 le référentiel de quantification des états propres $|JM\rangle$ dont l'axe des z est en général différent de

Vol. 17
1960

$\boldsymbol{k}$. La section efficace devient :

$$\frac{d\sigma}{d\Omega} = \left(\frac{Meg_N}{2mc}\right)^2 \sum_{i,f} \frac{\exp(-E_i/k_BT)}{\sum_j \exp(-E_j/k_BT)} \frac{p_f}{2p_0} \times$$

$$\times \{|\sum_{M'}\sum_{M} A^{f*}_{m'} A^{i}_{M} 1\langle \gamma JM'|P_+(\boldsymbol{k})|\gamma JM\rangle_1|^2$$

$$+|\sum_{M'}\sum_{M} A^{f*}_{M'} A^{i}_{M\ 1}\langle \gamma JM'|P_-(\boldsymbol{k})|\gamma JM\rangle_1|^2\} \quad (3.8)$$

4. EVALUATION DES ELEMENTS DE MATRICE DE L'OPERATEUR $P+$

Nous pourrions calculer directement les éléments de matrice de (3.8) en explicitant $P\pm$ selon (3.2b) et $|\gamma JM\rangle$ en fonctions propres de chaque électron. Ce processus serait très inélégant, mais de plus, il obligerait à un calcul formel différent pour chaque ion de terre rare et deviendrait impraticable dès que le nombre d'électrons est supérieur à un.

Suivant TRAMMEL et ayant remarqué que les états propres $|\gamma JM\rangle$ correspondent à $\boldsymbol{J},\boldsymbol{L},\boldsymbol{S}$ constants, nous utiliserons le formalisme des opérateurs tensoriels irréductibles. Pour cela nous allons faire apparaître dans $P\pm$ les harmoniques sphériques en développant $\exp(i\boldsymbol{k}\cdot\boldsymbol{r}_n)$ et $f(\boldsymbol{k}\cdot\boldsymbol{r}_n)$. Il vient :

$$P = \sum_n \sum_\nu i^\nu (2\nu+1)\{\tfrac{1}{2} f_\nu(kr_n) \times$$

$$\times [\boldsymbol{l}_n P_\nu(\cos\theta_n) + P_\nu(\cos\theta_n)\boldsymbol{l}_n] +$$

$$+ 2j f_\nu(kr_n) P_\nu(\cos\theta_n)\boldsymbol{s}_n\} \quad (4.1)$$

Avec

$$f_\nu(x) = \frac{2}{x^2}\int_0^x y j_\nu(y)\, dy$$

$$j_\nu(x) = \left(\frac{\pi}{2x}\right)^{1/2} J_{\nu+1/2}(x)$$

Nous obtenons :

$$\langle \gamma JM'|P|\gamma JM\rangle = \sum_\nu i^\nu (2\nu+1)\times$$

$$\times \left\{\sum_n \langle JM'|\tfrac{1}{2}\boldsymbol{l}_n P_\nu(\cos\theta_n) + \tfrac{1}{2} P_\nu(\cos\theta_n)\boldsymbol{l}_n|JM\rangle F^L_\nu(k)\right.$$

$$\left. + \sum_n \langle JM'|\boldsymbol{s}_n P_\nu(\cos\theta_n) + P_\nu(\cos\theta_n)\boldsymbol{s}_n|JM\rangle F^S_\nu\right\} \quad (4.2)$$

On a posé :

$$F^L_\nu(k) = \frac{\int f_\nu(kr)\psi^*_{4f}(r)\psi_{4f}(r) r' 2dr}{\int \psi^*_{4f}(r)\psi_{4f}(r) r' 2dr} \quad (4.3a)$$

$$F^S_\nu(k) = \frac{\int f_\nu(kr)\psi^*_{4f}(r)\psi_{4f}(r) r' 2dr}{\int \psi^*_{4f}(r)\psi_{4f}(r) r^2 dr} \quad (4.3b)$$

On notera dans (4.2) l'analogie formelle entre les deux parties intervenant dans l'élément de matrice : la partie "orbitale" et la partie de spin.

Nous sommes donc ramenés à trouver une somme d'opérateurs tensoriels irréductibles équivalant à $\boldsymbol{j}P_\nu(\cos\theta) + P_\nu(\cos\theta)\ \boldsymbol{j}$ où $\boldsymbol{j}$ est un certain moment cinétique.

Considérons l'opérateur tensoriel $\boldsymbol{Y}_k\ (\theta_n, \psi_n)$ dont les $2k+1$ composantes sont les "harmoniques sphériques" $\boldsymbol{Y}^q_k(\theta_n, \psi_n)$ on aura :

$$\langle JM'|\, Y^q_k(\theta_n,\psi_n)|JM\rangle$$

$$= (-)^{J-M} \frac{\langle JM'T-M|kq\rangle}{(2k+1)^{\frac{1}{2}}} \langle J||\, \boldsymbol{Y}_k(\theta_n,\psi_n)||J\rangle \quad (4.4)$$

C'est la formule (2.9) où nous avons remplacé le coefficient $3j$ par le coefficient de CLEBSCH–GORDON correspondant. Pour déterminer l'élément de matrice réduit nous le calculons dans la multiplicité l.†

$$\langle J||\, \boldsymbol{Y}_k(\theta_n,\psi_n)||J\rangle = \langle l||\, \boldsymbol{Y}_k(\theta_n,\psi_n)||l\rangle$$

$$= (-)^l \frac{(2l+1)\sqrt{2k+1}}{(4\pi)^{1/2}} \begin{pmatrix} l & k & l \\ 0 & 0 & 0 \end{pmatrix} \quad (4.5)$$

Pour simplifier l'écriture, nous allons choisir un opérateur tensoriel irréductible $\boldsymbol{y}_k$ tel que‡ :

$$\langle JM'|y^q_k|JM\rangle = (-)^{J-M}\langle JM'J-M|kq\rangle \quad (4.6)$$

et nous poserons

$$\mathscr{P}_k(M)_J = \langle JM|y^0_k|JM\rangle \quad (4.7)$$

Une forme explicite de $\mathscr{P}_k(M)_J$ sera (en remarquant que

† Cf : EDMONDS, p. 76.

‡ La convention de TRAMMEL diffère par le signe $(-)^M$ au lieu de $(-)^{J-M}$.

$2J-2M$ est pair) :

$$\mathscr{P}_k(M)_J = \left[\frac{(2k+1)!(2J-k)!k!k!}{(2J+k+1)!(2k)!}\right]^{1/2} \times$$

$$\times \sum_{\nu=0}^{k} (-)^\nu \frac{k(k-1)...(k-\nu+1)}{\nu!} \quad \frac{(J+M)...(J+M-k+\nu+1)}{(k-\nu)!} \quad \frac{(J-M)...(J-M-\nu+1)}{\nu!} \tag{4.8}$$

Remarquons que ce polynome en M de degré k a un sens même pour $M>J$ bien qu'il ne puisse plus alors représenter un coefficient de CLEBSCH-GORDON.
Comme

$$P_\nu(\cos\theta_n) = \left(\frac{4\pi}{2\nu+1}\right)^{1/2} Y_\nu^0(\theta_n,\psi_n)$$

on aura :

$$\langle JM'|P_\nu(\cos\theta_n)|JM\rangle$$
$$= \frac{2l+1}{(2\nu+1)^{1/2}}(-)^l \begin{pmatrix} l & \nu & l \\ 0 & 0 & 0 \end{pmatrix} \langle JM'|y_\nu^0|JM\rangle$$
$$= G(l|P_\nu|l)\langle JM'|y_\nu^0|JM\rangle \tag{4.9}$$

L'équation (4.2) prend maintenant la forme :

$$\langle JM'|P|JM\rangle$$
$$= \sum_\nu \sum_n G(l|P_\nu|l) i^\nu (2\nu+1) \times$$
$$\times \left\{ \frac{F_\nu^L}{2} \langle JM'|\boldsymbol{l}_n y_\nu^0(\theta_n,\psi_n) + y_\nu^0(\theta_n,\psi_n)\boldsymbol{l}_n|JM\rangle + \right.$$
$$\left. + F_\nu^S \langle JM'|\boldsymbol{s}_n y_r^0(\theta_n,\psi_n) + y_\nu^0(\theta_n,\psi_n)\boldsymbol{s}_n|JM\rangle \right\} \tag{4.10}$$

Nous sommes ramenés à déterminer l'équivalent d'un opérateur de la forme

$$\boldsymbol{j}\, y_\nu^0 + y_\nu^0 \boldsymbol{j}$$

Montrons que

$$j^\pm y_\nu^0 + y_\nu^0 j^\pm = \alpha_{\nu,\nu-1}^{(j)} y_{\nu-1}^{\pm 1} + \alpha_{\nu,\nu+1}^{(j)} y_{\nu+1}^{\pm 1} \tag{4.11}$$

Nous allons n'effectuer ce calcul que pour j^+, il se mène de la même manière pour j^-. Nous allons déterminer les coefficients $\alpha_{\nu,\nu-1}$ et $\alpha_{\nu,\nu+1}$. Prenons l'élément de matrice de (4.11) entre $\langle jm+1|$ et $|jm\rangle$, il vient :

$$\langle jm+1|j^+ y_\nu^0 + y_\nu^0 j^+|jm\rangle = \langle m+1|j^+|m\rangle \times$$
$$\times \{\langle m+1|y_\nu^0|m+1\rangle + \langle m|y_\nu^0|m\rangle\}$$
$$= \langle m+1|j^+|m\rangle \{\mathscr{P}_\nu(m+1)_j + \mathscr{P}_\nu(m)_j\}$$
$$= (-)^{j-m}\{\alpha_{\nu,\nu-1}^{(j)} \langle jm+1\, j-m|\nu-1,1\rangle +$$
$$+ \alpha_{\nu,\nu+1}^{(j)} \langle jm+1\, j-m|\nu+1,1\rangle\} \tag{4.12}$$

Pour déterminer les coefficients α nous allons exprimer les coefficients de CLEBSCH-GORDON de droite en fonction de ceux de gauche. Pour cela, remarquons que :

$$\mathscr{P}_n(m+1)_j = \sum_r C_{nr}^{(j)} \mathscr{P}_r(m)_j \tag{4.13a}$$

$$C_{nr}^{(j)} = \mathscr{P}_n(j+1)_j \mathscr{P}_r(j)_j + (-)^{n+r+1} \mathscr{P}_n(j)_j \mathscr{P}_r(j+1)_j \tag{4.14}$$

$C_{n\,n}^{(j)} = 1$ par égalité des puissances de m dans (4.13a)
Ces équations sont une conséquence de la relation :

$$\sum_{m=-j}^{j} \mathscr{P}_n(m)\, \mathscr{P}_r(m) = \delta_{n,r}$$

En tenant compte des relations de récurrence on écrira :

$$(-)^{j-m}\langle j,m+1,\, j-m|\nu,1\rangle$$
$$= [(j+m+1)(j-m)]^{1/2}[\nu(\nu+1)]^{-1/2} \times$$
$$\times [\mathscr{P}_\nu(m)_j - \mathscr{P}_\nu(m+1)_j]$$

et en reportant dans (4.12) :

$$\mathscr{P}_\nu(m)_j + \mathscr{P}_\nu(m+1)_j$$
$$= \alpha_{\nu,\nu-1}^{(j)} \left\{ \frac{\mathscr{P}_{\nu-1}(m)_j - \mathscr{P}_{\nu-1}(m+1)_j}{[\nu(\nu-1)]^{1/2}} \right\} +$$
$$+ \alpha_{\nu,\nu+1}^{(j)} \left\{ \frac{\mathscr{P}_{\nu-1}(m)_j - \mathscr{P}_{\nu-1}(m+1)_j}{[(\nu+1)(\nu+2)]^{1/2}} \right\} \tag{4.15}$$

En utilisant (4.14) et (4.13), il vient :

$$\alpha_{\nu,\nu+1}^{(j)} = -2[(\nu+1)(\nu+2)]^{1/2}(C_{\nu+1,\nu}^{(j)})^{-1}$$

$$\alpha_{\nu,\nu-1}^{(j)} = \frac{[\nu(\nu-1)]^{1/2}}{C_{\nu-1,\nu-2}^{(j)}} \left[\frac{2C_{\nu+1,\nu-2}^{(j)}}{C_{\nu+1,\nu}^{(j)}} - C_{\nu,\nu-2}^{(j)} \right] \tag{4.16}$$

Le lecteur montrerait que les autres coefficients que l'on pourrait introduire dans (4.11) sont nuls, ce qui démontre la validité du développement.

On notera que la simplicité du résultat provient du couplage de deux j égaux.

Vol. 17
1960

(1) *Calcul de l'élément de matrice "orbital".*

Nous allons nous placer pour calculer celui-ci dans la multiplicité l
Il vient :

$$\sum_\nu G(l|P_\nu|l)\left\{\frac{F_\nu^L}{2}\langle JM'|\sum_n(\boldsymbol{l}_n^\pm y_\nu^0(\theta_n,\psi_n)+ + y_\nu^0(\theta_n,\psi_n)\boldsymbol{l}_n^\pm)|JM\rangle\right\}i^\nu(2\nu+1)$$

$$=\sum_\nu i^\nu(2\nu+1)\frac{F_\nu^L}{2}G(l|P_\nu|l)\sum_n \times$$

$$\times\langle JM'|\alpha_{\nu,\nu+1}^{(l)}y_{\nu+1}^{\pm1}(\theta_n,\psi_n)+ + \alpha_{\nu,\nu-1}^{(l)}y_{\nu-1}^{\pm1}(\theta_n,\psi_n)|JM\rangle$$

$\alpha_{\nu,\nu\pm1}(l)$ sont définis par l'équation (4.16) où l'on fait $j=l$. il nous reste donc à déterminer

$$\sum_n\langle JM'|y_{\nu\pm1}^{\pm1}(\theta_n,\psi_n)|JM\rangle=(2\nu\pm2+1)^{-1/2}\times$$

$$\times\langle J||\sum_n\boldsymbol{y}_{\nu\pm1}(\theta_n,\psi_n)||J\rangle\langle JM'|y_{\nu\pm1}^{\pm1}|JM\rangle$$

L'élément de matrice réduit peut encore s'écrire,*

$$\langle J||\sum_n\boldsymbol{y}_{\nu\pm1}(\theta_n,\psi_n)||J\rangle=(-)^{L+S+J+\nu\pm1}(2J+1)\times$$

$$\times\begin{Bmatrix}L & J & S\\ J & L & \nu\pm1\end{Bmatrix}\langle L||\sum_n\boldsymbol{y}_{\nu\pm1}(\theta_n,\psi_n)||L\rangle$$

Pour calculer ce nouvel élément de matrice réduit, nous remarquons que :

$$\langle LL|\sum_n y_{\nu\pm1}^0(n)|LL\rangle$$

$$=\langle L||\sum_n\boldsymbol{y}_{\nu\pm1}(n)||L\rangle(2\nu\pm2+1)^{-1/2}\times$$

$$\times\langle LLL-L|\nu\pm1,0\rangle$$

$$=\langle L||\sum_n\boldsymbol{y}_{\nu\pm1}(n)||L\rangle\mathscr{P}_{\nu\pm1}(L)_L$$

* Cf : EDMONDS, *op cit.* Chapitre 7.

L'élément de matrice de gauche est celui d'un opérateur à un électron pris entre deux déterminants de SLATER orbitaux.

$$\langle LL|\sum_n y_{\nu\pm1}^0|LL\rangle$$

$$=\langle ll|y_{\nu\pm1}^0|ll\rangle+\langle ll-1|y_{\nu\pm1}^0|ll-1\rangle+ + \ldots+\langle ll-n+1|y_{\nu\pm1}^0|ll-n+1\rangle$$

$$=\mathscr{P}_{\nu\pm1}(l)_l+\mathscr{P}_{\nu\pm1}(l-1)_l+\ldots+\mathscr{P}_{\nu\pm1}(l-n+1)_l$$

C'est-à-dire :

$$\langle J||\sum_n\boldsymbol{y}_{\nu\pm1}(n)||J\rangle=(-)^{L+S+J+\nu+1}(2J+1)\times$$

$$\times\begin{Bmatrix}L & J & S\\ J & L & \nu\pm1\end{Bmatrix}\frac{\mathscr{P}_{\nu\pm1}(l)_l+\ldots+\mathscr{P}_{\nu\pm1}(l-n+1)_l}{\mathscr{P}_{\nu\pm1}(L)_L}$$

En posant avec TRAMMEL :

$$G(LSJ|\boldsymbol{y}_\nu(\boldsymbol{L})|LSJ)=(-)^{L+S+J+\nu+1}(2J+1)\times \times\begin{Bmatrix}L & J & S\\ J & L & \nu\end{Bmatrix} \tag{4.17}$$

$$G(l_1\ldots l_n|\boldsymbol{y}_\nu(\boldsymbol{l}_n)|l_1\ldots l_n)=\frac{\mathscr{P}_\nu(l)_l+\ldots+\mathscr{P}_\nu(l-n+1)_l}{n\mathscr{P}_\nu(L)_L} \tag{4.18}$$

et

$$\mathscr{G}_{\nu,\nu\pm1}^L=n\frac{2\nu+1}{2}G(l|P_\nu|l)\alpha_{\nu,\nu+1}^{(l)}\times \times G(LSJ|\boldsymbol{y}_{\nu\pm1}(\boldsymbol{L})|LSJ)G(l_1\ldots l_n|\boldsymbol{y}_{\nu\pm1}(\boldsymbol{l}_n)l_n\ldots l_1) \tag{4.19}$$

l'élément orbital devient :

$$\sum_\nu i^\nu F_\nu^L\{\mathscr{G}_{\nu,\nu-1}^L\langle JM'|y_{\nu-1}^{\pm1}|JM\rangle+ + G_{\nu,\nu+1}^L\langle JM'|y_{\nu+1}^{\pm1}|JM\rangle\} \tag{4.20}$$

(2) *Elément de matrice de spin.*

Comme $\boldsymbol{s}_n^\pm$ agissant sur $|JM\rangle$ ne change pas L on pourra écrire :

$$\sum_\nu i^\nu(2\nu+1)F_\nu^s\sum_n\langle JM'|\boldsymbol{s}_n y_\nu^0(n)+y_\nu^0(n)\boldsymbol{s}_n|JM\rangle G(l|p_\nu|l)$$

$$=\sum_\nu i^\nu(2\nu+1)F_\nu^s G(l|P_\nu|l)\frac{1}{\boldsymbol{n}}\frac{\mathscr{P}_\nu(l)_l+\ldots+\mathscr{P}_\nu(l-n+1)_l}{\mathscr{P}_\nu(L)_L}\{\langle JM'|\sum_n|\boldsymbol{s}_n y_\nu^0(L)+y_\nu^0(L)\boldsymbol{s}_n)|JM\rangle\}$$

Tableau 3. *Valeur des coefficients* $G(l|P_\nu|l)$, $G(\mathbf{l},...\mathbf{l}_n|y_\nu(\mathbf{l}_n)|\mathbf{l},...\mathbf{l}_n)$, $G(LSJ|\mathbf{y}_\nu(\mathbf{L})|LSJ)$ *et* α (*voir texte équations* (4.9), (4.16), (4.17) *et* (4.18)).

	ν	0	1	2	3	4	5	6	7
	$G(l\|P_\nu\|l)$	−2,6457		0,6110		−0,3760		0,3543	
Ce^{+++}	$G(l_1...\|l_n\mathbf{y}_\nu(\mathbf{l}_n)\|l_1...l_n)$	1	1	1	1	1	1	1	1
	$G(LSJ\|\mathbf{y}_\nu(\mathbf{L})\|LSJ)$	0,9258	0,9035	0,8571	0,7825	0,6701	0,4949	0	0
Pr^{+++}	$G(l_1..l_n\|\mathbf{y}_\nu(\mathbf{l}_n)\|l_1...l_n)$	1,2536	0,9910	0,5327	0	−0,4543	−0,6814	−0,5808	—
	$G(LSJ\|\mathbf{y}_\nu(\mathbf{L})\|LSJ)$	0,9045	0,8863	0,8497	0,7948	0,7216	0,6298	0,5194	0,3895
Nd^{+++}	$G(l_1...l_n\|\mathbf{y}_\nu(\mathbf{l}_n)\|l_1...l_n)$	1,3628	0,8498	0,1479	−0,2959	−0,2124	0,2601	0,5942	—
	$G(LSJ\|\mathbf{y}_\nu(\mathbf{L})\|LSJ)$	0,8771	0,8569	0,8170	0,7583	0,6823	0,5909	0,4867	0,3733
Ho^{+++}	$G(l_1...l_n)\|\mathbf{y}_\nu(\mathbf{l}_n)\|l_1...l_n)$	1,3628	0,6374	−0,1109	−0,2219	0,1593	0,1951	−0,4457	—
	$G(LSJ\|\mathbf{y}_\nu(\mathbf{L})\|LSJ)$	1,1435	1,1229	1,0823	1,0226	0,9457	0,8537	0,7493	0,6358
Er^{+++}	$G(l_1...l_n)\|\mathbf{y}_\nu(\mathbf{l}_n)\|l_1...l_n)$	1,3628	0,8498	0,1479	−0,2959	−0,2124	0,2601	0,5942	—
	$G(LSJ\|\mathbf{y}_\nu(\mathbf{L})\|LSJ)$	1,1094	1,0934	1,0617	1,0147	0,9532	0,8780	0,7205	0,621

Vol. 17
1960

	$^{(j)}\alpha_{2\nu,2\nu+1}$				$^{(j)}\alpha_{2\nu,2\nu-1}$			
j \ ν	0	1	2	3	0	1	2	3
5/2	−4,8305	−3,0425	−1,8257	0	0	2,0656	1,9518	0
3	−5,6569	−3,7033	−2,6968	0	0	2,4495	2,5071	1,6515
4	−7,3030	−4,9683	−4,1196	−3,0315	0	3,2041	3,5189	3,0728
9/2	−8,1241	−5,5857	−4,7673	−3,8270	0	3,5777	4,00	3,6642
5	−8,9448	−6,1968	−5,3936	−4,5472	0	3,9495	4,4721	4,2228
6	−10,5830	−7,4066	−6,6058	−5,8703	0	4,6903	5,3985	5,2822
15/2	−13,038	−9,2025	−8,3666	−7,7101	0	5,7966	6,7612	6,7937
8	−13,8567	−9,7979	−8,9443	−8,3020	0	6,1644	7,2110	7,2855

Or $\sum_n s_n^{\pm} = J^{\pm} - L^{\pm}$. Il vient pour le terme entre accolades :

$$\langle JM'|J^{\pm}y_\nu^0(L) + y_\nu^0(L)J^{\pm}|JM\rangle - \langle JM'|L^{\pm}y_\nu^0(L) + y_\nu^0(L)L^{\pm}|JM\rangle$$

D'après les propriétés déjà établies, nous écrirons

$$\langle JM'|J^{\pm}y_\nu^0(L) + y_\nu^0(L)J^{\pm}|JM\rangle = (-)^{L+S+J+\nu}(2J+1)\begin{Bmatrix} L & J & S \\ J & L & \nu \end{Bmatrix}\langle JM'|J^{\pm}y_\nu^0(J) + y_\nu^0(J)J^{\pm}|JM\rangle$$

$$= G(LSJ|\mathbf{y}_\nu(\mathbf{L})|LSJ)\{\alpha_{\nu,\nu+1}^{(J)}\langle JM'|y_{\nu+1}^{\pm 1}|JM\rangle + \alpha_{\nu,\nu-1}^{(J)}\langle JM'|y_{\nu-1}^{\pm 1}|JM\rangle\}$$

et

$$\langle JM'|L^{\pm}y_\nu^0(L) + y_\nu^0(L)L^{\pm}|JM\rangle$$

$$= G(LSJ|\mathbf{y}_\nu(\mathbf{L})|LSJ)\{\alpha_{\nu,\nu+1}^{(L)}\langle JM'|y_{\nu+1}^{\pm 1}|JM\rangle + \alpha_{\nu,\nu-1}^{(L)}\langle JM'|y_{\nu-1}^{\pm 1}|JM\rangle\}$$

En posant avec TRAMMEL :

$$\mathscr{G}_{\nu,\nu\pm1}^{(S)} = (2\nu+1)G(l|P_\nu|l)G(l,\ldots l_n|\mathbf{y}_\nu(\mathbf{l}_n)|l,\ldots l_n)\{\alpha_{\nu,\nu\pm1}^{(J)}G(LSJ|\mathbf{y}_\nu(\mathbf{L})|LSJ) - \alpha_{\nu,\nu\pm1}^{(L)}G(LSJ|\mathbf{y}_{\nu+1}(\mathbf{L})|LSJ)\} \quad (4.20)$$

l'élément de spin devient :

$$\sum_\nu i^\nu\{\mathscr{G}_{\nu,\nu+1}^{S}\langle JM'|y_{\nu+1}^{\pm 1}|JM\rangle + \mathscr{G}_{\nu,\nu-1}^{S}\langle JM'|y_{\nu-1}^{\pm 1}|JM\rangle\} \quad (4.20a)$$

Dans le tableau 3 nous avons tabulé les coefficients G et α, dans le tableau 4 les coefficients $\mathscr{G}$.* On remarque que pour les valeurs de ν différentes de zéro et un, nous n'obtenons pas les mêmes valeurs que TRAMMEL, chez qui une erreur de calcul s'est glissée.

Remarquons également que pour les terres rares $l = 3$, il s'ensuit que $G(l|P_\nu|l)$ qui est donné par (4.9) s'annule avec $\begin{pmatrix} 3 & \nu & 3 \\ 0 & 0 & 0 \end{pmatrix}$ Il faut $\nu + 2l$ pair et $0 \leqslant \nu \leqslant 2l$. La section efficace (3.8) devient :

* Les tableaux 3 et 4 et TRAMMEL donnent $(-)^\nu\mathscr{G}_\nu$.

$$\frac{d\sigma}{d\Omega} = \left(\frac{M_N e g_N}{2mc}\right)^2 \sum_{i,f}\frac{\exp(-Ei/k_BT)}{\sum_j \exp(-E_j/k_BT)}\frac{p_f}{2p_0}\{|\sum_\nu(-)^\nu[\mathscr{G}_{2\nu,2\nu+1}^{L}F_{2\nu}^{L}(k) + \mathscr{G}_{2\nu,2\nu+1}^{S}F_{2\nu}^{S}(k)]\langle\psi_f|y_{2\nu+1}^{1}|\psi_i\rangle +$$

$$+\sum_\nu(-)^\nu[\mathscr{G}_{2\nu,2\nu-1}^{L}F_{2\nu}^{L}(k) + \mathscr{G}_{2\nu,2\nu-1}^{S}F_{2\nu}^{S}(k)]\langle\psi_f|y_{2\nu-1}^{1}|\psi_i\rangle|^2 +$$

$$+|\sum_\nu(-)^\nu(\mathscr{G}_{2\nu,2\nu+1}^{L}F_2^{L}(k) + \mathscr{G}_{2\nu\,2\nu+1}^{S}F_{2\nu}^{S}(k))\langle\psi_f|y_{2\nu+1}^{-1}|\psi_i\rangle +$$

$$+\sum_\nu(-)^\nu(\mathscr{G}_{2\nu,2\nu-1}^{L}F_{2\nu}^{L}(k) + \mathscr{G}_{2\nu,2\nu-1}^{S}F_{2\nu}^{S}(k))\langle\psi_f|y_{2\nu-1}^{-1}|\psi_i\rangle|^2\} \quad (4.21)$$

Ce qui s'écrit après regroupement des termes :

$$\frac{d\sigma}{d\Omega} = \left(\frac{M_N e g_N}{2mc}\right)^2 \sum_{i,f}\frac{\exp(-Ei/k_BT)}{\sum_j \exp(-E_j/k_BT)}\frac{p_f}{2p_0}\left\{\left|\sum_{\nu=0}^{l}(-)^\nu[\mathscr{A}_\nu(k) - \mathscr{B}_{\nu+1}(k)]\right|\langle\psi_f|y_{2\nu+1}^{1}|\psi_i\rangle +\right.$$

$$\left.+\sum_{\nu=0}^{l}(-)^\nu(\mathscr{A}_\nu(k) - \mathscr{B}_{\nu+1}(k))\langle\psi_f|y_{2\nu+1}^{-1}|\psi_i\rangle|^2\right\} \quad (4.22)$$

Tableau 4. *Valeur des coefficients* $\mathcal{G}^L$ *et* $\mathcal{G}^S$ (*voir texte equations* (4.19) *et* (4.20))

	$\mathcal{G}^L_{2\nu,2\nu+1}$				$\mathcal{G}^S_{2\nu,2\nu+1}$				$\mathcal{G}^L_{2\nu,2\nu-1}$				$\mathcal{G}^S_{2\nu,2\nu-1}$			
ν	0	1	2	3	0	1	2	3	0	1	2	3	0	1	2	3
Ce^{+++}	6,7613	−4,4262	2,2582	0	−1,6903	0,8853	−0,3764	0	0	3,3806	−3,3197	1,8820	0	−1,3522	2,2132	−3,7639
Pr^{+++}	13,145	0	−3,9170	0	−4,3815	1,145	0,6525	−0,526	0	6,573	0	−3,264	0	−1,2655	−1,561	2,8455
Nd^{+++}	16,349	3,8078	2,1040	0	−7,006	0,4760	0,4676	0,8996	0	8,1731	2,8558	1,7535	0	−0,4954	−0,9809	−3,6607
Ho^{+++}	21,424	5,135	3,040	0	14,2825	1,027	1,520	5,1075	0	10,712	3,8512	2,5332	0	−0,47615	−0,7002	−1,949
Er^{+++}	20,862	5,0952	3,1264	0	10,429	−1,019	−1,5632	−5,563	0	10,430	3,8213	2,6053	0	0,4637	0,6947	2,0041

On a posé :

$$\mathscr{A}_\nu(k) = \mathscr{G}^L_{2\nu,2\nu+1}F^L_{2\nu}(k) + \mathscr{G}^S_{2\nu,2\nu+1}F^S_{2\nu}(k)$$
$$\mathscr{B}_\nu(k) = \mathscr{G}^L_{2\nu,2\nu-1}F^L_{2\nu}(k) + \mathscr{G}^S_{2\nu,2\nu-1}F^S_{2\nu}(k) \qquad (4.22a)$$

5. APPLICATION DE LA FORMULE DE SECTION EFFICACE (4.22).

(1) *Remarque générale*

Il reste à déterminer dans (4.22a) les valeurs de $F^L_{2\nu}(k)$ et $F^S_{2\nu}(k)$. Si l'on choisit pour $\psi_{4f}(r)$ l'expression (2.2), les intégrales de (4.3) s'effectuent algorithmiquement et on a, en posant $\xi = k^2a^2$

$$\begin{aligned}
F^L_0 &= (1-\tfrac{1}{2}\xi+\tfrac{3}{2^2}\xi^2+\tfrac{5}{4^2}\xi^3+\tfrac{3}{4^2}\xi^4+\tfrac{1}{4^2}\xi^5+\tfrac{1}{2^8}\xi^6)(1+\xi)^{-7}\\
F^L_2 &= (3\xi+\tfrac{15}{7}\xi^2+\tfrac{5}{2^2}\xi^3+\tfrac{3}{2^2}\xi^4+\tfrac{1}{2^2}\xi^5+\tfrac{1}{14^2}\xi^6)(1+\xi)^{-7}\\
F^L_4 &= \tfrac{2}{21}(44\xi^2+35\xi^3+21\xi^4+7\xi^5+\xi^6)(1+\xi)^{-7}\\
F^L_6 &= 4(\xi^3+\tfrac{3}{5}\xi^4+\tfrac{1}{5^2}\xi^5+\tfrac{1}{3^2\,5^2}\xi^6)(1+\xi)^{-7}\\
F^S_0 &= (1-7\xi+7\xi^2-\xi^3)(1+\xi)^{-8}\\
F^S_2 &= (6\xi-\tfrac{60}{7}\xi^2+\tfrac{10}{7}\xi^3)(1+\xi)^{-8}\\
F^S_4 &= \tfrac{8}{7}(11\xi^2-3\xi^3)(1+\xi)^{-8}\\
F^S_6 &= 16\xi^3(1+\xi)^{-8}
\end{aligned} \qquad (5.1)$$

Un certain nombre d'erreurs numériques rendent la tabulation de ces fonctions par TRAMMEL inutilisables pour les grandes valeurs de ν et pour certaines valeurs de ξ.

(2) *Atome polarisé*

Nous allons supposer que les atomes de terres rares sont dans l'état J_z maximal ($M = J$) par suite de l'influence d'un champ magnétique (champ moléculaire par exemple)

$$|\psi_f\rangle = |\psi_i\rangle = |JJ\rangle; \quad p_f = p_0$$

Soit β l'angle entre le vecteur $\boldsymbol{k}$ et la direction de $\boldsymbol{J}$, il vient:

$$\begin{aligned}
\langle JJ|y^{\pm1}_{2\nu+1}(k)|JJ\rangle_1 &= \sum_{q=-(2\nu+1)}^{2\nu+1} \mathscr{D}^{2\nu+1}_{q,\pm1}(\omega)\langle JJ|y^q_{2\nu+1}|JJ\rangle\\
&= d^{2\nu+1}_{0,\pm1}(\beta)\langle JJJ-J|2\nu+1,0\rangle\\
&= \mp\, P^1_{2\nu+1}(\cos\beta)\,\frac{(2J)!\,(4\nu+3)^{1/2}}{[(2J+2\nu+2)!(2J-2\nu-2)!(2\nu+1)(2\nu+2)]^{1/2}}
\end{aligned}$$

Pour $ka = 0$ (5.2) se réduit à :

$$\frac{d\sigma}{d\Omega} = \left(\frac{M_N e g_N}{2mc}\right)^2 \frac{3J}{(2J+1)(2J+2)} \times \times (\mathscr{G}^L_{0,1} + \mathscr{G}^S_{0,1})^2 \sin^2\beta \qquad (5.3)$$

On retrouve la loi classique de la dépendance angulaire de la section efficace. Si $ka \neq 0$ il y aura une déviation à la loi d'autant plus sensible que ka est grand, il faut remarquer que concurremment il y a une diminution appréciable de la section efficace.

Posons $$I(\beta,k) = \frac{1}{\sin^2\beta}\frac{d\sigma}{d\Omega}(\beta,k) \qquad (5.4)$$

Nous avons déterminé en fonction de β et pour diverses valeurs de k^2a^2 les rapports† :

$$R_1 = \frac{I(\beta,ka)}{I(0,ka)} \text{ et } R_2 = \frac{I(\beta,ka)}{I(0,0)}$$

Dans le cas du Néodyme pour $k^2a^2 = 0{,}1$ R_1 tombe à 0,55, R_2 valant 0,20 pour $\beta = 10°$. Si 2θ est l'angle de diffusion et $\lambda_0 \simeq 1$Å. la longueur d'onde des neutrons incidents :

$$ka = \frac{8\pi a_0 \sin\theta}{Z^*\lambda_0} \simeq 0{,}3$$

entraîne

$$\sin\theta \simeq 0{,}6,\ 2\theta \simeq 75°$$

Cet effet devrait pouvoir être mis en évidence expérimentalement.

† Nous traçons ici les rapports R_1 et R_2 dans le cas du Néodyme et de l'Holmium, Figs. 1(a), (b), (c) et (d).

$$\frac{d\sigma}{d\Omega} = \left(\frac{M_N e g_N}{2mc}\right)^2 \frac{2J}{(2J+1)(2J+2)} \left| \frac{\sqrt{3}}{\sqrt{2}}(\mathscr{A}_0 - \mathscr{B}_1)\sin\beta - \sqrt{\frac{7\,(2J-1)(2J-2)}{12\,(2J+3)(2J+4)}} \times \times (A_1 - B_2)P^1_3(\cos\beta) + \ldots \right|^2 \qquad (5.2)$$

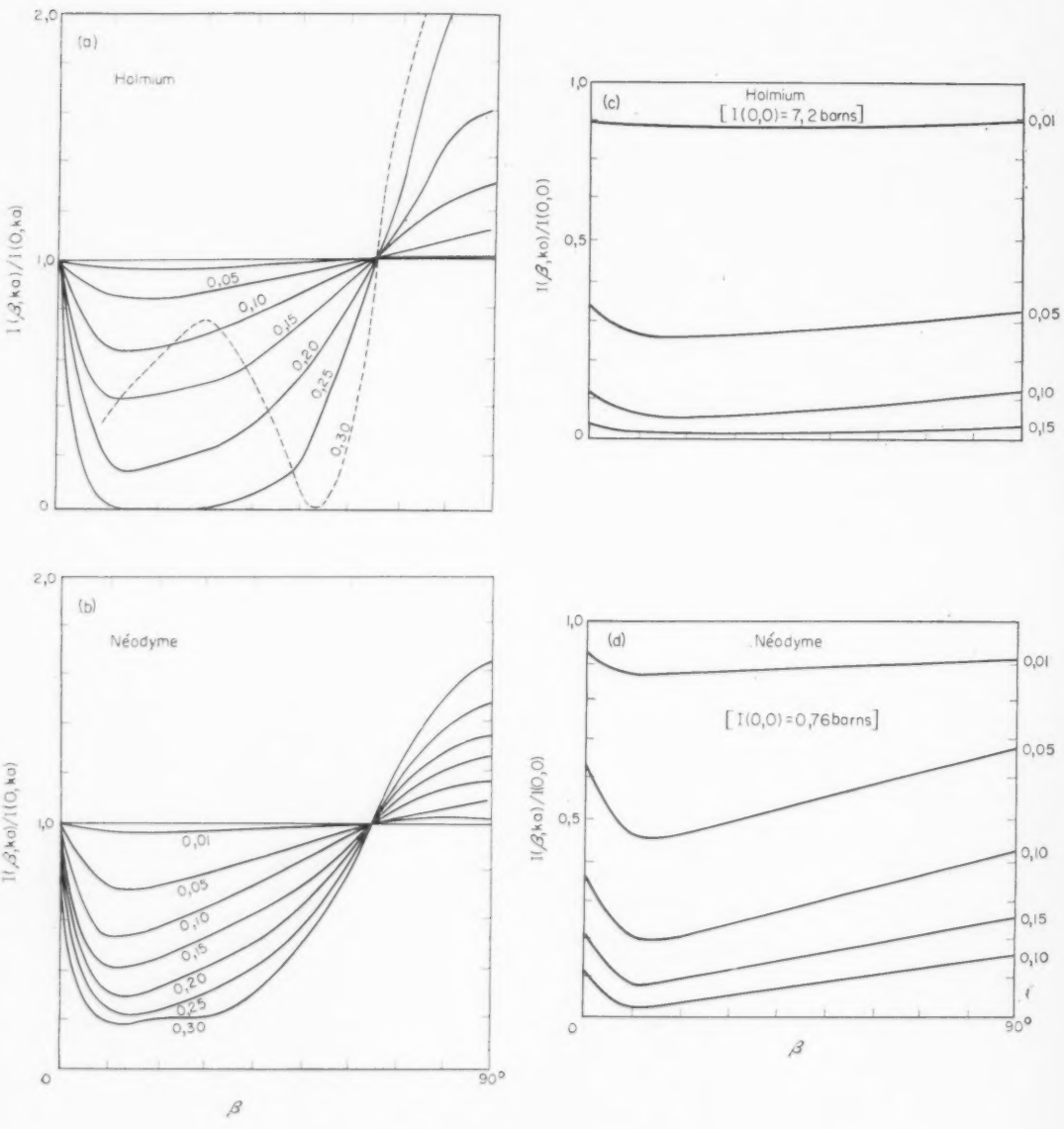

FIG. 1. Ecart à la loi $I \simeq \sin^2\beta$ tracé pour diverses valeurs de k^2a^2

(a) valeur du rapport R_2 pour l'Holmium
(b) ,, ,, ,, R_2 pour le Néodyme
(c) ,, ,, ,, R_1 pour l'Holmium
(d) ,, ,, ,, R_1 pour le Néodyne
(voir texte équation (5.4a)).

Vol. 17
1960

On peut en tous cas conclure qu'il y a quelque danger à adopter la loi classsique de dépendance angulaire de la section efficace si ka n'est pas suffisament petit ($<0{,}1$ par exemple).

(3) *Poudre cristalline avec ou sans champ cristallin*

Dans ce cas nous sommes amenés à calculer la valeur moyenne de la section efficace sur toutes les directions possibles des cristallites. Le référentiel 1 prend une direction quelconque par rapport à $\boldsymbol{k}$.

$$y^{\pm 1}_{2\nu+1}(k) = \sum_{q'=-(2\nu+1)}^{2\nu+1} \mathscr{D}^{2\nu+1}_{q',\pm 1}(\alpha,\beta,\gamma)\, y^{q'}_{2\nu+1} \qquad (1)$$

α, β, γ sont les angles d'EULER de la rotation qui amène le référentiel de $\boldsymbol{k}$ sur le référentiel 1. Compte tenu de l'orthogonalité des y et de la relation d'unitarité des matrices $\mathscr{D}$ il vient

$$\langle \mathscr{D}^{\nu}_{q,q'}(\omega)\mathscr{D}^{\nu}_{q'',q'''}(\omega)\rangle_{\substack{\text{moy}\\(\omega)}} = \frac{\delta\nu\nu'\delta qq'\delta q''q'''}{2\nu+1}$$

et

$$\frac{d\sigma}{d\Omega} = \left(\frac{M_N e g_N}{2mc}\right)^2 \sum_{i,f} \frac{p_f}{p_0} \frac{\exp(-E_i/k_BT)}{\sum_j \exp(-E_j/k_BT)} \times$$

$$\times \sum_{\nu=0}^{l} |\mathscr{A}_\nu - \mathscr{B}_{\nu+1}|^2 \frac{\mathscr{C}_\nu(f,i)}{4\nu+3} \qquad (5.6)$$

avec

$$\mathscr{C}_\nu(f,i) = \sum_{q=-(2\nu+1)}^{2\nu+1} |\langle \psi_f | y^q_{2\nu+1} | \psi_i \rangle|^2$$

(a) *Champ cristallin nul.* M est un bon nombre quantique et les $2J+1$ niveaux $|JM\rangle$ sont dégénérés

$$\psi_f = |JM'\rangle \quad \psi_i = |JM\rangle \quad p_f = p_0$$

$$\sum_f \sum_i \frac{\exp(-E_i/k_BT)}{\sum_j \exp[-E_j/k_BT]} \mathscr{C}_\nu(f,i) = \frac{4\nu+3}{2J+1}$$

La section efficace devient

$$\frac{d\sigma}{d\Omega} = \left(\frac{M_N e g_N}{2mc}\right)^2 \sum_{\nu=0}^{l} \frac{|\mathscr{A}_\nu(k) - \mathscr{B}_{\nu+1}(k)|^2}{2J+1} \qquad (5.7)$$

Pour ka inférieure à 0,4 on peut négliger dans (5.7) les termes $\nu > 0$. C'est la formule utilisée par TRAMMEL et c'est pourquoi les résultats obtenus par lui concordent avec l'expérience même si les valeurs des coefficients $\mathscr{A}_\nu$, $\mathscr{B}_{\nu+1}$ pour $\nu > 0$ sont fausses. Nous avons tracé la valeur de l'expression (5.7) en fonction de

$$\frac{\sin\theta}{\lambda_0} = \frac{kaZ^*}{8\pi a_0}$$

Pour Z^* nous avons interpolé et extrapolé dans la série des terres rares à partir des valeurs données par KOEHLER et WOLLAN pour Nd et Er. Les valeurs de Z^* utilisées sont reportées dans le tableau 1.

(b) *Champ cristallin non nul.* Nous avons vu que la multiplicité J est séparée en un certain nombre de multiplicités. Le neutron incident pourra induire des transitions élastiques entre états d'une même multiplicité ($p_f = p_0$) ou inélastiques entre deux multiplets :

$$\frac{\hbar^2}{2m}(p_f{}^2 - p_0{}^2) = E_i - E_f \qquad (5.8)$$

Si les états propres des multiplets ont la forme (3·7), alors† :

$$C_\nu(f,i) = \sum_{q=-(2\nu+1)}^{2\nu+1} |\sum_{M'}\sum_{M} A^{f*}_{M'} A^{i}_{M}(-)^{J-M} \times$$

$$\times \langle JJM' - M | 2\nu+1, 9\rangle|^2 = C_\nu(i,f) \qquad (5.9)$$

On peut remarquer que

$$\sum_f C_\nu(f,i) = \frac{4\nu+3}{2J+1}$$

Pour simplifier, nous allons supposer que la poudre cristalline est au zéro absolu, seul l'état fondamental est peuplé. Si b est la dégénérescence de cet état et $\psi_i{}^b$ ses fonctions propres, on aura :

$$\left(\frac{d\sigma}{d\Omega}\right)_{\text{élastique}} = \left(\frac{M_N e g_N}{2mc}\right)^2 \frac{1}{b} \sum_{i=0}^{b}\sum_{k=0}^{b}\sum_{\nu=0}^{l} \frac{|\mathscr{A}_\nu - \mathscr{B}_{\nu+1}|^2}{4\nu+3} \times$$

$$\times C_\nu(h,i)_{bb} \qquad (5.10)$$

Quant aux transitions inélastiques, il y en aura autant que de multiplets différents de l'état de

† Nous donnons les valeurs de ces coefficients dans le tableau 5 pour le cas du Cérium et des plus importants d'entre eux pour l'Holmium.

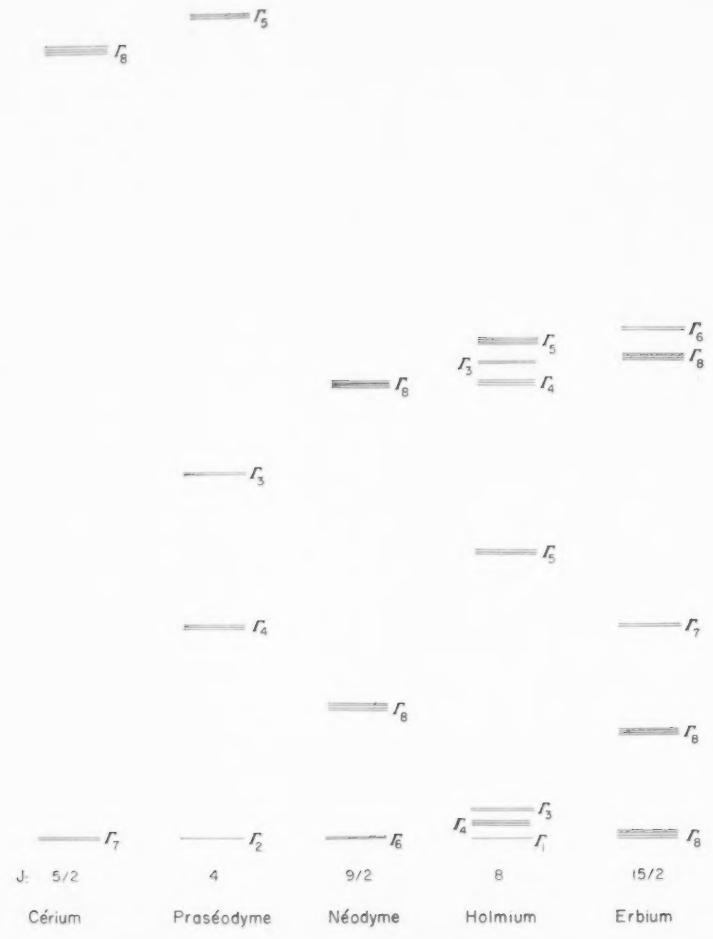

FIG. 2. Succession des niveaux d'énergie des différentes terres rares dans un champ cubique. (pour une même valeur du paramètre A)

base. Soit $\Gamma^{(c)}$ un tel multiplet dont les c fonctions de base sont $\psi_j{}^c$ on aura :

$$\left(\frac{d\sigma}{d\Omega}\right)_{\text{inél}}^{b\to c} = \frac{p_{cf}}{p_0}\frac{1}{b}\left(\frac{M_N e g_N}{2mc}\right)^2 \times$$

$$\times \sum_{i=0}^{b}\sum_{h=0}^{c}\sum_{\nu=0}^{l}\frac{|\mathscr{A}_\nu - \mathscr{B}_{\nu+1}|^2}{4\nu+3} C_\nu(h,i)_{b\to c} \quad (5.11)$$

La section efficace totale sera la somme de (5.10) et (5.11).

Remarque: Si l'énergie du neutron est grande devant la distance des niveaux $p_{cf} \simeq p_0$, en tenant compte de (5.9), on retrouve pour la section efficace totale la formule (5.7).

Les Figs. 3 donnent la variation en fonction de $\sin\theta/\lambda_0$ de la section efficace de l'ion libre.

Dans la Fig. 4 nous avons tracé la variation, en fonction du même paramètre, des sections efficaces "élastique" "inélastiques" et "totale" au zéro absolu pour diverses valeurs du paramètre A, dans le cas du Cérium. Nous pourrions également

Vol. 17
1960

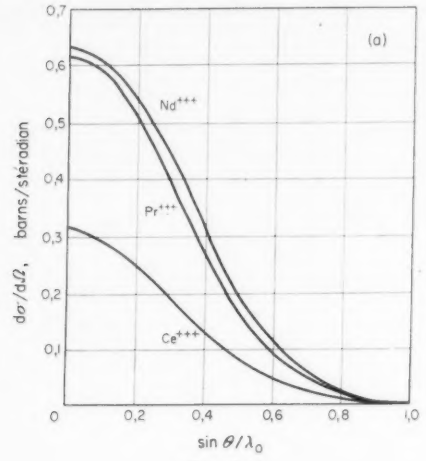

FIG. 3(a)

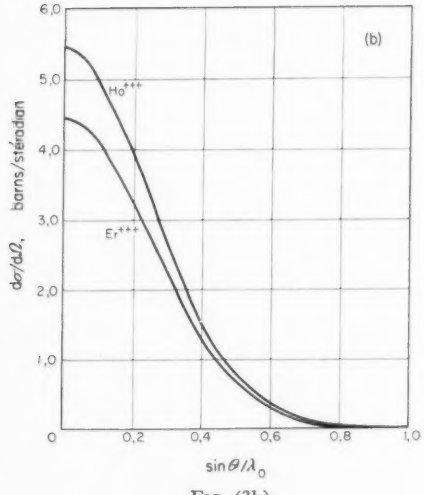

FIG. (3b)

FIG. 3. (a) Section efficace de l'ion libre en fonction de $\sin\theta/\lambda_0$ pour Ce^{+++}, Pr^{+++}, Nd^{+++}.
(b) Section efficace de l'ion libre en fonction de $\sin\theta/\lambda_0$ pour Ho^{+++} et Er^{+++}.

tracer cette variation pour les autres terres rares. Cependant, le grand nombre de figures alourdirait inutilement l'article.*

* Il est remarquable que dans le cas du Praséodyme au zéro absolu la seule transition importante soit inélastique.

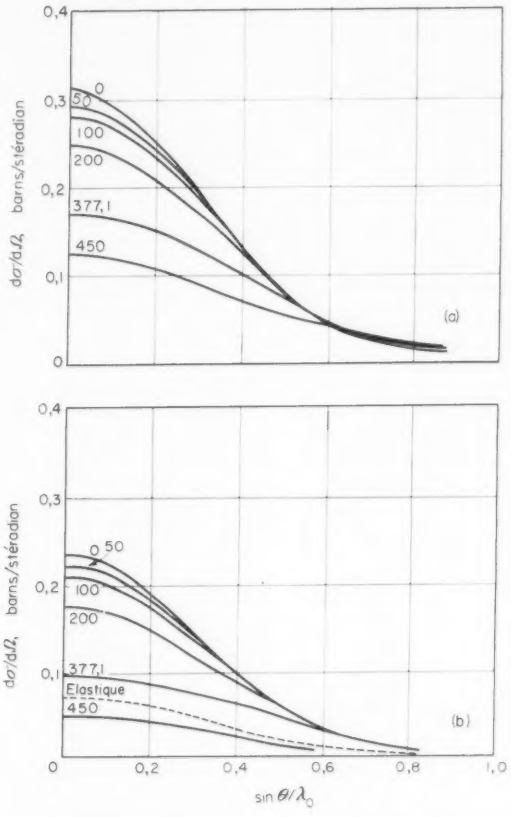

FIG. 4. Variation au zéro absolu des sections efficaces élastique (a) et inélastique (b) du Cérium dans un champ cubique, en fonction du paramètre $\sin\theta/\lambda_0$ pour diverses valeurs de la distance des niveaux. (377 cm^{-1} correspond à $A = 3300$ cm^{-1})

Remarquons qu'avec les valeurs de A choisies et pour des angles de diffusion assez petits la section efficace totale est peu différente de celle de l'ion libre (sauf pour le Cérium). Ceci provient de ce que les transitions entre niveaux éloignés ont une probabilité très faible de se produire. Ceci explique pourquoi KOEHLER et WOLLAN qui étudiaient la section efficace totale n'ont constaté qu'une faible variation de celle-ci avec la température.

Cependant les effets du champ cristallin peuvent être mis en évidence si on étudie les sections efficaces inélastiques.

Tableau 5. *Valeur des expressions* $\sum_{h,i} C\nu(hi)\Gamma_h\Gamma_i$ *dans un champ cubique (voir texte équation* (5.19)) *pour le Cérium* (a) *et pour certain niveaux de l'Holmium* (b)

(a)

ν	$\Gamma_7\Gamma_7$	$\Gamma_7\Gamma_8$	$\Gamma_8\Gamma_8$
0	0,2381	0,7619	1,2381
1	1,4815	0,8518	3,8148
2	1,2804	2,3862	4,9471
3	0	0	0

(b)

ν	$\Gamma_1\Gamma_4^{(1)}$	$\Gamma^{(1)}\Gamma^{(1)}$	$\Gamma_3^{(1)}\Gamma^{(1)}$	$\Gamma^{(2)}\Gamma^{(1)}$	$\Gamma_3^{(2)}\Gamma^{(2)}$	$\Gamma_3^{(2)}\Gamma_4^{(2)}$
0	0,1667	0,0379	0,3014	0,0390	0,2170	0,0967
1	0,1906	0,1197	0,4147	0,1343	0,0896	0,3037
2	0,1288	0,3725	0,2162	0,2633	0,2963	0,0969
3	0,0704	0,1822	0,1416	0,1862	0,1510	0,3548

ν	$\Gamma_5^{(1)}\Gamma_5^{(1)}$	$\Gamma_5^{(1)}\Gamma_4^{(1)}$	$\Gamma_5^{(1)}\Gamma^{(2)}$	$\Gamma_5^{(2)}\Gamma_5^{(2)}$	$\Gamma_5^{(2)}\Gamma_4^{(2)}$	$\Gamma^{(2)}\Gamma_4^{(2)}$
0	0,2877	0,0427	0,1125	0,2264	0,0745	0,2069
1	0,0	0,2689	0,1482	0,2215	0,3568	0,0070
2	0,1171	0,3725	0,5136	0,1536	0,2171	0,3766
3	0,8248	0,4378	0,4371	0,3934	0,1398	0,4946

6. DETECTION EXPERIMENTALE DES EFFETS DU CHAMP CRISTALLIN

L'équation de conservation d'enérgie (5.8) permet de définir à quelle condition on peut observer les effets du champ cristallin. Il faut que :

$$\frac{\hbar^2}{2M_N} p_0^2 > E_f - E_i$$

pour qu'une transition ait lieu.

Pour discuter ces éventualités nous allons étudier le cas de Ce^{3+} qui possède, dans un champ cubique les multiplets Γ_7 et Γ_8

Γ_7 est un doublet d'énergie : $-8A/105$

Γ_8 un quadruplet d'energie : $4A/105$

$$\frac{\hbar^2}{2M_N}(p_f^2 - p_0^2) = \frac{-12A}{105} = \Delta$$

si $\lambda_0 = 1{,}141$ Å on en tire

$$\lambda_f = \frac{2\pi}{\sqrt{(30{,}224 - 6{,}747\ 10^{-3}A)}} \qquad \begin{matrix} A \text{ en cm}^{-1} \\ \lambda_f \text{ en Å} \end{matrix}$$

Si $A = 3300$ cm^{-1} comme le signale KYNCH,

Vol. 17
1960

$\lambda_f = 2{,}22$ Å. Cette variation est facilement détectable avec un spectromètre à cristal.

La difficulté réside dans le choix du corps à étudier, car on veut éviter un trop grand foisonnement de raies de diffusion nucléaires. Pour avoir des sections efficaces assez fortes, la manipulation se fera aux petits angles ($\theta \simeq 0$). Pour ne pas compliquer inutilement l'appareillage la manipulation se fera à la température ambiante. Dans le cas du Cérium à ce moment et pour un angle 2θ donné, on détectera trois vecteurs d'onde différents pour les neutrons diffusés : p_0, p_1, p_2.
avec

$$p_1^2 - p_0^2 = \frac{2M_N}{\hbar^2}\Delta \text{ et } p_0^2 - p_2^2 = \frac{2M_N}{\hbar^2}\Delta$$

les sections efficaces inélastiques seront approximativement dans le rapport

$$\frac{p_2}{p_1}\exp(-\Delta/k_BT)$$

Nous avons tracé pour $\theta = 0$ la variation des sections efficaces élastiques inélastiques et totales en fonction de la température dans le cas du Cérium et de l'Holmium.* Nous avons choisi pour fixer les idées $A = 3300$ cm^{-1}. De plus, dans le cas de l'Holmium nous avons groupé les niveaux dont les distances ne conduisent pas à une variation appréciable de la longueur d'onde du neutron, ou bien dont les distances sont sensiblement égales. (Fig. 5).†

Remerciements—La detection expérimentale de cet effet sera effectuée à Saclay. Nous tenons à remercier M.P.G. DE GENNES et M. A. HERPIN, qui nous a suggéré ce problème, pour les nombreuses et fécondes discussions qui ont marqué son développement. Nous remercions également Mme PILLARD qui a effectué le calcul des coefficients $\mathcal{F}$, Mlle BORE qui a effectué celui des coefficients $\mathcal{C}_\nu$ et enfin, M. A. AMOUYAL qui a bien voulu mettre à notre disposition le calculateur électronique.

Note ajouttée sur l'épreuve: La détection experimentale de cet effet a été effectuée au spectomètre à temps de Vol par CRIBIER D. et JACROT B., *C.R. Acad. Sci. Paris* **250,** 2871–3, 25 Avril (1960).

* On pourra se procurer le détail des figures et tableaux pour les autres terres rares en le réclamant à l'un des auteurs. (D.S.J.).

† Nous reproduisons ci-après la distance des niveaux dans l'Holmium pour $A = 3300$ cm^{-1}.

$\Gamma_1\,\Gamma_4^{(1)} = 8{,}11$ cm^{-1}
$\Gamma_1\,\Gamma_3^{(1)} = 12{,}86$ cm^{-1}
$\Gamma_1\,\Gamma^{(1)} = 138{,}91$ cm^{-1}
$\Gamma_1\,\Gamma^{(2)} = 218{,}74$ cm^{-1}
$\Gamma_1\,\Gamma_3^{(2)} = 227{,}14$ cm^{-1}
$\Gamma_1\,\Gamma^{(2)} = 239{,}55$ cm^{-1}

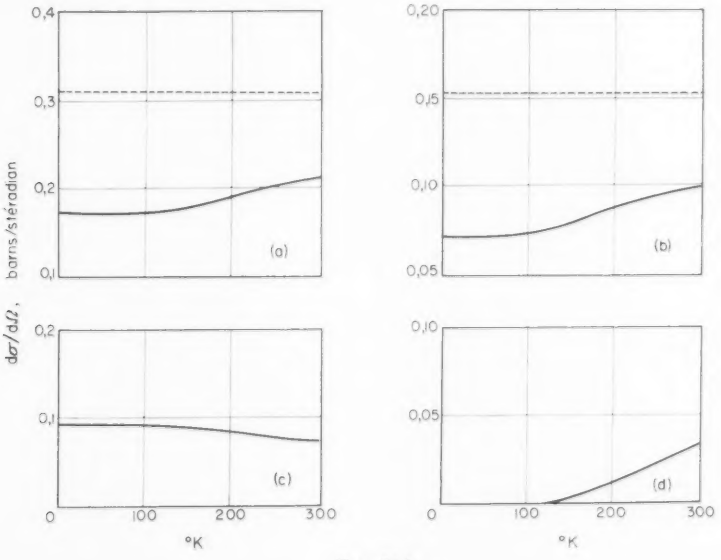

FIG. 5(a)

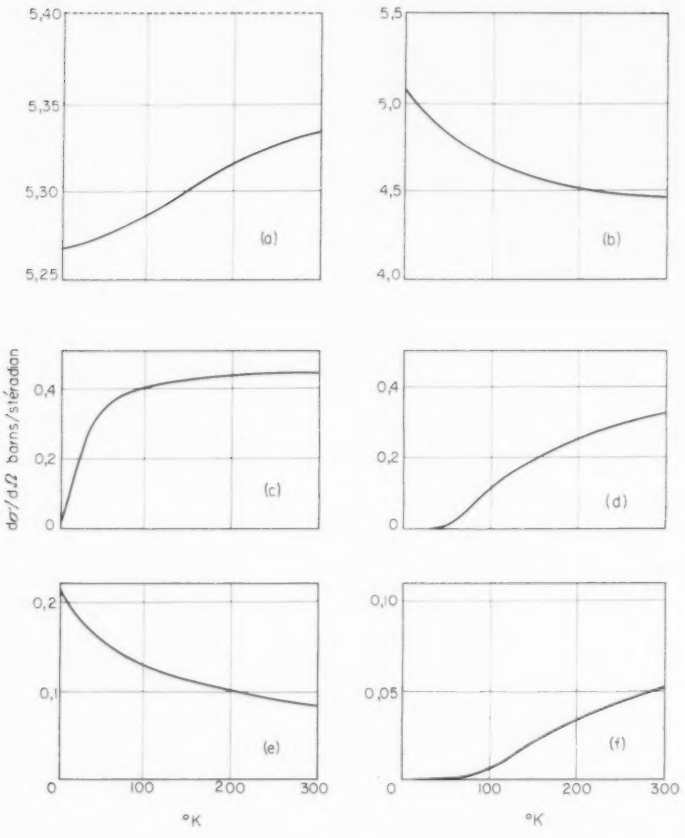

FIG. 5(b)

FIG. 5(i) Variation des différentes sections efficaces (Totale (a), élastique (b), inélastique $\Gamma_7 \rightarrow \Gamma_8$ (c) inélastique $\Gamma_7 \rightarrow \Gamma_8$ (d)) du Cérium avec la température pour $A = 3300\ \text{cm}^{-1}$, $\sin\theta = 0$, $\lambda_0 = 1.141\ \text{cm}^{-1}$.

(ii) Variation des diverses sections efficaces de l'Holmium avec la température pour $A = 3300\ \text{cm}^{-1}$, $\sin\theta = 0$, $\lambda = 1.141\ \text{cm}^{-1}$.

Un certain nombre de niveaux étant voisins ou pratiquement équidistants, on les a groupés pour obtenir les courbes reproduites.

Courbe (a) : Section efficace totale.

Courbe (b) : Section efficace quasi élastique. Elle comprend les transitions dans les ensembles: $\Gamma_1\Gamma^{(1)}\Gamma_3^{(1)}$, $\Gamma_5^{(1)}$, $\Gamma_4^{(2)}\Gamma^{(2)}\Gamma_5^{(2)}$

Courbe (c) : Section efficace inélastique. Elle comprend les transitions de l'ensemble $\Gamma_1\Gamma^{(1)}\Gamma_3^{(1)}$ à $\Gamma_5^{(1)}$ et de $\Gamma_5^{(1)}$ à l'ensemble $\Gamma^{(2)}\Gamma^{(2)}\Gamma_5^{(2)}$

Courbe (d) : Section efficace inélastique : Transitions inverses des précédentes.

Courbe (e) : Section efficace inélastique: Elle comprend les transitions de l'ensemble $\Gamma_1\Gamma_4^{(1)}\Gamma_3^{(1)}$ à l'ensemble $\Gamma_4^{(2)}\Gamma_3^{(2)}\Gamma_5^{(2)}$

Courbe (f) : Section efficace inélastique. Transitions inverses des précédentes.

Vol. 17
1960

BIBLIOGRAPHIE

1. TRAMMEL G. T., *Phys. Rev.* **92,** 1386 (1953).
2. KOEHLER W. C. et WOLLAN E. O., *Phys. Rev.* **92,** 1380 (1953); KOEHLER W. C., WOLLAN E. O. et WILKINSON K., *Phys. Rev.* **110,** 37 (1958).
3. BETHE H., *Ann. Phys. Lpz.* **3,** 133 (1929).
4. OPECHOWSKI V., *Physica* **7,** 552 (1940).
5. ABRAGAM A., *Résonance Electronique,* Vol. 1 p. 38, Institut National des Sciences et Techniques Nucléaires, Saclay (1956–7).
6. KYNCH G. J., *Trans. Faraday Soc.* **33,** 1402 (1937).
7. EDMONDS A., *Angular Momentum in Quantum Mechanics,* Princeton University Press (1957).
8. STEVENS K. W., *Proc. Phys. Soc. Lond.* **65,** 34, 209 (1952).
9. WIGNER E. P., *Gruppen Theorie und Ihre Anwendung auf die Quantem Mechanik und den Atomspektren* Fr. Vieweg, Braunschweig (1931) et Edwards Broth., Ann Arbor, Michigan (1944).
10. BETHE H. et VON DER LAGE C., *Phys. Rev.* **71,** 612 (1947).
11. ELLIOTT R., *Phys. Rev.* **96,** 280 (1951).
12. HALPERN O et JOHNSON P., *Phys. Rev.* **55,** 898 (1939).

J. Phys. Chem. Solids Pergamon Press 1960. Vol. 17, Nos. 1/2, pp. 138–142. Printed in Great Britain.

PRESSURE DEPENDENCE OF THE DIRECT ENERGY GAP IN GERMANIUM*

MANUEL CARDONA† and WILLIAM PAUL

Division of Engineering and Applied Physics, Harvard University, Cambridge, Massachusetts

(*Received* 19 *April* 1960)

Abstract—The pressure dependence of the energy gap corresponding to allowed optical transitions in germanium has been measured at room temperature and pressures up to 7000 kg/cm². This direct energy gap is found to increase at a rate of $1{\cdot}3 \pm 0{\cdot}1 \times 10^{-5}$ eV cm²/kg, in agreement with previous approximate determinations and with the pressure coefficient of the same energy gap in group 3–5 compounds.

INTRODUCTION

THE FUNDAMENTAL absorption edge in germanium can be considered as composed of two parts corresponding to disallowed and allowed optical transitions.[1] The former involves electron transitions from a valence band maximum at wave vector $k = 0$ to conduction band minima at the Brillouin zone boundary in the (111) directions; this process involves the absorption or emission of a phonon.[2] The latter, and higher energy, portion of the edge corresponds to allowed transitions between the valence band maximum energy state and states in the lowest conduction band minimum at $k = 0$. The minimum energy differences for both processes can be found from a detailed examination of the absorption edges, when, on occasion, the structure in the absorption edge resulting from the use of magnetic fields is helpful.[3,4]

PAUL and WARSCHAUER[5] measured the change of the indirect absorption edge with pressure up to 7000 kg/cm², and noted both a shift to higher energies and a change in the shape of the edge. Since the theory of the indirect transitions involves the states at $k = 0$ in the conduction band as intermediate states, an analysis of this shift and change of shape can be used to give both the pressure coefficient of the indirect energy gap and that of the "vertical" energy gap at $k = 0$. PAUL and WARSCHAUER found a result for the coefficient of the indirect energy gap in agreement with previously found values from resistivity experiments, i.e. 5×10^{-6} eV cm²/kg, within their limits of error. They determined a coefficient of 1×10^{-5} eV cm²/kg for the vertical energy gap at $k = 0$. Other workers[6] have found substantially greater coefficients for the indirect energy gap, but none of these have analysed their results in accordance with the sort of formulae believed to be applicable for indirect processes[7]; significantly, the results of PAUL and WARSCHAUER are in agreement with those of the other workers[6] when no correction is made for changes in shape of the absorption edge and a coefficient found from the photon energy corresponding to a fixed, chosen, absorption coefficient is computed. The coefficient found by PAUL and WARSCHAUER for the direct gap is, nevertheless, found with low accuracy, by this method.

FAN *et al.*, and NEURINGER[6] have also measured the pressure coefficient of the direct absorption edge to pressures of the order of 1000 kg/cm² and energies up to 0·80 eV. For the highest photon energies a pressure coefficient of about 1×10^{-5} eV cm²/kg was found. The agreement of their coefficient with that of PAUL and WARSCHAUER is

* This research was supported by the Office of Naval Research under Contract Nonr. 1866 (10).

† Now at R.C.A. Laboratories, Zurich, Switzerland.

not too meaningful, because the highest photon energy was still smaller than the accepted energy gap at $k = 0$, 0·805 eV.[3] The lack of completeness of all the previous determinations suggested the necessity of performing measurements of absorption coefficient as a function of pressure to photon energies larger than the accepted energy gap.

METHOD

The high pressure and optical apparatus used in these measurements has been described by PAUL and WARSCHAUER[5]. A Perkin–Elmer 12 C spectrometer was used, with glass optics. A Kodak Ektron PbS cell, cooled to dry ice temperature, was used as detector. Since the stability of this detector was poor, a measurement at a reference wavelength (a long wavelength reference) was made after each measurement at any other wavelength. All measurements at a given pressure were normalized to the same intensity at the reference wavelength.

The sample used was a high purity germanium single crystal thin film, whose thickness, 3·8μ, was determined from the interference pattern at wavelengths longer than those corresponding to the absorption edge. The film was free to move between two glass plates in its holder, so that the pressure applied to it was truly hydrostatic. The following sources of experimental error can be shown to be unimportant (a) changes in the intensity of the source, and in its spectral distribution (b) changes in the sensitivity of the detector, and in its spectral distribution (c) changes in the reflection coefficient of the sapphire window and the CS_2 pressure transmitting fluid (d) changes in the reflection coefficient of the glass plates holding the germanium film and the CS_2 (e) changes in the reflection coefficient of the sample and the CS_2 (f) distortion of the sapphire window with pressure (g) resolution of the spectrometer.

The discussion of Ref. (5) of the sources of error (a), (b) and (f) applies here. The sensitivity of the detector (objection (b)) does alter with time, but the continual referring of all measurements to the transmission at a long wavelength where the absorption coefficient is negligible eliminates any difficulties. Objections (c), (d) and (f) are also eliminated by the reference wavelength technique. Point (e) is less simple.

The energy transmitted by the sample at the reference wavelength is

$$I_{\text{ref}} = I_{0,\text{ref}}\{(1-R)/(1+R)\}$$

where I and I_0 are the transmitted and incident intensities and R is the reflection coefficient.

The energy transmitted in the region of high absorption is

$$I = I_0(1-R)^2 e^{-Kt}$$

where K is the absorption coefficient and t the sample thickness.

Apparently changes in the reflection coefficient of the interface between the germanium and the CS_2 do not affect equally the transmitted energies at the reference wavelength and wavelengths in the spectral region of high absorption; and the reference wavelength method does not correct for the change in reflectivity with pressure. It can be shown, fortunately, that the changes with pressure of the germanium[8] and CS_2 refractive indices[9] are small enough that negligible errors are committed by ignoring objection (e). The spectral dependences of the refractive index of germanium and CS_2 are also shown to be unimportant at the wavelengths of the measurement.

The pressure measurements were carried out at a mechanical slit width of 100μ, which corresponds to a spectral slit width of about 0·005μ. The absorption edge was measured at atmospheric pressure at slit widths of 50 and 100μ. A small displacement in wavelength was observed, much smaller than that caused by changes in pressure. Since the pressure shifts are essentially independent of photon energy in the range of energies employed, it is concluded that no significant error is introduced by the relatively poor resolution at mechanical slit widths of 100μ. The wide slit widths are, of course, almost mandatory in the high f number optical system that includes the pressure vessel. The resolution is such that fine structure due to excitons is not observable, but no errors are likely to be incurred in the deduced pressure coefficients thereby.

RESULTS AND DISCUSSION

The direct transitions can be made into the (000) conduction band states from the heavy or light hole mass bands. At $k = 0$, the transitions from the heavy mass band are forbidden by a group theoretical argument, provided spin–orbit coupling is neglected, while the transitions from the light mass band are not. It can be shown that the absorption coefficient due to the latter transitions only is given by

$$K = \frac{2e^2(2m^*)^{3/2}}{3ncm^2\omega\hbar^3}\,|\langle i|p|f\rangle_{k=0}|^2\,(\hbar\omega - Eg)^{1/2}$$

under the assumption that

$$\langle i|p|f\rangle_k = \langle i|p|f\rangle_{k=0},$$

that is, the matrix element is assumed constant and equal to its value at $k = 0$. In the above equation, n is the refractive index, c the velocity of light, ω the angular frequency, Eg the energy gap at $k = 0$, m the free electron mass, and m^* is given by

$$\frac{1}{m^*} = \frac{1}{m_e} + \frac{1}{m_{lh}}$$

m_e is the electron effective mass and m_{lh} the light hole mass.

Exciton effects that modify the spectral dependence of the absorption coefficient[10] are neglected again occur. The absolute magnitude of the absorption calculated then agrees well enough (within 20 per cent) with the experimental value. A curve of K^2 versus photon energy (Fig. 1)

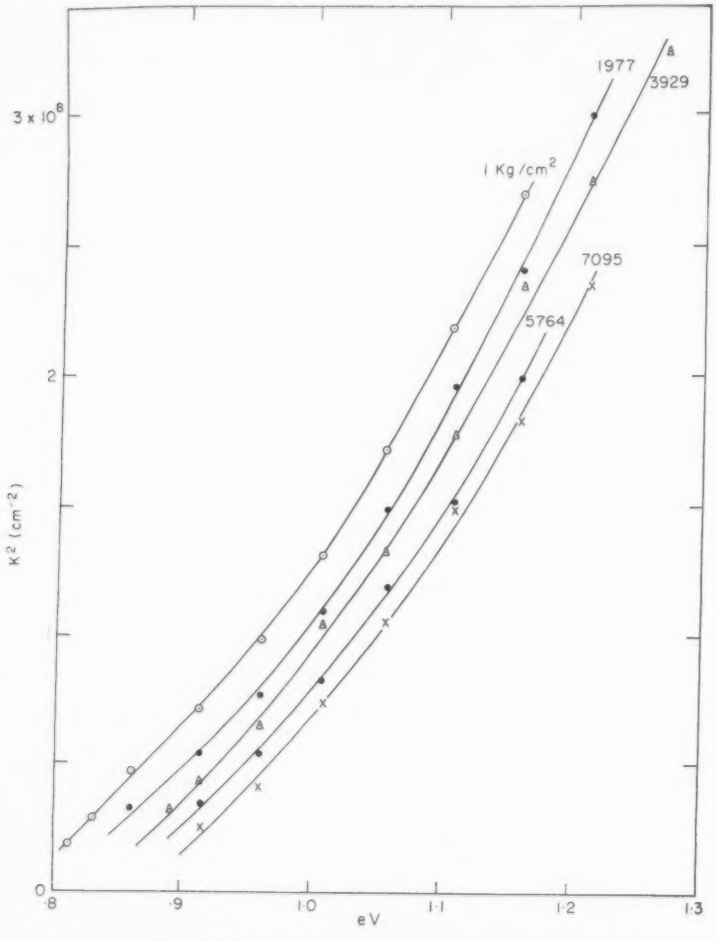

FIG. 1. The square of the absorption coefficient K vs. photon energy at several pressures.

for our determination of the pressure coefficient. The matrix element in the above equation can be estimated from the measured effective masses of the electrons and the light holes, and the formulae from the k.p. method[11] where they shows that, at energies $< 0{\cdot}95$ eV, at atmospheric pressure, K is approximately proportional to $(\hbar\omega - Eg)^{1/2}$. Above 0·95 eV, the K^2 curve deviates from linearity. This may be due to a number of causes, viz. (a) the onset of transitions from the

Vol. 17
1960

heavy mass hole band, which have an energy dependence of $(\hbar\omega - Eg)^{3/2}$. The extra energy term here comes from the dependence of the matrix element on the wave vector. (b) at high energies the conduction band will cease to be parabolic, and the absorption will increase faster than $(\hbar\omega - Eg)^{1/2}$ due to an increased density of final states for the transition. (c) The matrix element

shows the isoabsorption lines as a function of pressure. The decrease observed in the slope of these lines is within the limits of the experimental error. The line slopes show that the room temperature energy gap changes at a rate of

$$1{\cdot}3 \pm 0{\cdot}1 \times 10^{-5} \text{ eV cm}^2/\text{kg}$$

in agreement with the previous determinations,

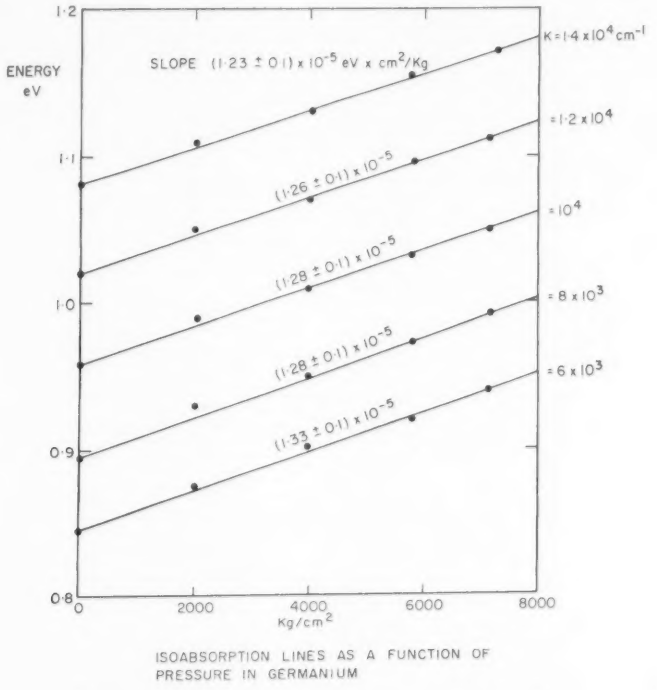

FIG. 2. Isoabsorption curves at several levels of absorption density.

for the allowed transitions may no longer be set equal to that at $k = 0$, but becomes dependent on $(\hbar\omega - Eg)$. The present data, which were obtained primarily to find the pressure coefficient of the gap, are inadequate for a detailed analysis of the shape of the absorption edge. Such an analysis is, in any case, not easy, since all of the modifications (a) (b) and (c) must be considered.

In Fig. 1, the measurements at 3929 and 7095 kg/cm² were taken on increasing the pressure while the measurements at 1977 and 5764 kg/cm² were taken on decreasing the pressure. Fig. 2

although the reasons for this agreement are not wholly understood.[12]

The pressure coefficient of the energy gap at $k = 0$ has also been determined for some intermetallic semiconductors. Thus, LONG[13] found a coefficient of $1{\cdot}4 \times 10^{-5}$ eV cm²/kg for InSb, and KEYES[13] $1{\cdot}55 \times 10^{-5}$ eV cm²/kg. WARSCHAUER and PAUL[14] found $1{\cdot}2 \times 10^{-5}$ eV cm²/kg for GaAs. EDWARDS *et al.*[15] have found similar coefficients in GaSb and GaAs in experiments to pressures of the order of 100,000 kg/cm². It is notable that the pressure coefficients of the energy gap at $k = 0$

in these materials are similar, despite the variation in the absolute magnitude of the energy gap at atmospheric pressure.

Acknowledgements—We are happy to acknowledge the help provided by Professor H. BROOKS and Dr. D. M. WARSCHAUER in the discussion and performance of this experiment. The single crystal film was provided through the good offices of Dr. ROGER NEWMAN and the General Electric Research Laboratory, Schenectady, to whom our thanks are also due.

REFERENCES

1. DASH W. and NEWMAN R., *Phys. Rev.* **99,** 1151 (1955).
2. MACFARLANE G. G. and ROBERTS V., *Phys. Rev.* **97,** 1714 (1955).
3. ZWERDLING S., LAX B. and ROTH L. M., *Phys. Rev.* **108,** 1402 (1957).
4. MACFARLANE G. G., MCLEAN T. P., QUARRINGTON J. E. and ROBERTS V., *Proc. Phys. Soc. Lond.* **71,** 863 (1958).
5. PAUL W. and WARSCHAUER D. M., *J. Phys. Chem. Solids* **5,** 89 (1958).
6. FAN H. Y., SHEPHERD M. L. and SPITZER W. G., *Photoconductivity Conference at Atlantic City,* 1954. p. 184. Wiley, New York (1956); NEURINGER L., *Phys. Rev.* **113,** 1495 (1959).
7. BARDEEN J., BLATT F. J. and HALL L. H., *Photoconductivity Conference at Atlantic City,* 1954. Wiley, New York (1956).
8. CARDONA M., PAUL W. and BROOKS H., *J. Phys. Chem. Solids* **8,** 204 (1959).
9. DANFORTH W. E. Jr., *Phys. Rev.* **38,** 1224 (1931).
10. ELLIOTT R. J., *Phys. Rev.* **108,** 1383 (1957); ELLIOTT R. J. and LOUDON R. J., *J. Phys. Chem. Solids* **8,** 382 (1959).
11. KANE E. O., *J. Phys. Chem. Solids* **1,** 82 (1956) .
12. PAUL W., *J. Phys. Chem. Solids* **8,** 196 (1959).
13. LONG D., *Phys. Rev.* **99,** 388 (1955); KEYES R. W., *Phys. Rev.* **99,** 490 (1955).
14. WARSCHAUER D. M. and PAUL W., unpublished work.
15. EDWARDS A. L., SLYKHOUSE T. E. and DRICKAMER H. G., *J. Phys. Chem. Solids* **11,** 140 (1959).

Vol. 17
1960

J. Phys. Chem. Solids Pergamon Press 1960. Vol. 17, Nos. 1/2, pp. 143–148. Printed in Great Britain.

ELASTIC CONSTANTS OF HEXAGONAL CADMIUM SULFIDE

D. I. BOLEF, N. T. MELAMED and M. MENES

Westinghouse Research Laboratories, Pittsburgh 35, Pennsylvania

(*Received* 25 *April* 1960)

Abstract—The adiabatic elastic constants of a single crystal of hexagonal cadmium sulfide were measured at 27°C. Measurements were made at 10 mc by means of an ultrasonic cw mechanical resonance technique. The elastic stiffness constants, in units of 10^{11} dynes/cm^2, are: $c_{11} = 8{\cdot}432$, $c_{33} = 9{\cdot}397$, $c_{44} = 1{\cdot}489$, $c_{12} = 5{\cdot}212$, $c_{13} = 4{\cdot}638$. Single crystal CdS has very low anisotropy, as indicated by the ratios $c_{11} - c_{12}/2c_{44} = 1{\cdot}08$ and $c_{33}/c_{11} = 1{\cdot}11$.

1. INTRODUCTION

THIS PAPER reports the results of the measurement of the adiabatic elastic constants at 27°C of single crystal hexagonal CdS. The acquisition of a large single crystal made possible the determination of all five of the required constants. To the authors' knowledge, this is the first determination of the complete set of elastic constants for a single crystal of the wurtzite structure.

The five elastic stiffness constants (c_{11}, c_{33}, c_{44}, c_{12}, and c_{13}) were determined from measurements of acoustic velocities. Eight acoustic velocities were measured along three separate crystallographic directions of propagation. These provided, in addition to the five elastic constants, three internal checks on the accuracy of the results. The measurements were made by means of a high frequency ultrasonic cw resonance technique described in detail in Ref. 1 and briefly in Section 2C. This technique is capable of yielding results of high precision and permits an accurate calculation of the end corrections due to the transducer and bond. The ultrasonic pulse technique was used for comparison with the cw results.

2A. FORMULAE FOR ELASTIC CONSTANTS

The determination of the elastic stiffness constants by ultrasonic techniques depends on measurements of the acoustic wave velocities. The relationships between the wave velocities and the elastic constants for a particular direction in hexagonal crystals are the following:[2]

(a) For propagation parallel to c-axis

$$\rho U_l^2 = c_{33}$$

$$\rho U_t^2 = c_{44}; \text{ (for any polarization)}$$

(b) For propagation parallel to a-axis

$$\rho U_l^2 = c_{11}$$

$$\rho U_t^2[001] = c_{44}; \text{ (polarized } \| \text{ } c\text{-axis)}$$

$$\rho U_t^2[210] = c_{66} = \tfrac{1}{2}(c_{11} - c_{12}); \text{ (polarized } \perp c\text{-axis)}$$

(c) For propagation 45° to c-axis

$$\rho U_t^2 = \tfrac{1}{2}(c_{66} + c_{44}); \text{ (polarized } \perp c\text{-axis)}$$

$$\rho U_q^2 = \tfrac{1}{4}(c_{11} + c_{33} + 2c_{44}) + \tfrac{1}{4}[(c_{11} - c_{33})^2 + 4(c_{13} + c_{44})^2]^{1/2}$$

$$\rho U_{qt}^2 = \tfrac{1}{4}(c_{11} + c_{33} + 2c_{44}) - \tfrac{1}{4}[(c_{11} - c_{33})^2 + 4(c_{13} + c_{44})^2]^{1/2}$$

In the above expressions the subscripts l and t designate respectively longitudinal and transverse mode propagation. The quasi-longitudinal and quasi-transverse waves, represented by ρU_{ql}^2 and ρU_{qt}^2 are coupled, and acoustical birefringence is generally observed. In the present instance no strong coupling was observed, although much better pulse and cw patterns were obtained for ρU_{ql}^2 than for ρU_{qt}^2.

2B. CRYSTAL PREPARATION

The single crystal used in these measurements was obtained from the Eagle–Picher Company,* and had been grown by vapor deposition. The shape of the crystal was irregular, but approximated a one inch cube; the weight before cutting was 48g. The CdS crystal was light amber in color and probably contained appreciably less than 1 per cent of impurities. The specimen was initially oriented with respect to the c axis [001] by an X-ray back reflection technique. A pair of faces on opposite sides of the crystal were ground

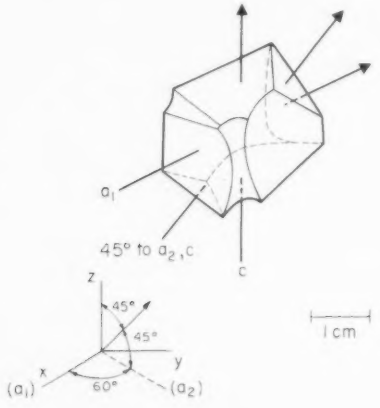

FIG. 1. Diagrammatic sketch of CdS crystal after cutting and grinding. Arrows indicate three directions of propagation perpendicular to three sets of plane-parallel faces.

perpendicular to the c-axis. Grinding was with AO-303½ emery powder on a cast iron lap, followed by polishing on onion skin paper with Linde A sapphire powder. Kerosene was used as the abrasive vehicle. The orientation of one of the faces was rechecked after polishing, and was estimated to be within 1½ degrees of the desired direction. The finished faces were flat and parallel to within 0·05 mil.

Two additional pairs of faces were ground; one pair perpendicular to the a-axis [010], and one pair perpendicular to an axis 45° to the a and c axes. In each case flatness and parallelism were within 0·05 mil. The cross sections were sufficiently large to permit the use of ½ in. diameter transducers for each set of faces. The acoustic path lengths were: ‖ c-axis, 2·0222 cm; ‖ a-axis, 2·4065 cm; 45° to a- and c-axes, 2·0945 cm. A diagrammatic sketch of the finished crystal, including directions of propagation, is shown in Fig. 1.

The transducers were x-cut and y-cut quartz crystals of the wraparound type. These were bonded to the specimen under pressure by means of salol (phenylsalicilate). The bond thicknesses were between 0·05 and 0·1 mil. Ground contact to the outer wraparound plating was accomplished by a gold-plated spring washer.

2C. TECHNIQUE

The technique used to measure acoustic velocities is designated "Method II" in Ref. 1. It consists in producing acoustic standing waves in a composite oscillator made up of the transducer,

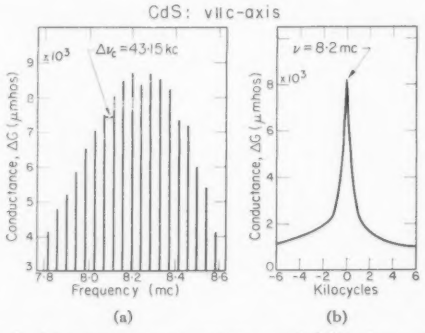

FIG. 2. (a) cw resonance spectrum of CdS. 8 mc shear mode propagated parallel to c-axis. ΔG is the change in conductance due to the composite oscillator.

(b) Line shape of individual resonance. The Q of the line is approximately 10^4.

bond, and specimen. The resonance frequencies of the composite oscillator are observed as conductance maxima on a Q-meter. If the sample has a high mechanical Q, the observed resonance maxima are sharp and the frequencies can be measured very accurately. A typical sharp-line spectrum is that obtained for CdS, and is shown in Fig. 2. The sharp peaks of Fig. 2(a) correspond to resonance maxima; the individual resonance maxima have the shape shown in Fig. 2(b). The frequency corresponding to the envelope maximum agrees closely with the transducer frequency ν_T which was independently measured by maximizing

* Eagle–Picher Company, Miami, Oklahoma.

Vol. 17
1960

the ratio of first pulse amplitude to the initiating pulse amplitude on the pulse-echo display.

Since the velocity of sound only in the specimen is of interest, one must express the specimen resonance frequencies in terms of the measured resonance frequencies of the composite oscillator. This can be done by analogy with the equivalent circuit of simple electrical transmission lines. The relationship is[1]:

$$v_{S,n} = \frac{2l_S}{n}\left[\nu_{C,n}\left(1-\frac{m_B}{m_S}\right)+\frac{m_T}{m_S}(\nu_{C,n}-\nu_T)\right] \tag{1}$$

where $m = \rho l$, ρ is the density, l the length, and the subscripts S, B, and T designate respectively the specimen, bond, and transducer. n is the effective number of half wavelengths in the specimen $n\lambda/2 = l_S$, at the observed resonant frequency $\nu_{C,n}$ of the composite oscillator. The expression for n in terms of the observed resonance maxima is:

$$n = \frac{\nu_{C,n}}{\Delta\nu_C}\left(1-\frac{m_T}{m_S}\right) \tag{2}$$

where $\Delta\nu_C$ is the measured frequency difference between adjacent half wave resonances $\nu_{C,n}$ and $\nu_{C,n-1}$. From equations (1) and (2) it is seen that the precision of the cw technique depends only upon the measurements of frequency, density, and length.

The procedure followed in the present work was to measure a number of resonance frequencies $\nu_{C,n}$ above and below the transducer frequency ν_T. From these, an average $\Delta\nu_C$ was computed, and n obtained by applying equation (2). Knowing n, equation (1) was then used to obtain the velocities of sound in the specimen. A typical set of calculations to obtain the velocity of sound is given in Table 1. In the case of the present sample, the large values of l_S allow one to neglect the terms containing m_B/m_S and m_T/m_S in equation (2) and to use, instead, a simplified form of equation (1):

$$v_S = \frac{2l_S}{n}\nu_{C,n} \tag{3}$$

without introducing an error of more than 0·05 per cent in the values of v_S. Equations (2) and (3) may be combined to obtain the expression

$$v_S = 2l_S\frac{\Delta\nu_c}{\left(1-\dfrac{m_T}{m_S}\right)}.$$

A scatter in the values of $\Delta\nu_c$, however, will then introduce a corresponding scatter in the values of v_s. If, as in the present work, the scatter in $\Delta\nu_c$ does not produce an ambiguity in the integer n, the error due to this scatter is eliminated by using $\Delta\nu_c$ *only* to obtain the proper value of n.

In addition to the cw measurements, the acoustic wave velocities were measured at 10 mc by the ultrasonic pulse-echo technique using a *rectified* wave train. It has been found[1] that the rectified pulse technique requires appreciable corrections

Table 1. *Calculation of acoustic wave velocity* v_2' *in* CdS (*bond neglected*)

$(1-m_T/m_S = 0{\cdot}9946)$

$\nu_{C,n}$*(Kc)	$(\Delta\nu_C)_{ave}$(Kc)	$\frac{\nu_{C,n}}{(\Delta\nu_C)_{ave}}$	$\left(1-\frac{m_T}{m_S}\right)\frac{\nu_{C,n}}{\Delta\nu_C}$	n	$\frac{2l_S}{n}$ (10^{-2} cm)	$v_2' = \frac{2l_S}{n}\nu_C$($10^5$ cm/sec)
9908·37						
9951·58		230·4	229·1	229	17661	1·7575
9994·85		231·4	230·1	230	17584	1·7575
10,037·92	43·19	232·4	231·1	231	17508	1·7574
10,081·11		233·4	232·1	232	17433	1·7574
10,124·30		234·4	233·1	233	17358	1·7574
10,167·49		235·4	234·1	234	17284	1·7573

* It has been found in practice that where there is an appreciable scatter in $\Delta\nu_C$ a consistent value of $(\Delta\nu_C)_{ave}$ is obtained by averaging frequency differences among mechanical resonance frequencies on the low frequency side of the central resonance.

Table 2. Measured acoustic wave velocities in CdS *at* 27°C

Direction of Propagation	Path Length (cm)	Mode	Direction of Particle Motion	Derived Elastic Constants	Symbol	Velocity (10^5 cm/sec)
$z = \parallel c$-axis	2·0222	Long.	z [001]	c_{33}	v_1	4·414 ± 0·005
		Trans.	y [210]	c_{44}	v_2'	1·7571 ± 0·001
		Trans.	x [010]	c_{44}	v_2'	1·7574 ± 0·001
		Trans.	45° to a	c_{44}	v_2''	1·7575 ± 0·001
$x = \parallel a$-axis	2·4065	Trans.	z [001]	c_{44}	v_3	1·7565 ± 0·001
		Trans.	y [210]	c_{66}, c_{12}	v_4	1·8271 ± 0·001
		Long.	x [010]	c_{11}	v_5	4·181 ± 0·004
45° to a-axis and c-axis	2·0945	Trans.	x [010]	c_{66}, c_{12}	v_6	1·794 ± 0·005
		Quasi-Long.	$y' = -45°$ to c (Fig. 1)	c_{13}	v_7	4·142 ± 0·005
		Quasi-Trans.	$z' = 90°$ to y'; 45° to c	c_{13}	v_8	2·116 ± 0·01

for end effects. The results of the pulse measurements were therefore compared with the corrected cw results. In the present measurements, the necessary correction to the velocity as measured by the rectified pulse technique amounted to 1·00 ± 0·05 per cent for a transducer thickness of 7·8 mils and an acoustic path length in the sample of 2·0222 cm.

3. RESULTS

The measured acoustic wave velocities at 27°C are listed in Table 2.* These were obtained directly from the cw measurements by the use of equation (3). The estimated maximum uncertainties in the values of the velocities are given in Table 3. The estimated errors due to angular misorientation were calculated using the formulae of WATERMAN[3].

Table 3. Estimated uncertainties for velocities

Lengths	
Specimen	0·04 per cent
Transducer	negligible
Bond	negligible
Frequency	0·01 per cent
Orientation	0·03 per cent
Neglect of $(1-m_B/m_S)\ v_{C,n}$ term	0·03 per cent
Neglect of $m_T/m_S\ (v_{C,n}-v_T)$ term	0·05 per cent
Maximum Probable Error	0·08 per cent

Table 4 gives the values of the elastic stiffness constants obtained from the measured velocities, as well as the elastic compliance constants s. The X-ray density $\rho = 4{\cdot}825$ g/cm^3 was used to calculate the elastic constants. The density was computed from the X-ray lattice constants $a = 4{\cdot}136$ Å and $c = 6{\cdot}713$ Å[4] and from the atomic weights Cd = 112·41 and S = 32·066. Table 4 includes additional properties calculated from the measurements: the linear compressibility K, parallel and perpendicular to the c-axis; the bulk modulus, B; and the anisotropies A_1 and A_2.

Internal checks were provided by the following comparisons:

For c_{44}:

$$(v_2)^2_{\text{ave}} = (3{\cdot}088 \pm 0{\cdot}002) \times 10^{10} \text{ cm}^2/\text{sec}^2$$

$$v_3^2 = (3{\cdot}085 \pm 0{\cdot}002) \times 10^{10} \text{ cm}^2/\text{sec}^2$$

For $1/2\ (c_{66}+c_{44})$:

$$v_6^2 = (3{\cdot}218 \pm 0{\cdot}002) \times 10^{10} \text{ cm}^2/\text{sec}^2$$

$$(v_2)^2_{\text{ave}} + v_4^2 = (3{\cdot}213 \pm 0{\cdot}004) \times 10^{10} \text{ cm}^2/\text{sec}^2$$

For c_{13}:

$$v_{13}^2 \text{ (from } \rho U_{ql}^2) = (9{\cdot}62 \pm 0{\cdot}15) \times 10^{10} \text{ cm}^2/\text{sec}^2$$

$$v_{13}^2 \text{ (from } \rho U_{qt}^2) = (9{\cdot}51 \pm 0{\cdot}40) \times 10^{10} \text{ cm}^2/\text{sec}^2$$

*All velocity measurements were taken under conditions of darkness.

Vol. 17
1960

Table 4. Elastic properties of CdS

Elastic stiffness constants (in 10^{11} dynes/cm^2)

C_{11}	C_{33}	C_{44}	C_{12}	C_{13}	C_{66}
8·432	9·397	1·489	5·212	4·638	1·610

Elastic compliance constants (in 10^{-12} cm^2/dyne)

S_{11}	S_{33}	S_{44}	S_{12}	S_{13}	$2(S_{11}-S_{12})$
2·104	1·602	6·716	−1·002	−0·545	6·212

$B = 6{\cdot}15 \times 10^{11}$ dynes/cm^2

$A_1 = \dfrac{C_{33}}{C_{11}} = 1{\cdot}11$

$A_2 = \dfrac{C_{66}}{C_{44}} = 1{\cdot}08$

$\dfrac{K_\parallel}{K_\perp} = \dfrac{5{\cdot}57 \times 10^{-13}}{5{\cdot}12 \times 10^{-13}} = 1{\cdot}09$

where v_{13} is a fictional velocity defined by the equation $\rho v_{13}^2 = c_{13}$.

Since the velocities used to obtain c_{13} are related quadratically to c_{13} and other elastic constants (See Section 2A), there result two possible values of c_{13}. The ambiguity may be resolved by applying the conditions of crystal stability[5] or by comparing compressibilities calculated from the elastic constants with independent measurements of the volume or linear compressibility. In the present case, the two values of c_{13} are 4·637 and −7·615 ($\times 10^{11}$ dynes/cm^2). Both values satisfy the stability criteria: $c_{13}^2 < c_{11}\,c_{33}$ and $c_{13}^2 < \frac{1}{2}\,c_{33} \times (c_{11}+c_{12})$. The bulk moduli $B =$

$$[2(s_{11}+s_{12})+s_{33}+4s_{13}]^{-1}$$

calculated from the two values of c_{13} are 6·15 and 1·35 ($\times 10^{11}$ dynes/cm^2) respectively. Although no value for the bulk modulus of CdS is given in the literature, these values may be compared with those obtained from BRIDGMAN'S[6] data for the volume compressibility of cubic ZnS, ZnSe, and ZnTe. At room temperature and atmospheric pressure, they are 7·95, 4·05, and 4·12 ($\times 10^{11}$ dynes/cm^2). Based on this comparison among similar crystals, the proper value for c_{13} is chosen as 4·637 ($\times 10^{11}$ dynes/cm^2). It is interesting to note that the value which best satisfies the stability criteria is the proper one to choose. This also is the case in hexagonal Co.[7]

4. DISCUSSION

A notable feature of CdS is its very low anisotropy. The anisotropies in elastic stiffness, as measured by c_{66}/c_{44} and c_{33}/c_{11} are respectively 1·08 and 1·11. The anisotropy in the linear compressibilities $K_\parallel/K_\perp$ is 1·09, where

$$K_\parallel = 2s_{13}+s_{33} = 5{\cdot}12 \times 10^{-13}\ \text{cm}^2/\text{dyne}$$

$$K_\perp = s_{11}+s_{12}+s_{13} = 5{\cdot}57 \times 10^{-13}\ \text{cm}^2/\text{dyne}.$$

This nearly isotropic behaviour may be related to the closeness of the c/a value of 1·624 to the ideal value of 1·633 for the hexagonal close-packed lattice. The hexagonal metals magnesium[8] and cobalts,[7] for example, with c/a ratios of 1·623, show anisotropies ($K_\parallel/K_\perp$) of 1·04 and 1·07, while hexagonal zinc,[9] with a c/a ratio of 1·86 has an anisotropy of 7·9.

In addition to c_{44} and c_{66} there is a third elastic constant $C = c_{11}+c_{12}+2c_{33}-4c_{13}$ which corresponds to a strain which changes the c/a ratio at constant volume. For CdS, $C = 13{\cdot}89 \times 10^{11}$ dynes/cm^2.

Four of the elastic constants had been measured previously by MASUMI and TANAKA[10]. c_{13} was

not obtained by these investigators. A comparison of their results with the present values indicates differences which vary from 1 per cent for c_{66} to 7 per cent for c_{11} and c_{33} and 14 per cent for c_{12}. In each case the previous values are too low. In all likelihood the discrepancy can be attributed to the use by MASUMI and TANAKA of a rectified pulse-echo technique at relatively low frequencies (5 mc) without the application of end corrections. Such corrections become important[1] for low frequencies and for thin samples such as were used by MASUMI and TANAKA.

Acknowledgements—We wish to thank R. FARICH and J. SCHAUB for aid in sample preparation, and Dr. A. TAYLOR and Miss BRENDA KAGLE for the back reflection X-ray photographs.

REFERENCES

1. BOLEF D. I. and MENES M., *J. Appl. Phys.* **31,** 1010 (1960).
2. See, for example, SLUTSKY L. J. and GARLAND C. W., *J. Chem. Phys.* **26,** 787 (1957).
3. WATERMAN P. C., *Phys. Rev.* **113,** 1240 (1959).
4. *National Bureau of Standards Circular* **539,** IV, 15 (1955).
5. ALERS G. A. and NEIGHBORS J. R., *J. Appl. Phys.* **28,** 1514 (1957).
6. BRIDGMAN P. W., *Proc. Amer. Acad. Arts Sci.* **74,** 21 (1940).
7. MCSKIMIN H. J., *J. Appl. Phys.* **26,** 406 (1955).
8. SLUTSKY L. J. and GARLAND C. W., *Phys. Rev.* **107,** 972 (1957).
9. ALERS G. A. and NEIGHBORS J. R., *J. Phys. Chem. Solids* **7,** 58 (1958).
10. MASUMI T. and TANAKA T., *J. Phys. Soc. Japan* **14,** 1313 (1959).

J. Phys. Chem. Solids Pergamon Press 1960. Vol. 17, Nos. 1/2, pp. 149–161. Printed in Great Britain.

THEORY OF SOLUBILITY OF INTERSTITIAL IMPURITIES IN GERMANIUM AND SILICON

K. WEISER

Research Laboratory, International Business Machines Corporation, Poughkeepsie, New York

(*Received* 27 *May* 1960)

Abstract—A theory of solubility is developed which is based on estimating the change in energy and in entropy when an impurity is placed in an interstitial site in the lattice. Two distinct cases are considered, namely, the case of the impurity remaining electrically neutral, and the case of the impurity becoming an ionized donor. The species which results in the greater gain in free energy will be predominant in the lattice.

I. INTRODUCTION

THE SOLUBILITY of impurities in germanium and silicon has been the subject of much investigation because of their great importance in determining the electrical properties of these semiconductors. The most recent summary of experimental results was made by TRUMBORE[1], and the thermodynamic principles which govern the solubility have been examined by several workers in the field.[2] Recently,[3] the author developed a theory for the solubility of certain substitutional impurities, stressing the importance of strain energy caused by an impurity as well as the role of the bond energy between an impurity and the surrounding host atoms. There is, however, no theory for the solubility of interstitial impurities.

An interstitial impurity is one which lodges in an empty crystal site instead of taking the place of a host atom as a substitutional impurity. Like substitutional impurities, an interstitial impurity may be either electrically active or it may be neutral. The existence of electrically active interstitial impurities has been unambiguously demonstrated only for the case of lithium,[4] whose fast diffusion and donor properties can scarcely be interpreted in any other way but on the basis of its existence as an interstitial impurity. There is also good evidence from diffusion experiments that an appreciable fraction of copper exists in the lattice as an ionized interstitial donor, at least at high temperature.[5] Such gases as hydrogen or helium, on the other hand, which are known to be soluble in germanium and silicon,[6] do not affect the electrical properties, and hence it is reasonable to assume that they also occupy interstitial positions.*

The theory presented here aims at an understanding of the factors which govern the solubility of both neutral and ionized interstitials. In particular, it attempts to show how one can predict whether an interstitial impurity will be ionized or neutral. It also attempts to predict the order of solubility within each category for various impurities.

II. THERMODYNAMIC FRAMEWORK

The fundamental condition of equilibrium governing the solubility of any impurity is that its chemical potential in the host crystal must equal its chemical potential in the external phase.[8]

The solubility of an impurity in the host crystal cannot, therefore, be considered independently of its thermodynamic properties in the external phase with which the solid is in equilibrium. If, for example, the pressure of the impurity in the vapor phase is changed, its chemical potential is also changed, and hence its solubility will be

* Oxygen represents a special case since it appears to occupy an interstitial position yet is chemically bonded to the host atoms.[7] Since this paper deals only with interstitial impurities which do not form such bonds, its solubility will not be considered here.

affected. The ratio of the concentration of the impurity in the solid, c_s, to that in the external phase c_{ext} is given by[8]:

$$\ln\frac{c_s}{c_{ext}} = -\frac{\Delta H_s^{ext}}{kT} + \frac{\Delta S_s^{ext}}{k}. \qquad (1a)$$

where ΔH_s^{ext} represents the energy* needed to transfer the impurity from the external phase into the crystal, and ΔS_s^{ext} is the "excess" entropy accompanying this transfer.† Since there will always be a vapor phase in equilibrium with the solid there will always be a distribution of the impurity between the two phases, which will be given by:

$$\ln\frac{c_s}{c_v} = -\frac{\Delta H_s^v}{kT} + \frac{\Delta S_s^v}{k} \qquad (1b)$$

where c_v is the concentration of the impurity in the vapor phase and ΔH_s^v and ΔS_s^v are the energy and entropy change involved in transferring the impurity from the vapor phase into the host crystal. If the impurity is a gas at the temperature of interest, i.e. it is above its critical point, the concentration in the vapor phase would ordinarily be known in any determination of its solubility, and hence equation (1b) would be useful. If, on the other hand, the impurity is either a solid or a liquid, it is generally introduced by dissolving it in the melt and then growing a crystal. Under these circumstances its concentration in the vapor phase is not usually known, and it is then convenient to consider the distribution of the impurity between the crystal and the melt. For a clearer understanding of the terms ΔH_s^{ext} and ΔS_s^{ext} in this case, it is desirable to break each one up into several parts, and to re-write equation (1a) as[2a]:

$$\ln\frac{c_s}{c_m} = -\frac{\Delta H_s^{cr} - \Delta H_m - H_f}{kT} + \frac{\Delta S_s^{cr} - \Delta S_m - S_f}{k} \qquad (1c)$$

The ratio c_s/c_m is the familiar "segregation constant" for crystal growing experiments with the superscript m standing for melt. H_f and S_f are the heat and entropy of fusion of the pure solute. ΔH_s^{cr} and ΔS_s^{cr} are the energy and entropy required to transfer the solute from its own crystalline lattice into the lattice of the host crystal, and ΔH_m and ΔS_m are the energy and entropy required to transfer the solute from its own molten state into the melt in equilibrium with the solid. Equation (1c) was first applied by THURMOND and STRUTHERS to impurity–semiconductor systems.[2a]

In this paper methods for estimating the energy and entropy of solid solution will be developed for both neutral and ionized interstitial impurities. In other words, the terms ΔH_s^v and ΔS_s^v of equation (1b), and ΔH_s^{cr} and ΔS_s^{cr} of equation (1c) will be estimated. It is clear from equation (1b) that if the impurity is a gas of known pressure such a theory can predict its solubility. Equation (1c), on the other hand, shows that if the impurity is a solid or liquid at the temperature of interest the theory can predict the segregation constant only if ΔH_m and ΔS_m are known from liquid state theory or from experiment. Fortunately, the latter is the case for many impurities of interest.[9]

The discussion will be limited to infinitely dilute solutions; absence of other impurities, which could interact with the impurity in question,[2d] is also assumed.

III. NEUTRAL IMPURITIES

(a) *Heat of solution*

Since the neutral interstitial impurities which have been observed are such gases as hydrogen or helium, the distribution between the solid and the vapor phase, equation (1b), is directly useful. For gases at moderate pressures, i.e. around one atmosphere or less, the interaction energy between atoms or molecules is negligible,[10] and hence the heat of solution, ΔH_s^v, will be given essentially by the interaction energy of the impurity with the surrounding host atoms. If an impurity on an interstitial site does not ionize, nor bind itself chemically to the surrounding host atoms its interaction with them must be of the van der Waals type characteristic of the interaction between atoms or molecules of saturated valence.[11] There

* ΔH_s^{ext} actually represents a change in enthalpy and differs from the change in energy by an amount $p\Delta V$, where ΔV is the change in volume accompanying the transfer of the impurity. At atmospheric pressures the difference is negligible.

† The word "excess" has to be inserted in order to differentiate ΔS from the ordinary entropy of solution $R \ln c$.[8]

Vol. 17
1960

will thus be an attractive and repulsive potential between the impurity and the host atoms.

Neglecting higher order terms in the distance between the atoms or molecules (i.e. neglecting dipole–quadrupole, quadrupole–quadrupole, etc. interactions) the London equation[12] for the attractive energy between two atoms or molecules 1 and 2 is given by:

$$U_{\text{att}} = -\frac{3}{2r^6}\alpha_1\alpha_2\frac{\Delta E_1 \Delta E_2}{\Delta E_1+\Delta E_2} \qquad (2)$$

In this equation, the α's stand for the polarizabilities, and the ΔE's stand for characteristic excitation energies of the species involved. London suggested that the ionization energies of the atoms or molecules should be used for the ΔE's, and with this approximation the expression has been used with good results to calculate both the attractive energy in gases[13] and heats of sublimation of molecular crystals.[14]

Since these "dispersion" forces are approximately additive,[13] the total attractive energy between the impurity atom and the host lattice is given by summing equation (2) over all the impurity–host atom pairs in the crystal. An interstitial atom has four nearest neighbors at the interatomic distance a_0, and six nearest neighbors at a distance $1{\cdot}14\,a_0$.[15] Contributions from host atoms of the second and third shell are negligible. Equation (2), applied to nearest neighbors, thus becomes:

$$U_{\text{att}} = -\frac{3}{2}\alpha_h\alpha_i\frac{(\text{I.P.})(E_h)}{(\text{I.P.})+(E_h)}\left(\frac{4}{a_0^6}+\frac{6}{(1{\cdot}14a_0)^6}\right) \qquad (2a)$$

where the subscripts h and i stand for host and impurity atoms respectively, and I.P. stands for the ionization potential of the impurity. A characteristic energy for the host crystal atoms, E_h was inserted to modify the London formula for the case where only one of the interacting atoms is free while the other one forms part of a crystal lattice. The probable value of E_h will be discussed below.

The impurity atom or molecule will also experience a repulsive potential in its interaction with the surrounding host atoms. The repulsion is that found between atoms with closed shells, or between molecules or ions.[11] A semi-rigorous theoretical treatment of the problem has been given only in a few instances,[16] and no simple analytical expression for the repulsive energy resulted from these attempts. Empirically it is found that expressions of the form $U = b\exp(-r/\rho)$, or $U = \lambda r^{-s}$ for the repulsive or overlap energy between two non-reacting atoms, ions or molecules, a distance r apart, can be used in the interpretation of gaseous virial coefficients and of the cohesive energy of ionic and molecular crystals;[17] b, ρ, λ and s are empirical parameters. If the two atoms are different the repulsive energy can be written as $\lambda_{12}\,r^{-s}$, where

$$\lambda_{12} = [\tfrac{1}{2}(\lambda_{11}^{1/s}+\lambda_{22}^{1/s})]^s;$$

λ_{11} and λ_{22} refer to the repulsive parameters for atoms of the same kind.[17] The experimental data can be fitted with s between 7 and 12, though for solids $s = 9$ seems to give the best results. If the interacting atoms are different any self-consistent scheme will, of course, give the same results, i.e. as long as the repulsive parameters for the individual atoms were chosen for the same value of s. The repulsive energy between the impurity and its ten nearest neighbors will be assumed to be given by:

$$U_{\text{rep}} = [\tfrac{1}{2}(\lambda_i^{1/9}+\lambda_h^{1/9})]^9\left[\frac{4}{a_0^9}+\frac{6}{(1{\cdot}14a_0)^9}\right] \qquad (3)$$

where λ_i is the repulsion parameter for the impurity, and λ_h is the characteristic repulsion parameter of the host atoms. It is assumed for the time being that the host atoms surrounding the impurity remain in their normal position and the effect of this assumption is examined later.

The total interaction energy of the neutral impurity and the host atoms will be given by adding equations (2a) and (3).

(b) *Entropy of solution*

We shall consider the impurity embedded in the solid as essentially still in the gaseous form since its interaction energy with the host crystal is much too small and in most cases actually of a repulsive nature (see Sec. IIIc) to be considered a heat of condensation which would be of the order of a few eV. For the same reason, we shall consider the vibrational modes of the solids as being essentially unaffected by the presence of a weakly

interacting impurity. The entropy of the solid will, therefore, be considered largely unchanged.

The only change in entropy which we will consider is that caused by a reduction of the phase space available to the impurity atom when it is immersed in the solid. Due to the presence of the host atoms which we will regard as hard spheres of diameter a_0, the volume available to the impurity atoms is $V_{at}-N(\pi/6)a_0^3$, where V_{at} is the atomic volume, and N is Avogadro's number. The change in entropy upon restricting a gas from a volume V to a volume V' is equal to $k \ln V'/V$,[10] and hence the change in entropy for the impurity atoms is given by:

$$\Delta S_s^v = k \ln \frac{V_{at}-N\frac{\pi}{6}a_0^3}{V_{at}} = k \ln 0{\cdot}7 \qquad (4)$$

for both silicon and germanium.

(c) *Estimate of interaction energies and solubilities of various neutral impurities*

According to equation (4) the entropy of solution should be approximately the same for all neutral impurities, and hence a theoretical estimate of the solubility rests on an estimate of the heat of solution. It will be clear from the discussion which follows that such an estimate can only be done very roughly. The attempt is important, however, in order to establish the order of magnitude of the heat of solution for the case of the impurity entering the lattice as a neutral solute as compared to the case when it enters it as an ionized solute.

If the parameters which appear in equations (2a) and (3) are known for the impurity, i.e. its polarizability, ionization potential and repulsion constant, an estimate of the heat of solution depends on a proper assignment of values for α_h, E_h and λ_h. It is tempting to obtain these parameters from experimental data since it is difficult to estimate them from bulk properties of the crystals, as will be seen below. If the theory is correct these constants can be calculated from a knowledge of the solubility of three neutral impurities for which α_i, I.P. and λ_i are known. Of the three impurities whose solubilities have been determined, the results for atomic hydrogen[6a,c] cannot be used since its repulsion parameter is not known. The results for molecular hydrogen[6b] and for helium[6a] are incompatible since with similar values of the impurity parameters their reported solubilities differ by more than four orders of magnitude. Of the two investigations the one of molecular hydrogen by THURMOND, GULDNER and BEACH[6b] appears more reliable since it was obtained by a straightforward method, while the data of VAN WIERINGEN and WARMOLZ for helium[6a] were obtained by a permeation technique which gave good results for atomic hydrogen, but showed much scatter for helium. It is, therefore, not possible to evaluate the host atom parameters from experimental results, and it is necessary to make at least a rough estimate of their values from the bulk properties of the host crystal. This can be done for α_h and E_h.

The polarizability of a host atom can be estimated approximately from the Lorentz–Lorentz equation relating the dielectric constant ϵ_0, to the atomic polarizability[18]:

$$\frac{\epsilon_0-1}{4\pi} = \frac{N\alpha}{1-\frac{4}{3}\pi N\alpha} \qquad (5)$$

N = number of atoms per cm^3. This equation, valid for cubic structures, applies only to isolated, non-interpenetrating atoms. It is difficult to estimate the error involved in applying it to the diamond lattice in which the wave functions of the atoms certainly do interpenetrate.* Equation (5) will, however, be used in the hope that it gives at least approximately the right result for α_h. Table 1 lists the estimated polarizabilities for diamond, silicon and germanium, together with the parameters used to calculate them. The last column lists the interatomic distance to the third power for these elements. It is gratifying to see that the calculated polarizabilities are approximately proportional to d_0^3, i.e. to the volume occupied per atom, as expected from the classical theory of atomic polarizability.[11]

As for E_h it is an energy characteristic of an excited state of the atom, and it must, therefore, lie somewhere in the conduction band. Its value should, therefore, lie between the energy gap[20] and the work function,[22] i.e. between about 1 and

* MOTT and GURNEY[18] have shown how to correct for this effect, but their method merely introduces a correction factor into the equation which cannot be determined *a priori*.

Vol. 17
1960

Table 1. *Estimated atomic polarizabilities in the diamond lattice from equation* (5)

	ϵ_0*	N†	α_h(cm^2)	d_0^3 (Å^3)[21]
Diamond	5·7	$17{\cdot}6\times10^{22}$	$1{\cdot}3\times10^{-24}$	3·7
Silicon	12·0	5·1	3·7	12·7
Germanium	16·0	4·5	4·5	14·5

* The dielectric constant for diamond was taken from the work of WHITEHEAD and HACKETT;[19] for germanium and silicon the values were taken from Conwell's review article.[20]

† Calculated from known densities, atomic weights and interatomic distances.[21]

5 eV for silicon and germanium. We shall take the arithmetic mean of 3 eV as an approximate value.

The magnitude of λ_h is the most difficult of all to estimate, and will be obtained from the experimental data on the solubility of molecular hydrogen, namely, 3×10^{18} cm^{-2} at the melting point of germanium.[6b] This value for c_s and a value for c_v calculated from ideal gas laws was used in equation (1b), together with equation (4) for the entropy of solution. With these

Table 2. *Calculated interaction energies and solubilities of various neutral impurities in germanium. Absence of chemical bonding is assumed. Host atoms parameters:* $\alpha_h = 4{\cdot}4\times10^{-24}$ cm^2, $E_h = 3$ eV, and $\lambda_h = 4\times10^{-82}$.

	U_{att} (eV)	U_{rep}† (eV)	$U_{int} = -U_{att}+U_{rep}$	Solubility* (atoms cm^3 at 1210°K)
H	0·31	assumed negligible	−0·31	10^{13}
H_2	0·43	0·47	0·04	10^{18}
He	0·11	0·18	0·07	10^{18}
Ne	0·22	0·46	0·24	10^{17}
A	0·87	2·38	1·41	10^{12}
N_2	0·93	2·84	1·91	10^{10}

* The concentration of the impurity in the gas phase was taken as that corresponding to one atmosphere pressure except for the case of atomic hydrogen where it was taken as the concentration produced by the thermal dissociation of molecular hydrogen at 1210°K.

† As was pointed out before, it was assumed in the above treatment of the repulsive energy that the host atoms surrounding the impurity remain in their normal position. If we make allowance for the possibility of these atoms moving away from the impurity the repulsive energy can be somewhat reduced. Let the total repulsive energy U_{rep}^{tot} be given by:

$$U_{rep}^{tot} = \lambda(i,h)\left[\frac{4}{(a_0+\Delta a_0)^9}+\frac{6}{(1{\cdot}14a_0+\Delta a_0)^9}\right]+8\pi\, G a_0(\Delta_a)^2$$

where the first term has been discussed before (see equation (3) and the second term represents the strain energy resulting from the expansion of the cavity of radius a_0 by an amount Δa.[25] Differentiating with respect to the radius, we can find a value which minimized the total repulsive energy, in a manner similar to the one employed by the author to calculate strain energies of substitutional impurities.[3] The resulting decrease depends on the value of λ_{12}. For small values of λ_{12} (e.g. H_2 or He), the repulsive energy is not changed appreciably, while for large values of λ_{12}, (e.g. A or N_2), the repulsive energy is reduced by at most 30 per cent. Since the estimates of λ_{12} are not believed to be accurate to within 30 per cent the details of the calculations are not included in this paper.

substitutions we obtain a heat of solution of 0·035 eV. With the known values for α_i,[13] I.P.[23] and λ_i[17] for molecular hydrogen and our estimated values of $E_h = 3$ eV and $\alpha_h = 4{\cdot}5 \times 10^{-24}$ cm^2 in equations (2a) and (3), we must use $\lambda_h = 4 \times 10^{-82}$ in order to obtain a total heat of solution of 0·035 eV.

Having found approximate values for the host atom parameters, it is possible to estimate the heat of solution of various impurities in germanium. Table 2 lists the results of the calculations.

Several conclusions are immediately obvious from Table 2: (a) The interaction energies are small (of the order of a few tenths of an electron volt) at least for the lighter elements. These results should be compared to the heat of solution for ionized impurities (Sect. IVa), which are generally considerably larger. (b) The theory predicts similar and large solubilities for the lighter elements, but drastically smaller solubilities for argon and nitrogen.* The reason is that the repulsive energy increases more rapidly with increasing size of the impurity than does the attractive energy. (c) Crystals grown in a hydrogen atmosphere should contain the gas in molecular rather than in atomic form.

As for comparison with experiment, the predicted solubility of atomic hydrogen is in satisfactory agreement with that found by FRANK and THOMAS[6c]. The theoretical results are based on the assumption that the repulsive energy is negligible, or that λ_i for hydrogen atoms, for which no experimental data are known, is considerably smaller than λ_h. The theory predicts a much larger solubility for helium than was found by VAN WIERINGEN and WARMOLTZ[6a], whose experiments may, however, be in error, Finally, it should be mentioned that one may expect the results for silicon to be similar to those for germanium since the host atom parameters α_h, E_h and λ_h are probably comparable for the two elements.

IV. IONIZED IMPURITIES

(a) *Heat of solid solution*

Those interstitial impurities which are known or thought to be ionized, e.g. Li or copper, are well below their critical points at the melting temperatures of germanium or silicon. According to the discussion in Section II the crystalline state of the impurity is, therefore, the most convenient reference state to use. The heat of solid solution can then be calculated by summing the energies involved in the steps necessary to transfer the impurity from its own crystal lattice into the host crystal at infinite dilution. The following sequence of steps can be postulated: (1) The impurity is evaporated from its crystalline lattice; E_1 = heat of sublimation, ΔH^v. (2) The impurity in the gas phase is ionized; E_2 = ionization potential, I.P. (3) The electron is dropped to the Fermi level of the host crystal; E_3 = work function of the host crystal, W.F.†[26] (4) The ion is placed in an interstitial site simultaneously with step 3 so as to preserve charge neutrality. The energy gained in this step is the polarization energy, which is liberated whenever a charge is embedded in a dielectric medium.[27] If the ion has appreciable size there will also be a repulsive potential between it and the surrounding host atoms, exactly as in the case of neutral impurities. Hence, $E_4 = -U_{\text{pol}} + U_{\text{rep}}$, where U_{rep} is given by equation (3). The total heat of solution, starting from the pure crystalline solute, will thus be given by:

$$\Delta H_s^{\text{cr}} = \Delta H^v + \text{I.P.} - \text{W.F.} - U_{\text{pol}} + U_{\text{rep}} \quad (6)$$

The first terms of equation (6) are readily measurable, and hence a theoretical estimate of the heat of solution depends on a calculation of U_{pol} and U_{rep}. An expression for the repulsive potential was already given in equation (3). An approximate value for the polarization energy can be obtained by assuming that the ion is in spherical cavity of radius R, surrounded by a continuous medium of dielectric constant ϵ. This model yields the expression[27]:

$$U_{\text{pol}} = \frac{e^2}{2R}\left(1 - \frac{1}{\epsilon}\right) \quad (7)$$

The result is of the order of 3 eV for germanium

* It must be emphasized again that absence of chemical bonding was assumed. If nitrogen behaves similarly to oxygen,[7] the above results do not, of course, apply.

† Since the work function represents the change in free energy when an electron is placed into the crystal, a quantity $T\,dW/dT$ must be subtracted from the experimental value to obtain the energy part of the work function. From measured values of dW/dT for germanium,[22] we conclude that this quantity is negligible.

or silicon, using for R the distance from the ion to a nearest host atom. In Section IVc and in the Appendix a more exact estimate will be discussed, but with this approximate value the following main conclusion about the solubility of an impurity as an ionized interstitial can be drawn from equation (6)*: The solubility will be appreciable only if the sum of the heat of sublimation and the ionization potential is small or comparable to the sum of the work function and the polarization energy. For germanium and silicon, this condition means that $\Delta H^v + \text{I.P.}$ must not be much larger than about 8 eV.

(b) *Entropy of solution*

The excess entropy of solution, ΔS_s^{cr} is the entropy change, as one g-atom of the impurity is transferred from its own lattice to an interstitial site in the host crystal. We can formally write this entropy change as:

$$\Delta S_s^{cr} = S_h + k \ln \sum_{i=1}^{3N} \frac{\nu_i'}{\nu_i} - S_i \qquad (8)$$

in the manner recently suggested by FREEDMAN and NOVICK[28]. Equation (8) expresses the entropy of the host crystal containing the impurity as the original entropy S_h plus a change in the entropy, $k \ln \Sigma \nu_i'/\nu_i$, caused by the presence of the ion and excess electron. The unprimed ν_i's are the characteristic frequencies of the host crystal, the primed ν_i's the frequencies after the introduction of the impurity. S_i is the entropy of the impurity in its crystalline state. We may estimate the magnitude of $k \ln \Sigma \nu_i'/\nu_i$ by considering the temperature dependence of the energy of polarization [equation (7)], and of the work function, the former giving the contribution of the ion, the latter that of the electron.[26,27]

$$k \ln \sum \frac{\nu_i'}{\nu_i} \approx \frac{d}{dT}\frac{e^2}{2R}\left(1 - \frac{1}{\epsilon}\right) + \frac{d}{dT}\text{W.F.}$$
$$\approx \frac{e^2}{2R}\frac{1}{\epsilon}\frac{\partial \ln \epsilon}{dT} + \frac{d}{dT}\text{W.F.} \qquad (9)$$

For germanium and silicon $d\text{W.F.}/dT$ was found to be negligible within experimental error.[22] From the experimental value for $d \ln \epsilon/dT$[29] one may therefore estimate $k \ln \Sigma \nu_i'/\nu_i$ to be equal to about 2×10^{-4} eV/deg for germanium or silicon.

(c) *Estimate of solubility of some ionized impurities.*

Comparison with experiment. For a quantitative estimate of the solubility of impurities as ionized interstitials a better evaluation of polarization energy than is given by equation (7) is needed. MOTT and LITTLETON[31] have shown how this problem can be solved to any degree of accuracy for a crystal lattice; this is done by actually computing the dipoles induced on the atoms of the crystal, and then summing their contribution to the potential at the charge site. In the Appendix some details of their method are described, and the results of its application to the case of a charge on an interstitial site in the diamond lattice are given. The computations, carried to a third order approximation, yield the value of 3·6 eV for both germanium and silicon. The use of the method is subject to the same criticism as the use of the Lorentz–Lorentz equation (equation 5) for the calculation of the polarizability per atom, namely, that it assumes non-interpenetrating atoms.

Unfortunately, no experimental verification of these calculations is possible. The only ionized impurity in germanium and silicon for which reliable experimental data of the solubility are available is lithium.[4] If the lithium pressure above the host crystal were also known as a function of temperature, the heat and entropy of solid solution could be obtained directly by the use of equation (1b), and an excellent check on the theory would be provided. Such data for lithium would be especially valuable since its ion is so small ($r = 0{\cdot}60$ Å) that the repulsive energy term of equation (6) is negligible; such data would therefore constitute an excellent check for the calculated value of the polarization energy. Unfortunately this information is not available although PELL[4a] has studied the distribution coefficients of lithium in both germanium and silicon as a function of temperature. According to equation (1c), however, such data yield heat and entropy terms from which one can only obtain the difference between the heat of solution in the solid and that in the melt, and similarly for the entropy. In many cases the

* In Section IVb it is shown that the entropy of solution is small so that the solubility is determined mainly by the heat of solution as in the case of neutral interstitials.

heats and entropies of solution in the melt, ΔH_m and ΔS_m, are known or else are small so that the temperature dependence of the distribution coefficient can be used to check the theory for the heat and entropy of solid solution.[3] In the case of lithium, however, PELL established that compounds exist between it and germanium and silicon, and hence the lithium in the melt may be chemically bonded. In any case, nothing is known experimentally for ΔH_m and ΔS_m in this case. We shall, therefore, use the theoretical result for the polarization energy, i.e. $U_{\text{pol}} = 3{\cdot}6$ eV, together with equation (3) for the repulsive energy, in estimating the heat of solid solution ΔH_s^{cr} for various impurities. For the entropy of solution, ΔS_s^{cr}, we shall use equations (8) and (9). With the theoretical values for ΔH_s^{cr} and ΔS_s^{cr} and the values for ΔH_m and ΔS_m which were recently deduced by THURMOND[9] from experimental data, equation (1c) can be used to calculate segregation constants for various ionized impurities. Table 3 lists the results, together with experimental values of the substitutional segregation constant (column 5). The last column gives the calculated ratio of interstitial to substitutional concentrations of the impurity.

It is first of all of interest to compare the results for the four elements listed in Table 3 relative to each other rather than to consider absolute values. The theory predicts that the ratio of the interstitial form to the substitutional form should be greatest for silver, followed by copper and nickel, and finally negligible for gold. In the case of silver the interstitial form is favored in spite of the large size of the ion because of the relatively small ionization potential. In the case of gold, the ratio is negligible because of the large ion size as well as because of the large ionization potential. The observed donor level in gold is therefore probably not due to interstitial gold.[32]

The case of copper merits special attention because of the considerable body of work done in investigating this element. Estimates of the ratio of ionized interstitial copper to substitutional copper, based on diffusion experiments, range from one per cent[5d] up to as much as fifty per cent.[5e] In any case, these estimates are higher by a factor of 10^4 to 10^5 than the ratio shown in Table 3. If the estimates based on diffusion are correct this discrepancy suggests that the calculated heat of solution, ΔH_s^{cr}, is too high by somewhat over 1 eV. The only theoretical calculations involved in the heat of solution are the polarization energy and the repulsive energy. The repulsive energy is only 0·2 eV, and hence, it would mean that the polarization energy should be larger, i.e. more negative, by about 1 eV. Such an error is possible, though unlikely. If the polarization energy is 4·6 eV instead of 3·6 eV all values would be raised by a factor of 10^4 so that, for example, the ratio of interstitial to substitutional silver would be of the order of unity. Another explanation which would reconcile the estimates derived from diffusion experiments and the values obtained

Vol. 17
1960

Table 3. Calculated ratios of interstitial to substitutional forms for various impurities in germanium (1210°K). *Full ionization of interstitials is assumed.*

	r(Å)[31]	U^*_{rep}(eV)	†ΔH_s^{cr}(eV)	k_{int} (calc.)	k_{subst} (exptl.)	$c_{\text{int}}/c_{\text{subst}} = k_{\text{calc}}/k_{\text{exptl}}$
Cu	0·96	0·2	2·9	10^{-11}	10^{-5}	10^{-6}
Ni	0·96	0·2	3·7	10^{-14}	10^{-6}	10^{-8}
Ag	1·26	0·9	2·9	10^{-11}	10^{-7}	10^{-4}
Au	1·37	1·4	5·8	10^{-21}	10^{-5}	10^{-16}

r = ionic radius.

* In estimating the repulsive energy with equation (3), we have used $\lambda_h = 0{\cdot}4 \times 10^{-81}$, as derived in Section IIIc. The repulsion parameter of the ion was estimated by interpolation from a plot of the λ values for positively charged ions listed by FOWLER[17] against their ionic radii.

† In calculating ΔH_s^{cr} (equation 6), the values for the heat of vaporization were taken from STULL and SIMKE[24], values for the ionization potentials from SLATER[11]. Values for the heats and entropies of fusion which appear in equation (1c) were also taken from STULL and SIMKE.

here, is based on a paper by KAUS[33]. KAUS suggests that for such elements as copper, silver or gold in an interstitial position in germanium or silicon, the donor electron may be less tightly held than by a hydrogen atom, but more tightly than by a lithium atom. In other words, the author postulates deep-lying donor levels for these elements, possibly buried in the valence band. If this picture is correct, it would mean that the copper is not fully ionized as is assumed here.

V. PREDICTION OF PREDOMINANT FORM OF THE IMPURITY IN THE LATTICE

The question finally arises how the theory can predict the predominant form in which a given impurity exists in the lattice. Some of the atoms of a given impurity may, for example, exist on substitutional sites, while others may be neutral interstitials and yet others may be ionized interstitials. The predominant species will be that which leads to a maximum decrease of the free energy when the impurity is introduced into the lattice. Since the contribution of the entropy to the free energy is small compared to that of the energy at the temperatures of interest here, it is simpler to examine the question with respect to the energy or heat of solution only.

As a first example, we shall discuss why lithium atoms enter germanium as ionized interstitials while hydrogen atoms enter as neutral interstitials. We assume both atoms to be initially in the vapor phase. From equation (6), subtracting ΔH^v and using $U_{\text{pol}} = 3{\cdot}6$ eV, we calculate $\Delta H_s^v = -3{\cdot}0$ eV, if lithium enters as an ionized impurity. From equations (2a) and (3), on the other hand, we estimate a ΔH_s^v of only $-0{\cdot}2$ eV, if it enters as a neutral impurity. In calculating the gain in energy for the latter case, we have neglected the repulsive energy, and we have estimated a rather high polarizability of $0{\cdot}4 \times 10^{-24}$ cm for the lithium atom. The actual gain in energy for the neutral case is, therefore, a good deal smaller, and the process may even require an expenditure of energy. It is clear, therefore, why lithium exists as an ionized interstitial. A similar calculation for hydrogen, on the other hand, shows that the opposite holds true, the incorporation as an ionized impurity requiring an energy of 5·1 eV while the incorporation as a neutral interstitial yields about 0·3 eV (Table 2). The difference between the two impurities lies mainly in the large difference in ionization potentials.

It is interesting to compare the approach used here to that used by REISS[34] and by KAUS[33] who arrived at the same conclusion on the basis of quantum mechanical calculations. Both of these authors calculated the energy of an *s*-electron of various impurities by solving the wave equation for the case of the impurity embedded in an interstitial spherical cavity surrounded by a dielectric medium (the semiconductor crystal). Inside the cavity the electron experiences a potential which is composed of the potential it sees in the isolated atom plus a contribution from the surrounding dielectric. Outside the cavity the potential is assumed to be given by an ordinary coulombic potential in a dielectric medium. The two methods differ in the degree of refinement used both in setting up the problem and in solving the wave equation.

For the purpose of comparing them to the method used in this paper it is merely important to look at the reason for the results obtained. For this purpose the method of REISS is particularly instructive. He shows that the ionization energy of a 1*s* electron (the valence electron of hydrogen) remains relatively unchanged by the presence of the dielectric, while the energy of a 2*s* electron (the valence electron of lithium) is radically reduced. The reason for the difference is that a 1*s* electron has appreciable density only in the vicinity of a Bohr distance from the impurity nucleus, and hence it does not appreciably feel the influence of the dielectric. A 2*s* electron, on the other hand, "spills over" the cavity wall, and is therefore greatly affected by the presence of the dielectric. In this approach to the problem, the basic reason for the difference between a 1*s* and 2*s* electron is the much larger distance of the latter from its nucleus. It is precisely this larger distance which is also responsible for its lower ionization energy in the isolated atom; this forms the explanation proposed in this paper for its tendency to enter as an ionized donor. Therein lies the connection between the two approaches. The method of REISS or of KAUS gives semiquantitative information about ionization energies in the crystals, i.e. impurity levels, while the method developed in this paper is more suitable for an estimate of solubilities of various impurities.

As another example, we shall consider the case of tin in germanium. Starting with a tin atom in the vapor phase, we estimate $\Delta H_s^v = -2{\cdot}7$ eV if the tin enters the lattice substitutionally.* If the tin enters as an ionized interstitial impurity, we estimate a heat of solution of only $-1{\cdot}4$ eV (from equation 6) neglecting the repulsive energy which would reduce the gain in energy. Clearly, one would expect tin to be predominantly a neutral, substitutional impurity, in accordance with experiment.

VI. CONCLUSIONS

If the thermodynamic potential of an impurity in the external phase in equilibrium with the host crystal is known (e.g. the pressure and temperature of the solute in the vapor phase), the solubility of an interstitial impurity can be predicted approximately by estimating the interaction energy of the impurity with the host crystal. The entropy changes of the host crystal and of the impurity must also be considered, but are of much less importance. Aside from an estimate of the interaction energy, it is also necessary to know various properties of both the impurity and the host crystal, such as the ionization potential, the work function, etc. In the theory developed here the interaction energy of an electrically neutral impurity is assumed to be of the Van der Waals type, consisting of an attractive potential and a repulsive potential caused by overlap of non-bonding electrons. The interaction energy of electrically active impurities is assumed to be given by the polarization of the lattice by the charge on the ion as well as by a repulsive energy as in the case of neutral impurities. The theory developed here attempts to make quantitative estimates of these interaction energies, and is then able to predict what the predominant form for a given impurity will be, as well as to make predictions about the relative solubilities of various elements within each group of interstitials. Absolute calculations of solubilities depend on experimental verification or modification of some of the parameters estimated by the theory.

* This value is obtained from the author's previous work on substitutional impurities.[3] The value of ΔH^s of that paper can be converted to ΔH_s^v by subtracting the heat of vaporization of tin.[24]

APPENDIX

CALCULATION OF POLARIZATION ENERGY PRODUCED BY AN INTERSTIAL CHARGE IN THE DIAMOND LATTICE

When a charge, e, is placed in the lattice, dipoles are induced on the atoms, and these dipoles give rise to a potential ϕ at the charge site. By a well known theorem of electrostatics the energy thus produced is given by:[35]

$$U_{\text{pol}} = \tfrac{1}{2} e\phi \tag{10}$$

The problem of an atomistic theory for the polarization energy, as opposed to the continuum theory which gives rise to equation (7), is to calculate first the dipoles induced on the atoms, and then sum their contribution to the potential at the charge site. It is assumed that the potential and the electric field E_0 at a point $(x_0y_0z_0)$ originating from a dipole at $(x_1y_1z_1)$ are given by[3b]:

$$\phi_0 = \frac{\boldsymbol{\mu} \cdot \boldsymbol{r}}{r^3} = -\boldsymbol{\mu}\nabla_0\left(\frac{1}{r'}\right) \tag{11a}$$

$$\boldsymbol{E}_0 = \nabla_0\left[\boldsymbol{\mu}\nabla_0\left(\frac{1}{r'}\right)\right] \tag{11b}$$

The subscript 0 indicates that the differentiation is to be carried out at $(x_0y_0z_0)$; r' is the distance between the points. The attack of MOTT and LITTLETON[30] on this problem proceeded along the following lines: At distances far from the charge, the lattice is broken into cubes of edge d (the interatomic distance). Each cube contains an atom and is considered uniformly polarized by the charge. The macroscopic equation for the polarization, $\boldsymbol{P}$, is then used to compute the dipole strength per atom, or rather per cube surrounding an atom:

$$\boldsymbol{\mu} = \boldsymbol{P}\, d^3 = \frac{\boldsymbol{D}-\boldsymbol{E}}{4\pi}\, d^3 = \frac{e}{4\pi}\left(1-\frac{1}{\epsilon}\right)\frac{\boldsymbol{r}_i}{r_i^3}\, d^3 \tag{12}$$

$\boldsymbol{D}$ is the displacement vector, $\boldsymbol{E}$ the electric field, ϵ the static dielectric constant, and r_i the distance from the charge to the atom in question. The direction of polarization is assumed to be along the radius vector and the interaction between the volume elements is neglected. In the zero order approximation equation (12) is assumed to apply to all the atoms in the crystal. This approximation underestimates the dipole moments induced on the

Vol. 17
1960

nearest neighbors since it ignores the fact that these atoms are not shielded from the field of the charge. Having assigned dipole moments to all the atoms, the potential at the charge site is then given by combining equations (11a) and (12):

$$\phi = \sum_i^{\infty} \frac{\mu_i}{r_i^2} = \frac{d^3e}{4\pi}\left(1-\frac{1}{\epsilon}\right)\sum_i^{\infty}\frac{1}{r_i^4} \tag{13}$$

In higher than zero order approximations, say in the n^{th} order approximation the dipoles up to and including the n^{th} shell are assumed to be unknown at the outset while the dipoles on the atoms beyond the n^{th} shell are approximated by equation (12). To calculate the dipole on an atom in one of the near shells one must first find the field at the site of the atom, and then multiply it by the atomic polarizability. The field is the vector sum of the field produced by the charge, and the fields produced by all the other dipoles in the crystal as given by equation (11b). For the n^{th} order approximation this procedure leads to the following set of n simultaneous linear equations for the dipoles in the first n shells:

$$\begin{aligned}
\mu_1 &= \alpha\left(\frac{e}{r_1^2}\right) + E_1(\textstyle\sum \mu_1) + E_1(\sum \mu_2) + \ldots E_1(\sum \mu_n) + E_1(\sum \mu_{\text{out}}) \\
\mu_2 &= \alpha\left(\frac{e}{r_2^2}\right) + E_2(\textstyle\sum \mu_1) + E_2(\sum \mu_2) + \ldots E_2(\sum \mu_n) + E_2(\sum \mu_{\text{out}}) \\
&\vdots \\
\mu_n &= \alpha\left(\frac{e}{r_n^2}\right) + E_n(\textstyle\sum \mu_1) + E_n(\sum \mu_2) + \ldots E_n(\sum \mu_n) + E_n(\sum \mu_{\text{out}})
\end{aligned} \tag{14}$$

In these equations α stands for the atomic polarizability, and the r_i's stand for the distance from the charge to the i^{th} shell. The symbols $E_i(\Sigma\mu_j)$ refer to the field produced by the dipoles of the j^{th} shell at an atom of the i^{th} shell. The symbols E_i $(\Sigma\,\mu_{\text{out}})$ refer to the field produced at an atom of the i^{th} shell by the dipoles beyond the n^{th} shell, where n is the order of the approximation; these dipoles are given by equation (12). Only the component of the field in the radial direction are considered. Having calculated the dipoles on the atoms it is a simple matter to compute the potential energy at the charge site by means of equation (11a).

$$\begin{aligned}
\phi &= \frac{d^3e}{4\pi}\left(1-\frac{1}{\epsilon_0}\right)\sum_j^{N}\frac{1}{r_j^4} \quad \text{zero order} \\
&= \frac{g_1\mu_1}{r_1^2} + \frac{d^3e}{4\pi}\left(1-\frac{1}{\epsilon_0}\right)\sum_j^{N>1}\frac{1}{r_j^4} \quad \text{1st order} \\
&\vdots \\
&= \frac{g_1\mu_1}{r_1^2} + \frac{g_2\mu_2}{r_2^2} + \ldots \frac{g_n\mu_n}{r_n^2} + \frac{d^3e}{4\pi}\left(1-\frac{1}{\epsilon_0}\right)\sum_j^{N>n}\frac{1}{r_j^4} \quad \text{n}^{\text{th}}\text{ order}
\end{aligned} \tag{15}$$

In these equations the g_i's stand for the number of atoms in the i^{th} shell at a distance r_i from the charge. The notation $\sum_j^{N>n}$ means that the summation is to be carried out over all the atoms beyond the n^{th} shell, where n is the order of the approximation. The method of MOTT and LITTLETON was applied to the case of an interstitial charge in the diamond lattice up to a third order approximation, 290 atoms surrounding the charge in 18

Table 4. Polarization energy by the method of MOTT *and* LITTLETON. *Charge on an interstitial site.**

	Zero Order	1st Order	2nd Order	3rd Order
Diamond	3·26	4·71	4·78	4·94
Silicon	2·38	3·55	3·55	3·64
Germanium	2·34	3·51	3·49	3·58

* The method was also applied to the case of a charge on a substitutional site. The results were remarkably similar to those shown above.

shells were included in the summations. Table 4 lists the results for diamond, silicon and germanium. The parameters which enter these calculations, namely, the interatomic distance d, the dielectric constant ϵ and the polarizability per atom α, were taken from Table 1.

The calculations were not carried beyond the third order because fourth shell atoms are no longer equivalent with respect to the charge. Thus, an atom at position 1/2, 1/2, 1/2 of the unit cell[15] has another atom between it and the charge at 0,0,0 (the center of the cell), whereas the atom at $1/2, -1/2, 1/2$ "sees" the charge directly. This non-equivalence necessitates breaking up the fourth shell into two groups of atoms, requiring five simultaneous equations for a fourth-order calculation. Similar difficulties arise for some of the shells beyond the fourth. It is clear from Table 4 that there is rapid convergence beyond the first order approximation, as was also found by MOTT and LITTLETON[30], and by RITNER, HUNTER and DUPRE[36] for the NaCI lattice. Furthermore, the uncertainty in the true value of α (see text) makes it doubtful that there is any point in carrying the calculation to a higher order of approximation.

REFERENCES

1. TRUMBORE F. A., *Bell Syst. Tech. J.* **39,** 205 (1960).
2. (a) THURMOND C. D. and STRUTHERS J. D., *J. Phys. Chem.* **57,** 831 (1953).
   (b) ORIANI R. A. and HALL R. N., *J. Phys. Chem. Solids* **6,** 97 (1958).
   (c) TRUMBORE F. A., ISENBERG C. R. and PORBAMSKI E. M., *J. Phys. Chem. Solids* **9,** 60 (1959).
   (d) REISS H., FULLER C. S. and MORIN F. J., *Bell Syst. Tech. J.* **35,** 535 (1956).
3. WEISER K., *J. Phys. Chem. Solids* **7,** 118 (1958).
4. (a) PELL E. M., *J. Phys. Chem. Solids* **3,** 74 (1957).
   (b) REISS H. and FULLER C. S., *J. Phys. Chem. Solids* **4,** 58 (1958).
5. (a) VAN DER MAESEN F. and BRENKMAN J. A., *J. Electrochem. Soc.* **102,** 229 (1955).
   (b) FULLER C. S. and DITZENBERGER J. A., *J. Appl. Phys.* **28,** 40 (1957).
   (c) GALLAGHER G. J., *J. Phys. Chem. Solids* **3,** 82 (1957).
   (d) FRANK F. C. and TURNBULL D., *Phys. Rev.* **104,** 617 (1956).
   (e) TWEET A.G., *J. Appl. Phys.* **28,** 2002 (1959).
6. (a) VAN WIERINGEN A. and WARMOLTZ N., *Physica* **22,** 849 (1956).
   (b) THURMOND C. D., GULDNER W. G. and BEACH A. L., *J. Electrochem. Soc.* **103,** 603 (1956).
   (c) FRANK R. C. and THOMAS J. E., Jr., *Bull. Amer. Phys. Soc.* (ser 2) **4,** No. 7 (1959).
7. (a) KAISER W., FRISCH H. L. and REISS H., *Phys. Rev.* **112,** 1546 (1958).
   (b) KAISER W., HROSTOWSKI H. J. and THURMOND C. D., *Bull. Amer. Phys. Soc.* (ser. 2) **5,** (1960).
8. See for example: STEINER L. E., *Chemical Thermodynamics,* Chapter XIII. McGraw Hill, New York (1948).
9. THURMOND C. D. and KOWALCHIK M., *Bell Syst. Tech. J.* **39,** 169 (1960).
10. See for example: GLASSTONE, S., *Textbook of Physical Chemistry.* Van Nostrand, New York (1946).
11. SLATER J. C., *Quantum Theory of Matter.* McGraw-Hill, New York (1951).
12. SEITZ F., *Modern Theory of Solids.* McGraw-Hill, New York (1940).
13. MARGENAU H., *Rev. Mod. Phys.* **11,** 1 (1939).
14. LONDON F., *Z. Phys. Chem.* **11B,** 222 (1930).
15. For a picture of the unit cell of the diamond lattice, see for example: KITTEL C., *Introduction to Solid State Physics,* Chapter 1. Wiley, New York (1953).
16. (a) BLEICK W. E. and MAYER J. E., *J. Chem. Phys.* **2,** 252 (1934).
   (b) SLATER J. C., *Phys. Rev.* **32,** 349 (1928).
17. FOWLER R. H., *Statistical Mechanics,* (2nd. Ed.) Cambridge (1936).

Vol. 17
1960

18. MOTT N. F. and GURNEY R. W., *Electronic Processes in Ionic Crystals*. Oxford University Press (1950).
19. WHITEHEAD S. and HACKETT W., *Proc. Phys. Soc., Lond.* **51,** 173 (1939).
20. CONWELL E. M., *Proc. Inst. Radio Engrs. N.Y.* **40,** 1327 (1952).
21. KITTEL C., *Introduction to Solid State Physics*. Wiley, New York (1953).
22. ALLEN F. G., *Tech. Rep.* 236, Cruft Laboratory, Harvard University, Cambridge, Mass.
23. *Handbook of Chemistry and Physics*, (38th Ed.) Chemical Rubber Co.
24. STULL D. R. and SINKE G. C., *Thermodynamic Properties of the Elements*, Advances in Chemistry, Series No. 18. Amer. Chem. Soc. (1956).
25. See for example: FRENKL J., *Kinetic Theory of Liquids*. Oxford University Press (1946).
26. HERRING C. and NICHOLS M. H., *Rev. Mod. Phys.* **21,** 185 (1949); see also Ref. (12).
27. BOETTCHER C. J. F., *Theory of Electrical Polarization*. Elsevier, New York (1952).
28. FREEDMAN J. F. and NOWICK A. S., *Acta Met.* **6,** 176 (1958).
29. CARDONA M., PAUL W. and BROOKS H., *J. Phys. Chem. Solids* **8,** 204 (1959).
30. MOTT N. F. and LITTLETON M. J., *Trans. Faraday Soc.* **34,** 485 (1938).
31. See for example: STERN K. and AMIS E. S., *Chem. Rev.* **59,** 1 (1959).
32. TYLER W. W., *J. Phys. Chem. Solids* **8,** 59 (1959).
33. KAUS P., *Phys. Rev.* **109,** 1944 (1958).
34. REISS H., *J. Chem. Phys.* **25,** 681 (1956).
35. See for example: HARNWELL G. P., *Principles of Electricity and Electromagnetism*. McGraw-Hill, New York (1949).
36. RITTNER E. S., HUTNER R. A. and DUPRE F. K., *J. Chem. Phys.* **17,** 198 (1949).

LETTERS TO THE EDITOR

Direct observation of open magnetic orbits

(*Received* 14 *March* 1960)

THE decisive influence of open magnetic orbits associated with multiply-connected Fermi surfaces on high-field magneto-resistance has been discussed by LIFSHITZ and PESCHANSKI[1]. Recently BLOUNT[2] has proposed that these orbits may be observed directly. We have also considered this possibility with a somewhat different emphasis on its experimental realizability.

It is simplest to begin by reviewing the detailed topology of open orbits in magnetic fields as analysed by LIFSHITZ and PESCHANSKI. They consider two sorts of Fermi surfaces:

(a) Those which have the form of an undulating cylinder.

(b) Those which can be represented by a three-dimensional grid of undulating cylinders.

Another category of Fermi surfaces is given by

(c) Those which can be represented by a two-dimensional grid of undulating cylinders.[3]

The most important result of LIFSHITZ and PESCHANSKI is that while in (a) open trajectories are encountered only when $H = H_x$ is perpendicular to the cylinder axis, in (b) open orbits are encountered much more frequently. More specifically, if H is plotted on a stereogram the domains of H which give open orbits are one-dimensional in case (a) and one or two-dimensional in case (b). The two-dimensional regions in case (b) always surround symmetry directions (denoted by Λ) for which there are no open orbits but for which different values of k_H give positive and negative mass orbits. It is this last feature that distinguishes (b) from (a); (c) is like (b) or (a) according to whether it has the feature or not.

The number of open orbits (which is proportional to $\Delta k_H/k_F$, where Δk_H is the range of k along H whose cross-sections give open orbits) is generally a finite fraction of the number of carriers. The number is constant for H in one-dimensional regions but is zero at the boundary (which includes Λ) of two-dimensional regions, rising to a maximum in the middle of these regions.

A characteristic feature of the open orbits in all cases is that in addition to the drift velocity along the magnetic field v_x (which is in general different for different open orbits) all open orbits have a drift velocity v_y in a plane perpendicular to the magnetic field. The direction of v_y is the same (for fixed H), for all open orbits (independent of k_H). In the one-dimensional regions this common direction (in k-space) is the principal axis of the cylinder to which H is perpendicular. In the two-dimensional regions the direction is given by $N = \Lambda \times H$. The orbit in *real* space thus has an additional drift velocity v_y parallel to $N \times H$, and the total drift velocity $v = v_x + v_y$ lies in the plane perpendicular to N.

Open orbits associated with one-dimensional regions are periodic with periodicity of the cylinder. Open orbits associated with two-dimensional regions are in general only quasi-periodic and much less likely to be observed. However, if the plane normal to N is a mirror plane the orbits will be periodic with periodicity K (where K is a fundamental reciprocal lattice vector parallel to N). The remarks of the last two paragraphs will be especially helpful later in discussing cyclotron resonance.

In addition to the open orbits described above LIFSHITZ and PESCHANSKI also discuss extended orbits, which in general are quasi-periodic. The regions where extended orbits may be expected are shown in LIFSHITZ and PESCHANSKI's stereogram (Fig. 3 of their paper).

We now examine the possibility of observing open orbits experimentally in the de Haas–van Alphen (dHvA) and cyclotron resonance, or Azbel'–Kaner (AK) effects. The results for magneto-acoustic resonance should be similar to those for cyclotron resonance.

It is natural, in examining the dHvA effect, to attempt to extend ONSAGER's semiclassical treatment[4, 5] of closed orbits based on the Bohr–Sommerfeld quantization rules to open orbits. It is easy to show that this cannot be done in a gauge-invariant fashion; thus no dHvA effect should be observed with open orbits.[6] This does not imply, however, that open orbits cannot give a *classical* AK effect, as stated by AZBEL' and KANER[7]. The principal difference between open orbits and closed orbits is the additional drift velocity v_y of open orbits. Even with H parallel to

Vol. 17
1960

the surface of the metal this additional drift velocity in general will contain a component parallel to the surface normal which will vitiate the AK effect. As we have seen, however, if in the one-dimensional regions the axis of the cylindrical Fermi surface is normal to the crystal surface or in the two-dimensional regions A is parallel to the crystal surface the drift velocity of *all* open orbits will also lie in this plane. This is just the requirement for the AK effect. A well resolved effect will probably be observed only if the motion is nearly periodic; for the two-dimensional regions this requires in addition that the crystal surface be parallel to a mirror plane.

With these conditions satisfied, if the open orbit is in the skin depth at time T_1 and returns to it at time T_2 the AK effect will measure the "cyclotron frequency" $\omega_c/2\pi = (T_2 - T_1)^{-1}$ directly. Moreover the largest effect will be obtained for $E_{rf} \| v_D = v_x + v_y$.

The foregoing discussion has assumed that $\omega_c(k_H)$ will be independent of k_H, which in general is not the case. If the open orbits come from a single undulating cylinder (H in a one-dimensional region) ω_c will take on extremal values (say at $k_H = 0$) and this will determine the value of ω_c observed [say $\omega_c(0)$]. For H in the two-dimensional regions no extremal is expected in general, but in certain cases ω_c for the open orbits may be confined to a narrow range so that oscillations may still be observable. We have in mind the open orbits that may be found in Cu, Ag and Au. According to SHOENBERG[8] the Fermi surface in these metals consists of large "bellys" connected by narrow "necks". The open orbits for H in two dimensional regions differ only by the amount of "neck" included, so that in this case ω_c may be sensibly constant for open orbits. A similar mechanism may make possible the observation of extended orbits.

The situation which obtains when the additional drift velocity v_y contains a component parallel to the surface normal has been discussed by BLOUNT[2]. He observes that by tipping the field H out of the surface it may be possible to find *some* orbits with drift velocities $v_H = v_X$ along H whose normal component cancels the normal component of v_y. A similar explanation for "tipped field" resonances has been proposed for closed orbits by CHAMBERS[9], HEINE[10] and PHILLIPS[11], though none of these authors could explain the observation in tin[12] of "*isolated* resonances" at angles so large as 30°. We agree with BLOUNT that open orbits may account for isolated large angle resonances in general symmetries.

Acknowledgements—Our thoughts on open orbits have benefited greatly from conversations with colleagues in the Mond Laboratory. We wish to express our appreciation particularly to Mr. M. G. PRIESTLY, Dr. D. SHOENBERG and Dr. A. B. PIPPARD for a number of helpful suggestions.

Royal Society Mond Laboratory J. C. PHILLIPS
Cambridge
England

References

1. LIFSHITZ I. M. and PESCHANSKI V. G., *Zh. exsp. teor. fiz.* **35,** 875 (1959).
2. BLOUNT E. I., *Phys. Rev. Letters* **4,** 114 (1960).
3. This case and the discussion of it were suggested by Dr. L. M. FALICOV.
4. ONSAGER L., *Phil. Mag.* **43,** 1006 (1952).
5. PIPPARD A. B., *Rep.* 10th *Solvay Cong.*, p. 123 (1955) (unpublished).
6. ZIL'BERMAN, G. E., *Zh. exsp. teor. fiz.* **6,** 299 (1958); **7,** 169 (1958). Note that in the latter the small oscillations stem from the cutoff of closed orbits, the open orbits contributing nothing.
7. AZBEL M. and KANER E. A., *Zh. exsp. teor. fiz.* **5,** 730 (1957).
8. SHOENBERG D., *Phil. Mag.*, to be published.
9. CHAMBERS R. G., *Canad. J. Phys.* **34,** 1395 (1956).
10. HEINE V., *Phys. Rev.* **107,** 431 (1957).
11. PHILLIPS J. C., *Phys. Rev. Letters* **3,** 328 (1959).
12. KIP A. F., LANGENBERG D., ROSENBLUM W. and WAGGONER G. F., *Phys. Rev.* **108,** 494 (1958).

The growth of single crystals of binary and ternary chalcogenides by chemical transport reactions

(*Received* 23 *February* 1960)

THE method of chemical transport reactions was used to grow single crystals of the following binary and ternary chalcogenides: ZnS, ZnSe, CdS, CdSe, MnS, SnS_2, In_2S_3, $ZnIn_2S_4$, $CdIn_2S_4$, $HgIn_2S_4$, $ZnIn_2Se_4$ and $CdIn_2Se_4$.

The term chemical transport reactions was first introduced by SCHÄFER *et al.*[1] who studied their

thermodynamics. Processes based on the same principle, however, have been known for a long time, e.g. the method of van Arkel–de Boer for preparing certain metals by thermal decomposition of their halides on a hot wire.

Transport reactions are based on the fact that a transport of matter can occur in a chemical system consisting of one solid and n gaseous components in equilibrium, if the equilibrium constant K is made to vary locally, e.g. by imposing a temperature gradient on the vessel containing the system. The simplest arrangement is a closed tube with a polycrystalline solid, e.g. ZnS, of temperature T_1 in one end, the other end being at T_2 (Fig. 1).

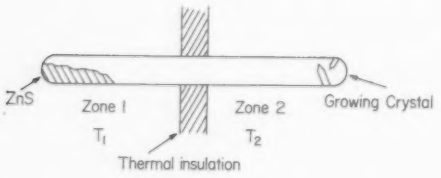

FIG. 1. Schematic arrangement for chemical transport reactions.

If nothing else is in the tube we have the trivial case $n = 1$. At temperatures high enough and for $T_1 > T_2$ normal sublimation of ZnS will occur.

By introducing a substance forming a volatile compound with ZnS, e.g. iodine, an equilibrium will establish of the form:

$$ZnS + I_2 \rightleftarrows ZnI_2 + \tfrac{1}{2}S_2 \quad (n = 3)$$

The different equilibrium conditions in both halves of the tube can lead to a deposition of ZnS in Zone 2 by transport via the gaseous mixture of ZnI_2 and S_2. Small amounts of iodine (the "transporter") are sufficient to transport practically unlimited amounts of ZnS because the I_2 liberated in Zone 2 will diffuse back and pick up more ZnS. From the relation:

$$\frac{d \ln K(T)}{dT} = \frac{\Delta H}{RT^2}$$

(K = equilibrium constant, ΔH = change in enthalpy) follows that the necessary condition for transport is $T_1 > T_2$ for reactions with $\Delta H > 0$ and $T_1 < T_2$ for reactions with $\Delta H < 0$.

Usually ZnS will deposit in polycrystalline form. However, single crystals are also obtainable if the experimental parameters are adjusted in such a way that—once a certain number of seeds are formed in Zone 2 (or introduced previous to the experiment)—the amount of material arriving in Zone 2 per unit time corresponds to the velocity of growth of the seeds.

If suitable transporters can be found this method is particularly useful for growing single crystals of materials with high melting or sublimation points because crystal growth can be achieved at much lower temperatures than have to be employed in conventional melting or vapour-phase techniques. In the case of zinc sulphide, e.g. we obtained at a growth temperature of 700°C crystals which were entirely cubic,[2] whereas crystals grown by "normal" sublimation at 1100° are usually mixtures of the cubic and the hexagonal phases.

Furthermore, it was found that if mixtures of different chalcogenides are used as feed material the transport method is also suitable for growing single crystals of ternary compounds, e.g. $ZnIn_2S_4$, $CdIn_2S_4$, $HgIn_2S_4$, materials known hitherto only in the polycrystalline state.[3]

We have employed the outlined principles to grow crystals of the various binary and ternary chalcogenides listed in Table 1. Iodine was used as a transporter in all experiments. It is, however, possible to use other substances, e.g. HI SnI_4, Br etc. Approximately 2 g of polycrystalline feed material were put into a quartz ampoule of 8 mm internal diameter and 200 mm length. After heating in a high vacuum to drive off adsorbed gases, iodine corresponding to a concentration of 5–6 mg/cm³ was condensed in with liquid air and the ampoule drawn off under vacuum. For crystal growth it was placed horizontally into a two-zone furnace, the feed material being in the hot zone. Growing times varied between 12 and 40 hr. For a given temperature gradient the transport rate R is roughly proportional to the cross-section of the tube q and to the square of the transporter concentration C. Typical values for ZnS are: $\Delta T = 1050° - 750°$, C = 5 mg I/cm³, $q = 0{\cdot}5$ cm² and $R = 20$ mg/hr.

Work on the optical and electrical properties of these crystals is in progress.

Table 1

Compound	Colour	Crystal shape	Maximal size (mm)	Transporter concentration (mg I/cm³)	Temperature gradient T_1 T_2
ZnS	White	Plates, rods, polyhedra	6 × 6 × 2	5	1050°–750°
ZnSe	Yellow		4 × 4 × 3	6	1050°–800°
CdS	Orange	hex. columns. polyhedra	5 × 1 × 1	5	1000°–400°
CdSe	Black	needles	5 × 1 × 1	6	1000°–500°
MnS	Dark green	plates	4 × 4 × 0·1	5	1000°–550°
SnS_2	Orange	plates	4 × 4 × 0·1	5	950°–600°
In_2S_3	Red	octahedra	4 × 4 × 4	6	950°–450°
$ZnIn_2S_4$	Yellow	thin plates	4 × 4 × 0·1	6	1000°–700°
$CdIn_2S_4$	Red	octahedra	4 × 4 × 4	6	1000°–600°
$HgIn_2S_4$	Black	octahedra	3 × 3 × 3	6	950°–650°
$ZnIn_2Se_4$	Dark red	polyhedra	3 × 3 × 3	6	1000°–700°
$CdIn_2Se_4$	Black	polyhedra	3 × 3 × 3	6	1000°–700°

Acknowledgements—Thanks are due to Messrs. H. U. Bölsterli and M. Lichtensteiger for their help in building equipment and carrying out many experiments.

Laboratories R.C.A. Ltd. R. Nitsche
Zurich
Switzerland

References

1. Schäfer H. *et al.*, *Z. anorg. Chem.* **286,** 27, 42 (1956); **290,** 279 (1957); **291,** 221, 294 (1957).
2. White J. C., R.C.A. Laboratories, Princeton, N.J., private communication.
3. Hahn H., *Z. anorg. Chem.* **263,** 177 (1950).

Generation of vacancies during plastic deformation of KCl crystals

(*Received* 17 *February* 1960; *revised* 4 *April* 1960)

Plastic deformation is known to produce detectable changes of conductivity in many types of solids. Following the interpretation of Seitz[1] these changes are generally ascribed to point defects which are created during the movement of dislocations. In ionic crystals the generated defects are charged, and take part directly to the conduction processes, thus increasing considerably the conductivity. This enhancement of conductivity is known as the Gyulai–Hartly effect and has already been observed by several workers in alkali halides.[2] However, a systematic study of its temperature dependence and of its annealing properties has yet been lacking. An investigation of the effect at low temperatures, where the point defects are not mobile, should also allow us to separate the two possible contributions (ionic and electronic) to the extra-conductivity. As is known, Tyler suggested that electrons are liberated during plastic flow and that the Gyulai–Hartly effect could be partially due to them.[3]

In the present experiments, the effect of plastic strain on the conductivity of KCl crystals was studied in the range of temperature from −170°C to +70°C. The crystals were mounted in a vacuum cryostat, and given a constant amount of strain (of the order of 5 per cent) by squeezing them uniaxially and homogeneously between two massive, insulated electrodes. The external current under a fixed applied field was measured during and after deformation by means of a vibrating-reed electrometer, whose output was fed into a pen recorder. The response time of the apparatus was kept as low as possible, in order to follow the conductivity decay soon after deformation. With a load resistor of $10^{10}\ \Omega$ the time constant was 0·3 sec and the sensitivity 10^{-14} A/division. The deformation was imparted to the crystal in a time of the order of the time constant of the apparatus.

In Fig. 1 the external current recorded during and after deformation is shown for three KCl

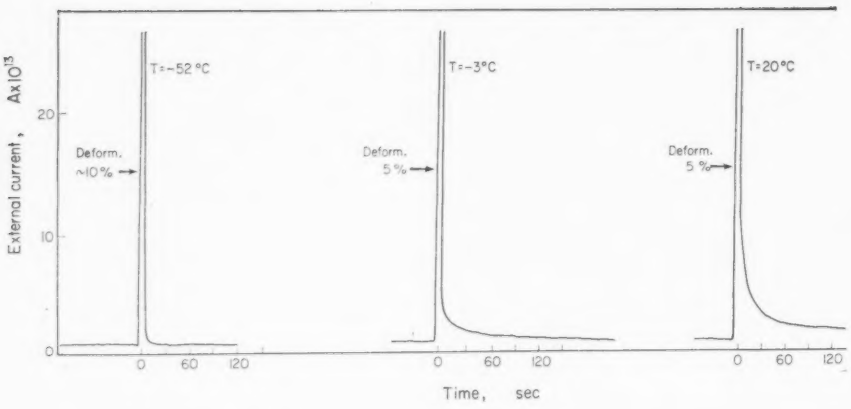

FIG. 1. External current as a function of time for three KCl crystals deformed at different temperatures. The end of the deformation is taken as time origin.

crystals deformed at different temperatures. It may be seen that two distinct effects are present. The first shows as a large sudden increase of conductivity during plastic strain: this effect is the only one that can be observed at temperatures between $-170°C$ and $-10°C$, and decays to zero after deformation in a time which is shorter than the time constant of our apparatus.* At temperatures higher than $-10°C$ there is an additional component, which appears as a tail of the initial peak and decays in a time of the order of minutes. This tail, which clearly represents the ionic contribution, can be easily separated; its time dependence is illustrated in Fig. 2, where the reciprocal of the conductivity is plotted as a function of time (taking the end of deformation as a time origin and considering the curve after a few seconds when the larger effect has already decayed). The straight lines of Fig. 2 clearly indicate that the decay of the extra-conductivity σ follows a hyperbolic law of the type:

$$\frac{1}{\sigma} = at + \rho_0, \qquad (1)$$

where the slope a is practically independent of temperature, whereas the intercept ρ_0 (i.e. the

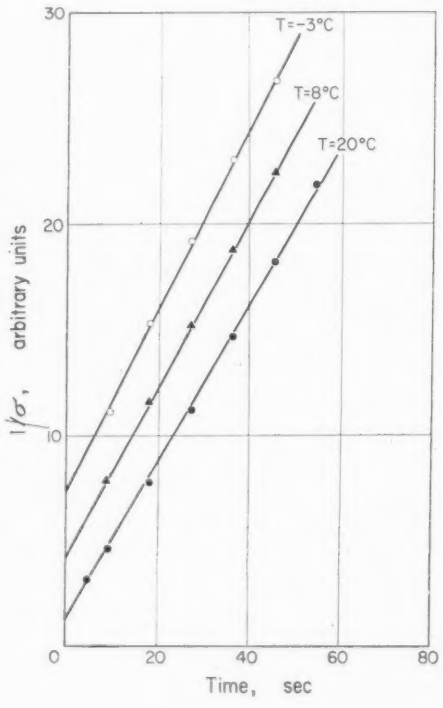

FIG. 2. Extra-resistivity as a function of time for three crystals deformed by the same amount (5 per cent) at different temperatures.

* A fast-decaying conductivity upon deformation has already been reported by GYULAI and BOROS[4].

Vol. 17
1960

extra-resistivity at $t = 0$) depends on temperature very strongly. A semilogarithmic plot of ρ_0 as a function of $1/T$ is given in Fig. 3: it is seen that ρ_0 fits the equation:

$$\rho_0 = C \exp(Q/kT) \qquad (2)$$

with $Q = 0{\cdot}45 \pm 0{\cdot}05$ eV and $C = \sim 2 \times 10^6 \Omega$cm.

According to SEITZ the Gyulai–Hartly effect is due to the presence of positive-ion vacancies, which have been created by sections of the moving

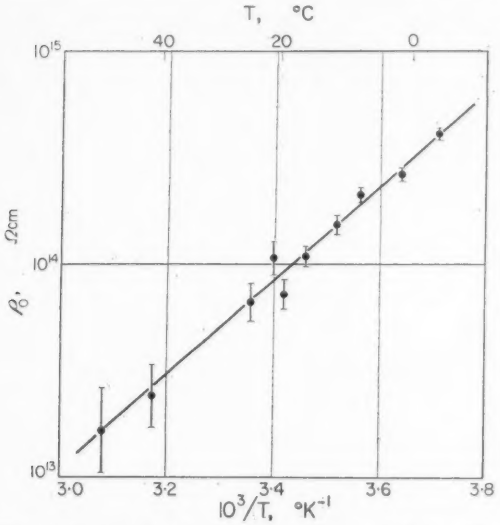

FIG. 3. Extra-resistivity extrapolated at $t = 0$ vs. $1/T$. Each point refers to a different crystal. Deformation was 5 per cent for all crystals.

dislocations; at ordinary temperatures, these vacancies are subsequently removed through migration and association with vacancies of the opposite sign. Assuming that positive- and negative-ion vacancies are created in equal numbers, and that only the former are mobile, equation (1) can be interpreted on the basis of a simple model. When interactions among vacancies are neglected, the rate of removal can be described by second-order kinetics:

$$-\frac{dn}{dt} = A \exp\left(-\frac{E}{kT}\right) n^2 \qquad (3)$$

where n is the number of excess vacancies present at time t, and E is the activation energy for migration of positive-ion vacancies. By integrating equation (3) one easily obtains the time dependence of the conductivity:

$$\frac{1}{\sigma} = \frac{1}{ne\mu} = \frac{A}{e\mu_0} t + \frac{\exp(E/kT)}{n_0 e \mu_0}, \qquad (4)$$

n_0 being the number of excess vacancies present at $t = 0$, and $\mu = \mu_0 \exp(-E/kT)$ being the mobility of positive-ion vacancies.

By comparing equations (1), (2) and (4) and assuming that n_0 does not depend on temperature, we obtain directly the value of the migration energy for a positive-ion vacancy, i.e. $E = Q = 0{\cdot}45$ eV. This figure is considerably smaller than that obtained from measurements of ionic conductivity and diffusion in undeformed crystals (0·68 eV).[5] The discrepancy probably means that the vacancies responsible for the excess conductivity move in highly distorted regions of the lattice: as is known the interaction of vacancies with each other or with dislocations can result in a lowering of the migration energy.

The behaviour of the initial effect (i.e. the sudden increase of conductivity during plastic deformation) was also investigated. Its main characteristics are:

(a) The total charge passing through the crystal during deformation is proportional to the applied field.*

(b) the effect is the same when the electrodes are painted on the lateral sides of the crystal, where no external forces are applied.

(c) The effect does not seem to depend very much upon temperature down to -100°C; below this temperature, however, it drops rapidly, almost vanishing at LNT. In our opinion the fast-decaying component of the conductivity is due to electrons liberated by the moving dislocations. However, further experiments are needed in order to confirm the electronic nature of the effect and eventually to explain the sudden reduction of "shubweg" at low temperatures.

Istituto di Fisica Dell'Universita' di Pavia
and P. CAMAGNI†
†*Comitato Nazionale Ricerche Nucleari*
Centro di Ispra G. CHIAROTTI
Italy A. MANARA†

* This shows that the effect is not the e.m.f. observed by FISHBACK and NOWICK[6] during inhomogeneous plastic deformation.

References

1. Seitz F., *Advanc. Phys.* **1,** 43 (1952).
2. Gyulai Z. and Hartly D., *Z. Phys.* **51,** 378 (1928); Stepanow A. W., *Z. Phys.* **81,** 560 (1933); Caffyn J. E. and Goodfellow T. L., *Nature, Lond.* **176,** 878 (1955); Fishback D. B. and Nowick A. S., *J. Phys. Chem. Solids* **5,** 302 (1958); Taylor A. and Pratt P. L., *Phil. Mag.* **3,** 1051 (1958).
3. Tyler W. W., *Phys. Rev.* **86,** 801 (1952).
4. Gyulai Z. and Boros J., *Math. Naturw. Anz. Ungar. Akad. Wiss.* **59,** 115 (1940).
5. Aschner J. F., thesis, University of Illinois, Urbana (1954).
6. Fishback D. B. and Nowick A. S., *Phys. Rev.* **99,** 1333 (1955).

Resonant absorption of gamma radiation in superconductors*

(*Received* 7 *March* 1960; *revised* 19 *April* 1960)

Resonant absorption of gamma radiation[1, 2, 3] (Mössbauer effect) in crystals may occur if the gamma ray recoil momentum is taken up by an entire macroscopic crystallite. This condition can be met for low energy gamma rays if the emitting and absorbing nuclei are embedded in crystalline lattices of adequately strong binding. Under these circumstances both the emission and absorption spectra have narrow peaks at identical energies, corresponding to no nuclear recoil, and the widths of these peaks approach the natural width of the excited level. Energy resolutions as large as 10^{15} have been observed in Zn^{67}[4] and Fe^{57}.[5] Perturbations at the nucleus of the order of small fractions of a μeV are readily made evident by a reduction in the amplitude of the nuclear resonance. These detectable shifts may be as small as the average energy change per atom in superconducting transitions (typically 10^{-8} eV[6]) and suggest that resonance absorption may be used to study the influence of superconductivity upon atomic nuclei.

Several effects may influence nuclear resonance absorption in a superconductor. Changes in the atomic volume and changes in the electronic configuration may modify the crystalline phonon spectrum. Such effects alter the effective Mössbauer temperature[7] and hence the no-phonon transition probability. A sum rule relating the gamma ray energy and the crystalline states to the no-phonon transition probability has been given by Lipkin[8]. Variations in the magnetic field at the superconductor nuclei can alter the nuclear Zeaman splitting, thereby changing the resonance condition and therefore the transmission through a superconducting resonant absorber.

Using the recently discovered[7] resonance in the 77 keV gamma level in Au^{197} we have searched for those effects in the intermetallic superconducting compounds Au_2Bi and $AuNb_3$. The $AuNb_3$ was prepared from commercially pure Nb and high purity Au by arc melting. The Au_2Bi was formed by freezing a melt containing 70 weight per cent of Bi. The excess Bi was then dissolved out using nitric acid. X-ray studies of both compounds revealed only lines corresponding to the compounds. No lines corresponding to pure elements were visible. Both compounds were pulverized and pressed with aluminum powder into $1\frac{1}{4}$ in. diameter absorbers of thickness 265 mg/cm^2 of Au_2Bi and 477 mg/cm^2 of $AuNb_3$. Thus each absorber contained approximately 200 mg/cm^2 of Au, facilitating comparison with a pure Au absorber.

A source of 77 keV Au^{197} gamma rays was prepared by neutron activation of enriched Pt^{196}. The resulting Pt^{197} decays by β^- emission with 18hr half-life to the 77 keV, 1·9 mμ sec level in Au^{197}, which then decays to the ground state of Au^{197}. Resonant capture of these 77 keV gammas was observed by measuring the transmission of this gamma ray through absorbing foils, first with the foils stationary and then with the source in motion relative to the absorbers. The speed used, 1·34 cm/sec, has been demonstrated[7] to be sufficient to Doppler shift the gamma rays by an energy greater than their natural width, thereby destroying the resonance condition. With a 200 mg/cm^2 pure Au absorber the counting rate increases over the stationary counting rate by a factor of $7{\cdot}7 \pm 0{\cdot}5$ per cent (after correction for background and unresolved X-rays). We denote this counting-rate change (resonance amplitude) by Δ. This resonance amplitude in pure Au is found to be independent of temperature from 1·6°K to 4°K.

* Work performed under the auspices of the U.S. Atomic Energy Commission.

Similar measurements were performed with the Au_2Bi absorber in the temperature range 1·6°K to 4°K. The counting-rate change, Δ, above the superconducting transition was $5{\cdot}5 \pm 0{\cdot}1$ per cent, and this number changes by less than 0·2 per cent upon passing through the transition. Concurrent susceptibility measurements on a sample of Au_2Bi from the same melt showed a superconducting transition at 1·76°K with a width of 0·1°K. This transition temperature is consistent with SCHOENBERG's earlier value of 1·73°K[9] and with the Leiden value of 1·84°K (quoted in Ref. 9). Fig. 1 shows the susceptibility (in arbitrary units) and Δ as functions of temperature. Temperatures were derived from helium vapor pressure using the T_{55E} scale.

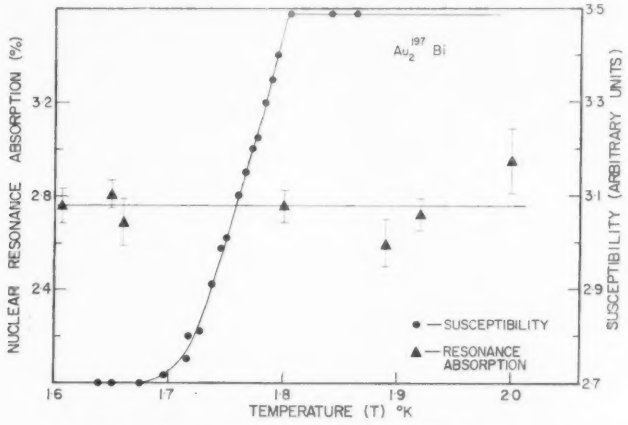

FIG. 1. Nuclear resonant absorption of 77 keV Au^{197} gamma radiation in Au_2Bi and the relative susceptibility of Au_2Bi in the neighborhood of the superconducting transition. No background correction has been made to the resonant absorption points.

Results similar to those obtained with the Au_2Bi absorber were found for $AuNb_3$. The transition temperature for this compound is reported to be 11·5°K[10] The Doppler shift velocity was again 1·34 cm/sec. The value of Δ was found to be $0{\cdot}74 \pm 0{\cdot}2$ per cent at temperatures below 4°K, and $0{\cdot}50 \pm 0{\cdot}26$ per cent above the superconducting transition temperature. The latter measurement was made during slow warming of the cryostat following evaporation of the helium bath, and the transition was observed from the susceptibility change.

The above results are consistent with the conclusion that no change in nuclear resonance absorption occurs in either Au_2Bi or in $AuNb_3$ as a result of the superconducting transition. For the $AuNb_3$ the restriction on the change in the resonance strength is rather weak, while for the Au_2Bi it may be concluded that the resonance is changed by no more than 2·5 per cent. In terms of upper limits on a possible shift in the nuclear transition with the onset of superconductivity, one may state that the shift is less than 2×10^{-8} eV in Au_2Bi and less than 4×10^{-7} eV in $AuNb_3$. Thus, in the case of Au_2Bi, any perturbation at the Au nucleus cannot be appreciably greater than the energy change per atom in the superconducting transition.[6]

Based upon these results a novel experiment may be proposed. Nuclear resonance absorption has been observed in ferromagnetic materials.[11] This resonance may be destroyed by an external magnetic field of only a few G.[12] Suppose a ferromagnetic superconductor[13] is formed containing an element with appreciable hyperfine structure in which nuclear resonance occurs. Then, if this material is placed in a permanent magnetic field the resonance is destroyed, and may be restored simply by lowering the temperature through the superconducting transition point. The magnetic

field will be expelled by the Meissner effect and the conditions for resonance at least partially restored. The degree of restoration will provide information related to the Matthias–Suhl model of ferromagnetic superconductors.[14]

While the experiment may be marginally possible in an ordinary superconductor using a suitably chosen isotope, (e.g. Zn^{67}) the effect will be largest in a ferromagnetic superconductor. In ordinary superconductors the magnetic field required to affect nuclear resonance will exceed the superconducting critical field.

We are presently attempting to increase the sensitivity of nuclear resonance as a probe through the use of resonance scattering of narrow gamma rays. It appears likely that a probe for superconductors may be made with a sensitivity approaching that which the Knight shift provides in ordinary materials.

Acknowledgements—We wish to thank B. MATTHIAS for several discussions and for suggesting various compounds and J. G. DASH for a number of discussions. The aid of the Omega West reactor group in source activation is acknowledged.

University of California P. P. CRAIG
Los Alamos Scientific Laboratory D. E. NAGLE
Los Alamos R. D. REISWIG
New Mexico

References

1. MÖSSBAUER R. L., *Z. Phys.* **151,** 124 (1958); *Naturwissenschaften* **45,** 538 (1958); *Z Naturf.* **14**a, 211 (1959).
2. CRAIG P. P., DASH J. G., MCGUIRE A. D., NAGLE D. E. and REISWIG R. D., *Phys. Rev. Letters* **3,** 221 (1959).
3. LEE L. L., Jr., MEYER-SCHUTZMEISTER L., SCHIFFER J. P. and VINCENT D., *Phys. Rev. Letters* **3,** 223 (1959).
4. NAGLE D. E., CRAIG P. P. and KELLER W. E., *Nature, Lond.* **186,** 707 (1960); CRAIG P. P., NAGLE D. E. and COCHRAN D. R. F., *Phys. Rev. Letters* **4,** 561 (1960).
5. POUND R. V. and REBKA G. A., *Phys. Rev. Letters* **4,** 274 (1960).
6. COOPER L. N., *Amer. J. Phys.* **28,** 91 (1960).
7. NAGLE D. E., CRAIG P. P., DASH J. G. and REISWIG R. D., *Phys. Rev. Letters* **4,** 237 (1960).
8. LIPKIN H., *Ann. Phys.* **9,** 332 (1960).
9. SHOENBERG D., *Nature, Lond.* **142,** 874 (1938).
10. MATTHIAS B. T., *Progress in Low Temperature Physics* (edited by GORTER C. J.) Vol. II. North Holland Publishing Company, Amsterdam (1957).
11. POUND R. V. and REBKA G. A., Jr., *Phys. Rev. Letters* **3,** 439 (1959).
12. PERLOW G. J., HANNA S. S., HAMERMESH M., LITTLEJOHN C., VINCENT D. H., PRESTON R. S. and HEBERLE J., *Phys. Rev. Letters* **4,** 74 (1960).
13. MATTHIAS B. T., SUHL H. and CORENZWIT E., *Phys. Rev. Letters* **1,** 449 (1958).
14. MATTHIAS B. T. and SUHL A., *Phys. Rev. Letters* **3,** 51 (1960).

On quadrupolar effects in alloys

(*Received* 15 *March* 1960)

IN A paper to appear shortly KOHN and VOSKO[1] explain the field gradients produced at the copper nuclei in the copper base alloys as due to the oscillating fluctuations of electronic density around the solute atoms. Their conclusions are in agreement with ROWLAND's experimental work[2] on a series of copper base alloys.

We wish to point out that we reached independently the same conclusions. Our work will be published in *J. Phys. Radium.*[3] It was initiated by the study of N.M.R. in cold worked copper done by AVERBUCH *et al.*[4], who found a λ factor of enhancement for elastic strain of the order of unity, against the value of 60 proposed by BLOEMBERGEN. This result shows that the size effects cannot predominate in producing field gradients in alloys; it is in agreement with ROWLAND's measurements[2] which were not known to us.

We have analysed the previous measurements by BLOEMBERGEN and ROWLAND[5] on Al base alloys: around each solute atom there are variations of electronic density decreasing in r^{-3} from the solute atom, as was pointed out by FRIEDEL[6]. To compute the field gradients we take into account the periodic structure by a simple extension of the Wigner–Seitz method[7] in the presence of a solute atom; the free electron results for the field gradient,

$$\propto \frac{\cos(2k_F r + \phi)}{r^3},$$

(where α and ϕ depend only on the scattering at the Fermi surface) are then simply multiplied by a factor μ which depends only on the matrix. The value of μ_{Al} obtained with orthogonalized plane waves is 5, while a value of 15 is needed to explain

the experimental results. In view of the approximations made this result can be considered to be satisfactory.

Our paper analyses the underlying assumptions in the use of the Wigner–Seitz approximation and in the computation of the field gradients. Our final method and results are essentially the same as KOHN's.

The main result of this study is to emphasize the importance of the long-range oscillations of electronic density, which can perturb the electronic density at large distances from the solute atom. This confirms the results already obtained in the Knight shift of dilute alloys.[8]

Service de Physique des Solides A. BLANDIN
B.P. 11 J. FRIEDEL
Faculte d' Orsay
(*S. et O.*)
France

References

1. KOHN W. and VOSKO S. H., *Phys. Rev.* **119,** 912 (1960).
2. ROWLAND T. J., *Phys. Rev.* **119,** 900 (1960).
3. BLANDIN A. and FRIEDEL J., to be published.
4. AVERBUCH P., DE BEREGEVIN F. and MÜLLER-WARMUTH W., *C.R. Acad. Sci., Paris* **249,** 2315 (1959).
5. BLOEMBERGEN N. and ROWLAND T. J., *Acta Met.* **1,** 731 (1953).
6. FRIEDEL J., *Phil. Mag.* **43,** 153 (1952).
7. ROTH L. M., Thesis, Harvard University (1957).
8. BLANDIN A. and DANIEL E., *J. Phys. Chem. Solids* **10,** 126 (1959).

Bismuth Fermi surface

(*Received* 22 *March* 1960)

AS AN ADDENDUM to the work on the single-OPW approximation in polyvalent metals,[1] a preliminary study of bismuth has been made. This does not add any striking new information on bismuth, partly because of the very extensive experimental work[2–6] which has given a great deal of information on the subject, partly because failure to include spin–orbit coupling explicitly leads to appreciable uncertainties, and partly because recent band calculations on bismuth by MASE[7] have allowed him to give what I believe to be the correct disposition of the Fermi surface within the Brillouin zone. It does, on the other hand, give another rather striking example of the insight that can be obtained by this very simple approach, and an illustration of the procedure for a case in which the lattice potential is quite important. What follows is a brief summary of this treatment.

The single-OPW Fermi surface has been constructed according to the procedures discussed previously.[1,8] The single-OPW sphere contains 10 electrons, since there are two pentavalent atoms per cell; this gives rise to segments of surface in bands 2–8. We expect that under the combined influence of the potential and of spin–orbit coupling this will be reduced to segments surrounding electrons in the sixth band and holes in the fifth, so we are interested only in the surface in these two bands. A section of these surfaces is shown in Fig. 1. The electron Fermi surface is expected to arise from either the surface *B* or the surface *C*. Experimentally it is known that the electron surface is elongated and is tipped slightly out of a plane perpendicular to the *c*-axis. It is clear from the symmetry of the point *B* that the addition of a potential and spin–orbit coupling could not give rise to such segments there, while

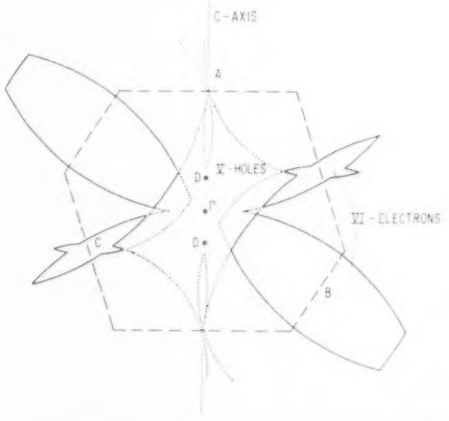

FIG. 1. Sections of the Fermi surface in the fifth and sixth bands according to the single-OPW approximation. The dashed lines give the outline of the Brillouin zone. The segments of surface are continued out of the reduced zone in order to give a better picture of their shape and connectivity. The section shown contains the *c*-axis and a principal reciprocal lattice vector.

they might easily appear at C. We note also that the two other electron surfaces may be generated from this one utilizing the three-fold symmetry around the c-axis. The hole surfaces presumably arise from the complex hole surface shown.

To see if the modifications we propose may reasonably be expected to arise from the addition of a potential and spin–orbit coupling, we first introduce a potential. Non-vanishing Fourier components of the potential exist for all reciprocal lattice vectors. JONES[9] has pointed out that with a slight movement of the two atoms in each unit cell with respect to each other, the Fourier components corresponding to wave numbers composed of odd numbers of principal reciprocal lattice vectors would vanish (they would have vanishing structure factor), and that in bismuth, such components will be smaller than the others. Jones pointed out that this effect is not large for large wave-numbers, but by keeping track of the structure factors of interest in our treatment, we see that these components are significantly smaller than those composed of even numbers of principal reciprocal attice vectors, and we do not include them explicitly. We assume that the components we keep have magnitude V/K^2, where V is an adjustable parameter and K is the magnitude of the reciprocal lattice vector in question. Such a form would be appropriate for a potential composed of Coulomb potentials on each atomic site. Proceeding as in our 4-OPW treatment of aluminum,[10] we treat bands 3–6 at B and bands 3–8 at C; all other bands having energies quite far removed from the Fermi energy at these points. As we increase V, we find that the sixth band energy is raised at B and lowered at C, confirming our supposition that the surface at B will disappear. We take a value of V which is 50 per cent larger than that required to make the sixth-band energy at B drop below that at C, and construct constant energy curves in the neighborhood of C, again following our procedure for treating aluminum.[10] The resulting curves are shown in Fig. 2.

The pointed portions of the $0{\cdot}9175E_0$ curve will be rounded off by the addition of the small matrix elements, making the shape more like that given by AUBREY and CHAMBERS[11]. The cusps associated with the lines of contact with the fifth band remain sharp when these are added. Addition of spin–orbit coupling, however, will lift the degeneracies associated with the lines of contact shown and introduce a tipping of the segments of electron surface. Spin–orbit coupling may also be expected to greatly reduce the unoccupied region of band 5 (the hole region) which would be very large in the above calculation with no spin–orbit coupling.

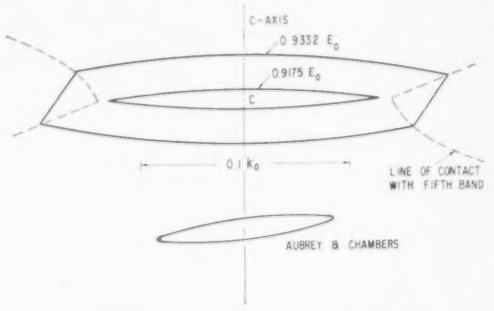

FIG. 2. Constant-energy curves near C according to a six-OPW approximation with certain small matrix elements neglected. The section is the same as that of Fig. 1. The Fermi surface proposed by AUBREY and CHAMBERS[11] is shown for comparison. E_0 is the single OPW Fermi energy and k_0 is the single-OPW Fermi wave number. The pointed ends of the $0{\cdot}9175E_0$ curve would be rounded by the inclusion of the small matrix elements. The degeneracy represented by the lines of contact would be lifted by spin–orbit coupling.

Finally, we examine the bands out of the plane shown in Figs. 1 and 2. We find that the energies of bands 5 and 6 rise together with the square of the displacement out of the plane of Figs. 1 and 2. This gives rise to segments of surface which are quite broad in this direction, though experimentally this is the narrowest dimension of the surface. Again, we may expect spin–orbit coupling to remove this discrepancy; the inclusion of spin–orbit coupling does not couple bands 5 and 6 at C, but a matrix element between them appears away from the plane of C and increases linearly with displacement. We may expect this to narrow the surface in the sixth band significantly, as well as to reduce the unoccupied region in the fifth band.

The final picture of the electron surface which we expect is shown in Fig. 3. The segments are located at the positions proposed by MASE[7], on the basis of his band calculations, but not in the positions proposed by JONES[12], who places them at

Vol. 17
1960

B in Figs. 1 and 3. MASE[7] has proposed that the hole surface is located at *A* in Figs. 1 and 3, while JONES[12] placed it at a position equivalent to *D*. Using the potential described above, a calculation of the bands along the line Γ-*A* indicated that the

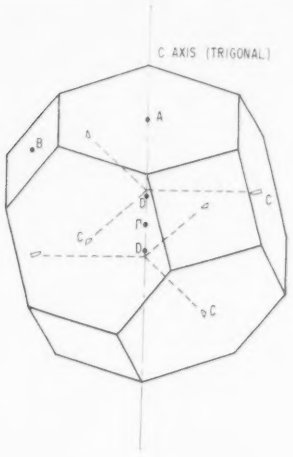

FIG. 3. The disposition of the electron Fermi surface at the centers of hexagonal faces. The segments lie approximately along lines perpendicular to and intersecting the *c*-axis, but are tipped slightly toward the point Γ. The sizes of the segments are approximately to scale. The figure represents a projection of the zone on a plane rotated 30° from that of Figs. 1 and 2 about an axis perpendicular to the c-axis and in the plane of Figs. 1 and 2.

holes are located at a position between *A* and *D*, but the inclusion of spin–orbit coupling might move it either way. Without adequate inclusion of spin–orbit coupling, we are unable to shed further light on this question.

Acknowledgement—The author has benefited from discussions of this problem with M. H. COHEN.

General Electric Research Laboratory
Schenectady
New York
W. A. HARRISON

References

1. HARRISON W. A., *Phys. Rev.* **118,** 1190 (1960).
2. SHOENBERG D., *Progress in Low-Temperature Physics*, Vol. II. North-Holland Publishing Co., Amsterdam (1957), (de Haas–Van Alphen Effect).
3. GALT J. K., YAGER W. A., MERRITT F. R. and CETLIN B. B., *Phys. Rev.* **114,** 1396 (1959), (cyclotron resonance).
4. ABELES B. and MEIBOOM S., *Phys. Rev.* **101,** 544 (1956), (galvanomagnetic properties).
5. SMITH G. E., *Phys. Rev.* **115,** 1561 (1959), (anomalous skin effect).
6. RENEKER D. H., *Phys. Rev.* **115,** 303 (1959), (magneto-acoustic attenuation).
7. MASE S., *J. Phys. Soc. Japan* **13,** 434 (1958); **14,** 584 (1959).
8. HARRISON W. A., *Phys. Rev.* **116,** 555 (1959).
9. See, for example, MOTT N. F. and JONES H., *The Theory of the Properties of Metals and Alloys* Chapter 5. Clarendon Press, Oxford (1936).
10. HARRISON W. A., *Phys. Rev.* **118,** 1182 (1960).
11. AUBREY J. E. and CHAMBERS R. G., *J. Phys. Chem. Solids* **3,** 128 (1957).
12. JONES H., *Proc. Roy. Soc.* **A147,** 396 (1934).

Spin resonance of electrons on donors in *p*-type silicon

(*Received* 7 *June* 1960)

WE HAVE observed paramagnetic resonance of donor impurities in *p*-type silicon. The experiments described here deal with processes occurring in compensated *p*-type silicon at liquid helium temperatures.

It is well known[1,2] that the "shallow" donor impurities, such as P, As, Sb and Bi are paramagnetic when present in neutral state of charge in silicon. Their hyperfine splittings allow an easy distinction among the different donors.

In *p*-type silicon, however, there is normally no paramagnetism associated with presence of donors as compensating impurities. These donors are positively charged having lost their electrons to the acceptor atoms.

We have used compensated *p*-type silicon crystals as indicated in Table 1. When kept in darkness no resonance was observed. Upon illumination of the samples with light of about 1μ wavelength electron–hole pairs are produced through band to band transitions. One observes appearance of resonance absorption typical of the donor present as compensation. The amplitudes of the lines increase with the photon flux absorbed, reaching eventually saturation. With light removed the amplitudes of the lines remain

unchanged for a period of at least several hours.

The resonance is due to electrons captured by the donors which become neutral and paramagnetic. Once captured, the electrons cannot, in a period of hours at helium temperatures, be thermally excited into the conduction band and could only recombine with free holes. The photoconductivity and photo-Hall experiments performed also at helium temperatures indicate that the carrier concentrations, under illumination never exceed 10^7 cm^{-3}. These carriers are identified as electrons from the sign of the Hall voltage. The holes must therefore be trapped, most probably at the boron centers which explains the very long time constants of the electrons on donors (Fig. 1). Dark conductivity of approximately 10^3 carriers-cm^{-3} is not sufficient for fast recombination of electrons and one observes an undiminished signal for a period of several hours.

Table 1

Crystal #[a]	Compensation	Room temperature resistivity (ohm–cm)	Concentration of donors (cm^{-3}) from	
			Resonance	Hall coefficient
B–11	P	0·8	$1{\cdot}5\times10^{15}$	5×10^{14}
B–17	P	1·1	3×10^{15}	6×10^{15}
B–19	As	1·0	5×10^{14}	7×10^{14}
B–20	As	2·0	6×10^{15}	3×10^{15}
B–24	P	0·9	7×10^{15}	3×10^{15}
B–23	As and P	1·1	1×10^{15}[b]	
B–18	Sb	0·9	1×10^{15}	2×10^{15}

[a] All the crystals were boron doped.

[b] Of each: As and P.

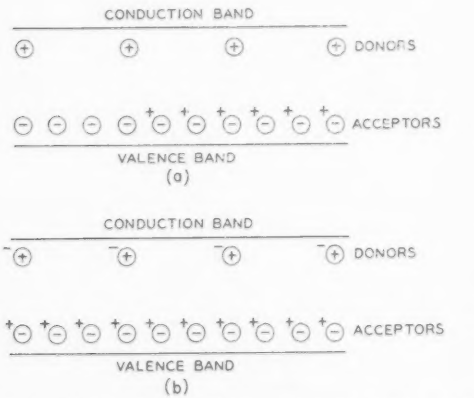

FIG. 1. Distribution of electrons among donors and acceptors at helium temperature. (a) Before light injection (b) After light injection.

The maximum amplitudes of the resonance lines have been compared to amplitudes of signals from samples with known donor concentrations (n-type). Care is required to take under consideration passage conditions while comparing the amplitudes. The concentrations obtained in such manner are listed in Table 1 together with the concentrations calculated from the Hall coefficient at low temperatures. Fair agreement of the two values, together with the saturation behavior of the amplitudes with flux makes us fairly certain that we observe resonance due to all donor atoms present. This method may be useful in determination of compensation in p-type silicon, both as to the type and concentration. We believe that it provides a more accurate determination of concentration than the Hall effect measurements.

In connection with these experiments we have estimated lifetime of electrons in p-type silicon at helium temperatures. This can be obtained from the steady state relation:

$$n = f\tau$$

where n is the steady state electron concentration under illumination, f the flux of photons absorbed

Vol. 17
1960

and τ the lifetime of electrons. The lifetimes thus obtained range between 10^{-9} and 10^{-8} sec and are approximately independent of the donor element present. With the additional knowledge of the concentration of donors we can estimate the cross section for capture of electrons at neutral acceptors (boron) to be of the order of 10^{-14} cm^2 at 1·2°K.

Acknowledgements—The authors would like to acknowledge profitable discussions with G. FEHER, W. L. BROWN and R. J. COLLINS.

Bell Telephone Laboratories
Murray Hill
New Jersey
U.S.A.

G. BEMSKI
B. SZYMANSKI

References

1. FLETCHER R. C., YAGER W. A., PEARSON G. L., HOLDEN A. N. and MERRITT F. R., *Phys. Rev.* **94,** 1392 (1954).
2. FEHER G., *Phys. Rev.* **114,** 1219 (1959).

BOOK REVIEW

Colloque National de Magnetisme Commemoratif de l'oeuvre de Pierre Weiss. Centre National de la Recherche Scientifique, Paris. 325 pp.

COMMEMORATING the fiftieth anniversary of the publication by PIERRE WEISS of his celebrated molecular field hypothesis, a Conference on Magnetism was held in Strasbourg in the summer of 1957. A volume has now appeared in which the papers and discussions which took place at that Conference are published. The impact which French science has had on the field of magnetism is universally recognized and is unparalleled in the history of science. Much of modern magnetism —which has seen such an intense flowering in recent years—can be traced directly to WEISS, his students, and "grand-students" many of whom now direct the many laboratories in France devoted in whole or in part to research in magnetism. The list of authors represented in this compilation includes a large number of scientific descendents of WEISS and at the same time is a veritable Who's Who in Magnetism.

The first few papers are concerned with modern developments associated with concepts first introduced by WEISS. The introductory paper by NÉEL —perhaps the foremost and most distinguished of WEISS's students—deals with the concept of molecular field and cites its importance in leading to an understanding of antiferromagnetism and ferrimagnetism as well as some tenable explanations of anomalies first observed by WEISS. Another paper by GUILLAUD and VAUTIER treats of another concept first advanced by WEISS—the domain—about which much new information has become available recently. The balance of the volume gives a good indication of the types of research currently in progress in the various French laboratories and covers a wide spectrum of magnetic effects. While it seems reasonable to suppose that most of the material contained in this volume will be published in one form or another in the various journals, as an up to date index of the extent, variety and caliber of the work in progress at perhaps the most important geographical center of research in magnetism, this volume should find its way into many a library with leanings towards magnetics.

J. E. GOLDMAN

BOOKS RECEIVED

Plansee Proceedings, 1958. *High Melting Metals* (Papers presented at the Third Plansee Seminar "*De Re Metallica*" held at Reutte/Tyrol in June 1958.) Edited by F. BENESOVSKY. Pergamon Press, 1959. xii+465 pp. Price £4. 3. 6.

R. HERMAN and R. HOFSTADTER: *High-Energy Electron Scattering Tables*. Stanford University Press, Stanford, California, 1960. 278 pp. Price $8.50.

W. HUME-ROTHERY: *Atomic Theory for Students of Metallurgy*. The Institute of Metals, London, 1960. 427 pp. Price 50s.

J. Phys. Chem. Solids Pergamon Press 1961. Vol. 17, Nos. 3/4, pp. 177–187. Printed in Great Britain.

ON THE METASTABLE γ-PHASE URANIUM–MOLYBDENUM ALLOYS

F. J. BLATT

Clarendon Laboratory, Oxford.*

(*Received* 9 *March* 1960)

Abstract—The experimental data of CHANDRASEKHAR and HULM (resistivity), of BERLINCOURT (Hall effect) and of GOODMAN *et al.* (specific heat) are examined within the framework of the band model suggested by FRIEDEL. It is shown that all available data are consistent with a reasonable density of states curve, and the qualitative features of that curve are in agreement with those deduced by FRIEDEL from the properties of pure uranium. Attention is directed to the thermoelectric power of these alloys as a means of further defining the band structure. Moreover, the thermoelectric power of certain uranium alloys may be large enough to be of practical interest.

1. INTRODUCTION

IN 1958 CHANDRASEKHAR and HULM[1] reported measurements of the resistivity and superconducting transition of a number of metastable γ-phase uranium–molybdenum alloys. One of the interesting properties of these alloys is the monotonic decrease of their resistivity with increasing temperature over the range investigated, 4–300°K.

The explanation for this anomalous behaviour suggested by CH is based on an expression given by JONES[2]. That relationship is appropriate to a metal in which there are two overlapping bands of which one is very narrow. Such a band structure was shown to be reasonable for α- and γ-phase uranium by FRIEDEL[3]. Moreover, CHANDRASEKHAR and HULM found that this same model could also account fairly well for the superconducting properties of the alloys.

Recently BERLINCOURT[4] remeasured the resistivities of a number of the alloys and also determined their Hall coefficients at 4·2°K, 77°K and 300°K. The Hall coefficients of all samples were positive and, with the exception of one alloy (11·6 per cent Mo), showed a positive temperature coefficient $\beta = (1/R)(dR/dT)$ of the order of 5×10^{-4}/°K.

BERLINCOURT concluded from what he considered to be a rather slow variation of the Hall coefficient R with temperature that the explanation for the negative temperature coefficient of resistivity put forth by CHANDRASEKHAR and HULM could not be correct because "such parameters would lead to a strongly temperature-dependent relaxation time for the broad band electrons and a correspondingly strong temperature dependence of the Hall coefficient, in contradiction with observation".[4] That conclusion is in error and in the following we shall show that FRIEDEL's two-band model as employed by CHANDRASEKHAR and HULM does, in fact, predict the observed temperature dependence of the Hall coefficient. Indeed, if anything it would seem at first sight that the temperature variation of the Hall coefficient is unusually *rapid*.

We shall consider the resistivity, Hall coefficient and specific heat in that order and shall attempt to deduce from this information a consistent picture of the band structure of the metastable γ-phase alloys. Finally, we shall turn our attention to the thermoelectric power of these alloys and show that a study of this phenomenon would be valuable not only in shedding further light on the band structure problem but may well prove to be of considerable practical interest.

* N.S.F. Post-doctoral fellow, on leave from Michigan State University, East Lansing, Michigan, U.S.A.

2. POSSIBLE ORIGINS OF A NEGATIVE TEMPERATURE COEFFICIENT OF RESISTIVITY

An anomalous temperature dependence of the resistivity may arise in a metal from a variety of causes, and we shall here consider briefly a few of these. We shall assume that the conduction electrons form a degenerate gas, so that the conductivity is given by

$$\sigma = -\int_0^\infty \sigma(\epsilon)\frac{\partial f_0}{\partial \epsilon}\,d\epsilon = \sigma(\eta) + \frac{\pi^2}{6}(kT)^2\left(\frac{\partial^2\sigma(\epsilon)}{\partial\epsilon^2}\right)_{\epsilon=\eta} \tag{1}$$

where

$$\sigma(\epsilon) = \frac{e^2}{12\pi^2\hbar^3}[\tau(\epsilon)\langle v_c(\epsilon)\rangle^2 N_c(\epsilon)] \tag{2}$$

Here $N_c(\epsilon)$ is the density of states in the conduction band,

$$\langle v_c(\epsilon)\rangle = (1/\hbar)\nabla_k\epsilon$$

is the expectation value of the velocity of an electron of energy ϵ in the conduction band, and $\tau(\epsilon)$ is the relaxation time. It will be convenient to write $[\tau(\epsilon)]^{-1} = QN_f(\epsilon)$; here $N_f(\epsilon)$ denotes the density of final states for the scattering processes which limit the conductivity, and Q is a quantity containing a variety of factors such as the number of defects (phonons and impurities) and the matrix elements for transitions of an electron from an initial state in the conduction band to some final state, which, for convenience, we assume to be of the same energy ϵ (i.e. we limit ourselves to elastic scattering only).

In normal metals it is the variation of Q with temperature that is responsible for the usual Bloch–Grüneisen temperature dependence of the resistivity.[5] Departures from the Bloch–Grüneisen law could arise from causes which we may classify as follows:

(1) An explicitly temperature-dependent scattering mechanism leading to an *anomalous* variation of Q with T. We would include here significant departures of the phonon spectrum from the Debye form; such departures will lead to deviations from the Bloch–Grüneisen law.

(2) A variation of $N_f(\epsilon)$ with ϵ sufficiently rapid to make the second term on the right-hand side of equation (1) of significant magnitude.

(3) A dependence of the band structure on temperature, leading to anomalous variations of $N_f(\epsilon)$, $N_c(\epsilon)$ and/or $v_c(\epsilon)$ with temperature.

As an example of mechanism (1) we may cite the generation of vacancies in metals at high temperatures. These defects present scattering centers to the conduction electrons and are believed to be responsible for anomalies of the resistivity near the melting point.[6]

The second mechanism is that considered by JONES[2]. It is assumed that the band structure of the metal is such that two bands overlap near the Fermi energy. One band, which we shall call the conduction band for convenience, is presumed to be rather broad (effective mass roughly equal to that of a free electron), whereas the second band is assumed narrow. Moreover, it is further assumed that the density of states in the narrow band greatly exceeds that in the conduction band at the Fermi energy, and that this density of states is a sensitive function of energy. It is this model which we shall consider shortly in more detail.

Finally, to turn to the third mechanism mentioned above, a variation of the band structure with temperature could arise from several causes. First, if the band structure is very sensitive to the lattice parameters, thermal expansion of the lattice will surely reflect itself in an alteration of the energy spectrum with temperature. Also, the electron–lattice interaction as such is known to affect the energy gap in semiconductors,[7] and the same mechanism may well play an important role in metals also. This possiblity has been suggested recently by ZIMAN[8].

3. THE JONES–FRIEDEL–CHANDRASEKHAR AND HULM MODEL

We assume that the band structure of a γ-phase uranium alloy is as shown schematically in Fig. 1 or Fig. 2. Fig. 1 shows the conduction and the narrow band as if both were of "standard" parabolic form. Fig. 2 is the band model suggested by FRIEDEL[3] for pure γ-phase uranium.

We shall now assume, as did JONES[2], that the only function which exhibits a rapid energy dependence near the Fermi energy is $N_f(\epsilon)$, the density of states in the narrow "f-band". We further restrict and simplify the analysis by assuming that the effective mass in this narrow band is

Vol. 17
1960

so large that the current is carried almost exclusively by the electrons (or holes) in the broad conduction band. Under these assumptions the

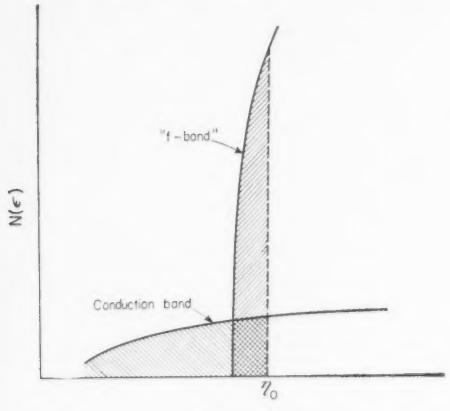

FIG. 1. Proposed band structure for γ-phase uranium, standard band approximation.

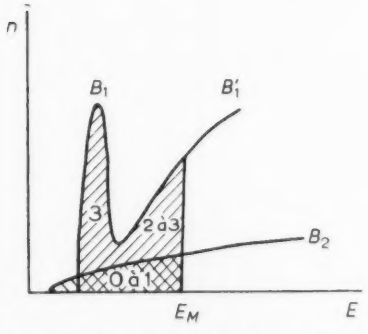

FIG. 2. Proposed band structure for γ-phase uranium, according to FRIEDEL.

resistivity,[2] Hall coefficient and thermoelectric power are given by the following expressions:

$$\rho(T)=\rho(\eta_0,T)\left[1-\frac{\pi^2}{6}(kT)^2\left\{3\left(\frac{N_f'}{N_f}\right)^2-\left(\frac{N_f''}{N_f}\right)\right\}\right] \quad (3)$$

$$R(T)=R(\eta_0,T)\left[1+\frac{\pi^2}{3}(kT)^2\left(\frac{N_f'}{N_f}\right)^2\right];$$

$$R(\eta_0,T)=\frac{1}{n_c e c} \quad (4)$$

$$S(T)=\frac{\pi^2k^2T}{6e}\left\{\left[\left(\frac{3}{\eta_0}\right)-2\left(\frac{N_f'}{N_f}\right)\right]+\right.$$
$$+\frac{\pi^2}{15}(kT)^2\left[42\left(\frac{N_f'N_f''}{N_f^2}\right)-\right.$$
$$\left.\left.-37\left(\frac{N_f'}{N_f}\right)^3-7\left(\frac{N_f'''}{N_f}\right)\right]\right\} \quad (5)$$

$$\cong-\frac{\pi^2k^2T^2}{3e}\left(\frac{N_f'}{N_f}\right)\left[1-\frac{\pi^2}{30}(kT)^2\left\{42\left(\frac{N_f''}{N_f}\right)-\right.\right.$$
$$\left.\left.-37\left(\frac{N_f'}{N_f}\right)^2-7\left(\frac{N_f'''}{N_f'}\right)\right\}\right] \quad (5a)$$

In the above expressions each prime (′) denotes differentiation with respect to ϵ, and all quantities within the brackets are to be evaluated at η_0, the Fermi energy at $T=0°K$. Equations (3)–(5) were obtained from the well known results for the transport coefficients[5] and the usual expansion of the relevant integrals in the degenerate limit.[9] In the spirit of the Jones model, we have retained, however, only terms of order $(N_f'/N_f)^2$ in equation (4) and have neglected terms of the form $(N_f'/\eta_0 N_f)$ and $(1/\eta_0)^2$. The corresponding simplification has also been employed in the derivation of equations (5) and (5a).

If we further assume that the f-band is of standard form the above equations reduce to

$$\rho(T)=\rho(\eta_0,T)\left[1-\frac{\pi^2}{6}\left(\frac{kT}{\Delta E}\right)^2\right] \quad (6)$$

$$R(T)=R(\eta_0,T)\left[1+\frac{\pi^2}{12}\left(\frac{kT}{\Delta E}\right)^2\right] \quad (7)$$

$$S(T)=S(\eta_0,T)\left[1+\frac{5\pi^2}{6}\left(\frac{kT}{\Delta E}\right)^2\right];$$

$$S(\eta_0,T)=\frac{\pi^2k^2T}{6e\Delta E}. \quad (8)$$

Here ΔE is the energy difference between the Fermi energy at $T=0°K$ and the edge of the f-band. Our previous assumption that $N_f'/N_f \gg 1/\eta_0$ is equivalent, in this special case, to the assumption $\Delta E \ll \eta_0$.

4. CORRELATION OF THE JONES–FRIEDEL–CHANDRASEKHAR and HULM MODEL WITH EXPERIMENTAL DATA

We shall now attempt to correlate the experimental results of CHANDRASEKHAR and HULM, BERLINCOURT and GOODMAN *et al.*[10] with the Friedel band model for γ-phase uranium. We shall use the "standard band" expressions, equations (6) and (7), as well as the more general formulae, equations (3) and (4). We consider, in turn, the resistivity, the Hall coefficient and the electronic specific heat,[10] and shall then attempt to deduce a consistent band model.

4a. *Resistivity*

The results of CHANDRASEKHAR and HULM are shown in Fig. 3, and these strongly suggest that equations (3) or (6) are applicable to these alloys. In the temperature range between 4°K and 100°K the changes in resistivity appear to obey the parabolic (i.e. T^2) dependence on temperature predicted by equations (3) and (6). At higher temperatures deviations from parabolic form are evident, and these may be due to a variety of causes. First, although at low temperatures it is reasonable to assume that $\rho(\eta_0, T)$ is independent of temperature—electron scattering arising primarily from the presence of stationary imperfections—at elevated temperatures electron–phonon scattering will play an important role. Consequently, since $\rho(\eta_0, T)$ is a monotonically increasing function of T (Bloch–Grüneisen function), we may expect just the sort of deviation from the form of equation (3) which the curves of CHANDRASEKHAR and HULM show at elevated temperatures. Another possibility is that the band structure itself is temperature dependent; in that case we would again expect to find some deviations from the prediction of equation (3) at elevated temperatures.

In Table 1 we have summarized the parameters which we obtain when we fit the curves of

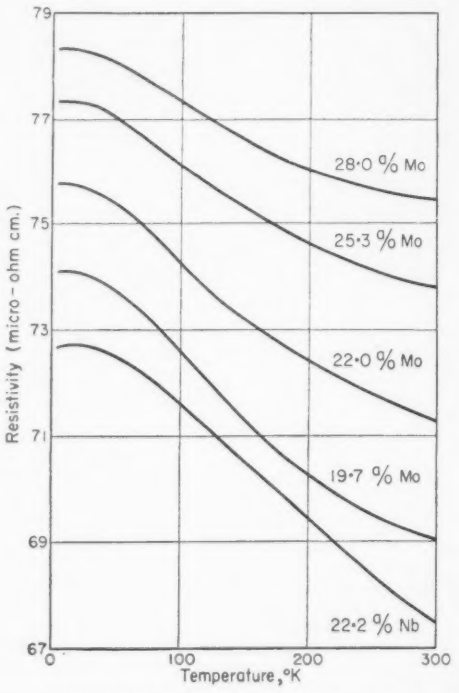

FIG. 3. Resistivity vs. temperature for some metastable γ-phase uranium alloys (according to CHANDRASEKHAR and HULM).

Table 1. *Parameters of the narrow band of γ-phase uranium–molybdenum alloys from resistivity results.*

Alloy, Mo concentration (%)	$P^2 = 3(N_f'/N_f)^2 - N_f''/N_f$; equation (3) $(\text{eV})^{-2}$	ΔE; equation (6) eV
11·6 (Be)	180	0·074
19·7 (CH)	165	0·078
22·0 (CH)	165	0·078
25·3 (CH)	135	0·086
28·0 (CH)	105	0·098

(Be) From results of BERLINCOURT[4].
(CH) From the results of CHANDRASEKHAR and HULM[1].

Vol. 17
1960

CHANDRASEKHAR and HULM and the one curve shown by BERLINCOURT to equations (3) and (6) in the temperature range between 4°K and about 100°K. We have not made use of BERLINCOURT's resistivity data for his other two alloys because he measured the resistivities of his 21·7 per cent and 30·5 per cent Mo alloys at three temperatures only.

Although it is perhaps hazardous to attach much significance to the numerical values of the parameter $P^2 = 3(N_f'/N_f)^2 - N_f''/N_f$ which, in the standard band limit, is just $(1/\Delta E)^2$, it is possibly of some significance that this parameter changes monotonically with increasing molybdenum concentration. If the standard band model were applicable to the *f*-band, we would conclude from Table 1 that this band is being filled gradually as we increase the molybdenum concentration, the Fermi energy moving farther from the band edge as molybdenum is added.

4b. *Hall effect*

BERLINCOURT's results on the Hall effect of these alloys provide perhaps the best arguments *against* mechanism (1), i.e. an anomalous temperature dependence of the relaxation time, as the mechanism responsible for the negative temperature coefficient of resistivity. For, contrary to BERLINCOURT's statement, a *temperature dependent* relaxation time does *not* lead to a temperature dependence of the Hall coefficient, R, provided the surfaces of constant energy in the conduction band are nearly spherical. If the energy surfaces in the conduction band have a more complicated shape R may vary with T as the dominant relaxation mechanism changes from scattering by impurities to scattering by phonons.

One must be careful, however, to distinguish between a relaxation time which is dependent on temperature and a relaxation time which *varies rapidly with electron energy*. In the latter case we see from equation (4) that the modification of the Fermi distribution with temperature can then lead to a temperature dependence of the Hall coefficient.

In fact, the alloys investigated by BERLINCOURT[4] display a rather pronounced temperature dependence of their zero-field Hall coefficients (see Fig. 4). Consequently, if we wish to ascribe this observation to an anomalous variation of $\tau(\epsilon)$ of the sort discussed earlier we should have to rely on mechanisms (2) or (3).

The Hall coefficient of each of the three alloys studied by BERLINCOURT is positive, suggesting that the current in the conduction band is, in fact, carried by "holes" rather than electrons.

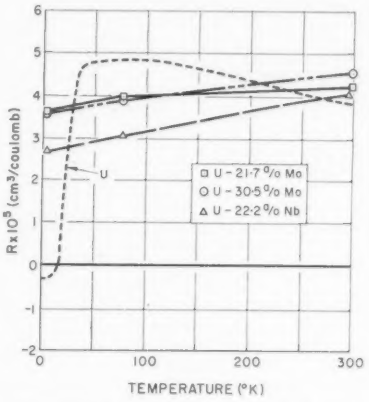

FIG. 4. Hall coefficient vs. temperature of some metastable γ-phase uranium alloys and of pure α-phase uranium (according to BERLINCOURT).

However one wishes to interpret the sign of R, the other information which we obtain from the data is that $|R|$ *increases* with increasing temperature, the behavior predicted by equations (4) and (7), regardless of the sign of R. We note, though, that although qualitatively the variation of R with temperature is correct (i.e. in agreement with the Jones–Friedel model), there would seem to remain a significant quantitative discrepancy, at least if we restrict ourselves to the standard band model, equation (7). From equations (6) and (7) we conclude that the fractional changes in R and ρ with temperature should be closely related, the fractional change in R being half that in ρ. Instead, we find that the fractional change in R is roughly an order of magnitude larger than that in ρ (neglecting the surprisingly large effect observed for the 11·6 per cent Mo alloy). Moreover, we note that whereas the predicted dependence of R on T is as T^2, the data of BERLINCOURT seem to suggest a variation with temperature rather less rapid. (With only three points available, 4·2°K, 77°K, and 300°K, it is difficult to deduce a temperature dependence.) The deviation from the expected T^2

Table 2. Parameters of the narrow band of γ-phase uranium–molybdenum alloys from results on resistivity, ρ, and Hall coefficient, R.

Alloy Mo conc. (%)	$(N_f'/N_f)^2$ (eV)$^{-2}$ (from R vs. T)	ΔE (eV) (from R vs. T)	ΔE (eV) (Table 1)	N_f''/N_f (eV)$^{-2}$ (calc.)	N_f''/N_f (eV)$^{-2}$ (stand. band)
11·6 (Be)	5550*	0·068*	0·074	+16300	−5500
21·7 (Be)	620	0·02	0·078	+ 1700	− 620
30·5 (Be)	520	0·022	0·11	+ 1480	− 520

(Be) From results of BERLINCOURT[4].

* From temperature dependence of R in the limit $H = 0$.

† Estimated by extrapolating result shown in Table 1.

behaviour is similar to the non-parabolic resistivity vs. temperature curves of CHANDRASEKHAR and HULM.

We have attempted to extract the appropriate band parameters from the Hall data. The results, shown in columns 2 and 3 of Table 2, are on even shakier foundations than those of Table 1. To obtain the results of Table 2 we have *assumed* that between 4·2°K and 77°K $R(T)$ is given correctly by equation (4) or (7), and have made use of the values of R at 4·2°K and 77°K only. For comparison with the resistivity results we have listed, in Column 4, the ΔE values as obtained from the resistivity results. The disagreement between these two ΔE values is so great that one must conclude that the standard band model cannot be applied to the narrow f-band.

If we reject the standard band model and, moreover, accept the numerical results shown in Table 1 and the first three columns of Table 2, we may then proceed to deduce numerical values for the quantity N_f''/N_f. The values of N_f''/N_f so calculated are listed in column 5 of Table 2; in the last column we have given the values of this same quantity according to the standard band model. It is apparent that, according to the data which we have examined so far, the true shape of the f-band does not even resemble a parabola near the Fermi energy; not only are the magnitudes of the values in the last two columns of Table 2 quite different, but their signs are opposite. We note, moreover, that both N_f'/N_f and N_f''/N_f are unusually large, so much so that the results must be viewed with considerable skepticism. These unreasonable magnitudes for the derivatives of N_f arise because we have assumed that the variation of R with T is exclusively the consequence of the peculiarities of the density-of-states function. The field and temperature dependences of the Hall coefficient of the 11·6 per cent Mo alloy (see Fig. 5) suggest some sort of spin order in the γ-phase, and it may well be this order which is in large measure responsible for the Hall effect anomalies.

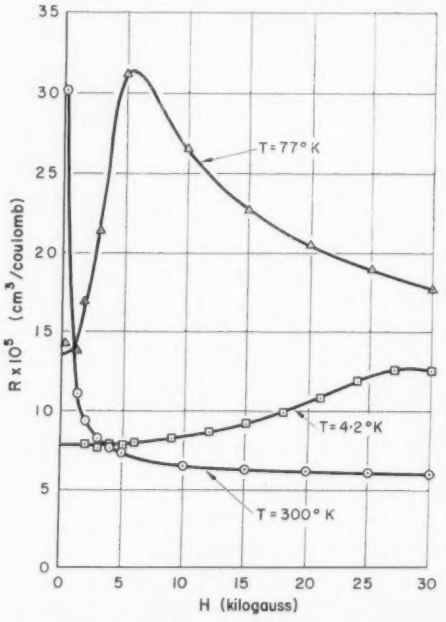

FIG. 5. Hall coefficient vs. magnetic field of a metastable γ-phase uranium alloy, containing 11·6 per cent Mo, at 4·2°K, 77°K and 300°K (according to BERLINCOURT).

Vol. 17
1960

The behaviour of the 11·6 per cent Mo alloy is most perplexing at first sight. A clue to a possible explanation of the field dependence of R may be obtained by plotting not the Hall coefficient, $R = E_H/JH$, but the Hall field, E_H, per unit current density, J, vs. H. This set of curves is shown in Fig. 6, and the shape of the curves

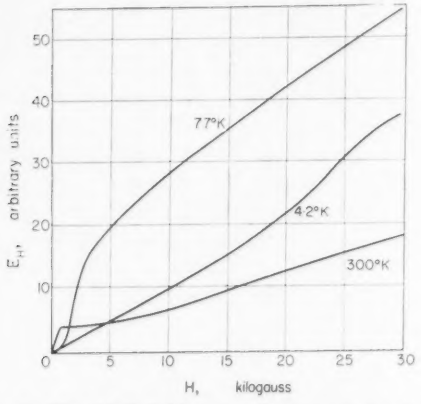

FIG. 6. The Hall field per unit current density vs. magnetic field of the 11·6 per cent Mo alloy studied by BERLINCOURT. These curves, corresponding to measurements carried out at 4·2°K, 77°K and 300°K were constructed from the curves given by BERLINCOURT, see Fig. 5.

corresponding to 77°K and 300°K now appear qualitatively similar to the corresponding curves for the ferromagnetic metals and alloys.[11] This similarity suggests that the origin of the anomalies of the Hall effect, and possibly also of the resistivity, may rest in a spin ordering in the γ-phase. Surely spin-orbit coupling will be quite large in the heavy transition metals and this could result in the "anomalous currents" which are believed to give rise to the "extraordinary" Hall effect in ferromagnetic metals.[12] Measurements of the magnetic susceptibility of these alloys as function of alloy composition and of temperature should help elucidate this question, as would studies of neutron diffraction.

4c. *Electronic specific heat*

If, for the moment, we revert once again to the standard band assumption for the narrow band it then follows from Table 1 that $N_f(\eta_0)$, being proportional to $(\Delta E)^{1/2}$, should increase with increasing molybdenum concentration. The results of GOODMAN *et al.*[10] which we have summarized in Table 3 show, however, that in the γ-phase alloys $N(\eta_0)$ *decreases* with increasing molybdenum concentration, showing again that the shape of the

*Table 3. Electronic specific heat and density of states of three metastable γ-phase uranium–molybdenum alloys.**

Alloy Mo conc. (%)	$\gamma = C_v/T$ mJ °K^{-2} mol^{-1}	$N(\eta_0) \times 10^{-22}$ (eV)$^{-1}$ cm^{-3}
17·8	15·1	30·2
21·6	14·9	29·8
29·6	14·2	28·4

* According to GOODMAN *et al.*[10]

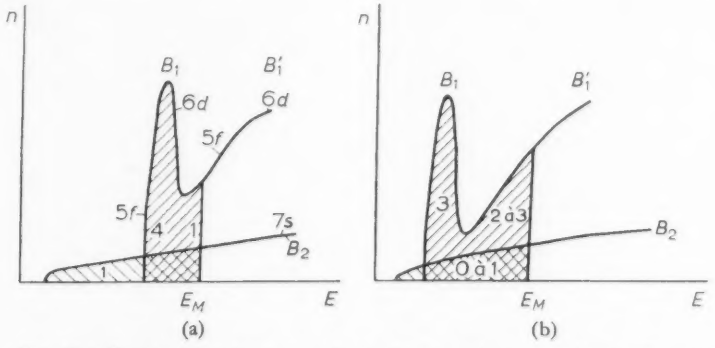

FIG. 7(a). Proposed band structure for α-phase uranium, according to FRIEDEL.
(b). Proposed band structure for γ-phase uranium, according to FRIEDEL.

narrow, high density-of-states band is *not* parabolic. The magnitude of the electronic specific heat, some twenty times that of silver, clearly demonstrates that the density of states at the Fermi energy is indeed quite large. Presumably, this large density of states is attributable to the *f*-band.

BAND STRUCTURE OF THE α- AND γ-PHASE ALLOYS

The band model proposed by FRIEDEL is shown in Figs. 7(a) and 7(b) and will serve as our guide in the following discussion. We first concentrate our attention on the γ-phase alloys and summarize the pertinent conclusions.

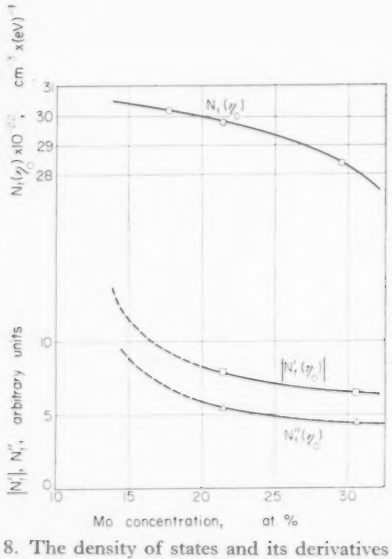

FIG. 8. The density of states and its derivatives at the Fermi energy as function of molybdenum concentration. Results deduced from temperature dependence of resistivity and Hall coefficient and concentration dependence of the electronic specific heat.

1. The density of states at the Fermi energy, $N_f(\eta_0)$, is unusually large and decreases with increasing molybdenum concentration (specific heat).

2. The logarithmic derivative of N_f at the Fermi energy is also of exceptional magnitude and also decreases with increasing molybdenum concentration (Hall effect).

3. The second derivative of N_f with respect to energy is *positive* at the Fermi energy; moreover, N_f''/N_f decreases with increasing molybdenum concentration (resistivity and Hall effect).

These conclusions are illustrated in Fig. 8.

We have deduced the positive curvature of the *f*-band near the Fermi energy from Hall and resistivity data on the metastable γ-phase uranium alloys. We agree here with FRIEDEL, who came to the same conclusion from considerations of the temperature dependence of the paramagnetic susceptibility of pure uranium. The agreement, however, is only qualitative, our numerical estimates for the slope and curvature of the *f*-band exceeding FRIEDEL's by about an order of magnitude. We have already commented on the unusual values of N_f'/N_f and N_f''/N_f as given in Table 2. We recall here again that these results were obtained with the aid of assumptions of questionable validity (spherical energy surfaces) and should therefore be viewed with some scepticism. Moreover, our conclusions are derived from data on *metastable* γ-phase *alloys* between 4°K and 300°K whereas FRIEDEL's are based on the properties of *pure* uranium *stable* in the γ-phase at a temperature near 1100°K: the quantitative difference is not surprising. Instead, it is perhaps rather gratifying that two quite different methods of analysis should lead to the same qualitative conclusions concerning the band structure of γ-phase uranium.

If we then accept this similarity between pure γ-phase uranium and the metastable alloys, we may add to items 1, 2, and 3, above, a fourth statement which further defines the shape of the density-of-states curve near the Fermi energy. We may *assume* that the thermoelectric power of the metastable γ-phase alloys is of the same sign as that of pure γ-phase uranium, namely positive. From equation (5) (see also FRIEDEL's equation 6) we then conclude:

4. The slope of N_f at the Fermi energy is *positive*. (*Assumed* sign of the thermoelectric power).

Let us now consider the band structure which would be consistent with items 1–4. The picture which we obtain is very nearly the same as that given by FRIEDEL, and is shown in Fig. 9. As the molybdenum concentration is increased either the Fermi energy shifts gradually to lower energies (resulting in lower values of N_f, N_f' and N_f'') or the band structure is modified in such a way as to lead to effectively the same result as regards the

Vol. 17
1960

density of states and its derivatives at the Fermi energy. Quite possibly, both effects may occur simultaneously.

We recall here that CHANDRASEKHAR and HULM also deduced that in the γ-phase alloys $N_f(\eta_0)$ decreased with increasing molybdenum concentration, a conclusion since fully confirmed by the work of GOODMAN and co-workers. CHANDRASEKHAR and HULM arrived at their conclusion from observations on the superconducting transition

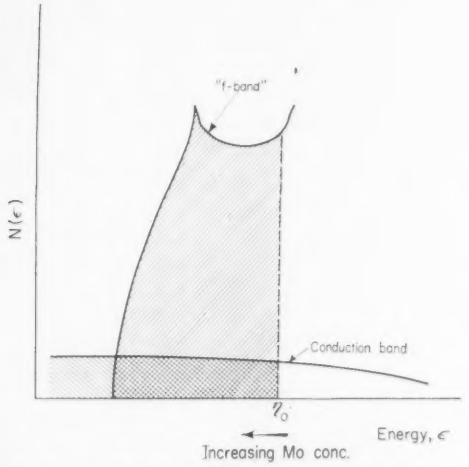

FIG. 9. One of the possible band structures for the metastable γ-phase uranium–molybednum alloys consistent with available data.

temperatures of the various alloys. Moreover, CHANDRASEKHAR and HULM pointed out that this change of N_f with molybdenum concentration may quite possibly explain the rather weak dependence of the residual resistivities of the alloys on molybdenum concentration. Normally, one expects—and generally finds—that the residual resistivity of an alloy is proportional to $c(1-c)$, where c is the solute concentration. The increase in residual resistivity of the metastable γ-phase uranium–molybdenum alloys is not nearly as rapid as the $c(1-c)$ relation predicts (see Fig. 10). We believe that CHANDRASEKHAR and HULM are correct in their suggestion that the relative insensitivity of the residual resistivity to alloy composition may be accounted for by the fact that as the number of scattering centers increases with increasing molybdenum concentration there occurs a

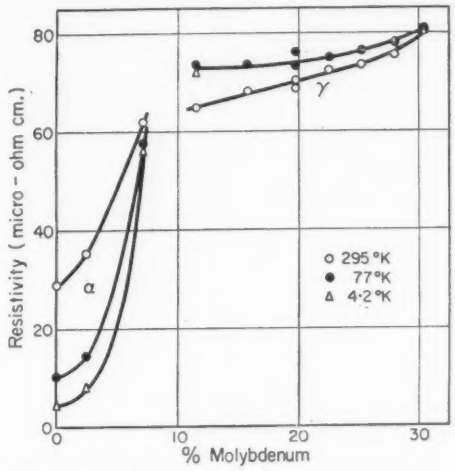

FIG. 10. Resistivity vs. composition for uranium–molybdenum alloys at three different temperatures. Most of the 4·2°K points are essentially coincident with the 77°K points in the γ-phase region and are therefore omitted. (According to CHANDRASEKHAR and HULM.)

simultaneous decrease of the density of states in the f-band at the Fermi energy, thus reducing the transition probability for each individual scattering event. These two effects, acting in opposite directions on the residual resistivity, apparently nearly cancel one another.

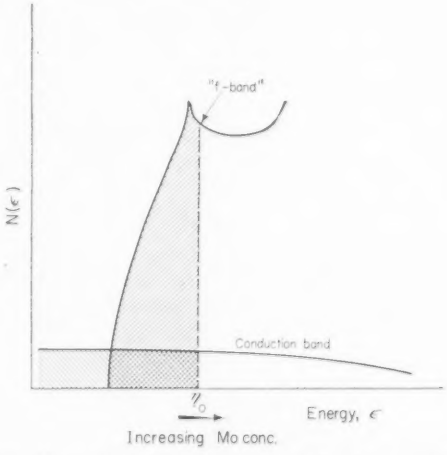

FIG. 11. A possible band structure for the metastable γ-phase uranium–molybdenum alloys; this model may be appropriate if the absolute thermoelectric power of these alloys is negative.

In the event that statement 4 above should prove incorrect we would need to revise our band model somewhat. The picture might then be more nearly as shown in Fig. 11. The Fermi energy is now located at a point at which the slope of the density-of-states curve is negative. In order that N_f, $|N_f'|$ and N_f'' decrease with increasing molybdenum concentration we would now have to stipulate that the Fermi energy shift to higher energies with increasing molybdenum concentration. Of course, in view of the relatively inadequate understanding of thermoelectricity in metals and the apparent sensitivity of thermoelectricity to the shape of the Fermi surface one would hesitate to interpret thermoelectric power data too rigidly. Quite possibly the question as to which of the two models (if either) is more nearly correct could be resolved better by a study of the soft X-ray bands of the alloys. Nevertheless, thermoelectricity of the alloys may be a rather interesting property to investigate.

In the α-phase the residual resistivities of the uranium–molbdenum alloys are also not proportional to $c(1-c)$. Here, however, the residual resistivity *increases too rapidly* with increasing c. CHANDRASEKHAR and HULM have suggested that in this phase an increase in molybdenum concentration *enhances* the density of states at the Fermi energy, and consequently the residual resistivity now increases not only by virtue of an increase in the number of scattering centers,—the factor $c(1-c)$—, but also by virtue of an increase in the transition probability for each collision. That $N_f(\eta_0)$ increases with molybdenum concentration in the α-phase is also consistent with the change in the superconducting transition temperature with c.[1] It may be more than fortuitous that as the limit of phase stability is approached (rougly 10 per cent Mo) the residual resistivities appear to approach the same value in both phases (see Fig. 10). This would seem to suggest that the limit of phase stability is related to the attainment of a critical, high density of states, a situation rather reminiscent of the Hume–Rothery rules.

6. THERMOELECTRIC POWER

According to equations (5) and (5a) the thermoelectric power of the metastable γ-phase uranium–molybdenum alloys should be unusually large if, indeed, the correct explanation for the temperature dependences of the resistivity and Hall coefficient is the one presented above, based on the Jones–Friedel band model. A measurement of the thermoelectric power would be of considerable value in further defining the form of the f-band, as was indicated already in the preceding section. If equation (5a) is an adequate approximation the magnitude of the thermoelectric power at low temperatures should be related simply to the temperature dependence of the Hall coefficient. The sign of the thermolectric power would serve to determine the sign of N_f' (within the qualifications mentioned earlier). Thus, a knowledge of the thermoelectric power would serve as a valuable check on the suggested location of the Fermi energy in the band scheme proposed by FRIEDEL.

A study of the thermoelectric power of these alloys may also be of some practical interest. We recall that recently MACDONALD *et al.*[13] have considered the possibility of refrigeration below helium temperature by means of Peltier cooling. They suggested that gold of very high purity may display the requisite properties which might make such cooling methods effective. It would seem that another likely candidate may be a uranium–molybdenum alloy near the α-/γ-phase stability limit. From the data of BERLINCOURT we find that the ratio $|N_f'/N_f|$ is about 75 $(\text{eV})^{-1}$ for the 11·6 per cent Mo alloy (see Table 2). If this result is correct the thermoelectric power of that alloy should be about 7·5 μV/°K at 4·2°K, i.e. nearly three orders of magnitude larger than that of "normal" metals at that temperature. It is conceivable that even larger values of $|N_f'/N_f|$ could be attained by suitably altering the alloy composition.

The disadvantage of these alloys as low temperature Peltier cooling elements lies in their transition to superconductivity near 2°K. On the other hand, they might prove superior to gold in the range above 4°K, and their preparation may not present metallurgical problems as severe as those encountered in the preparation of ultrapure gold. The alloys should also be more desirable than semiconductors which generally do not perform well at low temperatures.

7. CONCLUSION

We may summarize the discussion with the statement that it appears possible to reconcile the

Vol. 17
1960

resistivity, Hall effect, and specific heat data on the metastable γ-phase uranium–molybdenum alloys with the band model suggested by FRIEDEL. Modifications of that model may be required as new information (thermoelectric power, soft X-ray bands, magnetic susceptibility) becomes available. Also, we must not exclude the possibility that the anomalies discussed in this paper may find a more palatable explanation in terms of a model quite different from that adopted here. In particular the possible existence of an ordered spin structure in these alloys is suggested by the experimental data on at least one of the alloys.

Acknowledgements—The work described herein was performed during the tenure of an N.S.F. post-doctoral fellowship. I wish to thank the National Science Foundation for that grant and Professors W. E. LAMB, Jr. and B. BLEANEY for the hospitality extended to me during my stay at the Clarendon Laboratory, Oxford. I am also grateful to Professor J. FRIEDEL, Dr. W. M. LOMER, Dr. W. MARSHALL and Dr. B. R. COLES for valuable comments.

REFERENCES

1. CHANDRASEKHAR B. S. and HULM J. K., *J. Phys. Chem. Solids* **7,** 259 (1958).
2. JONES H., *Handbuch der Physik*, Vol. 19, p. 227. Springer Verlag, Berlin (1956).
3. FRIEDEL J., *J. Phys. Chem. Solids* **1,** 175 (1956).
4. BERLINCOURT T. G., *J. Phys. Chem. Solids* **11,** 12 (1959).
5. BLATT F. J., *Solid State Physics*, Vol. 4, p. 200. Academic Press, New York (1957).
6. MACDONALD D. K. C., *J. Chem. Phys.* **21,** 177 (1953).
7. FAN H. Y., *Phys. Rev.* **82,** 900 (1951); FAN H. Y., *Rep. Progr. Phys.* **19,** 10 (1956).
8. ZIMAN J. M., *Proc. Roy. Soc.* A**252,** 63 (1959).
9. WILSON A. H., *The Theory of Metals*. Cambridge University Press (1953).
10. GOODMAN B. B., HILLAIRET J., VEYSSIE J. J. and WEIL L., *C.R. Acad. Sci., Paris* **250,** 542 (1960).
11. JANO J. P., *Solid State Physics*, Vol. 5, p. 1, and references given therein. Academic Press, New York (1958).
12. ADAMS E. N. and BLOUNT E. I., *J. Phys. Chem. Solids*, **10,** 286 (1959).
13. MACDONALD D. K. C., MOOSER E., PEARSON W. B., TEMPLETON I. M. and WOODS S. B., *Phil. Mag.* **4,** 433 (1959).

J. Phys. Chem. Solids Pergamon Press 1961. Vol. 17, Nos. 3/4, pp. 188–195. Printed in Great Britain.

THE ABSORPTION SPECTRA OF MAGNESIUM AND MANGANESE ATOMS IN SOLID RARE GAS MATRICES*

O. SCHNEPP†

National Bureau of Standards, Washington 25, D.C.

(*Received* 7 *April* 1960; *revised* 3 *May* 1960)

Abstract—The absorption spectra of magnesium and of manganese in solid rare gas matrices have been investigated at liquid helium temperature. An absorption system of magnesium near 2850 Å and two for manganese near 4000 Å and 2800 Å have been observed. These absorptions lie very close to the wavelengths of allowed atomic transitions and it is concluded on the basis of the evidence presented here that the absorbing species are atoms which are, in general, trapped at more than one type of site. The crystal field causes the removal of the orbital degeneracy of the excited atomic *P* states; the splitting energy is observed to be of the order of 300 cm^{-1}. It is proposed that the removal of the degeneracy is due to asymmetric environments of the trapping site. Possible sites are discussed.

1. INTRODUCTION

In recent years there has been an increasing amount of activity in studies of "trapped radicals", i.e. unstable molecular or atomic species stabilized in small concentrations in solid deposits of inert gases at low temperatures.[1] Many molecular species of this type have been studied by optical spectroscopy and by electron spin resonance.[2] Only a very restricted number of atomic species had been studied by the "matrix isolation method" until a year ago. Trapped nitrogen and hydrogen[3] atoms had been investigated by electron spin resonance and nitrogen and oxygen atoms[4] had been studied in emission by optical spectroscopy.

The study of atomic species by optical spectroscopy has the advantage over the study of diatomic and polyatomic species in molecular crystal matrices inasmuch as the spectrum of the impurity atom may be expected to be much more sensitive to the immediate environment than diatomic or polyatomic molecules. The relatively high degeneracies which occur in atomic levels would, for example, be removed by lower than spherical symmetry of the impurity site in the solid. This expectation is fully supported by the observations on trapped nitrogen atoms.[4] The study of the absorption spectra of atoms dispersed in solids would then provide a tool for measuring the crystal field at a point in the crystal, similar to the way the crystal fields are studied in the investigations of the optical[5] and spin resonance[6] spectra of impurity ions in ionic crystals. The correlation between the spectra of free atoms and those of the atom trapped in an inert gas matrix like solid nitrogen or the solid rare gases would be considerably easier than for the ions since the crystal field effects are here expected to be very much smaller. On the other hand the optical absorption spectra of atoms of elements which are volatile at room temperature lie in wavelength regions which are experimentally more difficult to work in. But the experimental techniques used to date in the matrix isolation method all rely on a high vapor pressure of the substance to be studied.

It was in part the aim of this work to develop an experimental technique for the trapping of high temperature species in inert gas matrices at low temperatures, i.e. atomic or molecular products of vaporization of substances which have vanishingly small vapor pressure at room temperature. The apparatus developed allowed the deposition of the gaseous species in inert gas matrices

* This research was performed under the National Bureau of Standards Free Radicals Research Program, supported by the Department of the Army.

† On leave from the Department of Chemistry, Israel Institute of Technology, Haifa, Israel.

Vol. 17
1960

at 4·2°K if the parent substance had a vapor pressure of at least one μ Hg at 1200°C. It has also become clear how this apparatus should be improved for future studies to give better quantitative control over the amount and concentration of the stabilized species and to make the technique applicable to substances which reach a vapor pressure of one μ Hg only at even higher temperatures.

The absorption spectra of manganese and magnesium atoms in inert gas matrices at 4·2°K were studied by using the technique evolved. These spectra are described and interpreted in later sections of this paper in terms of the crystal field perturbations and the sites occupied by the impurity atoms.

2. EXPERIMENTAL

In Fig. 1 a schematic diagram of the evaporation furnace is shown. The copper electrodes, E, are soldered through kovar seals into a Pyrex tube, G. The other end of the Pyrex tube ends in a larger kovar graded seal which is soldered to a brass cylinder, B, provided with a flange, F. The copper electrodes are supported by an insulator, I. A tantalum boat was clamped between the ends of the copper electrodes and a brass cap, C, covered the boat and was held in position by means of a screw which clamped it to the insulator, I. The Pyrex tube, G, had a side-arm provided with a kovar seal to which a sintered glass twin lead-through, T was soldered. Thermocouple wires could be soldered into this lead-through. The cap, C, had an effusion hole, H, about 3 mm in diameter through which the atomic beam was directed to the cold deposition window.

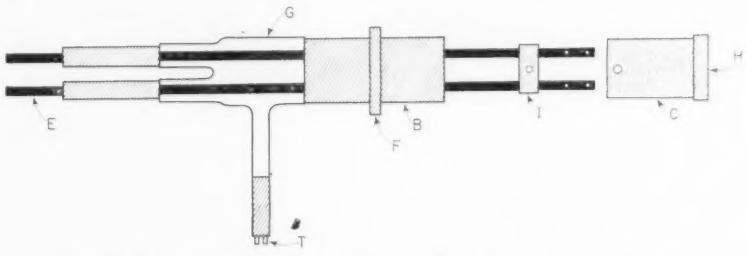

FIG. 1. Evaporation furnace attachment for low temperature Dewar.

The tantalum boat was heated by currents of up to 70 A, at 5 V. A high current 110 V to 5 V transformer was used for this purpose. The current was regulated by means of a rheostat in the primary circuit of the transformer, and the primary current was measured. The temperature of the boat was measured by using a chromel–alumel thermocouple up to 850°C. The thermocouple was spot-welded to the tantalum. Above 850°C an optical pyrometer was used.

The whole furnace assembly was held in a tubular sidearm of the helium dewar up to the flange, F. Rubber O-rings provided the vacuum seal around the brass cylinder, B. A shutter mounted in the sidearm allowed interruption of the flow of the hot vapor onto the deposition window. The beam of material admitted through the effusion hole, H, in the end face of the cap, C, impinged on the cold window at an angle of 45°.

The matrix material was admitted through a tube which also made an angle of 45° with the face of the deposition window but was on the opposite side of the normal to this window. The cold window was a sapphire window which was clamped to a copper mount by means of indium gaskets to insure good thermal contact. The copper mount was screwed into the cylinderical bottom of the helium container of the Dewar. The flow rate of the matrix gas was regulated by a needle valve and reproducible flow conditions were produced by reading the pressure on the low pressure side of the needle valve by means of a Pirani gauge.

The growth of layer thickness of the inert gas on the sapphire window per unit time was determined by observation of the interference colors when natural light was reflected from the window. The index of refraction of solid argon was

calculated by correcting the molar refractivity of the gas for density. This calculation gives a value of 1·24 for the refractive index of solid argon, in close agreement with experimental measurements,[7] and it is assumed that the indices of solid krypton and solid xenon lie between 1·25 and 1·30. By using these values we find that the flow rates of the rare gases used here correspond to rates of increase in layer thickness as follows:

argon	90 Å/min to 1350 Å/min
krypton	110 Å/min to 1650 Å/min
xenon	260 Å/min to 3900 Å/min

The flow rate most commonly used was twice the lower limit of the total range. The fastest flow rates used were fifteen times the slowest rates.

The rate of deposition of the metal atoms could only be crudely estimated in this experiment, although the vapor pressures[8] and the rates of vaporization[9] are comparatively well known for the metals investigated.

Comparison between the results of different experiments in this work show that the temperature of the metal was not reproducibly controlled. This is probably due to the fact that the temperature of the metal differed appreciably from that of the tantalum boat at the point of measurement. As a result, only crude estimates of metal atom flow rates and therefore metal atom concentrations in the matrices could be obtained here.

The spectrograph used was a medium Hilger quartz spectrograph, with a slit width of 10μ. The light source was a Hanovia high pressure 150 W xenon lamp. The emission spectrum of the iron arc was used for calibration.

It seems appropriate to indicate briefly what improvements need to be made in the experimental set-up described here in order that the concentration of trapped atoms in the matrix can be determined and a higher degree of reproducibility of the vaporization conditions attained. Instead of an open boat a closed effusion cell must be used in order to ensure uniform temperature of the sample and, therefore, reliable temperature measurements. If in such an arrangement conditions of effusive flow prevail a knowledge of the geometry of the apparatus permits accurate determination of the rate of flow from the effusion cell.

3. EXPERIMENTAL RESULTS

The absorption spectra of dispersions of magnesium and manganese in solid matrices of argon, krypton and xenon were photographed in the

Vol. 17
1960

Table 1. *Summary of wave numbers of absorption lines of magnesium and manganese atoms in rare gas matrices at* 4·2°K.

(a) Magnesium

Matrix	Wavelength (Å)	Wave numbers (cm^{-1})	Relative intensity
Free atom: $3s\,^1S - 3p\,^1P^\circ$	2852·120	35051	
Argon		34640 (80)	weak
		34920 (80)	weak
		35300 (80)	strong
		35540 (80)	medium (poor contrast)
		35810 (80)	medium (poor contrast)
Krypton		34700 (50)	weak
		34970 (40)	medium
		35130 (40)	strong
		35380 (30)	medium
		35590 (30)	medium
Xenon		33840 (60)	strong
		34050 (45)	strong
		34240(30)	strong

(b) Manganese, I

Matrix	Wavelength (Å)	Wave numbers (cm^{-1})	Relative intensity
Free atom:			
$a\ ^6S - z\ ^6P^\circ$	4034·490	24779	
	4033·073	24788	
	4030·755	24802	
Argon		24810 (80)	strong
		25040 (80)	medium
		25210 (80)	strong
		25440 (80)	weak
		25680 (80)	weak
Krypton		24600 (40)	medium
		24980 (70)	strong
		25210 (10)	weak
		25310 (10)	weak
		25630 (100)	strong
		25970 (40)	strong
		26220 (40)	medium
Xenon		23400 (240)	weak, very broad
		24340 (70)	weak
		25040 (70)	strong
		25310 (70)	strong
		25540 (70)	strong

(c) Manganese, II

Matrix	Wavelength (Å)	Wave numbers (cm^{-1})	Relative Intensity
Free atom:			
$a\ ^6S - y\ ^6P^\circ$	2801·084	35690	
	2798·270	35726	
	2794·817	35770	
Argon		35300 (70)	very weak
		35510 (70)	very weak
		35780 (70)	strong
		36030 (50)	strong
		36220 (50)	strong
		36490 (70)	very weak
		36740 (70)	medium
		36940 (70)	weak
Krypton		35130 (60)	very weak
		35380 (80)	very weak
		35640 (50)	strong
		35830 (60)	strong
		36050 (40)	strong
Xenon		34530 (80)	medium
		34720 (50)	strong
		34910 (40)	strong
		35340 (100)	strong, diffuse
		35540 (50)	very weak

Line widths are given in parentheses in units of cm^{-1}, following the wave numbers of the line centers in the same units.

region between 5000 Å and 2400 Å. Two absorption systems were observed for manganese and one for magnesium. These spectra remained unchanged over a wide range of concentrations, i.e. the spectra were not affected by changes in the rare gas flow rate by a factor of 15, as described in the preceding Section, nor by changes in evaporation rate or vapor pressure of the metal by at least a factor of ten. It can thus be concluded that the spectra observed remained unchanged over a range of concentrations which differed by more than a factor of 100. It is estimated that the concentrations were of the order of from 0·5 mole per cent to 100 times less. Above a certain limit of temperature of the metal to be vaporized, or above a certain limit of evaporation rate, no discrete spectra were observed, but grey dots could then be discerned in the deposit. These dots are presumed to be metallic particles.

The spectra observed are shown in Figs. 2, 3 and 4. The matrix material is given on the right of each spectrum and the atomic line or lines in the spectral region under study are indicated by black ink lines above the photographs. The spectra consist of broad lines, of width 30 cm^{-1} to 70 cm^{-1} which are usually superimposed on a region of continuous absorption. The wave numbers of the centers of the lines are summarized in Table 1, and those of the atomic lines are given for comparison. It is seen that in general the shifts in wave numbers from free atom to the matrix do not exceed 1000 cm^{-1} for the discrete components of the matrix spectra.

In Fig. 2 the absorption spectra of magnesium in argon, krypton and xenon matrices are presented. The argon spectrum is very diffuse but careful examination of the plate shows indications of a triplet structure in the intense part of the absorption. To longer wavelengths two weaker lines can be discerned, In krypton, five discrete lines are readily observable. Beginning at the short wavelength end the first three form a regular pattern with equal intervals. The first two are of about equal intensity while the third is appreciably more intense. The other two lines are again weaker. In the xenon matrix a clear triplet is observed. The center of gravity of absorption intensity in the matrix shifts progressively to longer wavelength with increasing atomic weight of the matrix material. Relative to the free atom spectrum there is a small shift to shorter wavelength for argon, almost no shift for krypton but a considerable shift to longer wavelength is observed for xenon.

Fig. 3 shows the spectra of manganese in the rare gas matrices near 4000 Å. Two photographs are shown for each matrix material with different absorption densities. The argon spectrum consists of three relatively closely spaced lines with equal intervals and two weaker lines which appear to shorter wavelengths. Beginning from the short wavelength side the krypton spectrum contains a group of three about equally spaced lines of which the first one is weaker than the other two. The second group consists of two lines of which the first one is more intense. The weaker of these two lines lies at the long wavelength edge of the absorption region. Between these two line groups there appear two very narrow weak lines. The xenon spectrum consists of a triplet of equally-spaced lines of similar intensities.

The shifts of the spectra with reference to the free atom spectrum are small. The center of gravity of absorption intensity of the argon spectrum is shifted slightly to shorter wavelength, that of the krypton spectrum more so and the xenon spectrum shift is intermediate between those of the argon and krypton spectra.

Fig. 4 shows the absorption spectra of manganese in the rare gas matrices near 2800 Å. The argon spectrum consists of a group of three lines of very similar intensities and a pair of weaker lines to shorter wavelength. Two photographs of the krypton spectrum with different absorption densities are shown and it is seen that this spectrum consists mainly of a group of three lines of which the shortest wavelength component is weaker than the other two. In addition, a weaker line is discernible to longer wavelength. The xenon spectrum is much more diffuse but some line structure is noticeable. There seem to be again three lines on the long wavelength side and a broad intense line appears to shorter wavelength. The center of gravity of the absorption intensity moves progressively to longer wavelength with increase in the atomic weight of the matrix material, such that the shift relative to the free atom spectrum is slightly to shorter wavelength in argon, almost zero for krypton but the shift for the xenon matrix is considerable in the direction of longer wavelength.

Vol. 17
1960

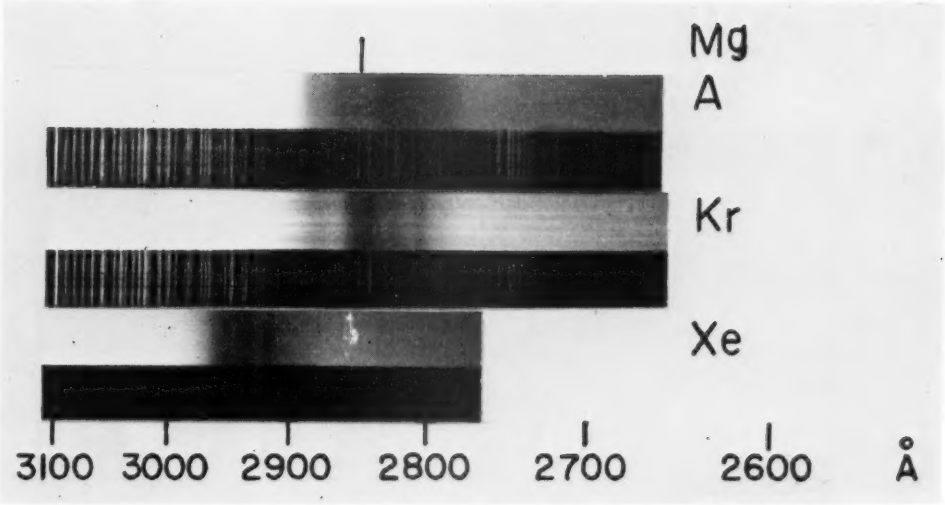

FIG. 2. The absorption spectra of magnesium atoms in solid matrices at 4·2°K. The spectra are marked according to the matrices used, A for argon, Kr for krypton and Xe for xenon. Alongside each spectrum an iron arc calibration spectrum is shown. Above the argon spectrum a single line indicates the position of the atomic magnesium line.

[*facing p.* 192

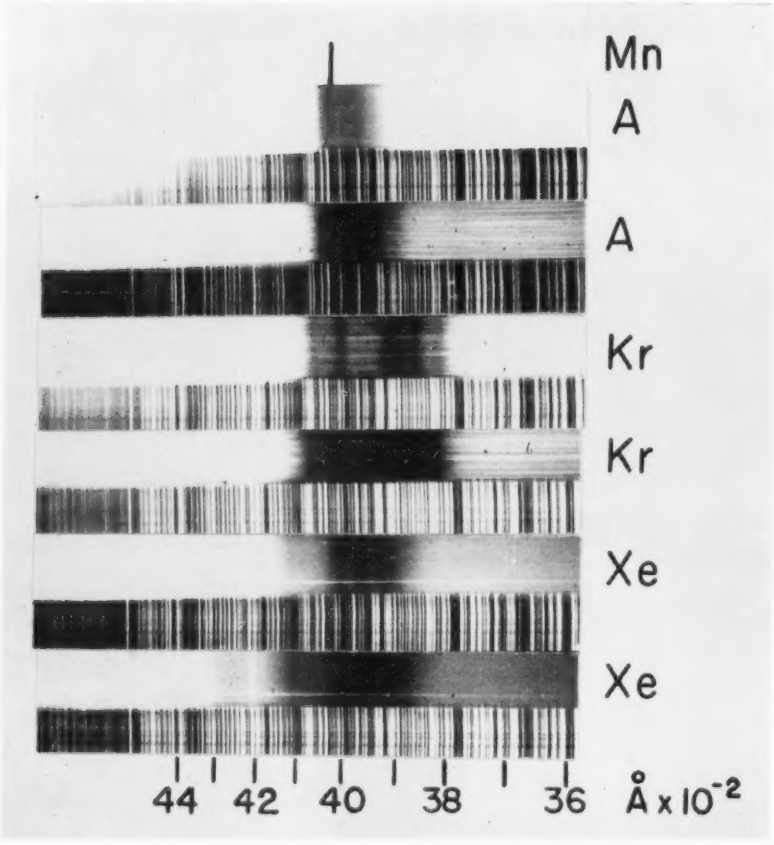

FIG. 3. The absorption spectra of manganese atoms in solid matrices at 4·2°K. The spectra are marked according to the matrices used, A for argon, Kr for krypton and Xe for xenon. Alongside each spectrum an iron arc calibration spectrum is shown. Two photographs showing different absorption intensities are shown for each matrix. The position of the atomic triplet is indicated by a single line above the first argon spectrum since its width covers all three components in this dispersion.

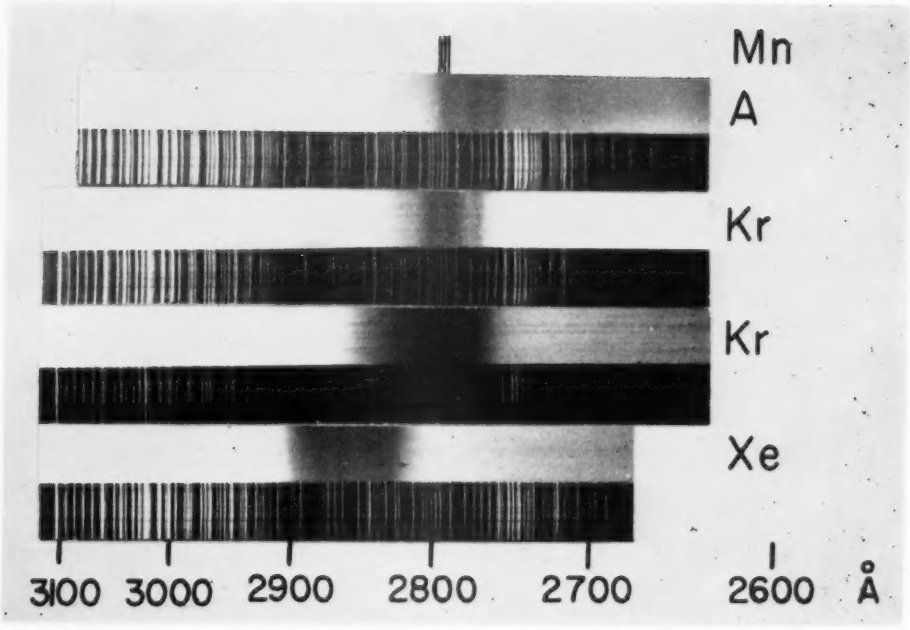

FIG. 4. The absorption spectra of manganese atoms in solid matrices at 4·2°K. The spectra are marked according to the matrices used, A for argon, Kr for krypton and Xe for xenon. Alongside each spectrum an iron arc calibration spectrum is shown. Two krypton spectra with different absorption intensities are also shown. The position of the atomic triplet is indicated by three closely-spaced lines above the argon spectrum.

BLANK
PAGE

Vol. 17
1960

It was obvious from the experimental observations that for all matrices the short wavelength system of manganese absorbs with considerably greater intensity than the long wavelength system. In order to determine the intensity ratio of these two absorption systems we compare the deposition times which were necessary to attain similar absorption intensities as determined by visual estimates directly from the plates. These comparisons were made on the basis of results obtained during the same experiment, the conditions of metal evaporation being kept constant. These estimates gave an intensity ratio of $4{\cdot}0 \pm 0{\cdot}3$. The results were consistent within the limits of error given for all three matrices.

For the case of the spectrum of manganese in krypton near 4000 Å, observations were made at different temperatures after the deposit had been prepared at liquid helium temperature. As described above, this spectrum consists mainly of one group of three lines on the short wavelength side and a second group of two lines on the long wavelength side. The sample was allowed to warm-up and the spectrum was observed as a function of temperature. The group of two lines decreased markedly in intensity near 20°K and was no longer observable at 40°K. The group of three lines, on the other hand, disappeared only above 50°K. It seems therefore that the two line groups are independent of one another and are characteristic of physically different and distinguishable species.

4. DISCUSSION

The ground state of the magnesium atom has the configuration $3s^2$ and it is therefore a ^1S state.[10] The lowest energy of an allowed atomic transition lies at 35051 cm^{-1} and the excited state involved is the ^1P state of the configuration $3s3p$. The ground state of manganese has the configuration $3d^54s^2$. The excited configuration $3d^54s4p$ gives rise to two ^6P terms, to which transitions from the ^6S ground state are allowed. These transitions consist of triplets whose components fulfill the selection rules $\Delta J = 0, \pm 1$. The wave numbers of these transitions are given in Table 1(b). It will be seen that the separations between the observed triplet components in the free atom spectra are of similar magnitude as the observed line widths in the matrix spectra. It is therefore not to be expected that these components will be resolved in this work.

The nature of the absorbing species in this work needs to be discussed. It was observed that the spectra remained unchanged over a very wide range of concentrations, i.e. for concentrations differing by at least a factor of 100. The highest concentrations for which these discrete spectra were observed were estimated to have a concentration of about 0·5 mole per cent. For concentrations greater than this no discrete spectra were observed. This fact indicates that nucleation occurs in more concentrated dispersions of magnesium or manganese atoms in rare gas matrices. Metallic particles are thus formed and these do not have discrete spectra. It may thus be concluded that species which give rise to the discrete absorption spectrum at low concentrations persist over a wide range of concentrations and disappear, presumably due to the onset of diffusion and metallic nucleation, when the concentration of the dispersed species exceeds a critical value. It is further to be noted that the three electronic absorption systems observed here lie very close to the spectra of the free atoms. Furthermore, the multiplet structure of the spectra is such as to support the assumption that the absorbing species are atoms imbedded in the matrix. The observation of triplets is understandable in terms of an asymmetric crystal field perturbation on the trapped atom in the excited P state. For cases where more than three components are observed it is proposed that more than one type of site is occupied by the atoms. This will be discussed in greater detail later in this Section. The conclusion that the absorbing species are atoms is further strongly supported by the observation that the absorption intensity ratio between the two manganese absorption systems agrees with that determined from atomic emission spectra.[11] For the purpose of this comparison the reported atomic emission intensities have to be corrected for the energy difference between the emitting states, due account being taken of the effective temperature of the source. The intensity ratio determined here as described in the preceding Section is $4{\cdot}0 \pm 0{\cdot}3$ while that obtained from atomic emission spectra for the most intense line in each system is 3·7. It is to be noted that the intensities of the strongest atomic transitions are not expected to be

appreciably affected by the weak perturbation of the solid matrix.*

It has been described that for the case of manganese dispersed in krypton five principal spectral components are observed near 4000 Å. On warming the deposit two of these lines have been observed to disappear near 20°K whereas the remaining group of three lines persisted up to 50°K. It must therefore be concluded that in this case the two line groups are characteristic of two different physical species. It is proposed here that these two species represent atoms of manganese located at different sites. One of these sites is asymmetric, i.e. the trapped atoms are perturbed by an immediate environment for which only twofold rotational symmetry axes exist. The second site has an immediate environment of higher symmetry, such that the perturbation causes a P state to split into two components. The low symmetry site is probably an impurity site in the lattice such that the lattice is strongly distorted in the neighborhood of the trapped atom. The higher symmetry site may be a surface site located on the surface of crystallites, at boundaries between crystallites, or in cracks or faults. A reasonable surface site would have hexagonal symmetry (point group C_{6v}) in the case of a cubic lattice, and a perturbation of this type would indeed split a P state into two components in a way similar to a perturbation of cylindrical symmetry. The assignment of the doublet absorption to a surface site is supported by the observation that the species responsible for this absorption disappears at very low temperature. It seems very reasonable to assume that the energy of activation for diffusion for a surface site is considerably lower than that for a site within the lattice. It is thus possible to account for the observed difference in stability of the two different sites on this basis. Another possible explanation for the disappearance of surface sites near 20°K depends on the fact that annealing processes have been reported[12] in such low temperature deposits on warming. In this case the crystallites would grow in size at this temperature, decreasing the total surface area and most of the surface sites would be converted into sites inside crystallites. If this latter process were of major importance, the intensity of the triplet absorption feature should increase in intensity as the doublet fades. This has not been observed. Although the separability of a pattern of five lines into two groups of two and three components respectively has been conclusively demonstrated for only one case, it seems justified to assume that the situation is analogous in all cases where five lines have been observed. It is thus concluded that the trapped atoms are located at more then one type of site in most of the cases studied here.

From Figs. 3 and 4 it is apparent that the spin orbit coupling in the free atom is small compared with the crystalline field splitting in the solid matrix. As a result we can in first approximation consider the splitting of the pure p-orbital and neglect the spin as has been done in our discussion so far. The subsequent introduction of the spin orbit coupling may cause an additional splitting of the orbital levels but this will, in the present case, only contribute to the width of the absorptions. Comparison of the spectra of manganese in the solid matrices with those of magnesium shows that the absorption lines are of similar width which proves that the observed line width is, however, determined by another factor, namely the distribution of crystalline field splittings. The atomic sites in the solid matrix are clearly not sharply defined although the experiment indicates that the sites are not entirely random either. On the other hand, some part of the trapped atoms does seem to be situated at random sites and to these the underlying continua, upon which the discrete absorption features are superimposed, can be attributed.

It is here proposed on the basis of the evidence presented that the excited P states involved in the transitions observed for magnesium and for manganese are split by the crystal field in the rare gas matrices. The perturbation energies for this interaction range from 200 cm^{-1} to 400 cm^{-1}. The shifts from free atom to matrix usually amount to less than 1000 cm^{-1} and in no case do they exceed 1500 cm^{-1}. The crystal field intensity therefore seems to be of the order of one hundredth of that

* *Note added in proof:* It has been pointed out to the author that two extremely intense lines of Mg II are located close to 2800 Å, and may interfere with the spectra of the neutral atoms observed here. It is not believed, however, that ionization is likely to occur in the evaporation furnace used as source in these experiments.

Vol. 17
1960

prevailing in ionic crystals. An alternate explanation of the splitting observed may be offered on the basis of a Jahn–Teller distortion of the lattice surrounding the excited trapped atom in the P state. The splitting energy observed here, however, seems too large if compared to corresponding splitting energies which have been ascribed to this effect in the ionic crystal case.[13]

A few remarks concerning the observed energy shifts from free atom to matrix need to be added. It is seen that the magnesium transition and the higher energy manganese transition behave similarly in this respect. Both are slightly shifted to shorter wavelength in argon, are hardly at all shifted in krypton but undergo a considerable shift to longer wavelengths in xenon. The trend is towards longer wavelength with increasing atomic weight of matrix material with a small difference between argon and krypton but a large jump in going from krypton to xenon. These two transitions are in the same wavelength region. The lower energy transition of manganese, on the other hand, shows a small shift for argon, a somewhat larger shift for krypton and again a smaller shift for xenon, all to shorter wavelength. This transition lies near 4000 Å, or at longer wavelengths than the other absorption systems investigated. The energy shifts are probably determined by two opposing types of interaction. On excitation, the electronic charge cloud surrounding the trapped atom tends to expand and therefore may cause stronger bonding interaction with the matrix atoms thus tending to lower the energy. On the other hand, it has recently been shown[14] that the surrounding "solvent" tends to restrict the electron cloud of the "solute" and thus raise its energy by a restricting box type effect. It is not believed that a scheme based solely on changes in polarizability[15] of the trapped atom with electronic excitation can give a full account of the shifts observed.

Acknowledgements—The author wishes to acknowledge many illuminating discussions with Dr. K. DRESSLER in the course of this work. He would also like to thank Dr. H. P. BROIDA who made this work possible and would express his gratitude to Dr. M. FOLMAN who read the manuscript and offered valuable suggestions for its improvement.

REFERENCES

1. WHITTLE E., DOWS D. A. and PIMENTEL G. C., *J. Chem. Phys.* **22,** 1943 (1954); NORMAN I. and PORTER G., *Nature, Lond.* **174,** 508 (1954).
2. FRANKLIN J. L. and BROIDA H. P., *Annual Reviews of Physical Chemistry* 1959, Annual Reviews, Stanford, California U.S.A. (1959).
3. COLE T. and HARDING J. T., *J. Chem. Phys.* **28,** 993 (1958); JEN C. K., FONER S. N., COCHRAN E. L. and BOWERS V. A., *Phys. Rev.* **112,** 1169 (1958); LIVINGSTONE R., ZELDES H. and TAYLOR E. H., *Disc. Faraday Soc.* **19,** 166 (1955); WALL L. A., BROWN D. W. and FLORIN R. E., *J. Phys. Chem.* **63,** 1762 (1959).
4. HERZFELD C. M. and BROIDA H. P., *Phys. Rev.* **101,** 606 (1956).
5. MCCLURE D. S., *Solid State Physics* (Edited by SEITZ F. and TURNBULL D.) Vol. IX. Academic Press, New York (1959).
6. See LOW W., *Paramagnetic Resonance in Solids,* Academic Press, New York (1959).
7. KRUGER J. and AMBS W. J., *J. Opt. Soc. Amer.* **49,** 1195 (1959).
8. STULL D. R., *Thermodynamic Properties of the Elements.* American Chemical Society, Washington (1956).
9. DUSHMAN S., *Vacuum Technique* Chapter 11. John Wiley, New York (1949).
10. MOORE C. E., *Atomic Energy Levels,* National Bureau of Standards Circular No. 467, Washington (1958).
11. CORLISS C. H., National Bureau of Standards, Washington. Private communication.
12. PEISER H. S., *Formation and Trapping of Free Radicals* (Edited by BASS A. M. and BROIDA H. P.) Chapter 9. Academic Press, New York (1960).
13. VAN VLECK J. H., *J. Chem. Phys.* **7,** 61, 72 (1939).
14. BROWN R. D. and COULSON C. A. *Calcul des Fonctions d'Onde Moleculaires,* p. 311. Editions du Centre National de la Recherche Scientifique, Paris (1958).
15. MCCARTY M., Jr. and ROBINSON G. W., *Mol. Phys.* **2,** 415 (1959).

J. Phys. Chem. Solids Pergamon Press 1961. Vol. 17, Nos. 3/4, pp. 196–202. Printed in Great Britain.

OXYGEN EXCHANGE BETWEEN SILICA AND HIGH PRESSURE STEAM*

W. G. SPITZER and J. R. LIGENZA

Bell Telephone Laboratories, Murray Hill, New Jersey

(*Received* 3 *May* 1960)

Abstract—When films of silica containing one type of oxygen isotope are exposed at elevated temperatures to high pressure steam containing a second oxygen isotope, the oxygen in the film is replaced by the isotope in the steam. The purpose of this study is to investigate the time, temperature and pressure dependencies of the exchange and to identify the oxygen-bearing species which diffuses from the steam into the silica. The concentration and distribution of the isotopes in the film are determined from the isotopic shift of one of the silica infrared absorption bands. Two models are proposed to account for the experimental results, and it is concluded on the basis of these models that the diffusing oxygen-bearing species is water. Because of independent experimental evidence, one of the two models considered is regarded as more likely. This model predicts the presence of silanol pairs, which are formed by the reaction between water and silicon–oxygen bonds, as well as water.

1. INTRODUCTION

WHILE oxygen exchange in silica has been previously reported,[1,2] very little quantitative information has been given concerning the exchange process. The work to be described here is a study of the exchange of oxygen between silica and high pressure steam in the silica phase. The purpose of this study is to investigate the time, temperature, and pressure dependencies of the exchange process and to identify the oxygen-bearing species which diffuses from the steam into the silica. Earlier experiments have shown that if a silica film, grown on a silicon substrate and containing one type of oxygen isotope is exposed to steam containing a second oxygen isotope at 923°K and 120 atm pressure, a considerable part of the original oxygen in the film is replaced by the isotope in the steam. While it may be expected that the extent of the exchange in the film will depend upon the time of exposure to the steam, the nature of the dependence has not been investigated. Infrared transmission measurements of the isotopic shift in the 9 μ silica absorption band were used to determine the extent of the exchange. In particular it was found that the exposure of a 6000 Å O^{16} film to O^{18} steam for five min at 923°K and 120 atm resulted in a thirty per cent exchange even though the thickness of new oxide grown during this time interval was small ($<$ 5 per cent) compared to the initial film thickness. Moreover, it was found that the thirty per cent exchange was uniform throughout the thickness of the film and the amount of exchange was independent of the presence of the silicon substrate. The same results were obtained when the film initially contained O^{18} and was treated with O^{16} steam. It was concluded that some oxygen-containing species diffuses into the silica film and diffuses sufficiently rapidly to maintain a uniform concentration throughout the film. The results obtained here support the previously reported conclusions and furnish information concerning the kinetics of the exchange process. They also indicate that the diffusing oxygen-containing species is water.

Two theories have been presented in the literature for the state of water in silica. One is that the water exists primarily as water molecules.[3] The other theory assumes that the water reacts with the silica to form internal silicon hydroxide groups

* This work was supported in part by the Signal Corps under Task 2 of Contract DA–36–039–sc–64618.

(silanol groups).[4] A model is proposed which is consistent with the results of the exchange experiments. This model indicates that both water molecules and silanol groups are present in the silica.

2. EXPERIMENTAL METHODS

The general procedure used to study the exchange process was to expose silicon previously oxidized in O^{16} steam to a known oxide thickness, to O^{18} steam for short periods of time at various temperatures and pressures. Infrared transmission measurements were then made of the oxides at the 9–10 μ silica absorption band to determine the extent of conversion. By etching the silica to different thicknesses the distribution of the oxygen exchange in the film was determined.

The silicon specimens prior to any oxidation were polished, single crystal, high resistivity ($\rho > 50\Omega$ cm), oxygen free wafers oriented in the $\langle 111 \rangle$ direction. The above conditions were chosen since the oxidation rate of silicon is known to be sensitive to crystal orientation and large impurity concentrations.[5] The silicon and water are placed in small metal bombs and raised to the oxidizing temperature in a suitable furnace. The lowest temperature used is above the critical point of water (647°K), so that the quantity of water used is just sufficient to reach the desired pressure at the oxidizing temperature. SiO_2^{16} films were grown from normal water which was purified by a double distillation in a silica still. The mixed (SiO_2^{16} and SiO_2^{18}) films were prepared by oxidizing a wafer bearing an SiO_2^{16} film in O^{18} steam. The O^{18} steam was produced from 90 per cent D_2O^{18} water after it was purified by a triple vacuum distillation. The lowest pressure which could be used, in the present work, was 25 atm because of the small bomb volume (0·6 ml). The amount of water to be placed in the bombs to reach this pressure could be delivered with an accuracy of only $\pm$ 5 per cent by using a pipette accurate to $\pm\ 2\times10^{-4}$ ml.

The infrared measurements were made with a single beam, double pass spectrometer with a sodium chloride prism. The spectral half width at 9 μ is 0·05 μ. Transmission measurements were made by placing the sample in the exit beam of the spectrometer and by using the conventional sample-in sample-out technique. The samples consisted of the polished silicon wafers with identical oxide films on the front and back surfaces. The wafers were made sufficiently thin (0·015 in.) that the product of the optical absorption coefficient of silicon[6] times the thickness is less than 0·1 for all wavelengths between 1·5 and 11·0 μ. Therefore any absorption in the 9 μ region will be primarily due to the silica films on the surfaces. The thicknesses of the silica films were determined from transmission interference fringes in the 1–6 μ region and published values of the refractive index for vitreous silica.[7] Previous measurements have shown these films to be vitreous silica.[8]

It is known[1] that the transmission minimum of O^{16} silica at 9·2 μ shifts to 9·6 μ for O^{18} silica. It is also known that the shift of this minimum in a case where the film contains both SiO_2^{16} and SiO_2^{18} is proportional to the relative concentration of either isotope. A measurement of the shift, therefore, gives the extent of conversion. It should be stressed that only the oxygen atoms which are chemically bonded to silicon atoms are of importance in these measurements. Since we are measuring the fundamental resonance vibrations of silica, the oxygen concentration which does not participate in the formation of SiO_2 will not have any pronounced effect on the wavelength of the fundamentals. The isotopic shift was determined from a direct comparison of the treated samples, those containing two oxygen isotopes, with an untreated sample of only one isotope where all samples have the same oxide thickness. The measurements were made in this manner to eliminate the small effect that the oxide thickness has on the wavelength of the transmission minimum.[9] In the cases where the distribution of an isotope in a film was desired, the shift was measured as a function of oxide thickness by thinning the films. The films were thinned by etching in dilute HF.[1]

3. EXPERIMENTAL RESULTS

Six identical silicon samples were oxidized in O^{16} steam until an oxide layer of about 6000 Å was produced in each case. Five of these specimens were then treated with O^{18} steam at 35 atm and 923°K. Although a different time of treatment was used for each of the five samples, in each case the time was sufficiently short that the change

in the film thickness due to the growth of new oxide was small (< 15 per cent) compared to the original thickness. The transmission of the samples was measured between 8·0 and 10·5 μ and the experimental curves are shown in Fig. 1.

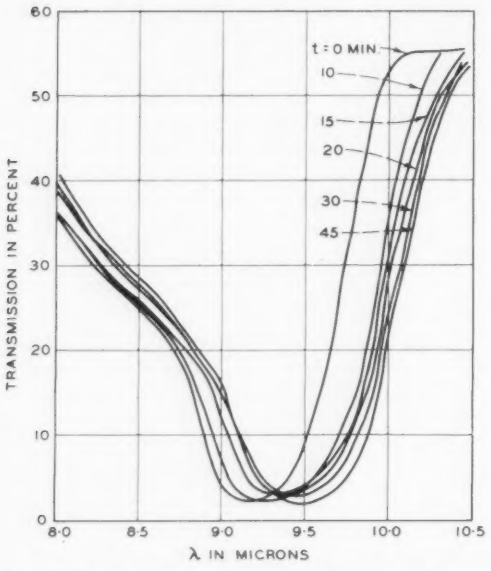

FIG. 1. Per cent transmission as a function of wavelength for six silicon specimens where each specimen has 6000 Å SiO_2 layer on the front and back surfaces. The $t = 0$ curve is for pure SiO_2^{16}. The other values of t give the time of exposure of SiO_2^{16} to O^{18} steam at 923°K and 35 atm pressure.

The times indicated on Fig. 1 are the times of treatment in the O^{18} steam, and as can be seen, the shift increases continuously with time. The shift is estimated from the change in the position of the transmission minimum and is therefore limited by the accuracy with which the minimum can be determined. Fig. 2 shows the shift in the minimum as a function of time for the data given in Fig. 1. The points of Fig. 2 follow a time dependence of the type,

$$S = S_\infty(1-e^{-\alpha t}) \qquad (1)$$

where S is the measured shift, S_∞ is the total possible shift for complete conversion (0·4 μ), and t is the time. The curve shown in Fig. 2 for $\alpha = 0{\cdot}031$ min^{-1} lies well within the experimental error for all of the measured points.

A similar set of measurements was made to determine the pressure dependence of the exchange. In this case, the samples were treated in O^{18} steam at 923°K for 10 minutes and at pressures from 35 to 150 atm. The solid dots in

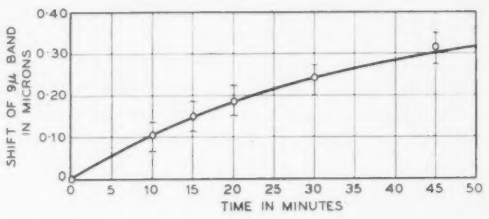

FIG. 2. The dots give the shift in the transmission minimum as a function of exposure time for the samples of Fig. 1. The solid curve is a plot of $S = S_\infty(1-e^{-\alpha t})$ where $\alpha = 0{\cdot}031$ min^{-1}, S is the observed shift, and S_∞ is the total shift between SiO_2^{16} and SiO^{18} (0·4 μ).

Fig. 3 show the shift of the minimum as a function of the pressure used during the treatment. The silica was then etched from the original 6000 Å to 3000 Å and the shift in the transmission minimum remeasured. The measured shifts for this thickness are given by the open circles in

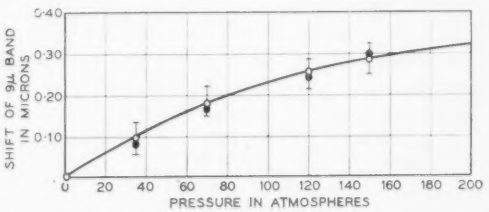

FIG. 3. Shift as a function of pressure for four samples of SiO_2^{16} films on silicon exposed to O^{18} steam at 923°K for 10 min. The open circles give the shift for the sample after thinning the oxide layers from 6000 Å to 3000 Å. The solid curve is a plot of $S = S_\infty(1-e^{-\beta p})$ where $\beta = 0{\cdot}0085$ atm^{-1}.

Fig. 3. In each case the shift for the two thicknesses agree within experimental error indicating the uniformity of the conversion with depth in the silica films. The data in Fig. 3 indicates that the pressure dependence of the shift is of the form

$$S = S_\infty(1-e^{-\beta p})$$

and the curve shown is for $\beta = 0{\cdot}0085$ atm^{-1}.

Vol. 17
1960

Because the power of the pressure will be of particular importance in the later discussion, Fig. 4 shows a semilog plot of $1-S/S_\infty$ vs. p and the experimental points clearly indicate that the shift is an exponential function of the first power of

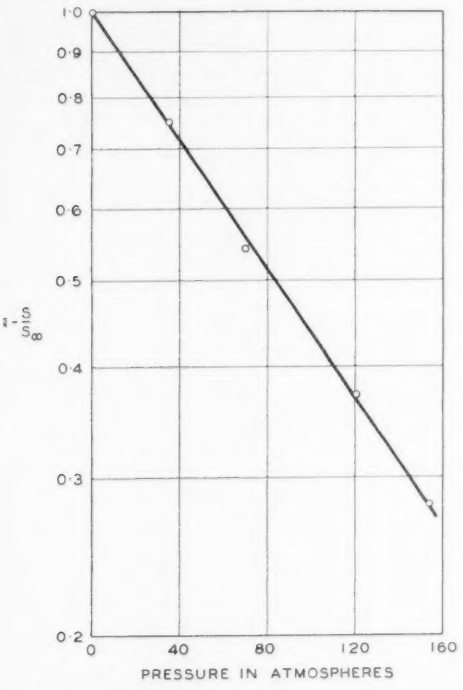

FIG. 4. A semilog plot of $1-S/S_\infty$ vs. the O^{18} steam pressure for the data of Fig. 3.

the pressure. The point at 35 atm in Fig. 3 duplicates the pressure and temperature used in the shift vs. time measurements for the 10 min sample. The agreement of the shift in the two cases is indicative of the consistency of the measurements.

The temperature dependence of the exchange has also been investigated. In these experiments the 6000 Å silica films were treated with O^{18} steam at 35 atm for 20 min and at temperatures between 773°K and 973°K. Fig. 5 gives the results of these measurements where, as in the previous measurements, the open circles give the shifts when the silica films have been thinned to 3000 Å. The curve in Fig. 5 is a theoretical one and is discussed in the next section.

4. THEORY AND DISCUSSION

Two different exchange mechanisms are considered each of which can give rise to an equation governing the exchange process which is in agreement with the experimental results. Since the exchanged oxygen is always distributed uniformly throughout the thickness of the films used in the present study, we will assume the following model for the diffusion mechanism. The water in the silica is in equilibrium with water in the steam phase and therefore the concentration of water

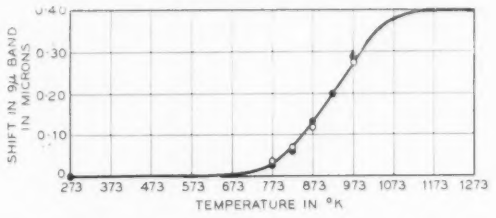

FIG. 5. The shift as a function of temperature. The O^{18} steam pressure is 35 atm and the exposure time is 20 min. The curve is calculated from equation (9).

in the silica is proportional to the steam pressure. Water enters the silica from the gas phase and occupies interstitial sites. Once in these sites the water molecule can diffuse by moving to adjacent interstitial positions, and it can react with the silica to exchange its oxygen with that of the silica. The end result of the exchange process is the reformation of a water molecule, but the initial steps in the exchange process may result in the production of new species which will always exist as long as water is present. The water moves through the lattice principally by interstitial diffusion, and at a much slower pace by the reformation of water molecules as a result of the exchange process.

The over-all exchange equation without regard to mechanism is

$$D_2O^{18}+Si—O^{16}—Si\equiv Si—O^{18}—Si+D_2O^{16} \quad (3)$$

We will consider two mechanisms for the exchange process. The first is the reaction (3) with no intermediate compound formation. This mechanism is the simplest one which can be proposed and will be developed in detail. It will be shown that this mechanism leads to exchange equations which are of the form of the experimental ones.

A second mechanism which does allow for intermediate compound formation is a reaction between the interstitial water molecule and a silicon oxygen bridge to form paired silanol groups. The slow step in the exchange is the condensation reaction of the pair to reform water and the silicon oxygen bridge. The silanol groups have a permanent existence and are in equilibrium with the interstitial water. This mechanism also leads to equations which are consistent with the experimental results, and is considered the more likely of the two because of independent experimental evidence for the existence of internal silanol groups in silica. It is known that when water is adsorbed on the surface of silica gel the water and silica react to form silanol groups.[10] It has also been observed in the high pressure steam oxidation of silicon that there is a definite pressure at any temperature beyond which silica cannot be grown. This effect has been attributed to the formation of silicic acids caused by a large concentration of silanol groups.[5] The silicic acids are soluble in the steam phase. The existence of silanol groups has also been proposed from an infrared study of the 2·7 μ band in silica.[4]

An equation governing the exchange can be derived for the first mechanism by assuming a reaction involving water in solution in the silica and the silicon oxygen bonds where the exchange reaction is given by equation (3). If at a time t the concentration of Si—O^{16}—Si is $\hat{O}^{16}$, of D_2O^{18} is O^{18}, of Si—O^{18}—Si is $\hat{O}^{18}$ and of D_2O^{16} is O^{16}, then

$$\frac{\partial \hat{O}^{18}}{\partial t} = k_1 \hat{O}^{16} O^{18} - k_1 \hat{O}^{18} O^{16}, \qquad (4)$$

where k_1 is bimolecular rate constant for the exchange process. We have assumed that the oxygens in the Si—O—Si bridge are immobile. If the initial values of $\hat{O}^{16}$ and O^{18} are a_0 and C_s, then at time t, $\hat{O}^{16} = a_0 - y$, $O^{18} = C_s$, $\hat{O}^{18} = y$ and $O^{16} = 0$. These values result from the assumption that the steam surrounding the specimen is in equilibrium with the water in solution in the silica. The value of $\hat{O}^{16}$ is reduced by the exchanged O^{18}. The O^{18} remains at C_s because of the equilibrium assumption and because of the uniform distribution in depth of the exchange. The O^{16} concentration remains near zero as this species diffuses out of the silica and becomes diluted by the gas phase. Under these conditions, equation (4) becomes

$$\frac{dy}{dt} = k_1 C_s (a_0 - y), \qquad (5)$$

where y is the $\hat{O}^{18}$ concentration, C_s is the solid solubility of water in silica, and a_0 is the total concentration of $\hat{O}^{16} + \hat{O}^{18}$. The solution of (5) is

$$y = a_0[1 - \exp(-C_s k_1 t)],$$

and since the shift is proportional to y/a_0,

$$S = S_\infty[1 - \exp(-C_s k_1 t)], \qquad (6)$$

where t is the time of treatment. Equation (6) is identical to the empirical equation (1) with $\alpha = k_1 C_s$. Assuming Henry's law holds, the concentration of water in the gas phase is proportional to the concentration of water in the silica, and we have

$$\frac{(H_2O)\ \text{silica}}{(H_2O)\ \text{gas}} = \frac{C_s}{C_g} = K_1,$$

where K_1 is the distribution coefficient between water in the gas phase and the silica phase. Since to a good approximation $pV = nRT$, and $C_g = n/V$, then

$$C_s = K_1 \frac{p}{RT} = \frac{p}{RT} \exp\left(\frac{\Delta S_1}{R}\right) \exp\left(-\frac{\Delta H_1}{RT}\right), \qquad (7)$$

where ΔH_1 is the enthalpy of solution of water in silica, ΔS_1 is the entropy of solution and p is the steam pressure. Equation (6) becomes

$$S = S_\infty\left\{1 - \exp\left[-\frac{p k_1 t}{RT} \exp\left(\frac{\Delta S_1}{R}\right) \times \right.\right.$$
$$\left.\left. \times \exp\left(-\frac{\Delta H_1}{RT}\right)\right]\right\}. \qquad (8)$$

At constant temperature $C_s = bp$, and (8) is of the form

$$S = S_\infty[1 - \exp(-k_1 b t p)]. \qquad (9)$$

Equation (9) is identical with the empirical relationship (2) used to obtain the curve in Fig. 3; the value of $k_1 bt$ is $8{\cdot}5 \times 10^{-3}\ \text{atm}^{-1}$. By using

Vol. 17
1960

the value of $k_1C_s = 3{\cdot}1\times10^{-2}$ min^{-1} determined from the shift as a function of time, with $t = 10$ min and $p = 35$ atm, one obtains $k_1bt = 8{\cdot}9\times10^{-3}$ atm^{-1}, which is in good agreement with the value given by the pressure measurement.

In order to fit the data for the shift as a function of temperature, equation (8) may be expressed as

$$S = S_\infty\left\{1-\exp\left[-\frac{k_1^0pt}{RT}\exp\left[\frac{\Delta S_1}{R}\right]\times\left(\exp\left[-\frac{\Delta H_1+E_A}{RT}\right]\right)\right]\right\}, \qquad (10)$$

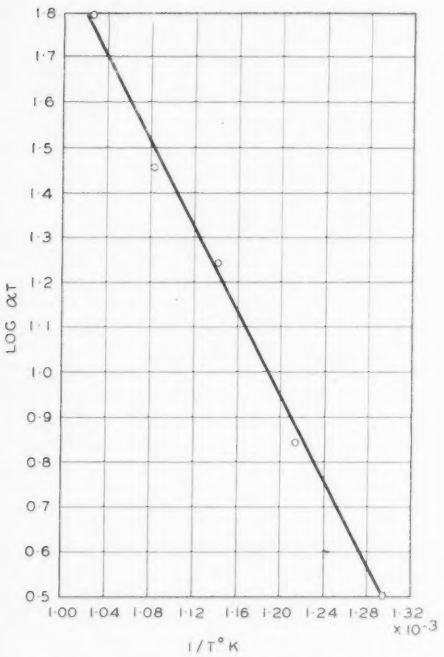

FIG. 6. A plot of log αT vs. $1/T$ where α is defined by $S = S_\infty(1-e^{-\alpha t})$. The values of α are obtained from the data given in Fig. 5.

where $k_1 = k_1^0\exp(-E_A/RT)$ and E_A is the activation energy for exchange. If we let

$$\alpha = k_1C_s = \frac{k_1^0p}{RT}\left[\exp\left(\frac{\Delta S_1}{R}\right)\right]\exp\left(-\frac{\Delta H_1+E_A}{RT}\right)$$

and plot log αT vs. $1/T$ the result should be a straight line assuming that the apparent activation energy is temperature independent. The values of α are obtained from $S = S_\infty(1-e^{-\alpha t})$ and the experimental shifts given in Fig. 5. The points calculated for the five temperatures of measurement are shown in Fig. 6. As can be seen the points lie close to a straight line. The slope and intercept of the line were calculated by using the method of averages and the value of α obtained was

$$\alpha = \frac{3{\cdot}6\times10^6}{T}\exp\left(-\frac{21{,}400}{RT}\right)\text{min}^{-1} \qquad (11)$$

for $p = 35$ atm. The value of

$$k_1^0\exp\left(\frac{\Delta S_1}{k}\right) \text{ is } 8{\cdot}5\times10^{22}\left(\frac{\text{molecules}}{\text{cm}^3}\right)^{-1}\text{sec}^{-1}$$

and the apparent activation energy is $\Delta H_1+E_A = 21{,}400$ cal/mol. The curve in Fig. 5 was calculated with (11) and $t = 20$ min. In this case also the agreement is quite satisfactory. At the present time, the authors have been unable to find estimates of ΔS_1 and ΔH_1.

The second mechanism for exchange involves two reactions. The first is a fast reaction between an interstitial water molecule and a silicon oxygen bridge to form a silanol pair

$$D_2O^{18}+Si{-}O^{16}{-}Si \xrightarrow{\text{fast}} Si{-}O^{16}D+DO^{18}{-}Si, \qquad (12)$$

followed by a slow condensation reaction within the silanol pair to form an exchanged oxygen bridge and an interstitial water molecule.

$$Si{-}O^{16}D+DO^{18}{-}Si \xrightarrow{\text{slow}} Si{-}O^{18}{-}Si+D_2O^{16}. \qquad (13)$$

The exchange rate is limited by the rate at which the paired silanol groups decompose and leads to an equation of the form of equation (10) if the concentration of silanol pairs is small compared to a_0, the concentration of silicon–oxygen bonds.

$$S = S_\infty\left\{1-\exp\left[\frac{k_2^0pt}{RT}\exp\left[\frac{\Delta S_1+\Delta S_2}{R}\right]\times\left(\exp\left[-\frac{\Delta H_1+\Delta H_2+E_A}{RT}\right]\right)\right]\right\}, \qquad (14)$$

where the quantities ΔS_2 and ΔH_2 are the entropy and enthalpy changes for reaction (12) respectively. At the present time, no estimate for ΔS_2 or ΔH_2 can be made.

The two silicon ions in a Si—O—Si bridge are at a fixed distance from each other. If this bridge reacts with a water molecule to form a silanol pair, another oxygen ion and two hydrogen ions must be inserted between them. This can only happen if the imposed strain is relieved by a shift in the positions of the ions in their immediate vicinity to decrease the void volume of the silica. In effect the silica would assume a more ordered quartz-like structure in the neighborhood of the silanol pairs. There is, in fact, a difference of 20 per cent in the void volumes of quartz and silica, the latter structure having the larger volume. According to this picture the stability of the silanol pair once formed, is due to a partial transition from the metastable silica structure to a thermodynamically stable quartz form. Therefore, the assumption, that the condensation of the silanol pairs is the slow step, is reasonable.

Thus the mechanisms we have considered lead to equations for the shift that are of the same form as the experimental equations and have the correct pressure, time and temperature dependencies. In both cases the reacting species is water which diffuses into the silica and is in equilibrium with the gas phase. The first mechanism will allow only for the existence of water in the silica, and the second, and more likely, mechanism predicts the presence of silanol pairs as well as water.

Acknowledgements—The authors wish to express their appreciation to L. E. HOWARTH for his aid with the infrared measurements and Miss R. E. COX for performing the steam oxidations. We also wish to thank D. KLEINMAN for his interest and helpful suggestions.

REFERENCES

1. LIGENZA J. R. and SPITZER W. G., *J. Phys. Chem. Solids*, to be published.
2. HUTCHISON D. A., *J. Chem. Phys.* **22,** 758 (1954).
3. OWEN A. E. and DOUGLAS R. W., *J. Soc. Glass Tech.* **43,** 159 (1959).
4. ADAMS R. V. and DOUGLAS R. W., *J. Soc. Glass Tech.* **43,** 147 (1959).
5. LIGENZA J. R., to be published.
6. KAISER W., KECK P. H. and LANGE C. F., *Phys. Rev.* **101,** 1264 (1956); COLLINS R. J. and FAN H. Y., *Phys. Rev.* **93,** 674 (1954).
7. RODNEY W. S. and SPINDLER R. J., *J. Res. Nat. Bur. Stand.* **53,** 185 (1954).
8. ATALLA M. M., *Proc. of the Conference on Elemental and Compound Semiconductors* (Edited by GATOS H.) Interscience, New York (1960).
9. BORN M. and HUANG K., *Dynamical Theory of Crystal Lattices*, p. 123. Oxford Press, London (1954).
10. ILER R. K., *The Colloid Chemistry of Silica and Silicates*. Cornell University Press, Ithaca, New York (1955).

J. Phys. Chem. Solids Pergamon Press 1961. Vol. 17, Nos. 3/4, pp. 203–209. Printed in Great Britain.

INFLUENCE OF TEMPERATURE AND BOMBARDMENT RATE ON DISORIENTATION OF SILVER SINGLE CRYSTALS BY ION BOMBARDMENT

G. J. OGILVIE* and A. A. THOMSON*

(*Received* 16 *May* 1960)

Abstract—Single crystals of silver with (110), (001) and (111) planes parallel to the surface, have been bombarded by positive ions of argon having an energy of 130 eV at constant temperatures in the range 100–400°C. Transmission electron diffraction patterns obtained from thinned regions in the crystals show that disoriented crystallites and stacking disorders are caused by the bombardment. The effects due to disoriented crystallites decrease in intensity as the temperature of bombardment increases. It is shown that the disorientation increases with increasing current density of ions and the change in disorientation with annealing is studied. The application of the results to the problem of producing clean surfaces by ion bombardment is discussed. It is shown that thermal annealing is not sufficient to account for the change in disorientation with bombardment temperature. The possibility is examined that point defects introduced by bombardment accelerate annealing.

1. INTRODUCTION

TRILLAT[1] showed that a single-crystal film of gold is progressively converted into a random polycrystalline aggregate by bombardment with 12 keV positive ions. A similar effect was studied in detail by OGILVIE[2] for thin single crystals of silver which had (110), (001) or (111) planes parallel to their surfaces. These crystals were bombarded at a number of ion energies in the range 12 eV–3 keV at a temperature always less than 80°C. It was shown that many small crystallites appear in the region of the surface of a crystal after bombardment, the orientation of these crystallites being related to the present parent orientation by tilts about axes lying in the plane of the surface of the crystal. These tilts may be as large as 35° but are usually less than 15°.

The experiments described below were carried out to determine in what way the disorientation caused by ion bombardment changes with the temperature of the crystal and the current density of positive ions. In addition, the way in which the disorientation is removed by annealing after bombardment was investigated.

* Division of Tribophysics, C.S.I.R.O., Melbourne.

2. EXPERIMENTAL PROCEDURE

(a) *Preparation of specimens*

Three single crystals of silver were made by casting in a graphite mould.[3] These crystals were in the form of thin sheets approximately $5 \times 2{\cdot}5$ cm which were then electropolished[4] to a final thickness of about 0·1 mm. One crystal had (110), another (001) and the third (111) planes nearly parallel to the surfaces of the sheets. Thin areas in each crystal were made by further electropolishing a small area of the crystal until a hole formed. This area was roughly defined either by holes in a protecting acrylic layer or by the cross section of small jets of electropolishing solution.[5]

(b) *Apparatus*

Argon ions were generated in an apparatus based on the Philips ionization gauge at a pressure of $1\text{–}2 \times 10^{-3}$ mm Hg. This apparatus and its method of operation have been described previously.[2] Ions of 130 eV energy were used because it was known[2] that marked disorientation occurred at this energy if the specimen temperature was below 100°C. Preliminary experiments established that if the specimen temperature was maintained at or less than 100°C, bombardment with 5×10^{17} ions/cm^2 was sufficient to give maximum disorientation. Therefore, the crystals were always bombarded with at least 10^{19} ions/cm^2 to ensure that a steady state had been achieved.

The specimens were heated in three ways:

(i) By bombarding with ions alone; for example, when a current density of 35 mA/cm^2 of ions was collected

by the specimen its temperature rose to, and remained steady at, 400°C.

(ii) By attaching heavy leads to the crystal and passing large currents through it.

(iii) By electron bombardment using a bare tungsten filament placed near the crystal and with 600 V between crystal and filament, a current of 7·5 mA/cm² was necessary to maintain a temperature of 400°C; a shield was placed between the crystal and the filament to prevent any evaporated tungsten condensing on the crystal.

(c) *Method*

The crystals were treated in the following ways:

(i) With the crystal heated by the discharge alone, bombardments were performed at 100°C and then in steps of 50°C up to 400°C. Above 400°C good electron diffraction patterns were not obtained; this may have been due to the loss of the thin areas caused by surface tension. The bombardment time varied from 30 min at 100°C (current density 0·4 mA/cm²) to 5 min at 400°C.

(ii) Some bombardments were carried out with a series of high current pulses so that, despite the high current densities, the temperature of the specimen did not rise above 100°C.

(iii) The temperature of the 111 crystal was held constant at 250°C by auxiliary resistance heating for positive ion currents in the range $2{\cdot}86 \times 10^{15}$ ions/cm²/sec to $1{\cdot}43 \times 10^{16}$ ions/cm²/sec.

(iv) After some bombardments a crystal was annealed by electron bombardment at a pressure of less than 10^{-4} mm Hg.

(d) *Electron diffraction*

Electron diffraction patterns were obtained from thin areas of the crystal near the holes, using 50 kV electrons. Although similar patterns were obtained from different areas in a crystal, in any given series of experiments the patterns were obtained from the same place. An area was considered satisfactory for diffraction if each pattern from it had the correct symmetry when the electron beam was perpendicular to the surface: that is, when that part of the crystal giving the diffraction pattern was not appreciably rotated with respect to the rest of the crystal.

3. RESULTS AND INTERPRETATION

(a) *The effect of specimen temperature on disorientation*

Figures 1, 3 and 5 are transmission electron diffraction patterns obtained from the crystals with (110), (001) and (111) planes parallel to the surface after bombardment at various temperatures. Figs. 2, 4 and 6 show the arrangement of the spots obtained from an unbombarded crystal. The diagrams also show the positions of the streaks and certain extra spots which appear in some diffraction patterns. The remaining spots, arcs, or rings in the diffraction patterns are due to disoriented crystallites and the orientation relationships between the crystallites and the parent crystal have been discussed in detail elsewhere.[2]

The patterns illustrate that the disorientation produced in the crystals by bombardment progressively decreases as the temperature of the crystal during bombardment increases.

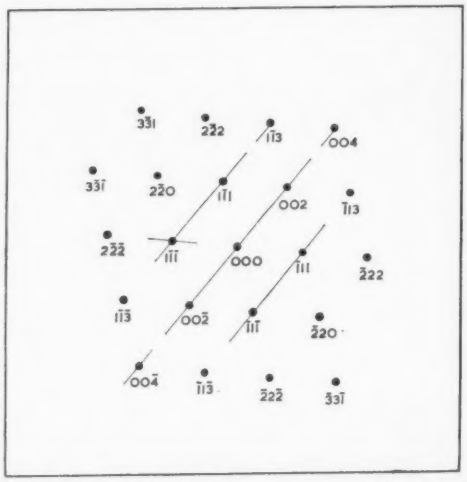

FIG. 2. Diagram showing the arrangement of spots obtained from an unbombarded crystal having (110) parallel to the surface with indices inserted. The position of the streaks obtained after bombardment are also shown.

In Fig. 1(a), obtained from the 110 crystal after bombardment at 100°C, there are almost complete spotty rings passing through spots with indices of the form 111, 002, 220 and 113 (see Fig. 2). Further out from the centre of the pattern (which is at 000) short spotty arcs are present. A proportion of the crystallites, therefore, appear to have random orientations and the remainder have a preferred orientation.

In Fig. 1(b), obtained after bombardment at 250°C, only occasional spots appear in place of the well defined rings of Fig. 1(a). Short arcs pass through some of the spots; for example the $\bar{1}1\bar{1}$, $1\bar{1}3$ and $\bar{3}31$. Consequently, the disoriented crystallites occupy a much smaller angular range. In this pattern there are sharp streaks passing

Vol. 17
1960

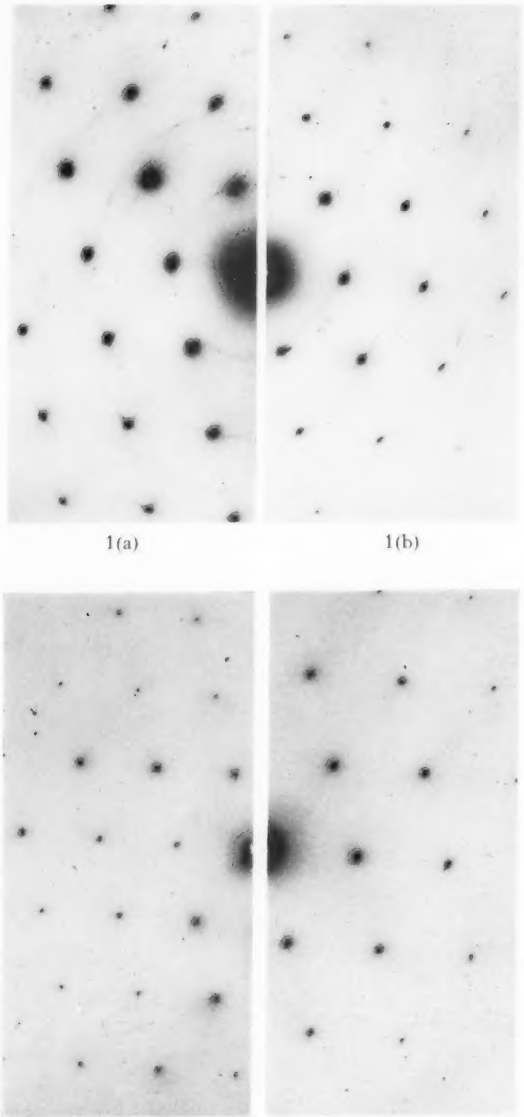

1(a) 1(b)

1(c) 1(d)

FIG. 1. Transmission electron diffraction patterns from the silver crystal with surfaces parallel to (110) bombarded with 10^{19} argon ions at 130 eV.

(a) Temperature during bombardment 100°C, current density equivalent to $3{\cdot}12 \times 10^{15}$ ions/cm^2/sec.
(b) Temperature during bombardment 250°C, current density equivalent to $1{\cdot}43 \times 10^{16}$ ions/cm^2/sec.
(c) Temperature during bombardment 300°C, current density equivalent to $6{\cdot}5 \times 10^{16}$ ions/cm^2/sec.
(d) Temperature during bombardment 400°C, current density equivalent to $2{\cdot}2 \times 10^{17}$ ions/cm^2/sec.

[*facing p.* 204

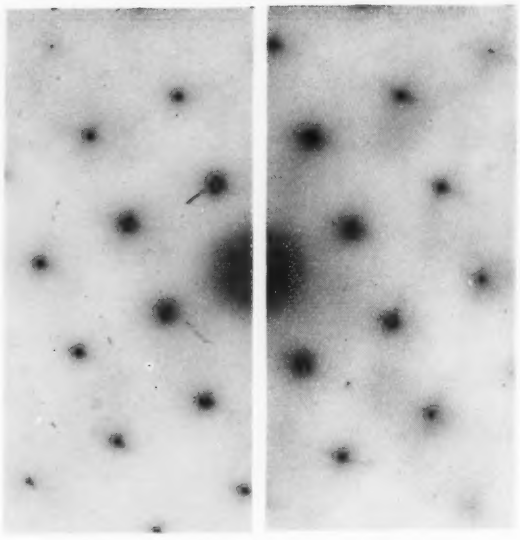

3(a) 3(b)

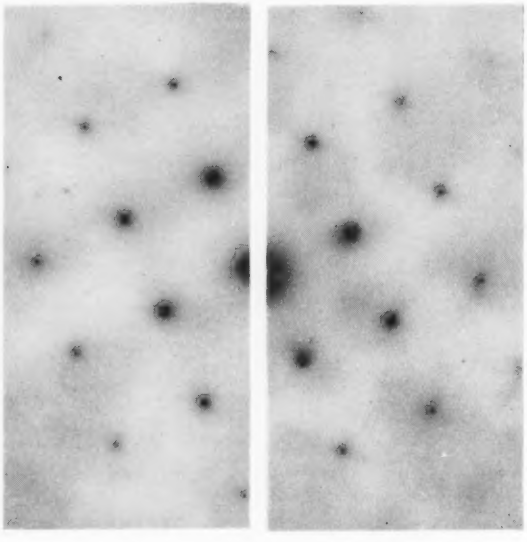

3(c) 3(d)

FIG. 3. Transmission electron diffraction patterns from the silver crystal with surfaces parallel to (001) bombarded with 10^{19} argon ions at 130 eV.

(a) Temperature during bombardment 100°C.
(b) Temperature during bombardment 200°C.
(c) Temperature during bombardment 350°C.
(d) Temperature during bombardment 400°C.

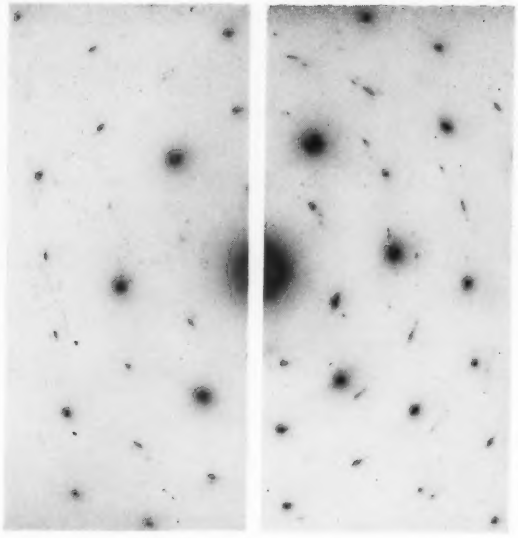

5(a) 5(b)

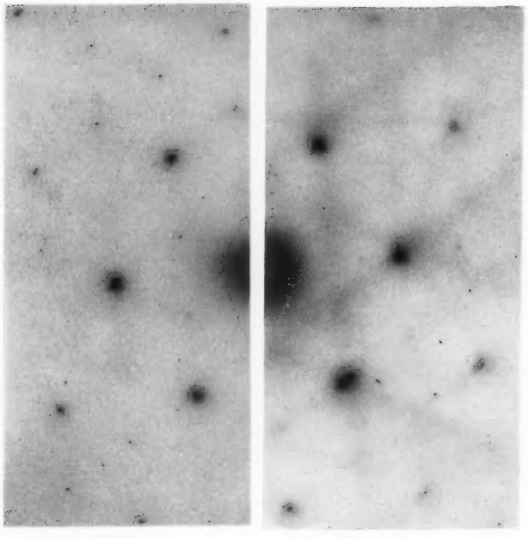

5(c) 5(d)

FIG. 5. Transmission electron diffraction patterns from the silver crystal with surfaces parallel to (111) bombarded with 10^{19} argon ions at 130 eV.

(a) Temperature during bombardment 150°C.
(b) Temperature during bombardment 250°C.
(c) Temperature during bombardment 350°C.
(d) Temperature during bombardment 400°C.

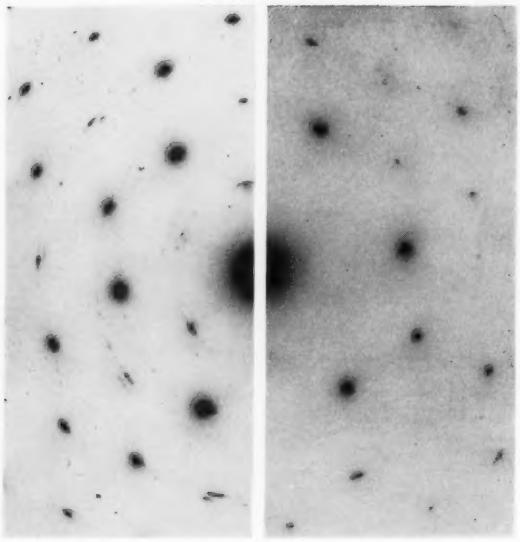

7(a) 7(b)

FIG. 7. Transmission electron diffraction patterns from the crystal with its surfaces parallel to (111).

(a) Bombarded with 5 sec pulses of 130 eV argon ions at a current density of $2{\cdot}2 \times 10^{17}$ ions/cm^2/sec at 1 min intervals.

(b) Annealed for 10 min at 400°C after the above treatment.

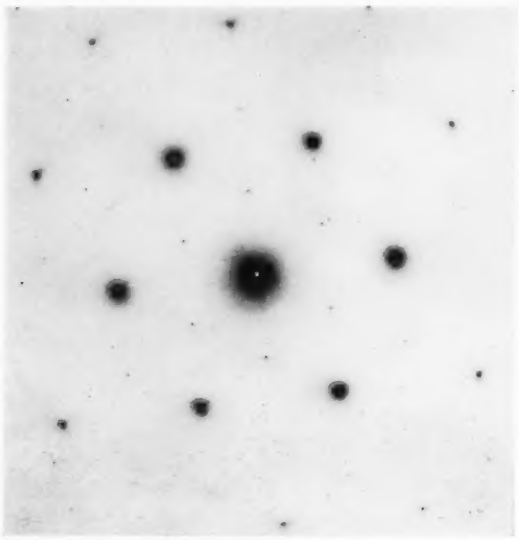

FIG. 8. Transmission electron diffraction patterns from the crystal with its surfaces parallel to (111) bombarded with 10^{19} argon ions at 130 eV. Temperature of bombardment 250°C, current density equivalent to $2{\cdot}86 \times 10^{15}$ ions/cm^2/sec, bombardment time 1 hr.

through the primary spots parallel to a line drawn between the 002 and the $00\bar{2}$ spots. Less intense streaks pass through the $\bar{1}11$ and the $\bar{1}1\bar{1}$ spots towards the centre of the pattern. This suggests that disorders exist in the crystal on planes perpendicular to the direction of the streaks and hence perpendicular to the crystal surface. These planes are {100} and {111}. It is likely that the disorders on the {111} planes are stacking faults.[5]

Figures 1(c) and 1(d), obtained after bombardment at 300°C and 400°C respectively, are very nearly identical and no rings, spots on the rings, or arcs through the primary spots can be seen. On the other hand the streaks which appear in the 250°C pattern (Fig. 1(b)) are still present. That is, disorientation is almost absent while stacking faults are still present.

Figure 3(a), obtained from the 001 crystal after bombardment at 100°C, shows intense arcs. The innermost arcs (lying on the 111 Debye–Scherrer circle) imply a minimum rotation of the crystallites, with respect to the parent crystal, of at least 35°. In the outer parts of the pattern there is a tendency for the spots from the crystallites to appear at the centres of the squares defined by the primary spots; that is, a preferred orientation is present.

Figure 3(b), obtained after bombardment at 200°C, shows little evidence of disorientation; very few spots, other than the spots from the parent crystal, can be seen. Diffuse streaks forming a cross centred on a primary spot—for example the $\bar{2}40$ spot (Fig. 4)—can be distinguished. Clearly, disorientation after bombardment at 200°C is much less than after bombardment at 100°C.

Figures 3(c) and 3(d) (350°C and 400°C respectively) show little evidence of disoriented crystallites. This implies that the tilts of the crystallites must be less than 9°. Diffuse crosses centered on the spots can be distinguished; for example, the $\bar{4}00$ spot in Fig. 3(c). These crosses tend to be obscured by the diffuse blackening around each primary spot but they are most easily seen in the 350°C pattern. The arms of the cross are directed parallel to ⟨110⟩. Since no pattern has been obtained in which the streaks extend all the way between two primary spots, it is unlikely hat these streaks are due to random disorders on (110) and $(1\bar{1}0)$ planes.

The streaks can be accounted for if stacking faults exist on {111} planes. Such faults would produce rods in reciprocal space passing through the lattice points in ⟨111⟩ directions. Electrons with 50 kV energy were used to obtain the diffraction patterns and this implies that the distribution of intensity in the diffraction patterns is, to a first approximation, a map of a plane in reciprocal space perpendicular to the electron beam and passing through the origin. A random crystallite

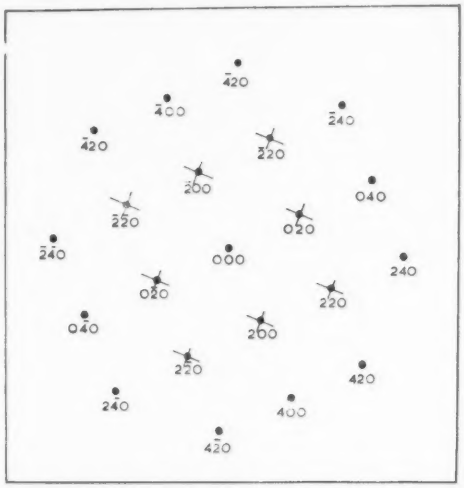

FIG. 4. Diagram showing the arrangement of spots obtained from an unbombarded crystal having (001) parallel to the surface with some indices inserted. The positions of the diffuse crosses obtained after bombardment are also shown.

will probably have some reciprocal lattice points lying close to the map plane and if the crystallite contains faults on all {111} planes the rods passing through a given lattice point will intersect the map at four places. If the electron beam is passing within a few degrees of the [100] direction these points will be arranged near to the corners of a square. The diagonals of the square define directions which lie very close to [110] and $[1\bar{1}0]$. It has already been shown that the orientations of crystallites in the surface of a bombarded silver crystal are predominantly related to the parent orientation by tilts about axes lying in or near the mean plane of the surface.[2] Imagine that the reciprocal lattice of each crystallite is superimposed on the reciprocal lattice of the parent to give a composite diagram. In this diagram the

reciprocal lattice points of the parent crystal lying in the plane of the map are at the middle of arcs centered on the origin and perpendicular to the map; that is to the photographic plate. Each point on these arcs (each of which decays in intensity with distance from its centre) would be associated with four spots on the plate; thus successive points on the arcs correspond with successive sets of four spots on the photographic plate. Hence, stacking faults on {111} planes of the crystallites would produce a cross on each primary spot on the plate, with the arms of each cross parallel to (110) and $(1\bar{1}0)$ and decaying in intensity with distance from the spot. Another possible explanation of this effect is that (110) and $(1\bar{1}0)$ planes have slightly variable spacings. The authors prefer the first explanation because more direct evidence for 111 faults has been found with the 110 crystal while the variable interplanar spacings necessary to account for this effect are unlikely in silver.

Figure 5(a), obtained from the 111 crystal after bombardment at 150°C, shows many intense short arcs implying a very marked preferred orientation. There is an almost complete, though faint, ring occupying the position of the 111 Debye–Scherrer circle with intense short arcs lying on it. This implies that some crystallites are tilted through an angle of at least $18\frac{1}{4}°$ with respect to the parent crystal.

Figure 5(b), obtained after bombardment at 250°C, is essentially the same as Fig. 5(a) except that the arcs have contracted almost to spots and there is no sign of any rings. This implies a very accurate preferred orientation of the crystallites. There are still some crystallites with a tilt of at least $18\frac{1}{4}°$.

In Fig. 5(c), obtained after bombardment at 350°C, the arcs have degenerated into spots and decreased in intensity particularly near the centre of the pattern. The maximum angle of tilt is clearly smaller. This trend is continued in Fig. 5(d) where there is practically no evidence for tilted crystallites in the pattern. The diffuse straight lines in the pattern are almost certainly Kikuchi lines, implying that considerable perfection exists in the diffracting volume.

The evidence presented above shows that disorientation produced by bombardment with argon ions decreases with increasing temperature of bombardment and becomes very small when the temperature rises to 400°C. However, the change in temperature was achieved by varying the ion current to the specimens, and, although at each temperature the bombardment times were such that disorientation was a maximum, it is possible that the ion current directly exerts an influence on the disorientation rather than indirectly through the temperature of the crystal. Consequently, a number of bombardments were performed with high current pulses.

Figure 7(a) is a diffraction pattern from the 111 crystal obtained after bombardment with 5 sec. pulses of $2{\cdot}2 \times 10^{17}$ ions/cm^2/sec at 1 min intervals. The specimen temperature oscillated between 60°C and 100°C. There is an almost complete, though faint, spotty ring—occupying the position of the 111 Debye–Scherrer circle—with intense short arcs lying on it. There are many intense short arcs in other parts of the pattern. This pattern is not very different to the 100°C pattern (Fig. 5(a)), where ions were continuously incident on the crystal and the same total number of ions were collected in the same time, although the peak current was that used previously to maintain the crystal at 400°C. The decrease in disorientation with increasing ion current and resultant increase in temperature is therefore due to the influence of the specimen temperature and not directly to the higher current densities of ions.

(b) *The influence of current density on disorientation at a given temperature*

These experiments were performed to determine if changing the mean current density of ions bombarding the crystal changed the resulting disorientation when the temperature of the 111 crystal was maintained at 250°C. By using resistance heating the ion current could be reduced; the minimum current used was equivalent to $2{\cdot}86 \times 10^{15}$ ions/cm^2/sec. The diffraction pattern (Fig. 8) shows a regular pattern of relatively faint spots which are identified in Fig. 6. There is no sign of rings or arcs due to disoriented crystallites. The outermost members of the array of extra spots occupy positions which could be accounted for if a strongly preferred orientation existed.[2] However, the inner spots are displaced toward the centre of the pattern from the predicted position by an appreciable distance. As the crystal was tilted about a direction parallel to

the photographic plate, the spots moved in a direction which was perpendicular to the tilt axis. This displacement was largest for the innermost spots. Assuming that all the spots in the array arise from a common cause it follows that in reciprocal space the lattice points are connected by rods which are perpendicular to the surface of the crystal. Consequently, disorders exist on (111) planes (those parallel to the surface of the crystal). These disorders are likely to be stacking faults.

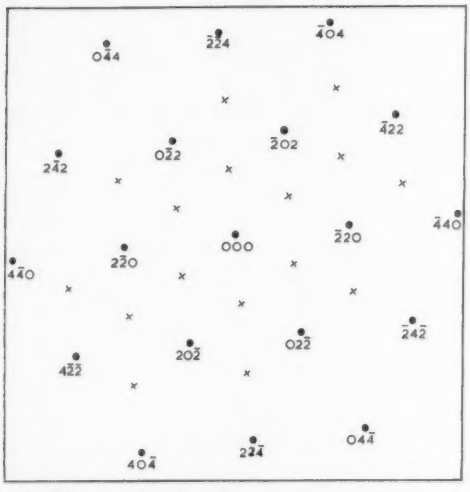

FIG. 6. Diagram showing the arrangement of spots obtained from an unbombarded crystal having (111) parallel to the surface. The positions of the spots caused by stacking faults on (111) planes are shown by small crosses.

Figure 5(b) was obtained from the same crystal after a bombardment with five times the current density at the same temperature. Here there is marked disorientation. In addition to the features already described previously (Section 3(a)) three spots lying just inside the position of the 111 Debye–Scherrer circle can be seen. These occupy the same positions as the innermost spots of the array in Fig. 8. The spots can be found in all the other patterns given in Fig. 5, and there is no marked change in intensity with temperature of bombardment.

After bombardments made with intermediate current densities the diffraction patterns showed different extents of disorientation, there being a regular decrease in disorientation with decreasing current density.

Some bombardments of a 111 crystal were made using current densities down to $3{\cdot}1 \times 10^{14}$ ions/cm^2/sec where the temperature of the crystal was less than 100°C. Under these conditions the disorientation was considerably less than for the 100°C bombardment (Fig. 5(a)) and was intermediate between the 250°C and 350°C patterns (Figs. 5(b) and 5(c)).

(c) *Annealing experiments*

The 111 crystal was bombarded at 100°C. After bombardment the diffraction pattern, which was similar to Fig. (5a), showed that the maximum angle through which crystallites were tilted was at least 20°. The crystal was then given a series of short annealing treatments at 250°C using electron bombardment heating. Electron diffraction patterns were obtained after each anneal. After annealing for one minute the diffraction pattern was practically unaltered; the maximum tilt was still about 20°. A further ten minutes annealing caused a change; the maximum observed tilt was then 12°. After heating for one hour no tilted crystallites were detected in the diffraction pattern which implied that the maximum tilt was less than 4°.

Figure 7(b) was obtained from the 111 crystal after a 10 minute anneal at 400°C. The crystal before annealing gave the diffraction pattern of Fig. 7(a). The pattern (Fig. 7(b)) shows that the disorientation is considerably reduced after annealing. All spots on the 111 Debye–Scherrer circle have disappeared and elsewhere in the pattern many arcs have entirely disappeared. Although some crystallites are tilted through at least $9\frac{1}{2}$° most have considerably smaller tilt angles. The disorientation is, however, still considerably greater than that found after bombarding the same crystal at 400°C (Fig. 5(d)). The spots identified in Section 3b as being due to stacking faults on (111) are very faint in this pattern.

4. DISCUSSION

The results show that the disorientation produced by ion bombardment is markedly dependent on the temperature at which the bombardment is carried out. Furthermore, it seems clear that if the temperature of a crystal is maintained constant, an increase in the bombardment rate increases

the disorientation. Consequently, in order to produce by bombardment a clean surface of a specimen which is in addition little changed by the treatment, high temperatures and low current densities should be used. Cleaning of surfaces by low energy ion bombardment has already been extensively investigated.[6,7,8] These studies were made with ion current densities of about 10–100 μA/cm^2; that is from 6×10^{13}–6×10^{14} ions/cm^2/sec. For a 111 silver crystal the disorientation resulting from a bombardment current of 50 μA/cm^2 (3×10^{14} ions/cm^2/sec) is still quite appreciable. This current is considered[8] to be about the minimum, using 100 eV ions, necessary to maintain a clean surface in a system in which the partial pressure of adsorbable impurities is 10^{-7} mm Hg.

Annealing after bombardment reduces the disorientation. There is no evidence of a new texture appearing as a consequence of annealing (Fig. 7(b)) and therefore it is likely that the crystallites are absorbed by the parent crystal; that is, there is no evidence of recrystallization. During annealing spots and arcs in the diffraction patterns tend to disappear from the central parts before disappearing from the periphery. Therefore, it is likely that crystallites making large angles with the parent crystal tend to be absorbed before those which make small angles with the parent.

A similar trend appears in the series of diffraction patterns with increasing temperature of bombardment. However, it does not necessarily follow that the smaller disorientation accompanying higher bombardment temperatures is primarily due to an increasing rate of absorption of crystallites. The following rough estimate of the thickness of the disoriented zone on the surface of the crystal and the rate at which it travels through the crystal is made to help test this possibility.

Koedam[9] has determined the number of silver atoms ejected for each incident positive argon ion in the energy range 50–300 eV using polycrystalline specimens. This number (the sputtering yield) is about 0·6 at 130 eV. When heated by the bombardment alone at 250°C the 111 crystal was bombarded by $1{\cdot}43\times10^{16}$ ions/cm^2/sec and this gives the rate of removal of silver to have been about 1000 Å/min. It was shown by Gillam[10] that a layer depleted in one constituent appeared at the surface of a bombarded alloy specimen and the thickness of this layer varied from 30 Å to 80 Å depending on the type of ion and its energy. This surface layer was disoriented in a similar fashion to the surface of a silver crystal. Consequently this would suggest that the crystallites at the surface of a bombarded silver crystal are not likely to extend more than about 100 Å into the crystal. If the thickness of the disoriented layer on the surface of the crystal is about 100 Å then the material in the disoriented layer at a given instant during the bombardment has all been removed from the specimen 6 sec later.

The annealing experiments demonstrate that negligible absorption of crystallites takes place in one minute at 250°C. After 10 minutes, absorption of a proportion of the crystallites had taken place; those tilted through large angles tending to disappear first. It is clear that absorption (due to annealing) is not fast enough to account for the decrease in disorientation with increasing temperature when the current density is high; but it is likely that this process becomes increasingly important with smaller current densities. It is possible, however, that the rate of absorption is increased by processes occurring during the bombardment. Point defects are probably introduced in large numbers during bombardment into a thin layer at the surface of the crystal because it has been established that such defects can aggregate to form stacking faults[11,12] and the electron diffraction patterns show evidence of considerable fault density. Mechanisms by which bombardment by heavy particles might produce point defects have been described.[13,14,15] Evidence[16] has accumulated to show that a high concentration of point defects can accelerate local or micro-diffusion. Furthermore, hardening by point defects can be reduced by plastic deformation.[17] But there is little evidence to show that a high concentration of point defects tends to accelerate annealing of a damaged metal. If it is assumed that the mechanism by which tilted crystallites are formed is independent of temperature, then the decrease in disorientation with increasing temperature (no auxiliary heating) would be mainly due to grain growth accelerated by the presence of a large concentration of point defects. However, the experiments do not give evidence to justify the above assumption and it is possible that the rate of

Vol. 17
1960

formation of tilted crystallites or the rate at which they tilt is dependent on temperature.

5. CONCLUSION

Silver crystals develop disoriented crystallites in their surfaces after bombardment with positive ions of argon with low energies. These crystallites tend to have preferred orientations. Stacking faults also appear after bombardment. The range of angles occupied by the disoriented crystallites decreases as the temperature during bombardment is increased, and also decreases as the current density of ions decreases.

It is suggested that point defects are introduced into the crystal by the impact of ions on its surface. It is shown that grain growth due to simple annealing is not fast enough to account for the decrease in disorientation with increasing temperature of bombardment. Therefore the possibility that annealing can be accelerated by the presence of point defects is considered and this possibility qualitatively fits the facts provided that the mechanism by which crystallites form is independent of temperature.

REFERENCES

1. Trillat J. J., *J. Chem. Phys.* **53,** 570 (1956).
2. Ogilvie G. J., *J. Phys. Chem. Solids* **10,** 222 (1959).
3. Sosnovsky H. M. C., *J. Phys. Chem. Solids* **10,** 304 (1959).
4. Tegart W. J. McG., *The Electrolytic and Chemical Polishing of Metals*, p. 63. Pergamon Press, London (1956).
5. Whelan M. J. and Hirsch P. B., *Phil. Mag.* **2,** 1121, 1303 (1957).
6. Farnsworth H. E., Schlier R. E., George T. H. and Burger R. M., *J. Appl. Phys.* **29,** 1150 (1958).
7. Honig R. F., *J. Appl. Phys.* **29,** 549 (1958).
8. Wolsky S. P., *Phys. Rev.* **108,** 1131 (1957).
9. Koedam M., *Physica* **24,** 692 (1958); **25,** 742 (1959).
10. Gillam E., *J. Phys. Chem. Solids* **10,** 55 (1959).
11. Hirsch P. B., Silcox J., Smallman R. E. and Westmacott K. H., *Phil. Mag.* **3,** 897 (1958).
12. Silcox J. and Hirsch P. B., *Phil. Mag.* **4,** 72 (1959).
13. Seitz F. and Koehler J. S., *Solid State Physics*, Vol. II, p. 307 (edited by Seitz F. and Turnbull D.) Academic Press, New York (1956).
14. Silsbee R. H., *J. Appl. Phys.* **28,** 1246 (1957).
15. Leibfried G., *J. Appl. Phys.* **30,** 1388 (1959).
16. Dienes G. J. and Vineyard G. H., *Radiation Effects in Solids.* Interscience, New York (1957).
17. Cottrell A. H., *Vacancies and other Point Defects in Metals and Alloys*, Symposium, Institute of Metals Monograph and Report Series, No. 23, London.

J. Phys. Chem. Solids Pergamon Press 1961. Vol. 17, Nos. 3/4, pp. 210–219. Printed in Great Britain.

PHOTOCAPACITANCE EFFECTS IN ADDITIVELY COLORED ALKALI HALIDE CRYSTALS

D. KAHN and A. J. GLASS*

R.I.A.S., Baltimore, Maryland

(*Received* 10 *March* 1960)

Abstract—Additively colored alkali halide crystals are placed between current blocking electrodes and an increase in the capacitance and conductance of the crystal is found on illumination. A measurement of these quantities at frequencies between 2 and 1000 c/s has shown that the observed behavior follows quite closely a linearized theory developed by J. Ross Macdonald. The region of application of the theory has been examined experimentally, and results show that the theory may be used for larger applied voltages than assumed in the theory. An analysis of the experimental data indicates that the field induced electrode breakdown for the larger voltages ($\sim$5 V r.m.s.) is of such a nature that the equivalent circuit describing the crystal continues to be valid. This has also been observed by others. Using the results of the theory the mobility of KI and KBr crystals at room temperature has been measured. These determinations agree substantially with measurements by others using Hall effect methods. Measurements at low frequencies have revealed phenomena due to the finite recombination rate of the conduction electrons and ionized *F*-centers. From our analysis of this behavior, the capture cross section of an ionized *F*-center in KBr has been found to be $3{\cdot}1 \times 10^{-15}\sqrt{\gamma}$ cm^2, where γ is the ratio of the effective electron mass (polaron) to the free electron mass. The recombination rate constant in KBr has also been measured.

Vol. 17
1960

1. INTRODUCTION

The properties of electronic conduction in alkali halide crystals are of interest from several points of view. Nevertheless, comparatively little experimental work on conductivity has been carried out on these crystals. The rather low mobility in this type of crystal (1–10 cm^2/V sec) and the small carrier concentrations result in a correspondingly high resistivity ($\sim 10^9$–10^{10} ohm cm) which makes most of the usual methods of semiconductor physics difficult to apply.

The low mobility results from the large interaction between the conduction electron and the lattice vibration phonons, which is, in itself, a topic of much theoretical interest. Because of the interesting analogy between the conduction electron–phonon field interaction and the nuclear interaction with its meson field, the rest energy and effective mass of a conduction electron in an alkali halide crystal has been the subject of several field theoretical investigations.[1–6]

Although the polaron rest energy calculations are in reasonably good agreement, the calculated values of the polaron rest mass vary over a wide range.

In view of the field theoretical interest in this problem as well as the general interest in problems of electron conduction, it seemed worthwhile to develop methods for investigating the conduction parameters of alkali halide crystals, taking into account their high resistivity. The methods used in the experimental investigation described below do not depend upon any special properties of the alkali halide crystals, and the words "conduction band electron" will be used henceforth instead of "polaron".

Some measurements of the mobility using the Hall effect have been made in spite of the high resistivity of the alkali halide crystals. By constructing an a.c. amplifier with a very high input impedance, Macdonald was able to measure the mobility of KBr.[7] Using a method which essentially measures the Hall angle, Redfield measured the mobility of NaCl, KCl, KBr and KI at liquid

* Present address: Department of Physics, Yale University, New Haven, Connecticut.

nitrogen temperatures and 200°K.[8] The method seems difficult to apply because of the large crystal impedance, and the reported errors range from 25 to 100 per cent of the mobility value. More recently BROWN has extended the method of REDFIELD to lower temperature where the increased mobility reduces the crystal impedance considerably.[9] His results appear to fit well with those obtained by REDFIELD.

investigated in some detail and is discussed at some length below.

The determination of the admittance of the crystal is made by measuring the voltage drop across a resistor in series with the crystal. In practice this resistor is the grid resistor of the meter or amplifier circuit and is lower than the crystal impedance by a factor of at least 10^3. The specific resistivity ρ of the illuminated crystals is

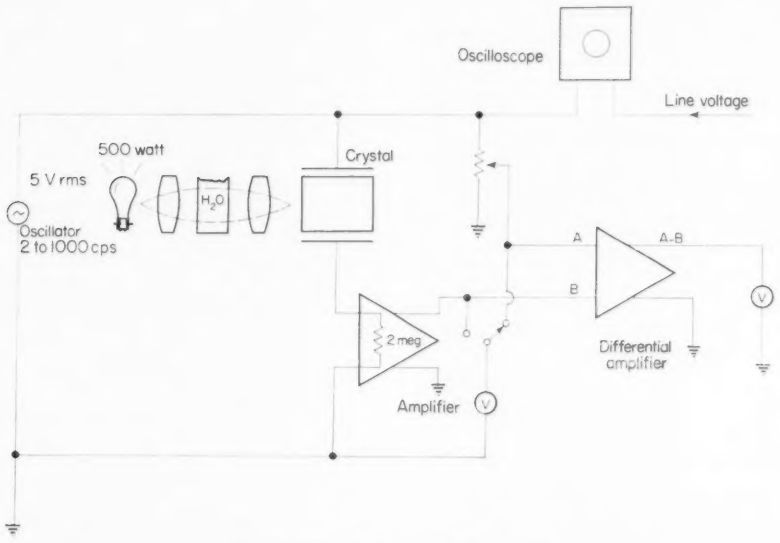

FIG. 1. Circuit diagram of apparatus.

The use of the photocapacitance effect described in this investigation circumvents the difficulties of working with high impedance materials and gives mobility results that agree with other investigators using Hall effect measurements.

2. EXPERIMENTAL METHOD

For high impedance materials a method of determining the mobility and other conduction parameters, whereby the impedance of the measuring instrument is in series with the crystal impedance, is desirable. Such a method used in this investigation is shown in Fig. 1. It is important to realize that the contacts to the crystal are such that a negligible current passes between the crystal and the electrodes in either direction (current blocking electrodes). The nature of these contacts has been

of the order of 10^9 ohm cm. The phase of the displacement current in the crystal with respect to the applied voltage is determined by measuring the difference between two voltages of equal amplitude. one having the phase of the displacement current and one having the phase of the driving voltage. These two parameters, the phase and the displacement current, allow one to calculate the conduction electron density and mobility as will be shown later.

The crystals are additively colored by heating them in a metal vapor of the crystal anion in a sealed, double-temperature bomb and are then quickly cooled to room temperature to avoid any coagulation of the *F*-centers into larger aggregates.[10] These large colored crystals are then cleaved into smaller crystals and electrodes applied in the form of an air-drying silver paint.[11] After

several days, this paint dries into a tough, low resistance coating which adheres satisfactorily to the alkali halide crystal. The paint seems to contain only organic binders and does not affect the crystal in any observable way.

The crystals are placed in a dry atmosphere and are illuminated in these experiments by light from a 500 W projection lamp. A heat absorbing filter in a water bath is interposed between the light and the crystal to filter out the long wavelength radiation. In some instances, an aqueous solution of $Fe(NH_4)_2(SO_4)_2 \cdot 6H_2O$ is also used to filter out the near infrared[12] and the crystal is cooled by air passed through silica gel.

In making the measurements, a fixed voltage of 5 V r.m.s. is applied across the crystal and the amplitude of the current passed through the crystal is read on the Ballantine meter-amplifier, which is in series with the crystal. The frequency of the applied voltage is determined by the Lissajous pattern displayed on the scope. Data were taken from 2–1000 c/s.

The output of the meter-amplifier is applied to one side of the differential amplifier. To the other side is applied a signal of the same amplitude as the meter-amplifier, output, but of the same phase as the voltage impressed across the crystal. This latter signal is obtained by attenuating the output of the oscillator with a voltage divider which introduces negligible phase shift at the frequencies employed. The resultant voltage read on the meter is a simple function of the phase difference between the two signals put into the differential amplifier. Phase shifts through the meter-amplifier and elsewhere in the circuitry are determined by calibrating the equipment with test capacitors and resistors.

3. THEORY

When these prepared crystals are illuminated and an alternating voltage is applied to the crystal, an a.c. admittance is measured which is different from that of the same crystal in the dark. This difference is due to the presence of electrons excited into the conduction band of the illuminated crystal with the absoprtion of light by the F-centers in the crystal.[13] Both a small signal linearized theory and a nonlinear theory of this effect in crystals have been developed in great detail by MACDONALD[14,15]. The small signal theory is linearized to the extent that terms containing harmonics of the applied a.c. voltage are eliminated. The time independent portions of the negative and positive charge densities are assumed to be equal and constant over the crystal; although this assumption can be shown not to be necessary for the theory to be valid.[16] Under these assumptions, the current in the illuminated crystal subjected to an applied a.c. voltage $V_1 \exp(i\omega t)$ is

$$\frac{J_1}{V_1} = i\omega C_g + G_p(\omega) + i\omega C_p(\omega) \qquad (1)$$

where $C_g = \epsilon A/4\pi L$ is the usual dielectric capacitance of a crystal of length L, cross-sectional area A, and dielectric constant ϵ. In effect C_g is the measured capacitance of the unilluminated crystal. In general, the space charge capacitance C_p and conductance G_p are very complicated expressions and are given by MACDONALD[14].

In certain cases, these expressions may be simplified. When the F-center ionization rate constant k_1 is much smaller than the recombination rate constant k_2, the density of conduction electrons will be much less than the density of F-centers. This is the case for a low rate of F-center ionization. If n_0, the average negative charge density is much smaller than the F-center density but not too small (i.e. $n_0 = 10^7$–10^{10} cm^{-3}), then G_p and C_p are simply

$$G_p = \frac{G_\infty \omega^2}{\omega_0^2 + \omega^2} = \frac{e\mu n_0 A}{L} \times \frac{\omega^2}{\omega_0^2 + \omega^2} \qquad (2)$$

and

$$C_p = \frac{C_0 \omega_0^2}{\omega_0^2 + \omega^2} = A\left(\frac{\epsilon e^2 n_0}{8\pi kT}\right)^{1/2} \times \frac{\omega_0^2}{\omega_0^2 + \omega^2}. \qquad (3)$$

where ω_0 is defined by the relation $\omega_0 = G_\infty/C_0$.

Thus, a measurement of C_p and G_p at suitable frequencies will determine C_0 and G_∞, and, hence, the average conduction electron density n_0 and mobility μ.

4. EXPERIMENTAL RESULTS

Inasmuch as the interpretation of the experimental results obtained in this investigation is based on the predictions of this theory, its validity was investigated by several different methods, especially since MACDONALD found results which could not be explained using his

Vol. 17
1960

linearized theory.[17] The theory is based on the usual equations for diffusion conductivity with the additional assumptions of zero current flow across the electrodes and bimolecular recombination, i.e. the conduction electrons come only from the photoexcitation of an F-center and are trapped finally by an ionized F-center (halogen ion vacancy).

The assumption of electron diffusion will be valid as long as a current carrier gains less than kT of energy from the electric field between lattice collisions. The low mobility of the conduction electrons in the alkali halides ensure that this assumption is valid for accelerating fields up to 10^5 V cm^{-1}. This is much larger than the fields produced in our crystals except very near the electrodes.

The validity of the assumption of bimolecular recombination can be demonstrated by measuring the dependence of C_0 on the intensity of illumination. A detailed balance argument for a bimolecular recombination process leads to the result that n_0 is proportional to the square root of the intensity of illumination I and hence by the definition of C_0 we would expect the relation $C_0 \propto I^{1/4}$. This was found to be the case in a KBr crystal. MACDONALD, however, did not observe the light dependence expected from his linearized theory.[17] The reason for this discrepancy is not clear and is being investigated.

The assumption of no current flow at the electrodes is the most critical assumption and has been tested at some length. The possibility of electrode breakdown will depend strongly on the crystal field at the electrode caused by the charge migration. If the average charge density liberated by the F-band light is large enough, the induced fields in the crystal will be very steep at each electrode and the center of the crystal will be essentially field free. If we denote the ratio of the crystal length to the r.m.s. Debye shielding length ($\sqrt{2}$ times the distance on which a field due to a charge excess decreases by a factor of $1/e$) by M, then one would expect the field at the electrode to be at least of the order of MV_L/L. where V_L is the applied voltage. For the crystals used in this investigation M is of the order of 100. An expression for the crystal field may be found if the applied voltage is appreciably larger than $kT/e \sim 0{\cdot}03$ V.[16,18] Under this condition the field near the electrode rises exponentially to a value of

$$E_L = 4\left(\frac{2\pi kTn_0}{\epsilon}\right)^{1/2} \sinh\frac{eV_L}{kT2}.$$

For an applied voltage of 5 V r.m.s. and an n_0 of 10^8 cm^{-3}, E_L is of the order of 10^9 V cm^{-1}. From this argument one would expect that there would be electrode breakdown for applied voltages larger than kT/e and the assumption of no current flow would be invalid.

That electrode breakdown does indeed take place can be demonstrated by measuring the d.c. behavior of illuminated crystals. As an example of the behavior of the d.c. current, Fig. 2 shows

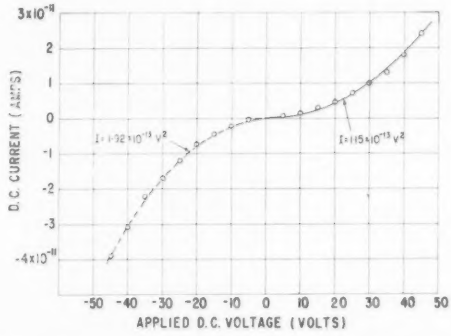

FIG. 2. Variation of d.c. current with applied voltage in an illuminated KBr crystal containing F-centers with one painted silver and one colloidal graphite electrode. A positive direction of the voltage corresponds to the silver electrode being positive.

data taken using an additively colored KBr crystal with a cross-sectional area of 0·108 cm^2 with one colloidal graphite electrode and one painted silver electrode. The crystal current in the dark was linear in voltage and corresponded to a resistance of 9×10^{13} ohms. The current density under illumination can be represented quite will in either direction by the equation $J = aV_L^2$, where for both directions a is of the order of 10^{-13} A/V^2 cm^2. The data were taken from -45 V to 45 V in 5 V steps. This result indicates the formation of a space charge at each of the crystal electrode interfaces which prevents the free passage of electrons. This is certainly to be expected in view of the fact that cleaving the crystal

will result in the production of considerable damage at the surface, with the formation of deep traps which would trap electrons and produce a narrow region of negative space charge acting as a current barrier.[19] The V^2 dependence of the leakage current on the voltage is what one would expect for a phenomenon of this type.

Although electrode breakdown is to be expected and does in fact exist, nevertheless, the results of a linear theory based on the assumption of no electron current flow can be shown to be still applicable. This is found to be true for both a.c. and d.c. measurements of crystal impedance.

The capacitance of several KBr crystals was measured in this laboratory as an applied a.c. voltage of 5 c/s was varied from 17 mV r.m.s. (which is low enough so that the linear theory should be valid) to 5 V r.m.s. The measured capacitance was constant within the errors of the measurement (~ 3 per cent). We have never observed any decrease in the capacity of an illuminated crystal as the frequency decreases which is what one would expect if electrical leakage were to reduce the space charge capacitance.

Since the space charge capacitance C_0 is the result of current blocking at the electrodes, it serves as a sensitive indicator of the electrode behavior. A number of experiments have indicated that C_0 is remarkably voltage independent over large ranges of the applied voltage. MACDONALD found relatively little harmonic generation when a.c. voltages up to 2000 V r.m.s. were applied to the crystal.[17] DONALD applied an a.c. potential of 9 V r.m.s. to KBr crystals at frequencies of $\sim \frac{1}{4}$ c/s and above with a super-imposed d.c. field and found no change in the a.c. capacitance for applied d.c. voltages below 100 V.[20]

The d.c. behavior of the space charge capacitance was investigated by observing the discharge curve of an illuminated F-centered crystal. Discharge curves of a colored KBr crystal in series with a 10^{12} ohm resistor are shown in Fig. 3. The slopes of the discharge curves using a semi-logarithmic plot are proportional to $-G_p/C_p$ and are equal to within 10 per cent when the charging potential is varied from 4–20 V, implying that no striking voltage dependence of the space charge exists. This is also borne out by the straightness of the curves. Similar results have been observed by others.[21]

The experimental results discussed above indicate that the space-charge capacitance is voltage independent for applied voltages much larger than kT/e, whereas a voltage independent capacitance is a consequence of the small signal theory only, where the applied voltage is taken to be much less than kT/e. A resolution of this inconsistency may lie in the breakdown of the assumption, in the

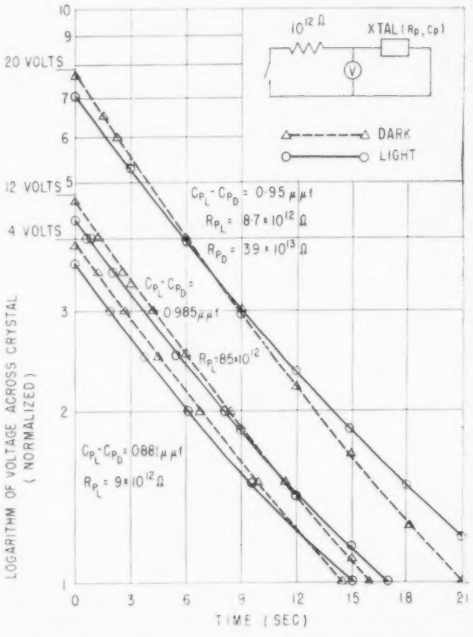

FIG. 3. Discharge curve for illuminated and dark additively colored KI crystal with 4, 12, and 20 volts initially across crystal. The normalization of each pair of curves is different.

small signal theory, of completely blocking electrodes. In fact, a d.c. argument shows that if the breakdown current is proportional to the square of the applied voltage, then the induced space charge capacitance is voltage independent. If one assumes a leakage current at the electrodes (at $x = \pm L/2$) equal to a V_L^2 then we can write the equation for d.c. current due to the negative charge carriers in the form

$$\mu kT\frac{dn}{dx} + e\mu n\frac{dV}{dx} = aV_L^2 \qquad (4)$$

Let us consider first the positive half of the crystal

only. Since the electron charge density at the positive electrode is so much larger than the positive charge density, we may ignore any positive charge. Eliminating the charge density by using Poisson's equation and integrating once we obtain

$$\frac{kT}{e}\frac{dE}{dx}+\frac{1}{2}E^2 = -\frac{4\pi a}{\epsilon\mu}V_L{}^2x \qquad (5)$$

Integrating over the positive half of the crystal equation (5) becomes

$$\frac{kT}{e}(E_L-E_0)-\left[\frac{1}{2}EV\right]_0^{L/2}+\frac{1}{2}\int_0^{L/2}V\frac{dE}{dx}dx$$

$$= -\frac{2\pi a V_L{}^2L^2}{\epsilon\mu} \qquad (6)$$

Since electrode breakdown occurs only when the fields at the electrodes are very steep, this condition ensures a very large charge concentration at each electrode causing an essentially field free region throughout the crystal except at the electrodes. Under these conditions $E_0 = 0$ and the third term on the right hand side of equation (6) may be ignored compared to the second since

$$\int_0^{L/2}V\frac{dE}{dx} \ll V_L\int_0^{L/2}\frac{dE}{dx}dx = V_LE_L{}^* \qquad (7)$$

If our applied voltage V_L is large compared to kT/e as it will be for the case of possible electrode breakdown, the first term on the right hand side will be much smaller than the second term and we may rewrite equation (6) as

$$E_L = +\frac{4\pi a}{\epsilon\mu}V_LL^2 \qquad (8)$$

The differential capacitance at each electrode C_d is defined as the change in charge per unit area on the crystal electrode per unit change of potential at the electrode or, using equation (8)

$$C_d \equiv \frac{d\sigma_L}{dV_L} = \frac{\epsilon A}{4\pi}\frac{dE_L}{dV_L} = \frac{aA}{\mu}L^2 \qquad (9)$$

This differential capacitance is independent of the applied voltage and thus one would expect that an exponential discharge curve could be observed even if there were some leakage at the electrodes.

The combined results of these tests of crystal behavior lead us to expect the results of the linearized space charge theory of MACDONALD to be valid for the conditions used in our experiments.

The data of Table 1 contain the numerical values obtained for two specimens, one KBr, and the other KI. The F-center concentration f_0 was determined from the absorption spectrum of the specimen, using SMAKULA's formula.[22] The value given for G_∞ is the high frequency limiting value of the admittance. The value of C_0 is equal to 1·4 times the low frequency limit of the solid curves in Figs. 4 and 5 as will be explained below. The value μ_H for KBr is the Hall mobility measured by MACDONALD and ROBINSON in both additively colored and X-ray colored crystals.[7] The value μ_0 for KBR is the average of the Hall mobility for about ten specimens measured by ONUKI and KAWAMURA using the method of MACDONALD[23]. REDFIELD, in 1954 reported a Hall mobility of 30 ± 15 cm^2 V^{-1} sec^{-1} for KI at 200°K.[24] It is noteworthy that

Table 1. *Experimental values for mobility in additively colored* KBr *and* KI *crystals at room temperature*

	KBr	KI
A	0·136 cm^2	0·0386 cm^2
L	0·754 cm	0·544 cm
C_g	0·077 $\mu\mu$f	0·0312 $\mu\mu$f
f_0	$6{\cdot}5\times10^{15}$ cm^{-3}	$1{\cdot}2\times10^{17}$ cm^{-3}
C_0	2·88 $\mu\mu$f	5·05 $\mu\mu$f
G_∞	326 $\mu\mu$mhos	118 $\mu\mu$mhos
M	37·9	162
n_0	$3{\cdot}48\times10^8$ cm^{-3}	$12{\cdot}6\times10^9$ cm^{-3}
ρ	$5{\cdot}63\times10^8$ ohm cm	$6{\cdot}02\times10^8$ ohm cm
μ	32·2 cm^2/V sec	0·825 cm^2/V sec
μ_H	7·5–12·5 cm^2/V sec	
μ_0	38^{+8}_{-11} cm^2/V sec	

* This derivation assumes that the zero of potential, midway between the potentials applied to the electrodes, is also the potential of the field free region of the crystal. This is correct only for small carrier concentrations. For larger carrier concentrations, the results still are valid but the equations should be modified to contain the potential of the field free region V_D explicitly.[15]

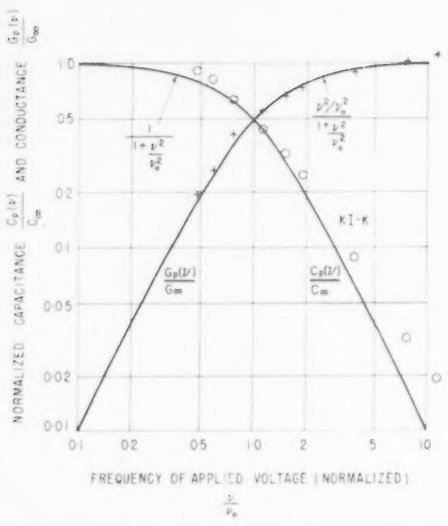

FIG. 4. Frequency dependance of normalized space charge capacitance and conductance in illuminated KI containing F-centers.

using additively colored crystals, space charge-capacitance greater than 50 times the geometrical capacitance is obtained.

Fig. 4 shows the comparison of experiment and theory for a potassium iodide crystal. The continuous curves are those of equations (2) and (3). For this crystal, ν_0 was only 5·3 c/s which is why the data does not extend to frequencies lower than $\nu = 0{\cdot}5\ \nu_0$. These curves were fitted to the data at $\nu = \nu_0$. In this region measurements of both G_p and C_p are relatively accurate. At higher frequencies measurements of C_p suffer from the fact that since C_p is found by subtracting the capacitance of the dark crystal from that of the illuminated crystal; as these quantities become equal, the error becomes very large.

The rise in the experimental value of C_p above the curve at low frequencies is due to the fact that in these crystals we do not have an infinite recombination rate of conduction band electrons and ionized F-centers.

This rise is illustrated better in Fig. 5 which shows the comparison of theory and experiment for the case of a colored KBr crystal. Here again the continuous curves represent equations (2) and (3). These two curves were fitted using the value of G_p at high frequencies (G_∞) and the crossover point of the two curves (ν_0). This choice fixes the low frequency limit of the capacitance curve. In this determination $\nu_0 = 25{\cdot}5$ c/s.

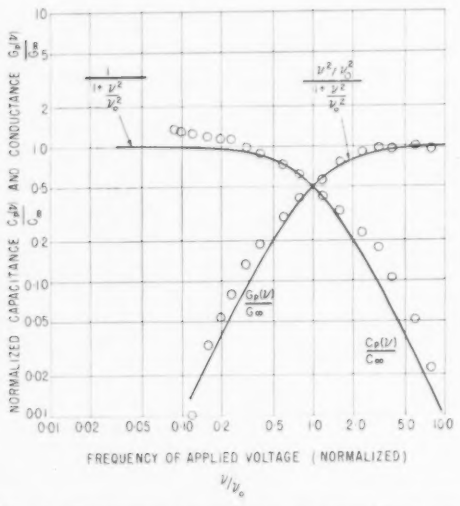

FIG. 5. Frequency dependance of normalized space charge capacitance and conductance in illuminated KBr containing F-centers.

The rise of both $G_p(\nu)$ and $C_p(\nu)$ above the continuous curves at low frequencies is due to the fact that the mean lifetime τ_r of an electron ejected from an F-center before recapture by an ionized F-center used in this experiment is long compared to the ordinary dielectric relaxation time τ_D and is comparable to the period of the alternating voltage applied to the crystal. The increase in C_p and G_p reflects the increasing amount of change of the space distribution of the ionized F-centers, brought about by the varying number of conduction electrons captured per unit volume, as the applied voltage is lowered in frequency. If the period of electron motion in the crystal is short compared to the mean lifetime for capture, the distribution of ionized F-centers will be symmetrical about the center of the crystal (where it would be a maximum). When the period of the applied voltage is long compared to the mean lifetime of the conduction electron, the ionized F-center density will follow the applied voltage and will change appreciably in time.

The effects of the long lifetime may be summarized in the circuit shown in Fig. 6. The

Vol. 17
1960

conductance $G_{r\infty}$ is that due to the movement of the ionized F-center distribution. At high frequencies, since this conductance is much smaller than G_∞, this branch of the circuit adds nothing to the current in the crystal so that the effective space charge capacitance is C_∞ instead of C_0. At low frequencies the limiting value of the capacitance is C_0 and both arms of the circuit contribute to the

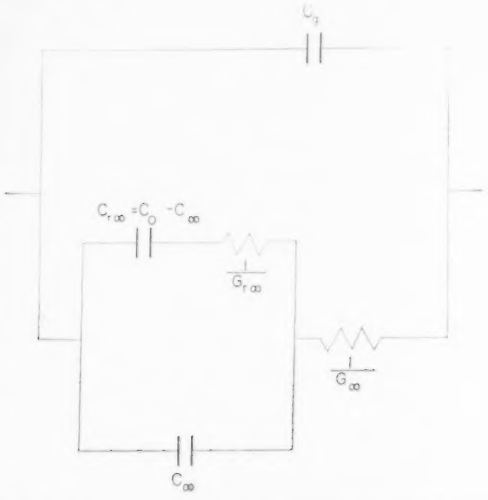

FIG. 6. Equivalent circuit of an illuminated crystal with a noninfinite recombination rate.

admittance. It can be shown that when the electron density is sufficiently large, the ratio of C_0 to C_∞ should be $\sqrt{2}$.[14] As can be seen from Fig. 5, the ratio of $C_p(\nu)$ to C_0 at 2 c/s is $\sim 1{\cdot}3$ and still rising slowly. That this addition to the capacitance is due to the phenomenon postulated above may also be shown by plotting the difference of the measured capacitance curve and the continuous curve in Fig. 5. This difference, as can be seen from the equivalent circuit of Fig. 6, should have the same shape as the capacitance curve in Figs. 4 and 5. To show this we have plotted

$$\frac{C_0-C_\infty}{C_p(\nu)-\left(\dfrac{C_\infty \nu_0^2}{\nu^2+\nu_0^2}\right)}-1 \text{ vs. } \nu^2,$$

where

$$\frac{C_\infty \nu_0^2}{\nu^2+\nu_0^2}$$

is the value of the continuous capacitance curve and C_0 is taken as $\sqrt{2}C_\infty$. This curve should be a straight line through the origin if the added capacitance is due to recombination effects. That this is so is shown in Fig. 7. The scatter of the two higher frequency points is probably due to the subtraction

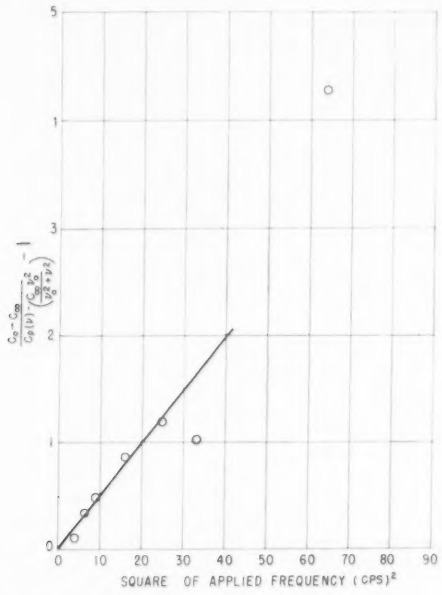

FIG. 7. Plot of

$$\frac{C_0-C_\infty}{C_p(\nu)-\left(\dfrac{C_\infty \nu_0^2}{\nu^2+\nu_0^2}\right)}-1$$

vs. the square of the applied frequency for the illuminated KBr crystal shown in Fig. 5.

process causing a large relative error. The slope of this curve is equal to

$$\frac{(C_0-C_\infty)^2}{G_{r\infty}^2}.$$

From the measured slope, $G_{r\infty}$ is found to be $23{\cdot}7\ \mu\mu$ mhos.

The ratio of the mean lifetime for conduction electron capture τ_r to the dielectric relaxation time, τ_D, denoted by ξ may be determined from a knowledge of $G_{r\infty}$ and G_∞. Since in our crystals

$M \gg 1$ we may write

$$\frac{G_{r\infty}}{G_\infty} = \frac{M}{\sqrt{2\xi}} \tag{14}$$

Using our determined values of M, G_∞ and $G_{r\infty}$, we find that $\xi = 364$ which implies that the recombination constant for conduction electrons to be captured by ionized F-centers in KBr is $k_2 = 3{\cdot}34 \times 10^{-8}$ cm^3 sec^{-1}.[14] This value of the recombination rate leads to a mean lifetime for ionized F-center capture of a conduction electron in the KBr crystal by an ionized F-center investigated of 0·086 sec. This long lifetime is mainly due to the fact that the density of capturing centers, the ionized F-centers, is only $3{\cdot}48 \times 10^8$ cm^{-3}. It should be noted that this lifetime is not the same as that for the capture of a conduction electron into a trap shallow compared to the F-center excitation energy but somewhat deeper than kT. This shallow trapping lifetime is much shorter as can be easily seen by suddenly interrupting the light beam. Some preliminary experiments show that this lifetime is shorter than 10^{-3} sec. Since the crystals are illuminated continuously. the resultant rapid shallow trapping and re-excitation will not affect the observed phenomena at the low frequencies used in this investigation.

The conduction electrons in the alkali halide crystal have such a low density that their velocity distribution follows a Maxwell–Boltzmann distribution (i.e. non-degenerate). Since the ionized F-centers are not mobile the recombination rate of electrons and ionized F-centers may be thought of as the collision rate between a set, n, of particles with a Maxwell–Boltzmann velocity distribution and a set, p, of particles with zero velocity. If the cross section for collision is S the rate is $Sn_0p_0\bar{v}$. For small applied voltages the average recombination rate in the crystal will be $k_2n_0p_0 = k_2n_0^2$. This must equal the expression $Sn_0p_0^2(2kT/m_p)^{1/2}$, where S is the cross section for the capture of an electron by an ionized F-center and m_p is the conduction electron effective mass or polaron mass. If we represent the ratio of the effective mass to the free electron mass by γ we have $S = 3{\cdot}1 \times 10^{-15}\sqrt{(\gamma)}$ cm^2.

One may also note that since we have found k_2 experimentally, our knowledge of k_2 and n_0 allows us in principle to calculate k_1, the dissociation constant. If the light intensity in the crystal is measured, then the quantum yield of electrons ejected into the conduction band may be determined. Heretofore, only the product of this yield and the mean "range" before capture of the electrons per unit field strength has been measured. If k_1, however, is to be equal to the probability of an F-center electron being excited into the conduction band per absorbed photon, a very large field must be applied to the crystal to remove the excited electron before it is recaptured by the halogen ion vacancy from which it came.

5. CONCLUSIONS

The data obtained in this investigation are in striking agreement with the predictions of the linearized a.c. theory of photocapacitative effects developed by MACDONALD. Using techniques described in this report a large number of the parameters associated with electron conductivity in colored alkali halide crystals may be determined with good accuracy and relative ease.

Although the 5 V r.m.s. applied across the crystal is large compared to kT/e in contradistinction to the requirements of the linearized theory, no behavior that could be attributed to a non-linear theory was detected and the relations between the quantities expected from a linearized theory were verified. An extrapolation of the applied voltage from a region where the assumptions of the theory are valid to a region where electrode breakdown effects would be expected to occur also did not reveal any non-linear effects.

One possible explanation of the validity of the theoretical results for the applied voltages used in this experiment lies in the nature of the breakdown current as discussed at length above. Another explanation may be the fact that the current leakage through the crystals measured at zero frequency is very much smaller than the a.c. currents in the illuminated crystal. The d.c. admittance was generally of the order of 10^{-12}–10^{-13} mhos. The success of the linearized theory may also be due to the fact that at the frequencies used in this work the electrons did not have sufficient time to build up a high enough charge density at the electrodes to cause appreciable leakage. This does seem to be the case for the positive ionized F-center distribution.

Vol. 17
1960

The experimental results of this investigation and the observations by others mentioned above, while attesting to the usefulness of the MACDONALD theory, do not explain those results obtained by MACDONALD which are contrary to the predictions of the theory, principally the behavior under varying illumination and the slope of log $C_p(\omega)$ with frequency at frequencies above ω_0. Both these descrepancies are being investigated. It has been found that in crystals having been illuminated for several hours the slope of log $C_p(\omega)$ with frequency does decrease from 2 as predicted by the theory to 1·5 or 1. Slopes less than 2 were observed by MACDONALD[17]. Spectrophotometric curves show that prolonged illumination of the crystals does produce some coagulation of the *F*-centers with a production of other shallower traps. It may be that an excessive number of such traps is responsible for the change of slope of log $C_p(\omega)$. MACDONALD also found a large number of shallow traps ($\sim$0·04 eV) in his crystals.

In view of the satisfactory agreement of our mobilities with the Hall mobility measurements that have been reported in the literature, this method is being extended to other materials and temperatures.

REFERENCES

1. FRÖHLICH H., *Advanc. Phys.* **3,** 325 (1954).
2. SCHULTZ T. D., *Electron–Lattice Interactions in Polar Crystals*, M. I. T., Solid State and Molecular Theory Group, Tech. Rpt. No. 9, Aug. 20, 1956. This report contains an excellent review of work done prior to its publication.
3. ALLCOCK G. R., *Advanc. Phys.* **5,** 412 (1956).
4. BUIMISTROV V. M. and PEKAR S. I., *Sov. Phys. JETP* **6,** 977 (1958).
5. LIEB E. H. and TAMAZAKI K., *Phys. Rev.* **111,** 728 (1958).
6. SEWELL G. L., *Phil. Mag.* **3,** 1361 (1958).
7. MACDONALD J. R. and ROBINSON J. E., *Phys. Rev.* **95,** 44 (1954).
8. REDFIELD A. G., *Phys. Rev.* **94,** 537 (1954).
9. BROWN F. C. and INCHAUSPÉ N., International Symposium on Color Centers in Alkali Halides, Oregon State College, Sept. 8–11 (1959).
10. SCOTT A. B. *et al.*, *J. Phys. Chem.* **57,** 757 (1953).
11. Silver Paint No. 4817 mfd. by E. I. DuPont de Nemours and Co.
12. WITHROW R. B., *Plant Physiol.* **32,** 355 (1957).
13. MOTT N. and GURNEY R., *Electronic Processes in Ionic Crystals*, 2nd Ed. Oxford University Press (1948).
14. MACDONALD J. R., *Phys. Rev.* **92,** 4 (1953).
15. MACDONALD J. R., *J. Chem. Phys.* **30,** 806 (1959).
16. KAHN D. and GLASS A. J., R.I.A.S. Tech. Report 59–2 (Feb. 1959).
17. MACDONALD J. R., *J. Chem. Phys.* **23,** 275 (1955).
18. MACDONALD J. R. and BRACHMAN M. K., *J. Chem. Phys.* **22,** 1314 (1954); MACDONALD J. R., *J. Chem. Phys.* **22,** 1317 (1954).
19. MOTT N. and GURNEY R., *Electronic Processes in Ionic Crystals*, 2nd Ed., p. 173. Oxford University Press (1948).
20. DONALD D. K., Technical Report No. 125, Lab. for Ins. Research, M. I. T., Feb. 1958.
21. VON HIPPEL A. *et al.*, *Phys. Rev.* **91,** 568 (1953).
22. SEITZ F., *The Modern Theory of Solids* p. 662. McGraw-Hill, New York (1940).
23. ONUKI M., and KAWAMURA H., *J. Phys. Soc. Japan* **14,** 967 (1959).
24. REDFIELD A. G., *Phys. Rev.* **94,** 537 (1954).
25. SEITZ F., *Rev. Mod. Phys.* **26,** 7 (1954).

J. Phys. Chem. Solids Pergamon Press 1961. Vol. 17, Nos. 3/4, pp. 220–228. Printed in Great Britain.

THE EFFECTS OF GAMMA RADIATION ON SOLIDS. EXO-ELECTRON EMISSION FROM IRRADIATED IRON OXIDE CATALYSTS

E. J. GIBSON

Warren Spring Laboratory, Stevenage, Herts.

(*Received* 10 *February* 1960)

Abstract—The results are presented of an exploratory study into the emission of exo-electrons from powdered iron oxide catalysts for the Fischer–Tropsch synthesis after exposure to gamma radiation. It is considered that the evidence supports the theory that emission centres consist of oxygen ion vacancies containing trapped electrons. The role of irradiation appears to be the filling of the vacancies with electrons.

Vol. 17
1960

As part of a study of the effect of radiation on solid catalysts, a search has been made for physical measurements which will show a change in the properties of the catalyst surface on irradiation. This paper presents the results of an exploratory investigation of the phenomenon known as exo-electron emission, that is the emission of low energy electrons from a surface at excitation energies below the photo-electric threshold of the metal. The emission of low energy electrons from irradiated solids as a result of thermal- or photo-stimulation has been measured in a number of studies.[1–6] It has been suggested that the emission is associated with the discharge of colour centres, or, in oxides,[2] with the presence of electrons trapped at oxygen ion vacancies. Also Nassenstein[7] has reported that silver catalysts having different activities for the oxidation of ethylene, emitted electrons at different temperatures on heating up to reaction temperature (200°C).

Some preliminary experiments were carried out at the National Engineering Laboratory, D.S.I.R. Unreduced mill-scale catalysts were exposed to light of known wavelength in the range 4300 to 7000 Å, and the emission measured with an open Geiger counter,[2] using a mixture of argon and ethyl alcohol as counting gas. No emission was obtained from unirradiated samples, but doses of X-rays as small as 0·2 rad resulted in an appreciable emission.

The present study is concerned entirely with certain iron oxide catalysts for the Fischer–Tropsch synthesis. These catalysts did not give any emission on heating unless they had previously been subjected to X- or gamma radiation. As the acivitty of these catalysts for the Fischer–Tropsch reaction is increased by irradiation, it seemed possible that a study of the emission phenomenon would give information regarding those changes that take place in the catalyst on irradiation which result in an increase in catalytic activity.

EXPERIMENTAL

The equipment used for the emission measurements was a methane-flow proportional counter (U.K.A.E.A. type 1077B). It was modified by removing the flat sample platform and replacing it by a platform with a 1·5 cm diameter well which could hold a small quantity of powdered catalyst, see Fig. 1. The necessary leads for heating the catalyst, measuring its temperature, and carrying the accelerating potential to the grid over the catalyst sample were all led up through the stem of the heater assembly.

The heater was capable of raising the catalyst to 350°C. The temperature was raised by increasing the voltage to the heating coil in steps of 20 V,

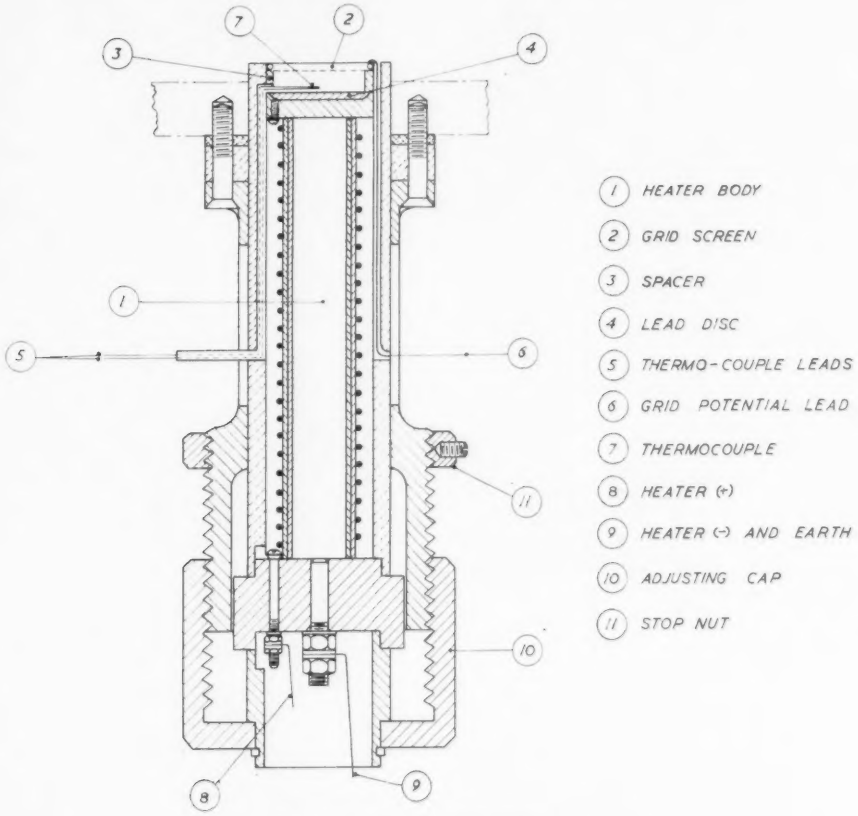

FIG. 1. Catalyst heating assembly.

giving heating rates which varied between 6° and 12°/min from run to run, but which were reasonably constant in any one run. Readings of temperature and count-rate were taken every minute.

It was found necessary to run the heater up to at least 200°C with the methane flowing before inserting the sample, otherwise spurious pulses were obtained at about 100°C. It is thought that these were due to water adsorbed in porous insulating materials used in parts of the platform assembly.

The accelerating grid, which was maintained at a positive potential of 108 V with respect to the catalyst, lay about 2 mm above the catalyst surface and flush with the bottom of the counting chamber.

The linear amplifier (U.K.A.E.A. type 1049B) was operated with a total gain of about 20,000. The count rate was registered on a ratemeter (U.K.A.E.A. type 1037).

The course of an experiment was as follows-:

About 0·5 ml catalyst was placed in a tube of 13 mm internal diameter and evacuated at 10^{-3} mm Hg for half an hour at room temperature. The tube was filled with oxygen-free nitrogen and placed in the radiation field of a Co^{60} source of about 90 c. The dose-rate for the catalysts used was slightly greater than 10^5 rads/hr.

Immediately following the irradiation period, some of the sample was poured into the sample well, the accelerating grid put in place, and the platform assembly screwed up into position. The chamber was purged with methane at 100 ml/min for 15 min and then the rate of flow was reduced to 40 ml/min for the remainder of the experiment.

Table 1. *Composition of mill-scale catalysts*

Catalyst No.	3	18	2425
Mill-scale Batch No.	II	VI	VII A
Composition (wt. per cent)			
Fe	66·8	73·5	71·2
Al_2O_3	3·6	0·1	1·9
SiO_2	1·6	0·5	1·9
Cr_2O_3	nil	0·5	nil
Mn_3O_4	0·6	0·7	1·0
Alkali content of catalyst (parts by weight K_2O per 100 parts Fe)	2·0	2·0	2·0
Roasting temperature (°C)	1000	1000	1300

CATALYSTS

Catalysts Nos. 3, 18, and 2425 were prepared from rolling-mill-scale by impregnation with potassium carbonate from solution followed by roasting for 4 hr at 1000°C or above. The composition of the mill-scales, and roasting temperatures of these catalysts are given in Table 1.

Measurements of electrical resistivity and thermoelectric power have indicated that these solids are *n*-type semiconductors.

RESULTS

Samples of mill-scale catalysts which had been subjected to gamma radiation and subsequent

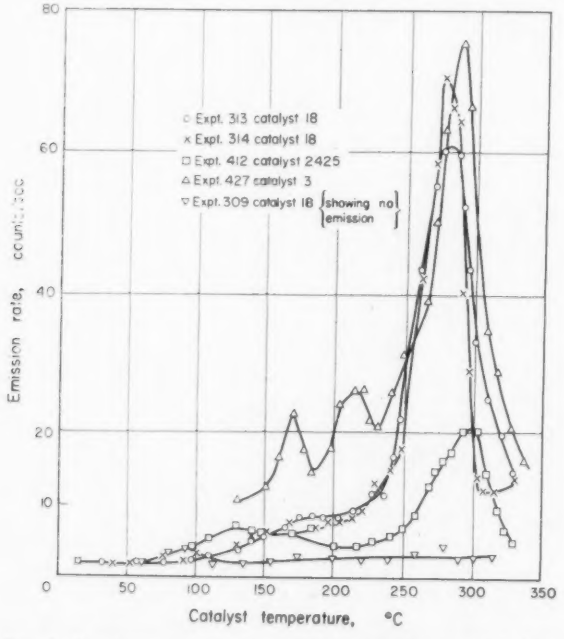

FIG. 2. Specimen curves demonstrating exo-electron emission.

heating in the proportional counter gave emission peaks at 300 ± 20°C; some typical results are shown in Fig. 2.

The presence of adsorbed gases on the surface was found to affect the magnitude of the emission with some samples, and when a series of samples were required for comparative tests, it was found necessary to evacuate them all simultaneously. Small, low-temperature emission peaks were observed in some cases—for example a peak was often observed at 160–170°C; these are probably ascribable to adsorbed gases.

Effect of heat treatment on emission

Catalysts 3 and 18 gave an emission when irradiated without any prior heat treatment, but it was found that the magnitude of the emission at 300°C could be markedly altered by certain treatments before irradiation. Some results obtained with catalyst 18 are shown in Table 2; all samples were cooled to room temperature before irradiation.

A sample which was heated to 450°C *in vacuo* but not irradiated gave no emission.

Table 2. Effect of heat treatment on exo-electron emission.

Heat treatment			Maximum emission rate
Duration (hr)	Air pressure	Temperature (°C)	(counts/sec)
0	—	—	40
18	10^{-3} mm Hg	450	320
3	1 atm	1300	0

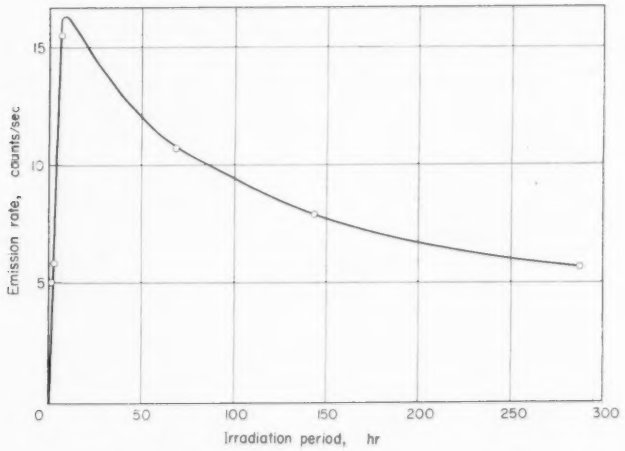

FIG. 3. Effect of radiation dosage on the maximum emission rate.

A further illustration of the effect of heat treatment is provided by an experiment with catalyst 2425. This catalyst did not give an emission after irradiation without a prior heat treatment, but when a sample was heated to 450°C for 6 hr at 10^{-3} mm Hg, cooled to room temperature, irradiated in nitrogen and its emission measured, a peak emission of 21 counts/sec was obtained.

Effect of total dose

Although it has not proved possible thus far to

obtain quantitatively reproducible data on the variation of the magnitude of the emission with increase in total radiation dose, sufficient data have been obtained to establish the general picture.

The count rate at the temperature of peak emission rises linearly with increase in radiation dose up to about 10^6 rads, and thereafter decreases in a non-linear manner up to the maximum doses used (4×10^7 rads). One set of results obtained with catalyst 18 is shown in Fig. 3. To eliminate any effect due to variations in the rate of heating, the total number of counts registered between the temperatures marking the beginning and end of the emission peak were plotted for one series of results and the same variation with radiation dose was observed as is shown in Fig. 3.

Stability of the emission centres

Although normally the catalyst was put into the counter immediately after the irradiation, experiments in which the emission was measured at varying periods of time after the end of the irradiation showed that if the samples were kept in nitrogen in the dark for up to 24 hr, the same emission was obtained on heating. However, if the samples were left open to the air for a few hours, a reduced emission was obtained on heating. Longer exposure to air did not appear to have much effect, and after leaving for 24 hr, a substantial emission was still obtained.

In one series of experiments, sufficient catalyst 18 was irradiated for several emission measurements, the dose being 8×10^6 rads. A peak emission of 61 counts/sec was obtained immediately after irradiation; the remainder of the sample was left open to the air, samples being taken for emission measurement after 4 hr and 28 hr. A peak emission of 42 counts/sec was obtained in both cases.

The length of time during which electrons are emitted at the temperature of peak emission was determined by holding the catalyst heater at this temperature and noting the change in count-rate with time. In Fig. 4 is shown the results of three experiments. The decay falls into two sections and in the first section at least, appears to be exponential; insufficient data are available for the form of the second part of the decay curve to be established.

The rate of decay in the first part has a half life of 1·2 to 1·5 minutes and is fairly reproducible.

DISCUSSION

The main points requiring discussion are (1) what light do these experiments throw on the nature of the centres responsible for emission, and (2) what is the role of gamma radiation in producing these centres. It is difficult to discuss

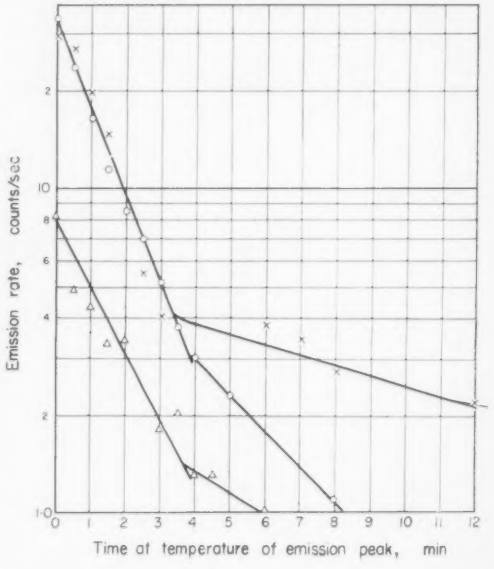

FIG. 4. Decay of emission rate at the temperature of peak emission.

the relevance of this phenomenon to the radiation-induced increase in catalytic activity until more experimental evidence is available on the factors controlling the increase in activity.

Nature of the emission centres

It has been suggested that exo-electron emission has its origin in a structure similar to that giving rise to thermoluminescence, and in some cases[8] it has been found that the variation of thermos stimulated electron emission with temperature i-closely parallel to the variation of thermoluminescence with temperature. Furthermore, instances have been reported[6,9,10] in which intensity of

Vol. 17
1960

luminescence at the peak of the glow-curve from irradiated solids increases to a maximum and then declines as the dose of radiation is increased; a similar effect of increase in radiation dose on the intensity of electron emission has been observed in the present work.

NASSENSTEIN[4] has suggested that a formula proposed for luminescence[11] could be used to estimate the thermal excitation energy of emission centres,

$$E_{\text{therm}} \sim 25\, kT_{\text{excit}} \qquad (1)$$

where E_{therm} is the thermal excitation energy, and T_{excit} is the excitation temperature in °K. Values of excitation energies calculated from the temperature of peak emission by the above formula are shown in column 7 of Table 3.

GROSSWEINER[13] has developed equations for calculating the trap depth and mean life-time at the peak of first order luminescence glow-curves. The equation giving trap depth is

$$E = \frac{1{\cdot}51\ T_p T_m}{(T_p - T_m)} \qquad (2)$$

where E = trap depth in electron volts
T_p = temperature at the peak of the emission curve
T_m = temperature at which the low temperature side of the emission peak reaches half its maximum value.

The mean life-time for decay at the temperature of peak emission is given by the equation

$$-\frac{n_p}{dn_p/dt} = \frac{2T_p(T_p - T_m)}{3T_m\beta} \qquad (3)$$

where β is the rate of warming.

Table 3. Results calculated from emission curves.

Experiment No.	Catalyst No.	Period of irradiation (hr)	Rate of heating (°C/min)	Trap depth (eV) (from Eq. 2)	Mean lifetime (min) (from Eq. 3)	Excitation energy (eV) (from Eq. 1)
312	18	24	10	1·4	2·0	1·2
313	18	68	10	1·8	1·5	1·2
327	18	69	12·5	1·7	1·3	1·25
328	18	140	9	1·7	1·9	1·22
330	18	6·7	10	1·7	1·7	1·25
332	18	140	9	2·6	1·2	1·25
412	2425	16	7	1·4	1·9	1·22
427	3	40	6·5	2·0	2·1	1·22
428	3	40	8·5	2·4	1·3	1·2

These equations provide an alternative method of calculating the excitation energy of the trapped electrons, and the values of the trap depth and of the mean life-time of the centres at the temperature of peak emission calculated using these formulae are shown in columns 5 and 6 of Table 3. If thermoluminescence and exo-electron emission do have their origin in the same type of structure, then the excitation energy necessary to cause emission should be equivalent to the trap depth. The values obtained for trap depth are somewhat higher and more variable than those obtained from the temperature of peak emission alone, the most probable value being about 1·8 eV, about

50 per cent higher than the value obtained using the other equation.

Using the relationship $E_{opt} \sim 2E_{therm}$,[12] where E_{opt} is the optical excitation energy, the values of the optical excitation energy can be calculated. The values obtained using E_{therm} from equation (1) lie between 2·4 and 2·5 eV; these should be compared with values of 2·64 to 2·71 eV obtained by GRUNBERG[2] and others for a range of other oxides: the values obtained using the trap depth from equation (2) are somewhat higher than this, with a mean value of about 3·6 eV. It should be remembered that in this work, the catalysts are not a single oxide but a mixture of oxides, and a close agreement between energy values now reported and those obtained with pure oxides would not necessarily be expected.

Some support for the use of GROSSWEINER's equations in this work is obtained by comparing the values of mean life-time of the emission centres at the temperature of peak emission obtained from his equations with those observed. The calculated figures are shown in column 6 of Table 3, and lie in the range 1·3 to 2·1 min. The values obtained from the curves shown in Fig. 4 are 1·7 and 2·1 min; the two sets of figures are in fair agreement.

It thus seems reasonable to conclude that the phenomenon of exo-electron emission requires the presence of electrons in traps, and from a comparison of the figures presented here with those obtained by GRUNBERG, it seems likely that in the present instance the traps are oxygen ion vacancies. This is in accord with the fact that these catalysts behave as *n*-type semiconductors.

The effect of adsorbed gases on the emission phenomenon has been demonstrated with two catalysts. Other workers[3] have also attributed some emission peaks to the presence of adsorbed gases.

Heating to 450°C *in vacuo* will remove any gases which are physically adsorbed, and also some chemisorbed gases. In view of the theory that the emission is dependent upon the existence of oxygen ion vacancies, it is worth examining the possibility that oxygen is removed from the surface by this treatment. BEVAN *et al.*[14] give 0·3 T_m (where T_m is the melting point in °K) as the lowest temperature at which oxygen can be regarded as mobile or removable from the surface of an oxide; this corresponds to 280°C for pure Fe_2O_3.

These workers observed changes in electrical conductivity due to the removal of surface oxygen at 410°C and 10^{-5} mm Hg with Fe_2O_3. It seems probable that oxygen was removed from the surface layers by heating to 450°C *in vacuo* in our experiments.

It should be noted that catalysts 3 and 18 from which an emission was obtained without any prior vacuum heat treatment, were prepared by sintering at 1000°C, and when heated to 1300°C in air failed to give any emission, while catalyst 2425, which gave no emission without a vacuum heat treatment, was prepared by sintering at 1300°C. These results only conform with the theory proposed if heating to 1300°C in air produces a surface in a higher state of oxidation than that obtained by heating to 1000°C, and if this change is reversible by heating *in vacuo* at 450°C. Such changes would seem unlikely on the basis of present knowledge, but current work in this laboratory, is showing that the surfaces of iron oxides are very variable in composition and the question should be regarded as open at the moment.

The role of irradiation

The main effect of bombardment with electromagnetic radiation is the production of excited electrons and positive holes. The mechanism for electron emission proposed by GRUNBERG and WRIGHT[2] requires the presence of electrons trapped in shallow (low energy) surface sites (of unknown composition) as well as electrons trapped at oxygen ion vanancies (F' centres) and it is possible that both types of trap are filled during irradiation. We have observed that exposure to air or oxygen at room temperature for several hours after irradiation results in a small reduction in emission, whereas there was no reduction if the sample was maintained in nitrogen. It appears therefore that some of the centres responsible for emission can "decay" through oxidation but the "spontaneous decay" observed by GRUNBERG is very slow if it occurs at all. This implies that the shallow traps are continually being replenished at room temperature, and that the removal of F' centres by diffusion is very slow. It seems likely that the main role of gamma radiation is to create F' centres by filling existing vacancies with electrons. It is of interest however to consider

the possible formation of vacancies as a result of atomic displacements produced by irradiation.

Using data from DIENES and VINEYARD[15], it is possible to estimate the vacancy concentration brought about by a given dose of radiation. Assuming an atomic displacement requires 25 eV, the threshold energy for displacement of an oxygen ion is 0·16 MeV, and for displacement of an iron ion is 0·44 MeV. The cross section for displacement of oxygen and iron atoms by Compton electrons from 1 MeV gamma rays is 0·13 and 0·05 barns respectively; thus for Fe_2O_3, there will be approximately four times as many oxygen displacements as iron displacements.

If it is assumed that the depth of catalyst which contributes to the emission is limited to 30 Å (see Ref. 2), the weight of catalyst on the counter platform from which emission would be detected is about 3×10^{-6}g. The number of oxygen displacements by Compton electrons in this material due to a dose of 7×10^5 rads ($1{\cdot}3\times10^{14}$ eV) would be 6×10^6.

Further there is the possibility of displacements occurring through multiple ionization by the mechanism proposed by VARLEY[16]. Of the $1{\cdot}3\times10^{14}$ eV absorbed in the surface layer, not more than 1 MeV would be used in producing each Compton displacement, i.e. not more than 6×10^{12} eV in total. There would also be a small amount of energy used in vacancy production by photo-electrons—probably not more than a tenth of this amount. The net energy available for multiple ionization will therefore be approximately $1{\cdot}2\times10^{14}$ eV, enough to produce at least 10^{12} ion pairs. Existing evidence indicates[15] that a $(p+1)$-fold ionization is 100 times less likely to occur than a p-fold ionization; one would therefore expect about 10^8 triply-ionized oxygen atoms to be produced, each of which might result in a displacement. Also it is suggested that in alkali halides the cross section for displacement by ionization may be 30 times that for displacement by direct collision. It seems clear therefore that a total of at least 10^7 oxygen displacements could occur.

This figure must now be compared with the total number of electrons counted. In one experiment, the total number of counts registered on a scaler by a catalyst which had received 7×10^5 rads was 23,670. Assuming 15 per cent of the emitted electrons enter the counter and the efficiency for detection is 50 per cent, the total number of electrons emitted was approximately $3{\cdot}2\times10^5$. This estimate could be too low because the efficiency for collecting and counting the emitted electrons is lower than that estimated, or too high because of the possibility of a centre being responsible for the emission of more than one electron. Even if this estimate is low by a factor of 10, it is still possible for all the electron emission centres to have been produced as a result of atomic displacements.

Although this necessarily rough calculation indicates that the production of vacancies through atomic displacements could give rise to sufficient emission centres, two observations make it unlikely that the contribution from this source is very great. Firstly, the evidence that a very large increase in emission is obtained when a sample is heated *in vacuo* before irradiation, and secondly, that the maximum emission is obtained after a dose of about 10^6 rads. One might expect a continued increase in emission beyond this dose if new centres were being created by atomic displacements. The fall in emission after higher doses of radiation suggests that some of the centres are being destroyed; this might be established by an investigation of the effect of irradiation dose-rate on the emission.

If the emission centres are produced as a result of the radiation exciting electrons into vacancies already present, then a much lower energy radiation ought to produce the same effect. This point has not yet been investigated in detail although it was found that irradiation with ultra-violet light (energy about 3·5 eV) did not produce any emission centres, whereas irradiation with Co (α) radiation (7 kV) did.

It is not yet clear what the relationship is between the production of emission centres and the increase in catalytic activity brought about by irradiation. It has proved difficult to obtain quantitatively reproducible data for the variation of catalytic activity with the dose of radiation absorbed, but increases in activity of 50 per cent have been obtained after doses as low as 10^5 rads.

It has also been found that the activity of some catalysts can only be increased by radiation if adsorbed gases are first removed.

Finally, it should be said that these results can

only be regarded as applying to the catalysts used in this work, and quantitative differences would be expected when using pure Fe_2O_3 or other iron oxide catalysts. It is recognized that much more accurate and reliable results would be obtained by using a more refined technique for measuring the intensity of emission, the most important feature of which would be the substitution of an electron multiplier working in high vacuum for the proportional counter.

Acknowledgements—The work described in this paper formed part of the programme of the Fuel Research Board of the Department of Scientific and Industrial Research and the paper is published by permission of the Director of The Warren Spring Laboratory. The assistance of Mr. R. W. CLARKE, Mr. D. POPE and Mr. P. WATSON with various parts of the experimental work is gratefully acknowledged. It is also a pleasure to record my thanks to Dr. L. GRUNBERG and Dr. K. H. WRIGHT of the National Engineering Laboratory, D.S.I.R., for their helpfulness in discussions of this subject and for making some preliminary measurements. The figures are Crown copyright and are published by permission of the Controller, H.M. Stationery Office.

REFERENCES

1. *Acta Phys. Austr.* **10,** (1957). Papers presented to meeting of Austrian Physical Society, September, 1956.
2. GRUNBERG L. and WRIGHT K. H. R., *Proc. Roy. Soc.* **A232,** 403 (1955).
3. HIESLAMAIR H. and MÜLLER H., *Z. Phys.* **152,** 642 (1958).
4. NASSENSTEIN H., *Z. Naturf.* **109,** 944 (1955).
5. BOHUN A., *J. Phys. Radium* **17,** 783 (1956).
6. HENSLER J. R., *Nature, Lond.* **183,** 672 (1959).
7. NASSENSTEIN H. and MENOLD R., *Naturwissenschaften* **43,** (21), 492 (1956).
8. HANLE W., *Acta Phys. Austr.* **10,** 339 (1957).
9. HECKELSBERG L. F. and DANIELS F., *J. Phys. Chem.* **61,** 414 (1957).
10. KRAMER J., *Acta Phys. Austr.* **10,** 327 (1957).
11. RANDALL J. T. and WILKINS M. H. F., *Proc. Roy. Soc.* A**184,** 366 (1945).
12. MOTT N. F. and GURNEY R. W., *Electronic Processes in Ionic Crystals*, p. 162. Clarendon Press, Oxford (1957).
13. GROSSWEINER L. J., *J. Appl. Phys.* **24,** No. 10, 1306 (1953).
14. BEVAN D. J. M., SHELTON J. P. and ANDERSON J. S., *J. Chem. Soc.*, p. 1729 (1948).
15. DIENES G. J. and VINEYARD G. H., *Radiation Effects in Solids.* Interscience, London (1957).
16. VARLEY J. H. O., *Nature, Lond.* **174,** 886 (1954).

J. Phys. Chem. Solids Pergamon Press 1961. Vol. 17, Nos. 3/4, pp. 229–231. Printed in Great Britain.

THE IONIC DISTRIBUTION IN THE GARNETS $Gd_3Al_3Fe_2O_{12}$ AND $Y_3Al_3Fe_2O_{12}$

C. E. MILLER

Bell Telephone Laboratories, Murray Hill, New Jersey

(*Received* 18 *May* 1960; *revised* 23 *June* 1960)

Abstract—An analysis of quantitative X-ray powder diffraction intensity data has been made with the purpose of determining the ionic distribution in $Gd_3Al_3Fe_2O_{12}$ and $Y_3Al_3Fe_2O_{12}$. It has been found that the exact distribution cannot be determined in this manner. However, the distribution recently deduced by Geller is compatible with the results of the X-ray analysis.

INTRODUCTION

IN A RECENT paper[1] GELLER calculated the ionic distribution in several substituted rare earth iron garnet systems. His results indicated that the fraction of aluminum ions in tetrahedral sites is 0·62 in $Gd_3Al_3Fe_2O_{12}$.

The present study of the Al–Fe distribution in $Gd_3Al_3Fe_2O_{12}$ and $Y_3Al_3Fe_2O_{12}$ is based on quantitative X-ray intensity data. The yttrium compound gave a better diffraction pattern with measurable lines over a wider angular range, presumably because of the reduced fluorescence. The replacement of gadolinium by yttrium should have little effect on the ionic distribution.

EXPERIMENTAL

Preparation of specimens

The compounds were prepared by coprecipitation of the metal hydroxides from a stoichiometrically proportioned solution of the metal nitrates. The mixture of hydroxides for each compound was calcined at 800°C for 16 hr to form the oxides.*[2] The oxide mixtures were compacted into pellets and fired for two hours at 1350°C. The fired ceramic discs were then pulverized, recompacted and refired through a total of four cycles, that is, until the sharpness of the lines on the X-ray powder photograph of each specimen indicated complete combination to a single garnet phase.

* The author is indebted to D. W. MITCHELL of these Laboratories for providing the calcined oxide mixtures.

Diffraction data

The X-ray powder photographs were taken with Straumanis-type Norelco cameras of 114·59 mm diameter using CrK radiation. The specimens used for quantitative diffraction intensity analysis were prepared by grinding the ceramics to pass through a 400 mesh screen and mixing the powder with a small amount of petrolatum as binder. The sample was placed in a specimen spinner in a Norelco diffractometer and irradiated with Cu$K\alpha$ radiation. The areas of the recorded diffraction lines were measured with a Keuffel and Esser compensating polar planimeter.

Crystallographic data

The lattice constants, determined from measurement of the powder photographs and the diffractometer patterns are:

$Gd_3Al_3Fe_2O_{12}$	12·267 Å ± 0·003 Å
$Y_3Al_3Fe_2O_{12}$	12·161 Å ± 0·003 Å†

IONIC DISTRIBUTION FROM X-RAY DIFFRACTION ANALYSIS

Relative intensities were calculated‡ for models with 52 per cent, 62 per cent and 72 per cent of the aluminum ions in tetrahedral sites. Corrections

† This value is in agreement with that previously found for this compound.[2]

‡ $I_{hkl} = p[F_{hkl}]^2$ L·P × 10^{-6}, where p = multiplicity factor, F = structure amplitude, L·P = Lorentz-polarization factors.

Table 1. *Observed and calculated intensities of* $Y_3Al_3Fe_2O_{12}$ *and* $Gd_3Al_3Fe_2O_{12}$

	$\{Y_3\}[Al_yFe_{2-y}](Al_zFe_{3-z})O_{12}$				$\{Gd_3\}[Al_yFe_{2-y}](Al_zFe_{3-z})O_{12}$			
		I_c				I_c		
$h^2+k^2+l^2$	I_0	$z = 1{\cdot}86$	$z = 1{\cdot}56$	$z = 2{\cdot}16$	I_0	$z = 1{\cdot}86$	$z = 1{\cdot}56$	$z = 2{\cdot}16$
6	32	35	31	40	116	175	116	134
8	3	6	12	2	31	32	43	22
14	21	25	22	29	85	90	83	97
16	61	56	53	59	88	79	75	83
20	179	232	243	222	373	402	419	387
22	n.o.	0	0	0	n.o.	6	5	6
24	63	72	66	77	117	114	107	121
26	10	10	10	10	12	10	10	10
30	35	35	33	37	79	75	72	78
32	5	7	9	5	18	16	19	13
38	37	42	39	47	85	88	84	92
40	n.o.	0	0	0	n.o.	6	8	4
46	n.o.	3	2	3	15	12	12	14
48	31	36	40	33	62	67	72	62
52	73	75	77	72	115	117	121	113
54	13	13	11	13	37	32	30	33
56	75	78	74	82	106	105	100	110
62	4	6	5	7	21	20	18	21
64	24	27	27	27	48	44	43	45
70	n.o.	1	1	1	n.o.	6	6	6
72	n.o.	1	1	1	n.o.	5	6	4
80	17	18	17	19	31	26	25	27
84	41	41	43	40	70	74	77	72
86	4	4	3	4	15	13	13	14
88	14	13	12	14	21	19	18	20
94	n.o.	4	4	5	12	13	12	13
104	n.o.	5	6	4	12	11	13	9
110	6	6	5	6	18	15	14	16
116	39	38	39	36	70	68	70	65
118	n.o.	3	2	3	n.o.	7	7	7
120	19	18	17	18	28	25	24	26
126	n.o.	6	5	4	14	15	14	14
128	18	17	17	17				
144	9	6	6	7				
148	13	10	10	10				
152	23	18	19	19				
166	5	6	5	7				
176	13	12	14	11				
180	31	30	30	28				
184	9	10	10	10				
192	15	10	10	10				
206	n.o.	6	5	7				
208	n.o.	7	6	7				
212	32	33	34	31				
216	35	32	31	34				

n.o. = not observed.

All lines not listed were either space group absences or not observed with calculated intensities all less than 5.

Vol. 17
1960

were made for dispersion of the Cu$K\alpha$ radiation by the metal ions.[3] Both the real and imaginary parts of the corrections were included. The atomic scattering factors for Y^{3+}, Gd^{3+}, and Fe^{3+} were taken from the tables of THOMAS and UMEDA[4], those for Al^{3+}, from VIERVOLL and ØGRIM[5]. The scattering factors for O^{2-} are those of BERGHUIS *et al.*,[6] arbitrarily modified such that $f_0^{2-} = 10{\cdot}00$ at $\sin\theta/\lambda = 0$ and $f_0^{2-} = f_0$ for all values of $\sin\theta/\lambda \geqslant 0{\cdot}20$. The temperature factors used were 0·1 for Gd^{3+}, 0·3 for Y^{3+}, 0·6 for octahedral $Fe^{3+}-Al^{3+}$, 0·8 for tetrahedral $Fe^{3+}-Al^{3+}$ and 1·20 for O^{2-}. These values are in accord with those either determined or found to be reasonable in previous garnet work (see e.g. Refs. (7), (9) and pertinent references in those papers). The atomic scattering factors were adjusted to values proportional to the $Fe^{3+}-Al^{3+}$ ionic distribution in the octahedral and tetrahedral sites.

The original calculation of the intensities*[7] for the 62 per cent model was made using the yttrium–iron garnet oxygen coordinates: (−0·027, 0·057, 0·149).[8] It appeared that the agreement could be improved by refinement of the oxygen coordinates. In yttrium–iron garnet, the octahedral Fe–O distance is 2·00 Å and the tetrahedral distance 1·88 Å.[8] The octahedral Al–O distance has been found to be 1·95 Å in the natural silicate garnet grossularite;[9] the tetrahedral Al–O distance in yttrium–aluminum garnet is 1·77 Å.[10] These values were weighted for the 62 per cent distribution and new metal–oxygen distances computed from them. In this model the octahedral distance is 1·97 Å and the tetrahedral distance is 1·81 Å. New oxygen coordinates (−0·035, 0·054, 0·148) were calculated to fit these distances and used in the subsequent calculations. The results are shown in Table 1. It seems probable that further refinement of the oxygen coordinates could improve the agreement for particular reflections, but is not required for the purpose of the experiment.

* The calculated intensities were computed on the IBM 704 computer using the Fortran program devised by R. G. TREUTING.[7]

DISCUSSION

There is rather close agreement (Table 1) between the observed relative intensities and those calculated for each of the three trial distributions. The 220 and 211 reflections appear to be most sensitive to the ionic distribution: these reflections are relatively insensitive, within reason, to temperature factors. As for the remaining reflections, there is really no choice among the three distributions. Thus, any conclusions relative to the best model must depend only on these two reflections. Obviously, a conclusion based on these two reflections will lack precision. However, there is some indication that the fraction of Al^{3+} ions in tetrahedral sites lies within the values (Table 1) $0{\cdot}52 < z/3 < 0{\cdot}72$ and *perhaps* closer to 0·62 than to the other values. In any event, the distribution predicted by Geller:

$$\{Gd_3\}[Al_{1.14}Fe_{0.86}](Al_{1.86}Fe_{1.14})O_{12}$$

is compatible with the results of the X-ray diffraction analysis.

REFERENCES

1. GELLER S., *J. Phys. Chem. Solids* **16,** 21 (1960).
2. GILLEO M. A. and GELLER S., *Phys. Rev.* **110,** 73 (1958).
3. DAUBEN C. H. and TEMPLETON D. H., *Acta Cryst., Camb.* **8,** 841 (1955).
4. THOMAS L. H. and UMEDA K., *J. Chem. Phys.* **26,** 296 (1957).
5. VIERVOLL H. and ØGRIM O., *Acta. Cryst., Camb.* **2,** 277 (1959).
6. BERGHUIS J., HAANAPPEL I. M., POTTERS M., LOEPSTRA B. O., MACGILLAVRY C. H. and VEENENDAAL A. L., *Acta Cryst., Camb.* **8,** 478 (1955).
7. GELLER S., MILLER C. E. and TREUTING R. G., *Acta Cryst., Camb.* **13,** 179 (1960).
8. GELLER S. and GILLEO M. A., *J. Phys. Chem. Solids* **3,** 30 (1957).
9. ABRAHAMS S. C. and GELLER S., *Acta Cryst., Camb.* **11,** 437 (1958).
10. PRINCE E., Fourth International Congress, International Union of Crystallography, Montreal, 10–19 July 1957, Abstract No. 6.28, *Acta Cryst., Camb.* **10,** 787 (1957).

J. Phys. Chem. Solids Pergamon Press 1961. Vol. 17, Nos. 3/4, pp. 232–245. Printed in Great Britain.

PROPERTIES OF LITHIUM HYDRIDE—II OPTICAL ABSORPTION BY COLOR CENTERS*

F. E. PRETZEL

Los Alamos Scientific Laboratory, University of California

and

C. C. RUSHING†

University of Florida

(*Received* 16 *May* 1960)

Abstract—The optical properties of color centers involving trapped electrons in LiH show that properties of the crystalline media other than the lattice parameter are important in relation to the energy of the optical absorption bands. The *F* band in LiH is found at 2·4 eV instead of at 4·8 eV, as predicted by the Ivey formula for *F* bands in the alkali halides. Other properties of the *F* band in LiH are consistent with expectations from the *F*-center model and with the high vibrational frequency and high cation-vacancy mobility in LiH crystals. The *M* band, Li-colloid band and other bands in LiH are also shifted to lower energy; therefore, the sequence of bands in LiH is comparable to the familiar sequence found in KCl.

The principal *V* band in LiH is at 3·5 eV. The properties of the center responsible for the *V* band are consistent with those of an H_2 molecule trapped at an anion site. This is the same as one proposed for the V_1 center in KCl.

"Impurity" bands are found both in "pure" and in Mg-doped LiH crystals. Bands due to Mg colloid and *Z*-type centers are found, along with a series of fine-structure lines like those previously reported only in LiF.

Vol. 17
1960

INTRODUCTION

RADIATION-INDUCED optical absorption bands have been examined in single crystals of LiH, and the results have been interpreted in terms of the color-center models developed for the alkali halides. These models were described by SEITZ in two review articles in 1946 and 1954,[1] and they were subsequently revised at International Symposia on Color Centers at Chicago in 1956 and Corvallis, Oregon, in 1959. The color-center models have been used to interpret optical absorption spectra of alkaline earth halides, alkaline earth oxides and alkali azides[2]—all of which are crystallographically less similar to the alkali halides than the alkali hydrides.

The only previously reported work on color centers in alkali hydrides is that of JOHNSON[3], who studied the optical absorption in films of NaH and KH built up by the successive evaporation of metal onto a window followed by reaction with hydrogen. JOHNSON reported the observation of *F* bands at 360 mμ in NaH and 480 mμ in KH, in agreement with predictions from the Ivey formula for *F* bands in the alkali halides.[4]

Although most of the properties of color centers observed in LiH are consistent with the color-center models, the energies of the optical absorption bands are much less than those predicted from the Ivey formulae.‡ For this reason we have taken care to reproduce our measurements under

* Work performed under the auspices of the U.S. Atomic Energy Commission.

† Guest scientist under the L.A.S.L. Summer Program.

‡ These results were first given in a paper by PRETZEL to the American Physical Society (*Bull. Amer. Phys. Soc.* (ser. 2) **2**, 155 (1957)) and again in revised form at the 1959 Symposium on Color Centers. An anomaly also appears in the energy of the fundamental ultraviolet absorption bands in LiH which was discussed in Paper I of this series.[5]

varying conditions, and with LEWIS we have made concurrent measurements of paramagnetic resonance (ESR) absorption by the crystals (which are reported in Paper III of this series).[6] Non-stoichiometric LiH crystals containing an excess of Li metal were prepared, but quenching these crystals to room temperature produced Li colloid rather than *F* centers. The rapid aggregation of *F* centers to form Li colloid in LiH at room temperature is evidently related to the high mobility of cation vacancies as deduced from electrical conductivity measurements (see Paper I). For this reason most of the irradiations and measurements designed to study the *F* band in LiH were performed at low temperature.

EXPERIMENTAL

The LiH and LiD plates used for the optical absorption studies were about 8 mm square and from 0·2 to 2 mm thick. The plates were cleaved from the single crystals described in Paper I, which contains a description of the purity, physical properties and composition of the LiH crystals employed. To prevent corrosion of the LiH crystal surfaces, all plates were cleaved and mounted in the absorption cells inside a dry box containing argon; the plates were then kept under vacuum inside the absorption cells. Some colored crystals were similarly transferred to the absorption cells with minimum warming and exposure to light.

Neutrons, X-rays and γ-rays and β-rays from LiT incorporated in a few of the samples were used to color the LiH crystals for optical absorption studies. (The tritium β-rays in the LiH+LiT crystals acted as a constant source for kinetic studies.) The γ-irradiations were carried out using a 750 Curie Co^{60} source at room temperature. Low-temperature irradiations of several samples were performed inside the optical absorption cells by using X-ray or neutron beams directed through the Be windows in the cells. The X-ray source used was a GE Model XRD machine with a Cu target operated at 40 keV and 20 mA. J. E. DUMMER, of this Laboratory, examined the X-ray beam from this machine at the position of the samples. The center of a 1 mm LiH plate was found to be in an X-ray flux of 25 r/sec with 8 to 10 keV average energy at that geometry. Neutron irradiation was carried out using a beam of $\sim 10^9$ n/sec cm^2 from the 5 MW swimming-pool reactor at this Laboratory. Neutron irradiations were also carried out on samples sealed inside cooled Nylon "rabbits" which were repeatedly passed through the 5×10^{11} n/cm^2 sec flux region of a 25 kW homogeneous reactor and recooled under liquid nitrogen. Doses from $0{\cdot}3$ to $1{\cdot}5\times10^{14}$ n/cm^2 were obtained in this way without warming the samples above 200°K during the irradiation.

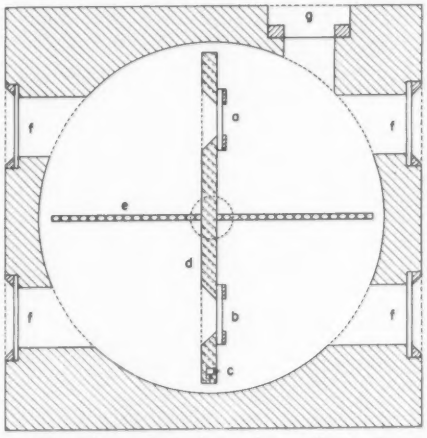

FIG. 1. Double optical absorption cell for Beckman DK-2 spectrophotometer: (a) reference crystal, (b) colored crystal, (c) sample thermocouple, (d) Cu support, (e) Cd septum, (f) quartz windows, (g) 0·18 mm Be window for exposing sample to X-rays or neutrons with sample holder rotated 90° counterclockwise.

Two of the small optical absorption cells used were comparable to the cell described by CASLER *et al.*[7] and were made of stainless steel with quartz windows. A large double cell was constructed to hold both sample and uncolored reference plates in the respective beams inside the cell compartment of a Beckman DK-2 spectrophotometer. This arrangement has the advantage of displaying the radiation-induced absorption bands in the sample against an approximately flat background by cancelling out the effects of the tail of the 252 mμ fundamental LiH absorption band in the near-ultraviolet region. The large cell holds 1·5 l. of coolant in the Dewar-like upper portion, and it is also equipped with a thermocouple and an electrical heater for control of the sample temperature. Fig. 1 is a horizontal cross

section through the lower part of the cell showing the relative placement of sample and reference crystals on the Cu holder with respect to the quartz windows of the cell and the Be window used for neutrons or X-rays. The Cd septum between the reference and sample protects the reference crystal from exposure to scattered neutrons, X-rays, or intense bleaching light.

Most optical absorption measurements were made using a Beckman DK-2 spectrophotometer and results were verified by running some spectra also in a Cary Model-11 instrument, which was also useful for strongly colored crystals because of its extended density range. The spectra were recorded with liquid nitrogen in contact with the crystal holders to improve spectral resolution and minimize possible bleaching of the sample. and those given in the figures of this paper were taken at 80°K unless another temperature is specified.

Optical bleaching was done using a wolfram-filament microscope lamp or an AH-4 mercury-vapor lamp as the light source, except for those bands which required less intense light and could be bleached in the spectrophotometer. A green filter with maximum transmission at 550 mμ was used to obtain F light, and a blacklight filter which transmitted the Hg lines in the 365 mμ region was used for bleaching in the V bands. A polaroid filter was used in conjunction with the source of F light to study symmetry effects of F to M-band bleaching. A Nicol prism was installed between the cell and phototube compartments of the spectrophotometer to analyze for dichroism produced by bleaching with polarized light. The apparatus was tested with X-ray-colored NaCl and KCl crystals which were bleached at 300°K with F light polarized in the direction of [110] crystal axes to produce M bands. The crystals were cooled to 80°K before the polarized bleaching light was turned off. The resulting dichroism was found to have a maximum negative value at the F band and a maximum positive value at the M band, in agreement with results on KCl reported by VAN DOORN[8]. Similar, though less conclusive, results were obtained for LiH, with the only region of positive dichroism under the M band.

The absorption spectra have been replotted as absorption coefficient (α) in cm^{-1} vs. photon energy in eV in Figs. 2 through 13. The spectra have been analyzed to estimate the widths of the component bands and to compare the shapes to the normal Gaussian or Lorentzian distribution. The F band is represented by an asymmetric Gaussian (or Pekarian[9]) distribution with an approximately 0·8 eV width at half maximum.

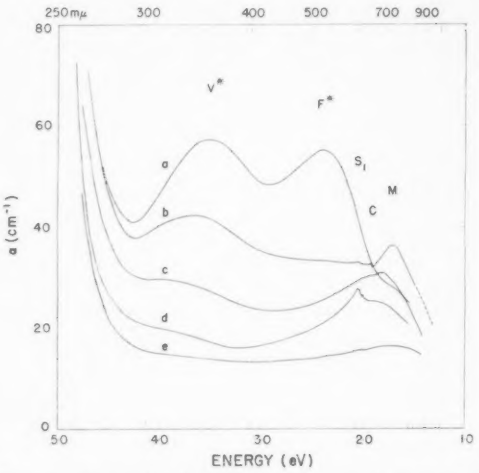

FIG. 2. Absorption bands in LiH crystal exposed to 9×10^{13} n/cm^2 at 80°–200°K: (a) after irradiation – – $N \approx 2{\cdot}8\times10^{17}$ F centers/cm^3, (b) after 2 min bleach with "white" light at 300°K, (c) after 5 min bleach with "white" light at 300°K, (d) after 3 weeks dark storage at 300°K, (e) after bleaching (d) with "white" light at 300°K for 30 min.

An estimate of the concentration of F centers in a given LiH crystal may be obtained from the peak absorption coefficient (α_{max}) by substituting the half-width ($W_{1/2} = 0{\cdot}8$ eV) and the refactive index ($n = 1{\cdot}985$) into the modified form of SMAKULA's equation,[10] $Nf = 1{\cdot}28\times10^{17}[n/(n^2+2)^2]\, W_{1/2}\, \alpha_{max}$, which becomes $N = 7{\cdot}0\times10^{15}\, \alpha_{max}$ if it is assumed that $f = 0{\cdot}82$ as found by BATE and HEER[11] for LiF.

ABSORPTION BANDS IN "PURE" LiH

1. *Major bands formed by intense irradiation at low temperature*

A typical result of the low-temperature irradiation of LiH to produce color-center concentrations of the order of $(1\rightarrow4)\times10^{17}$/cm^3 is given in the first curve of Fig. 2. Two complex bands are the

Vol. 17
1960

major products: the V^* band at 3·5 eV and the F^* band at 2·4 eV. The F-center paramagnetic resonance (ESR) was found in samples whose optical spectra are represented by curve *a*, Fig. 2. The connection between the F-center ESR and the 2·4 eV optical absorption was established by making parallel measurements on samples which were differentially bleached to produce the M band as indicated by curve *b*, Fig. 2 or which contained an electron-trapping impurity.†

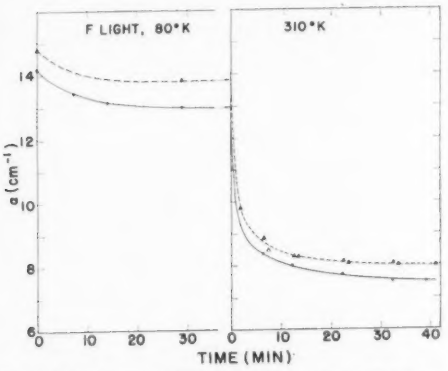

FIG. 3. Bleaching of F^* and V^* bands in LiH crystal colored by X-rays at 200°K. First bleached ~9 per cent of bands by F light at 80°K, and thermally bleached 38 per cent in dark at 310°K. Both curves correspond to an exponential (1st order) bleaching mechanism: —— F^* band, – – – – V^* band.

The complementary character of the V^* band and the F^* band was established by bleaching studies using either F light at 80°K or thermal bleaching at ~310°K as shown in Fig. 3. The mutual annihilation of centers responsible for the V^* and F^* bands by excitation of F-center electrons with F light leads to the conclusion that trapped holes, or V centers, are responsible for the V^* band.

The designation of the F^* and V^* bands of Fig. 2 as complex bands was chosen in the light of evidence which indicates that other weaker bands exist under the broad overlapping envelope of curve *a*. However, the two maxima at 3·5 eV and 2·4 eV are typical of the simplest centers which evidently correspond to the V_1 and F bands in the alkali halides. The tail of the 252 mμ fundamental absorption band is shown on the high-energy side of Fig. 2. to illustrate the comparatively narrow confines of the spectral range in which radiation-induced color-center absorption in LiH has been found. Because the simpler color-center bands in LiH are also comparatively broad and frequently overlap each other, it is often difficult to obtain conclusive evidence on the shape of individual spectral bands.

† The details of these experiments are contained in Paper III.

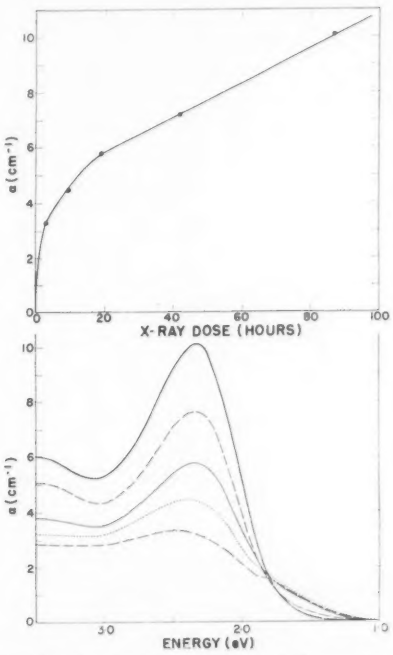

FIG. 4. F-band growth in LiH crystal X-rayed at 80°K. Lower part shows spectra of F^* band after: – – 3 hr, ····· 9·5 hr, —— 19 hr, – – 42 hr, —— 87 hr. Upper part shows corresponding growth curve for F^* band with linear portion corresponding to the absorption of 18 keV/F center.

2. *F Band*

The growth of the F band (+satellites) in a LiH crystal X-rayed at 80°K is given in Fig. 4. The shape of the growth curve as a function of X-ray dose is similar to those obtained for alkali halide samples[12] and a similar explanation for it may be given: the first rapid growth occurs

because electrons are trapped at free (or readily freed) anion vacancies in the LiH crystal, whereas the linear portion of the curve extending beyond 7×10^{16} F centers/cm^3 corresponds to the energy required also to produce the anion vacancies from sources normally present in the crystal.*

The maximum of the F band in Fig. 4 is at a lower energy than normally observed, but the reason for this anomaly is revealed by bleaching the final spectrum of Fig. 4 with F light at 80°K and then at 200°K, as shown in Fig. 5. A narrower (0·5 eV wide) band with its maximum at 2·10 eV was found under the F band; this band is more stable towards bleaching light and is similar to the F band in shape. It has been called the A band by analogy to bands found in the alkali halides.† Correction for absorption in the A band and approximate corrections for the V- and K-band absorption on the other side of the F band resulted in the F-band curve shown in the upper part of Fig. 5, with the maximum in the normal position at 2·4 eV.

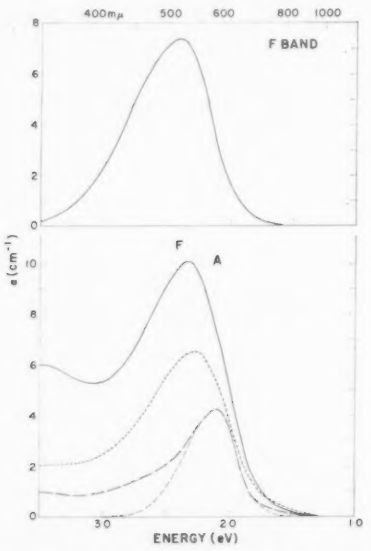

FIG. 5. Analysis of F^* band formed at 80°K. Lower part shows: — F* band formed by X-rays in Fig. 4, ····· F^* band after 2·5 hr bleach in F light at 80°K, – – A band after bleaching the F band with F light for 8 hr at 200°K, – – – – A band corrected for other bands. Upper part shows F band corrected for absorption by A, V and K bands in LiH. The half-width of the F band at 80°K is 0·05 eV, and the spectrum corresponds to $5{\cdot}1\times10^{16}$ F centers/cm^3 and $1{\cdot}7\times10^{16}$ A centers/cm^3.

The half-width of the F band at 80°K is 0·75 eV according to Fig. 5, but other analyses have led to larger values; hence 0·8 eV was chosen to calculate approximate F-center concentrations from the modified form of Smakula's equation given previously. Measurements indicate that the change in half-width at 300°K is probably less than 10 per cent from the 80°K value. The presence of other centers in the samples with absorption bands overlapping the F band made it impossible to measure the temperature dependence of the F band directly.

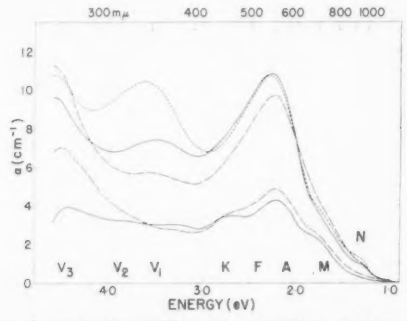

FIG. 6. Complexity of V bands and F^* band formed by 80°K X-irradiation and optical bleaching: —— after 8 hr X-irradiation, — — after 15·5 hr X-irradiation, —— after 61 hr X-irradiation, — — after 20 min F light bleach, – – – – after 96 hr total X-irradiation with intermediate optical bleach.

Other minor absorption bands are illustrated in Fig. 6, including the K band, impurity bands and possibly a metastable F' band, which may all contribute to the broad general rise in absorption under the F band during the early stages of X-ray coloring. The K band is named by analogy to alkali halide spectra, and no proof for the existence

* Note that this energy requirement is high in LiH, about 18 keV/F center. The rates of F-center production by various kinds of ionizing radiation will be described in a subsequent paper.

† LÜTY reported at the 1959 Symposium on Color Centers that the center responsible for the A band in KCl is an electron trapped by a vacancy pair. If the 2·10 eV band in LiH does not show similar dichroism, the designation should probably be changed.

Vol. 17
1960

of an F' band was obtained from attempts to observe the reversible $F \rightarrow F'$ transition in bleaching experiments.

3. *V Bands*

The presence of more than one V band in LiH crystals X-rayed at 80°K is also illustrated in Figs. 6 and 7. The V_1 band at 3·5 eV is predominant in heavily irradiated samples; but the presence of the V_2 band at approximately 3·9 eV is assumed to be responsible for the shift of the V^*-band maximum toward 3·65 eV, as shown in the upper curves of both figures. Improved resolution of the V_1 and the V_2 bands is shown in the upper 80°K spectrum of Fig. 7 which is comparable to the spectrum found at 300°K. An incompletely resolved V_3 band near 4·5 eV also contributes to the variation observed in the V^*-band region of Figs. 6 and 7.† Although concentrations of V_1 centers were similar to those of F centers ($\geqslant 10^{17}$/cm^3) in neutron irradiated LiH crystals, the observed concentrations of the other V bands did not exceed 5×10^{16}/cm^3.

Although the initial growth of the V bands during low-temperature irradiation is not as regular as the growth of the F band, low-temperature bleaching consistently indicated the mutual annihilation of V_1 and F centers comparable to Fig. 3. A slight increase of V_1-band bleaching was observed relative to that of the F band in Fig. 6 which apparently corresponds to the transformation of some of the V_1 centers to V_3 centers. The more generally observed inequality of V_1- and F-band bleaching is the type shown in Fig. 2, in which the F centers are destroyed more rapidly than the V_1 centers to produce M centers. From an analysis of the differences between various spectra and from bleaching studies, it is deduced that the V_1 band is comparable to the F band in width (0·83 ± 0·05 eV) and that it probably has a more symmetrical Gaussian band shape than the F band.

† Care must be taken in interpreting the spectra obtained beyond 4 eV in Figs. 6 and 7 even though the uncolored reference LiH crystal was cleaved from the same plate as the sample. The fundamental band absorption in the reference forces the spectrophotometer slit to open rapidly and reduces the resolution of the instrument. It is not certain whether the 4·5 eV band is a resolved band or a radiation-induced extension of the fundamental band to lower energy.

4. *M, N and R Bands*

The M band in LiH is at 1·7 eV (Fig. 2). It is produced by optically bleaching the F band at 300°K. The properties of the M center in LiH are analogous to those found for M centers in the alkali halides insofar as they have been studied. M centers may be an intermediate in the formation of Li colloid from F centers, as shown in the bleaching results of Fig. 2. The M band is about one-half as wide as the F band (0·4 eV), and there are indications of the development of dichroism in the M band in LiH bleached with polarized F light similar to that found in the alkali halides. No paramagnetic resonance associated with the M band has been found within the limits of sensitivity of the apparatus in samples containing $\sim 5 \times 10^{16} M$ centers/cm^3.

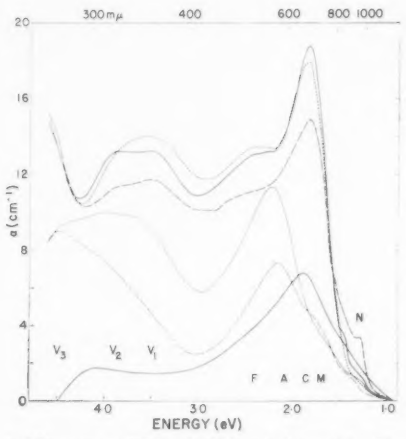

FIG. 7. V bands and Li colloid band formed by X-raying LiH at 300°K: —— spectrum of crystal of Fig. 6 after total 105 hr X-irradiation at 80°K with intermittent optical bleaching, — — after 50 min F-light bleach at 160°K, —— after 16·5 hr additional X-irradiation starting at 80°K but mainly at 300°K, - - - - same spectrum at 300°K, — — after 110 min bleach with "white" light at 80°K, —— after 19 hr thermal bleach at 300–370°K.

The N band is at 1·3 eV and is about 0·2 eV wide (Fig. 7). The N band has also been observed with some F band in relatively thick LiH films of imperfect structure. In some spectra there are indications of weak absorption bands in the 1·4 to 1·6 eV range, which may correspond to the R bands in the alkali halides.

5. Li-*Colloid band*

Colloid bands have been observed in LiH crystals, with maxima from 1·85 to 1·91 eV and with half-widths from 0·4 to 1·0 eV, depending upon the conditions of precipitation which influence the Li particle size and the particle-size distribution. Narrow colloid bands are formed by allowing a colored LiH crystal to warm to room temperature in the X-ray beam as illustrated in the upper curves of Fig. 7. The narrow colloid band sharpens on cooling the crystal to 80°K,

FIG. 8. Li colloid band in LiD crystals: —— formed by exposure to $3{\cdot}4\times10^6$ r of γ-rays at 300°K,— — formed by warming from 80°K to 300°K during X-irradiation as in Fig. 7 and plotted to double scale for comparison.

and it can be partly bleached by irradiating the sample with light absorbed in the colloid band at 80°K.* Larger colloidal particles are typically more resistant to bleaching conditions as illustrated by the broad Li-colloid band in Fig. 7.

A LiD crystal was exposed to $3{\cdot}4\times10^6$ r of Co^{60} γ-radiation at 300°K to produce the intense colloid band shown in Fig. 8. Paramagnetic resonance measurements on this sample showed the presence of Li metal.† LiH is an excellent material for the study of colloid precipitation by the paramagnetic resonance method, and a study of Li-colloid formation in LiH has been made which will be reported in this series.

"IMPURITY" ABSORPTION BANDS

The connection between the Mg band and a specific impurity in a LiH crystal is rather conclusive, but no comparable evidence exists for the origin of other bands described in this section. Some can be produced at intensities which are dependent on the general purity of the host crystal. Others are listed here because they have shapes or structures which are not typical of bands found in "pure" alkali halides and because the trapping centers have a low effective cross section and/or are present at low concentrations in the crystal. The latter condition may exist for any complex defect in the crystal, which may or may not include an impurity ion.

1. Mg *Band*

The Mg band at 3·1 eV is over 1 eV wide, and it appears in LiH+0·001 MgH_2 crystals under conditions which would produce Li colloid in "pure" LiH. Samples with about 0·1 molar per cent MgH_2 contain this additive in an aggregated form at room temperature, as indicated by the low-temperature break in the conductivity curve of the Mg-doped LiH crystal of Fig. 3 in Paper I. The reaction $MgH_2+2Li\rightarrow Mg+2LiH$ is thermodynamically favored, which agrees with the experimental observation that the Mg band is more resistant to optical or thermal bleaching than the Li-colloid band.‡

The *F* and *V* bands are formed in Mg-doped crystals irradiated at a low temperature, as illustrated in Fig. 9, but the *V** band is relatively more intense than in a "pure" crystal. The rate of formation of *F* centers in the Mg-doped crystals is about twice that for "pure" LiH crystals, possibly because the impurity increases the concentration of vacancy sources in the crystal. Bleaching the *F* band reveals an excess of *V* centers

* DEXTER predicted differential bleaching in colloid bands because of the higher fraction of light absorbed by the fine particles.[13]

† Similar results have been reported by DOYLE *et al.*[14]

‡ The Mg band may be similar to the Ca band found in KCl containing 3×10^{18} $CaCl_2/cm^3$.[15] The effectiveness of even lower concentrations of divalent cations ($\sim 2\times10^{17}/cm^3$ of Ca^{++} or Sr^{++}) for the prevention of alkali colloid precipitation in additively colored KCl has also been demonstrated.[16]

Vol. 17
1960

in the Mg-doped crystal. The direct effect of electron trapping by the MgH_2 impurity to form Mg colloid is illustrated in the spectra of Fig. 9. The preponderance of V bands formed by X-irradiation at 300°K was demonstrated by bleaching the F band to show the Mg plus V bands underneath.

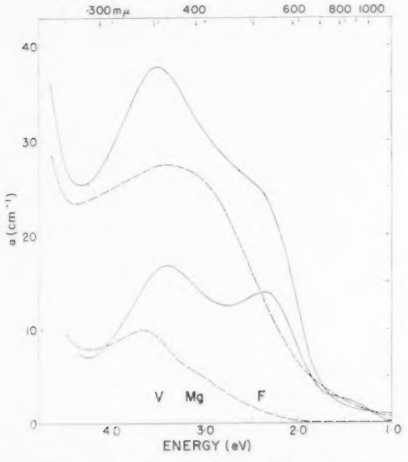

FIG. 9. Absorption bands formed in Mg-doped LiH containing ~0·1 molar per cent MgH_2 after exposure to X-rays: —— after 15·5 hr X-irradiation at 200°K, — — after 1 hr F light at 80°K followed by 20 hr in dark at 300°K, —— after 24 hr additional X-irradiation at 300°K, — — after 12 hr bleaching with V^* light (365 mμ – – AH-4 lamp) at 300°K.

The regular formation of the Mg band by β-radiation at 300°K in a similarly doped LiD crystal containing a trace of LiT is shown in Fig.10. The initial spectra are complicated by the V bands, but the Mg band is predominant in the final ones. The rate of formation of the Mg band was linear to about 10^{18} Mg centers/cm³ (based on Smakula's equation) with some deviation from linearity at 2×10^{18}/cm³. The energy required per Mg center is only 3 eV calculated from the known concentrations of LiT and the linear portion of the growth curve. The time lapse of 1107 days at 300°K required to produce the final curve of Fig. 10 indicates that the reaction producing the Mg colloid is essentially irreversible. The dashed curves indicate the comparatively slow rate at which Li colloid was formed in the upper portion of the LiD+LiT crystal which contained Mg in the form of stable MgO instead of MgH_2. Paramagnetic resonance measurements showed the presence of Li metal in the sample cleaved from the upper part of the crystal, but resonances corresponding to either the Mg band or V centers were not found in the sample from the lower part. This is consistent with expectations since Mg colloid should not be paramagnetic.

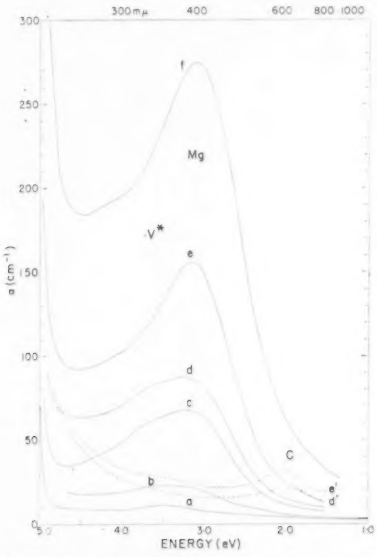

FIG. 10. Mg band formed by β-irradiation in Mg-doped LiD crystal stored at room temperature. Solid curves for sample containing 6×10^{19} MgD_2/cm³ and $1\cdot0\times10^{16}$ LiT/cm³ after: (a) 10 days, (b) 43 days, (c) 193 days, (d) 234 days, (e) 528 days, (f) 1107 days. Dashed curves show Li-colloid band formed in sample from the part of the crystal containing MgO instead of MgD_2 after: (d') 263 days, (e') 537 days.

2. *Z Bands*

A band found at about 2·2 eV in LiH and LiD was erroneously reported as the F band in the 1957 paper (see footnote on page 1). Although the 2·2 eV band has many characteristics of an F band it was found that: (1) the 2·2 eV band was not formed by irradiation at low temperature, but that thermal bleaching was required to resolve it; (2) the intensity of the 2·2 eV band generated corresponded to about 10^{16} centers/cm³ in the most favorable crystals, but it was undetectable in the purest LiH crystals prepared. Magnesium

was added to segregate oxide in the preparation of the crystals in which the strongest 2·2 eV bands were produced; therefore, it is reasonable to call this band a Z band* by analogy to the bands found in $NaCl+CaCl_2$ and $KCl+SrCl_2$.[17] The MgH_2 aggregates may be much more efficient traps for the electrons released by F centers on

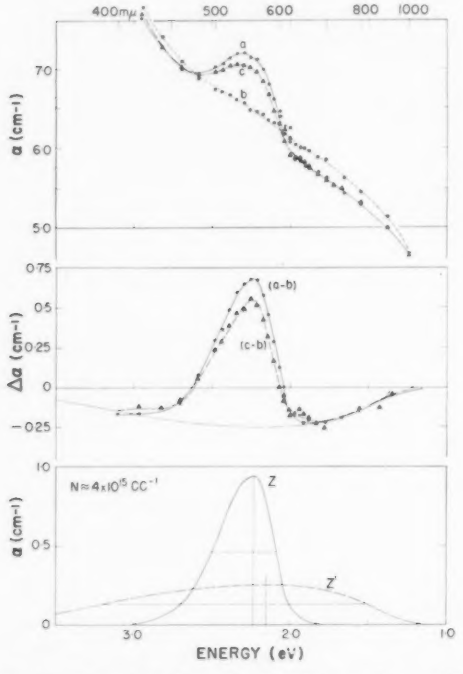

FIG. 11. Z bands in Mg-doped LiD crystal containing some oxide. Upper part: (a) Z band formed by ultraviolet irradiation of cloudy crystal, (b) Z' band formed by 1 hr exposure to 570 mμ light in the spectrophotometer, (c) Z-band recovery after thermally bleaching the Z' band for 20 hr in the dark at ~300°K. Middle part: difference-curves obtained from bleaching study. Lower part: Z bands deduced by the analysis indicated above.

bleaching than simpler traps which might involve isolated Mg^{++} ions. If this is true, it will explain the absence of Z bands in the spectra of the $LiH+MgH_2$ crystals of Figs. 9 and 10.

* Only one band was found in LiH which may correspond to either the Z_1 or Z_2 band found in the alkali halides; therefore no attempt has been made to distinguish between the models proposed for these bands.

The Z band can be bleached by Z light in a spectrophotometer at 80°K to form a broad Z' band with a maximum at about 2·1 eV, which in turn bleaches thermally to reform the Z band within 8 hr at 300°K. This reversible bleaching is entirely analogous to the $F-F'$ transition in KCl,[1] and it even proceeds more easily. This property of the Z band has been used to analyze complex spectra for the presence of the Z band or to obtain the shape of the Z bands in cloudy crystals as illustrated in Fig. 11. It was found that multiple repetitions of the $Z \rightarrow Z' \rightarrow Z$ bleaching cycle led to approximately 10 per cent loss in Z center concentration per cycle, which occurred primarily during the thermal recovery phase. That a fixed concentration of trapping centers remained in these crystals was demonstrated by irradiating such a crystal with ultraviolet light in the tail of the fundamental absorption band. The original concentration of Z centers was rapidly restored, and continued irradiation of the crystal with ultraviolet light had no significant effect on the spectrum.

The comparative thermal stability of the Z band in LiH has made it possible to study the effects of temperature and crystal composition on the band without undue interference from overlapping bands. These results are valuable because no way has yet been found to make comparable studies on the F band, and the work of CAMAGNI and CHIAROTTI[18] on Z bands in $KCl+SrCl_2$ indicates that the properties of F and Z bands are similar. A LiD ($+MgD_2$) crystal containing $1{\cdot}6\times10^{16}$ Z centers/cm^3 was used to study the effect of temperature on the Z-band shape at 80°, 160° and 296°K. The total area under the curves remained constant within 0·4 per cent during the decrease of the Z-band half-width from 0·390 eV at 296°K to 0·348 eV at 80°K. The position of maximum absorption also shifted from $2{\cdot}21_4$ eV at 296°K to $2{\cdot}22_0$ eV at 80°K.†

A comparable crystal of LiH was not found for analysis of the temperature dependence of the

† The analysis of RUSSELL and KLICK[19] for the effect of temperature on the half-widths of F bands was applied to these data. For the Z band in LiD the values $h\nu_g = 0{\cdot}05_2$ eV and $A = 0{\cdot}350$ eV were derived for the expression for the half-width, $W_{1/2} = A[\coth(h\nu_g/2kT)]^{1/2}$. In the formula, A is a constant which is equal to the half-width at 0°K and ν_g is the vibrational frequency of the F center in the ground state.

Vol. 17
1960

Z band, but bleaching studies similar to those illustrated in Fig. 11 gave 0·47 eV for the 80°K half-width of the Z band at a maximum of $2{\cdot}19_5$ eV. (The corresponding values for LiD studied in the same way are 0·41 eV for the 80°K half-width and 2·22 eV for the Z-band maximum.) In either case the Z band in LiH is significantly wider than in LiD, and the shift of the Z-band maximum to higher energy in LiD is expected from the reduction in lattice parameter and in zero-point vibrational energy compared to LiH.

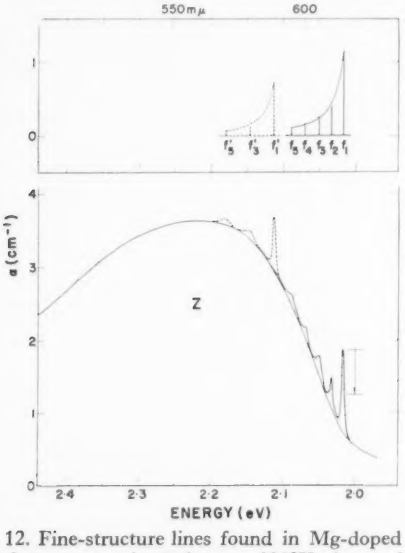

FIG. 12. Fine-structure lines found in Mg-doped LiD. after long storage in dark at ~300°K since coloring. Lower part shows Z band with: ——f series originally present, and – – – –f' series developed after $Z \rightarrow Z' \rightarrow Z$ bleaching cycle with the corresponding drop in the f_1 line indicated. Upper part shows the analysis of the f series and f' series with weak curves indicating the $i^{1\cdot4}$ intensity dependence found for each series.

3. *Fine-structure lines*

A series of fine-structure lines, f lines, comparable to those previously reported in LiF by DELBECQ and PRINGSHEIM[20], have been found in LiH. The f lines have been found in thick crystals containing a slight electron excess (a faint blue color), but whose spectra show no other band at a measurable intensity. However, they are normally associated with either the S or Z bands which are formed under similar conditions.

Two sets of fine-structure lines in LiD are shown on the low-energy side of Z band in Fig. 12. The first series of lines (called the f series) consists of five lines, with the strongest f_1 line at 2·016 eV and successive f_2, f_3, f_4 and f_5 lines regularly spaced at +0·017 eV intervals. An optical-thermal $Z \rightarrow Z' \rightarrow Z$-band bleaching cycle influenced the f series of lines, which are also sensitive to the bleaching conditions. The net result was that the intensity of the f series was reduced (as indicated for the f_1 line in Fig. 12) and a new f' series of lines appeared. The f' series consists of an f_1' line at 2·112 eV and two more lines called f_3' and f_5' spaced at +0·034 eV intervals from the first member. The numbering of the f' series was chosen because the spacing is precisely double that of the f series and because a log–log plot of line intensity vs. line number (i in f_i or f_i') showed that the relative line intensity for each series was a function of $i^{-1.4}$ with the f' lines counted this way. This phenomenon might be explained if some change of composition or reorientation of components in a complex trapping center took place during the bleaching cycle which would be responsible for the 0·096 eV increase in the transition energy of the first line and also for a change in spectroscopic selection rules to eliminate the even-numbered members of the f' series.

The analysis of the fine-structure lines was rarely as straightforward as in the preceding example. The even-numbered members of the f series were also either weakened or absent in some crystals, and at times other lines were observed that were not members of either series. The results obtained for the fine-structure lines in LiH were similar to those for LiD, but not as accurate. The f_1 line appears at 2·004 eV, the f_1' line is at 2·091 eV and the average spacing is 0·016 eV for a five-membered series in LiH. Results published for the comparable five-membered series found on the low-energy side of the 380 mμ band in LiF[20] give the f_1 line at $3{\cdot}171_3$ eV and an average spacing of $0{\cdot}029_4$ eV.* The proposal that the line spacing is related to one of the fundamental vibrational frequencies of the

* The same spacing was found for a series of four emission lines in the 595 → 569 mμ range of the luminescence spectrum of LiF by KAPLANSKII. FEOFILOV, working with polarized luminescence, found evidence that the center responsible for the lines is oriented along the [110] crystal axes.[21]

LiF crystal[20] does not fit the results for LiH. Although the vibrational frequencies of the crystals decrease in the order of LiH > LiD > LiF, the fine-structure spacing *increases* in the same sequence (but the difference between LiH and LiD may not be significant). The spacing of the purely vibrational levels of the free Li_2 molecule[22] is larger than any spacing between series members (0·044 eV); therefore, the observed trend of the line spacings could be produced if the Li_2 molecular force constant were reduced in proportion to some function of the dielectric constant of the crystalline media.

Although no suitable model for the center responsible for fine-structure lines has been found, the character of the *f* series is in excellent agreement with expectations for an electronic transition to five vibrational levels of the excited state. The temperature effect on the resolution of *f* lines in LiH is also consistent with a 0·017 eV spacing between vibrational levels. No lines are resolved at 296°K ($kT = 0{\cdot}026$ eV); there is a faint indication of structure at 160°K ($kT = 0{\cdot}014$ eV); and structure is fully revealed at 80°K, with the first line $\sim 0{\cdot}005$ eV wide ($kT = 0{\cdot}007$ eV).

4. *S Bands*

Two other bands have been observed in irradiated LiH crystals subsequently subjected to prolonged thermal bleaching at 300°K; because of their sharply peaked appearance, these have been called *S* bands. The S_1 band at 2·05 eV occurs in both LiH and LiD crystals, and it is illustrated in Figs. 2 and 13. The S_1 band is 0·22 eV wide and is decidely more peaked than a Lorentzian curve. Since the S_1 band appears on thermally bleaching the fine-particle colloid band in the purest crystals, its occurrence could be explained if it represents one electron (or more) trapped at the Li-colloid nucleus. The Li precipitation nuclei are presumably complex and may include impurities such as Cu, Fe, Na and O, which are usually present at concentrations of at least $3 \times 10^{16}/cm^3$ in the LiH crystals.*

The S_2 band at 2·32 eV is formed under similar conditions, but it is most pronounced in impure crystals which also exhibit the *Z* bands. The S_2 band is less peaked than the S_1 band but is narrower (0·11 eV), as shown in Fig. 13. Colloid and *Z* bands are also present in the spectrum of Fig. 13, where the *Z* band was largely converted to *Z′* band to better show the S_2 band.

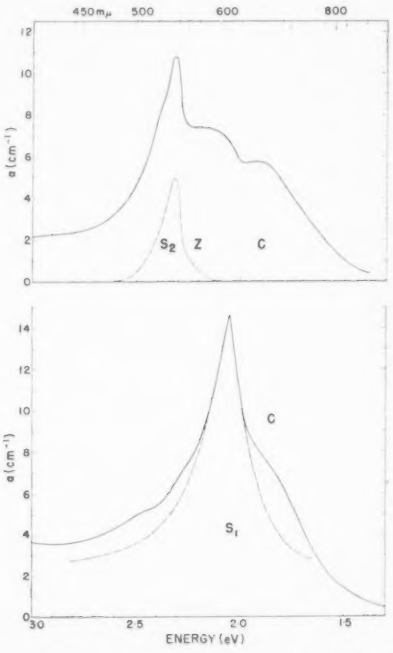

FIG. 13. Sharp impurity bands formed by dark thermal bleaching of narrow colloid bands in LiH. Lower part shows: —— S_1 band formed in "pure" LiH after X-irradiation at 80°K followed by bleaching, — — corrected S_1 band. Upper part shows: —— S_2 band plus others formed in Mg-doped LiD crystal irradiated at low temperature and then bleached, — — S_2 band corrected for absorption in *Z*, *Z′* and colloid bands.

DISCUSSION

The *F* band in LiH has two striking properties compared to the *F* bands generally found in alkali halide crystals: (1) the energy is only one-half of the value predicted from the Ivey formula, and (2) temperature has little effect on the width of the band or on the band maximum. From the lattice parameter of LiH and the Ivey formula, a calculated *F*-band energy of 4·8 eV (approximately the same as for the *F* band in LiF) is obtained instead of the measured value of 2·4 eV. A modified

* The S_1 band may be analogous to the 222 mμ band in LiF which appears under similar conditions.[20]

Vol. 17
1960

form of an empirical relation proposed by LEVY[23] was used to attempt corrrection for the large difference between the dielectric constants of LiH and LiF, since the lattice parameters are nearly the same. The ratio of the high-frequency dielectric constants of the two materials was multiplied by the F-band energy in LiF to obtain a result which is in excellent agreement with the observed value:

$$E_{\max}(\mathrm{LiH}) = \frac{n^2(\mathrm{LiF})}{n^2(\mathrm{LiH})}$$

$$E_{\max}(\mathrm{LiH}) = \frac{(1{\cdot}92)}{(3{\cdot}94)}\,4{\cdot}96 = 2{\cdot}4\ \mathrm{eV}.$$

The temperature effect on the F band in LiH and LiD was not measured directly because of complications mentioned earlier, but it is known to be small. However, we have used the data for the effect of temperature on the Z bands to estimate the probable effect on the F bands. The value of $h\nu_g = 0{\cdot}05_2$ eV for the Z band in LiD is near to the fundamental infrared vibration $h\nu_t = 0{\cdot}05_4$ eV, and a similar correspondence was observed for the F bands in a number of alkali halides.* The use of $h\nu_g = 0{\cdot}07_0$ eV for the F band in LiH (from $h\nu_t = 0{\cdot}072$ eV) leads to a calculated 296°K width of 0·80 eV compared to 0·75 eV found at 80°K. These results are within the uncertainty of the experimental F-band width determinations in LiH. By a similar analysis, the F band in LiD should be 0·70 eV wide at 80°K if the 0·80 eV width is assumed at 296°K. It may be possible to detect such a difference between the LiD and LiH F-band widths at 80°K in suitable samples. The relative Z-band widths in LiD and LiH are consistent with this interpretation and with indications that the electron is more tightly bound to the impurity center as compared to the F center. An inter-comparison of extrapolated half-widths of F bands at 0°K shows the sequence of widths LiH > LiD > LiF > NaCl > KBr in agreement with the expectation that these values are related to the zero point energies ($1/2h\nu_g$) of the F center in each crystal.

The effect of isotopic composition on the position of the F-band maximum in LiH and LiD has not been observed for similar reasons, but such an effect has been observed for the Z band (0·025 eV), the f line (0·012 eV) and the f_1' line (0·021 eV). In all cases the energy of the band is greater in LiD, as might be expected from the smaller lattice parameter of LiD compared to LiH. The energy difference expected from the Ivey formula for F bands is 0·04 eV, but 0·02 eV would result if all the values calculated from the Ivey formula were scaled down to fit the experimental value for the F band in LiH.

In addition to the F band, all of the other absorption bands produced by electron-excess centers in LiH are also displaced toward low energy compared to the positions of comparable bands in LiF or to the predictions from the Ivey formulae. The relative position of the major bands is maintained, although the displacement of the more complex bands is somewhat less than that of the F band. Thus the sequence F, Z, colloid, M, N band is the same as that found in KCl with the possible exception of the R bands. The series of five fine-structure lines is also displaced toward lower energy in LiH compared to LiF.

The diamagnetic character of the V_1 center in

* An intercomparison between $h\nu_g$ for the F band and $h\nu_t$ for fundamental infrared absorption in five alkali halides for which data is available led to the following table:

Salt	LIF	NaCl	KCl	KBr	KI
$h\nu_t$(eV)	0·039	0·020	0·018	0·014	0·012
$h\nu_g$(eV)	0·037	0·018	0·011	0·011	0·015

Most of the values of $h\nu_g$ were taken from a paper by RUSSELL and KLICK[19] except the value for LiF which was obtained in this laboratory. The large deviation of $h\nu_g$ for KCl may be related to a larger degree of relaxation around the F center in this crystal compared to the others. Russell and Klick have shown that in any case the values of ν_g are low compared to the frequency of the longitudinal waves, $\nu_l = (\epsilon_s/\epsilon_0)^{1/2}\nu_t$, in the perfect lattice. The symbols, ν_t,ϵ_s and ϵ_0, refer to the infrared absorption frequency and to the static and high-frequency dielectric constants respectively.

LiH, as evidenced by the absence of an ESR associated with the V_1 band, is consistent with KÄNZIG's findings on V_1 centers in KCl and KBr.[25] He proposed that the center responsible for the V_1 band in these alkali halides is a halogen molecule trapped at a halide ion site, and he used this model to explain various bleaching characteristics of the samples. These low-temperature bleaching studies indicate that transformations can occur between the paramagnetic V center (X_2^- molecule ion in two adjacent X^--ion sites) and H center (X_2^- molecule ion in a single X^--ion site) and the diamagnetic V_1 center and a postulated interstitial X^- ion without significant F center destruction. Similar paramagnetic centers have not been detected in LiH irradiated at 78°K, although both H and V centers have been found in LiF X-rayed at 78°K,[25] but the search for paramagnetic V centers in LiH should be extended to lower temperatures. If it is assumed that paramagnetic V centers analagous to those found in the alkali halides are relatively unstable in LiH, then the transformations found above should occur less readily and V_1 centers may be stable to higher temperatures as also proposed by KÄNZIG[25]. The H_2 molecule also fits into the H^--ion site in LiH and, because of its high dissociation energy compared to the halogen molecules and the low electron affinity of atomic hydrogen compared to halogen atoms, the H_2 molecule is relatively stable toward the capture of two electrons to produce an interstitial H ion as one of the products. It appears that it may be necessary to supply an anion vacancy to contain the extra H^- ion produced by bleaching a V_1 center in LiH. These considerations are consistent with the observations indicating high thermal stability for some V_1 centers in LiH compared to those found in the alkali halides.*

It is interesting to note that the position of the V_1 band is relatively constant for a number of crystals despite large differences in crystalline anion species and lattice parameter. The V_1 band is at 3·5 eV in LiH, 3·4 eV in KCl and approximately 3·0 eV in KBr.[26] The possible V-type band in LiF at 3·6 eV is also consistent with this observation, but the experimental evidence on V_1 centers is not adequate to support further speculation on this point.

The variable resistance of F and V_1 bands to mutual bleaching at low temperatures can be explained if we postulate the existence of another type of V center in LiH crystals which is the equivalent of a self-trapped double hole. Such a center can be compared to the self-trapped hole (or V center) of KÄNZIG's but, because of the small size of the H_2 molecule, it is probably better to consider it as a V_1-center–anion-vacancy complex. This positively-charged complex center could be bleached readily by combination with a pair of electrons to produce two H^- ions in the normal lattice positions. On the other hand, the V_1 center would recombine more easily with help from lattice defects capable of supplying the anion vacancy needed to accommodate the extra H^- ion produced by bleaching. The existence of two V centers absorbing at about 3·5 eV would explain the difference in bleaching characteristics illustrated in Fig. 3 because the small percentage of complexes would be optically bleached with ease at 80°K whereas the V_1 centers would bleach more readily under thermal activation. Two other observations are also consistent with this interpretation: (1) the fraction of easily bleached (complex) centers is greatest in crystals irradiated at the lowest temperatures, and (2) the yield of color centers increases with temperature. The V_1-center–anion-vacancy complex should dissociate into its component parts at elevated temperatures because of charge repulsion. This process suggests that V_1 centers may be produced in LiH either by the dissociation of complexes or, more directly, by the combination of an irradiation-produced H^+ ion with a H^- ion in the lattice by a mechanism similar to that proposed by VARLEY[27].

No specific models are proposed for the centers responsible for the V_2 and V_3 bands in LiH. HERSH[28] observed the similarity between the optical absorption of the halogen X^- complex ions in solution and the V_2 and V_3 bands in potassium halide crystals, but there is no evidence for a comparable H_3^- complex ion. The observation of increased absorption in the V_3 band in LiH following optical bleaching with F light could be explained if the absorbing center were an anion vacancy instead of a complex V center; in this case the V_3 band should be called an α band. The

* Further evidence on this point will be included in a subsequent paper.

Vol. 17
1960

complex V bands in LiH could also be the result of absorption by complex centers involving an H_2 molecule and an impurity ion. Centers of the $Cl_2^- - Ba^{++}$ complex type were observed by HAYES and NICHOLS in KCl and KBr doped with divalent impurities.[29] The extensive V_1 center production observed in irradiated $LiH + MgH_2$ crystals, in which electrons are trapped by Mg centers, is comparable to the enhanced production of self-trapped holes (Cl_2^- molceule ions) in KCl doped with Ag, Tl or Pb to serve as electron traps which was observed by DELBECQ *et al.*[30]

Acknowledgements—The authors are indebted to W. B. LEWIS for paramagnetic resonance measurements which have made possible the interpretation of the optical spectra. We are also grateful to G. V. GRITTON for aid in the preparation of samples and to R. J. FRIAUF for his co-operation in experiments which have confirmed some of the results contained in this report. M. THORPE assisted us with the neutron irradiations and A. ZELTMAN helped us with the Co^{60} gamma source. F. JOHNSON kindly supplied us with a copy of his unpublished work on NaH and KH, and discussions with many workers have helped us in the direction of this research and in the interpretation of the results. Among those who have especially helped us in this way are B. GOURARY, C. DELBECQ, P. PRINGSHEIM and A. B. SCOTT.

Correction added in proof: Experimental measurements show that the oscillator strength for the F band in LiH is approximately $f = 0{\cdot}1$ rather than $0{\cdot}82$ assumed in this paper. Estimates of F-center concentrations should be increased, and other calculations based on these should be revised accordingly.

REFERENCES

1. SEITZ F., *Rev. Mod. Phys.* **18,** 384 (1946); **26,** 7 (1954).
2. For example see: AMELINCKX S., BONTINCK W., DEKEYSER W. and SEITZ F., *Phil. Mag.* (ser. 8) **2,** 355 (1957); WERTZ J. E., AUZINS P., WEEKS R. A. and SILSBEE R. H., *Phys. Rev.* **107,** 1535 (1957); CLARKE F. P., *Phil. Mag.* (ser. 8) **2,** 607 (1957); CUNNINGHAM J. and TOMPKINS F. C., *Proc. Roy. Soc.* **A251,** 27 (1959).
3. JOHNSON F., *Columbia Radiation Laboratory Progress Report*, pp. 30–35. (Aug. 31, 1955).
4. IVEY H. F., *Phys. Rev.* **72,** 341 (1947).
5. PRETZEL F. E., RUPERT G. N., MADER C. L., STORMS E. K., GRITTON G. V. and RUSHING C. C., *J. Phys. Chem. Solids* **16,** 10 (1960).
6. LEWIS W. B. and PRETZEL F. E., *J. Phys. Chem. Solids* (to be published).
7. CASLER R., PRINGSHEIM P. and YUSTER P., *J. Chem. Phys.* **18,** 887 (1950).
8. VAN DOORN C. Z., *Philips Res. Rep.* **12,** 309 (1957).
9. MARKHAM J. J. and KONITZER J. D., *J. Chem. Phys.* **29,** 673 (1958).
10. SMAKULA A., *Z. Phys.* **59,** 603 (1930).
11. BATE R. T. and HEER C. V., *J. Phys. Chem. Solids* **7,** 14 (1958).
12. HESKETH R. V., *Phil. Mag.* (ser. 8) **4,** 114 (1959).
13. DEXTER D. L., *Solid State Physics* **6,** 353 (1958).
14. DOYLE W. T., INGRAM D. J. E. and SMITH M. J. A., *Phys. Rev. Letters* **2,** 497 (1959).
15. HEILAND G. and KELTING H., *Z. Phys.* **126,** 689 (1949).
16. WATSON L. R. and SCOTT A. B., *J. Chem. Phys.* **30,** 342 (1959).
17. SEITZ F., *Phys. Rev.* **83,** 134 (1951).
18. CAMAGNI P. and CHIAROTTI G., *Nuovo Cim.* (ser. 9) **11,** 1 (1954).
19. RUSSELL G. A. and KLICK C. C., *Phys. Rev.* **101,** 1473 (1956).
20. DELBECQ C. J. and PRINGSHEIM P., *J. Chem. Phys.* **21,** 794 (1953); PRINGSHEIM P., *Z. Phys.* **136,** 573 (1954).
21. KAPLIANSKII A. A., *Optik i Spektrosk.* (U.S.S.R.) **3,** 267 (1959); FEOFILOV P. P., *Ibid* 268, in English translation.
22. MAYER J. E. and MAYER M. G., *Statistical Mechanics*, p. 468. John Wiley, New York (1940).
23. LEVY M., *Nature, Lond.* **177,** 241 (1956).
24. HEILMANN G., *Z. Phys.* **152,** 368 (1958); GOTTLIEB M. JR., *J. Opt. Soc. Amer.* **50,** 343 (1960).
25. KÄNZIG W. and WOODRUFF T. O., *J. Phys. Chem. Solids* **9,** 70 (1959); CASTNER T. G. and KÄNZIG W., *J. Phys. Chem. Solids* **3,** 178 (1957).
26. MARKHAM J. J., *J. Phys. Chem.* **57,** 762 (1953).
27. VARLEY J. H. O., *J. Nuclear Energy* **1,** 130 (1954).
28. HERSH H. N., *J. Chem. Phys.* **27,** 1330 (1957); **30,** 790 (1959).
29. HAYES W. and NICHOLS G. M., *Phys. Rev.* **117,** 993 (1960).
30. DELBECQ C. J., SMALLER B. and YUSTER P. H., *Phys. Rev.* **111,** 1235 (1958).

J. Phys. Chem. Solids Pergamon Press 1961. Vol. 17, Nos. 3/4, pp. 246–253. Printed in Great Britain.

MAGNETIC SUSCEPTIBILITY AND GALVANOMAGNETIC EFFECTS IN PURE AND *P*-TYPE TELLURIUM

GASTON FISCHER

Division of Pure Physics, National Research Council, Ottawa, Canada

and

F. T. HEDGCOCK

Department of Physics, University of Ottawa, Ottawa, Canada

(*Received* 7 *March* 1960; *revised* 25 *April* 1960)

Abstract—The magnetic susceptibility, resistivity and Hall constant of samples of tellurium of various charge carrier densities have been measured between 4·2°K and 500°K. Pure tellurium shows a temperature independent susceptibility between room temperature and the temperature of liquid helium. All heavily doped samples show a temperature dependent diamagnetism which is thought to arise from the free charge carriers. The magnetic susceptibility and galvanomagnetic effects are interpreted with a simple two band model. Hole effective masses, based on the two band interpretation of the susceptibility measurements, are found to range from 0·14 m to 0·24 m. An impurity scattering effective mass of 0·2 m is found for the holes in the most degenerate sample. Magnetic evidence for the trapping of charge carriers can be seen in the liquid helium region and an estimate of 0·004 eV is obtained for the activation energy of hole formation. All samples show an unexplainable temperature dependent paramagnetic contribution to the susceptibility above room temperature.

Vol. 17
1960

1. INTRODUCTION

EXPERIMENTAL studies on the magnetic properties of semiconductors[1] have shown that useful information about the electronic band structure of semiconductors can be derived from such measurements. With this in mind, measurements have been made of the magnetic susceptibility, Hall coefficient and resistivity of pure and doped tellurium at temperatures in the liquid helium region as well as near the melting point.

Investigations of the electrical properties of samples of pure and doped tellurium by KRONMÜLLER *et al.*[2] and FUKUROI *et al.*[3] have shown that these are semiconductors which exhibit both an intrinsic and extrinsic conductivity region. Early magnetic measurements[4] on tellurium have shown a mean mass susceptibility at room temperature which is diamagnetic and of the order of $-0{\cdot}31 \times 10^{-6}$ e.m.u./gm. Experiments on the temperature dependence of the diamagnetic anisotropy of single crystals of tellurium alloys were made by RAO and GOVINDARAJAN[5] to decide whether or not tellurium was a metal. More recent experiments with pure tellurium have been reported by BUSCH and VOGT[6] who observed a change of the susceptibility on melting. However, because of insufficient data no attempt has been made to interpret the magnetic results in relation to the band structure of tellurium.

2. EXPERIMENTAL METHOD

The specimens were prepared with tellurium from A. D. MACKAY which was zone refined and melted in glass tubes with the desired impurity added. The alloys were then homogenized at 440°C for several days.

The room temperature absolute susceptibility was determined to an accuracy of 3 per cent with a microbalance which was fitted into a vacuum case. The low temperature susceptibilities were measured with an automatically recording microbalance[8] and are determined with a relative accuracy of 0·2 per cent. Since the presence of any ferromagnetic impurity would greatly alter

Table 1

Sample	Doping (atomic per cent)	Charge carrier concentration at 100°K (per cm^3)	$-\chi$ at 300°K (e.m.u./gm.)
1	0·1 I	$3{\cdot}5\times10^{16}$	$0{\cdot}29\times10^{-6}$
2	0·1 Sb	$1{\cdot}3\times10^{19}$	$0{\cdot}30\times10^{-6}$
3	0·1 Sb	$1{\cdot}5\times10^{19}$	$0{\cdot}30\times10^{-6}$
4	0·1 Sn	$2{\cdot}2\times10^{17}$	$0{\cdot}30\times10^{-6}$
5	1 Sn	$3{\cdot}5\times10^{17}$	$0{\cdot}30\times10^{-6}$
6	zone refined	1×10^{15}	$0{\cdot}29\times10^{-6}$

the measured susceptibilities, all specimens were examined for ferrous impurity. None of the samples showed a field dependent susceptibility which would have evidenced impurities of this kind.

The resistivity and Hall coefficient measurements were made with an apparatus described by DAUPHINÉE and MOOSER[9].

3. EXPERIMENTAL RESULTS

Table 1 gives a list of the alloys studied and the corresponding value of the charge carrier concentration at 100°K as determined from the Hall coefficient. The absolute mass susceptibility at room temperature is also given and all values appear equal within experimental errors. All samples are *p*-type. The charge carrier density in the iodine doped sample is in good agreement with that of a sample of similar impurity content used by KRONMÜLLER *et al.*[2] Our antimony-doped samples, however, contain nearly three times as many acceptors as their equivalent alloys. The two samples of nominal composition 0·1 and 1 per cent tin have very nearly indentical properties with concentrations of about 3×10^{17} acceptors per cm^3. A micrographic inspection revealed that these two samples contain appreciable amounts of insoluble precipitates between the grain boundaries of the tellurium crystallites. We think, therefore, that the solubility limit of tin

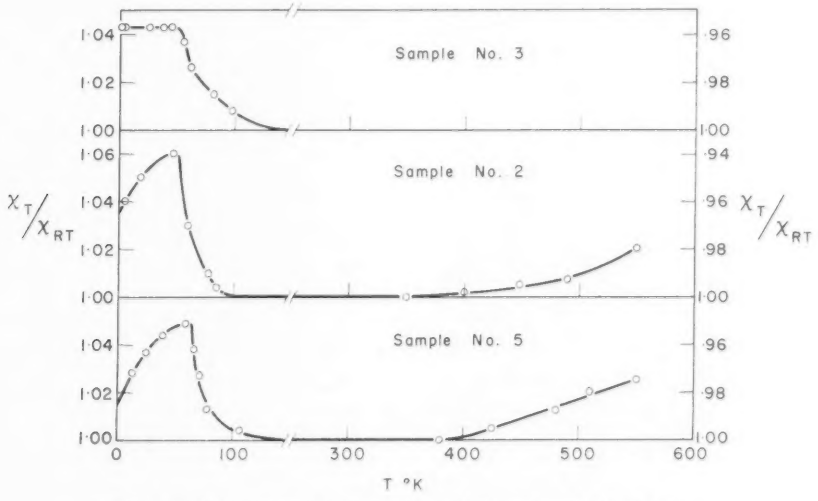

FIG. 1. Relative susceptibility of three tellurium alloys (c.f. Table 1) vs. temperature.

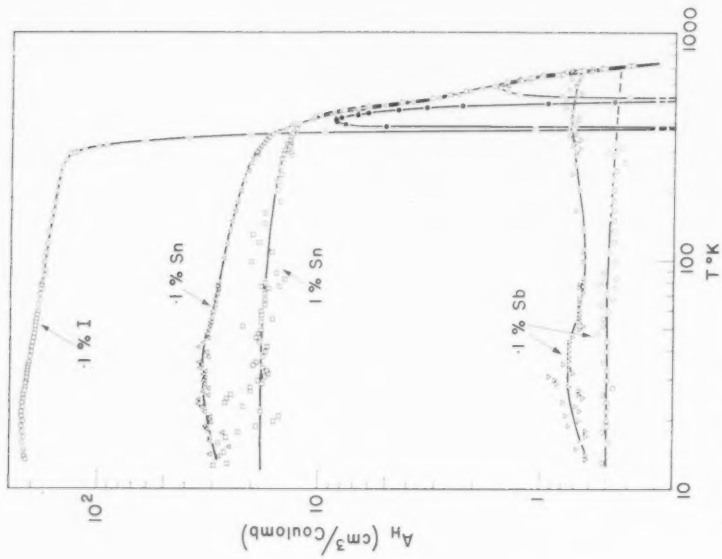

FIG. 3. Hall coefficient of various tellurium alloys vs. temperature.

Vol. 17
1960

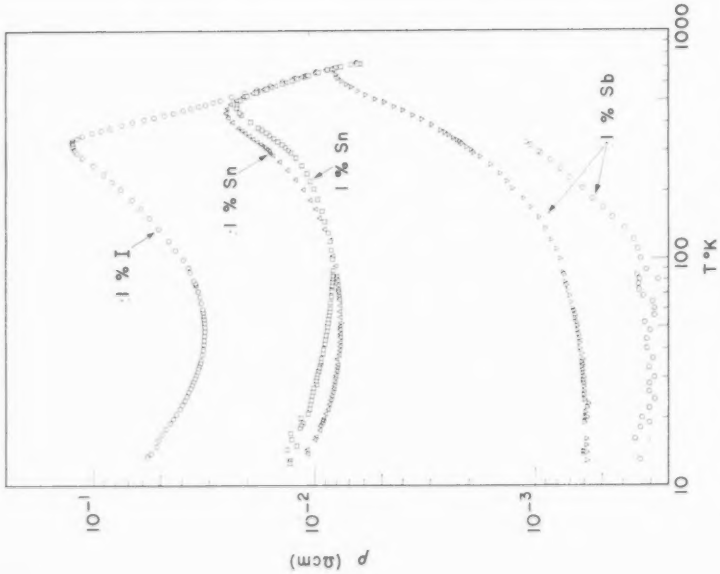

FIG. 2. Resistivity of various tellurium alloys vs. temperature.

in tellurium is between 10^{-3} and 10^{-2} atomic per cent.

The absolute susceptibility of the samples shown in Table 1 are in reasonable agreement with the accepted value of $0{\cdot}31\times10^{-6}$ e.m.u./gm.,[10] and the result obtained with the purest sample is in good agreement with the more recent value of $2{\cdot}90\times10^{-7}$ e.m.u./gm. reported by YUAN[11]. The absolute susceptibility of specimens 2 and 5 had to be determined from powdered samples. The error in these results can be as much as 5 per cent because of the uncertainties related to packing and to sample container. The magnetic susceptibility of pure tellurium was temperature independent in the whole range from 6°K to room temperature, and so was that of the 0·1 per cent iodine sample. Fig. 1 shows the relative susceptibility of the other tellurium alloys as a function of temperature while Figs. 2 and 3 show the resistivity and Hall coefficient of the same samples. It will be noticed that all samples become more diamagnetic as the temperature is lowered and all but sample 3 have a maximum in their diamagnetic susceptibility occurring around 20 to 30°K. The Hall coefficients of these samples are approximately constant below room temperature and down to about 25°K. Below 25°K the Hall coefficient of some samples seems to decrease slightly with decreasing temperature.

4. DISCUSSION OF RESULTS

4:1 *Magnetic susceptibility of a semiconductor*

Let us first review the magnetic properties of semiconductors. Following BUSCH and MOOSER[1], the total mass susceptibility of a semiconductor can be written as the sum of three components: the lattice susceptibility χ_L, which is the susceptibility of the electrons in the valence band and is diamagnetic; the susceptibility of the free charge carriers χ_f, which is the susceptibility of electrons in the conduction band or of holes in the valence band; and the susceptibility of trapped carriers χ_b.

The charge carrier susceptibility can be written as

$$\chi = \frac{N_f\mu^2}{\rho kT}\left(1-\frac{m^2}{3m^{*2}}\right)\frac{F'_{1/2}(\eta)}{F_{1/2}(\eta)} \qquad (1)$$

where N_f is the number of charge carriers per cm^3,

μ is the Bohr magneton.
m and m^* are the free and effective charge. carrier masses for motion in a magnetic field,†
ρ is the density of the material,
k is the Boltzmann constant,
T is the absolute temperature,
η is the reduced Fermi energy (ζ/kT),
$F_{1/2}(\eta)$ is the Fermi integral, and
$F'_{1/2}(\eta)$ is the first derivative of $F_{1/2}(\eta)$. Values of these integrals and derivatives have been tabulated by MCDOUGALL and STONER[12].

When η is less than 2, the degeneracy factor $F_{1/2}(\eta)/F_{1/2}(\eta)$ is approximately 1 and the charge carrier susceptibility is proportional to T^{-1}. The first term in equation (1) represents the spin paramagnetism, and the second term the Landau diamagnetism of the free charge carriers.

The susceptibility of N_b electrons (or holes) trapped in impurity sites can be written as

$$\chi_b = \frac{N_b}{\rho}\left(\frac{\mu^2}{kT}-\frac{e^2K^2m^2a_h^2}{6m^{*3}c^2}\right) \qquad (2)$$

where K is the dielectric constant of the material, a_h is the first Bohr radius of the hydrogen atom while the other symbols have the same meaning as before. The first term in equation (2) is again the paramagnetic component due to the spin, and the second term the Langevin diamagnetism of the trapped electrons or holes.

4:2 *Determination of the Fermi energy in a degenerate semiconductor*

As can be seen from equation (1), before the charge carrier susceptibility can be estimated a value of the reduced Fermi energy is required. Assuming that in a highly doped semiconductor, impurity scattering dominates in the low temperature region and that a mean free path can be ascribed to the charge carriers which is

† The magnetic susceptibility effective mass is identical with the density of states effective mass only when the energy surfaces are spheres in wave-vector space and the bands are non-degenerate.

proportional to the square of the charge carrier kinetic energy, the Hall coefficient becomes

$$|A_H| = \frac{3}{16\pi e}\left(\frac{h^2}{2m^*kT}\right)^{3/2}\frac{F_{1/2}(\eta)}{[F_2(\eta)]^2} \qquad (3)$$

where

$$F_\alpha(\eta) = \int_0^\infty x^\alpha(1+e^{x\eta})^{-1}\,dx$$

and the carrier density is given by

$$p = 4\pi h^{-3}(2m^*kT)^{3/2}F_{1/2}(\eta) \qquad (4)$$

The usefulness of equations (3) and (4) in determining the Fermi energy from measured values of $|A_H|$ is limited because m^* is usually not known. To obtain some indication of the degree of degeneracy of our samples we shall use the values tabulated by FINLAYSON *et al.*[13] which are based on equation (3) and assume an effective mass ratio of unity. The reduced Fermi energies derived in this manner are given in Table 2 and η as a function of T is shown in Fig. 4 for sample 2. It is seen that samples 2 and 3 obtain rather high positive values of η, indicating an appreciable degree of degeneracy. All other samples can be regarded as non-degenerate, and classical statistics applied. In the classical limit the factor $F'_{1/2}(\eta)/F_{1/2}(\eta)$ of equation (1) becomes unity, and an effective mass can readily be deduced from the susceptibility measurement.* The same factor is appreciably different from unity for samples 2 and 3, and can only be calculated if η is known. Since the η values reported in Table 2 were obtained from the Hall coefficient with the implication of an effective mass ratio of unity it is inconsistent to use them now, to obtain another value of m^* from the susceptibility experiments. However, effective mass values obtained in this way appear to be rather insensitive to the inconsistency of the method. It can be seen in Table 2 that values of m^* obtained as described above for the degenerate samples 2 and 3 agree fairly well with those of samples 4 and 5 treated classically. The data for sample 2 shown in Fig. 4 includes χ_f as a function of $F'_{1/2}(\eta)/F_{1/2}(\eta)T$ as well as the percentage change in p as a function of T as derived from equation (4). Included in Table 2 are values of the Hall mobility deduced from Hall coefficient and conductivity (see Figs. 2 and 3). The hole mobilities are seen to decrease with increasing charge carrier concentration and the susceptibility effective masses seem to increase with concentration. Although the susceptibility effective mass is not identical with the mobility effective mass, we would expect that both should be governed by a similar concentration dependence. Indeed, our mobilities are compatible with an increase in m^* and a decrease in relaxation time with increasing concentration. It is somewhat surprising that KRONMÜLLER *et al.*[2] have reported a hole mobility which is substantially *lower* in their purest sample than in almost all of their doped samples. The high mobilities that we observed in our purer samples are a result of the long annealing of the samples which probably removes most dislocations.[15]

MANSFIELD[14] has shown that for a completely degenerate semiconductor the mobility should be fairly insensitive to the number of ionized scattering centres. This appears to be the case for tellurium where the mobilities listed in Table 2 become approximately constant for the samples with highest impurity content. MANSFIELD[14] also shows that an "impurity scattering effective mass" may be estimated from the conductivity of a degenerate sample at low temperatures. The analysis as applied to our most degenerate sample (sample 3) yields a value of m^*/mK of $7{\cdot}2\times10^{-3}$, where K is the dielectric constant of tellurium. Using the extrapolated value of 4·8 for the

* The calculation of effective masses contained in Table 2 are based on the temperature dependence of the relative susceptibility of the alloy and the absolute susceptibility of pure tellurium. In the region of constant N_f and assuming $N_b \ll N_f$.

$$\frac{\chi(T)}{\chi(\text{R.T.})} = \frac{\chi_f(T)+\chi_{\text{Te}}}{\Delta\chi+\chi_{\text{Te}}}$$

where $\Delta\chi$ includes χ_f(R.T.) + susceptibility of precipitated impurity etc. Then provided $\Delta\chi/\chi_{\text{Te}} \ll 1$

$$\frac{\chi(T)}{\chi(\text{R.T.})} = \frac{\chi_f}{\chi_{\text{Te}}}+1$$

where χ_{Te} is taken to be $0{\cdot}290\times10^{-6}$ e.m.u./gm. The maximum error introduced by assuming the value of $\Delta\chi/\chi_{\text{Te}} < 1$ is approximately eight per cent. This is certainly within the accuracy of 15 per cent claimed for the effective masses in Table 2.

Vol. 17
1960

Table 2

Sample	p from 40 to 100°K (cm^{-3})	μ_p from 40 to 100°K (cm^2/V sec)	η at 40°K	m^*/m $\pm$ 0·03
6	1×10^{15}	1×10^{4}		
1	$3{\cdot}5\times10^{16}$	5×10^{3}	$-2{\cdot}8$	—
4	$2{\cdot}2\times10^{17}$	$3{\cdot}3\times10^{3}$	$-1{\cdot}14$	0·14
5	$3{\cdot}5\times10^{17}$	$2{\cdot}6\times10^{3}$	$-0{\cdot}50$	0·15
2	$1{\cdot}3\times10^{19}$	$1{\cdot}2\times10^{3}$	5·3	0·20
3	$1{\cdot}5\times10^{19}$	$1{\cdot}5\times10^{3}$	6·0	0·24

refractive index as reported by Moss[15], yields for m^* a value of approximately 0·2 m. The fact that the value of m^* derived from electron transport data is in such close agreement with those obtained from the magnetic susceptibility would lead one to believe that the Fermi surface in tellurium is fairly simple and nearly spherical.

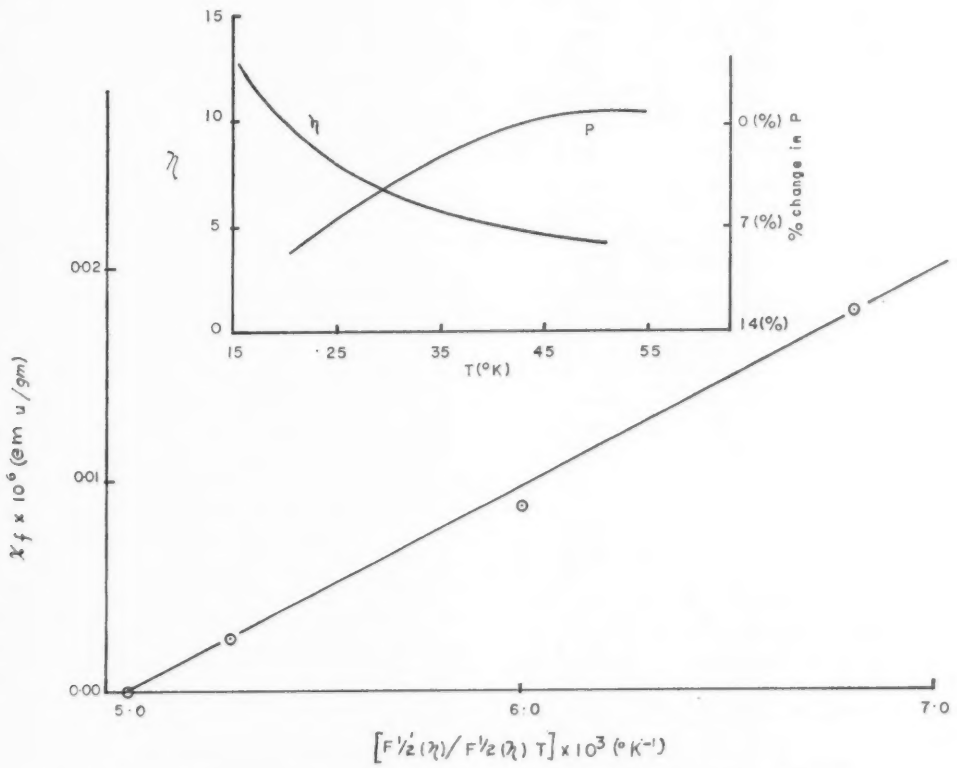

FIG. 4. Temperature dependence of the reduced Fermi energy and hole concentration as calculated from equations (3) and (4) for sample 2. Inset shows charge carrier susceptibility λ_f as a function of $F_{1/2}(\eta)/F_{1/2}(\eta)T$ for sample 2.

4:3 *Determination of the activation energy for holes in tellurium.*

As can be seen in Fig. 4, below 40°K the calculated number of holes is seen to decrease with decreasing temperature in contrast to the apparent increase as indicated by assuming the Hall coefficient to be inversely proportional to the number of free carriers. The increase in the number of trapped holes occurs in the region of the susceptibility maximum. Assuming the effective mass of a trapped hole to be the same as when activated, an estimate of the bound carrier susceptibility χ_b yields a negligible contribution to the total susceptibility above 10°K. If the decrease in the diamagnetism at low temperatures is due to the decrease in the number of free holes, then the decrease in the free charge carrier susceptibility can be written[7]

$$\Delta\chi_f = N[1-\exp(-\Delta E/2kT)]\frac{\mu^2 m^2}{3\rho m^* 2kT} \quad (5)$$

where N is the total number of carriers, ΔE the activation energy for hole formation, and the other symbols have the same meaning as before. A graphical estimate of the activation energy based on equation (5) yields a value of 0·004 eV and is in good agreement with the value of 0·005 eV deduced from a hydrogenic model of extrinsic tellurium based on the same effective mass.

Sample 3 exhibits a constant diamagnetism in the very low temperature region, implying a vanishing activation energy and completely degenerate behaviour of the charge carriers.* For completely degenerate charge carriers in a parabolic band equation (1) reduces to the temperature independent form

$$(\chi_f)_0 = 4m^*\mu^2(3\pi^2 N_f)^{1/3}\left[1-1/3\left(\frac{m}{m^*}\right)^2\right] \quad (6)$$

where the degeneracy of states in the valence band, exclusive of spin, is assumed to be one. The above equation yields a value of $0{\cdot}010\times10^{-6}$ e.m.u./gm. for the charge carrier susceptibility at the absolute zero as compared with the extrapolated value of $0{\cdot}013\times10^{-6}$ e.m.u./gm. observed for sample 3. Since this agreement is within the experimental error in the effective mass, we conclude that the degeneracy of states in the valence band must be one (i.e. only one maximum at the top of the valence band).

4:4 *High temperature results*

The magnetic susceptibility of the samples measured between room temperature and 550°K are shown in Fig. 1. All the samples studied, including the purest tellurium, show a slight increase in the paramagnetism as the temperature is raised. These measurements are in agreement with those of YUAN[11] who observed a slight increase in the paramagnetism before melting. The Hall coefficient shows the usual conversion from *p*- to *n*-type in the region of 500°C, as can be seen in Fig. 3. Since the number of charge carriers in the intrinsic region increases with increasing temperature, the effective mass of the carriers would have to be greater than $m/\sqrt{3}$ in order that χ_f be positive. We cannot afford an explanation of this behaviour in any of the proposed band structures of tellurium suggested so far.

5. CONCLUSIONS

Below room temperature the magnetic and galvanomagnetic properties of tellurium can be explained with a simple two-band model. Since samples containing different kinds and amounts of foreign elements always are more *p*-type than pure tellurium, experiments give information mainly about the valence band. The present investigation would indicate a non-degenerate and nearly spherical valence band. The band is not quite parabolic. At the top of the band, when 2×10^{17} holes per cm^3 are left, the effective mass is about 0·14 m_0, while it becomes 0·24 m_0 when the band contains $1{\cdot}5\times10^{19}$ holes per cm^3. The hole mobility in pure and annealed tellurium is close to 10^4 cm^2/V sec below about 150°K, in comparison with $1{\cdot}5\times10^3$ cm^2/V sec in pure but unannealed material.[2] Our experimental results would also be compatible with a three-band model recently proposed by MOOSER and PEARSON[19]. This latter model is capable of explaining the galvanomagnetic properties of tellurium above room temperature, but so far no explanation can be given for the decrease in diamagnetism observed in tellurium above 300°K.

* BOWERS[18] has observed similar behaviour in the magnetic susceptibility of highly doped germanium samples.

Vol. 17
1960

Acknowledgements—The authors would like to thank Dr. J. S. DUGDALE for helpful discussions and criticism. One of the authors (F.T.H.) wishes to mention the support of this research given by the Defence Research Board of Canada.

REFERENCES

1. BUSCH G. and MOOSER E., *Helv. Phys. Acta* **26,** 611 (1956).
2. KRONMÜLLER H., JAUMANN J. and SEILER K., *Z. Naturf.* **11a**, 243 (1956).
3. FUKUROI T., TANUMA S. and MUTO Y., *Tohoku Univ. Sci. Rep.* **6,** 18 (1954).
4. OWEN M., *Ann. Phys.* **37,** 657 (1912); MACLENNAN J. C. and COHEN E., *Trans. Roy. Soc. Canad.* **23,** 159 (1929); RAO S. R., *J. Mysore Univ.* **B5,** number 269 (1945). (See also for references to earlier Indian publications).
5. RAO S. R. and VOGINDARAJAN S. R., *Proc. Indian Acad. Sci.* **A10**, 235 (1939).
6. BUSCH G. and VOGT. O., *Helv. Phys. Acta.* **30,** 224 (1957).
7. HEDGCOCK F. T., *J. Electronics* **2,** 513 (1957).
8. HEDGCOCK F. T. and MUIR W. B., *Rev. Sci. Instrum.* April (1960).
9. DAUPHINÉE T. M. and MOOSER E., *Rev. Sci. Instrum.* **26,** 660 (1955).
10. *Tables de constantes et données numériques*, Vol. VII. Masson et Cie (1957).
11. YUAN SI, private communication.
12. MCDOUGALL J. and STONER E. C., *Phil. Trans. Roy. Soc.* **237,** 67 (1938).
13. FINLAYSON D. M., JOHNSON V. A. and SHIPLEY F. M., *Phys. Rev.* **87,** 1141 (1952).
14. MANSFIELD R., *Proc. Phys. Soc. Lond.* **69B,** 76 (1956).
15. FISCHER G., WHITE G. K. and WOODS S. B., *Phys. Rev.* **106,** 480 (1957).
16. CALLEN H. B., *J. Chem. Phys.* **22,** 518 (1954).
17. MOSS T. S., *Proc. Phys. Soc. Lond.* **65B,** 62 (1952).
18. BOWERS R., *Phys. Rev.* **108,** 683 (1957).
19. MOOSER E. and PEARSON W. B., *J. Phys. Chem. Solids* **7,** 65 (1958).

J. Phys. Chem. Solids Pergamon Press 1961. Vol. 17, Nos. 3/4, pp. 254–258. Printed in Great Britain.

THRESHOLD CONCENTRATION FOR THE EXISTENCE OF FERROMAGNETISM IN DILUTE ALLOYS*

M. COOPERSMITH and R. BROUT

Laboratory of Atomic and Solid State Physics and Department of Physics
Cornell University, Ithaca, New York

(*Received* 15 *April* 1960; *revised* 7 *May* 1960)

Abstract—Previous calculations by BROUT for a magnetically dilute system give a value of $x_0Z = 1$ for the suppression of ferromagnetism, where x_0 is the concentration below which ferromagnetism does not exist and Z is the number of nearest neighbors. Only nearest neighbor exchange forces are assumed to exist. This value was obtained using the first term in the cluster expansion of $1/N \langle \log \langle Z \rangle_R \rangle_C$. In the present paper, we shall find a more exact expression for x_0Z by evaluating the higher order terms in the cluster expansion. We find that $x_0Z \simeq 4/3$ for simple, body-centered and face-centered cubic lattices.

IN A previous article by BROUT[1], a crude estimate of the critical concentration needed to suppress ferromagnetism in dilute ferromagnets was given as $x_0 = 1/Z$. Here x_0 is the critical concentration and Z is the number of first neighbors. The interaction is assumed to be of the Ising variety (i.e. $v_{ij\mu_i\mu_j}$ where v_{ij} vanishes except for nearest neighbors and $\mu_i = \pm 1$).

It is the purpose of this article to extend the calculation given in Ref. 1 (second virial coefficient) to higher powers of x in order to arrive at a more reliable estimate of x_0 for the same model. For simple cubic (s.c.) and body-centered cubic (b.c.c.) lattices the calculation is carried out to x^5. For the face-centered cubic lattices the calculation is carried to x^4. All three calculations give $x_0Z \simeq 4/3$.

Unfortunately it is difficult to give accurate estimates of convergence, but in all cases considered, going from the next highest to the highest order included in the calculation does not affect the result by more than a few per cent. This is seen from equations 1(a), 1(b) and 1(c). This indicates, but does not prove, that our estimates are reliable to a few per cent for the assumed model of interaction.

In an article by SATO *et al.*[2] comparison of their theory with experiment is quoted. In Table 2 we present this Table with the present work included in the last column.

It should be cautioned however that agreement with experiment is probably fortuitous in that we have assumed a simple Ising model interaction with only near neighbor forces. We have included the Table in the present work in order to compare with the theory of Ref. 2.

FIG. 1. Example of the comparison of the present notation with that of Ref. 1.

The Curie point is obtained for $H = 0$ from the equation

$$\frac{1}{N}\frac{\partial^2}{\partial R^2}\langle \log \langle Z \rangle_R \rangle_C|_{R=0} = 0 \qquad (1)$$

where we use the notation of Ref. 1. In the second derivative the Curie temperature, T_c occurs in the form $\tanh [J(r_i)/kT_c]$. Hence, putting $\tanh \beta_c J = 1$ yields a relation for x_0 needed to suppress ferromagnetism. In the present notation a diagram with n vertices denotes the sum of all semi-invariants with the same skeletal diagram in the old notation.[1] An example is given in Fig. 1. We

* This work has been partially supported by the Office of Naval Research.

Vol. 17
1960

Table 1. *Evaluation of diagrams for* (*a*) *simple cubic,* (*b*) *body-centered cubic and* (*c*) *face-centered cubic lattices*

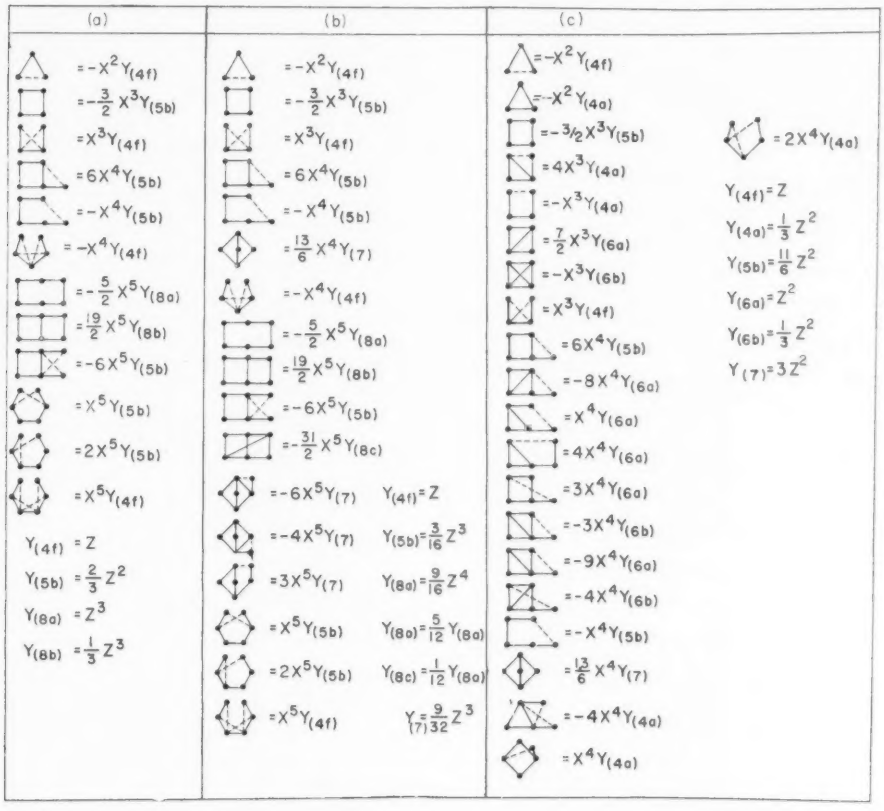

Table 2. *Comparison of various theoretical values with experimentally determined values of* x_0 *for b.c.c. and f.c.c.*

	C–W	C–V	A–C–N	Expt.	C–E
Fe–Cr	0	0·14	0·25	~0·20	0·17
Fe–Au	0	0·09	0·17	~0·14	0·11

distinguish between internal and external dotted lines in a diagram. A dotted line is internal if the diagram remains irreducibly linked when the dotted line is removed. An example is given in Fig. 2(a). A dotted line is external if the diagram becomes reducibly linked when the dotted line is removed, an example of which is Fig. 2(b). Internal dotted-line diagrams are merely corrections to the prototype solid-line diagram needed to insure only one particle on a lattice site. These diagrams can be eliminated simply by counting the number of ways to place the prototype diagram

on the lattice keeping the vertices distinct. External dotted-line diagrams represent a new type of bond which must be evaluated separately and which makes an important contribution to the final result.

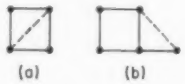

FIG. 2. Examples of internal and external line graphs.

In the Appendix we give the rules for evaluating a diagram and also derive a number of interesting theorems concerning the relationships between different types of diagrams. For the present we state the results for the three cubic lattices. For the simple cubic lattice we have:

$$\frac{1}{N}\frac{\partial^2}{\partial R^2}\langle\log\langle Z\rangle_R\rangle_C|_{R=0} = 0 = -1+xZ-6x^2 -30x^3+114x^4+102x^5+\ldots \quad (1a)$$

for the body-centered cubic lattice,

$$\frac{1}{N}\frac{\partial^2}{\partial R^2}\langle\log\langle Z\rangle_R\rangle_C|_{R=0} = 0 = -1+xZ- -8x^2-144x^3+784x^4-832x^5+\ldots \quad (1b)$$

for the face-centered cubic lattice,

$$\frac{1}{N}\frac{\partial^2}{\partial R^2}\langle\log\langle Z\rangle_R\rangle_C|_{R=0} = 0 = -1+xZ- -60x^2+216x^3+576x^4+\ldots \quad (1c)$$

Approximate solutions obtained by iteration are given by $x_0Z = 1{\cdot}29$, $x_0Z = 1{\cdot}39$ and $x_0Z = 1{\cdot}36$. We therefore conclude that $x_0Z \simeq 4/3$ for all lattices.

APPENDIX

We prove some interesting theorems concerning diagrams evaluated in

$$\frac{1}{N}\frac{\partial^2}{\partial R^2}\langle\log\langle Z\rangle_R\rangle_C|_{R=0}.$$

FIG. 3. Diagram contributing to the coefficient of x^3.

To illustrate the method of evaluating complicated diagrams we consider Fig. 3. The contribution is to the coefficient of x^3 and is equal to

$$\frac{1}{N}\frac{\partial^2}{\partial R^2}\left\{\sum_{i>j>k>l}^{\infty}\left\langle\sum_{n=4}\frac{M_n^{(3)}}{n!}(-\beta)^n\right\rangle_C\right\}\Bigg|_{R=0} \quad (A1)$$

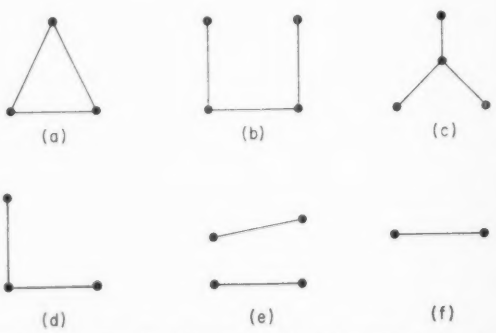

FIG. 4. Correction diagrams in the evaluation of Fig. 3.

where $M_n^{(i)}$ means that contribution to M_n arising from diagrams of a particular skeletal type "i". Now

$$M_n^{(3)} = M_n^{(v_{ij\mu_i\mu}+v_{jk\mu_j\mu_k}+v_{ki\mu_k\mu_i}+v_{kl\mu_k\mu_l})} - M_n^{(v_{ij\mu_i\mu_j}+v_{jk\mu_j\mu_k v_{ki}+\mu_k\mu_l})} - 2M_n^{(v_{ij\mu_i\mu_j}+v_{jk\mu_j\mu_k}+v_{kl\mu_k\mu_l})} - - M_n^{(v_{jk\mu_j\mu_k}+v_{kl\mu_k\mu_l}+v_{ki\mu_k\mu_l})} + 5M_n^{(v_{ij\mu_i\mu_j}+v_{jk\mu_j\mu_k})} + M_n^{(v_{ij\mu_i\mu_j}+v_{kl\mu_k\mu_l}} - 4M_n^{(v_{ij\mu_i\mu_j})} \quad (A2)$$

We rewrite this as follows:

$$M_n^{(3)} = M_n^{(v_{ij\mu_i\mu_j}+v_{jk\mu_j\mu_k}+v_{ki\mu_k\mu_i}+v_{kl\mu_k\mu_l})} - [M_n^{(v_{ij\mu_i\mu_j}+v_{jk\mu_j\mu_k}+v_{ki\mu_k\mu_l})} - - 3M_n^{(v_{ij\mu_i\mu_j}+v_{jk\mu_j\mu_k})} + 3M_n^{(v_{ij\mu_i\mu_j})}] - 2[M_n^{(v_{ij\mu_i\mu_j}+v_{jk\mu_j\mu_k}+v_{kl\mu_k\mu_l})} - 2M_n^{(v_{ij\mu_i\mu_j}+v_{jk\mu_j\mu_k})} - - M_n^{(v_{ij\mu_i\mu_j}+v_{kl\mu_k\mu_l}} + 3M_n^{(v_{ij\mu_i\mu_j})}] - 5[M_n^{(v_{ij\mu_i\mu_j}+v_{jk\mu_j\mu_k})} - 2M_n^{(v_{ij\mu_i\mu_j})}] - - [M_n^{(v_{ij\mu_i\mu_j}+v_{kl\mu_k\mu_l})} - 2M_n^{(v_{ij\mu_i\mu_j})}] - 4M_n^{(v_{ij\mu_i\mu_j})} \quad (A3)$$

$$= M_n^{(v_{ij\mu_i\mu_j}+v_{jk\mu_j\mu_k}+v_{ki\mu_k\mu_i}+v_{kl\mu_k\mu_l})} - M^{(4a)} - M_n^{(4b)} - M_n^{(4c)} - M_n^{(4d)} - M_n^{(4e)} - M_n^{(4f)} \quad (A4)$$

Vol. 17
1960

Substituting equation A4 into A1, we can extend the sum down to $n = 1$ since equation A2 vanishes for for $n = 1, 2, 3$. We thus get for the contribution of Fig. 3 to A1:

$$\frac{1}{N}\frac{\partial^2}{\partial R^2}\Big\{\sum_{i>j>k>l}\langle\log\langle\exp[-\beta(v_{ij}\mu_i\mu_j+v_{jk}\mu_j\mu_k+v_{ki}\mu_k\mu_i+v_{kl}\mu_k\mu_l)]\rangle_R$$

$$-(4a)-(4b)-(4c)-(4d)-(4e)-(4f)\rangle_c$$

$$=\frac{N^3}{4!}\times 4\times 3\frac{\partial^2}{\partial R^2}\{\langle\log[\cosh\beta J_{12}\cosh\beta J_{23}\cosh\beta J_{31}\cosh\beta J_{34}+$$

$$+\sinh\beta J_{12}\sinh\beta J_{23}\sinh\beta J_{31}\cosh\beta J_{34}+$$

$$+R^2(\sinh\beta J_{12}\sinh\beta J_{23}\sinh\beta J_{31}\sinh\beta J_{34}+$$

$$+2\sinh\beta J_{12}\sinh\beta J_{23}\sinh\beta J_{34}\cosh\beta J_{31}+$$

$$+5\sinh\beta J_{12}\sinh\beta J_{23}\cosh\beta J_{31}\cosh\beta J_{34}+$$

$$+4\sinh\beta J_{12}\cosh\beta J_{23}\cosh\beta J_{31}\cosh\beta J_{34}+$$

$$+\text{terms involving } R^4]-\text{correction diagrams}\rangle_c\}|_{R=0}$$

$$=N^3\langle(\tanh\beta J_{12}\tanh\beta J_{23}\tanh\beta J_{31}\tanh\beta J_{34}+2\tanh\beta J_{12}\tanh\beta J_{23}\tanh\beta J_{34}+$$

$$+5\tanh\beta J_{12}\tanh\beta J_{23}+4\tanh\beta J_{12})/(1+\tanh\beta J_{12}\tanh\beta J_{23}\tanh\beta J_{31})-$$

$$\text{correction diagrams}\rangle_c$$

$$=x^3Y_{(3)}\{(\tanh^4\beta J+2\tanh^3\beta J+5\tanh^2\beta J+4\tanh\beta J)/(1+\tanh^3\beta J)-\text{correction diagrams}\} \qquad \text{(A5)}$$

where we have put $v_{ij} = -J_{ij}$ and have evaluated the average for nearest neighbor interaction. $Y_{(i)}$ equals the number of ways of placing the diagram of Fig. i on the lattice. The generalization to any diagram is obvious from the above evaluation. It is particularly advantageous to evaluate the diagrams of Figs. 5(a), (b) and (c) as

FIG. 5. Diagrams of general interest in the calculation of more complicated diagrams.

these occur frequently in the evaluation of more complicated diagrams. For the following, it is convenient to put $X = \tanh\beta J$.

To evaluate Fig. 5(a) we have:

$$(4b)_{n+1} = X^n+2X^{n-1}+3X^{n-2}+\ \ldots\ +nX-$$

$$-2(4b)_n-3(4b)_{n-1}-\ \ldots\ -n(4f) \qquad \text{(A6)}$$

where $(i)_n$ refers to a diagram of the type of Fig. i with n vertices.

Using induction we have

$$(4f) = X,\ (4b)_n = X^{n-1},$$

hence

$$(4b)_{n+1} = X^n$$

The final answer for the contribution to

$$\frac{1}{N}\frac{\partial^2}{\partial R^2}\langle\log\langle Z\rangle_R\rangle_C|_{R=0}$$

is

$$-x^nY(5b)_nX^n \qquad \text{(A7)}$$

where the minus sign comes about because of the dotted line.

Fig. 5(b) gives:

$$(5b)_n = \frac{n(X^{n-1}+X^{n-2}+\ \ldots\ +X^2+X)}{1+X^n}-$$

$$-n(4b)_n-n(4b)_{n-1}-\ \ldots\ -n(4f)$$

$$=n\left[\frac{X^{n-1}+X^{n-2}+\ \ldots\ +X}{1+X^n}-\right.$$

$$\left.-(X^{n-1}+X^{n-2}+\ \ldots\ +X)\right]$$

$$=-n\frac{X^n}{1+X^n}(X^{n-1}+X^{n-2}+\ \ldots\ +X) \qquad \text{(A8)}$$

Evaluating the summations and averages the final answer is

$$-x^{n-1}Y_{(5b)_n}\frac{X^n}{1+X^n}(X^{n-1}+X^{n-2}+\ldots+X) \tag{A9}$$

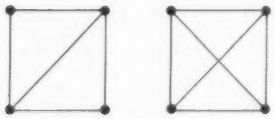

FIG. 6. Diagrams contributing to the coefficient of x^3.

Finally, for Fig. 4(c) we obtain:

$$(3)_n = \frac{X^{n+1}+\text{ terms contributing to the numerator of } (5b)_n + 2(X^n+X^{n-1}+\ldots+X^2)+X}{1+X^n} -$$

$$-\text{correction terms of } (5b)_n -$$

$$-2(X^n+X^{n-1}+\ldots+X^2)-X-(5b)_n$$

$$=-2\frac{X^{n+1}}{1+X^n}(X^{n-1}+\ldots+X)$$

FIG. 7. Diagram contributing to the coefficient of x^4.

The final answer is

$$4x^nY_{(5b)_n}\frac{X^{n+1}}{1+X^n}(X^{n-1}+\ldots+X)=-4xX(5b)_n \tag{A10}$$

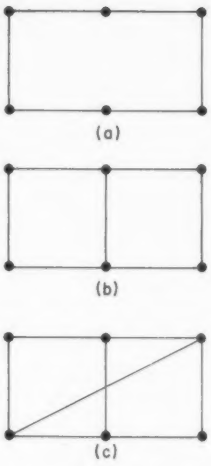

FIG. 8. Diagrams contributing to the coefficient of x^5.

Using the evaluations of Fig. 5(a), (b) and (c) and the rule for evaluating diagrams the following diagrams

FIG. 9. Diagram contributing to the coefficient of x^3.

have been calculated. Their values are listed for reference in Tables 1(a), (b) and (c). In the following we have put $X \equiv \tanh\beta J = 1$.

Vol. 17
1960

REFERENCES

1. BROUT R., *Phys. Rev.* **115,** 824 (1959).
2. SATO H., ARROTT A. and KIKUCHI R., *J. Phys. Chem. Solids* **10,** 19 (1959).

J. Phys. Chem. Solids Pergamon Press 1961. Vol. 17, Nos. 3/4, pp. 259–266. Printed in Great Britain.

THE RELATION OF TRANSITION PARAMETERS FOR LINEAR PROCESSES TO MEASURABLE PARAMETERS IN FERRIMAGNETIC RESONANCE

P. E. SEIDEN*†

Institut Fourier, University of Grenoble, Grenoble, France

(*Received* 11 *April* 1960; *revised* 17 *May* 1960)

Abstract—Expressions are derived for linear processes that relate the fundamental transition parameters for relaxation in ferrimagnetic resonance to measureable parameters such as linewidths and relaxation times. These calculations include the effect of the reaction of spinwaves back onto the uniform precession. Previous calculations by others have neglected this effect and the consequences of its neglect are discussed.

INTRODUCTION

THE PROCESSES believed to contribute to ferrimagnetic relaxation have been discussed in general by a number of authors.[1–4] We shall use here the description of these processes given by CALLEN[4] which considers both direct and indirect relaxation of the uniform precession explicitly. The first process considered is the direct relaxation of the uniform precession into the lattice; i.e. the destruction of a uniform precession magnon and the creation of a lattice phonon. This process, following the notation of CALLEN, will be denoted by the transition parameter $\lambda_{0\sigma}$. The second process we consider is the destruction of a uniform precession magnon (wavenumber $k = 0$) and the creation of a spinwave‡ magnon ($k \neq 0$), denoted by λ_{0k}. The third process is the destruction of a spinwave magnon and the creation of a lattice phonon, denoted by $\lambda_{k\sigma}$. The spin–lattice parameters ($\lambda_{0\sigma}$ and $\lambda_{k\sigma}$) represent the transition from a particular spinwave k to all phonons σ. The spin–spin parameter (λ_{0k}) represents the transition from the uniform precession to a particular spinwave k.

Most previous approaches at the determination of the relaxation parameters from measureable quantities utilized one or another of the presently available phenomenological equations of motion. The equations most used for resonance phenomena are unsuitable in their original forms, since they do not supply us with the three independent parameters needed for the processes described above. These equations are the LANDAU–LIFSHITZ[5] equation:

$$\dot{\boldsymbol{M}} = -\boldsymbol{M}\times\boldsymbol{H} - \lambda\boldsymbol{M}\times(\boldsymbol{M}\times\boldsymbol{H}) \tag{1}$$

or its modification by GILBERT[6]:

$$\dot{\boldsymbol{M}} = -\gamma\boldsymbol{M}\times\boldsymbol{H} - \lambda\boldsymbol{M}\times\dot{\boldsymbol{M}} \tag{2}$$

and the BLOCH–BLOEMBERGEN[7] equations:

$$\dot{M}_{x,y} = -\gamma(\boldsymbol{M}\times\boldsymbol{H})_{x,y} - \frac{M_{x,y}}{T_2} \tag{3}$$

$$\dot{M}_z = -\gamma(\boldsymbol{M}\times\boldsymbol{H})_z - \frac{M_0 - M_z}{T_1} \tag{4}$$

where T_1 and T_2 are the longitudinal and transverse relaxation times respectively. CALLEN[4] has formulated a phenomenological equation which does satisfy the requirements of the processes we

* National Science Foundation Postdoctoral Fellow.

† Present address, IBM Research Center, Yorktown Heights, New York.

‡ The $k \neq 0$ magnons created are not strictly spinwaves but are normal modes of the sample. However for the purposes of this paper we will use the term spinwave for these modes.

are considering. This equation is:

$$\dot{\boldsymbol{M}} = \alpha \boldsymbol{M} - \gamma \boldsymbol{M} \times \boldsymbol{H} - \lambda \boldsymbol{M} \times (\boldsymbol{M} \times \boldsymbol{H}) \qquad (5)$$

where α and λ have been derived on a quantum mechanical basis as a function of M, H, and the three transition parameters. FLETCHER, *et al.*[8] have recently proposed a set of equations which are equivalent to equation (5) decomposed along another set of axes. These equations, given below, were derived by the classical energy balance approach.

$$\dot{M}_{x,y} = -\gamma(\boldsymbol{M} \times \boldsymbol{H})_{x,y} - \\ - \frac{M_{x,y}}{2} \left(\frac{1}{T_{10}} + \sum_k \frac{1}{T_{2k}} \right) \qquad (6)$$

$$(\dot{M_0 - M_z}) = \gamma(\boldsymbol{M} \times \boldsymbol{H})_z - \\ - \frac{M_x^2 + M_y^2}{2M_0} \left(\frac{1}{T_{10}} - \frac{1}{T_{1k}} \right) - \frac{M_0 - M_z}{T_{1k}} \qquad (7)$$

where the relaxation times T_{10}, T_{1k} and T_{2k} are related to the transition parameters as follows:

$$T_{10} = \frac{1}{\lambda_{0\sigma}} \qquad T_{1k} = \frac{1}{\lambda_{k\sigma}} \qquad T_{2k} = \frac{1}{\lambda_{0k}}$$

The difficulty with the above equations however, is that the results derived from them have neglected the reaction of the spinwaves on the uniform precession, i.e. it is usually assumed that the number of spinwave magnons (N_k) is very small compared to the number of uniform precession magnons (n_0). This is not necessarily the case in all ferrimagnetics. We will derive here expressions relating the transition parameters to experimentally measured quantities without the restriction $n_k \ll n_0$. Also in these derivations we will not find it necessary to use a phenomenological equation of motion.

LINEWIDTHS AND A LINEAR SATURATION RELATION

The restriction that we will make in this calculation is to consider only linear* processes and therefore we can not expect to encounter the non-linear effects of SUHL[9]. This however does not eliminate the possibility of having $n_k \approx n_0$, since to remain in the linear region we must only require that:

$$n_0 \ll M_0/\gamma\hbar \qquad (8)$$

and:

$$n_k \ll M_0/\gamma\hbar \qquad (9)$$

where M_0 is the saturation magnetization, γ is the gyromagnetic ratio, and $\hbar$ is Planck's constant divided by 2π. The ratio n_k/n_0 is not thereby restricted. Although the calculation that follows will not assume small signal conditions explicitly the neglect of non-linear terms implicitly makes this assumption. The criterion for the range of applicability will be discussed in terms of SUHL's theory.

In deriving the linear saturation relation we shall begin with CALLEN's[4] analysis of the three transitions that we are considering. The interaction term in the Hamiltonian for the uniform precession-phonon transition is given as:

$$\mathscr{H}_{0\sigma} \sim [b_\sigma^+ S_0^- + b_\sigma^- S_0^+] \qquad (10)$$

where S_0^+ and S_0^- are the creation and destruction operators for the uniform precession magnons and b_σ^+ and b_σ^- are similar operators for phonons. Similarly for the uniform precession-spinwave transition we have:

$$\mathscr{H}_{0k} \sim [S_k^+ S_0^- + S_k^- S_0^+] \qquad (11)$$

where S_k^+ and S_k^- are creation and destruction operators for spinwaves. For the spinwave-phonon transition the interaction term is:

$$\mathscr{H}_{k\sigma} \sim [b_\sigma^+ S_k^- + b_\sigma^- S_k^+] \qquad (12)$$

The matrix elements of equation (10) are:

$$|\langle b_\sigma^+ S_0^- \rangle|^2 \sim (n_\sigma + 1) n_0 \qquad (13)$$

where n is the number of phonons: and:

$$|\langle b_\sigma^- S_0^+ \rangle|^2 \sim n_\sigma (n_0 + 1) \qquad (14)$$

so that the probability for the transition becomes:

$$P_{0\sigma} \sim (n_\sigma + 1) n_0 - n_\sigma (n_0 + 1) = n_0 - n_\sigma \simeq n_0 \qquad (15)$$

* The term linear as used in this paper refers to the rate equations that govern the occupation numbers of the spinwave states.

Vol. 17
1960

Similarly for equations (11) and (12);

$$P_{0k} \sim n_0 - n_k \tag{16}$$

$$P_{k\sigma} \sim n_k - n_\sigma \simeq n_k \tag{17}$$

We now depart from CALLEN's formulation by not assuming $n_k \ll n_0$, however we will neglect the number of phonons, n_σ, with respect to n_0 and n_k. In doing this we assume that the lattice is thermostated by the surroundings so that n_σ is constant and can be accounted for by using the measured saturation magnetization at the temperature at which we desire the transition parameters. From equations (15)–(17) we may now write the equations for the rate of change of n_0 and n_k.

$$\dot{n}_0 = -\lambda_{0\sigma} n_0 - \sum_k \lambda_{0k}(n_0 - n_k) + \frac{\chi'' h^2}{2\hbar} \tag{18}$$

$$\dot{n}_k = \lambda_{0k}(n_0 - n_k) - \lambda_{k\sigma} n_k \tag{19}$$

The last term in equation (18), where h is the linearly polarized r.f. magnetic field and χ'' is the imaginary part of the diagonal component of the r.f. magnetic susceptibility tensor, represents the number of uniform precession magnons created by the r.f. magnetic field perun it time. At equilibrium we have:

$$\dot{n}_0 = \dot{n}_k = 0 \tag{20}$$

and we can solve equations (18) and (19) for n_0 and n_k.*

$$n_0 = \left(\lambda_{0\sigma} + \sum_k \frac{\lambda_{0k}\lambda_{k\sigma}}{\lambda_{0k} + \lambda_{k\sigma}}\right)^{-1} \frac{\chi'' h^2}{2\hbar} \tag{21}$$

$$n_k = \frac{\lambda_{0k}}{\lambda_{0k} + \lambda_{k\sigma}} \left(\lambda_{0\sigma} + \sum_k \frac{\lambda_{0k}\lambda_{k\sigma}}{\lambda_{0k} + \lambda_{k\sigma}}\right)^{-1} \frac{\chi'' h^2}{2\hbar} \tag{22}$$

The ratio of these equations immediately enables us to determine the effect of assuming $n_k \ll n_0$.

$$\frac{n_k}{n_0} = \frac{\lambda_{0k}}{\lambda_{0k} + \lambda_{k\sigma}} \tag{23}$$

It is then seen that if $n_k \ll n_0$ we must have $\lambda_{k\sigma} \gg \lambda_{0k}$. It should also be noticed that the upper limit on the total number of spinwave magnons relative to the number of uniform precession magnons depends directly on the number of independent spinwave modes excited.† The maximum number of spinwaves are excited if $\lambda_{0k} \gg \lambda_{k\sigma}$ for each independent mode, under this condition $n_0 = n_k$ and the ratio

$$\sum_k n_k / n_0$$

is then just equal to the number of independent spinwave modes excited and can be very much greater than one.

The total number of independent spinwave modes excited (K) is then important for the determination of

$$\sum_k n_k / n_0$$

and, as will be seen later, for the interpretation of data. It must be pointed out that this analysis has not taken into account the transitions between $k \neq 0$ spinwaves. Actually equation (19) should contain a term

$$-\sum_j \lambda_{kj}(n_k - n_j)$$

where j is another spinwave mode, however to avoid the mathematical complications caused by this term we will make certain assumptions about the parameter λ_{kj}. We will assume that λ_{kj} is either zero or infinity, i.e. the interaction between the spinwaves is so weak that it may be neglected or is so strong that the interacting spinwaves may be treated as one mode since the strong interaction tends to equalize their populations instantly. Therefore what we mean by independent modes are those whose interaction with other modes may be neglected. This means the value K to be used in these calculations is not necessarily equal to the greatest number of modes into which one can scatter a uniform precession magnon. The problem

* Equations similar to these were derived previously[10] for the case of only one independent spinwave mode. The results given in that paper are then special cases of the results obtained here.

† In this paper the term spinwave is defined as one magnon of any k. Spinwave mode is taken to be synonymous with normal mode. An independent spinwave mode is a mode or group of modes whoes interaction with all other modes (except $k = 0$) can be neglected.

of the value to be taken for K must be investigated for each system along with $\lambda_{0\sigma}$, λ_{0k}, and $\lambda_{k\sigma}$.

We will now relate n_0 and n_k to the magnetization of the sample. CALLEN[4] has shown that the number of $k \neq 0$ magnons is given by:

$$M = M_0 - \sum_k \gamma\hbar n_k \tag{24}$$

and for an ellipsoid of revolution about the axis of the d.c. magnetic field the number of $k = 0$ magnons is:

$$M_z = M - \gamma\hbar n_0 \tag{25}$$

M_z is related to M and the transverse magnetization by:

$$|M_+|^2 + M_z^2 = M^2 \tag{26}$$

where M_+ is the circularly polarized component of transverse magnetization ($M_x + iM_y$). Since:

$$\chi'' = \frac{M^+}{h} \tag{27}$$

we have:

$$-(\chi'')^2h^2 = -2\gamma\hbar n_0 M + \gamma^2\hbar^2 n_0^2 \tag{28}$$

Substituting for M by equation (24) and for n_0 and n_k by equations (21) and (22) we obtain:

$$-\chi'' = -\gamma M_0\left(\lambda_{0\sigma} + \sum_k \frac{\lambda_{0k}\lambda_{k\sigma}}{\lambda_{0k}+\lambda_{k\sigma}}\right)^{-1} + \\ + \frac{\gamma^2}{4}\chi''h^2\left(\lambda_{0\sigma} + \sum_k \frac{\lambda_{0k}\lambda_{k\sigma}}{\lambda_{0k}+\lambda_{k\sigma}}\right)^{-2} \times \\ \times\left(2\sum_k \frac{\lambda_{0k}}{\lambda_{0k}+\lambda_{k\sigma}} + 1\right) \tag{29}$$

In the small signal region where we may neglect the terms containing h^2 we find that the susceptibility is given by:

$$\chi_0'' = \frac{M_0}{\Delta H} = \gamma M_0\left(\lambda_{0\sigma} + \sum_k \frac{\lambda_{0k}\lambda_{k\sigma}}{\lambda_{0k}+\lambda_{k\sigma}}\right)^{-1} \tag{30}$$

so that:

$$\Delta H = \frac{1}{\gamma}\left(\lambda_{0\sigma} + \sum_k \frac{\lambda_{0k}\lambda_{k\sigma}}{\lambda_{0k}+k_\sigma}\right) \tag{31}$$

Equation (29) may then be solved for χ'' to obtain:*

$$\frac{\chi''}{\chi_0''} = \frac{1}{1 + \frac{1}{4}\frac{h^2}{(\Delta H)^2}\left(2\sum_k \frac{\lambda_{0k}}{\lambda_{0k}+\lambda_{k\sigma}} + 1\right)} \tag{32}$$

Equation (31) may now be used to assist in evaluating the transition parameters from the data. However before we can apply equation (32) to saturation measurements we must examine the consequences entailed by restricting this analysis to linear transitions. SUHL[9] has shown that nonlinear effects cause a premature saturation in ferrimagnetics and if the threshold field for this process is not greater than the r.f. magnetic field required for linear saturation, equation (32) cannot be used. SUHL has shown that the threshold r.f. magnetic field for nonlinear effects is given by:

$$h_c = \Delta H\sqrt{\left(\frac{\Delta H_k}{4\pi M_0}\right)} \tag{33}$$

where ΔH_k is the linewidth of the spinwave whose population begins to increase greatly at threshold causing the susceptibility to decline. The r.f. field at which the susceptibility is reduced to one half the small signal value is given by:

$$\frac{1}{4}\frac{h_{\frac{1}{2}}^2}{(\Delta H)^2}\left(2\sum_k \frac{\lambda_{0k}}{\lambda_{0k}+\lambda_{k\sigma}} + 1\right) = 1 \tag{34}$$

To use equation (32) we must have $h_c^2/h_{\frac{1}{2}}^2 > 1$. This ratio is seen to be:

$$\frac{h_c^2}{h_{\frac{1}{2}}^2} = \frac{\Delta H_k}{16\pi M_0}\left(2\sum_k \frac{\lambda_{0k}}{\lambda_{0k}+\lambda_{k\sigma}} + 1\right) \tag{35}$$

This ratio will be greater than one if $\Delta H_k > 16\pi M_0$. Experiments[8,13,14] have shown that this is not the case for most ferrites, although it can occur.[14] Even if this condition does not

* In a previous calculation[11,12] an attempt was made, which used the small signal approximation, to derive a relation that would indicate the onset of linear saturation. The relation obtained is not a special case of equation (32) because the small signal assumption is not valid in this region.

Vol. 17
1960

hold we may still have:

$$\Delta H_k \sum_k \frac{\lambda_{0k}}{\lambda_{0k}+\lambda_{k\sigma}} > 8\pi M_0 \tag{36}$$

if the number of independent modes is large enough. Since the largest value the ratio $\lambda_{0k}/\lambda_{0k}+\lambda_{k\sigma}$ may have is one, we must have:

$$K\Delta H_k > 8\pi M_0 \tag{37}$$

where we assume $\lambda_{0k} \gg \lambda_{k\sigma}$. As previously mentioned the number of independent modes (K) must be investigated for each material. The value we should use for K is not presently known for any material but it does not seem probable that equation (36) will prevail for most ferrimagnetics. Therefore, except for special cases, equation (32) cannot be used since the observable saturation will be due to nonlinear effects.

Although we may not in general use the saturation phenomena in ferrimagnetics to assist in evaluating the transition parameters by means of equation (32), we may still use the saturation phenomena by applying the results of SUHL's nonlinear theory and using equation (33) for the determination of ΔH_k. Since ΔH_k is defined by SUHL as a linewidth expressing the net loss mechanism of the spinwaves, we may write:

$$\gamma\Delta H_k = \lambda_{k\sigma} \tag{38}$$

The $\lambda_{k\sigma}$ determined in this manner is that of the spinwave that is responsible for the onset of the saturation effect as described by SUHL[9]. A similar interpretation is applicable to the low d.c. magnetic field instability described by SUHL[9] and the parallel field instability described by SCHLÖMANN[14].

MEASUREMENT OF THE TRANSITION PARAMETERS BY A MODULATION TECHNIQUE

FLETCHER *et al.*[8] have recently described a modulation method for the determination of the transition parameters in ferrimagnetics. Their method consists of modulating the microwave signal at a frequency ω and measuring components at 2ω, generated in the sample, proportional to M_z and M^2 (see Ref. 8 for complete details). They have derived the relation given below for the square of the ratio of these components (R^2). In deriving this relation it was necessary to assume that for the spinwaves excited $\lambda_{k\sigma}$ is independent of k, i.e. it has the same value for all spinwave modes excited.

$$R^2 = \frac{1+\left(\frac{2\omega}{\lambda_{k\sigma}}\right)^2\left[\frac{T_2}{\frac{2}{\lambda_{k\sigma}}+\left(1-\frac{\lambda_{0\sigma}}{\lambda_{k\sigma}}\right)T_2}\right]^2}{1+\left(\frac{2\omega}{\lambda_{k\sigma}}\right)^2} \tag{39}$$

T_2 is given by:

$$T_2 = \frac{2}{\gamma\Delta H} \tag{40}$$

and can be evaluated from equation (6) as:

$$T_2 = \frac{2}{\lambda_{0\sigma}+\sum_k \lambda_{0k}} \tag{41}$$

From equation (31) it is seen that the expression for T_2 including reaction terms is:

$$T_2 = \frac{2}{\lambda_{0\sigma}+\sum_k \frac{\lambda_{0k}\lambda_{k\sigma}}{\lambda_{0k}+\lambda_{k\sigma}}} \tag{42}$$

As we should expect this expression reduces to equation (41) if $\lambda_{k\sigma} \gg \lambda_{0k}$ for each spinwave mode.

Returning to the calculation for R^2, we may eliminate T_2 from equation (39) by using equation (41) and we find:

$$R^2 = \frac{1+\left(\frac{2\omega}{\lambda_{k\sigma}}\right)^2\left(\sum_k \frac{\lambda_{0k}}{\lambda_{k\sigma}}+1\right)^{-2}}{1+\left(\frac{2\omega}{\lambda_{k\sigma}}\right)^2} \tag{43}$$

We have derived an expression for R^2 in the manner of FLETCHER *et al.* except that we have used equations (18) and (19) containing the reaction terms. We find that:

$$R^2 = \frac{1+\left(\frac{2\omega}{\lambda_{k\sigma}+(K+1)\lambda_{0k}}\right)^2}{1+\left(\frac{2\omega}{\lambda_{0k}+\lambda_{k\sigma}}\right)^2} \tag{44}$$

In deriving this expression it is found that it is necessary to make the same assumption about λ_{0k} that has already been made about $\lambda_{k\sigma}$. That is in the calculation of R^2 including reaction terms it is necessary to assume that for the excited spinwave modes λ_{0k} is independent of k.

Since it was necessary to assume λ_{0k} and $\lambda_{k\sigma}$ are independent of k in the analysis of the modulation method as repeated here including the reaction terms, the modulation method is therefore not as general as one might have hoped. If one avoids this assumption the calculation's complexity greatly increases, however since the present information on the transition parameters and K is rather scarce, this assumption is perhaps good for a first attempt at the evaluation of these parameters.

LONGITUDINAL RELAXATION TIME

In connection with their work on the modulation technique FLETCHER *et al.* have derived an expression for an effective longitudinal relaxation time by considering the steady state energy and comparing it with the steady state energy predicted by equations (3) and (4). They obtain:

$$T_1 = \frac{T_2}{2}\left(1+\sum_k \frac{\lambda_{0k}}{\lambda_{k\sigma}}\right) \tag{45}$$

Repeating the calculation using equations (21) and (22) we find:

$$T_1 = \frac{T_2}{2}\left(1+\sum_k \frac{\lambda_{0k}}{\lambda_{0k}+\lambda_{k\sigma}}\right) \tag{46}$$

This equation yields the result that:

$$\frac{2T_1}{K+1} \leqslant T_2 \leqslant 2T_1 \tag{47}$$

The limit $T_2 = 2T_1$ applies when

$$\sum_k \lambda_{0k}/\lambda_{k\sigma} \ll 1$$

and therefore, by equation (22)

$$\sum_k n_k \ll n_0.$$

This is the case previously discussed by FLETCHER *et al.* The limit $T_2 = 2T_1/K+1$ applies when $\lambda_{0k} \gg \lambda_{k\sigma}$ and therefore $n_0 = n_k$.

We will now consider some experimental measurements to see how these are effected by the inclusion of the spinwave reaction terms. SPENCER and LECRAW[15] have recently published measurements of T^1, obtained from modulation measurements, using equations (39) and (45). The values for well polished single crystal yttrium iron garnet at 2·5°K are given as:

$$T_1 = 1{\cdot}3\times10^{-6}\text{ sec} \qquad T_2 = 0{\cdot}81\times10^{-6}\text{ sec}$$

where T_2 is obtained from a linewidth measurement by equation (40). Inserting these values in equations (45) we obtain:

$$\sum_k \frac{\lambda_{0k}}{\lambda_{k\sigma}} = 2{\cdot}2$$

Equations (44) and (46) should properly be used instead of equations (39) and (45). Using the above value of

$$\sum_k \lambda_{0k}/\lambda_{k\sigma}$$

in equation (43) to find the experimentally measured value of R^2 and then using this value together with equations (44) and (46) we find:

$$T_1 = \frac{T_2}{2}\left(1+\frac{2{\cdot}2K}{6{\cdot}4+K}\right) \tag{49}$$

or:

$$0{\cdot}53\times10^{-6}\text{ sec} \leqslant T_1 \leqslant 1{\cdot}3\times10^{-6}\text{ sec} \tag{50}$$

The smaller value applies if $K = 1$ and the larger if K is very large. The value for large K is just that obtained by SPENCER and LECRAW because to be able to neglect reaction terms it is only necessary to have $n_k \ll n_0$ for each independent spinwave mode. The fact that

$$\sum_k \lambda_{0k}/\lambda_{k\sigma} = 2{\cdot}2$$

and therefore

$$\sum_k n_k/n_0 = 2{\cdot}2$$

only means that K must be very large if $\lambda_{0k} \ll \lambda_{ko}$.

The assumption of large K might be acceptable for a well polished sample of yttrium iron garnet

Vol. 17
1960

if the scattering into spinwaves is not mostly due to the remaining surface imperfections. This is because we might expect that if the bulk of the scattering is due to volume scatterers of various sorts and sizes, which occur since the crystal is not perfect, we then would excite a great number of modes slightly and would therefore have small λ_{0k} and large K. If the surface imperfections are causing the scattering, as is the case with more poorly polished samples, the assumption of large K is probably not justified since the important spinwaves would be those whose wavelengths are of the same order as the size of the surface imperfections and these modes will be excited heavily. Also as soon as one mode is heavily excited the reaction terms must be included, at least for this mode, and the value of K is no longer important for establishing the validity of neglecting reaction terms. The value of K, however, is still important for understanding the basic processes in the system and as we have previously indicated, the investigation of the independent modes deserves considerable attention.

It would seem that since the parameters $\lambda_{0\sigma}$, λ_{0k}, and $\lambda_{k\sigma}$ (or the inverse parameters T_{10}, T_{2k}, and T_{1k}) are basically more fundamental than T_1 it is more reasonable to discuss them directly than to calculate a T_1 from them. Also there is a difficulty in defining a unique T_1 in analogy with paramagnetic resonance. FARRAR[16] has measured the relaxation time for a sample of polished yttrium iron garnet by directly observing the decay of ΔM_z after rapidly turning off the microwave power. However FARRAR's relaxation time, which we call T_1^*, is not necessarily equal to the T_1 determined by the steady state energy balance approach. To find T_1^* we must solve the equation of motion for (M_0-M_z). Consider equations (6) and (7) for the case of no microwave magnetic field. The transverse equation may be solved to yield:

$$M_+ = C\exp[i\gamma H_0-(1/T_2)]t \tag{51}$$

The equation for (M_0-M_z) may be rewritten as:

$$\frac{d(M_0-M_z)}{dt} = -\frac{|M+|^2}{2M_0}\left(\frac{1}{T_{10}}-\frac{1}{T_{1k}}\right)- -\frac{M_0-M_z}{T_{1k}} \tag{52}$$

Substituting equation (51) for M_+ we have:

$$\frac{d(M_0-M_z)}{dt}+\frac{M_0-M_z}{T_{1k}}+ +\frac{C^2}{2M_0}\exp[-(2t/T_2)]\left(\frac{1}{T_{10}}-\frac{1}{T_{1k}}\right)=0 \tag{53}$$

The solution to this equation is not a single exponential but is in fact a sum of two exponentials. The solution is of the form:

$$(M_0-M_z) = C_1\exp[-(t/T_{1k})]+ +C_2\exp[-(2t/T_2)] \tag{54}$$

Therefore T_1^* is not a unique relaxation time. One might hope to evaluate T_{1k} from T_1^* if $T_1^* > T_2/2$, which is actually the case experimentally. However the equation of motion that we have used here does not include the effect of reaction terms. One must first find equations of motion that take the reaction terms into account and then solve them for (M_0-M_z). The above calculation is only to point out that one must be careful in using a quantity of the type of T_1 and not assume too much of an analogy with paramagnetic resonance and the results of the Bloch–Bloembergen equations.

EQUATIONS OF MOTION

If we again assume, as we have done in the analysis of the modulation technique, that λ_{0k} and $\lambda_{k\sigma}$ are independent of k, we may very simply derive equations, similar to equations (6) and (7), including the effect of the reaction terms. This is done by taking equations (18) and (19) and eliminating n_0 and n_k by equations (24) and (25). We then have:

$$\frac{d(M-M_z)}{dt} = -(\lambda_{0\sigma}+K\lambda_{0k})(M-M_z)+ +\lambda_{0k}(M_0-M)+\frac{\gamma}{2}\chi''h^2 \tag{55}$$

$$\frac{d(M_0-M)}{dt} = K\lambda_{0k}(M-M_z)- -(\lambda_{0k}+\lambda_{k\sigma})(M_0-M) \tag{56}$$

Since we have established that the linear process

approximation is only valid for the small-signal region we will incorporate the small signal approximation here and let:

$$M = \sqrt{(M_x^2+M_y^2+M_z^2)} \simeq M_z+\frac{M_x^2+M_y^2}{2M_0} \quad (57)$$

so that equation (55) becomes:

$$\frac{1}{2M_0}\frac{d(M_x^2+M_y^2)}{dt} = -[(K+1)\lambda_{0k}+\lambda_{0\sigma}]\times \times\frac{M_x^2+M_y^2}{2M_0}+\lambda_{0k}(M_0-M_z)+\frac{\gamma}{2}\chi''h \quad (58)$$

and the sum of equations (55) and (56) is:

$$\frac{d(M_0-M_z)}{dt} = -\frac{M_x^2+M_y^2}{2M_0}(\lambda_{0\sigma}-\lambda_{k\sigma})- -\lambda_{k\sigma}(M_0-M_z)+\frac{\gamma}{2}\chi''h^2 \quad (59)$$

Making equations (58) and (59) consistent with the following equation of motion for no loss:

$$\dot{\boldsymbol{M}} = -\gamma \boldsymbol{M}\times\boldsymbol{H} \quad (60)$$

we obtain the equations of motion as:

$$\dot{M}_{x,y} = -\gamma(\boldsymbol{M}\times\boldsymbol{H})_{x,y}-[(K+1)\lambda_{0k}+\lambda_{0\sigma}]\times \times\frac{M_{x,y}}{2}+M_0\lambda_{0k}\frac{(M_0-M_z)}{M_{x,y}} \quad (61)$$

$$(\dot{M}_0-M_z) = \gamma(\boldsymbol{M}\times\boldsymbol{H})_z-\frac{M_x^2+M_y^2}{2M_0}(\lambda_{0\sigma}-\lambda_{k\sigma})- -\lambda_{k\sigma}(M_0-M_z) \quad (62)$$

By comparison with equations (6) and (7) we see that the equation of motion for the z-component of the magnetization is unchanged by the inclusion of the reaction terms. The transverse equation, however, has gained an additional term which is inversely proportional to the transverse magnetization.

Equation (5) can also be used as an equation of motion if desired. All that is necessary to put it in the proper form is to derive α and λ in terms of the three transition parameters as CALLEN[4] has done but use equations (18) and (19) in place of the analogous equations without the reaction terms.

REFERENCES

1. AKHIESER A., *J. Phys., Moscow* **10,** 217 (1946).
2. KITTEL C. and ABRAHAMS E., *Rev. Mod. Phys.* **25,** 233 (1953).
3. BLOEMBERGEN N. and WANG S., *Phys. Rev.* **93,** 72 (1954).
4. CALLEN H. B., *J. Phys. Chem. Solids* **4,** 256 (1958).
5. LANDAU L. and LIFSHITZ L., *Phys. Z. Sowjet.* **8,** 153 (1935).
6. GILBERT T. A., Armour Research Institute Unpublished Reports.
7. BLOCH F., *Phys. Rev.* **70,** 460 (1946).
8. FLETCHER R. C., LECRAW R. C. and SPENCER E. G., *Phys. Rev.* **117,** 955 (1960).
9. SUHL H., *J. Phys. Chem. Solids* **1,** 209 (1957).
10. SEIDEN P. E., *C.R. Acad. Sci., Paris* **250,** 2530 (1960).
11. SEIDEN P. E. and SHAW H. J., *J. Appl. Phys.* **31,** 225S (1930).
12. SEIDEN P. E., *Report M.L.* 657, Oct. 1959. W. W. Hansen Laboratories of Physics, Stanford University.
13. SEIDEN P. E. and SHAW H. J., *Proc. Inst. Radio. Engrs. N.Y.* **48,** 122 (1960).
14. SCHLÖMANN E., GREEN J. J. and MILANO U., *J. Appl. Phys.* **31,** 386S (1960).
15. SPENCER E. G. and LECRAW R. C., *Phys. Rev. Letters* **4,** 130 (1960).
16. FARRAR R. T., *J. Appl. Phys.* **29,** 425 (1958).

Vol. 17
1960

J. Phys. Chem. Solids Pergamon Press 1961. Vol. 17, Nos. 3/4, pp. 267–277. Printed in Great Britain.

NUCLEAR QUADRUPOLE SPIN–LATTICE RELAXATION IN SOLIDS*

M. J. WEBER†

Department of Physics, University of California, Berkeley 4, California

(*Received* 11 *July* 1960)

Abstract—Nuclear quadrupole spin–lattice relaxation in solids has been investigated using pulsed nuclear induction techniques. By selective excitation of the quadrupolar spin system, several new modes of relaxation are observed. Measurements of these modes are used to determine the individual transition probabilities W_1 and W_2 associated with $\Delta m = \pm 1$ and ± 2 quadrupole spin–lattice relaxation. W_1, W_2, and the spin–lattice relaxation time T_1 of the Cl^{35} pure quadrupole resonance in p–$C_6H_4Cl_2$, $KClO_3$, and $NaClO_3$ have been measured in the temperature range 77–300°K. The BAYER theory of quadrupole spin–lattice relaxation is applied to p–$C_6H_4Cl_2$ to calculate W_1 and W_2. From the BAYER theory and the separate measurement of W_1 and W_2, information is obtained about the lifetime of excited torsional states and the mode of torsional oscillation which provides the dominant relaxation contribution in p–$C_6H_4Cl_2$. Measurements of the spin–lattice relaxation in $NaClO_3$ and $KClO_3$ are compared with CHANG's theory of quadrupole relaxation. The experimental results suggest that the model used by CHANG to describe the fluctuating internal electric field gradient in $NaClO_3$ responsible for the Cl^{35} relaxation is inadequate.

1. INTRODUCTION

A NUMBER of detailed theories of nuclear quadrupole spin–lattice relaxation have been developed.[1–4] These theories differ principally in the model used to define the source of the electric field gradient at the nucleus and the manner in which the quadrupole interaction is thermally modulated. For each model, an explicit calculation is made of the transition probabilities generated by the time-dependent quadrupole Hamiltonian. Since the quadrupole Hamiltonian operator[5] has off-diagonal matrix elements leading to relaxation transitions in which the nucleus changes its magnetic quantum number m by ± 1 and ± 2, one must compute two transition probabilities to describe the observed spin–lattice relaxation process. These two probabilities will not be equal, in general, since not only do they involve different spin operators, but, more important, they involve different components of the fluctuating crystalline electric field gradient tensor.

The experimental verification of spin–lattice relaxation theories rests upon the measurement of the rate or characteristic time of the relaxation and its temperature dependence, and upon relating the results to calculated transition probabilities. For the case of quadrupole relaxation in a quadrupolar spin system, two complications are present. First, unlike the equally spaced nuclear Zeeman energy levels produced by a magnetic field, the separations between adjacent energy levels arising from nuclear quadrupole coupling in solids are all unequal.[6] Second, whereas in magnetic dipole relaxation only $\Delta m = \pm 1$ relaxation transitions are present, there are two possible transitions active in quadrupole relaxation, $\Delta m = \pm 1$ and $\Delta m = \pm 2$, with transition probabilities W_1 and W_2 respectively. Due to the more complicated energy level scheme and the presence of two different relaxation transitions, it is not generally possible to assign a unique characteristic relaxation time to a quadrupolar spin system. Observable resonances between successive levels will, in general, have different modes and rates of

* Supported in part by the Office of Naval Research and the National Security Agency.

† Submitted by M. J. WEBER in partial fulfillment of the requirements for the degree of Doctor of Philosophy, University of California. Present Address: Research Division, Raytheon Company, Waltham 54, Massachusetts.

relaxation.[7] A careful analysis is usually required to see explicitly how the relaxation of a specific resonance line proceeds and how the two transition probabilities W_1 and W_2 enter.

To obtain complete confirmation of the theoretical predictions of quadrupole relaxation theories, it is desirable to determine experimentally W_1 and W_2 separately. Since these transition probabilities are proportional to different components of the fluctuating electric field gradient tensor, they provide a sensitive and critical test of the model chosen to describe the source of the crystalline electric field gradient. The primary purpose of the experiments discussed in this paper is to measure the individual probabilities W_1 and W_2 using pulsed nuclear induction techniques. The measurements obtained for several non-cubic solids containing quadrupolar spin systems are compared with the predictions of the quadrupole spin–lattice relaxation theories of BAYER[1] and CHANG[4] and the validity of these theories is discussed.

In this paper we will consider only the relaxation of nuclei with spin $I = 3/2$. The study of the quadrupole relaxation of nuclei with $I > 3/2$ can be made using a straightforward extension of the techniques developed in this paper.* For the case of $I = 3/2$ the pure quadrupole resonance spectrum consists of a single observable transition.[6] A simple analysis shows that the quadrupole spin–lattice relaxation is characterized by a single relaxation time which is inversely proportional to the sum of W_1 and W_2. To determine W_1 and W_2 separately, a small Zeeman magnetic field is applied to the spin system to remove the Kramer's $\pm m$ degeneracy of the quadrupole energy levels and thereby introduce additional observable transitions. Since these transitions involve the resonance of different portions of the total quadrupolar spin system, by selectively exciting and observing the relaxation of these component resonance lines, additional information about the relaxation process is obtained. We now analyze the time dependence of the quadrupole spin–lattice relaxation for the case of a quadrupolar spin system with Zeeman field splitting.

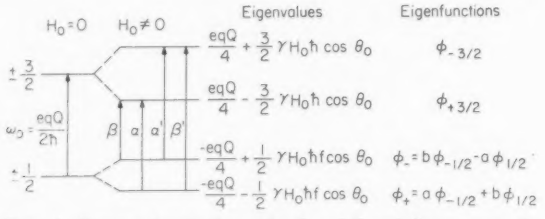

FIG. 1. Energy levels for spin $I = 3/2$ axially symmetric quadrupole interaction perturbed by a small magnetic field H_0 applied to an angle θ_0 with respect to the symmetry axis of the electric field gradient. Parameters are

$$a^2 = \left(\frac{f-1}{2f}\right),\ b^2 = \frac{f+1}{2f},\ f^2 = 1+4\tan^2\theta_0.$$

2. SPIN–LATTICE RELAXATION

In zero magnetic field, the spin $I = 3/2$ quadrupole spectrum consists of a single frequency transition between the two doubly degenerate quadrupole energy levels $\pm 1/2$ and $\pm 3/2$. If a small external magnetic field H_0 is applied to remove the $\pm m$ degeneracy, the spectrum is split into four component lines shown as transitions α, α', β, β' in Fig. 1. The electric field gradient at the nucleus is assumed to have axial symmetry. If the lines are separated by a field $H_0 \gg \Delta H$, where ΔH is the equivalent resonance line width in Oe the individual resonance lines will not overlap appreciably and any cross relaxation via spin–spin

* If the nuclei of interest have spin $I \geqq 2$, the pure quadrupole resonance spectrum[6] will consist of two or more distinct resonance lines. Each line will exhibit a different mode of relaxation and will involve a different functional combination of W_1 and W_2. The measurement and analysis of the relaxation of two modes will provide two data sufficient to determine the two transition probabilities W_1 and W_2.

Vol. 17
1960

interactions will be negligible.[8] Since the coupling between the nuclear spin system and the lattice in a solid via electric quadrupole interactions is, in general, several orders of magnitude greater than via magnetic dipole interactions,[9] the former will be considered to be the sole spin–lattice relaxation mechanism present.

The rate equations for the spin state populations N_i, where $i = 3/2,\ -3/2,\ +,\ -$, designates the eigenstates in Fig. 1, subject to $\Delta m = \pm 1$ and ± 2 quadrupole spin–lattice relaxation transitions with probabilities W_1 and W_2, respectively are

$$\begin{aligned}\frac{dN_{\pm 3/2}}{dt} &= -(W_1'+W_2')N_{\pm 3/2} \\ &\quad +(b^2W_1+a^2W_2)N_{\pm}+(a^2W_1+b^2W_2)N_{\mp}, \\ \frac{dN_{\pm}}{dt} &= -(W_1+W_2)N_{\pm} \\ &\quad +(b^2W_1'+a^2W_2')N_{\pm 3/2} \\ &\quad +(a^2W_1'+b^2W_2')N_{\mp 3/2}. \end{aligned} \tag{1}$$

The quantities a and b are functions of the angle θ_0 between the magnetic field direction and the symmetry axis of the electric field gradient and are defined in Fig. 1. The unprimed and primed transition probabilities indicate upward and downward transitions, respectively, and are weighted by the appropriate Boltzmann factor for the system. Since the magnetic field splitting is assumed to be very much smaller than the quadrupole energy level separation, i.e. $\gamma\hbar H_0 \ll eqQ$, the Boltzmann factors for each relaxation transition are taken to be equal.

The general solutions of (1) are expressed in terms of the net macroscopic nuclear magnetization associated with the four observable transitions α,α', β,β', i.e.

$$M_{\alpha,\alpha'} \propto (N_{\pm}-N_{\pm 3/2}),\ M_{\beta,\beta'} \propto (N_{\mp}-N_{\pm 3/2}).$$

These are given by

$$\begin{aligned} M_{\alpha,\alpha'}(t) &= b^2M_0+C_1\exp[-2(W_1+W_2)t] \\ &\quad \pm C_2\exp[-2(b^2W_1+a^2W_2)t], \\ M_{\beta,\beta'}(t) &= a^2M_0+C_3\exp[-2(W_1+W_2)t] \\ &\quad \pm C_4\exp[-2(a^2W_1+b^2W_2)t], \end{aligned} \tag{2}$$

where

$$\begin{aligned} 2C_1 &= M_\alpha(0)+M_{\alpha'}(0)-2b^2M_0, \\ 2C_2 &= M_\alpha(0)-M_{\alpha'}(0), \\ 2C_3 &= M_\beta(0)+M_{\beta'}(0)-2a^2M_0, \\ 2C_4 &= M_\beta(0)-M_{\beta'}(0). \end{aligned} \tag{3}$$

$M(0)$ is the initial value of magnetization at time $t = 0$. M_0 is equal to one-half the thermal equilibrium magnetization of the total unperturbed quadrupolar spin system.

From (2) we see that both the α,α' lines and β,β' lines, which are symmetrically displaced from the pure quadrupole resonance frequency, form a pair of relaxation modes with a time dependence made up of a linear combination of two exponential terms. This particular transient recovery arises from cross communication between the Zeeman lines introduced by relaxation transitions which transfer spins from eigenstates associated with one line to new eigenstates associated with a different line. Note that a^2 and b^2, which are a measure of the admixture of the $\phi_{1/2}$ and $\phi_{-1/2}$ states in the new magnetic states ϕ_+ and ϕ_-, enter as multipliers of W_1 and W_2 in the second exponential term in (2). Since these quantities are a function of the angle θ_0 of the applied magnetic field, the relative contributions of W_1 and W_2 to the relaxation of the given line can be varied.

In the limit of zero applied magnetic field, the intensity of the β,β' lines goes to zero and the α,α' lines coalesce into a single observable transition. The relaxation of this resonance is described by the sum of $M_\alpha(t)$ and $M_{\alpha'}(t)$ in (2) and is given by

$$\begin{aligned} M(t) &= 2M_0+\left(\frac{M_+(0)+M_-(0)-2M_0}{2}\right) \\ &\quad \times \exp[-2(W_1+W_2)t]. \end{aligned} \tag{4}$$

Since the approach to equilibrium of a spin 3/2 quadrupolar spin system has a simple exponential time dependence given by (4), it is possible to define a spin–lattice relaxation time

$$T_1 = [2(W_1+W_2)]^{-1}. \tag{5}$$

T_1 is measured by observing the relaxation of the zero field resonance.

3. EXPERIMENTAL TECHNIQUES

The longitudinal relaxation of the z-component

of nuclear magnetization has been observed and measured using pulsed nuclear magnetic induction techniques.[10] In this method a short intense pulse of resonant r.f. is applied to excite the spin system and to establish the initial conditions at $t = 0$ in (3). At some later time a second "inspection" r.f. pulse is applied to examine the relaxation of the system toward equilibrium. Since the amplitude of the resulting free nuclear precession signal is proportional to the associated z component of nuclear magnetization present when the r.f. pulse is applied, the height of the signal following the second pulse, relative to that of the first, is a direct measure of the longitudinal relaxation during the interval between pulses. By making a series of measurements at various pulse separations, the transient recovery of the spin system during relaxation is determined. Equation (2) describes the observable time-dependent behavior and value of magnetization at time t.

The determination of the individual probabilities W_1 and W_2 for quadrupolar spin–lattice relaxation is carried out by applying a small magnetic field to the sample. One of the Zeeman component lines of the resulting quadrupole spectrum is selectively excited and its relaxation observed. The measurement of the transient recovery (2) of any one of the α, α', β, β' groups of spin states combined with the measurement of T_1 from the zero magnetic field resonance is sufficient to evaluate the two exponential terms in (2) and thereby W_1 and W_2.

It should be noted that the measurement of a finite W_2 establishes that quadrupole spin–lattice relaxation is present, since if the relaxation was due to magnetic dipole interactions only $\Delta m = \pm 1$ transitions would occur. The observed W_1 will include contributions from both magnetic dipole and electric quadrupole interactions, however, as mentioned earlier, the latter is usually the dominant relaxation mechanism by several orders of magnitude. This determination of the quadrupolar nature of the relaxation mechanism by using pulse techniques and observing the dynamic recovery of a selected portion of the nuclear spin system is the transient analog of earlier experiments performed by POUND[9] using continuous wave, steady-state saturation techniques. POUND, however, studied systems of magnetic energy levels perturbed by the presence of small quadrupole interactions, whereas in the present experiments we study systems of quadrupole energy levels perturbed by small Zeeman magnetic fields.

It is desirable that certain conditions be satisfied when frequency separation techniques of selective excitation are used in pulsed nuclear induction experiments. First, the frequency separation of adjacent resonance lines and the r.f. pulse time should be such that the Fourier frequency spectrum of the r.f. pulse used to excite one line will not have frequency components of sufficient intensity to produce an observable excitation of adjacent lines. Second, a given resonance line must not overlap another if a clean selective excitation of a single line is to be obtained using linearly polarized r.f.* For an applied magnetic field H_0, the frequency separations[6] of component lines of the quadrupole spectrum are of the order of γH_0. Thus if

$$\gamma H_0 \gg 2\pi/t_w, \tag{6}$$

where t_w is the r.f. pulse time width, the first condition is satisfied. A fundamental requirement of pulsed nuclear induction experiments is[10]

$$1/t_w \gg \gamma \Delta H, \tag{7}$$

where ΔH is the equivalent resonance line width. The fulfillment of (6) and (7) insures that $H_0 \gg \Delta H$ and, therefore, the second condition above is automatically satisfied.

The pulsed r.f. oscillator and the receiver used to observe the free magnetic precession signals in these quadrupole resonance experiments were similar to apparatus described elsewhere.[6,12] The r.f. equipment was operated in the frequency region around 30 Mc/sec. Measurements of the spin–lattice relaxation were recorded using a gated "boxcar" integrator.[13] A Helmholtz coil was used to provide the small, homogeneous magnetic field for experiments involving Zeeman field splitting.

4. DISCUSSION OF EXPERIMENTAL RESULTS

(a) *Paradichlorobenzene—Bayer theory*

The spin–lattice relaxation of the chlorine nucleus in paradichlorobenzene has been examined to verify the BAYER theory[1] of the quadrupole spin–lattice relaxation, and to illustrate the usefulness of the additional information obtained by measuring

* Selective excitation of overlapping quadrupole resonance lines can be achieved by the use of circularly polarized r.f. See Refs. (8) and (11).

Vol. 17
1960

W_1 and W_2 separately. p–$C_6H_4Cl_2$ was chosen for this study since the quadrupole resonance spectrum has been thoroughly investigated,[14] the crystal structure is known,[15] and the modes and frequencies of molecular motions have been well established.[16] The two chlorine atoms in the p–$C_6H_4Cl_2$ molecule are bonded to the benzene ring at opposite corners. The field gradient at the position of the Cl nucleus is produced primarily by the C—Cl covalent bond and is the same at each site.

The spin–lattice relaxation time T_1 of Cl^{35} in a single crystal of p–$C_6H_4Cl_2$ was measured at room temperature at 34·26 Mc/sec and a value of 22 milliseconds observed, in agreement with previous data.[17] W_1 and W_2 were determined separately by applying a magnetic field making equal angles $\theta_0 = \tan^{-1}\sqrt{(2)}$ with respect to the two inequivalent Cl–Cl directions in the p–$C_6H_4Cl_2$ unit cell, and observing the relaxation of one of the β,β' Zeeman component lines. Using the time-dependent recovery predicted by equation (2), values of $W_1 = 4{\cdot}8\ \text{sec}^{-1}$ and $W_2 = 17{\cdot}9\ \text{sec}^{-1}$ were measured with an estimated error of $\pm 3\ \text{sec}^{-1}$.

BAYER's relaxation theory is based upon the effect of molecular torsional motions in crystals. These torsional motions are continuously interrupted by interaction with other vibrational and rotational degrees of freedom of the molecule and lead to random fluctuations of the electric field gradient seen by the nuclei. If the associated Fourier spectrum of electric field fluctuations has frequency components in the order of the quadrupole resonance frequency, electric quadrupole relaxation transitions will be induced. These random fluctuations are treated using a stochastic theory similar to that used by BLOEMBERGEN *et al.*[18] in the treatment of nuclear spin relaxation. The "correlation" functions for the torsional motions are characterized by τ_a, the lifetime of a molecule in an excited torsional state.

The theory is developed for a spin 3/2 quadrupole system having an axially symmetric field gradient. Treatment is made of a simplified case in which the molecule containing the nucleus of interest is assumed to undergo torsional oscillations about an axis perpendicular to the z principal axis of the electric field gradient. This corresponds to the $27\ \text{cm}^{-1}$ and $54\ \text{cm}^{-1}$ molecular torsional oscillations in p–$C_6H_4Cl_2$ which have been determined by Raman spectra studies.[16] BAYER's theoretical probabilities for $\Delta m = \pm 1$ and ± 2 relaxation transitions are given by

$$W_1 = \frac{3}{2}\frac{(\hbar\omega_Q)^2}{\hbar\omega_t^3 A\tau_a} \times \frac{2-e^{-x}}{e^x-1}, \qquad (8)$$

$$W_2 = \frac{3}{8}\frac{(\hbar\omega_Q)^2\tau_a}{(A\omega_t)^2} \times \frac{4\cosh x - 3}{(e^x-1)^2}.$$

ω_t is the torsional frequency, A is the corresponding moment of inertia of the molecule, ω_Q is the quadrupole resonance frequency, and x is defined as $\hbar\omega_t/kT$, where T is the absolute temperature.

To compare the BAYER theory directly with experiment, the value of the lifetime τ_a of a molecule in an excited torsional state is required. Since no independent measurements of τ_a are available, BAYER's theoretical values of W_1 and W_2 in (8) were related by (5) to the experimentally measured T_1 and possible values of τ_a found from the resulting quadratic equation using known values of ω_t, A, and ω_Q. The results are given in Table 1 for both the $27\ \text{cm}^{-1}$ and $54\ \text{cm}^{-1}$ torsional motions, together with the corresponding ratio of W_2 to W_1.

Table 1. *Excited torsional state lifetimes τ_a based on the Bayer theory using the measured value of $T_1 = 22$ milliseconds at* 300°K

Torsional frequency	τ_a(sec)	W_2/W_1
$27\ \text{cm}^{-1}$	$2{\cdot}1\times10^{-12}$ $6{\cdot}7\times10^{-12}$	0·3 3·2
$54\ \text{cm}^{-1}$	$1{\cdot}1\times10^{-13}$ $1{\cdot}4\times10^{-10}$	$8{\cdot}3\times10^{-4}$ 1400

Knowledge of T_1 and BAYER's theoretical predictions yields the four possible alternatives for τ_a given in Table 1, but does not establish which value, if any, is correct. This can be done, however, by utilizing the additional datum provided by the separate determination of W_1 and W_2. Within experimental error, the ratio W_2/W_1 was found to range from ~ 2–12. The only value of τ_a in Table 1, which gives a ratio W_2/W_1 consistent with experimental observation is $\tau_a = 6{\cdot}7\times10^{-12}$ sec

obtained from the 27 cm^{-1} oscillation. This is a reasonable value for τ_a and satisfies the requirement $\omega_l^2\tau_a^2 \gg 1$.

As a further test of the theory, the temperature dependence of the relaxation was measured in the region 77–300°K. The results are plotted in Fig. 2 together with the theoretical curve predicted by the BAYER theory using the known temperature dependence of the quadrupole resonance and torsional vibration frequencies. Agreement between

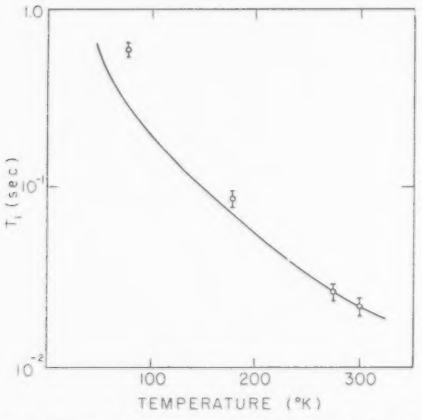

FIG. 2. T_1 vs. temperature for Cl^{35} in p–$C_6H_4Cl_2$. The solid curve is the theoretical plot using the BAYER theory and $\tau_a = 6{\cdot}7 \times 10^{-12}$ sec for the 27 cm^{-1} torsional oscillation.

theory and experiment becomes progressively poorer at lower temperatures. This is probably due to BAYER's simplifying assumptions concerning the character and lifetime of torsional states and the treatment of only one mode of torsional vibration. By extending the BAYER theory to include relaxation effects due to a general molecular and lattice vibration[19] and the influence of possible C—Cl bond stretching, the discrepancy might be remedied.

In addition to measuring the temperature dependence of T_1, the ratio W_2/W_1 was also determined at 77°K. The result was $W_2/W_1 \approx 1$ with an estimated error of $+1$, $-1/2$. The BAYER theory predicts a more rapid decrease of W_2 than W_1 as the temperature is lowered so that in the region $T = 77$°K, $W_2/W_1 \sim 1$. This agreement with experiment is fortuitous, however, due to the discrepancy between the calculated and observed T_1 at this temperature.

We conclude that the BAYER theory can account for the observed relaxation of the chlorine nuclei in paradichlorobenzene, with evidence that the 27 cm^{-1} torsional motion provides the operative relaxation mechanism. Although an independent value of the excited torsional state lifetime is not available, the separate evaluation of W_1 and W_2 has provided additional information which more completely justifies the choice of τ_a. In previous work it has been assumed from the BAYER theory that $\Delta m = \pm 2$ transitions are the dominant source of the relaxation. Our results establish that W_2 is only about three times larger than W_1 in p–$C_6H_4Cl_2$ at room temperature. However, W_1 and W_2 are of the same order of magnitude at 77°K.

(b) *Potassium chlorate*

The spin–lattice relaxation of the Cl^{35} quadrupole resonance in a single crystal of $KClO_3$ has been investigated. $KClO_3$ has a monoclinic structure with two molecules per unit cell.[20] The molecules alternate in their orientation to one another; however, they are chemically and physically equivalent in regard to their quadrupole resonance and Zeeman splitting properties. The electric field gradient at the chlorine site is due principally to ionic and covalent bonding within the chlorate group and is very nearly axially symmetric. The Cl^{35} quadrupole resonance frequency is 28·1 Mc/sec at room temperature.

The individual quadrupole spin–lattice relaxation probabilities W_1 and W_2 have been measured by applying a magnetic field of 75 gauss at $\theta_0 = 0$ and observing the relaxation recovery of one of the α resonance lines. The experimental data is plotted in Fig. 3. The prediction in (2) of a relaxation time dependence formed of a linear combination of two exponential terms is well established. Using the measured spin–lattice relaxation time at room temperature of $T_1 = 21$ milliseconds and (2), we find $W_1 = 18{\cdot}5$ sec^{-1} and $W_2 = 5{\cdot}4$ sec^{-1}, with an estimated error of ± 2 sec^{-1}. Measurements at temperatures of 300, 273, 195, and 77°K indicate that the ratio W_1/W_2 is approximately constant within experimental error over this temperature range. The T_1 values were: 300°K, 21 msec; 273°K, 26 msec; 195°K, 50 msec; 77°K, 455 msec. Discussion of these results and comparison with

Vol. 17
1960

theory is postponed to Section 4(c) where spin–lattice relaxation in a similar chlorate group in $NaClO_3$ is considered.

Another experiment was performed to verify further the $\alpha-\alpha'$ coupled relaxation predicted by (2). Two independent pulsed r.f. oscillators were tuned to the frequencies of the α and α' resonances and their outputs coupled into a two-coil r.f. output

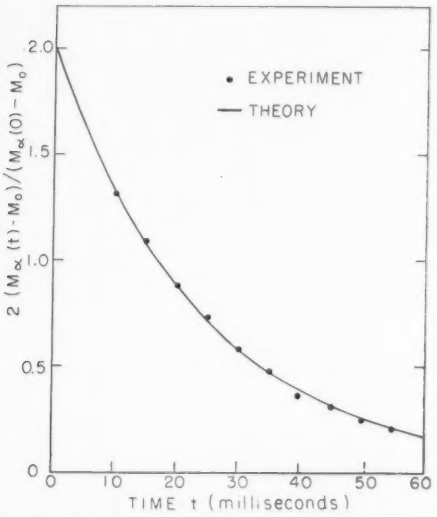

FIG. 3. Spin–lattice relaxation of α resonance line of Cl^{35} in $KClO_3$. The solid curve is given by $\exp(-t/T_1)+\exp(-2W_1t)$, where $T_1 = 21$ msec and $2W_1 = 37$ sec^{-1}.

head[8] which consisted of a solenoidal r.f. coil located inside an orthogonal Helmholtz r.f. coil. The solenoidal coil held the sample and served as a receiver coil for the observation of the free magnetic-induction signals. The α spin system was initially excited by an r.f. pulse from the appropriate oscillator. At a later time an r.f. pulse from the other oscillator was applied to observe the time-dependent behavior of the α' spin system. The data is plotted in Fig. 4 together with the theoretical $M_{\alpha'}(t)$ curve predicted by (2) using known values of W_1 and W_2. Due to cross-coupling between the $\alpha-\alpha'$ systems introduced by $\Delta m = \pm 2$ relaxation transitions, there is a transient increase in the polarization of the α' system. This behavior of $M_{\alpha'}(t)$ is characteristic of the transient Overhauser effect discussed by SOLOMON[21].

Free induction signals of the α and α' resonances exhibit an increased decay lifetime relative to that of the zero field resonance. This is due to the presence of the magnetic field which divides possible spin transitions into two groups of different frequencies thereby reducing the mutual spin–spin flipping contribution to the resonance line width. The expected increase in decay lifetime can be estimated by calculating the second moment of the line shape in the presence of large Zeeman splitting with appropriate truncation of the dipolar

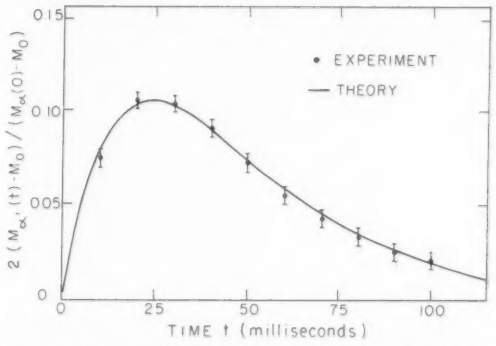

FIG. 4. Spin–lattice relaxation of α' resonance line of Cl^{35} in $KClO_3$ following initial excitation of the α resonance line. The solid curve is given by $\exp(-t/T_1)-\exp(-2W_1t)$, where $T_1 = 21$ msec and $2W_1 = 37$ sec^{-1}.

Hamiltonian. The broadening of quadrupole spectra due to magnetic dipole–dipole interactions has been treated by ABRAGAM and KAMBE[22]. Their results are applied to $KClO_3$ by considering (1) chlorine nuclei as resonant spins interacting among themselves and (2) chlorine nuclei interacting with unlike, nonresonant potassium nuclei. A mean square frequency deviation of $\Delta\omega^2 = 4{\cdot}9\times10^5$ sec^{-2} is found. When a large magnetic field is applied, only one of the α, α' spin groups may be treated as resonant nuclei. The calculation is modified to include interactions with (1) resonant chlorine nuclei, (2) nonresonant chlorine nuclei, and (3) potassium nuclei. A concentration factor[23] is introduced into the calculation to define the probability that a lattice site is occupied by a resonant or nonresonant chlorine. The results predict an α line width reduced by approximately 5 per cent. This is in agreement with the observed increase in decay lifetime.

(c) *Sodium chlorate—Chang theory*

CHANG[4] has developed a general theory of quadrupole spin–lattice relaxation in solids based on the interaction of the quadrupole moment of the nucleus with the fluctuating crystalline electric field gradient produced by thermal lattice vibrations of neighboring electronic charges. The theory is applied to sodium chlorate to calculate the rate and temperature dependence of the chlorine spin–lattice relaxation. The field gradient at the chlorine site in $NaClO_3$ is assumed to be axially symmetric and generated by a single equivalent charge replacing the three oxygens on the pyramidal ClO_3^- ion and located on the symmetry axis at an equilibrium distance R from the chlorine. This field gradient is described by

$$q = -\frac{c}{eQ}(r-b), \tag{9}$$

where Q is the nuclear electric quadrupole moment. This expression is equivalent to the first two terms in a Taylor expansion of the quadrupole coupling constant eqQ in powers of the small relative displacement of the chlorine and the single equivalent charge. The constants b and c are to be determined by experiment and may be considered to include any shielding or covalency effects.

Using this simplified model of the field gradient at the chlorine nucleus (9) and a density of states of lattice waves given by a Debye spectrum, CHANG has calculated the quadrupole relaxation transition probabilities for Raman processes involving the inelastic scattering of two lattice phonons. The results are

$$W_1 = K(cb)^2 I_1(T),$$
$$W_2 = K(eqQ)^2 I_2(T), \tag{10}$$

where

$$K = \frac{3}{4}\left(\frac{kT}{h}\right)^3 (MR^2)^{-2}.$$

M is the density of the crystal and I_1 and I_2 are complicated integrals involving an integration over the Debye spectrum of lattice vibrations and are calculated numerically. CHANG has evaluated W_1 and W_2 in (10) and has compared their sum in (5) with experimentally measured T_1's. By proper choice of the parameters in the theory, agreement within a factor of two between theory and experiment was found over the temperature range 373–77°K. These results are shown in Table 2. Recent measurements[24] have confirmed the correctness of the temperature dependence of T_1 in the temperature interval 300–10°K. The measurement of T_1, however, does not provide as critical a test of the correctness of the model used to describe the fluctuating internal electric fields as does the separate measurement of W_1 and W_2.

Table 2. Temperature dependence of the quadrupole coupling constant, the theoretical relaxation time T_1 based on Chang's theory, and the experimental T_1 for Cl^{35} in sodium chlorate

T(°K)	$(eqQ/2h)$ (Mc/sec)	Calculated T_1 (sec)	Observed T_1 (sec)
77	30·624	1·6	0·96 ± 0·05
150		0·25	
194	30·325		0·130 ± 0·005
217		0·11	
273	30·033	0·060	0·065 ± 0·010
297	29·930	0·046	0·045 ± 0·002
324	29·792		0·032 ± 0·002
340	29·683	0·028	0·025 ± 0·003
373	29·519	0·017	0·017 ± 0·002

W_1 and W_2 were measured separately by applying a magnetic field to a single crystal of $NaClO_3$ in the crystalline (100) direction. For this direction the magnetic field makes equal angles $\theta_0 = \tan^{-1}\sqrt{(2)}$ with the four body diagonals of the cubic $NaClO_3$ unit cell[20] which form the z-principal axes for the chlorine field gradient of the four molecules. One of the β Zeeman lines of the resultant three-component quadrupole spectrum was selectively excited and its relaxation recovery compared with the time-dependence given in equation (2). The results of a series of measurements at room temperature and 29·93 Mc/sec were $W_1 = 8{\cdot}5\ \text{sec}^{-1}$, $W_2 = 2{\cdot}7\ \text{sec}^{-1}$ with an estimated error of $\pm 1\ \text{sec}^{-1}$. Measurements at 77°K gave values of $W_1 = 0{\cdot}28\ \text{sec}^{-1}$ and $W_2 = 0{\cdot}24\ \text{sec}^{-1}$ with an estimated error of $\pm 0{\cdot}15\ \text{sec}^{-1}$.

From CHANG's theory and equation (10) the theoretical ratio of W_1 to W_2 is given by

$$\frac{W_1}{W_2} = \frac{(cb)^2 I_1}{(eqQ)^2 I_2} \simeq \tfrac{1}{2}(cb/eqQ)^2, \tag{11}$$

Vol. 17
1960

where $I_2 \lesssim 2I_1$ as computed[11] by Chang using known elastic constants for $NaClO_3$. Since the temperature dependences of W_1 and W_2 in (10) are approximately equal, the ratio (11) should be nearly constant as a function of temperature. This is observed, within experimental error, for both $NaClO_3$ and $KClO_3$. From CHANG's computations, the value of $(cb/eqQ)^2$ was $\lesssim 50$ and thus $W_1 \lesssim 25\ W_2$. The observed value of $W_1/W_2 \sim 3$ at room temperature differs greatly from this value.

A possible source of the discrepancy between the theoretical and experimental ratio W_1/W_2 may be the evaluation of the constants b and c in (9) since they enter in the expression for W_1 but not for W_2. These constants are estimated by combining the known temperature dependence of the linear thermal expansion coefficient of the $NaClO_3$ crystal and the temperature dependence of eqQ for chlorine in equation (9). To take into account the possible tighter bonding of the oxygen ions to the chlorine ion than the average for the crystal, CHANG has introduced a multiplicative factor f into the thermal expansion coefficient for $NaClO_3$, where $f \leqq 1$. The values of f used were of order 0·2–0·3 and were chosen to obtain agreement with the experimental T_1 at room temperature since there was not enough independent information available to estimate f accurately. These values of f, however, yield ratios $W_1/W_2 \sim 25$. If one takes $f = 1$, W_1 is reduced and $W_1 \sim 9\ W_2$ which is still beyond experimental error. In addition, experimental and theoretical T_1's no longer agree unless the parameter R is greatly reduced from its value of $1{\cdot}46 \times 10^{-8}$ cm, which is not very reasonable. Smaller values of f tend to increase W_1/W_2.

The transition probabilities W_1 and W_2 are derived from the off-diagonal $\Delta m = \pm 1$ and ± 2 operators of the time-dependent quadrupole Hamiltonian given by

$$\mathscr{H}_{\pm 1} = A(I_{\pm}I_z + I_zI_{\pm})(V_{xz} \mp iV_{yz}) \qquad (12)$$

and

$$\mathscr{H}_{\pm 2} = \frac{A}{2} I_{\pm}^2 (V_{xx} - V_{yy} \mp 2iV_{xy}).$$

In (12),

$$A = \frac{eQ}{4I(2I-1)} \text{ and } V_{kl} = \frac{\partial E_l}{\partial x_k} = \frac{\partial^2 V}{\partial x_k \partial x_l},$$

where V is the crystalline field potential at the nuclear position. We see from (12) that W_1 and W_2 are proportional to different components of the electric field gradient tensor and therefore their relative magnitudes will be sensitive to the model chosen to describe the fluctuating field gradient. Therefore, the W_1/W_2 discrepancy probably originates in the one-dimensional, two-body relaxation mechanism based on the motion of a single equivalent charge used by CHANG to describe the source of the fluctuating field gradient in $NaClO_3$. This model appears to be too great a simplification of the motion within the chlorate group.

That the fluctuating electric field gradient responsible for the chlorine relaxation arises principally from charge motion within the chlorate group is suggested by several pieces of evidence.

(1) Since the chlorine in the chlorate ion is bonded to the three oxygens by S–P hybridized trigonal-pyramid orbitals, the field gradient as seen by the chlorine is due principally to the associated charge distribution.

(2) The quadrupole resonance frequencies and the spin–lattice relaxation times of chlorine in several chlorates (Na, K, Rb, Ba) are of the same order of magnitude although the lattice structures are dissimilar, thereby indicating that the influence of the cations is small.

(3) In both $NaClO_3$ and $KClO_3$, which have chlorate groups of substantially the same size and shape, the relative magnitudes of W_1 and W_2 are equal within experimental error, although the lattice arrangements of cations and chlorate ions are different.

Possible relaxation contributions from the sodium ion in $NaClO_3$ can be estimated. CHANG has considered the relative motion of the Na ion and the Cl ion in an $NaClO_3$ molecule as an alternate source of the fluctuating field gradient. The computed relaxation times due to this effect, however, are ~ 100 times too long. This particular sodium ion, however, is not the nearest neighbor of the chlorine nucleus. There are six nearest neighbor Na^+ of the chlorine situated in a distorted NaCl lattice structure. The relaxation produced by these charges can be estimated using the model and theory developed by VAN KRANENDONK[2]. Again the results yield T_1's several orders of magnitude too long, a difference much greater than can presently be accounted for by an enhancement factor

due to anti-shielding[2] or covalency.[3] Any relaxation contribution due to the sodium ions in $NaClO_3$ therefore must be small.

To treat thoroughly the relaxation in $NaClO_3$ or the other chlorates an exact calculation of the field gradient tensor components from knowledge of electronic wave functions for the thermally distorted lattice would be desirable, however, very difficult with the information presently available. Alternatively, treatment could be made of the various vibrational modes of the chlorate group as known from Raman spectra studies. Starting from a generalized theory of the influence of lattice vibrations on the off-diagonal elements of the quadrupole interaction Hamiltonian, normal modes of vibrations are established, and CHANG's or BAYER's relaxation theory could then be extended to make an explicit calculation of the relaxation.

Raman spectra data[25] has identified several low-frequency lines $\sim 100\ cm^{-1}$ associated with translatory and rotatory motions of the ClO_3^- ion in $NaClO_3$. Two approximately normal modes of vibration[19] can be established which provide rotation of the principal axis of the chlorine field gradient tensor. These oscillations are just the type of motions treated by BAYER in his theory of quadrupole spin–lattice relaxation. By extending the BAYER theory to include these two modes of torsional oscillation and considering a single characteristic $\tau_a \sim 6 \times 10^{-13}$ sec, for both modes, a calculated $T_1 \approx 46$ milliseconds at room temperature and a ratio $W_1/W_2 \sim 3$ is obtained. In the absence of independent measurements of τ_a, the choice of τ_a was made to provide the best agreement with the experimental data. Although the agreement for both T_1 and W_1/W_2 is good, only order-of-magnitude agreement is to be expected in view of the simplified treatment and assumptions made concerning the complete chlorate group motions. A similar treatment of the spin–lattice relaxation of Cl^{35} in $KClO_3$ again gives order-of-magnitude agreement with experimental results.

5. SUMMARY

By studying the relaxation of selected portions of a multi-level quadrupolar spin system using pulsed nuclear induction techniques, additional information about the spin–lattice relaxation process is obtained. In particular it is possible to establish whether the dominant relaxation mechanism which brings the spin system into thermal equilibrium with the lattice is quadrupolar in origin and to measure the individual probabilities for $\Delta m = \pm 1$ and ± 2 quadrupole relaxation transitions. The experimental results provide valuable information about the different components of the fluctuating crystalline electric fields in solids and aid in verifying the correctness of various proposed theories of quadrupole spin–lattice relaxation.

The techniques of selective excitation and investigation of nuclear spin relaxation,[8] may have additional usefulness in the study of spin–lattice interactions. At low temperatures nuclear spin–lattice relaxation in solids via quadrupolar interactions becomes very slow. Nuclear relaxation through interaction with small amounts of paramagnetic impurities in the material is nearly temperature independent and thus at sufficiently low temperatures may become a competitive process. The presence of relaxation via paramagnetic impurities could be established by a detailed comparison of the temperature dependence of W_1 and W_2, since W_1 would include the effects of both quadrupole and magnetic impurity relaxation whereas W_2 is generated solely by quadrupole spin–lattice interactions.

Acknowledgement—The author would like to express his sincere appreciation to Professor E. L. HAHN for many helpful discussions and for his continued interest in this work.

REFERENCES

1. BAYER H., *Z. Phys.* **130,** 227 (1951).
2. VAN KRANENDONK J., *Physica* **20,** 781 (1954).
3. YOSIDA K. and MORIYA T., *J. Phys. Soc. Japan* **11,** 33 (1956).
4. CHANG C. E., Office of Scientific Research report, available from Department of Physics, University of Washington, Seattle, Washington.
5. COHEN M. H. and REIF F., Nuclear Quadrupole Effects in Nuclear Magnetic Resonance, *Solid State Physics*, Vol. V. Academic Press, New York (1957).
6. DAS T. P. and HAHN E. L., Nuclear Quadrupole Resonance Spectroscopy, *Solid State Physics*, Supplement 1. Academic Press, New York (1958).
7. SHULER K. E., *Phys. Fluids*, **2,** 442 (1959).
8. WEBER M. J. and HAHN E. L., *Phys. Rev.* **120,** 365 (1960); WEBER M. J., Thesis, University of California (unpublished).

9. POUND R. V., *Phys. Rev.* **79,** 685 (1950).
10. HAHN E. L., *Phys. Rev.* **80,** 580 (1950); PAKE G. E., Nuclear Magnetic Resonance, *Solid State Physics*, Vol. II. Academic Press, New York (1956).
11. WEBER M. J. and HAHN E. L., *Bull. Amer. Phys. Soc.* **3,** 324 (1958).
12. BLOOM M., HAHN E. L. and HERZOG B., *Phys. Rev.* **97,** 1699 (1955).
13. HOLCOMB D. F. and NORBERG R. E., *Phys. Rev.* **98,** 1074 (1955); KAPLAN D. E., Thesis, University of California (unpublished).
14. DEAN C., Thesis, Harvard University, 1952 (unpublished).
15. CROATTO U., BEZZI S. and BUA E., *Acta. Cryst., Camb.* **5,** 825 (1952).
16. SAKSENA B. D., *J. Chem. Phys.* **22,** 1618 (1955).
17. WOESSNER D. E. and GUTOWSKY H. S., *J. Chem. Phys.* **27,** 1072 (1957).
18. BLOEMBERGEN N., PURCELL E. M. and POUND R. V., *Phys. Rev.* **71,** 466 (1947).
19. KUSHIDA T., *J. Sci. Hiroshima Univ.* **A19,** 427 (1955).
20. WYCKOFF R. W. G., *Crystal Structures*. Interscience, New York (1957).
21. SOLOMON I., *Phys. Rev.* **99,** 559 (1955).
22. ABRAGAM A. and KAMBE K., *Phys. Rev.* **91,** 894 (1954).
23. KITTEL C. and ABRAHAMS E., *Phys. Rev.* **90,** 238 (1953).
24. BENDER P. A., JENNINGS D. A. and TANTTILA W. H., *J. Chem. Phys.* **32,** 499 (1960).
25. KUMARI C. S., *Proc. Ind. Acad-Sci.* **A28,** 500 (1948).

J. Phys. Chem. Solids Pergamon Press 1961. Vol. 17, Nos. 3/4, pp. 278–283. Printed in Great Britain.

PREPARATION AND PROPERTIES OF $CdSnAs_2$

A. J. STRAUSS and A. J. ROSENBERG*

Lincoln Laboratory,† Massachusetts Institute of Technology, Lexington 73, Massachusetts

(*Received* 1 *July* 1960)

Abstract—*n*-type samples of $CdSnAs_2$ (melting point = 590°–600°C) have been prepared by freezing from the melt. The highest room temperature Hall mobility attained was $1{\cdot}2 \times 10^4$ cm²/volt sec for a sample with a free electron concentration of $5{\cdot}5 \times 10^{17}$ cm^{-3}. From infrared absorption data the energy gap is estimated to be approximately 0·23 eV at room temperature. The absorption edge shifts to shorter wavelengths with increasing electron concentration. The electrical and optical data indicate that the conduction band of $CdSnAs_2$ is characterized by a low electron effective mass, of the order of a few hundredths of the free electron mass.

INTRODUCTION

THE SYNTHESIS of ten intermetallic semiconductors of the composition $A^{II}B^{IV}C^{V}_2$—where A^{II} is Cd or Zn, B^{IV} is Si, Ge, or Sn, and C^{V} is P or As—has been reported.[1,2] Except for $ZnSnAs_2$, these compounds crystallize in the tetragonal chalcopyrite structure, in which each atom is tetrahedrally bonded. They are isoelectronic with the III–V compounds, from which they are formally derived by the ordered substitution of one Group II and one Group IV atom for each pair of Group III atoms. An electron mobility of 3000 cm²/volt sec has been reported for $CdSnAs_2$,[1] but no other data on the electrical properties of the II–IV–V compounds have been published. Energy gaps for six of the compounds (not including $CdSnAs_2$) have been estimated from optical absorption measurements.[2]

The present investigation was undertaken because of our interest in compound semiconductors with high carrier mobilities. Its most notable result has been the preparation of $CdSnAs_2$ with a room temperature Hall mobility of $1{\cdot}2 \times 10^4$ cm²/volt sec at an electron concentration of $5{\cdot}5 \times 10^{17}$ cm^{-3}. This mobility is by far the highest reported for any ternary compound, and is exceeded at room temperature only by values measured for four binary compounds with the zinc blende structure—InSb, InAs, HgTe, and HgSe. Infrared transmission measurements indicate that the energy gap of $CdSnAs_2$ is probably about 0·23 eV at room temperature. The absorption edge shifts to shorter wavelengths with increasing electron concentration as observed in the case of *n*-type InSb[3] and InAs.[4]

SAMPLE PREPARATION

Samples of the compound were synthesized by melting stoichiometric quantities of the elements in evacuated and sealed quartz tubes. Three different crystallization techniques were used: vertical Bridgman, quenching, and slow cooling. The Bridgman apparatus consisted of two resistance furnaces, the lower at 750°C for melting the material and the upper at 600°C for maintaining the arsenic vapor pressure at approximately one atmosphere. Directional freezing was accomplished by lowering the sample tube out of the apparatus at 0·1 in/hr. The ingot prepared in this manner consisted mostly of polycrystalline $CdSnAs_2$ as a single phase, but the last-to-freeze portion contained two phases, due to the loss of arsenic by condensation on the upper part of the sample tube. The single phase material was threaded with many fine cracks, but it was possible to isolate a crack-free sample for electrical measurements. The grain size of this sample was only about 20 μ, as estimated from a Laue pattern.

Quenched samples were prepared by immersing quartz tubes containing the molten compound in

* Now at TYCO, Inc., Waltham, Massachusetts.

† Operated with support from the U.S. Army, Navy, and Air Force.

liquid nitrogen. The ingots obtained were virtually free of cracks but were polycrystalline, with an estimated grain size of only 10 μ.

A number of samples were prepared by slow cooling in the course of thermal analysis experiments performed to determine the freezing point of $CdSnAs_2$. In these experiments, a chromel–alumel thermocouple was inserted into a re-entrant in the bottom of a quartz sample tube. The sample tube was placed in a massive stainless steel cylinder, and the whole assembly was heated in a well-insulated vertical resistance furnace until the compound had been melted. The furnace power was then reduced sufficiently to establish a cooling rate of approximately 1 deg/min until freezing (non-directional) was completed, after which the furnace was turned off. Although the ingots prepared in this manner were very severely cracked, the grain size was much larger than for the Bridgman-grown and quenched ingots. In several cases, it was possible to obtain crack-free single crystals of the order of 1 cm in their longest dimension.

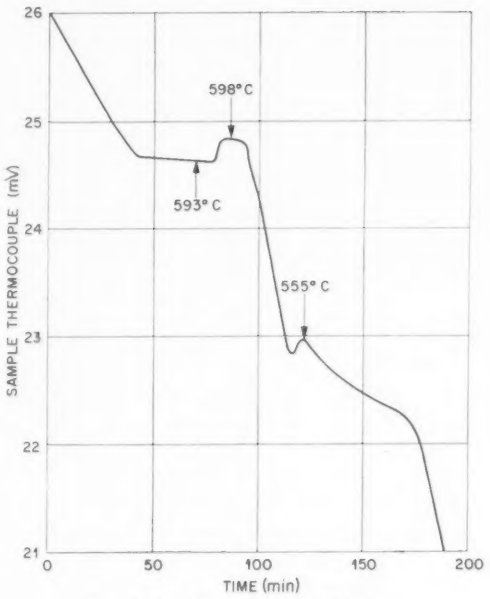

FIG. 1. Cooling curve for $CdSnAs_2$.

THERMAL ANALYSIS

Three cooling curves and two heating curves have been determined in thermal analysis experiments on $CdSnAs_2$. The solid–liquid transformation occurs between 590°C and 600°C; a more exact value for the transition temperature cannot be given, since both cooling and heating curves reveal complexities in the phase diagram which are not well understood. One of the cooling curves is shown in Fig. 1, while a heating curve is shown in Fig. 2. Fig. 1 shows only the voltage readings for the thermocouple inserted into the re-entrant in the sample tube, while Fig. 2 also gives the differences between these readings and those for a thermocouple inserted into the wall of the stainless steel cylinder. Both curves shown exhibit three thermal arrests, rather than the single temperature plateau characteristic of a solid–liquid transformation in a simple phase diagram. The other curves obtained have the same general features but are somewhat different in detail.

The presence of two plateaus in the cooling curves suggests the existence of a metastable solid phase whose liquidus temperature, at the composition corresponding to $CdSnAs_2$, is lower than the liquidus temperature of the stable compound. If this is the case, sufficient supercooling of the stable phase permits crystallization of the metastable phase, and the initial plateau is observed. This phenomenon occurs in the Cd–Sb

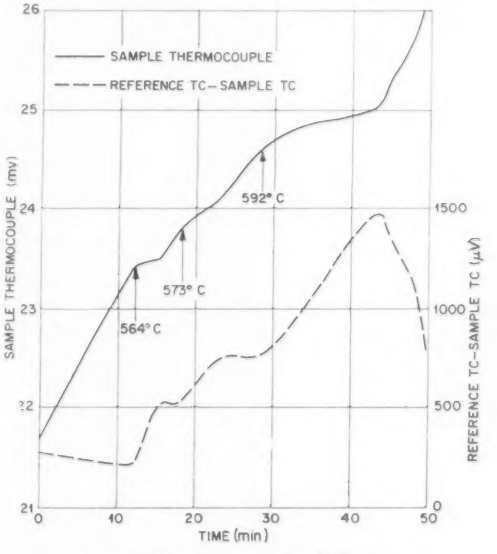

FIG. 2. Heating curve for $CdSnAs_2$.

system, where the metastable phase Cd_3Sb_2 crystallizes from a slowly cooled melt of the composition CdSb, even though its liquidus is approximately 50°C below that of the stable compound CdSb.[5] If the metastable phase then transforms rapidly into the stable phase, and the transformed solid comes into contact with the remaining liquid, crystallization of the stable phase is nucleated. The temperature then rises rapidly to the stable liquidus, and a second plateau is observed. This type of nucleation frequently occurs in alloys of CdSb with ZnSb.[6] The third arrest, beginning at 552°C in Fig. 1, could result from an allotropic transformation of the stable phase, whether this phase had been formed by direct crystallization from the melt or by transformation of metastable material.

While the model proposed can explain the cooling curves obtained for $CdSnAs_2$, it does not account for the observed heating curves. On the basis of this model, the heating curves should exhibit a thermal arrest at 540–560°C due to the allotropic transformation of the stable phase, followed by a plateau at the melting point of the high-temperature form. Instead, the measured curves exhibit three poorly defined arrests, all of which begin at significantly higher temperatures than 560°C, and the last of which extends to a slightly higher temperature than the upper plateau in the cooling curve. It is clear, therefore, that a more extensive investigation of the Cd–Sn–As system will be required to elucidate the phase diagram in the vicinity of $CdSnAs_2$.

LATTICE PARAMETERS

X-ray diffractometer measurements on two powdered samples of $CdSnAs_2$, one prepared by slow cooling and the other by quenching, gave the same results within the limits of experimental error. The following average values were obtained for the tetragonal lattice parameters: $a = 6{\cdot}093 \pm 0{\cdot}003$, and $c/a = 1{\cdot}959 \pm 0{\cdot}006$. These data are in agreement with the published values of $6{\cdot}09_2$ and $1{\cdot}95_7$, respectively.[1]

ELECTRICAL PROPERTIES

The Hall coefficient (R_H) at 7800 G and resistivity (ρ) were measured by conventional d.c. potentiometric techniques on crack-free samples of $CdSnAs_2$ prepared by the three methods described above. All samples were *n*-type. Data for resistivity, carrier concentration ($1/R_He$), and Hall mobility (R_H/ρ) at room temperature and liquid nitrogen temperature are given in Table 1, together with values for the thermoelectric power at room temperature. Fig. 3 shows the temperature dependence of ρ and R_H for sample A of Table 1 between 85°K and 350°K.

All the samples measured were extrinsic over the temperature range investigated. It can therefore be concluded that the intrinsic carrier concentration in $CdSnAs_2$ at 300°K is less than 5×10^{17} cm^{-3}

Table 1. *Properties of n-type* $CdSnAs_2$

Sample	Method of preparation	300°K				77°K		
		ρ (ohm-cm)	n (cm^{-3})	μ_n (cm^{2}V^{-1}sec^{-1})	α (μVdeg^{-1})	ρ (ohm-cm)	n (cm^{-3})	μ_n (cm^{2}V^{-1}sec^{-1})
A	Bridgman	$4{\cdot}2 \times 10^{-4}$	$2{\cdot}7 \times 10^{18}$	$5{\cdot}6 \times 10^{3}$	-54	$3{\cdot}7 \times 10^{-4}$	$2{\cdot}8 \times 10^{18}$	$6{\cdot}1 \times 10^{3}$
2	Quenched	$1{\cdot}1 \times 10^{-3}$	$2{\cdot}5 \times 10^{18}$	$2{\cdot}4 \times 10^{3}$	-51			
1A	Slow-cooled	$3{\cdot}6 \times 10^{-4}$	$2{\cdot}9 \times 10^{18}$	$6{\cdot}1 \times 10^{3}$		$3{\cdot}4 \times 10^{-4}$	$2{\cdot}8 \times 10^{18}$	$6{\cdot}6 \times 10^{3}$
4A	Slow-cooled	$9{\cdot}3 \times 10^{-4}$	$5{\cdot}5 \times 10^{17}$	$1{\cdot}2 \times 10^{4}$	-111	$8{\cdot}2 \times 10^{-4}$	$5{\cdot}5 \times 10^{17}$	$1{\cdot}4 \times 10^{4}$
4B	Slow-cooled	$5{\cdot}4 \times 10^{-4}$	$1{\cdot}1 \times 10^{18}$	$1{\cdot}1 \times 10^{4}$	-83			
4C	Slow-cooled	$1{\cdot}1 \times 10^{-3}$	$5{\cdot}8 \times 10^{17}$	$1{\cdot}0 \times 10^{4}$	-119	$9{\cdot}5 \times 10^{-4}$	$5{\cdot}4 \times 10^{17}$	$1{\cdot}2 \times 10^{4}$
5A	Slow-cooled	$8{\cdot}9 \times 10^{-4}$	$2{\cdot}8 \times 10^{18}$	$2{\cdot}5 \times 10^{3}$	-71	$8{\cdot}3 \times 10^{-4}$	$3{\cdot}0 \times 10^{18}$	$2{\cdot}5 \times 10^{3}$

Vol. 17
1960

and that the lattice mobility of electrons at the same temperature is at least 12,000 cm^2/volt sec.

The mobilities of the various samples, with one or perhaps two exceptions, exhibit the usual variation with impurity concentration and crystal perfection. The highest mobilities were observed

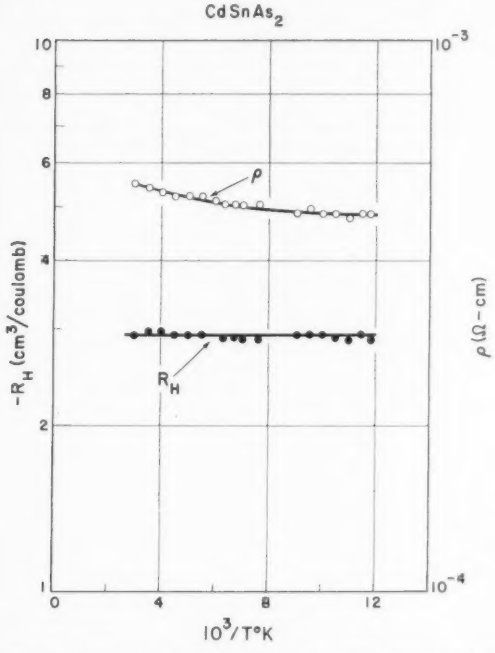

FIG. 3. Temperature dependence of electrical resistivity and Hall coefficient for *n*-type $CdSnAs_2$.

in the three samples of lowest carrier concentration, all of which were single crystals prepared by slow cooling. Among the other samples, all of which have carrier concentrations of approximately 3×10^{18} cm^{-3}, the polycrystalline quenched sample and one slow-cooled single crystal have mobilities of about 2500 cm^2/volt sec. Although the quenched and Bridgman samples have approximately the same grain size, the quenched sample might be expected to contain a higher density of imperfections, and its lower mobility is therefore reasonable. On the other hand, the fact that one of the slow-cooled crystals has the same mobility as the quenched sample is anomalous. In addition, it is rather surprising that the other slow-cooled crystal does not have a higher mobility than the Bridgman sample, in view of the great difference in their grain sizes.

INFRARED TRANSMISSION

Infrared transmission data detween 2 and 15 μ for samples 4C and 5A of Table 1 are shown in Fig. 4. The measurements were made at room temperature with a Perkin–Elmer Model 221 double beam spectrophotometer. Both curves are

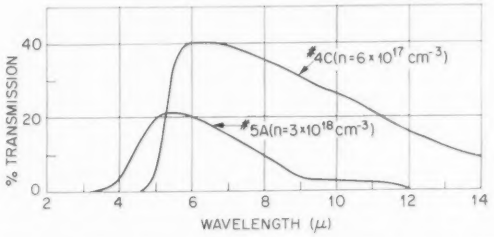

FIG. 4. Infrared transmission of *n*-type $CdSnAs_2$ at room temperature. Sample thickness: 4C, 200 μ; 5A, 80 μ.

seen to exhibit typical semiconductor features: an opaque region at the shortest wavelengths which results from interband absorption, a relatively sharp absorption edge, and a partially transparent region beyond the edge in which free carrier absorption is predominant. The gradual decrease in transmission observed on the long wavelength side results from the usual increase in free carrier absorption with increasing wavelength. Since sample 4C contains only one-fifth the free electron concentration of sample 5A, its transmission beyond the edge is much greater than for sample 5A, although it is more than twice as thick as sample 5A. In fact, it seems probable that between 6 μ and 7 μ the transmission for sample 4C is determined mostly by reflection losses, with absorption playing only a minor role.

The absorption edge for sample 5A is located at shorter wavelengths than the edge for sample 4C. Similar shifts of the absorption edge to higher energies with increasing electron concentration have been observed for *n*-type InSb[3] and InAs.[4] These shifts are attributed to the low density of states in the conduction bands of these compounds.[7,4] When the free electron concentration is sufficient to fill an appreciable fraction of the

lower states in the conduction band, photons of higher energy are required to promote electrons from the valence band to higher unoccupied states. Therefore the shift of absorption edge in $CdSnAs_2$ may be taken as evidence for a low electron effective mass in this compound. From the absorption edge for sample 4C, the energy gap for $CdSnAs_2$ is estimated to be approximately 0·23 eV; the data for InSb suggest that further decreases in free electron concentration will not shift the edge much further.

BAND STRUCTURE

Although the present experimental data are too limited to permit a detailed discussion of the band structure of $CdSnAs_2$, it is clear from the infrared transmission measurements that at room temperature the optical energy gap ($\sim$ 0·23 eV) is significantly less than the gap for InAs (0·35 eV),[8] the isoelectronic III–V compound. GOODMAN[2] found that the II–IV–V_2 chalcopyrites which he investigated also have lower energy gaps than the related III–V compounds. As in numerous other cases, the reduction in energy gap is correlated with a reduction in cohesive energy, as shown by the decrease in melting point from 943°C for InAs[9] to 590–600°C for $CdSnAs_2$. These effects are presumably associated with the reduction in the average electronegativity difference of the atoms from 0·3 for InAs to 0·25 for $CdSnAs_2$, on PAULING's scale.[10]

It was noted previously that $CdSnAs_2$ resembles InSb and InAs in exhibiting a shift of its optical absorption edge to higher energy with increasing electron concentration. These three compounds, together with HgSe, also exhibit marked similarities in their electrical and thermoelectric properties, as shown in Table 2. These similarities indicate that the conduction band of $CdSnAs_2$, like those of the other compounds, is characterized by a low electron effective mass of the order of a few hundredths of the free electron mass. They also suggest that the conduction band of $CdSnAs_2$ may have the non-parabolic form described by KANE for InSb,[11] which probably is also characteristic of HgSe, as HARMAN has recently suggested.[12]

Table 2. Properties of high-mobility compound semiconductors (300°K)

	$CdSnAs_2$		InSb		InAs		HgSe	
n (cm^{-3})	α ($\mu V deg^{-1}$)	μ ($cm^2V^{-1}sec^{-1}$)	α^a ($\mu V deg^{-1}$)	μ^b ($cm^2V^{-1}sec^{-1}$)	α^c ($\mu V deg^{-1}$)	$\mu^{d,e}$ ($cm^2V^{-1}sec^{-1}$)	α^f ($\mu V deg^{-1}$)	μ^f ($cm^2V^{-1}sec^{-1}$)
$5·5\times10^{17}$	−111	$1·2\times10^4$	−106	$2·5\times10^4$	−140	$1·3\times10^4$	−91	$1·7\times10^4$
$1·1\times10^{18}$	−83	$1·1\times10^4$	−82	$1·9\times10^4$	−110	$1·0\times10^4$	−70	$1·2\times10^4$
$2·7\times10^{18}$	−54	$5·6\times10^3$	−51	$1·3\times10^4$	−75	$0·9\times10^3$	−49	$7·0\times10^3$

(a) BARRIE R. and EDMOND J. T., *J. Electronics* **1,** 161 (1955).
(b) HARMAN T. C. and STRAUSS A. J. (unpublished).
(c) Estimated from data of WEISS H., *Z. Naturf.* **11a,** 131 (1956).
(d) HARMAN T. C., GOERING H. L. and BEER A. C., *Phys. Rev.* **104,** 1562 (1956).
(e) SCHILLMAN E., *Z. Naturf.* **11a,** 463 (1956).
(f) HARMAN T. C. (private communication).

Acknowledgements—The authors are indebted to Mr. A. A. MENNA and Mrs. L. B. FARRELL for assistance in the experimental work.

REFERENCES

1. FOLBERTH O. G. and PFISTER H., *Halbleiter und Phosphore*, p. 474. Vieweg, Braunschweig (1957).
2. GOODMAN C. H. L., *Nature, Lond.* **179,** 838 (1957).
3. TANENBAUM M. and BRIGGS H. B., *Phys. Rev.* **91,** 1561 (1953).
4. TALLEY R. M. and STERN F., *J. Electronics* **1,** 186 (1955).
5. HANSEN M., *Constitution of Binary Alloys* (2nd Ed.) p. 438. McGraw-Hill, New York (1958).
6. STRAUSS A. J., Semiconductor Symposium of the Electrochemical Society, October, 1959 (unpublished).

Vol. 17
1960

7. BURSTEIN E., *Phys. Rev.* **93,** 632 (1954).
8. DIXON J. R., *Bull. Amer. Phys. Soc.* (ser. 2) **4,** 133 (1959).
9. VAN DER BOOMGAARD J. and SCHOL K., *Philips Res. Rep.* **12,** 127 (1957).
10. PAULING L., *The Nature of the Chemical Bond* (3rd Ed.) p. 93. Cornell University Press, Ithaca, New York (1960).
11. KANE E. O., *J. Phys. Chem. Solids* **1,** 248 (1957).
12. HARMAN T. C., *Bull. Amer. Phys. Soc.* (ser. 2) **5,** 152 (1960).

J. Phys. Chem. Solids Pergamon Press 1961 Vol. 17, Nos. 3/4, pp. 284–291. Printed in Great Britain.

THEORY OF THE MAGNETIC SUSCEPTIBILITY OF HOLES IN GERMANIUM*

J. M. LUTTINGER and P. J. STILES

University of Pennsylvania, Philadelphia, Pennsylvania

(*Received* 13 *June* 1960)

Abstract—The theory of the magnetic susceptibility of free holes is given. A general method of calculation which will work for degenerate as well as simple bands is described, and applied to the valence band of Ge. Results are given for both Maxwell–Boltzmann and Fermi–Dirac statistics, and the possibility of comparison with experiments is discussed.

1. INTRODUCTION

IN THIS brief paper we shall deal with the magnetic susceptibility of free holes in the valence band of Ge. There has been some experimental work on this subject in recent years.[1,2,3,4] As we shall see below it is quite difficult to make an accurate comparison of the theory given here with the experiments, because many other contributions to the susceptibility mask that of the free carriers. However, this theory is presented in the hope that it will perhaps stimulate research in an interesting range, and also for its intrinsic methodological interest.

The susceptibility is treated in the effective mass limit of degenerate band theory, using the general formalism of KOHN and LUTTINGER[5]. To the best of our knowledge such a calculation (which would be valid for low hole concentrations) has not been carried out previously.

In Section 2 we outline a general method for obtaining the field independent susceptibility. This method is essentially the same as that used by SCHAFROTH in connection with the Meissner effect in superconductors. Instead of an homogeneous external field, a periodic slowly varying field is used. This enables one to use ordinary perturbation theory on the field in a very straightforward manner.[6] The result for the homogeneous field is obtained by letting the spatial variations of the field approach zero. The result is first given for Maxwell–Boltzmann statistics. It is obtained for Fermi–Dirac statistics by a simple transformation. We may mention that two other methods of calculation, that of PEIERLS[8] and the direct summation over the energy levels in a magnetic field did not prove immediately applicable in the degenerate band problem.

Section 3 deals with the detailed application of the general method to germanium. Finally, in Section 4, numerical results are given and the range of applicability is discussed.

2. GENERAL METHOD OF CALCULATION

The magnetic susceptibility of a system of N non-interacting particles with a Hamiltonian $\mathscr{H}$ and with discrete energy levels is easily calculated with Maxwell–Boltzmann statistics.[9] The free energy F and the partition function Z are given by

$$\exp(-\beta F/N) = Z \equiv \text{Trace} \times \times \exp(-\beta\mathscr{H}) \equiv \text{Tr}\exp(-\beta\mathscr{H}) \quad (2.1)$$

where $\beta = 1/kT$ and $\mathscr{H} = \mathscr{H}_0 + \mathscr{H}'$, $\mathscr{H}_0$ being the Hamiltonian when the magnetic field $H = 0$, and $\mathscr{H}'$ being the magnetic perturbing term. The Hamiltonian in the presence of a magnetic field will contain terms linear and quadratic in H. We use the following notation, $\mathscr{H} = \mathscr{H}_0 + \mathscr{H}_1 + \mathscr{H}_2$, where $\mathscr{H}_0$ is the unperturbed Hamiltonian, $\mathscr{H}_1$ is linear, and $\mathscr{H}_2$ is quadratic in the field. Therefore, we have $\mathscr{H}' = \mathscr{H}_1 + \mathscr{H}_2$. Since in the absence of permanent moments, the lowest order term in the magnetic field in the free energy is proportional to

* This work was supported in part by the Office of Naval Research.

Vol. 17
1960

H^2, we must calculate Z correct to second order in H. The expansion of $\mathrm{Tr}\exp[-\beta(\mathscr{H}_0+\mathscr{H}')]$ where $\mathscr{H}_0$ and $\mathscr{H}'$ do not necessarily commute is well known.[11] The results are

$$\mathrm{Tr}\exp[-\beta(\mathscr{H}_0+\mathscr{H}')] = [\mathrm{Tr}\exp(-\beta\mathscr{H}_0)]\{1-\beta\langle\mathscr{H}'\rangle_0+ + \Big\langle\int_0^\beta ds(\beta-s)\mathscr{H}'\exp(-s\mathscr{H}_0)\mathscr{H}'\exp(s\mathscr{H}_0)\Big\rangle_0+ + \text{higher order terms in } \mathscr{H}'\} \tag{2.2}$$

where $\langle\ \rangle_0$ denotes an average with respect to the distribution function $\exp(-\beta\mathscr{H}_0)/\mathrm{Tr}\exp(-\beta\mathscr{H}_0)$. We insert $\mathscr{H}'=\mathscr{H}_1+\mathscr{H}_2$ into equation 2.2 and obtain

$$Z(\beta) = Z_0(\beta)\{1-\beta\langle\mathscr{H}_2\rangle_0+ + \int_0^\beta ds(\beta-s)\langle\mathscr{H}_1\exp(-s\mathscr{H}_0)\mathscr{H}_1\exp(s\mathscr{H}_0)\rangle_0+\ \ldots\} \tag{2.3}$$

With equation 2.1, we have an expression for the change in the free energy.

$$F = -\frac{N}{\beta}\log Z \tag{2.4a}$$

$$= -\frac{N}{\beta}\{\log Z_0+\log[1-\beta\langle\mathscr{H}_2\rangle_0+\int_0^\beta ds(\beta-s)\times \times\langle\mathscr{H}_1\exp(-s\mathscr{H}_0)\mathscr{H}_1\exp(s\mathscr{H}_0)\rangle_0+\ \ldots]\} \tag{2.4b}$$

$$= F_0+\Delta F \tag{2.4c}$$

When we expand the logarithm in equation (2.4b) we obtain,

$$\Delta F = N\Big\{\langle\mathscr{H}_2\rangle_0-\frac{1}{\beta}\int_0^\beta ds(\beta-s)\times \times\langle\mathscr{H}_1\exp(-s\mathscr{H}_0)\mathscr{H}_1\exp(s\mathscr{H}_0)\rangle_0+\ \ldots\Big\} \tag{2.5}$$

We now work in a representation "l" where $\mathscr{H}_0$ is diagonal, that is $\mathscr{H}_0\psi_l=\epsilon_l\psi_l$. Then the averages may be expressed as

$$\langle\mathscr{H}_2\rangle = [\sum_l\exp(-\beta\epsilon_l)]^{-1}\sum_l\mathscr{H}_{2ll}\times \times\exp(-\beta\epsilon_l) \equiv Z_0^{-1}\sum_l\mathscr{H}_{2ll}\exp(-\beta\epsilon_l) \tag{2.6}$$

and

$$\langle\mathscr{H}_1\exp(-s\mathscr{H}_0)\mathscr{H}_1\exp(s\mathscr{H}_0)\rangle_l = \sum_{l'}|\mathscr{H}_{1ll'}|^2\exp(-s\omega_{l'l}) \tag{2.7}$$

where $\omega_{l'l}=\epsilon_{l'}-\epsilon_l$. With the definition of the function $f(\omega_{l'l})$ as

$$f(\omega_{l'l}) \equiv \int_0^\beta ds(\beta-s)\exp(-s\omega_{l'l}) = \frac{\beta\omega_{l'l}-1+\exp(\beta\omega_{l'l})}{(\omega_{l'l})^2} \tag{2.8}$$

we may now write

$$\Delta F = \frac{N}{Z_0}\sum_l\Big\{\mathscr{H}_{2ll}-\frac{1}{\beta}\times \times\sum|\mathscr{H}_{1ll'}|^2f(\omega_{l'l})\Big\}\exp(-\beta\epsilon_l) \tag{2.9}$$

In order to use perturbation theory, we shall choose the field

$$\boldsymbol{H} = (0,\ 0,\ A_0K\sin Ky) \tag{2.10}$$

which may be obtained from the vector potential

$$\boldsymbol{A} = (A_0\cos Ky,\ 0,\ 0) \tag{2.11}$$

We choose K such that $a \ll 1/K \ll L$. We also choose periodic boundary conditions for K. "a" is a typical lattice parameter and "L" is a typical linear dimension of the crystal. With K chosen this way we would expect to observe the effects of a macroscopic field. We now have $\Delta F = f(A_0, K)$, which we must relate to the susceptibility.

If the system has a susceptibility χ, and magnetization $I(\boldsymbol{r})$ in a certain region would be given by $I(\boldsymbol{r}) = \chi H(\boldsymbol{r})$ where $H(\boldsymbol{r})$ is the magnetic field

in that region. Therefore the change in the free energy, ΔF, would be given by[12]

$$\Delta F = \tfrac{1}{2}\int_V I(\mathbf{r})H(\mathbf{r})\,d\mathbf{r} = \tfrac{1}{2}\chi\int_V H^2(\mathbf{r})\,d\mathbf{r} \quad (2.12)$$

or

$$\Delta F/V = \tfrac{1}{2}\chi\frac{1}{V}\int_V H^2(\mathbf{r})\,d\mathbf{r} = \tfrac{1}{2}\chi\overline{H^2} \quad (2.13)$$

To calculate $\overline{H^2}$ easily we choose a cubic crystal of volume L^3, then we have for $\overline{H^2}$ with previously chosen periodic boundary conditions for K,

$$\overline{H^2} = \frac{1}{L^3}\int_V A_0K^2\sin^2Ky\,dxdydz = \frac{A_0^2K^2}{2} \quad (2.14)$$

We may now write for the susceptibility.

$$\chi = -\frac{4\Delta F}{A_0^2K^2V} \quad (2.15)$$

or using equation (2.9)

$$\chi_{mB} = \frac{-4n}{Z_0A_0^2K^2}\sum_l\left\{\mathscr{H}_{2ll} - \frac{1}{\beta}\times\right.$$

$$\left.\times\sum_{l'}|\mathscr{H}_{1ll'}|^2f(\omega_{l'l})\right\}\exp(-\beta\epsilon_l) \quad (2.16)$$

where $n = N/V$, the number of particles per unit volume (1/cm^3). Here we label χ as χ_{mB} because this is the susceptibility calculated with Maxwell–Boltzmann statistics. To determine $\mathscr{H}_1$ and $\mathscr{H}_2$ in general we must make the substitution $k_\alpha \to P_\alpha - (e/c)A_\alpha$. A simple example is the free particle:

$$\mathscr{H} = \frac{\left(\mathbf{p} - \frac{e}{c}\mathbf{A}\right)^2}{2m} = \mathscr{H}_0 + \mathscr{H}_1 + \mathscr{H}_2 \quad (2.17a)$$

$$\mathscr{H}_1 = \frac{-e}{2mc}(\mathbf{A}\cdot\mathbf{p} + \mathbf{p}\cdot\mathbf{A}) = -\mu_B(\mathbf{A}\cdot\mathbf{p} + \mathbf{p}\cdot\mathbf{A}) \quad (2.17b)$$

$$\mathscr{H}_2 = \frac{e^2}{2mc^2}\mathbf{A}^2 = 2m\mu_B^2\mathbf{A}^2 \quad (2.17c)$$

where $\hbar$ is taken as 1 from now on, and $\mu_B = e/2mc$ is the Bohr magneton. If $\mathbf{A}\cdot\mathbf{p} = \mathbf{p}\cdot\mathbf{A}$, we may write for equation (2.16)

$$\chi_{mB} = -\frac{8n\mu_B^2}{Z_0A_0^2K^2}\sum_l\left\{mA_{ll}^2 - \frac{2}{\beta}\times\right.$$

$$\left.\times\sum_{l'}|\mathbf{A}\cdot\mathbf{p}_{ll'}|^2f(\omega_{l'l})\right\}\exp(-\beta\epsilon_l) \quad (2.18)$$

and with

$$\mathbf{A} = (A_0\cos Ky,\ 0,\ 0)$$

$$\chi_{mB} = -\frac{8n\mu_B^2}{Z_0K^2}\sum_l\left\{m\cos^2Ky_{ll} - \frac{2}{\beta}\times\right.$$

$$\left.\times\sum_{l'}|\cos KyPx_{ll'}|^2f(\omega_{l'l})\right\}\exp(-\beta\epsilon_l) \quad (2.19)$$

The great simplification achieved by using the vector potential of the form $\sim\cos Ky$ is that the matrix elements have the form

$$\sim\int_V\exp(-i\mathbf{k}\cdot\mathbf{r})\cos Ky\exp(i\mathbf{k}\cdot\mathbf{r})\,d\mathbf{r}.$$

If we treat K as a vector in the y direction, that is

$$\cos Ky = \tfrac{1}{2}[\exp(i\mathbf{K}\cdot\mathbf{r}) + \exp(-i\mathbf{K}\cdot\mathbf{r})]$$

we note that the integral is non-zero only if $k'-k+K=0$ or $k'-k-K=0$ because of its periodic form. Hence the value of the integral is proportional to $(\delta_+ + \delta_-)$ where $\delta_\pm = \delta_{\mathbf{k}'-\mathbf{k}} \pm \mathbf{K}$. The delta functions leave our expression for χ_{mB} a function of $\mathbf{k}$ and $\mathbf{K}$. We then expand χ_{mB} in a power series in $\mathbf{K}$. At this point, we take the limit as $\mathbf{K}$ approaches zero (which corresponds to a uniform field) in the ensuing expression and we are left with an expression for the susceptibility. For the free particle we obtain for χ_{mB},

$$\chi_{mB} = -\tfrac{1}{3}\mu_B^2n\beta, \quad (2.20)$$

the usual Landau result.

By applying the known transformation of WILSON and SONDHEIMER[9], we obtain from Maxwell–Boltzmann the corresponding result for Fermi–Dirac statistics. This result is valid as long

Vol. 17
1960

as the Hamiltonian is a quadratic function of the momentum.

3. THE VALENCE BAND IN GERMANIUM

The valence band of germanium is characterized by three doubly-degenerate bands, the highest two being degenerate at $k = 0$ and the third is separated from these two by an amount ΔE at $k = 0$. We do not consider the contribution of the latter to the susceptibility here. The Hamiltonian for a hole in the valence band is of the form of a four by four matrix. The Hamiltonian for this case with the magnetic field present is given as,[13]

$$\mathscr{H} = \frac{1}{m}\left\{\left(\gamma_1+\frac{5\gamma_2}{2}\right)\frac{k^2}{2} - \gamma_2(k_x^2J_x^2+k_y^2J_y^2+k_z^2J_z^2) - \right.$$
$$-2\gamma_3(\overline{k_xk_y}\,\overline{J_xJ_y}+\overline{k_yk_z}\,\overline{J_yJ_z}+\overline{k_zk_x}\,\overline{J_zJ_x})+$$
$$\left.+\frac{e}{c}\mathrm{K}\boldsymbol{J}\cdot\boldsymbol{H}+\frac{e}{c}q(J_x^3H_x+J_y^3H_y+J_z^3H_z)\right\} \tag{3.1}$$

The J's appearing in the Hamiltonian correspond to angular momentum matrices for spin 3/2. The k's are understood to be $k_\alpha = p_\alpha-(e/c)A_\alpha$ and $\overline{k_xk_y}$ is the symmetrized product, $\frac{1}{2}(k_xk_y+k_yk_x)$. With the Hamiltonian in its present form, the unperturbed energies are not isotropic functions of k.

Theoretical estimates as well as some cyclotron resonance data indicate that q is very small, so that we approximate $\mathscr{H}$ by taking $q = 0$. Because in germanium $(\gamma_2-\gamma_3)/(\gamma_2+\gamma_3) \sim 0{\cdot}15$ we further approximate the Hamiltonian by setting $\gamma_2 = \gamma_3 = \bar{\gamma}$ and use as a value for $\bar{\gamma}$ that of $(\gamma_2+\gamma_3)/2$. This greatly simplifies the calculations, for now the energy is an isotropic function of k. By the means of the identity

$$\sum_{\alpha,\beta}(\overline{k_\alpha k_\beta})(\overline{J_\alpha J_\beta}) = (\boldsymbol{k}\cdot\boldsymbol{J})^2 - \frac{e}{2c}(\boldsymbol{J}\cdot\boldsymbol{H}) \tag{3.2}$$

where again $k_\alpha = p_\alpha-(e/c)A_\alpha$, we may rewrite the expression for the Hamiltonian as

$$\mathscr{H} = \frac{1}{m}\left\{\left(\gamma_1+\frac{5\bar{\gamma}}{2}\right)\frac{k^2}{2} - \bar{\gamma}(\boldsymbol{k}\cdot\boldsymbol{J})^2+\right.$$
$$\left.+\left(\kappa+\frac{\bar{\gamma}}{2}\right)\frac{e}{c}(\boldsymbol{J}\cdot\boldsymbol{H})\right\} \tag{3.3}$$

To calculate the susceptibility we must first put $k_\alpha = p_\alpha-(e/c)A_\alpha$ in the Hamiltonian and obtain

$$\mathscr{H} = \mathscr{H}_0+\mathscr{H}_1+\mathscr{H}_2 \tag{3.4a}$$

$$\mathscr{H}_0 = \frac{1}{m}\left\{\left(\gamma_1+\frac{5\bar{\gamma}}{2}\right)\frac{p^2}{2} - \bar{\gamma}(\boldsymbol{p}\cdot\boldsymbol{J})^2\right\} \tag{3.4b}$$

$$\mathscr{H}_1 = \frac{-e}{mc}\left\{\left(\gamma_1+\frac{5\bar{\gamma}}{2}\right)\left(\frac{\boldsymbol{p}\cdot\boldsymbol{A}+\boldsymbol{A}\cdot\boldsymbol{p}}{2}\right) - \right.$$
$$-\bar{\gamma}[(\boldsymbol{p}\cdot\boldsymbol{J})(\boldsymbol{A}\cdot\boldsymbol{J})+(\boldsymbol{A}\cdot\boldsymbol{J})(\boldsymbol{p}\cdot\boldsymbol{J})]+$$
$$\left.+\left(\kappa+\frac{\bar{\gamma}}{2}\right)(\boldsymbol{J}\cdot\boldsymbol{H})\right\} \tag{3.4c}$$

and

$$\mathscr{H}_2 = \frac{e^2}{mc^2}\left\{\left(\gamma_1+\frac{5\bar{\gamma}}{2}\right)\frac{A^2}{2} - \bar{\gamma}(\boldsymbol{A}\cdot\boldsymbol{J})^2\right\} \tag{3.4d}$$

The energy levels corresponding to $\mathscr{H}_0$ are

$$\epsilon_1 = \epsilon_4 = \frac{(\gamma_1+2\bar{\gamma})}{2m}k^2 \tag{3.5a}$$

and

$$\epsilon_2 = \epsilon_3 = \frac{(\gamma_1-2\bar{\gamma})}{2m}k^2 \tag{3.5b}$$

With the gauge chosen as in Section 2, that is $\boldsymbol{A} = (A_0\cos Ky,\ 0,\ 0)$, we have for $\mathscr{H}_1$ and $\mathscr{H}_2$,

$$\mathscr{H}_1 = -2A_0\mu_B\left\{\left(\gamma_1+\frac{5\bar{\gamma}}{2}\right)p_x\cos K_y - \right.$$
$$-\bar{\gamma}[\cos KyJ_x(\boldsymbol{p}\cdot\boldsymbol{J})+(\boldsymbol{p}\cdot\boldsymbol{J})J_x\cos Ky]+$$
$$\left.+\left(\kappa+\frac{\bar{\gamma}}{2}\right)K\sin KyJ_z\right\}$$
$$\equiv -2A_0\mu_B\mathscr{H}'_1 \tag{3.6a}$$

and

$$\mathscr{H}_2 = 2mA_0^2\mu_B^2\left\{\left(\gamma_1+\frac{5\bar{\gamma}}{2}\right)\cos^2Ky - 2\bar{\gamma}J_x^2\cos Ky\right\}$$
$$\equiv 2mA^2\mu^2\mathscr{H}'_2. \tag{3.6b}$$

At this point, two alternative methods of calculation may be used. The matrix elements of $\mathscr{H}'_1$ and $\mathscr{H}'_2$ can be calculated directly from the eigenfunctions

of $\mathscr{H}_0$ (which have the form $\psi_i = u_i(\boldsymbol{k}) \exp(i\boldsymbol{k}\cdot\boldsymbol{r})$. This we did not do. What appeared to be a shorter method of calculation was to write (by means of certain projection operators) the expression for ΔF as a trace, and to make use of the invariance properties of the trace with respect to the choice of basis functions. This is illustrated by the following procedure. In the expression for χ_{mB}, the index "l" denotes a sum over the degenerate bands and a sum over k, that is

$$\sum_l = \sum_{i=1}^{4} \sum_k .$$

We rewrite the expression for χ_{mB} as,

$$\chi_{mB} = \frac{-8\mu_B^2 n}{Z_0 K^2} \sum_{i=1}^{4} \sum_k \Big\{ m(\mathscr{H}'^{ii}_{2kk}) - \frac{2}{\beta} \sum_{j=1}^{4} \sum_k |\mathscr{H}'^{ij}_{1kk'}|^2 f(\omega^{k'k}_{ji}) \Big\} \exp[-\beta\epsilon_i(k)] \tag{3.7}$$

A typical matrix element may be represented as

$$\mathscr{H}'^{ij}_{1kk'} = \frac{1}{V} \int_V \exp(-i\boldsymbol{k}\cdot\boldsymbol{r}) U_i^*(\boldsymbol{k}) \mathscr{H}'_1 U_j(\boldsymbol{k}') \times \times \exp(i\boldsymbol{k}'\cdot\boldsymbol{r})\, d\boldsymbol{r} \tag{3.8}$$

We define $\mathscr{H}'_{1kk}$ by its relationship to the matrix elements as

$$\mathscr{H}'^{ij}_{1kk'} \equiv U_i^*(\boldsymbol{k}) \mathscr{H}'_{1kk'} U_j(\boldsymbol{k}) \tag{3.9}$$

The U's are four-component vectors and the $\mathscr{H}'$'s are four by four matrices so that this representation of $\mathscr{H}'^{ij}_{1kk'}$ is like a scalar product of $U_i^*(\boldsymbol{k})$ and $\mathscr{H}'_{1kk'} U_j(k)$. From equation (3.8) we see that $\mathscr{H}'_{1kk'}$ will be $\sim (\delta_+ + \delta_-)$ as in the case of the free particle.

The two necessary projection operators are constructed as

$$\Lambda^+(k) = \frac{\mathscr{H}_0 - \epsilon_1}{\epsilon_2 - \epsilon_1} \tag{3.10a}$$

and

$$\Lambda^-(k) = \frac{\mathscr{H}_0 - \epsilon_2}{\epsilon_1 - \epsilon_2} \tag{3.10b}$$

and have the following properties:

$$\Lambda^+(k)\psi_1(k) = \Lambda^+(k)\psi_4(k) = \Lambda^-(k)\psi_2(k) = \Lambda^-(k)\psi_4(k) = 0$$

and

$$\Lambda^+(k)\psi_2(k) = \psi_2(k), \text{ etc.}$$

We can now make replacements of the type

$$|\mathscr{H}'^{22}_{1kk'}|^2 + |\mathscr{H}'^{23}_{1kk'}|^2 + |\mathscr{H}'^{32}_{1kk'}|^2 + |\mathscr{H}'^{33}_{1kk'}|^2 = \mathrm{Tr}(\mathscr{H}'_{1kk'} \Lambda^+(k') \mathscr{H}'_{1k'k} \Lambda^+(k)) \tag{3.11}$$

in the expression for χ_{mB} and obtain

$$\chi_{mB} = -\frac{8\mu_B^2 n}{Z_0 K^2} (S_1 + S_2). \tag{3.12}$$

S_1 and S_2 are defined as

$$S_1 \equiv \sum_k \{\mathrm{Tr}(\mathscr{H}'_{2kk} \Lambda^-(k)) \exp[-\beta\epsilon_2(k)] + \mathrm{Tr}(\mathscr{H}'_{2kk} \Lambda^+(k)) \exp[-\beta\epsilon_1(k)]\} \tag{3.13a}$$

and

$$S_2 \equiv -\frac{2}{\beta} \sum_k \sum_{k'} \{\mathrm{Tr}(\mathscr{H}'_{1kk'} \Lambda^-(k') \mathscr{H}'_{1k'k} \Lambda^-(k)) f(\omega^{k'k}_{11}) \exp[-\beta\epsilon_1(k)] + \mathrm{Tr}(\mathscr{H}_{1kk'} \Lambda^+(k') \mathscr{H}_{1k'k} \Lambda^+(k)) f(\omega^{k'k}_{22}) \exp[-\beta\epsilon_2(k)] + \mathrm{Tr}(\mathscr{H}'_{1kk'} \Lambda^+(k') \mathscr{H}'_{1k'k} \Lambda^-(k)) f(\omega^{k'k}_{12}) \exp[-\beta\epsilon_2(k)] + \mathrm{Tr}(\mathscr{H}'_{1kk'} \Lambda^-(k') \mathscr{H}'_{1k'k} \Lambda^+(k)) f(\omega^{k'k}_{21}) \exp[-\beta\epsilon_1(k)]\}$$

Vol. 17
1960

The evaluation of the traces in the expressions for S_1 and S_2 is straightforward but tedious. These traces involve products of the J's up to the eighth power. They were evaluated by choosing a particular representation for the J's, and calculating the traces in S_1 and S_2 directly.

When the traces are performed, the resulting expression for S_2 is a function of k and K (as $\mathscr{H}'_{1kk'}$ is $\sim(\delta_+ + \delta_-)$) and the expression for S_1 is already a function of k alone. Taking at this point the limit as K approaches zero in the expression for χ_{mB} (equation 3.12), we are left with the field independent part of the susceptibility for a homogeneous field. This is

$$\chi_{mB} = -\tfrac{1}{3}\mu_B^2 n\beta\gamma_1^2 W \tag{3.14}$$

where

$$W \equiv 1 - 15\left(\frac{\kappa}{\gamma_1}\right)^2 + \left[\frac{36}{5} + \frac{6111}{128}\left(\frac{\kappa}{\gamma_1}\right)^2 + \right.$$
$$\left. + 36\frac{\kappa\bar{\gamma}}{\gamma_1} - \frac{49}{10}\left(\frac{\bar{\gamma}}{\gamma_1}\right)^2\right]F -$$
$$- \left[30\frac{\bar{\gamma}\kappa}{\gamma_1^2} - \frac{25}{3}\frac{\bar{\gamma}}{\gamma_1}\right]G, \tag{3.15}$$

$$G \equiv \frac{(\gamma_1+2\bar{\gamma})^{3/2} - (\gamma_1-2\bar{\gamma})^{3/2}}{(\gamma_1+2\bar{\gamma})^{3/2} + (\gamma_1-2\bar{\gamma})^{3/2}}, \tag{3.16a}$$

and

$$F \equiv 1 - \frac{\gamma_1}{3\bar{\gamma}}G \tag{3.16b}$$

If we now apply the transformation[9] from Maxwell–Boltzmann to Fermi–Dirac statistics we obtain

$$\chi_{FD} = \chi_{mB} F_{1/2}(\eta)/F_{1/2}(\eta) \tag{3.17}$$

with η now defined by the equation

$$F_{1/2}(\eta) = \frac{nh^3}{(mkT)^{3/2}}\frac{\pi^2}{2^{1/2}}\frac{1}{\omega}\left(\frac{\gamma_1}{\bar{\gamma}}\right)^{3/2} \tag{3.18}$$

Here ω is the degeneracy at $k = 0$ (4 for Ge), and $\bar{\gamma}$ is defined as

$$\bar{\gamma} \equiv \gamma_1[(\gamma_1+2\bar{\gamma})^{3/2} + (\gamma_1-2\bar{\gamma})^{3/2}]^{2/3} \times$$
$$\times [2(\gamma_1+2\bar{\gamma})^{3/2}(\gamma_1-2\bar{\gamma})^{3/2}]^{-2/3} \tag{3.19}$$

We may write down the low temperature susceptibility, that is

$$\lim_{T\to 0} \chi_{FD} = -\frac{4\pi m\mu_B^2}{3h^2}\left(\frac{3n}{\pi}\right)^{1/3}(\omega^{2/3}\bar{\gamma}\gamma_1 W), \tag{3.20}$$

where the necessary $\hbar$'s have been inserted in equations (3.18) and (3.20).

The susceptibility of the valence band is plotted as a function of T and n in the region of interest in Fig. 1.[13] In Table 1 the numerical values of the constants used are listed.

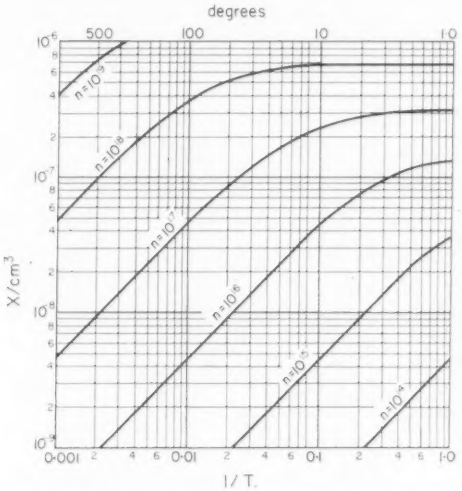

FIG. 1. The susceptibility of the valence band of Ge as a function of T and n.

Table 1

Constant	Value[14]
γ_1	13·2
γ_2	4·1
γ_3	5·6
γ	4·85
K	3·9

4. DISCUSSION

In any attempt to compare experimental values of the susceptibility to values predicted by formulae

developed here, those factors which limit the reliability of both the experimental and predicted values should be taken into consideration.

First let us consider the predicted values. As the susceptibility was calculated on the basis of the effective mass limit, we would expect that for low concentrations any error introduced by using this model would be negligible. We shall see later that we expect little error in the predicted value at concentrations which could give us a reliable experimental value to compare with. Therefore the only foreseeable error in the predicted value would come from the approximation in the Hamiltonian when we set $\gamma_2 = \gamma_3$. We assume an error of the order of 15 per cent was introduced by doing this. By means of perturbation theory one could calculate this correction, but we have not done this because it is quite tedious and not yet called for by the data.

It seems therefore that the value of the susceptibility inferred from experimental data is the main cause of a limited range of comparison. To begin with, the present method used to measure the susceptibility of n holes in the valence band is one of subtraction. The total susceptibility (per cm^3) of a germanium crystal of G atoms/cm^3, L impurity atoms/cm^3, and n holes/cm^3 in the valence band would be given by the following formula,

$$\chi_T = \chi_{FD} + G\chi_{\mathrm{Ge}} + (L-n)\chi_{\mathrm{imp}}$$

where χ_{Ge} is the susceptibility/atom of a pure Ge crystal; χ_{imp} is the susceptibility/atom of an unionized impurity atom. To determine χ_T one first measures the total susceptibility (1/cm^3) of a "pure" crystal (to determine χ_{Ge}) and also the total susceptibility (1/cm^3) of a crystal with impurities and from these two values (and a previous expression for χ_{imp}) one obtains χ_{FD}. In the range which we feel the formulae may be applied, the contribution for the holes ranges from 1 to 1/200 of the contribution of the host crystal depending on the temperature and concentrations. Another experimental difficulty is that though values within a given series of measurements are highly reproducible, when the experiment is performed at another time, the results are not as reproducible. These two facts together would lead to a shift of the absolute value of the susceptibility but would not change the general features of a susceptibility curve if the concentration of holes as a function of temperature was available.

The most important restriction comes from the effect of so-called "Impurity Banding". For those concentrations ($n > 5\times 10^{16}$/cm^3) in which impurity band conduction is observed, the likelihood of comparison is limited in at least two ways. Firstly, by reducing the accuracy of the evaluation of the number of holes in the band (the number of holes in the valence band, not the number of carriers), and secondly by introducing a direct contribution to the susceptibility. As the second is not well understood at the present time, it would seem that only for concentrations of holes of $< 5\times 10^{16}$ can one expect comparison with this theory.

REFERENCES

1. Bowers R., *Phys. Rev.* **108,** 683 (1957).
2. Stevens D. K., Cleland I. W., Crawford J. H., Jr. and Schweinler H. C., *Phys. Rev.* **100,** 1084 (1955).
3. Hedgecock F. T., *Canad J. Phys.* **34,** 43 (1956); *J. Electronics* **2,** 513 (1957).
4. van Itterbuck A. and Duchateau W., *Physica, Eindhoven* **22,** 699 (1956).
5. Kohn W. and Luttinger J. M., *Phys. Rev.* **97,** 869 (1955).
6. In order to examine the ease of application of this method, we have calculated the diamagnetic susceptibility of Bloch electrons which was previously calculated by a different method by Hebron and Sondheimer[7]. Our results were in complete agreement with theirs. This method was previously used in an unpublished diamagnetism calculation of Kohn and Luttinger.
7. Hebron J. E. and Sondheimer E. H., *Phys. Rev. Letters* **2,** 150 (1959).
8. Peierls R. E., *Quantum Theory of Solids* p. 144. Oxford University Press (1955).
9. See, for example, Wilson H. A., *The Theory of Metals*, p. 164. Cambridge University Press (1953). Wilson outlines a general method of relating thermodynamical quantities calculated by Maxwell–Boltzmann statistics to those calculated by Fermi–Dirac statistics. We employ the transformation to relate χ_{mB} the Maxwell–Boltzmann susceptibility or the susceptibility in the classical region to χ_{FD} the susceptibility which is correct in all regions. The results are in this case that

$$\chi_{FD} = \chi_{mB}F'_{1/2}(\eta)/F_{1/2}(\eta)$$

where

$$F_{1/2}(\eta) = \int_0^\infty [\exp(x-\eta)+1]^{-1}\times x^{1/2}\,dx$$

and

$$F'_{1/2}(\eta) = (\partial/\partial\eta)F_{1/2}(\eta)$$

are familiary known as Fermi–Dirac integrals.

Vol. 17
1960

The above relationship only holds for a Hamiltonian which is quadratic terms in k.

10. McDOUGALL J. and STONER E. C., *Phil. Trans.* a**237,** 67 (1938).
11. BROWN H. and LUTTINGER J. M., *Phys. Rev.* **100** 685 (1955).
12. PANOFSKY W. K. H. and PHILLIPS M., *Classical Electricity and Magnetism* p. 153. Addison-Wesley, New York (1955).
13. LUTTINGER J. M., *Phys. Rev.* **102,** 1030 (1956).
14. BROWN H., Thesis, University of Michigan (unpublished).

J. Phys. Chem. Solids Pergamon Press 1961. Vol. 17, Nos. 3/4, pp. 292–300. Printed in Great Britain.

ETUDE SPECTROPHOTOMETRIQUE DE LA SERIE JAUNE DE Cu_2O AUX BASSES TEMPERATURES

S. NIKITINE, J. B. GRUN et M. SIESKIND

Laboratoire de Spectroscopie et d'Optique du Corps Solide, Institut de Physique, Université de Strasbourg (France)

(*Received* 30 *May* 1960)

Résumé—L'intensité d'oscillateur des raies d'absorption de la série "jaune" des cristaux de Cu_2O a été déterminée expérimentalement à différentes températures (77, 20 et 4°K) par une méthode spectrophotométrique. L'intensité d'oscillateur de la première raie ($n = 2$) est $f_2 = 2{,}8 \times 10^{-6}$; les intensités d'oscillateur relatives $f_0(n) = f_n/f_2$ n'ont pu être calculées avec une précision suffisante à partir des données expérimentales que pour les premières raies de la série. La valeur de f_2 ainsi que l'intensité d'oscillateur relative dans la série sont en bon accord avec la théorie d'ELLIOTT[1] des transitions excitoniques défendues.

Cet argument joint aux autres arguments déjà connus[1,2] permet d'affirmer que la série "jaune" de Cu_2O appartient a un spectre excitonique défendu (spectre de deuxième classe).

On a montré que le maximum du coefficient d'absorption K_{max} d'une raie décroît avec le nombre quantique n suivant la loi $K_{max} \propto 1/n^2$ pour $n \geqslant 3$.

Ces raies ont une forme asymétrique. On a introduit un paramètre pour caractériser cette propriété et on a étudié la variation de ce paramètre avec n. La forme de la première raie ($n = 2$) diffère beaucoup de la forme des autres raies de la série.

Les résultats de nos mesures montrent que la durée de vie des excitons croît avec n; ce résultat n'est pas inconsistant avec la théorie de TOYOZAWA[12].

Abstract—The "yellow" series of absorption lines in Cu_2O crystals has been studied by spectrophotometric methods at different temperatures down to liquid helium. The experimental values of the oscillator strength of the absorption lines have been determinated. The oscillator strength of the first lines ($n = 2$) is $f_2 = 2{\cdot}8 \times 10^{-6}$; the relative oscillator strength $f_0(n) = f_n/f_2$ has been calculated from experimental data for different lines. $f_0(n)$ is however determined with a sufficient accuracy for the very first lines of the series only. Both the value of f_2 and the relative oscillator strength in the series are in good agreement with ELLIOTT'S[1] theory of forbidden exciton transitions. These arguments added to others already known[1,2] give a very solid basis to the interpretation of the "yellow" series of Cu_2O as a forbidden exciton spectrum.

It has been shown that the maximum of the coefficient of absorption in a line K_{max} decreases with the quantum number n according to a law $K_{max} \propto 1/n^2$ for $n \geqslant 3$.

The lines are of a very assymetric form. A parameter is introduced to characterize this property. The variation of this parameter with n is investigated. The form of the first line ($n = 2$) differs very much from the form of the other lines of the series.

According to our data, the life time of excitons increases with n; this result is not inconsistent with TOYOZAWA's theory.[12]

INTRODUCTION

LES SPECTRES de raies d'absorption que l'on observe avec des cristaux de Cu_2O ont été attribués à des transitions de deuxième classe (faiblement interdites) vers des états excitoniques P[1,2]. Toutefois, cette attribution reposait sur des arguments qualitatifs ou semi quantitatifs. Peu de données quantitatives ayant été obtenues jusqu'à présent sur les spectres en question, nous nous sommes proposés de reprendre l'étude de la série "jaune" de Cu_2O pour être en mesure d'effectuer une comparaison quantitative de la théorie d'ELLIOTT[1] des transitions excitoniques de deuxième classe avec des données expérimentales.

Nous avons déjà donné les premiers résultats de nos études dans une communication présentée au Congrès de Bologne.[3] Nous avons pu obtenir depuis un grand nombre de données nouvelles dont la comparaison avec la théorie fait l'objet de ce mémoire.

RAPPEL DE LA THEORIE DES SPECTRES EXCITONIQUES

La théorie d'ELLIOTT prévoit deux classes de spectres excitoniques.

Les transitions de première classe (4) correspondent à des spectres permis. Elles se produisent pour $\vec{K} = 0$ et $\Delta\vec{K} = 0$, où $\vec{K}$ est le vecteur d'onde et seules des transitions vers les états excitoniques S sont permises. La théorie prévoit que les spectres de raies doivent être hydrogénoïdes :

$$\nu_n = \nu_\infty - \frac{R_e}{n^2} \text{ avec } n = 1, 2, \ldots \infty \qquad (1a)$$

où ν_n est le nombre d'onde de la nième raie, ν_∞ celui de la limite de la série, R_e le nombre de Rydberg excitonique et n le nombre quantique. Par ailleurs, les intensités d'oscillateur des raies de la série varient comme :

$$f_n = \frac{C_1}{\epsilon^3 n^3} \qquad (2)$$

où C_1 est une constante que l'on peut calculer à priori dans certains cas et ϵ la constante diélectrique. L'ordre de grandeur de C_1 peut être prévu dans la plupart des cas.

L'un de nous a montré[2] que la théorie de cette classe de transitions décrit, quelquefois jusque dans les détails d'une façon remarquable, les spectres de certaines substances (CuI, CuCl, HgI_2, PbI_2, etc.).

Quand les transitions de première classe sont interdites, en raison de la structure des bandes électroniques ($C_1 = 0$), une deuxième classe de transitions peut être prévue. Elle est faiblement interdite. Dans ce cas, $\Delta\vec{K} = 0$, $\vec{K} \neq 0$ mais très petit. On montre qu'alors, seules des transitions vers des états P excitoniques, sont permises. De ce fait, les raies de la série obéissent encore à une loi hydrogénoïde, mais la raie correspondant à $n = 1$ est interdite :

$$\nu_n = \nu_\infty - \frac{R_e}{n^2} \qquad \begin{matrix} n = 2, 3, \ldots \infty \\ n \neq 1. \end{matrix} \qquad (1b)$$

Par ailleurs, le facteur f est donné par la formule :

$$f_n = \frac{C_2}{\epsilon^5} \frac{n^2 - 1}{n^5}$$

C_2 est une constante qui est difficile à calculer dans l'état actuel de la théorie, mais dont on peut estimer l'ordre de grandeur. L'un de nous a montré[2] que dans cette évaluation, on pouvait préciser que, dans les spectres de deuxième classe, l'absorption devait être beaucoup plus faible que dans les spectres de première classe. Une évaluation grossière a été faite et montre que le rapport des facteurs f pour la raie $n = 1$ d'un spectre de première classe et pour la raie $n = 2$ d'un spectre de deuxième classe est de l'ordre de 10^{-3}, en admettant que les deux spectres comparés appartiennent à deux corps ayant des ϵ du même ordre. Or, l'absorption dans Cu_2O est effectivement beaucoup plus faible que dans CuI, dont le spectre est un cas typique pour les transitions de première classe. Cet argument, ainsi que le fait que les séries de raies observées avec la cuprite[5,6,7,8], commencent avec la raie $n = 2$ (la raie $n = 1$ est également observable quelquefois, mais elle est très faible. Elle est probablement observable dans des cristaux possédant de fortes tensions,[3] ont conduit[1] et[2] à l'estimation que les spectres de la cuprite étaient dus à des transitions excitoniques de deuxieme classe.*

Mais, il est certain que des données quantitatives doivent être apportées à l'appui de cette classification. En effet, l'attribution des spectres d'autres substances à la première classe aurait pu être faite en se basant sur l'intensité de l'absorption car elle est très grande. Ce fait élimine l'attribution de ces spectres à des impuretés ou défauts éventuels [2cdf]. Dans le cas de la cuprite, cet argument n'est plus valable car l'intensité d'absorption est de l'ordre de grandeur de celle que pourraient donner des impuretés ou des défauts éventuels.

* L'effet Zeeman étudié par GROSS *et al.*[6] est également une preuve de l'origine excitonique du spectre de la cuprite, mais ne donne pas d'indication directe quant à la nature de la transition excitonique.

Ainsi, l'attribution des spectres de Cu_2O, bien que plausible, n'était pas démontrée rigoureusement.

Une étude quantitative approfondie paraît donc indispensable pour pouvoir statuer sur cette attribution.

COMPARAISON DES DONNEES EXPERIMENTALES AVEC LA THEORIE

Il est évident qu'un élément essentiel de comparaison des données expérimentales avec la théorie est obtenu en mesurant les valeurs expérimentales f_{exp} de l'intensité d'oscillateur des raies et en les comparant avec les valeurs théoriques de la formule suivante :

$$f_{exp} = \frac{m_0 c^2}{\pi N e^2} \int nK \, d\nu \qquad (4)$$

Dans cette formule, m_0 est la masse de l'électron au repos, c la vitesse de la lumière, N le nombre d'atomes par unité de volume et e la charge de l'électron; n est l'indice de réfraction du cristal et K le coefficient d'absorption défini par la formule:

$$J = J_0(1-R)^2 e^{-Kx} \qquad (5)$$

où x est l'épaisseur du cristal, J_0 l'intensité de lumière incidente et J l'intensité de la lumière

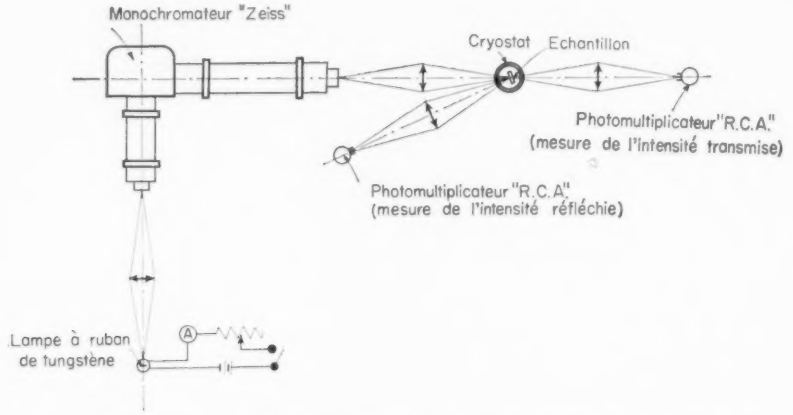

FIG. 1. Montage pour la mesure absolue des coefficients d'absorption et de réflexion.

f_{th}. Comme C_2 ne peut pas être calculé à priori avec précision, la comparaison portera sur :

(a) l'ordre de grandeur des f_{th} que l'on peut évaluer et la valeur des f_{exp}.

(b) la variation de f_{exp} avec n.

Nous avons, en plus, obtenu des données expérimentales qui ne sont pas prévues par la théorie dans son état actuel. Il serait important de développer la théorie dans ce sens.

L'évaluation de f_{exp} peut être faite par différentes méthodes.[2,9] Mais, seule la méthode de KRAWETZ[10] est applicable à Cu_2O, la dispersion anormale n'étant pas observable avec ce corps, les raies étant trop faibles.

La méthode de KRAWETZ repose sur l'application transmise. R est le coefficient de réflexion de Cu_2O. On peut se contenter de cette formule approchée négligeant les termes correspondant aux interférences car la densité optique de nos échantillons dans cette partie du spectre est déjà appréciable.

n varie peu dans la région spectrale où se trouve la série jaune et peut être considéré avec une bonne précision comme constant* et remplacé par une valeur moyenne $\bar{n} = 2{,}75$. On peut alors écrire la formule de KRAWETZ sous une forme plus simple :

$$f_{exp} = aS \qquad (6)$$

* Ce fait ressort avec certitude de nos expériences. Nous n'avons trouvé ni dispersion anormale, ni anomalies du coefficient d'absorption au voisinage des raies. Ces deux faits sont concordants et sont dus à la circonstance que les raies d'absorption sont faibles.

Vol. 17
1960

où $S = \int K\,dv$ est l'intégrale de la courbe d'absorption de la raie étudiée et a une constante.

Comme, dans le cas de Cu_2O, il y a par cellule élémentaire deux fois plus d'atomes de cuivre que d'oxygène et que l'on ne sait pas lequel de ces atomes est responsable de l'absorption, il est préférable de définir f par cellule élémentaire et non par atome. Dans ce cas, pour Cu_2O, on a :

$$f_{\text{exp}}^{V_0} = 2{,}4 \times 10^{-10} S \qquad (7)$$

Le problème consiste donc finalement á évaluer S.

MONTAGE EXPERIMENTAL

Le montage expérimental* comportait (Fig. 1) une source S qui était une lampe à filament de tungstène alimentée au moyen d'une batterie d'accumulateurs, qui permettait d'obtenir un courant constant et une brillance constante. La constance du courant était contrôlée par enregistrement durant toute la mesure.

L'image de S était projetée sur la fente d'entrée d'un monochromateur à trois prismes Zeiss dont la bande passante était 0,5 Å dans la région spectrale considérée.

Pour mesurer les intensités transmises et réfléchies par l'échantillon, l'image de la fente de sortie du monochromateur était projetée sur l'échantillon au moyen d'une lentille L_1. Cet échantillon était légèrement incliné par rapport à l'axe du montage, de façon à envoyer le faisceau réfléchi au moyen d'une lentille L_2 sur un premier photomultiplicateur P_1. Le faisceau transmis dans l'axe du montage était envoyé au moyen d'une autre lentille L_3 sur un deuxième photomultiplicateur P_2.

Pour mesurer l'intensité de la lumière incidente J_0 au moyen des deux photomultiplicateurs P_1 et P_2, on déplaçait le cryostat verticalement dans deux positions différentes, de façon à :

(a) faire passer la lumière directement sur P_2 sans traverser le cristal;

(b) faire tomber la lumière incidente sur un miroir argenté qui la réfléchissait sur P_1.

La coefficient de réflection du miroir avait été mesuré préalablement, ce qui permettait de tenir compte de son pouvoir réflecteur.

La source S ayant une intensité rigoureusement constante, on mesurait d'abord l'intensité incidente pour un grand nombre de longueurs d'onde avec P_1 et P_2. On remettait ensuite en place le cristal et on déterminait, au moyen de P_1 et P_2, l'intensité transmise et réfléchie par le cristal pour les mêmes longueurs d'onde que précédemment. Après cette deuxiéme série de mesures, on reprenait quelques points dans les mêmes conditions que lors de la première série de mesures, pour s'assurer que l'intensité de S n'avait pas changé pendant les mesures. Le courant passant par S était d'ailleurs contrôlé par enregistrement.

Les photomultiplicateurs P_1 et P_2 étaient du type R.C.A. I.P. 21 S4. Le courant, à la sortie, était mesuré avec des galvanomètres A.O.I.P. sensibles à 10^{-9}A sans amplification.

On peut estimer qu'avec les précautions prises, les erreurs commises dans les mesures photométriques étaient de l'ordre de $\pm$ 2 pour cent.

Alors que l'épaisseur de cristaux de CuI et PbI_2 pour la mesure de f doit être de l'ordre de quelques dixièmes de micron, dans le cas de Cu_2O, par suite de la faible absorption, nous avons pu utiliser des lames cristallines de 10 à 20 μ. L'épaisseur de ces lames a été mesurée à l'aide d'un palmer permettant d'évaluer le demi-micron. Mais, cette épaisseur était légèrement variable d'un point à un autre d'un échantillon; il en résultait une incertitude de l'ordre du micron.

On peut finalement estimer que K était déterminé à $\pm$ 5 pour cent près. La précision était un peu moins bonne sur les sommets des raies d'absorption.

DESCRIPTION QUALITATIVE DU SPECTRE D'ABSORPTION

Les Figs. 2(a) et (b) représentent la courbe d'absorption† d'un échantillon de 10 μ d'épaisseur dans la région de la série "jaune" pour $T = 4{,}2$°K. Avant d'en tirer des données quantitatives, quelques remarques générales sont nécessaires.

En premier lieu, il faut noter que l'absorption dans les raies de la série jaune se superpose à un fond continu qui commence à devenir important

* Nous remercions M. BIELLMANN pour son aide au cours du montage de cette installation spectrophotométrique.

† Le fond continu se trouvant du côté des grandes longueurs d'onde au-delà des deux bords rouges est probablement dû à une imprécision dans la détermination de R, la réflexion pouvant comporter une petite part de réflexion diffuse.

dans le rouge à partir des deux bords. Ce fond continu a fait l'objet d'une étude approfondie qui sera le sujet d'une prochaine publication. Il résulte de cette étude qu'il est légitime de considérer ce fond continu comme étant indépendant de l'absorption dans les raies de la série. Il est

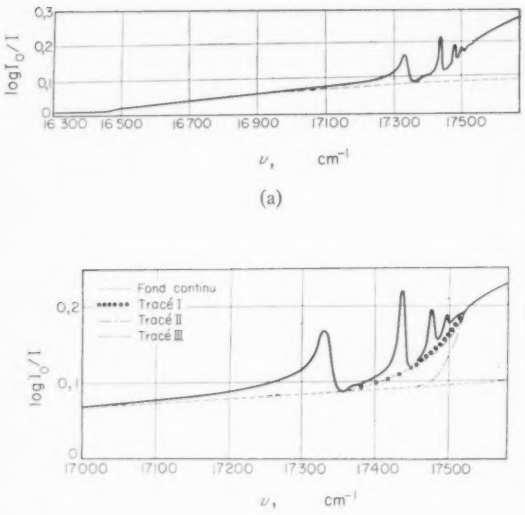

FIG. 2 (a) Courbe d'absorption d'un échantillon de Cu_2O de 10 μ d'épaisseur à 4,2°K. (b) Courbe d'absorption d'un échantillon de Cu_2O de 10 μ d'epaisseur à 4,2°K (série jaune).

donc nécessaire de soustraire de l'absorption totale dans la région spectrale où se trouve la série, l'absorption du fond continu étudiée par ailleurs. On peut observer que la forme de raie $n = 2$ est très différente de la forme des autres raies de la série. Elle est beaucoup plus large et beaucoup plus dissymétrique.

Il est ensuite remarquable que toutes les raies soient dissymétriques, mais qu'elles deviennent de moins en moins dissymétriques quand n croît. Les raies deviennent également beaucoup plus fines quand n croît.

La série converge vers un bord qui forme une transition continue avec une courbe d'absorption croissante.

Dans toute cette région spectrale, le coefficient d'absorption K est de l'ordre de 2 à 5×10^2 cm.

EVALUATION DES INTENSITES D'OSCILLATEUR f_{exp} A PARTIR DE LA COURBE D'ABSORPTION

Pour évaluer l'absorption intégrale S dans les raies, nous avons soustrait de l'absorption dans le spectre, le fond continu, étudié dans un travail à paraître. Il résulte de cette étude que le coefficient d'absorption dans le fond continu varie très exactement comme $(\nu - \nu_i)^{1/2}$ où ν_i est le nombre d'onde du bord limitant cette absorption dans le rouge (ceci est rigoureux à la température de l'He liquide. A haute température, il y a en fait superposition de deux spectres continus de même nature, mais décalés l'un par rapport à l'autre. Les deux spectres peuvent être d'ailleurs décrits par la théorie d'ELLIOTT[1]). Il est alors possible d'extrapoler la formule trouvée pour cette partie de la courbe d'absorption dans le fond continu, jusque vers la série jaune. La soustraction ne présente donc pas un caractère arbitraire, tout au moins au début de la série jaune.

Par ailleurs, ce spectre continu doit se raccorder au spectre continu que l'on observe, du côté des grandes fréquences, au-delà de la série jaune. La théorie ne donne aucune indication quant au raccord de ces deux spectres. Devant cette incertitude, nous avons raccordé à l'estime (Fig. 2) les deux spectres continus suivant deux tracés (I) et (II). Nous avons soustrait ensuite cette absorption continue (I) et (II) de l'absorption totale et obtenu ainsi deux tracés de l'absorption dans les raies.

Pour les courbes obtenues à 4,2°K, ces différents tracés n'influent pratiquement pas sur la valeur de l'intégrale S des raies $n = 2$ et $n = 3$; mais le calcul de S devient hasardeux à cause de la différence entre les deux tracés pour les raies de nombre quantique $n > 3$. On ne peut donner alors que des ordres de grandeur pour ces raies.

Pour la température de l'azote liquide, le calcul de S est déjà incertain pour $n = 3$, mais reste raisonnablement précis pour $n = 2$. Pour la température de l'hydrogène liquide. l'incertitude sur les valeurs de S est intermédiaire. A partir des valeurs de S ainsi obtenues, nous avons calculé les intensités d'oscillateur des différentes raies à différentes températures et pour les deux tracés (I) et (II). Nous avons groupé, dans le Tableau 1, les résultats obtenus avec un même échantillon.

Ces mesures ont été reprises pour différents

Vol. 17
1960

Tableau 1. *Intensités d'oscillateur des raies de la série jaune de* Cu_2O *pour les tracés* (I) *et* (II), *aux températures de l'*He, *l'*H_2 *et* N_2 *liquides.*

	$T = 4°K$				$T = 20°K$				$T = 77°K$				
n	$f_{(I)}10^6$	$f_{0(I)}(n)$	$f_{(II)}10^6$	$f_{0(II)}(n)$	$f_{(I)}10^6$	$f_{0(I)}(n)$	$f_{(II)}10^6$	$f_{0(II)}(n)$	$f_{(I)}10^6$	$f_{0(I)}(n)$	$f_{(II)}10^6$	$f_{0(II)}(n)$	théor. $f_0(n)$
2	2,8	1	2,8	1	2,8	1	3,3	1	2,8	1	3,1	1	1
3	1,0	0,36	1,4	0,5	1,0	0,36	2,2	0,67	1,0	0,36	2,8	0,9	0,34
4	0,3	0,11	0,8	0,29	0,3	0,11	1,0	0,30	0,3	0,11	0,9	0,29	0,14
5	0,1	0,04	0,3	0,11	0,15	0,05	0,4	0,12	—	—	—	—	0,08

échantillons. On en déduit des valeurs concordantes des facteurs f à 3 pour cent près, tout au moins pour les premières raies, L'incertitude sur les raies $n > 3$ provient uniquement de l'incertitude sur le tracé du fond continu. Le Tableau 2

Malheureusement, la constante C_2 de la formule (3) ne peut être calculée avec précision. A priori, on ne peut en donner qu'un ordre de grandeur. Nous nous contenterons de comparer la valeur de f_2 de Cu_2O à celle de f_1 de CuI, qui présente un

Tableau 2. *Comparaison des intensités d'oscillateur de trois échantillons d'epaisseurs différentes pour les raies* $n = 2$ *et* $n = 3$ *à la température de l'*He *liquide.*

	Echantillon 1, $e = 10\ \mu$		Echantillon 2, $e = 12\ \mu$		Echantillon 3, $e = 14\ \mu$			
n	$f_{(I)}10^6$	$f_{(II)}10^6$	$f_{(I)}10^6$	$f_{(II)}10^6$	$f_{(I)}10^6$	$f_{(II)}10^6$	$\overline{f_{(I)}}10^6$	$\overline{f_{(II)}}10^6$
2	2,8	2,8	2,9	2,9	2,6	2,6	2,8 ± 6%	2,8 ± 6%
3	1,0	1,4	1,1	1,6	0,9	1,3	1,0 ± 10%	1,4 ± 10%

donne cette comparaison pour les deux premières raies de la série, à la température de l'He liquide.

Comme le montre le Tableau 1, la valeur de f pour une raie donnée ne varie pas beaucoup avec la température.

COMPARAISON DES VALEURS DE f_{exp} AVEC LA THEORIE

Il est important de comparer les valeurs de facteurs f ainsi déterminés avec la théorie d'ELLIOTT[1] des transitions vers des états excitoniques.

Nous avons dit que le spectre de Cu_2O a été comparé à un spectre de deuxième classe (faiblement interdit) prévu par la théorie d'ELLIOTT. spectre de première classe. Le rapport des valeurs expérimentales

$$\frac{f_{2exp}(Cu_2O)}{f_{1exp}(CuI)} = 0{,}7 \times 10^{-4}$$

est bien de l'ordre de grandeur prévu dans un calcul très approximatif.*[2] La comparaison quantitative ne peut être menée plus loin, tant que le calcul à priori de C_2 ne sera pas effectué.

Mais on peut conduire néanmoins la comparaison plus loin en étudiant les intensités relatives $(f_n/f_2)_{exp}$. La théorie prévoit que ce rapport

* Notons que $f_{2exp}(Cu_2O)$ et $f_{1exp}(CuI)$ ont été évalués par cellule élémentaire.

(C_2 restant constant) est :

$$f_0(n) = \frac{f_n}{f_2} = 10{,}6 \times \frac{n^2-1}{n^5}$$

La comparaison ne peut être faite avec précision que pour $n = 3$ et à la température de l'hélium, par suite de l'incertitude du tracé du fond continu. Mais, pour la raie $n = 3$, l'accord avec la théorie est bon ($\pm$ 15 pour cent environ), comme l'indiquent les valeurs données dans le Tableau 1.

Comme il n'était pas possible de conclure pour les raies de nombre quantique $n > 3$, nous avons tenté de faire le raisonnement inverse. Nous avons supposé que la formule (3) s'appliquait à la série jaune et nous avons construit, à partir des valeurs de f données par cette formule, le fond continu qu'il faudrait soustraire pour obtenir un tel résultat. Ce fond continu (III) est porté sur la Fig. 3. On voit qu'il n'est pas inconsistant avec la courbe expérimentale.

Nous croyons que cette discussion a apporté un élement qualitatif nouveau : ordre de grandeur de f, et un élement quantitatif : valeur de $f_0(n)_{exp}$ en faveur de l'interprétation de la série jaune de la cuprite et son attribution à des transitions excitoniques de deuxième classe. En ajoutant ces arguments nouveaux à ceux qui avaient été donnés précédemment, il nous semble qu'il reste peu de doutes en ce qui concerne cette interprétation.

VALEURS DU COEFFICIENT D'ABSORPTION MAXIMUM K_{max} DES RAIES DE LA SERIE JAUNE

Les valeurs de K_{max} du coefficient d'absorption maximum des raies sont naturellement également affectées par l'incertitude du tracé du fond continu.

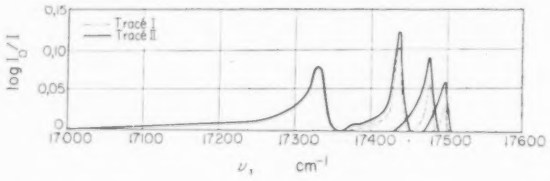

FIG. 3. Profiles de raies de la série jaune de Cu_2O correspondant aux tracés I et II.

Malgré cette incertitude, on peut noter que K_{max} diminue lorsque le nombre quantique n augmente. Il semble que cette variation soit, pour les raies correspondant à $n \geqslant 3$, assez voisine de $K_{max} \propto 1/n^2$. Cette variation ne s'applique pas à la raie $n = 2$, qui est très large et dont la valeur de K_{max} est aberrante. Ces valeurs sont données dans le Tableau 3 pour les deux tracés (I) et (II) et pour différentes températures, mais pour le même

Tableau 3. *Coefficients maxima d'absorption en* cm^{-1} *de la série jaune de* Cu_2O *pour les tracés* (I) *et* (II) *aux températures de l'*He, *l'*H_2 *et* N_2 *liquides.*

	$T = 4°K$		$T = 20°K$		$T = 77°K$	
n	$K^{max}_{(I)}10^{-2}$	$K^{max}_{(II)}10^{-2}$	$K^{max}_{(I)}10^{-2}$	$K^{max}_{(II)}10^{-2}$	$K^{max}_{(I)}10^{-2}$	$K^{max}_{(II)}10^{-2}$
2	1,8	1,8	1,8	1,9	2,0	2,2
3	2,4	2,8	2,1	2,9	1,8	2,8
4	1,3	2,0	1,1	1,9	1,0	1,7
5	0,6	1,4	0,6	1,1	—	—

Vol. 17
1960

échantillon. Il ne paraît pas possible de conclure au sujet de la variation thermique de K_{max}.

LARGEUR ET DISSYMETRIE DES RAIES

Comme nous l'avons dit, les raies de la série jaune de la cuprite sont très dissymétriques. Pour caractériser cette dissymétre, nous avons mesuré, à partir de l'abscisse du maximum de chaque raie, une demi-largeur vers les grandes valeurs de ν : $\Delta\nu^+_{1/2}$, et une demi-largeur vers les petites valeurs de ν : $\Delta\nu^-_{1/2}$. Nous suggérons de prendre, pour paramètre exprimant la dissymétrie d'une raie, la quantité :

$$\delta = \frac{\Delta\nu^-_{1/2} - \Delta\nu^+_{1/2}}{\Delta\nu^-_{1/2} + \Delta\nu^+_{1/2}}$$

$\delta = 1$ pour une raie complètement dissymétrique ($\Delta\nu^+_{1/2} = 0$ par exemple), $\delta = 0$ pour une raie symétrique ($\Delta\nu^-_{1/2} = \Delta\nu^+_{1/2}$).

Il est facile de voir que la dissymétrie des raies diminue quand le nombre quantique des raies augmente dans la série.

Par ailleurs, $2\overline{\Delta\nu}_{1/2} = \Delta\nu^+_{1/2} + \Delta\nu^-_{1/2}$ diminue également lorsque le nombre quantique augmente.

Les valeurs de $\overline{\Delta\nu}_{1/2}$ dépendent beaucoup du tracé du fond continu. Il est assez difficile de se prononcer sur la loi suivant laquelle cette décroissance se produit. Notons que si l'on admet la formule d'ELLIOTT sur la variation de f dans la série et la validité de la loi $K_{max} \propto 1/n^2$ pour $n \geqslant 3$, la variation de $\overline{\Delta\nu}_{1/2}$ devrait être de la forme :

$$\Delta\nu_{1/2} \propto \frac{n^2-1}{n^3} \text{ pour } n \geqslant 3$$

en supposant f proportionnel au produit $K_{max} \times 2\Delta\nu_{1/2}$.

Il est à noter que si l'on admet la relation classique entre la durée de vie et la demi largeur de la raie, on devrait conclure que les excitons de nombre quantique élevé sont plus stables que les excitons de nombre quantique faible, malgré les valeurs en sens contraire des énergies de liaison.*

* Le Prof. YOCCOZ a pu montrer, à partir de la théorie de TOYOZAWA, que la largeur des raies devrait décroitre comme $1/n^6$ quand la masse totale de l'exciton est grande et qu'elle serait constante quand la masse de l'exciton est faible. Nos valeurs correspondraient à un cas intermédiaire.

Tableau 4. *Demi-largeur* (*en* cm^{-1}) *des raies de la série jaune de* Cu_2O *aux températures de l'*He, *l'*H_2 *et* N_2 *liquides pour les tracés* (I) *et* (II).

		Tracé (I)				Tracé (II)			
	n	$\overline{\Delta\nu}_{1/2}$	$\Delta\nu^-_{1/2}$	$\Delta\nu^+_{1/2}$	δ	$\overline{\Delta\nu}_{1/2}$	$\Delta\nu^-_{1/2}$	$\Delta\nu^+_{1/2}$	δ
$T = 4°K$	2	15	20	10	0,33	15	20	10	0,33
	3	5,5	7	4	0,25	6,5	8	5	0,25
	4	4	4	4	0	6,5	8	5	0,23
	5	3	3	3	0	6	8	4	0,33
$T = 20°K$	2	15	22	8	0,45	16,5	24	9	0,45
	3	5,5	7	4	0,25	12,5	17	8	0,36
	4	5	5	5	0	10	14	6	0,4
$T = 77°K$	2	18,5	25	12	0,35	22,5	30	15	0,33
	3	7	8	6	0,14	12	16	8	0,33
	4	4	4	4	0	8	10	6	0,25

Les données concernant la largeur des raies sont réunies dans le Tableau 4.

Il y a lieu de noter que les formules empiriques suggérées sont affectées par l'incertitude du tracé du fond continu. Elles sont des approximations grossières.

CONCLUSIONS

Cette étude nous a permis de déterminer les valeurs expérimentales des intensités d'oscillateur des raies de la série jaune de Cu_2O. Cette détermination a été faite avec une bonne précision pour la raie $n = 2$ et une assez bonne précision pour la raie $n = 3$; pour les raies de nombre quantique plus élevé, nous n'avons pu que déterminer un ordre de grandeur des intensités d'oscillateur. L'ordre de grandeur de l'intensité d'oscillateur f_2 pour $n = 2$ est celui que l'on peut prévoir pour des transitions de deuxième classe. Le rapport $f_0(3) = f_3/f_2$ est en bon accord avec la formule d'ELLIOTT pour ce genre de transitions. Ces données apportent des arguments nouveaux en faveur de l'interprétation des raies de la série jaune comme transitions de deuxième classe. De ce fait, cette attribution ne paraît plus être mise en doute.

Par ailleurs, nous avons montré que la forme de la raie $n = 2$ est très différente de celle des autres raies, comme si cette raie était de nature différente.

Les valeurs de K_{max} décroissent dans la série suivant une loi qui est assez voisine de $1/n^2$.

Les raies sont très dissymétriques, mais la dissymétrie diminue quand n augmente. Par ailleurs, la largeur des raies diminue quand n augmente. Ceci indiquerait une plus grande durée de vie des excitons. Sur l'orbite de nombre quantique $n = 2$ à 4°K elle est $\tau \sim 1{,}8 \times 10^{-13}$ sec. Ces dernières données ne sont pas prévues par la théorie. Il serait souhaitable que celle-ci soit développée dans ce sens.

Remerciements—Nous remercions vivement le Dr. ELLIOTT (Oxford) pour la communication des résultats de ses études théoriques avant leur publication et pour de nombreuses discussions importantes. Nous remercions également le Prof YOCCOZ (Strasbourg) pour des discussions stimulantes sur les questions théoriques concernant nos travaux.

BIBLIOGRAPHIE

1. ELLIOTT R. J., R.R.E. Memorandum, N. 1342 (1957); *Phys. Rev.* **108,** 1384 (1957); *J. Phys. Chem. Solids* **8,** 382 (1959).
2. (a) NIKITINE S., *J. Chim. Phys.* 621 (1958).
   (b) NIKITINE S., *Phil. Mag.* **4, 37,** 1 (1959).
   (c) NIKITINE S., *J. Phys. Chem. Solids* **8,** 190 (1959).
   (d) NIKITINE S., Congrès de Bologne (à paraître).
   (e) NIKITINE S., EL KOMOSS S. G., REISS R. et RINGEISSEN J., *J. Chim. Phys.* 665 (1958).
   (f) NIKITINE S., REISS R. et SIESKIND M., *C.R. Acad. Sci. Paris* **246,** 3439 (1958).
3. NIKITINE S., GRUN J. B. et SIESKIND M., Congrès de Bologne (à paraître).
4. voir aussi DRESSELHAUS G., *J. Phys. Chem. Solids* **1,** 14 (1956); *Phys. Rev.* **106,** 16 (1957).
   HAKEN H., Rapport sur l'état actuel des recherches sur l'exciton, *Halbleiterprobleme* IV, (édité par SCHOTTKY W.). Vieweg, Brunswick (1958).
5. HAYASHI M. et KATZUKI K., *J. Phys. Soc. Japan,* **7,** 599 (1952).
6. GROSS E. F. et KARRYEFF N. A., *Dokl. URSS,* **84,** 47, 261 (1952); GROSS E. F. et ZAKHARTCHENIA B. P., *Dokl. URSS,* 745 (1953); GROSS E. F., *Nuovo Cim. Suppl.,* Vol. III, Serie X, n°4 (1956).
7. NIKITINE S., PERNY G. et SIESKIND M., *C.R. Acad. Sci. Paris* **238,** 67, 1987 (1954); *J. Phys. Radium* **15,** 18 (1954); NIKITINE S., COUTURE L., PERNY G. et SIESKIND M., *C.R. Acad. Sci. Paris* **238,** 1786 (1954).
8. APFEL H. S. et HADLEY L. N., *Phys. Rev.* **100,** 1689 (1955).
9. NIKITINE S. et REISS R., *J. Phys. Chem. Solids* **16,** 237 (1960).
10. REISS R., *Cahiers de Physique,* **104,** 129 (1959).
11. PERNY G., Thèse (à paraître).
12. TOYOZAWA, *Prog. Theor. Phys., Osaka* **20,** 53 (1958).

Vol. 17
1960

J. Phys. Chem. Solids Pergamon Press 1961. Vol. 17, Nos. 3/4, pp. 301–307. Printed in Great Britain.

DONOR EQUILIBRIA IN THE GERMANIUM–OXYGEN SYSTEM*

C. S. FULLER, W. KAISER and C. D. THURMOND

Bell Telephone Laboratories, Incorporated, Murray Hill, New Jersey

(*Received* 6 *July* 1960)

Abstract—Donor equilibria involving the reaction of oxygen have been determined in a series of oxygen-doped Ge crystals of known oxygen concentrations. The intrinsic electron concentration is shown to be an important factor in determining the equilibrium. The results confirm that four oxygen atoms are involved in the formation of one donor. The standard enthalpy change (71 kcal, 3·1 eV) for the donor formation is somewhat greater than that expected for a GeO_4 structure. The entropy (48 e.u.), however, appears to be much too large for a simple rearrangement model.

I. INTRODUCTION

THE REACTIONS of oxygen leading to donor formation in silicon have been the subject of a considerable number of investigations over the past five years.[1] Investigation of the kinetics of the donor formation indicated that an aggregation of oxygen atoms takes place upon annealing and, in particular, that a structure consisting of four oxygen atoms is formed which has donor properties.[2,3] More recently ELLIOTT[4] found, in germanium, that donors attributable to oxygen are formed upon annealing. A more detailed study of the donor formation in oxygen-doped germanium has been reported by BLOEM *et al.*[5] who described their results qualitatively in terms of temperature dependent equilibria between neutral oxygen atoms and a donor consisting of four oxygen atoms.

$$4N \rightleftarrows D \tag{1}$$

where N represents the neutral oxygen atom and D represents the donor. We have investigated the formation of donors over a wide temperature range in germanium single crystals having well-defined oxygen concentrations. It is shown that the concentrations of donors formed can be accounted for quite well if each donor is assumed to contain four oxygen atoms. However, in order to obtain satisfactory agreement with experiment, we have found it necessary to introduce the intrinsic carrier concentration into the equilibrium equation (1), which then may be written

$$4N \rightleftarrows D \rightleftarrows D^+ + e^- \tag{2}$$

since ionization of the donor is essentially complete in these experiments. In equation (2) the donor ion, D^+, is assumed to be composed of four oxygen atoms surrounding a Ge atom of the crystal and may be designated GeO_4.

In the later discussion, we take up some subsidiary factors affecting the equilibrium as well as a comparison of the results with similar data for silicon containing oxygen.

II. EXPERIMENTAL

A. *Materials and measurement*

The crystals, containing oxygen in various concentrations, were prepared by growing from melts under different partial pressures of oxygen in argon. Infra-red absorption measurements, made at 11·7 microns, showed the crystals employed to be uniform in oxygen concentration to within about 5 per cent. The absorption measurements themselves in this range are precise to a few per cent. The infra-red determinations were standardized by means of gas analysis on a separate series of oxygen-doped Ge crystals.[6,7] Specimens for the resistivity and Hall effect measurements

* A preliminary account of this work has appeared in *J. Phys. Chem. Solids* **16,** 161 (1960).

Table 1. *Equilibrium donor concentrations in* 10^{16} *cm*$^{-3}$ *for various oxygen contents and temperatures.*

Oxygen conc. $cm^{-3} \times 10^{-16}$		Reaction Temperature, °C							
		350	385	435	470	500	517	527	560
a	b								
9	7·6	1·90	1·22	0·17	None c	None			
19	17·3	4·34	3·47	2·07	0·25	,,			
25	20·8	5·20	4·50	2·80	0·71	,,			
d	25·2	6·3	5·7	3·7	1·66	,,			
40	38·4	9·6	8·2	6·3	4·10	1·15	0·14	None	
39	40·4	10·1	9·2	7·3	4·77	2·17	0·59	,,	
44	44·0	11·0	9·8	7·7	5·30	2·63	0·45	,,	
49	51·2	12·8	12·3	9·9	7·3	4·00	2·05	0·79	
60	59·2	14·8	14·1	11·6	8·5	5·80	3·00	1·79	
120	129·2	32·3	30·0	28·7	23·4	20·2	18·8	15·4	9·5
$n_i \times 10^{-16}$		20	30	62	100	140	150	160	200

a. As determined by infra-red absorption.
b. $4D^+$ at 350°C.
c. "None" corresponds to $< 10^{14}$ cm^{-3}.
d. Not determined.

were taken immediately adjacent to the specimens used for oxygen analysis. The oxygen contents of the crystals used in this work ranged from 0·9 to $12{\cdot}0 \times 10^{17}$ atoms cm^{-3}* (Table 1).

Hall measurements were made on standard bridges,[8] using a field of 1600 Oe. Resistivity measurements were made upon rectangular bars ($2 \times 2 \times 15$ mm^3) by means of a four-point probe device.[4] The accuracy in the resistivity measurements was better than 1 per cent.

B. *Annealing procedure*

Since the crystals undergo reactions as a consequence of heating during crystal growth, it is essential before each run to heat each specimen to near the melting point of Ge and to quench rapidly from this temperature. Because contamination by copper nearly always occurs when Ge is heated to high temperatures, the following procedure was followed: The resistivity specimens were cleaned by means of a light etch in mixed HF and HNO_3, rinsed in pure water, plated lightly in a gold cyanide plating bath and finally given a rinse in pure water. The dry specimens were sealed under about 10 mm air pressure in quartz tubes, heated for $1\frac{1}{2}$ min at 915°C, and quenched in water to near room temperature in less than 5 sec. In this way the starting resistivities (after removal of the surface plating by grinding off several mils) were always above 2 ohm cm for the crystals containing $6{\cdot}0 \times 10^{17}$ cm^{-3} oxygen or less.

Anneals were carried out in furnaces controlled to $\pm$ 1°C. All resistivity measurements were made after quenching to 25 $\pm$ 1°C. The rates of cooling to room temperature were less than 3 sec and in no case were they found to affect the results. No reaction was observed at room temperature for long times.

Annealing temperatures ranged from 329 to 560°C for times (in some cases as long as 1000 hours which were sufficient to attain near-equilibrium concentrations as discussed below. The pertinent data are given in Table 1. Tests at 325°C for over 1000 hr showed the same equilibrium value as obtained after a long time at 350°C.

The concentrations of donors formed in Ge are much greater under comparable conditions than in Si.[5] Most important, the rates of donor formation in Ge are at least 500 times greater than in Si for similar temperatures and oxygen concentrations.

C. *Calculation of donor concentrations*

In order to convert the resistivity changes observed upon annealing into donor concentrations,

* All oxygen contents are in atoms cm^{-3}.

Vol. 17
1960

it is necessary to know the electron mobilities as a function of donor concentration. The mobility values employed are shown in Fig. 1 and represent an average of our determinations, those of DEBYE

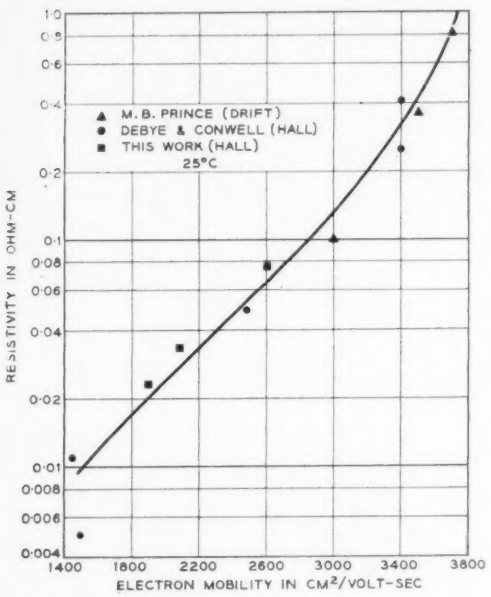

FIG. 1. Relation between resistivity (25°C) and mobility used to calculate electron (donor) concentrations.

and CONWELL[8] and of PRINCE[10]. The maximum error in mobility is about 5 per cent. No attempt has been made to correct Hall mobilities to drift mobilities since, for low fields μ_H/μ is very nearly unity.

The Hall coefficients of a number of samples have been measured as a function of temperature. It is found that the donors formed after annealing to equilibrium are essentially fully ionized at room temperature. A detailed account of this work will be given in a separate article.

D. *Determination of equilibrium donor concentrations*

In order to be sure that true equilibrium values for the donors are measured, it is necessary to follow the changes in donor concentration with time of annealing. It has been found that the donors saturate with time and that the saturation (equilibrium) values decrease markedly with temperature.[5] A series of curves of this kind for a crystal containing $3{\cdot}6\times10^{17}$ cm^{-3} oxygen is shown in Fig. 2. However, the behavior, depending on the oxygen content and particularly upon the annealing temperature, is often less simple. It is found for example that after sufficiently long reaction times the donors always decrease. This occurs more rapidly at the higher temperatures (above 470°C) especially for the higher oxygen concentrations. Observations of this kind are expected at high temperatures where oxide precipitation occurs. In fact the formation of a precipitated GeO_2 phase and a corresponding decrease in oxygen in solid solution has been observed by optical means.

Of more concern is the formation of a maximum followed by a plateau. Such a behavior has also been noted in Si containing oxygen[3] and is shown for Ge containing oxygen in Fig. 3. A crystal with $6{\cdot}0\times10^{17}$ atoms/cm^{-3} of oxygen was annealed at 500°C. A maximum prior to a lower plateau is clearly shown. Evidence that the plateau is an equilibrium concentration was obtained by annealing a similar sample at 472°C for 25 min, at which time a considerably higher donor concentration had been formed than in the crystal annealed at 500°C. When the temperature was raised to 501°C, the donor concentration fell to a value approximately the same as found in the crystal annealed at 500°C, as shown in Fig. 3.

Similar procedures were employed to determine the positions of the equilibria for annealing temperatures above 500°C. Because of the maxima mentioned and the loss of oxygen into precipitate aggregates, which occurs more rapidly as the temperature is increased, the equilibria for the higher temperatures are not as precisely determinable as those for the lower temperatures (below 500°C).

III. RESULTS AND DISCUSSION

The results of the determination of the donor equilibrium concentrations at the different temperatures are shown in Table 1 for all of the oxygen doped crystals. If it is assumed that a donor containing 4 oxygen atoms comes to equilibrium with dissolved oxygen atoms, the relationship between the ionized donor concentration, D^+, measured at room temperature, and the equilibrium oxygen concentration, N, can be expected

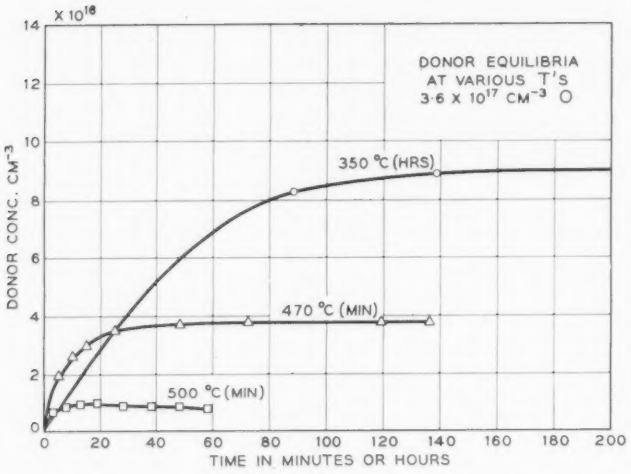

FIG. 2. Increase in donor concentration with time of anneal at 350°C, 470°C, and 500°C for a crystal of Ge originally containing $4{\cdot}0\times10^{17}$ cm^{-3} dissolved oxygen.

to be given by the following equilibrium expression when the solid solutions are very dilute.

$$\frac{D^+}{N^4} = \text{constant} \qquad (3)$$

Equation (3), however, is correct only as long as the concentration of the donor, D^+, is much less than the concentration of intrinsic electrons, n_i, at the equilibrium temperature. This condition is not met, however, for a number of the samples studied, as can be seen by comparing D^+ with n_i as a function of temperature[11] in Table 1. From the charge balance relationship and the electron hole equilibrium, a corrected equation is obtained

$$\frac{D^+[D^+ + (D^{+2} + 4n_i^2)^{1/2}]}{2N^4} = K \qquad (4)$$

Since the concentration of oxygen atoms is the difference between the original oxygen concentration, N_0, and the oxygen contained in the donor ion, D^+, equation (4) becomes

$$\frac{D^+[D^+ + (D^{+2} + 4n_i^2)^{1/2}]}{2(N_0 - 4D^+)^4} = K \qquad (5)$$

Equation (5) has been tested in the following manner. It is first noted that the measurements on the crystals annealed at 350°C indicate that practically all of the oxygen has been converted to a donor ion containing 4 oxygen atoms. Fig. 4 is a plot of the equilibrium donor ion concentration at

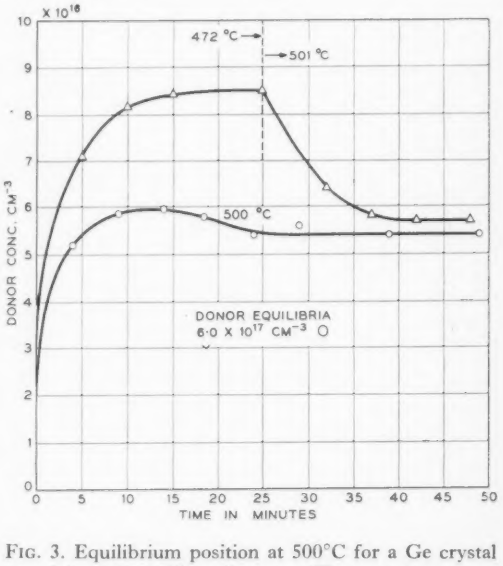

FIG. 3. Equilibrium position at 500°C for a Ge crystal containing $6{\cdot}0\times10^{17}$ cm^{-3} oxygen. The upper curve was obtained by reacting initially at 472°C to produce a concentration of donors in excess of the equilibrium concentration at 500°C.

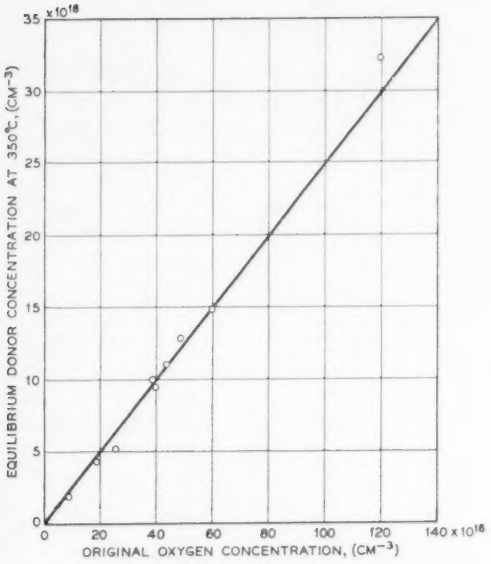

FIG. 4. Plot of equilibrium donor concentration at 350°C vs. original oxygen concentration as determined by infra-red absorption for crystals given in Table 1. The line is drawn to have a slope of 1/4.

350°C as a function of the total oxygen concentration in the crystal as measured by infra-red absorption (calibrated by vacuum fusion gas analysis). The line through the points is of slope 1/4. This is the behavior predicted from equation (5) if K is a relatively large number. It is not possible to obtain a value of K from the measurements at 350°C, since the term $(N_0-4D^+)^4$, which is very sensitive to experimental error, occurs in the denominator of equation (5). At each of the other temperatures, however, the experimental measurements can be used to obtain values of K.

It is believed that it is possible to obtain a better evaluation of N_0 by using the electrical measurements on the 350°C annealed samples as a measure of the oxygen concentration rather than the infra-red absorption measurements. The absorption measurements were not made on the same samples as those used for electrical measurements, but on samples lying adjacent to these samples in the same crystal. The scatter of points around the line of slope 1/4 in Fig. 4 is believed to arise from differences in oxygen concentration arising from small inhomogeneities in the crystal. Column b of Table 1 gives the corrected values of the oxygen concentration which were used to obtain equilibrium constants.

In Fig. 5, the various values of $2K$ at each temperature have been plotted as a function of $1/T$. Both the spread and distribution of points are shown. A line given by the following equation has been drawn through the data.

$$\log 2K = \frac{15560}{T} - 55{\cdot}38 \qquad (6)$$

An average value of the equilibrium constant has been obtained from equation (6) at each of the

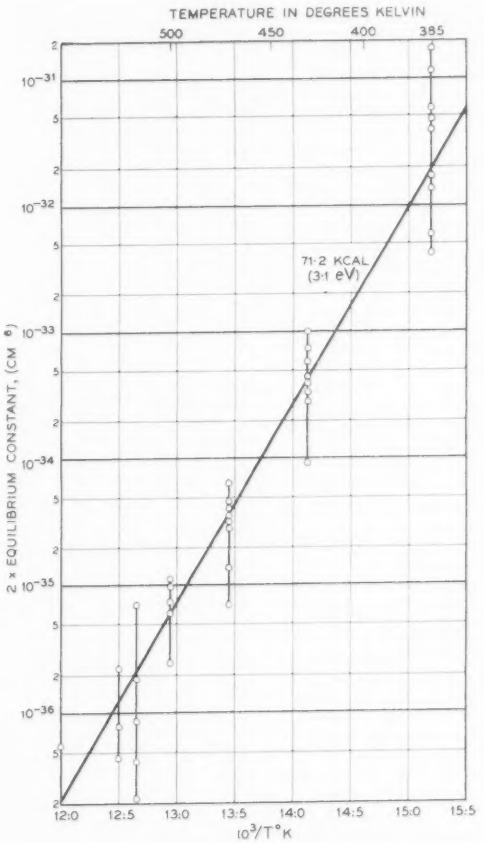

FIG. 5. Semi-log plot of twice the equilibrium constant, $2K$, vs. reciprocal of absolute temperature. The vertical lines and points show the range and distribution of values calculated from data of Table 1 using equation (5). The line corresponds to the equation, $\log 2K = 15560/T - 55{\cdot}38$.

experimental anneal temperatures and the relationship between the donor ion concentration and oxygen concentration has been calculated using equation (5). These calculated curves are shown in Fig. 6 where it is seen that a reasonably

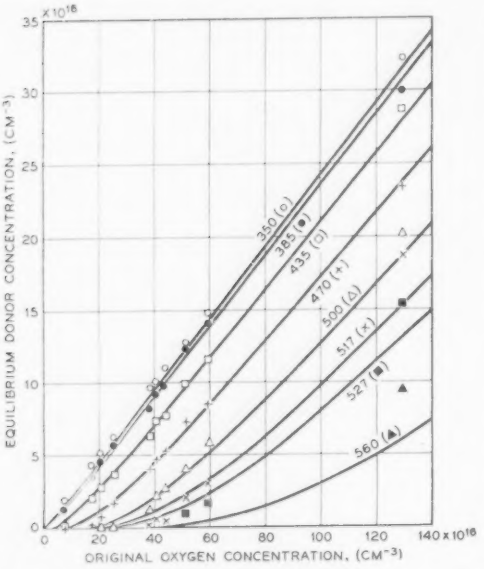

FIG. 6. Equilibrium donor concentrations at various temperatures (indicated on the figure) plotted against original oxygen content (see text). The data are taken from Table 1. The curves are calculated (equation 5) using values of K corresponding to each temperature and taken from the line in Fig. 5.

good fit to the data has been obtained. This fit suggests that oxygen atoms dissolved in solid Ge come into equilibrium with a 4 oxygen atom complex which is also in solid solution. The magnitude of the equilibrium constant and its temperature dependence should give additional information about this reaction.

The equilibrium constant K is related to a standard heat of reaction, ΔH^0, and a standard entropy change, ΔS^0, by the following relationship.

$$\log K = -\frac{\Delta H^0}{4{\cdot}575T} + \frac{\Delta S^0}{4{\cdot}575} - 2\log N_L \quad (7)$$

In this expression, N_L is the number of germanium atoms per unit volume in pure Ge and is $4{\cdot}45 \times 10^{22}$ atoms cm^{-3}. It follows that $\Delta H^0 = -71$ kcals per 4 oxygen atoms and $\Delta S^0 = -48$ entropy units per 4 oxygen atoms.

It may be asked whether these values of ΔH^0 and ΔS^0 are reasonable for the reaction being considered. It will now be shown that the magnitudes of these two numbers, especially the value for ΔS^0, are larger than is to be expected for this reaction. This conclusion suggests that we do not as yet have a complete understanding of these solid solutions and additional work will be necessary before this is achieved.

The model considered here envisages an oxygen atom bound to two adjacent Ge atoms when it is in the atomic state as in the oxygen–silicon system. When the 4 oxygen atom complex forms, it would be reasonable to suppose that around a particular Ge atom, 4 oxygen atoms disrupt the 4 normal Ge–Ge bonds. Thus, each oxygen atom is bound to one common Ge atom and to one other Ge atom. This reaction requires 4 Ge–O bonds of one type to be broken and 4 Ge–O bonds of another type to be made. The value of ΔS^0 to be expected for this type of reaction is around zero, rather than the -12 e.u. per oxygen atom we find experimentally.

The heat of the reaction, ΔH^0, can be estimated by using the temperature dependence of the solubility of oxygen in germanium, ΔH^*, which is 27·6 kcal or 1·2 eV.[7] If it is assumed that the Ge–O bond in the GeO_4 complex is no stronger than the Ge–O bond in GeO_2 (glass) it can be shown that $-\Delta H^0$ would be expected to be less than 2(1·2) or 2·4 eV. The experimental value of 3·1 eV is appreciably larger than this.

IV. COMPARISON WITH Si

Because of the much slower rate of reaction in oxygen-doped Si crystals, equilibria of the kind discussed above are difficult to establish except at temperatures so high that only small donor concentrations exist. As has been pointed out[5] donor generation in oxygen-doped Si is much less at the same temperature than in Ge containing the same amount of oxygen. For example at 450°C, Si containing 10^{18} cm^{-3} oxygen generates a maximum of about 2×10^{16} cm^{-3} donors[3] compared to an estimated $2{\cdot}5 \times 10^{17}$ cm^{-3} donors for a similar Ge crystal. In other words, in spite of a much lower intrinsic electron concentration, the generation of donors, as measured at room temperature

Vol. 17
1960

is much less in the case of Si. Furthermore, it does not appear possible to explain this difference as being due simply to a difference in the ionization energies of the donors in the two cases. Both infra-red absorption[12] measurements and Hall measurements[13] show levels for the donors in Si which lie in the range 0·03 to 0·06 eV. Likewise the behavior of these donors in p-type Si is such as to suggest that deeper ionization levels are not present. Both the rate of generation of donors and the equilibrium constant are very much smaller for Si than for Ge. Because, however, the position of the equilibria in Si are very difficult to determine, a quantitative comparison over a temperature range is not as yet possible.

VI. SUMMARY

An investigation of donor equilibria resulting from the reactions of oxygen in Ge crystals of known oxygen concentrations has been made. The oxygen concentrations studied varied from 0·9 to $12{\cdot}0 \times 10^{17}$ cm^{-3} as determined by infra-red absorption. Reaction temperatures ranged from 325°C to 560°C. Donor concentrations were determined by quenching the reactions to 25°C and measuring resistivity. Hall effect determinations showed that the donors formed are essentially completely ionized at 25°C.

The results show that the intrinsic electron concentration is an important factor in the position of the donor equilibrium. A mass-action treatment including the hole–electron equilibrium enables a quantitative expression to be deduced for the equilibrium constant. Calculations based on this expression agree well with the experimental results for temperatures below 500°C, giving support to the GeO_4 model. At higher temperatures the reactions become more complicated as evidenced by the formation of the maximum in Fig. 3. As a result the equilibrium concept discussed in equations (1) to (5) should be considered only an approximation (see Fig. 6 for $T > 500$°C).

A comparison of the results with those observed in Si shows a very close similarity suggesting that, although the reactions are about 500 times slower in Si and much lower equilibrium donor concentrations exist at comparable temperatures, nevertheless the reaction mechanisms and donor structures must be essentially the same in the two cases.

Acknowledgements—The authors are greatly indebted to the following persons who have contributed valuable assistance in the course of this work: M. Kowalchik for help in growing the Ge crystals, F. H. Doleiden and J. P. Maita for assisting with the Hall and resistivity measurements, Katherine Wolfstirn for aid with the calculations and drawings and George Wheatley for assistance with the infra-red measurements.

REFERENCES

1. Kaiser W., Frisch H. L. and Reiss H., *Phys. Rev.* **112,** 1546 (1958) and references in this paper.
2. Kaiser W., *Phys. Rev.* **105,** 1751 (1957).
3. Fuller C. S. and Logan R. A., *J. Appl. Phys.* **28,** 1427 (1958).
4. Elliott G., *Nature, Lond.* **180,** 1350 (1959).
5. Bloem J., Haas C. and Penning P., *J. Phys. Chem. Solids* **12,** 22 (1959).
6. Guldner W. G. and Beach A. L., *A.S.T.M. Spec. Tech. Pub.* #222 (1958).
7. Kaiser W. and Thurmond C. D., to be published.
8. Debye P. P. and Conwell E. M., *Phys. Rev.* **93,** 693 (1954).
9. Valdes L. B., *Proc. Inst. Radio Engrs. N.Y.* **42,** 420 (1954).
10. Prince M. B., *Phys. Rev.* **92,** 681 (1953).
11. Morin F. J. and Maita J. P., *Phys. Rev.* **94,** 1525 (1954).
12. Hrostowski H. J. and Kaiser R. H., *Phys. Rev. Letters* **1,** 199 (1958).
13. Morin F. J. *et al.*, *Phys. Rev.* **96,** 833 (1954).

J. Phys. Chem. Solids Pergamon Press 1961. Vol. 17, Nos. 3/4, pp. 308–317. Printed in Great Britain.

CRITICAL MAGNETIC SCATTERING OF NEUTRONS IN MAGNETITE

T. RISTE

Institutt for Atomenergi, Kjeller, Norway*

(*Received* 11 *July* 1960)

Abstract—The angular distribution of neutrons inelastically scattered from magnetite is analyzed for temperatures in the neighbourhood of the Curie temperature. The breakdown of the spin wave theory in this temperature region reported earlier by RISTE *et al.* (*J. Phys. Chem. Solids* **9**, 153 (1959)) is discussed. Values of the parameters characterizing the critical fluctuations are deduced from the experiments and compared with theoretical predictions by DE GENNES and VILLAIN (*J. Phys. Chem. Solids*, **13**, 10 (1960)). Some quantitative aspects of the scattering indicate that kinematical braking of the fluctuations, as predicted by the latter authors, may exist. A tentative value of the diffusion constant A_1 is derived.

I. INTRODUCTION

THIS PAPER is the third in a series dealing with the magnetic neutron scattering from Fe_3O_4. In the first paper[1] (hereafter referred to as I) the magnetic Bragg reflections were found to decrease in a way following approximately the behaviour of a Brillouin function. The decrease in the elastic intensity was accompanied by a simultaneous increase in the inelastic intensity, the latter component giving coherent diffuse peaks in the neighbourhood of the magnetic Bragg reflections. In the second paper[2] (hereafter referred to as II) it was shown that the diffuse peaks could be ascribed to spin wave scattering over a considerable range of temperatures and angles. The strong increase in the intensity of the diffuse peaks when approaching the Curie temperature from either side, was explained by VAN HOVE[3] as being due to the strong increase in the fluctuations of the magnetization in this temperature region. The scattering on these fluctuations is called critical scattering and is the main subject of this paper.

The theoretical work by VAN HOVE has been extended by ELLIOTT and MARSHALL[4] and by DE GENNES[5]. The theoretical work has formed the basis for the analyses of several experiments on iron by GERSCH *et al.*[6], by ERICSON and JACROT[7] and by LOWDE[8].

The spin arrangement in magnetite is rather complicated. In view of the experimental results to be discussed below, DE GENNES and VILLAIN[9] undertook a study of the whole problem of magnetic inelastic neutron scattering from crystals of composite spin arrangements, with special consideration to the case of magnetite. Our analysis will be based mainly on their paper.

The theory will be briefly reviewed in Section 2. Section 3 gives the experimental technique. The experimental results will be given in Section 4 and discussed in Section 5.

2. THEORY

It is now a well-established experimental fact that magnetic diffuse peaks exist in the neutron diffraction pattern from magnetic substances. VAN HOVE[3] has shown that these peaks are due to fluctuation of the domain magnetization from its temperature average. The temperature average itself is easily observable as the elastic magnetic Bragg peak, it is unequal to zero only for $T < T_C$. The calculation of the fluctuations is a statistical problem and an analysis of the diffuse scattering may conversely give information about the statistical properties of the system of magnetic

* Work sponsored jointly by Institutt for Atomenergi, Norway, and Reactor Centrum Nederland, the Netherlands.

Vol. 17
1960

spins. The scattering in the diffuse peaks is coherent and must be due to correlated fluctuations of spins on different sites. If $\boldsymbol{S}_0(0)$ denotes the spin at the origin at time zero and $\boldsymbol{S}_R(t)$ the spin at position $\boldsymbol{R}$ at time t, the relevant function, in terms of which to discuss this problem is

$$\gamma'(\boldsymbol{R},t) = \langle \boldsymbol{S}_0(0) \cdot \boldsymbol{S}_R(t) \rangle - \langle \boldsymbol{S}_0 \rangle \cdot \langle \boldsymbol{S}_R \rangle \quad (1)$$

It gives the fluctuating part of the spin correlation, i.e. the deviation from its asymptotic value. The last product gives the elastic Bragg scattering, for $T > T_C$ these terms are equal to zero and all the intensity is found in the diffuse peaks. The neutron scattering due to $\gamma'(\boldsymbol{R},t)$ is in general inelastic, but under critical conditions, i.e. for temperatures close to T_C, the inelasticity becomes weak. Thus the time dependence of the function and the energy changes in the scattering may be neglected. It is convenient to start our review of the theory with the simplest case, the paramagnetic temperature region.

A. $T > T_C$

It was shown by VAN HOVE[3] that under critical conditions the correlation function for a simple ferromagnet takes the form

$$\gamma'(R,0) = \frac{v_0}{4\pi r_1^2 R} S(S+1) \exp(-\kappa_1 R) \quad (2)$$

r_1 gives the intensity and κ_1^{-1} the range of the fluctuations. v_0 is the volume per magnetic atom.

DE GENNES[5] has shown the following connection with the susceptibility:

$$\sum_{\boldsymbol{R}} \langle \boldsymbol{S}_0 \cdot \boldsymbol{S}_R \rangle \exp(i\boldsymbol{\varkappa}\boldsymbol{R}) = S(S+1) \frac{\chi(\boldsymbol{\varkappa})}{\chi_0} \quad (3)$$

$\chi(\boldsymbol{\varkappa})$ is the wavelength-dependent susceptibility giving the response of the spin system to a field of wave vector $\boldsymbol{\varkappa}$. χ_0 is the paramagnetic susceptibility in the absence of the exchange interactions. This gives readily

$$(\kappa_1 r_1)^2 = \frac{\chi_0}{\chi(0)} \quad (4)$$

Further, since the scattering cross section is the Fourier transform of the correlation function, one obtains:

$$\left(\frac{d\sigma}{d\Omega}\right)_{\text{fluct}} = \frac{2}{3}\left(1{\cdot}91 \frac{e^2}{mc^2}\right) S(S+1)|F(\kappa)|^2 \frac{\chi(\boldsymbol{\varkappa})}{\chi_0} \quad (5)$$

$F(\kappa)$ is the magnetic form factor. For $\boldsymbol{\varkappa}$ close to a reciprocal lattice vector $2\pi\boldsymbol{\tau}$ one may expand $\chi(\boldsymbol{\varkappa})$ in series of $|\boldsymbol{\varkappa}-2\pi\boldsymbol{\tau}|$ to obtain

$$\left(\frac{d\sigma}{d\Omega}\right)_{\text{fluct}} = \frac{2}{3}\left(1{\cdot}91 \frac{e^2}{mc^2}\right)^2 S(S+1) \times \times \frac{|F(\kappa)|^2}{r_1^2[\kappa_1^2 + |\boldsymbol{\varkappa}-2\pi\boldsymbol{\tau}|^2]} \quad (6)$$

In their extension of the formulae above to more complicated spin arrangements, DE GENNES and VILLAIN[9] have introduced the susceptibility tensor $\chi_{ij}(\boldsymbol{\varkappa})$ where i and j denote the spins at position $\boldsymbol{r}_i$ and $\boldsymbol{r}_j$ in the unit cell. κ_1^{-1} has as before the meaning of a correlation range and is a constant for the crystal, r_1 will on the other hand depend on $\boldsymbol{\varkappa}$. Equation (4) will then take the form

$$[\kappa_1 r_1(0)]^2 = \frac{\sum_i \chi_{0^i}}{\sum_{ij} \chi_{ij}(0)} \quad (7)$$

and the cross section formula corresponding to (6) reads

$$\left(\frac{d\sigma}{d\Omega}\right)_{\text{fluct}} = \frac{2}{3}\left(1{\cdot}91 \frac{e^2}{mc^2}\right)^2 \frac{1}{z_i} \sum_{i=1}^{z_i} S_i(S_i+1) \times \times \frac{|F(\kappa)|^2}{r_1^2(\tau)[\kappa_1^2 + |\boldsymbol{\varkappa}-2\pi\boldsymbol{\tau}|^2]} \quad (8)$$

z_i is the number of sublattices.

B. $T < T_C$

If the z-axis is chosen along the direction of magnetization, we now have to distinguish the susceptibilities and correlations in the different spin components: ϵ, $\eta = x, y, z$. Instead of formula (5) we get

$$\left(\frac{d\sigma}{d\Omega}\right)_{\text{fluct}} = \left(1{\cdot}91 \frac{e^2}{mc^2}\right)^2 \frac{k_B T}{g^2 \mu_B{}^2} |F(\kappa)|^2 \sum_{ij} \sum_{\epsilon\eta} \times \times \chi_{ij}^{\epsilon\eta}(\boldsymbol{\varkappa}) \left[\delta_{\epsilon\eta} - \frac{\kappa_\epsilon \kappa_\eta}{\kappa^2}\right] \times \exp i\boldsymbol{\varkappa}(\boldsymbol{r}_i - \boldsymbol{r}_j) \quad (9)$$

The factor in the brackets shows that the cross section depends on the direction of the magnetization relative to the scattering vector. In the same way as for $T > T_C$ one may expand $\chi_{ij}(\mathbf{x})$ in terms of constants r_1 and κ_1, κ_1 will however depend upon the direction of propagation of the fluctuations relative to the magnetization.

C. *Calculation of r_1 and κ_1*

DE GENNES and VILLAIN[9] have given a method for performing the expansion of $\chi_{ij}(\mathbf{x})$ which is applicable also in the case of complicated spin arrangements. Their method is based on a local form of the molecular field theory. In the calculations on magnetite they used the interactions which were deduced by NÉEL[10] from susceptibility measurements. If A and B denote the ions on tetrahedral and octahedral sites, respectively, the values of the exchange integrals deduced by NÉEL were:

$$\frac{J_{AA}}{k_B} = -18^0 \quad \frac{J_{AB}}{k_B} = -23^0 \quad \frac{J_{BB}}{k_B} = 0^0 \tag{10}$$

The calculations on (111), the predominant magnetic reflection, yielded the following results:

$$\text{for } T > T_C\text{: } r_1 = 2{\cdot}44\,\text{Å}$$

$$\text{and } \kappa_1^2 = 0{\cdot}494\frac{T-T_C}{T_C}\,\text{Å}^{-2} \tag{11}$$

$$\text{for } T < T_C\text{: } r_1 = 2{\cdot}44\,\text{Å}$$

$$\text{and } \kappa_{1z}^2 = 1{\cdot}12\frac{T-T_C}{T_C}\,\text{Å}^{-2} \tag{12}$$

A closer examination of their calculations shows that the results of equations (11) and (12) are independent of the relative strength of the AA and AB interactions.

It is also possible to perform a separate calculation of κ_1^2, following a method which has been used for α-Fe_2O_3[11]. In the case of $T > T_C$ we obtain

$$\kappa_1^2 = 0{\cdot}78\frac{T-T_C}{T_C}\,\text{Å}^{-2} \quad \begin{matrix}(\text{only } AA \text{ interactions}\\ \text{counted})\end{matrix} \tag{13}$$

$$\kappa_1^2 = 0{\cdot}46\frac{T-T_C}{T_C}\,\text{Å}^{-2} \quad (AB \text{ interactions}) \tag{14}$$

$$\kappa_1^2 = 0{\cdot}62\frac{T-T_C}{T_C}\,\text{Å}^{-2} \quad (BB \text{ interactions}) \tag{15}$$

The molecular field calculations furthermore gave the general results that the range of the transverse fluctuations is infinite, i.e. $\kappa_{1x} \equiv 0$. The Bethe–Peierls–Weiss method provides a different statistical method for calculating r_1 and κ_1,[4] this method is, however, not applicable to magnetite. The first calculation by ELLIOTT and MARSHALL[4] yielded a finite range of the transverse fluctuations. It gave in fact $\kappa_{1x} > \kappa_{1z}$. DE GENNES has informed us that there is an error in their calculation, when corrected the BPW method also gives $\kappa_{1x} \equiv 0$.

D. *The time-dependence of the fluctuations*

Up to this point we have left the time-dependence of the fluctuations and the associated inelasticity of the neutron scattering out of consideration. The most extensive exposition of this problem is found in the work by DE GENNES and VILLAIN[9] and the following is a short review of their results.

The problem is conveniently discussed in magnetization space. We consider the case where we have two sublattices with magnetization M_1 and M_2 respectively, as illustrated in Fig. 1.

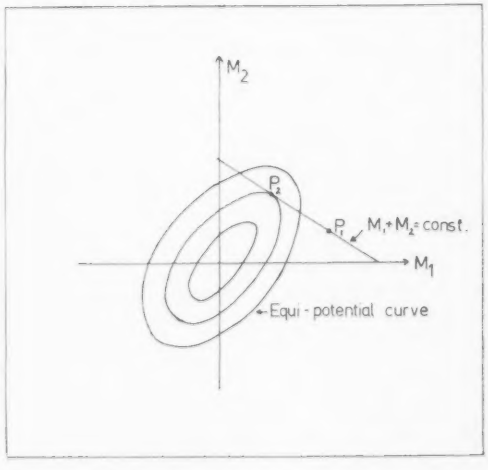

FIG. 1. Diagram used by DE GENNES and VILLAIN (Ref. 9) for discussing time dependence of spin fluctuations in ferrimagnet of two sublattices.

Vol. 17
1960

When $T > T_C$ the point of equilibrium is at the origin. If a fluctuation has brought the point which represents the physical system to P_1, the point afterward tends to move along the line $M_1+M_2 =$ constant, since the total magnetization is a constant of the motion. The representative point will move towards the point P_2 which corresponds to a minimum of the thermodynamic potential. Superimposed on this movement there is a drift towards the origin. This drift is braked by a motion along the family of lines $M_1+M_2 =$ const., the latter motion itself is, however, not braked. In this way there will be two components in the fluctuations: a rapid one, corresponding to transfer of magnetization between the sublattices, and a slow one, corresponding to a quenching of the magnetization over long distances. The two components give rise to inelastic and quasielastic scattering of neutrons respectively. The scattering near a reciprocal lattice point will now correspond to a certain combination of the sublattice magnetizations given by the structure factor. In a simple ferromagnet the structure factor of any reflection is proportional to the magnetization and the scattering is quasielastic. In the ferrimagnetic case, when $\pi \neq 0$, the structure factor can be decomposed in two parts: one part which is proportional to the magnetization and one part which is proportional to the difference between the sublattice magnetizations. In ferro- and ferrimagnetic structures we therefore expect to find a so-called kinematical braking of fluctuations with wave vectors close to $2\pi\tau$. It gives scattering with momentum distribution given by formula (6) and frequency (or energy) distribution for any q given by

$$p_q(\omega) = \frac{\Lambda_1 q^2}{\omega^2+\Lambda_1^2 q^4} \qquad (16)$$

$$(q = |\mathbf{\varkappa}-2\pi\boldsymbol{\tau}|)$$

which contains Λ_1, the diffusion coefficient of the magnetization.

When the temperature approaches T_C, there is also a slowing down of the relaxation which is called thermodynamic braking. It is due to the fact that certain ordered configurations are nearly stable in this temperature region, leading to short range order. The effect on Λ_1 is to make it approach zero, this has also been established experimentally by ERICSON and JACROT[7]. The thermodynamic braking is effective even in antiferromagnets where the kinematical one is completely absent.

At the same time as $\Lambda_1 \to 0$ theory predicts that also $\kappa_1 \to 0$. The critical scattering should therefore be found close to the reciprocal lattice points and be characterized by small energy and momentum transfers.

The cross section formula (6) has to be supplemented by formula (16) if it is to give also the energy distribution of scattered neutrons. It is, however, not necessary to assume that all the scattering is elastic in order to arrive at (6). It is sufficient to make the assumptions that the energy and momentum transfers are small and independent of each other and further that the frequency spectrum has a Lorentzian form as given by (16). The integration over ω will then give only a constant factor in the cross section formula.

3. THE EXPERIMENTAL TECHNIQUE

The technique was described in detail in II. It consists of taking a vertical survey of the peak while keeping the crystal angle of misset $(\theta-\theta_B)$ constant. This technique is particularly well suited for the spin wave region in which it was found to yield results consistent with direct observations of the energy exchange.[2,12] At any missetting we could then pick out the inelastic component with a rather well defined energy transfer $\hbar\omega$ determined by $\theta-\theta_B$. As long as the spin wave approximation is valid this technique also means selecting scattering by spin fluctuations with wave vector $\mathbf{\varkappa} = 2\pi\boldsymbol{\tau}+\boldsymbol{q}$ where q is connected with ω through the spin wave dispersion relation. Fig. 2(a) shows the well known reciprocal lattice construction for this case. The existence of a scattering surface of this type for the spin wave case may be said to be well established.

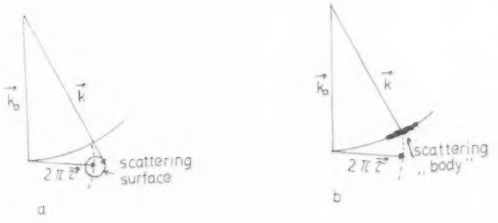

FIG. 2. Reciprocal lattice constructions for diffuse neutron scattering (a) in spin wave region and (b) at Curie temperature.

At high temperatures the spin wave picture breaks down and our experimental method is not able to assess the situation. Theory predicts that at T_C the picture is almost certainly as in Fig. 2(b). There is no dispersion relation which connects momentum and energy transfers and we may therefore have the situation depicted with zero energy transfer and non-zero momentum transfer.

In cases where the scattering is inelastic and the angular width of the observable peak is not too wide, it seems reasonable to assume that at a certain value of $\theta-\theta_B$ we are still selecting scattering which goes with a mean energy transfer given by this

setting. When making observations near the wings of the peak, the selection of momentum or wave vector for the fluctuation doing the scattering is also quite good. It thus seems that one should obtain $p_q(\omega)$ by making observations at a certain angle of latitude near the wing of the peak for several values of $\theta - \theta_B$.

The measurements were all made on single crystals of magnetite, Fe_3O_4. Further details about samples and the way of mounting them are given in II.

4. EXPERIMENTAL RESULTS

First we want to give some qualitative aspects of the scattering. In Fig. 3 the intensity integrated over the diffuse peak has been plotted for several settings of the crystal and over a wide temperature range. The experiments which led to these curves also showed that in the critical region the peak width increased linearly with the angle of misset. Thus we have found that critical scattering is most predominant for small momentum and energy transfers. When approaching T_C from above, the diffuse peak width was strongly decreasing, this may be interpreted as an increase in the dimensions

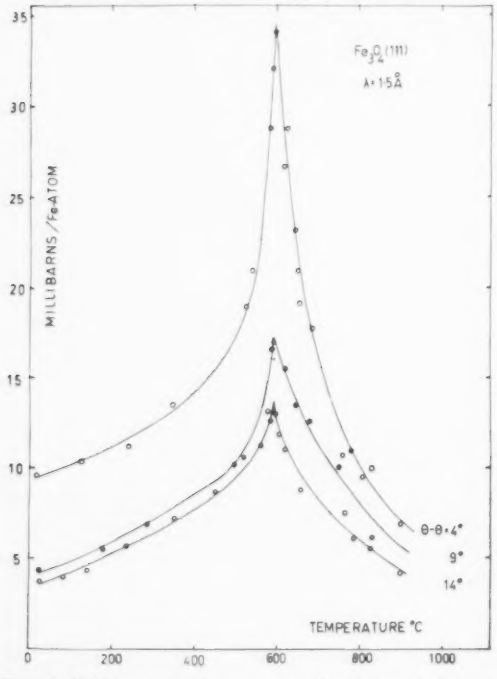

FIG. 3. Diffuse scattering cross section integrated over scattering surface as a function of temperature, as observed for different settings from Bragg position of crystal.

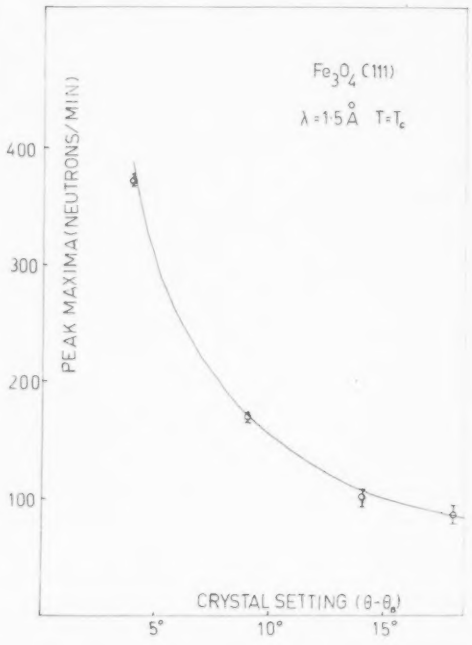

FIG. 4. Diffuse peak maxima, after correcting for instrumental broadening, plotted vs. crystal setting. Curve plotted from formula (18) in text with $\kappa_1 = 0$.

of the fluctuating regions. In this way the curves in Fig. 3, together with the above-mentioned observations on the peak widths, indicate that as T_C is approached, there is an increase both in the relaxation time and the correlation range of the fluctuations. Thus our observations support the qualitative predictions given by VAN HOVE[3].

We shall now proceed to a quantitative analysis of the critical scattering and start with the experimental results at the Curie temperature.

A. $T = T_C$

At this temperature theory predicts zero values of Λ_1 and κ_1 so that the wave vectors of scattered neutrons have to end close to the sphere of reflection, as shown in Fig. 2(b). The intensity in the peak maxima will depend on the crystal missetting

Vol. 17
1960

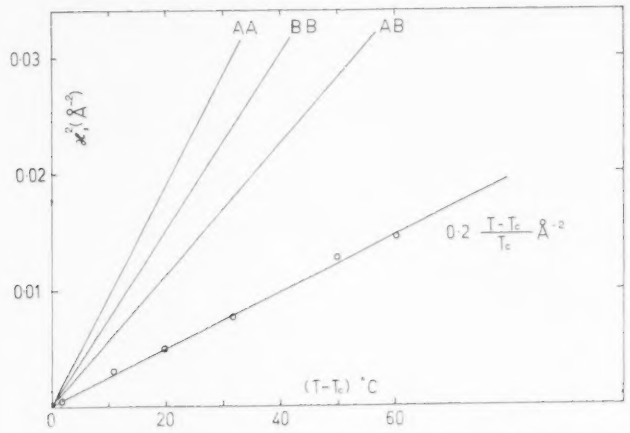

FIG. 5. Experimental values of parameter κ_1 deduced from diffuse peak maxima at $\theta - \theta_B = 4°$ and theoretical values calculated from molecular field theory, taking indicated interactions into consideration.

according to

$$\frac{d\sigma}{d\Omega} \sim [\kappa_1^2 + 4\pi^2\tau^2(\theta-\theta_B)^2]^{-1} \qquad (17)$$

This formula is easily obtained from equation (6) and is deduced for the case of a monochromatic beam incident upon the crystal. In the case of a white incident beam, as was used in the present case, one may easily show that the intensity in the peak maxima will be given by

$$I_{\max} \sim [\kappa_1^2 + 4\pi^2\tau^2(\theta-\theta_B)^2]^{-1/2} \qquad (18)$$

In Fig. 4 we see that the observed intensity distribution, when correcting for instrumental broadening of the peaks, has indeed such a simple behaviour and gives $\kappa_1 = (0 \pm 0{\cdot}01)$ Å.

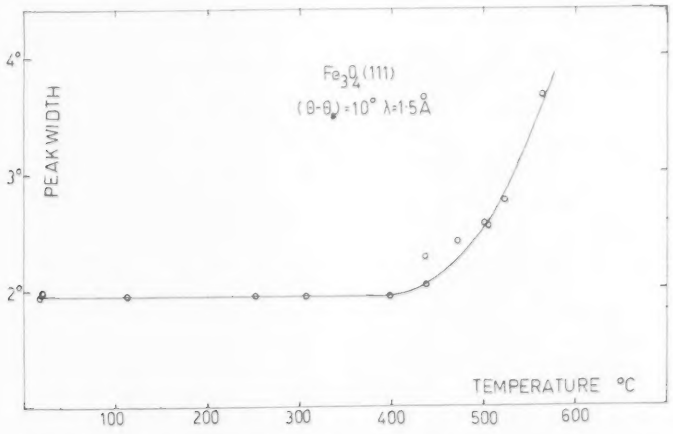

FIG. 6. Width of diffuse peaks due to transverse fluctuations observed at $\theta - \theta_B = 10°$, after correcting for instrumental broadening, plotted vs. temperature.

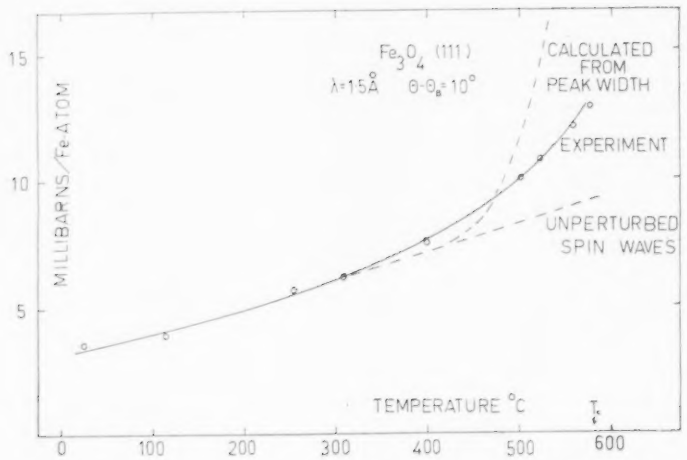

FIG. 7. Integrated cross section of same diffuse peaks as in previous figure.

The intensity at $\theta-\theta_B = 4°$ corresponds to $(8{\cdot}6 \pm 0{\cdot}5)$ barns (sterad × iron atom)$^{-1}$. According to formula (8) this gives $r_1 = (4 \pm 0{\cdot}1)$ Å which is considerably higher than the theoretical value of 2·42 Å.

B. $T > T_C$

If one neglects the temperature variation of r_1, which is predicted to be as $r_1^2 = r_1^2(T_C) \times T_C T^{-1}$, one may according to formula (18) derive the temperature behaviour of κ_1 from the temperature variation of the peak maximum for a fixed crystal setting. The deduced values of κ_1^2, which are shown in Fig. 5, are seen to have the predicted linear behaviour, but with an appreciably lower slope of

$$\kappa_1^2 = (0{\cdot}2 \pm 0{\cdot}01)\,\frac{T-T_C}{T_C}\,\text{Å}^{-2} \qquad (19)$$

C. $T < T_C$

In II it was found that the diffuse intensity could be explained by means of spin wave theory over a considerable range of temperatures. Fluctuations in the transverse (i.e. x and y) spin components, of which spin waves are a special case, may be observed in isolation by magnetizing the crystal along the scattering vector. This is readily seen from formula (9) because with this direction of the magnetic field the factor in the brackets is equal to 4/3 for the transverse components, but equal to zero for the longitudinal (z) component. Figs. 6 and 7 give the observed temperature variation of the width and intensity respectively of diffuse peaks at $\theta-\theta_B = 10°$ which are due to transverse spin fluctuations. Fig. 6 shows that "something" is happening to the spin waves which makes the peak broaden out. Recalling from II the connection between the peak width and the effective exchange integral (J), it might simply mean a decrease of J which should then vary as the inverse of the peak width. This would, however, affect $g(\omega)$, the number of quantum states corresponding to the frequency ω. A simple calculation gives $g(\omega) \sim J^{-3/2}$. The associated temperature variation of scattered neutrons, being proportional to $g(\omega)\,[\exp(\hbar\omega/k_B T)-1]^{-1}$, should then be as the dotted curve in Fig. 7.

The intensity component due to the longitudinal fluctuations is derived by subtracting the transverse component from the total intensity. Fig. 8 shows an example of such a decomposition. If we should derive κ_{1z} by the same procedure as for $T > T_C$, we would have to correct for experimental broadening. The shape of the longitudinal curve is, however, rather poorly established, and we have preferred to neglect the temperature variation of the peak width and compare the integrated intensity with the calculations on differential cross sections. Fig. 9 gives our experimental points and a theoretical

Vol. 17
1960

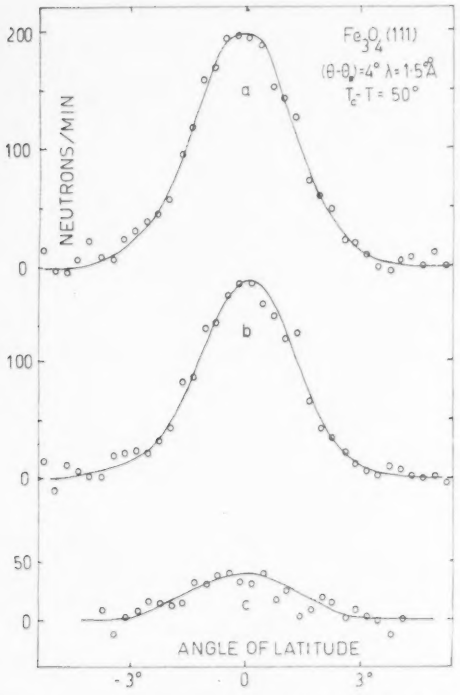

FIG. 8. Decomposition of diffuse peak (a) $\theta-\theta_B = 4°$ and $T = T_C-50°$ into peaks due to transverse (b) and longitudinal fluctuations (c).

curve calculated by DE GENNES and VILLAIN[9]. The normalization to the same values at T_C is arbitrary.

D. *The time dependence of the fluctuations*

The analysis of the critical scattering has so far been in the static approximation, i.e. the energy change has been neglected. At the end of Section 3 we have suggested a method for obtaining the frequency distribution $p_q(\omega)$ for a wave vector q which gives scattering near the wing of a diffuse peak. Some observations at a counter angle of $\sim 3°$ from the maximum of the diffuse peaks, corresponding to $q \sim 0{\cdot}23$ Å^{-1}, are shown in Fig. 10. It is seen from Fig. 8 that all the experimental points fall approximately on the same Lorentzian curve, corresponding to a value $\Lambda_1 = 7{\cdot}5 \times 10^{-3}$ c.g.s. Using the formula given by DE GENNES[5] for a paramagnet of simple cubic structure taking only the AB interactions into account, we obtain a theoretical value of $5{\cdot}6 \times 10^{-3}$. We see that Λ_1 is independent of temperature in the region of observation, indicating that fluctuations of this wave vector are not subject to thermodynamic braking. Kinematical braking is on the other hand active so as to make the diffusion approximation valid. The presence of the strong critical scattering for wave vectors close to $2\pi\tau$ is, however, highly suggestive of thermodynamic braking.

5. DISCUSSION

The general picture of the temperature variation of the intensity is in agreement with the theoretical predictions, as explained in the beginning of the previous section. We may distinguish between two temperature regions for the spin fluctuations, in one of them spin waves dominate and in the other critical fluctuations. The transition region is the most difficult one to explain.

When comparing Figs. 6 and 9, it looks as if the onset of longitudinal fluctuations coincides with a perturbation of the spin waves of the same vector. Results of the same kind were observed at $\theta-\theta_B = 4°$. If we define the critical region as the one where longitudinal fluctuations occur, then Fig. 14 in II implies that the transition temperature between the two regions is dependent upon the wavelength of the fluctuation. Why this is so is not understood.

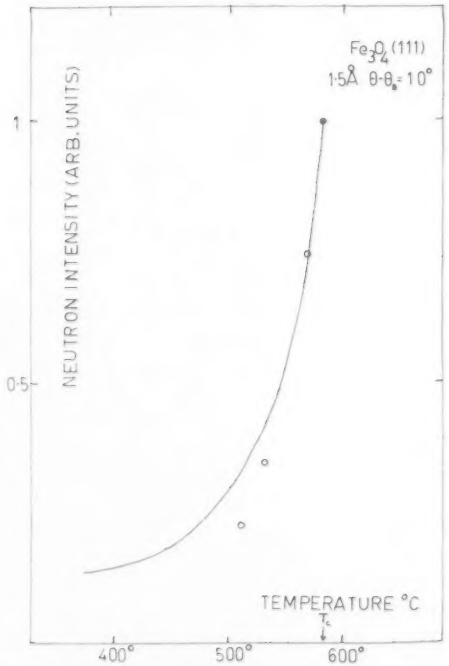

FIG. 9. Integrated diffuse peaks due to longitudinal spin fluctuations at $\theta-\theta_B = 10°$, compared with differential cross section at same setting. Values arbitrarily normalized to coincide at T_C.

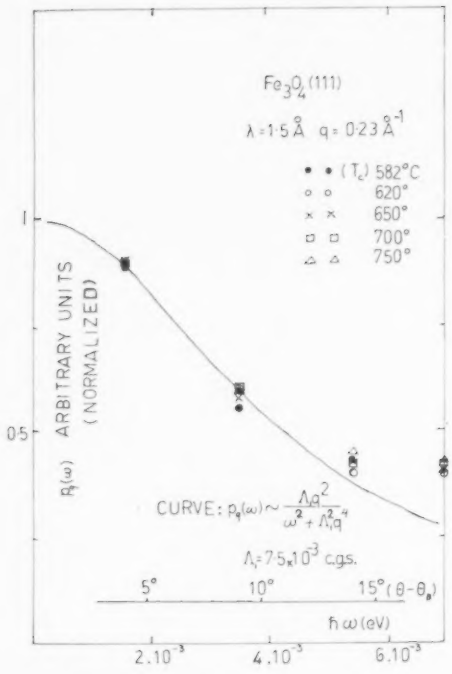

FIG. 10. Observed frequency distribution of spin fluctuations with wave vector $q = 0{\cdot}23$ Å^{-1} for different temperatures compared with Lorentzian curve, as given by formula (16) in text.

Our experiments can give some information about the behaviour of spin waves in the critical region. Fig. 6 indicates that the spin wave frequency decreases as the Curie temperature is approached. If the one-to-one correspondence between frequency and wave vector is preserved, the cross section should behave as the upper curve in Fig. 7. Since the intensity falls below, we conclude that the one-to-one correspondence is destroyed and that a mixing of the energy states must occur. Thus the fluctuations of the transverse components of the magnetization are not fully described by spin wave theory in the critical region.

In the paper by DE GENNES and VILLAIN[9] it was predicted that the frequencies of the different spin wave modes should decrease roughly as the spontaneous magnetization. Such a decrease of the frequency does in fact lead to a curve which is qualitatively in agreement with Fig. 6. The decrease of the magnetization also determines the intensity of the longitudinal fluctuations. This makes one understand why the onset of longitudinal fluctuations coincides with the perturbation of the spin waves. The problem why the different spin wave modes behave differently remains unsolved, however.

Our experimental values of r_1 and κ_1 deviate markedly from the calculated ones. Their product

$$(r_1\kappa_1)^2_{\text{obs}} = (3{\cdot}2 \pm 0{\cdot}3)\frac{T-T_C}{T_C}$$

does on the other hand agree favourably with the calculated value

$$(r_1\kappa_1)^2_{\text{calc}} = 2{\cdot}9\,\frac{T-T_C}{T_C}$$

given by DE GENNES and VILLAIN. The latter value is consistent with susceptibility data. The discrepancy of r_1 and κ_1 could mean that the basic equation for the molecular field calculations, which assumes a linear relation between the moment on one site and the moments of the surrounding atoms, is a poor approximation. It is unlikely that the discrepancy should be due to the fact that we make use of formulae which are given in the static approximation. To make this approximation valid it is not necessary that the scattering is elastic, it is sufficient that the frequencies have a Lorentzian distribution. The latter distribution seems justified from the data on iron by ERICSON and JACROT[7].

In Ref. (11) it is concluded that the predicted kinematical braking of the fluctuations in Fe_3O_4 must be the reason why the diffuse peaks are broader than the corresponding ones in α-Fe_2O_3. As to the experimental value deduced above for Λ_1, the value leans heavily on the correctness of the experimental method and should be regarded only as tentative. The agreement with the Lorentz curve in Fig. 10 may be fortuitous and should be checked by direct observation of the energy changes.

Acknowledgements—The author wishes to thank Dr. A. W. MCREYNOLDS for communicating some results of unpublished work showing the same qualitative aspects as reported above. He is also indebted to Professor L. VAN HOVE and to Drs. P. G. DE GENNES and

J. VILLAIN for helpful discussions of their theoretical work. The experimental assistance of Mr. K. BLINOWSKI is gratefully acknowledged.

REFERENCES

1. MCREYNOLDS A. W. and RISTE T., *Phys. Rev.* **95,** 1161 (1954).
2. RISTE T., BLINOWSKI K. and JANIK J., *J. Phys. Chem. Solids* **9,** 153 (1959).
3. VAN HOVE L., *Phys. Rev.* **95,** 1374 (1954).
4. ELLIOTT R. J. and MARSHALL W., *Rev. Mod. Phys.* **30,** 75 (1958).
5. DE GENNES P. G., *Contribution a l'étude de la diffusion magnetique des neutrons,* Presses Universitaire de France (1959).
6. GERSCH H. A., SHULL C. G. and WILKINSON M. K., *Phys. Rev.* **103,** 525 (1956).
7. ERICSON M. and JACROT B., *J. Phys. Chem. Solids* **13,** 235 (1960).
8. LOWDE R. D., *Rev. Mod. Phys.* **30,** 69 (1958).
9. DE GENNES P. G. and VILLAIN J., *J. Phys. Chem. Solids* **13,** 10 (1960).
10. NÉEL L., *Ann. Phys.*, Paris **3,** 137 (1948).
11. RISTE T. and WANIC A., this journal, following paper.
12. BROCKHOUSE B. N., *Phys. Rev.* **106,** 859 (1957).

J. Phys. Chem. Solids Pergamon Press 1961. Vol. 17, Nos. 3/4, pp. 318–333. Printed in Great Britain.

A NEUTRON DIFFRACTION STUDY OF SPIN FLUCTUATIONS IN α-Fe_2O_3*

T. RISTE and A. WANIC†

Institutt for Atomenergi, Kjeller, Norway‡

(*Received* 11 *July* 1960)

Abstract—Diffuse scattering experiments on neutrons in α-Fe_2O_3 are found to reveal the linear dispersion relation for antiferromagnetic spin waves. The spin waves propagate with a velocity of $3{\cdot}8 \times 10^6$ cm sec^{-1}, corresponding to a value of $-3{\cdot}5 \times 10^{-3}$ eV for the strongest exchange integral. The spin fluctuation scattering in the critical region agrees with calculations based on a local form of molecular field theory.

I. INTRODUCTION

IN RECENT years neutrons have proved to be very useful when investigating elementary excitations in solids and liquids. The thermal neutrons obtainable from nuclear reactors turn out to have the right energies and momenta for such investigations. In magnetic inelastic scattering the technique has developed along two lines. When the intensity is adequate one performs a direct energy analysis of the scattered beam,[1] otherwise one makes observation on the geometry of the coherent inelastic diffraction peaks.[2] The former method is of course in general superior, but the latter method has proved to be adequate in the spin wave region.

In the discussion of magnetic neutron scattering it is useful to introduce the spin correlation function, a concept which VAN HOVE[3] has defined by the relation

$$\gamma(\boldsymbol{R},t) = \langle \boldsymbol{S}_0(0) \cdot \boldsymbol{S}_{\boldsymbol{R}}(t) \rangle \qquad (1)$$

It expresses the directional correlation between a spin at the origin at time zero and a spin at the position $\boldsymbol{R}$ at time t, averaged over the thermal distribution.

The correlation function expresses the cooperative properties of the spin system and is therefore particularly useful when making observations on coherent neutron scattering. In order that an array of spins shall give coherent magnetic scattering, it is necessary not only that the spins have ordered positions, but also that their directions are ordered.

In ferro-, ferri- and antiferromagnetic substances the ordered alignment exists over regions or domains which are large on an atomic scale. The average long range order of a domain is easily observed from the magnetic Bragg reflections and may be expressed by the asymptotic part of the correlation function: $\gamma(\infty, t)$. In an antiferromagnet it is convenient to consider the correlation between spins within the same sublattice, its asymptotic part is proportional to the square of the sublattice magnetization. The temperature variation of the sublattice magnetization, a quantity which is otherwise hard to observe, is easily observed from the antiferromagnetic Bragg reflections. The decrease of the sublattice magnetization, when going from lower temperatures to the Néel point, is a consequence of the natural tendency towards disorder as the temperature is raised. The competing tendency of antiferromagnetic order as a result of the still existing exchange interactions is, however, at the same time active. At any time there is then a statistical chance of a spin order deviating from the temperature average. The excursions or the fluctuations of the sublattice

* A smaller part of the present work was published in *Nature* **185**, 450 (1960).

† On leave from the Institute of Nuclear Research, Krakow, Poland; now back there.

‡ Work sponsored jointly by Institutt for Atomenergi, Norway, and Reactor Centrum Nederland, the Netherlands.

Vol. 17
1960

magnetization in a domain from its average value reach a maximum at the Néel temperature and give rise to the critical scattering. The fluctuations are in general of short or intermediate range, i.e. confined to a fluctuating region of finite dimensions, and give diffraction peaks which are more diffuse than the sharp Bragg reflections.

If one only asks about the range of the correlation, it is sufficient to consider the spatial part of the correlation function and leave the time dependence out of consideration. Since the time dependence of the correlation function is intimately connected to the energy changes in the scattering, a slow time dependence of the correlation function results in quasi-elastic scattering. If one neglects the energy changes in the scattering, the so-called elastic approximation is applied and information about the correlation function is obtained in the static approximation.

Experiments of this type on antiferromagnetic crystals have earlier been performed only in the so-called critical region,[4] i.e. near the Néel temperature, and in the paramagnetic region.[5] In the critical region data were analysed in the static approximation. The present paper is the first attempt to study spin fluctuations in an antiferromagnet from the spin wave region up to the paramagnetic region. Since no direct energy analysis of the scattered beam could be made, the interpretation will be seen to be less certain at some points.

Before going over to the experiments and their interpretation, we will give a short review of the relevant theories.

2. THEORY

The experiments of SHULL *et al.*[6] showed unambiguously that the spins of an antiferromagnet are aligned antiparallel in a regular way to give a zero net moment. This justifies the starting point of an earlier theoretical work by HULTHÉN[7] on antiferromagnetic spin waves. He showed that, assuming an ordered antiferromagnetic ground state, the lowest excited states corresponded to the so-called spin waves. According to the spin wave theory the disorder introduced in the ordered spin system, as the temperature is raised from absolute zero, will propagate as a wave through the lattice. The wavelength will be quantized by the periodic structure of the lattice. HULTHÉN found that the antiferromagnetic spin waves travel with a velocity c_m independent of the wavelength, or expressed differently

$$\omega = c_m q \tag{2}$$

where ω is the frequency and q the wave number of the spin wave respectively. We see that a quantization of the momentum $\hbar q$ through the wavelength gives a simultaneous quantization of the energy $\hbar\omega$. Such an energy quantum has been called a magnon in analogy to a phonon, the quantum of a lattice vibration. In an inelastic magnetic scattering process a neutron will exchange momentum $\hbar q$ and energy $\hbar\omega$ with the spin system and may be said to excite or absorb spin waves carrying the same quanta. We therefore see that an analysis of the magnetic inelastic scattering gives a unique possibility of verifying directly the dispersion relation above.

The simple form of the dispersion relation above has earlier been predicted for some simple antiferromagnetic spin arrangements. GOEDKOOP[8] has recently shown that it is valid also in general cases. He gives the method for calculating c_m for different spin arrangements. GOEDKOOP has also given the method for calculating the intensity of spin wave scattering for each set of planes of an antiferromagnetic crystal, this involves calculating a relative structure factor.

As the temperature of the crystal is raised, a greater number of spin waves will be excited and will give an increase in the scattering cross section. Thus the temperature variation of the intensity gives direct information about the statistical behaviour of spin waves.

The theoretical work on antiferromagnetic spin waves has mostly been concerned with the question of the ground state. It is, however, reasonable that most of the discussion on ferromagnetic spin waves is also valid in the antiferromagnetic case. Thus we must expect the theory to break down when the number of excited spin waves gets too high. If the only result were a decrease of the spin wave velocity, the associated temperature variation of the cross section could easily be calculated.[9] It is also possible that the one-to-one correspondence between frequency and wave vector (expressed by equation 2) will break down. If the distribution of wave numbers corresponding to a frequency ω is smeared out, one must expect a change in the

intensity corresponding to a single line in the energy spectrum of scattered neutrons. What we have called "smearing out" is usually called mixing of states with different q values.

Conventional magnetic and thermodynamic measurements will in most cases give some quantity which is integrated over the whole spin wave spectrum. In antiferromagnetics the spin wave theory gives a magnetic T^3 term in the specific heat and a negative T^2 term in the saturation magnetization. The latter behaviour has been verified by high field nuclear magnetic resonance.[10]

It should be mentioned that the concept of correlation function expressed by equation (1) is useful also in the spin wave region. The operators corresponding to the spin vectors may be calculated in the spin wave approximation. When the spin wave theory breaks down, no explicit calculation of the correlation function or the scattering cross section is possible. In this case the scattering is with great advantage discussed in terms of the qualitative aspects of the correlation function. The cross section for inelastic scattering is given by its Fourier transform[11]:

$$\frac{d^2\sigma}{d\Omega d\omega} = \left(1{\cdot}91\frac{e^2}{mc^2}\right)^2 \frac{k}{k_0}|F(\kappa)|^2 \int \frac{dt}{2\pi}\exp(-i\omega t) \times$$

$$\times \sum_{ij}\sum_{\epsilon\eta}[\langle T^{\epsilon}_{i,\kappa}(0)T^{\eta}_{j,-\kappa}(t)\rangle - \langle T^{\epsilon}_{i,\kappa}\rangle\langle T^{\eta}_{j,-\kappa}\rangle \times$$

$$\times \exp[i\boldsymbol{\varkappa}(\boldsymbol{r}_i-\boldsymbol{r}_j)]\left(\delta_{\epsilon\eta}-\frac{\kappa_\epsilon\kappa_\eta}{\kappa^2}\right)] \qquad (3)$$

where we have introduced the vector

$$\boldsymbol{T}_{j,\kappa} = \sum_{Rj} \boldsymbol{S}_{R_j}\exp[i\boldsymbol{\varkappa}(R_j-\boldsymbol{r}_j)] \qquad (4)$$

The position coordinate of an ion has been written as

$$\boldsymbol{R}_l = \boldsymbol{r}_l+\nu_a\boldsymbol{a}+\nu_b\boldsymbol{b}+\nu_c\boldsymbol{c}.$$

ν_a, ν_b, ν_c are integers and $\boldsymbol{a}$, $\boldsymbol{b}$, $\boldsymbol{c}$ are the translation vectors of the crystal. The other symbols of formula (3) have the following meaning: e^2/mc^2 is the classical electron radius, $\boldsymbol{k}$ and $\boldsymbol{k}_0$ the outgoing and incoming wave vectors of the neutron respectively and $F(\kappa)$ a magnetic form factor assumed equal for all the atoms. ϵ and η denote any of the components x, y, z of a vector. The momentum transfer is given by

$$\hbar\boldsymbol{\varkappa} = \hbar(\boldsymbol{k}_0-\boldsymbol{k})$$

and the energy transfer by

$$\frac{\hbar^2}{2m_0}(k_0^2-k^2).$$

m_0 is the neutron mass. If $2\pi\boldsymbol{\tau}$ denotes any of the reciprocal lattice vectors of the crystal, we can write the momentum transfer as

$$\hbar\boldsymbol{\varkappa} = \hbar 2\pi\boldsymbol{\tau}+\hbar\boldsymbol{q}.$$

The first term on the right then denotes the momentum given to the neutron by the crystal as a whole and the second term by the quantum doing the inelastic scattering, if the spin wave theory is valid $\boldsymbol{q}$ denotes the wave vector of the magnon. The scattering cross section is in the static approximation obtained from formula (3) by putting k equal to k_0, integrating over ω and assuming κ independent of ω.

Our scattering formula is seen to give inelastic components due to fluctuations in the x, y and z spin components. The fluctuations in the x and y components, i.e. transverse to the magnetization, are in the lower temperature region described by the spin wave theory. When considering scattering due to fluctuations in the z-components, the longitudinal fluctuations, we see that the last term in the brackets is proportional to the sublattice magnetization. Longitudinal fluctuations therefore gain in intensity as the sublattice magnetization decreases, this has been discussed qualitatively already in the introduction. Critical fluctuations in antiferromagnets have been treated theoretically only little compared with those in ferromagnets. In ferromagnets VAN HOVE[3] showed that the fluctuations could be characterized by a range κ_1^{-1} and a diffusion constant Λ_1, related to their relaxation time. ELLIOTT and MARSHALL[12] and DE GENNES and HERPIN[13] have established some relations between the values of these constants below and above the critical temperature. They found that the behaviour of κ_1 was such that the slope of the intensity when approaching T_c from below was in the ratio of about -2 to the slope when approaching T_c from above. ELLIOTT and MARSHALL have found that κ_1 for antiferromagnets behaves similarly to the one for ferromagnets.

Vol. 17
1960

In the calculation of κ_1 DE GENNES and VILLAIN[11] have introduced the wavelength-dependent susceptibility tensor $\chi(\boldsymbol{\varkappa})$, giving the response of the magnetization to a field with wave vector $\boldsymbol{\varkappa}$, and shown that it is related to the spin correlations. Thus the cross section may in the static approximation be written as

$$\left(\frac{d\sigma}{d\Omega}\right)_{\text{fluct}} = \left(1{\cdot}91\,\frac{e^2}{mc^2}\right)^2 \frac{k_B T}{g^2\mu_B{}^2}\,|F(\kappa)|^2 \sum_{ij}\sum_{\epsilon\eta} \chi_{ij}(\boldsymbol{\varkappa}) \times$$

$$\times \left[\delta_{\epsilon\eta} - \frac{\kappa_\epsilon \kappa_\eta}{\kappa^2}\right] \exp\left[i\,\boldsymbol{\varkappa}(\boldsymbol{r}_i - \boldsymbol{r}_j)\right] \qquad (5)$$

A similar formula has been given by KRIVOGLAZ[14].

The relaxation of the fluctuations have also been calculated by DE GENNES and VILLAIN[11], part of their results have been quoted elsewhere.[9] In the case of antiferromagnets they found that the relaxation of critical fluctuations were braked only by a thermodynamic mechanism.

3. EXPERIMENTS

Our experiment was made on a natural geological specimen of α-Fe_2O_3, hematite, from Elba. The crystal had a volume of about 200 mm^3 and a spectrochemical analysis showed that the content of metal impurities was 0·15 per cent. The structure of hematite is rhombohedral with the iron atoms lying in layers normal to the trigonal axis.

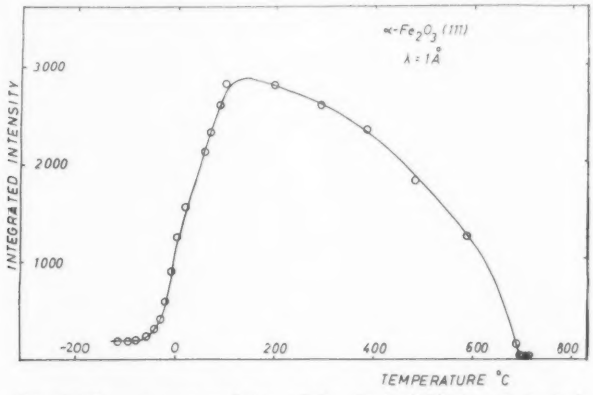

FIG. 1. Temperature variation of the elastic (111) rhombohedral reflection.

Provided we keep the restriction that $|T-T_N|/T_N \ll 1$ and $\boldsymbol{\varkappa}$ is close to $2\pi\boldsymbol{\tau}$, $\chi(\boldsymbol{\varkappa})$ can for certain crystal structures be expanded in terms containing only $|\boldsymbol{\varkappa}-2\pi\boldsymbol{\tau}|$ and constants related to the crystal structure and the magnetic interactions. The final formula is

$$\left(\frac{d\sigma}{d\Omega}\right)_{\text{fluct}} = \left(1{\cdot}91\,\frac{e^2}{mc^2}\right)^2 |F(\kappa)|^2 S(S+1) \times$$

$$\times \sum_{ij}\sum_{\epsilon\eta} r_1{}^{-2}[\kappa_1{}^2 + (\boldsymbol{\varkappa}-2\pi\boldsymbol{\tau})^2]^{-1} \times$$

$$\times \left[\delta_{\epsilon\eta} - \frac{\kappa_\epsilon \kappa_\eta}{\kappa^2}\right] \exp\left[i\,\boldsymbol{\varkappa}(\boldsymbol{r}_i - \boldsymbol{r}_j)\right] \quad (6)$$

In the Appendix this expansion is carried out for the case of hematite.

SHIRANE *et al.*[15] have recently given the following parameters: $a_0 = 5{\cdot}424$ Å, $\alpha = 55°17'$. The magnetic structure has been determined by SHULL *et al.*[6], who showed that below a Néel point of about 700°C hematite may exist in two antiferromagnetic states. Below approximately −20°C the magnetic axis lies along the trigonal axis. This will in the following be called state I. Above the transformation temperature, in state II, the spins are in the (111) planes. Within each plane the spins are ferromagnetically coupled and adjacent planes are antiferromagnetically coupled.

A. *The elastic intensity component*

The transformation between the states will be clearly visible in a neutron diffraction diagram,

because the scattering cross section contains a factor given by the last parenthesis in formula (3). An elastic reflection involves scattering on the z-components of the spins, in which case the factor takes the form $[1-(\kappa_z/\kappa)^2]$. Thus, when going from state I to II, the factor changes its value from zero to one for the (111) reflection.

In Fig. 1 we have plotted the temperature variation of this reflection. The strong increase seen when going from -100°C to 100°C is due to the abovementioned transition. The further decrease when going up towards the Néel temperature of 696°C is due to the decrease of the sublattice magnetization. We see that the transition extends over a temperature region of nearly 200°. A very similar curve has been obtained in magnetization experiments by LIN[16]. Sharper transitions of about 10° have earlier been reported by CORLISS *et al.*[17] BACON[18] has observed that the nature of the transition may vary from one sample to the other. In some samples he has found reminiscence of the high temperature phase even at liquid nitrogen temperature, thus supporting the present observations. Our curve is taken using a plutonium-filtered beam of 1 Å neutrons and second order contamination of $\frac{1}{2}$ Å neutrons can be excluded.

B. *The spin wave component*

The technique for studying the inelastic reflections which we have used is described in detail elsewhere.[2] It consists of taking vertical profiles of the peaks at different angles of misset of the crystal from its Bragg position. In the spin wave region each angle of misset $(\theta-\theta_B)$ defines an average energy transfer for the inelastic scattering and the corresponding peak width (Γ) is proportional to the momentum transfer. Thus a plot of Γ vs. $(\theta-\theta_B)$ gives the dispersion relation. The earlier experiments on magnetite revealed the quadratic dispersion relation for ferromagnetic spin waves.[2] The present experiments on hematite gave the curve on Fig. 2, which shows that the linear dispersion relation of equation (2) is valid. The magnon velocity can be calculated from the slope of the line using the formula given by ELLIOTT and LOWDE[19]:

$$\Psi = \sin 2\theta_B \left[\left(\frac{c_m}{v}\right)^2 - 1\right]^{-1/2} (\theta-\theta_B) \qquad (7)$$

Ψ is the total semiangle of the peak and v the neutron velocity. Our data give $c_m = 3{\cdot}8\times10^6$ cm sec^{-1} which is about five times faster than the phonon velocity in the same substance. (A rough estimate of the phonon velocity from the Debye

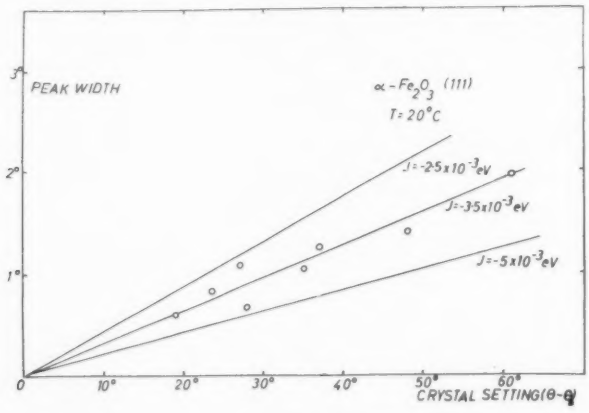

FIG. 2. Connection between crystal setting and diffuse peak width after correction for instrumental broadening. Straight lines have been calculated for different spin wave velocities corresponding to the indicated values of the predominant exchange integral.

Vol. 17
1960

temperature gave a value of $7{\cdot}6\times10^5$ cm sec^{-1}.) GOEDKOOP has given a theoretical formula for the connection between the spin wave velocity and the exchange integral.[8] By solving the secular equation arising from a Heisenberg type exchange coupling between the spins of the iron atoms, he found the formula:

$$c_m = -2^{5/2}\frac{Sa}{\hbar}\sum_i z_i J_i \qquad (8)$$

S is the iron spin, z_i the number of neighbours having the exchange integral J_i and a the base of the unit cell in hexagonal coordinates. The latter formula was calculated taking only the two strongest interactions into account and assuming that the spin waves are propagating in the base plane.

The observed value of the magnon velocity corresponds to

$$\sum_i z_i J_i = -2{\cdot}1\times10^{-2}\text{ eV}.$$

This figure is consistent with the value of $-1{\cdot}8\times10^{-2}$ eV found for Fe_3O_4, because hematite has a critical temperature of 969°K compared with 855°K for magnetite. In hematite $z = 6$ for the interaction which is supposedly the strongest one, this corresponds to $J = 3{\cdot}5\times10^{-3}$ eV as indicated in Fig. 2.

When applying formula (7) to our experimental data, we had of course to correct for instrumental broadening of the peaks. The instrumental or resolution function is given by the profile of the peak at the Bragg setting $\theta = \theta_B$. Assuming Gaussian forms of this profile and of the observed diffuse peak, the corrected full width at half maximum (Γ) of the diffuse peak is simply given by $\Gamma = (\Gamma_{obs}^2 - \Gamma_B^2)^{1/2}$. Γ_{obs} and Γ_B denote the observed full widths at half maximum for the diffuse and the Bragg peaks respectively. The theoretical shape of the diffuse peak, as calculated by ELLIOTT and LOWDE[19], is however quite different: the peak is flat with the sides cut sharply off at an angle Ψ given by formula (7). The connection between Ψ and Γ can now be found by measuring out the full width at half maximum of the curve one obtains by folding the theoretical peak profile with our experimental function.

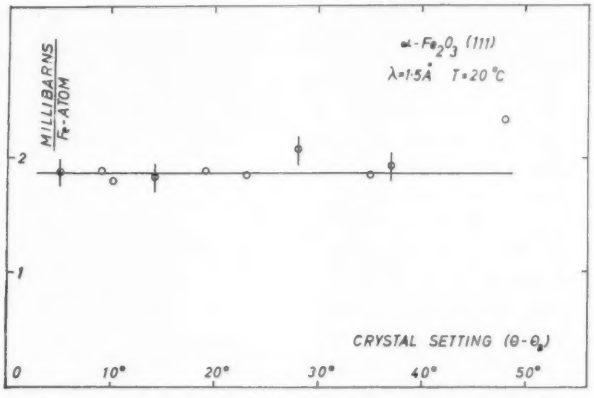

FIG. 3. Diffuse peak cross section plotted vs. crystal setting.

The value of the exchange integral that we have found, may be used in a calculation of the diffuse scattering cross section. ELLIOTT and LOWDE[19] have shown that the cross section integrated over the whole diffuse peak for a simple class of antiferromagnets is independent of the crystal missetting. Their treatment has been generalized by GOEDKOOP[8] to include also the case of hematite. His formula for the intregrated cross section reads:

$$\sigma^T = 2\pi\left[1+\left(\frac{\kappa_z}{\kappa}\right)^2\right]\frac{k_B T}{E}\left(1{\cdot}91\frac{e^2}{mc^2}\right)^2\times$$
$$\times\frac{(-2S\sum_i z_i J_i)}{m_0 c_m^2}S\left|\frac{F(\tau)}{F_0^{rev}}\right|^2\tanh^{-1}\frac{v}{c_m} \qquad (9)$$

where E is the neutron energy. $F(\tau)/F_0^{\text{rev}}$ is a relative structure factor where "rev" indicates that the "down" spins have been reversed so that they all point "up". At room temperature it gives a value of 1·66 millibarns per iron atom when putting $[1+(\kappa_z/\kappa)^2] = 1{\cdot}66$ which is found from Fig. 1 when correcting for extinction. Our observed values are plotted in Fig. 3 and show the predicted behaviour in being independent of the crystal missetting. The diffuse peak intensity has been put on an absolute scale by comparing with the (222) Bragg reflection which is of pure nuclear origin and has negligible extinction. The observed value of 1·86 millibarns is a little higher than predicted, but the agreement is sufficiently good in view of the different uncertainties in estimating $[1+(\kappa_z/\kappa)^2]$, the temperature factors and c_m.

It remains to be proved that the observed diffuse peaks are indeed due to antiferromagnetic spin waves and not to lattice vibrations, which also would show a linear dispersion relation. Since the nuclear structure factor of the (111) reflection is zero, such vibrations could only manifest themselves as magnetic vibrational scattering. This kind of scattering, being elastic in the magnetic sense, obeys the factor $[1-(\kappa_z/\kappa)^2]$. The spin wave cross section, which involves scattering on the x and y components, contains the factor $[1+(\kappa_z/\kappa)^2]$ as shown above. In a ferromagnet one is able to change the value of κ_z by applying an external field in different directions and thus change the direction of the spins with respect to the reflecting plane. In an antiferromagnet the spin direction cannot be changed markedly by an external field. In hematite, however, we have seen from Fig. 1 that there is a transition which simulates the effect of an external field on a ferromagnet.

From Fig. 1 and the fact that the inelastic scattering is proportional to the absolute temperature, it may be inferred that when the crystal is cooled from 20°C to −35°C the intensities due to spin waves and lattice vibrations should change by +9 and −71 per cent respectively. Experimentally an increase of 10 ± 5 per cent was obtained, showing that the diffuse peaks must be of almost pure spin wave origin. A theoretical estimate of the magneto-vibrational scattering, made from the formula given by LOWDE[20], showed that at 20°C it would be only about 10 per cent of the spin wave scattering. Also, since the phonon velocity is about one fifth of the magnon velocity, the phonon peaks will be about five times wider than the magnon peaks and will merge into the isotropic background.

C. *The transition from spin waves to critical fluctuations*

In Fig. 4 are shown some diffuse peaks taken at a crystal missetting of 14° for different temperatures. It is seen that, when starting from room

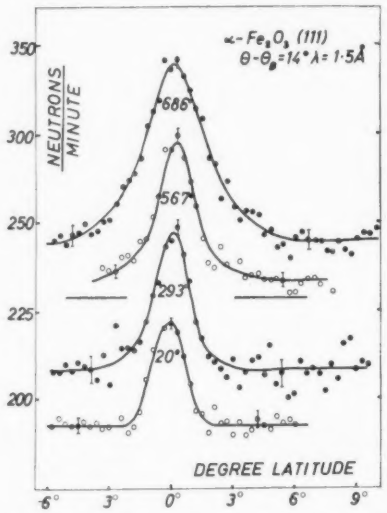

FIG. 4. Profile of diffuse peak at $\theta-\theta_B = 14°$ taken at different temperatures.

temperature, the only effect of increasing the temperature is at first to change the intensity but not the width of the peaks. When approaching the Néel temperature, however, one sees a pronounced increase in the peak width. The peak width Γ, which has been discussed earlier, is plotted in Fig. 5. The curve bears a strong resemblance to the observations in magnetite.[2] As for magnetite, we find that the temperature T_1, where the sudden increase of Γ occurs, depends on the crystal missetting or, which is the same, on the magnon energy. In Fig. 6 we see the observed connections between T_1 and the magnon energy. In the same figure is plotted the curve which was observed for magnetite. In magnetite we found that the sudden increase of Γ was accompanied by

Vol. 17
1960

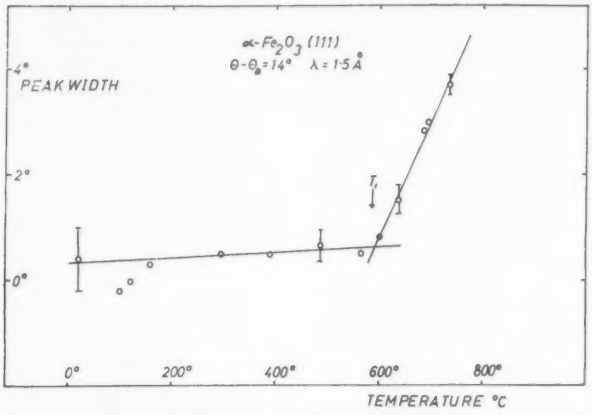

FIG. 5. Width of diffuse peaks, after correction for instrumental broadening, as function of temperature.

the onset of fluctuations in the z-components of the spin. This point cannot be checked for hematite, because the method of distinguishing the different intensity components by applying an external field is useless in an antiferromagnet. The experiments on magnetite further showed that the broadening applied to the peaks due to spin waves or transverse fluctuations.[9]

In Fig. 7 one sees the temperature variation of the diffuse peak cross section at $\theta-\theta_B = 14°$. In the low temperature region the experimental errors are of the size of the experimental points. The curve drawn through the points in the region of transition from state I to II has the shape calculated from Fig. 1. There is no discontinuity at the corresponding T_1 of about 600°C. Instead we see that there is a tendency of the cross section to exceed the linear temperature variation predicted by formula (9) already at much lower temperatures. The proportionality in T was arrived at by assuming Bose–Einstein statistics and a magnon energy much less than k_BT, which also is the case in our experiments. A clearer picture of the general temperature behaviour of the cross section is seen

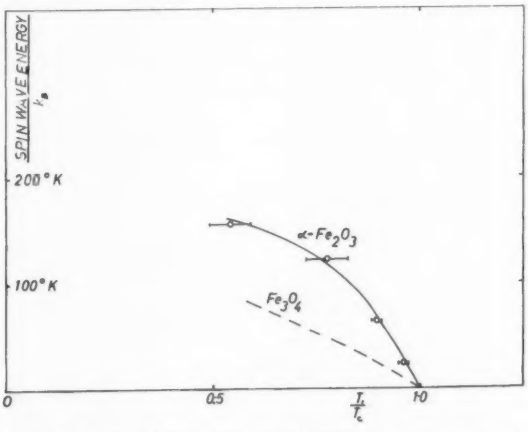

FIG. 6. Connection between observed temperature of broadening (T_1) of diffuse peaks and magnon energy. The curve for Fe_3O_4 is taken from Ref. 2.

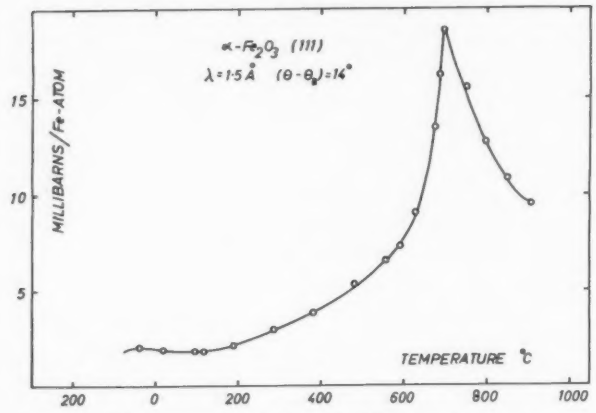

FIG. 7. Temperature variation of diffuse peak cross section at $\theta-\theta_B = 14°$.

from Fig. 8. The diffuse peak intensity seems to contain two components:

(a) A general inelastic component which is independent of the crystal missetting.

(b) A component of critical scattering which is of appreciable intensity only in the vicinity of the Bragg setting and disappears completely at missettings as high as 35°.

Concerning (a) we see that the general inelastic component, which can be studied in isolation at $\theta-\theta_B = 35°$, has a temperature behaviour which is described quite well by $[1-M_T{}^2M_0{}^{-2}]$. M_T denotes the sublattice magnetization and M_0 its saturation value. The quantity in brackets is easily derived from Fig. 1 at least in state II, since the intensity of the Bragg peak is at any temperature proportional to $M_T{}^2$. It seems surprising that the cross section at any spin wave energy should be governed by this quantity. One should rather expect that this factor applies to the cross section when integrated over all energies and directions, as would be observed in transmission measurements with a polycrystal. Our observations therefore indicate a mixing of the spin wave states when the temperature is raised to about half the Néel temperature. The constancy of the

Vol. 17
1960

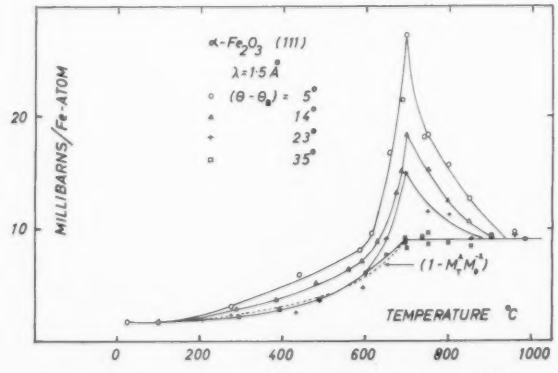

FIG. 8. Temperature behaviour of cross section at different missettings. Broken curve is calculated from relative value of sublattice magnetization $M_TM_0{}^{-1}$, derived from Fig. 1.

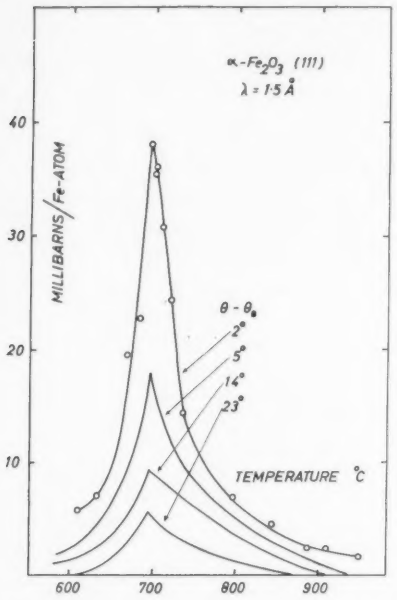

FIG. 9. Critical scattering component derived from curves like in Fig. 8, after subtracting general inelastic component as explained in the text.

peak width even at temperatures high enough for the intensity to exceed the linear slope, indicates that a state characterized by a frequency ω is mixed with states having values of q both smaller and greater than given by equation (2).

D. *The critical component*

Concerning (b) this critical component can simply be derived from the curves of Fig. 8 by subtracting the general inelastic term. After carrying out this subtraction, we obtain the curves of Fig. 9. The ratio between the slopes of the intensity below and above the Néel temperature is seen to be approximately -2, in agreement with the general predictions on the constant κ_1 for ferromagnets, as mentioned earlier.

The expression for the differential cross section has been given by formula (6). It may be shown that in the white beam technique this leads to the following dependence for the peak maxima

$$I_{\max} \sim r_1^{-2}(\tau)[\kappa_1^2 + 4\pi^2\tau^2(\theta-\theta_B)^2]^{-1/2} \qquad (10)$$

Thus the dependence of $I_{\max}$ on $(\theta-\theta_B)$ is very simple when $\kappa_1 \ll 2\pi\tau(\theta-\theta_B)$. Our data at $T = T_N$, shown in Fig. 10, show the predicted behaviour. The agreement between the theoretical curve and the experimental points sets an upper limit of $\sim 10^{-4}$ Å^{-2} on κ_1^2 at T_N. The curve has been drawn with a value of 1·68 Å for r_1 (111), this value is calculated in the Appendix using molecular field theory. The intensity at $\theta-\theta_B = 4°$ corresponds to a cross section of 46 millibarns per steradian and magnetic ion.

The temperature variation of the cross section is contained in κ_1. In Fig. 11 is shown the temperature variation of κ_1^2 obtained from the peak maximum at $\theta-\theta_B = 4°$ when correcting for

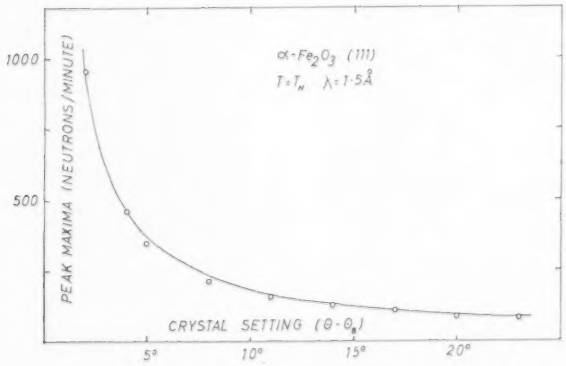

FIG. 10. Diffuse peak maxima for $T = T_N$. Curve has been drawn for $\kappa_1 = 0$ and $r_1 = 1{\cdot}68$ Å, which are theoretical values calculated in the Appendix.

experimental broadening. For $T < T_N$ the data have been left out because of the inaccuracy of this correction when the broadening is weak. According to theory κ_1^2 should be proportional to $(T-T_N)$ when the correlation range (κ_1^{-1}) is long compared to the interatomic distance. At $T \gg T_N$ one expects departure from this behaviour, in

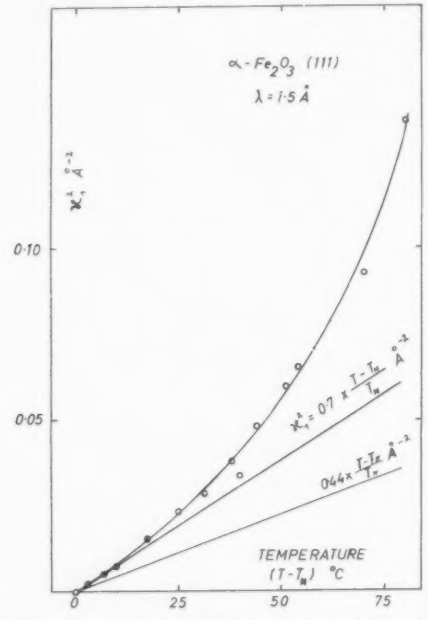

FIG. 11. Temperature variation of κ_1^2 as obtained from peak maximum at $\theta-\theta_B = 4°$. Lines have been calculated with different assumptions for interactions, as explained in the text.

the paramagnetic limit $\kappa_1^2 \to \infty$ because the spins will be uncorrelated. It is seen from Fig. 11 that there is a gradual departure from a linear slope near T_N, it is however difficult to assign an accurate value to this slope. Two theoretical curves are drawn, the calculations are found in the Appendix. The value of $\kappa_1^2 = 0{\cdot}44(T-T_N)/T_N$ is obtained when taking only the supposedly strongest interaction into account, this is the Fe–O–Fe superexchange bond which forms an angle closest to 180°. The value $\kappa_1^2 = 0{\cdot}7(T-T_N)/T_N$ is obtained when taking only the second strongest interaction into account. If one uses the thermodynamic relation $r_1^2\kappa_1^2 = (T-T_N)/T_N$ one gets $\kappa_1^2 = 0{\cdot}6\,(T-T_N)/T_N$ from the calculated value of r_1^2.

We have so far not discussed the intensity component which is observed at the Bragg position for $T > T_N$. The intensity is of antiferromagnetic origin since the nuclear structure factor is zero. There is no visible broadening of the peaks at this setting, they always appear with the same width as the Bragg peaks at lower temperatures. The integrated intensity of the peak varies according to Fig. 12, the curve has been corrected for higher order contamination. It is seen that the intensity

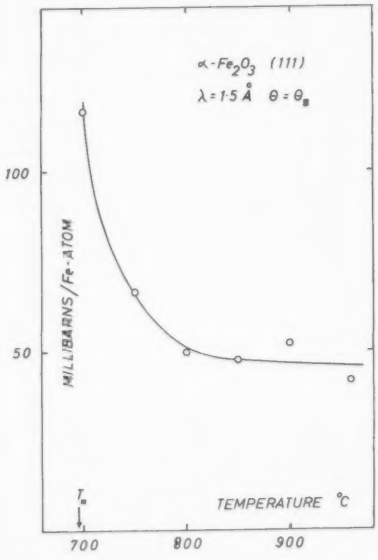

FIG. 12. Temperature variation of integrated peak at Bragg setting for $T > T_N$.

does not come down to the level observed at other crystal settings.

When comparing with the experimental results for Fe_3O_4,[9] we see that the diffuse peaks of α-Fe_2O_3 are much narrower than the corresponding ones in Fe_3O_4. We mention as a typical example that the diffuse peak at T_N and $\theta-\theta_B = 4°$ for α-Fe_2O_3 had a corrected width of only 1·6°, whereas the corresponding peak for Fe_3O_4 had a width of 3·3°.

4. CONCLUSION

From the experimental results presented here one can conclude that the magnetic inelastic scattering of neutrons from α-Fe_2O_3 is well

Vol. 17
1960

described by spin wave theory up to about half the Néel temperature. In this temperature region there is a one-to-one correspondence between spin wave frequency and wavelength. At higher temperatures there is at first a slow tendency for the scattered intensity to supersede its theoretical value, this is interpreted as a spreading out of the momentum spectrum of spin waves characterized by a single frequency, i.e. as a mixing of states. This tentative conclusion can only be checked by analysing the spectrum of scattered neutrons with a good resolution of energy and momentum.

At a temperature which we have indicated by T_1, there is a sudden broadening of the spin wave peaks. The connection between T_1 and the spin wave energy is found to be very similar to the case of magnetite reported earlier.

The observed picture of the temperature variation and the angular distribution led us to conclude that one could distinguish between two intensity components, a general inelastic one and a critical one. This agrees with the predictions by VAN HOVE[3] and by DE GENNES and VILLAIN[11].

In the spin wave region the energy is in a simple way related to the crystal setting, as discussed before. In the critical and the paramagnetic region it still seems reasonable to assume that the greatest energy transfers are observed at the largest missettings. Information on the momentum transfer, or the wave vectors of the fluctuations, is of course obtained from the peak width. Our observations therefore show that the general inelastic component has a wide distribution in energy and momentum. The intensity of this component is approximately constant for $T > T_N$.

The curves of Fig. 9 show that the critical scattering is restricted to small energy and momentum transfers, as predicted first by VAN HOVE[3]. The detailed study of the critical scattering near T_N shows that its behaviour is well predicted by calculations based on a local form of the molecular field theory, a method first given by DE GENNES and HERPIN[13]. This is perhaps surprising in view of the disagreement observed for Fe_3O_4.[9]

A comparison between the critical scattering in ferrimagnetic Fe_3O_4 and antiferromagnetic α-Fe_2O_3 is of interest. These compounds contain the same atomic species and the interactions are very similar. The comparison between peak widths given in the previous section, shows that enhanced scattering at the critical temperature, or critical scattering, is in the antiferromagnetic case even more restricted to wave vectors close to certain reciprocal lattice vectors.

The scattering by a fluctuation with a definite wave vector is expected to increase if the relaxation is markedly braked. As a result of the braking the range of the fluctuation will increase and thus also the coherent inelastic scattering. From the observed intensity distribution we conclude that processes which tend to brake the relaxation of the fluctuations are in the antiferromagnetic case only found when the wave vectors are close to the reciprocal lattice vectors. Recalling now what was mentioned in Section 2 about processes braking the fluctuations, this indicates that thermodynamic braking processes are active only for wave vectors which deviate little from the reciprocal lattice vectors. Kinematic braking processes are on the other hand active over a wider range of wave vectors, this is the reason for the broad peaks observed in Fe_3O_4.

It is also interesting to note that there is no anomaly in the diffuse scattering in the transition region from state I to state II. This means that the spin order within the domain remains the same (apart from the Brillouin-type decrease with temperature) during the transition, and that the domains remain with unchanged dimensions. If the transition from one state to the other would occur by growing around nuclei of the new phase one should expect fluctuations of the domain size which would be accompanied by diffuse scattering. Consequently the domain as a whole must have the direction of its antiferromagnetic axis changed as it goes through the transition. The reason why the width of the transition as shown in Fig. 1 is broader than found by some other experimenters, is due to the fact that some crystals are more inhomogeneous than others so that the transition temperature may be different for different domains within the same sample. This is proved by the curves on Fig. 13. Sample I in this figure refers to the sample which gave the curve in Fig. 1. The other curve is obtained with a small sample, having a volume of only 2 mm^3, which was cut out from sample I. It is seen that the small sample has a much narrower transition than the big one.

Our experiments do not enable us to determine the relative strength of the exchange integrals.

The observed connection between peak width and crystal setting in Fig. 2 only gives the effective exchange integral

$$\sum_i z_i J_i$$

The intensity distribution seen from Fig. 3 confirms the linear dispersion relation, but gives no new information about the exchange integrals.

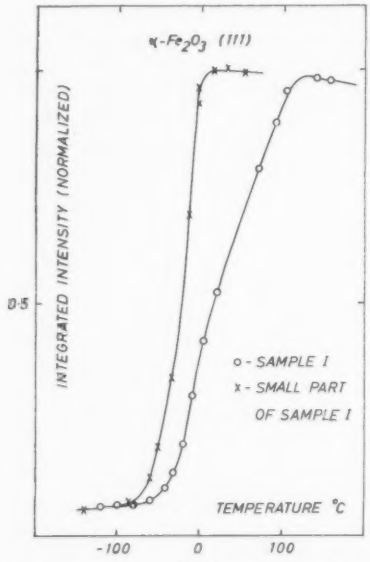

FIG. 13. Temperature variation of elastic reflection when antiferromagnetic spins rotate from low temperature alignment along [111] into (111).

In the critical region our calculations of r_1 show that the value of this constant is independent of the exchange integral. κ_1 is on the other hand sensitive to the model of the interactions. In our case, however, the range of the fluctuations decreases so quickly when increasing $(T-T_N)$ that it is difficult to state anything about the individual J_i's.

Acknowledgement—The authors want to thank Dr. J. A. GOEDKOOP for many stimulating discussions on the theoretical aspects of spin wave scattering.

APPENDIX

It is seen from formula (5) that the cross section may be found from the wavelength-dependent susceptibility $\chi(\kappa)$. This quantity will be calculated below, following a method given by DE GENNES[21].

In Ref. (8) we find the following information about the magnetic structure of hematite:

Hematite has four sublattices. Spins in the same sublattice are located in planes normal to the rhombohedral axis. If consecutive planes (and sublattices) are denoted 1, 2, 3 and 4, the spin sequence is $+--+$. A spin in sublattice 1 is in superexchange coupling through intervening atoms with the spins in the other sublattices, the dominating interactions are supposedly those with sublattice 2 and 3. In molecular field theory the same idea is expressed by saying that the spins on sublattice 2 and 3 give a Weiss field at sublattice 1, the direction of the field being opposite to the spin direction in 2 and 3. The magnetic moment carried by the spin on 1 is in equilibrium under the action of these Weiss fields and the external field. This can be expressed in the following set of equations:

$$\begin{aligned} \boldsymbol{M}_1 &= \frac{C'}{T}(\boldsymbol{H}-\lambda\boldsymbol{M}_3-\tfrac{1}{2}\epsilon\boldsymbol{M}_2) \\ \boldsymbol{M}_2 &= \frac{C'}{T}(\boldsymbol{H}-\lambda\boldsymbol{M}_4-\tfrac{1}{2}\epsilon\boldsymbol{M}_1) \\ \boldsymbol{M}_3 &= \frac{C'}{T}(\boldsymbol{H}-\lambda\boldsymbol{M}_1-\tfrac{1}{2}\epsilon\boldsymbol{M}_4) \\ \boldsymbol{M}_4 &= \frac{C'}{T}(\boldsymbol{H}-\lambda\boldsymbol{M}_2-\tfrac{1}{2}\epsilon\boldsymbol{M}_3) \end{aligned} \qquad \text{(A.1)}$$

C' is the Curie constant, λ and ϵ are molecular field constants of which λ is supposed to be the greater. The factor $\frac{1}{2}$ arises because each spin has six of the stronger bonds, but only three of the weaker ones.

At $T = T_N$ we shall have a nonvanishing set of values of $\boldsymbol{M}$, when putting $H = 0$. Putting the determinant of the equations equal to zero, we obtain:

$$T_N = C'(\lambda \pm \tfrac{1}{2}\epsilon) \qquad \text{(A.2)}$$

The upper sign should be chosen because it gives the highest value of T_N.

By adding the equations (A.1), we obtain:

$$\boldsymbol{M} = \frac{C'}{T}\left(4\boldsymbol{H}-\lambda\boldsymbol{M}-\frac{\epsilon}{2}\boldsymbol{M}\right) \qquad \text{(A.3)}$$

where

$$\boldsymbol{M} = \boldsymbol{M}_1+\boldsymbol{M}_2+\boldsymbol{M}_3+\boldsymbol{M}_4 \qquad \text{(A.4)}$$

This gives

$$\begin{aligned} \chi &= 4\frac{C'}{T}\left[1+\frac{C'}{T}(\lambda+\tfrac{1}{2}\epsilon)\right]^{-1} \\ &= \chi_0\left[1+\frac{C'}{T}(\lambda+\tfrac{1}{2}\epsilon)\right]^{-1} \end{aligned} \qquad \text{(A.5)}$$

Vol. 17
1960

We are next going to introduce the wavelength-dependent susceptibility giving the response of the sublattice magnetization to a field which changes direction when going from an "up" spin to a "down" spin. The origin is chosen at a spin in sublattice 1.

Introducing

$$M_3 = \tfrac{1}{4}M(\boldsymbol{\varkappa})\exp(-i\boldsymbol{\varkappa}\boldsymbol{R}_3)$$
$$M_2 = \tfrac{1}{4}M(\boldsymbol{\varkappa})\exp(-i\boldsymbol{\varkappa}\boldsymbol{R}_2) \qquad \text{(A.6)}$$

we have the equivalent equation of (A.1):

$$\tfrac{1}{4}M(\boldsymbol{\varkappa}) = \frac{C'}{T}\left[H(\boldsymbol{\varkappa})-\lambda\langle M_3\rangle-\frac{\epsilon}{2}\langle M_2\rangle\right] \qquad \text{(A.7)}$$

The averages are taken over the nearest neighbours in the sublattices denoted by the index.

If

$$S_n = \frac{1}{z_n}\sum\exp(-i\boldsymbol{\varkappa}\boldsymbol{R}_n)$$

then equation (A.7) may be written:

$$\tfrac{1}{4}M(\boldsymbol{\varkappa}) = \frac{C'}{T}\left[H(\boldsymbol{\varkappa})-\lambda S_3(\boldsymbol{\varkappa})\tfrac{1}{4}M(\boldsymbol{\varkappa})-\right.$$
$$\left.-\frac{\epsilon}{2}S_2(\boldsymbol{\varkappa})\tfrac{1}{4}M(\boldsymbol{\varkappa})\right] \qquad \text{(A.8)}$$

which gives

$$\frac{\chi_0}{\chi(\boldsymbol{\varkappa})} = 1+\frac{C'}{T}\lambda S_3(\boldsymbol{\varkappa})+\frac{C'}{T}\frac{\epsilon}{2}S_2(\boldsymbol{\varkappa}) \qquad \text{(A.9)}$$

In the notation of formula (5) the term in the denominator should more properly have been written

$$\sum_j \chi_{ij}(\boldsymbol{\varkappa})$$

with $i = 1$ and $j = 2,3$.

When calculating the quantities S_3 and S_2, it is convenient to index the lattice on a hexagonal unit cell. The cell dimensions are $a = 5{\cdot}03$ Å and $c = 13{\cdot}73$ Å. With the origin at an atom in sublattice 1 the coordinates of the atoms in sublattice 3 are:

$$\tfrac{1}{3},\ \tfrac{2}{3},\ \tfrac{1}{6}$$
$$-\tfrac{2}{3},-\tfrac{1}{3},\ \tfrac{1}{6}$$
$$\tfrac{1}{3},-\tfrac{1}{3},\ \tfrac{1}{6}$$
$$\tfrac{2}{3},\ \tfrac{1}{3},-\tfrac{1}{6}$$
$$-\tfrac{1}{3},\ \tfrac{1}{3},-\tfrac{1}{6}$$
$$-\tfrac{1}{3},-\tfrac{2}{3},-\tfrac{1}{6}$$

and in sublattice 2

$$\tfrac{1}{3},\ \tfrac{2}{3},\ \tfrac{1}{6}-2u$$
$$-\tfrac{2}{3},-\tfrac{1}{3},\ \tfrac{1}{6}-2u$$
$$\tfrac{1}{3},-\tfrac{1}{3},\ \tfrac{1}{6}-2u$$

where $u = 0{\cdot}145$.

This gives:

$$S_3 = \frac{1}{3}\left\{\cos\left[\frac{a}{3}(\kappa_x+2\kappa_y)+\frac{c}{6}\kappa_z\right]+\right.$$
$$+\cos\left[\frac{a}{3}(-2\kappa_x-\kappa_y)+\frac{c}{6}\kappa_z\right]+$$
$$\left.+\cos\left[\frac{a}{3}(\kappa_x-\kappa_y)+\frac{c}{6}\kappa_z\right]\right\} \qquad \text{(A.10}$$

Our experiments were performed on the (003) reflection with the [010] axis mounted vertical. Denoting the crystal setting as usual by $(\theta-\theta_B)$ the coordinates of κ are in the elastic approximation given by:

$$\kappa_x = \tfrac{2}{3}2\pi\tau\sin(\theta-\theta_B)$$
$$\kappa_y = -\frac{1}{\sqrt{3}}2\pi\tau\sin(\theta-\theta_B)$$
$$\kappa_z = 2\pi\tau\left[1-2\sin^2\frac{\theta-\theta_B}{2}\right]\approx 2\pi\tau$$

For small values of $(\theta-\theta_B)$ we easily obtain:

$$S_3 = -[1-5{\cdot}3(\theta-\theta_B)^2] = -[1-2{\cdot}8|\boldsymbol{\varkappa}-2\pi\boldsymbol{\tau}|^2] \qquad \text{(A.11)}$$

The expansion of S_2 gives a complex term, this is, however, cancelled by an equivalent term of opposite sign when expanding with the origin in sublattice 4. When omitting the complex term, we obtain:

$$S_2 = -0{\cdot}68[1-2{\cdot}8|\boldsymbol{\varkappa}-2\pi\boldsymbol{\tau}|^2] \qquad \text{(A.12)}$$

Due to the crystal symmetry the expansions of S_3 and S_2 are in fact invariant by a rotation around the c-axis, the plane normal.

Inserting the expansion in formula (A.9), we obtain:

$$\frac{\chi_0}{\chi(\boldsymbol{\varkappa})} = 1-\frac{C'}{T}(\lambda+0{\cdot}34\epsilon)[1-1{\cdot}68^2|\boldsymbol{\varkappa}-2\pi\boldsymbol{\tau}|^2] \qquad \text{(A.13)}$$

Thus the condition for critical scattering is:

$$(\lambda+0{\cdot}34\epsilon)\frac{C'}{T_N} = 1 \qquad \text{(A.14)}$$

It is easy to show that our equations (A.2), (A.5) and (A.14) are not compatible with susceptibility data, but it is possible that a set of consistent equations might be obtained by also including other magnetic interactions. When comparing (A.13) with equations (5) and (6), we see that $r_1 = 1{\cdot}68\,(T_N/T)^{1/2}$(Å). Close to T_N the temperature variation of r_1 may be neglected.

Our next task is to find κ_1, the inverse of the range of the fluctuations.

From (A.11) and the last two equations we have:

$$\frac{\chi_0}{\chi(\mathbf{x})} = 1+\frac{T_N}{T}S_3(\mathbf{x}) \qquad \text{(A.15)}$$

which together with equation (6) gives the thermodynamic relation

$$\kappa_1^2 r_1^2 = \frac{T-T_N}{T_N} \qquad \text{(A.16)}$$

which in our case gives

$$\kappa_1^2 = 0{\cdot}6\,\frac{T-T_N}{T_N}$$

It is also possible to perform a separate calculation of κ_1 without making use of the connection with r_1 as expressed by (A.16). We then proceed in the same way as DE GENNES[21]. Retaining only the supposedly strongest interaction, we have corresponding to (A.1):

$$M_1(0) = -\frac{\lambda C'}{zT}\sum_i M_3(\boldsymbol{R}_i) \qquad \text{(A.17)}$$

$$M_3(\boldsymbol{R}_i) = -\frac{\lambda C'}{zT}\sum_j M_1(\boldsymbol{R}_i+\boldsymbol{R}_j) \qquad \text{(A.18)}$$

The summation over i and j means a summation over all the z nearest neighbours connected through the strongest interaction. Combining the last two equations, we obtain:

$$M_1(0) = \frac{\lambda^2 C'^2}{z^2T^2}\sum_{ij} M_1(\boldsymbol{R}_i+\boldsymbol{R}_j) \qquad \text{(A.19)}$$

and further

$$M_1(0) = \frac{\lambda^2C'^2}{T^2}M_1(0)+\frac{\lambda^2C'^2}{z^2T^2}\times$$

$$\times\Big[\sum_{\substack{ij\\ j\neq 0}} M_1(\boldsymbol{R}_i+\boldsymbol{R}_j)-(z^2-z)M_1(0)\Big] \qquad \text{(A.20)}$$

$$M_1(0) = \frac{\lambda^2C'^2}{T^2}M_1(0)+$$

$$+\frac{\lambda^2C'^2}{T^2}\frac{z-1}{z}[\bar{M}_{nn}-M(0)] \qquad \text{(A.21)}$$

where $\bar{M}_{nn}$ denotes the average magnetic moment per ion in the shell of next nearest neighbours of strongly interacting ions.

With the assumption of long range correlations the quantity in the brackets may be found from the expansion.

$$M_\nu(x) = M(0)+\left(\frac{\partial M}{\partial x}\right)_0 x_\nu + \frac{1}{2}\left(\frac{\partial^2 M}{\partial x^2}\right)_0 x_\nu^2+\ \ldots \qquad \text{(A.22)}$$

where x_ν is the component along grad M of the position vector of the ν 'th ion. This expansion gives:

$$\bar{M}_{nn} = M(0)+\frac{1}{z_{nn}}\left(\frac{\partial M}{\partial x}\right)_0\sum_{\nu=1}^{z_{nn}} x_\nu^2+$$

$$+\frac{1}{2z_{nn}}(\nabla^2 M)_0\sum_{\nu=1}^{z_{nn}} x_\nu^2 \qquad \text{(A.23)}$$

Since the next nearest neighbours under consideration have a center of symmetry in (000), we get:

$$\bar{M}_{nn}-M(0) = \frac{1}{2z_{nn}}(\nabla^2 M)_0\sum_{\nu=1}^{z_{nn}} x_\nu^2 \qquad \text{(A.24)}$$

In hematite

$$\sum_\nu x_\nu^2$$

depends upon the direction of the gradient. We can obtain a mean value of this sum by averaging over three mutually orthogonal directions, one along the c-axis and two in the base plane. We thus obtain

$$\overline{\sum_\nu x_\nu^2} = 197\ \text{Å}^2.$$

From our last equation and (A.21) we obtain

$$\kappa_1^2 = 2\,\frac{T^2-\lambda^2C'^2}{\lambda^2c'^2}\,\frac{z}{z-1}\,\overline{\left(\frac{z_{nn}}{\sum_\nu x_\nu^2}\right)} \qquad \text{(A.25)}$$

From (A.14) we have $\lambda C' = T_N$, when putting $\epsilon = 0$, which gives

$$\kappa_1^2 = 0{\cdot}44\,\frac{T-T_N}{T_N}\,\text{Å}^{-2} \qquad \text{(A.26)}$$

which is valid for $0 < T-T_N \ll T_N$.

One must expect that the latter method of calculating κ_1 is a good approximation when the range of the correlations is long. This restriction on κ_1 may limit the validity of (A.26) to a very small temperature interval.

Vol. 17
1960

By the same method one may calculate κ_1 when also the interaction characterized by ϵ is included. In the special case where $\lambda = 0$, we obtain:

$$\kappa_1^2 = 0{\cdot}7\,\frac{T-T_N}{T_N}\,\text{Å}^{-2} \qquad \text{(A.27)}$$

REFERENCES

1. Brockhouse B. N., *Phys. Rev.* **106,** 859 (1957).
2. Riste T., Blinowski K. and Janik J., *J. Phys. Chem. Solids* **9,** 153 (1959).
3. Van Hove L., *Phys. Rev.* **95,** 1374 (1954).
4. McReynolds A. W. and Riste T., *J. Phys. Radium* **20,** 175 (1959).
5. Iyengar P. K. and Brockhouse B. N., *Bull. Amer. Phys. Soc.* **3,** 195 (1958).
6. Shull C. G., Strauser W. A. and Wollan E. O., *Phys. Rev.* **83,** 333 (1951).
7. Hulthén L., *Proc. Acad. Sci. Amst.* **39,** 190 (1936).
8. Goedkoop J. A., *J. Phys. Chem. Solids,* to be published.
9. Riste T., this journal, preceding paper.
10. Johnson F. M. and Nethercott A. H., *Phys. Rev.* **114,** 705 (1959).
11. de Gennes P. G. and Villain J., *J. Phys. Chem. Solids* **13,** 10 (1960).
12. Elliott R. J. and Marshall W., *Rev. Mod. Phys.* **30,** 75 (1958).
13. de Gennes P. G. and Herpin M., *C.R. Acad. Sci., Paris* **243,** 1611 (1956).
14. Krivoglaz M. A., *Dokl. Akad. Nauk S.S.R.* **1,** 51 (1958); *Soviet Physics Doklady* **3,** 61 (1958).
15. Shirane G., Pickart S. J., Nathans R. and Ishikawa Y., *J. Phys. Chem. Solids* **10,** 35 (1959).
16. Lin S. T., *J. Appl. Phys.* **30,** 306S (1959).
17. Corliss L. M., Hastings J. and Goldman J. E., *Phys. Rev.* **93,** 893 (1954).
18. Bacon G. E., private communication.
19. Elliott R. J. and Lowde R. D., *Proc. Roy. Soc.* **A230,** 46 (1955).
20. Lowde R. D., *Proc. Roy. Soc.* **A221,** 206 (1954).
21. de Gennes P. G., private communication.

LETTERS TO THE EDITOR

On the transition to metallic behavior in zinc oxide

(*Received* 31 *May* 1960)

IN A RECENT study of the capacitance of the zinc oxide electrolyte interface[1,2] we observed a strikingly sharp change (amounting almost to a discontinuity) in the flat-band potential,* occurring at a donor density of about 3×10^{18} cm^{-3}. Fig. 1 shows the experimental results for one particular

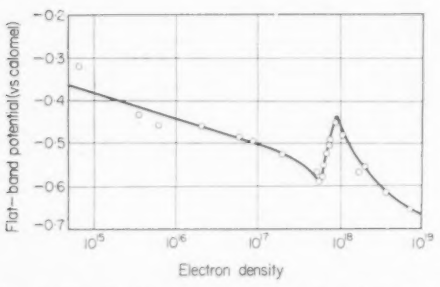

FIG. 1. The flat-band potential as a function of electron density for crystals freshly etched in H_3PO_4. (See Ref. 1.)

surface pretreatment (H_3PO_4 etch) and one ambient solution (KCl). Other things being simple (and there is no reason to think they are not simple in the case of zinc oxide), the variation of the flat-band potential under constant surface treatment should be exactly equal in magnitude and of opposite sign to the variation of the Fermi energy (with respect to some fixed energy in the bulk of the crystal, e.g. the conduction band edge). We speculated briefly that the "discontinuity" in flat-band potential did in fact reflect a discontinuity in Fermi energy but did not elaborate.

Since then it has been suggested[3] that this is qualitatively just the behavior to be expected of a system when the wave functions of the bound donor-states start to overlap and the transition to metallic behavior occurs. According to MOTT[4] this transition should be quite sharp. In the present note we wish to point out that all available data support this interpretation almost quantitatively.

The first such datum is the donor concentration (3×10^{18} cm^{-3}) at the transition point. This "scales" reasonably well from the transition point in germanium ($\sim5\times10^{16}$ cm^{-3}) observed by FRITSCHE[5]. The ionization energy of indium donors in zinc oxide is about 0·075 eV[6] compared to 0·01 eV in FRITSCHE's experiments with germanium while the respective dielectric constants are about 8·5[6] and 16. Thus, the apparent Bohr radius in germanium is about 4·0 times as great as in zinc oxide. The concentration at the transition point in zinc oxide should therefore be about 64 times that in germanium, within experimental error of the observed ratio ($3\times10^{18}/5\times10^{16}$) of 60. Actually the simple theory used here is probably in greater error than are the experiments.

The conductivity data of THOMAS[7] on indium-doped zinc oxide crystals also support the argument for a very sharp transition to metallic behavior. His data are shown in Fig. 2. The important and, to our knowledge, previously unrecognized feature of these data is that for crystals of room-temperature conductivity greater than about 15(Ω-cm)$^{-1}$ the curves show positive curvature while below this value the curvature is negative. This is in a direction to make the very low-temperature conductivity finite and temperature-independent at high donor density, but essentially zero at low donor density. The interesting features to note here are that the change is fairly abrupt and that the donor concentration at the 15(Ω-cm)$^{-1}$ demarcation point is about 3×10^{18}, just the concentration at the discontinuity in flat-band potential. Clearly the low-temperature behavior is metallic above this concentration while at lower concentrations it is that of a typical semiconductor.

At elevated temperatures, of course, where an appreciable fraction of the donor states are ionized, one expects a far more complex situation, with conduction-band and impurity-band conduction both playing significant roles. It is therefore not surprising that one does not observe the abrupt "phase"-transition by conductance measurements at elevated temperature. The interesting feature of our flat-band potential measurements is that the transition remains quite sharp, energywise

* The flat-band potential is defined as the potential (with respect to some fixed reference electrode) of the semiconductor when the "bands are flat" right up to the surface; there is no charge on the semiconductor under these conditions if "surface-states" are absent.

Vol. 17
1960

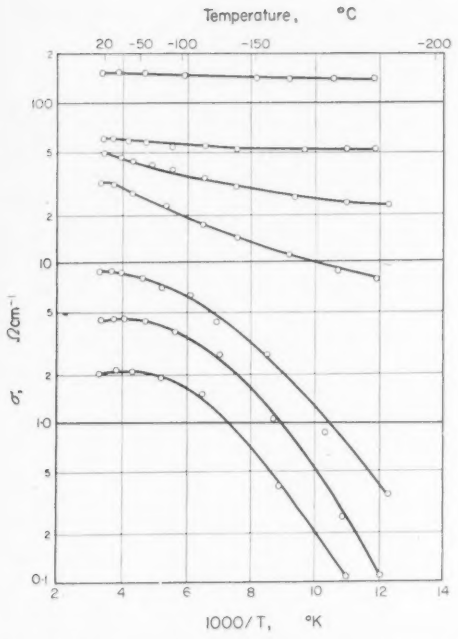

FIG. 2. The conductivity of indium-doped zinc oxide crystals as a function of temperature. (After THOMAS.)

at least, even at room temperature and in the presence of a random donor distribution. MOTT's theory predicts a discontinuous change only for a perfect lattice.

There are still many features of the flat-band potential data which require explanation. In particular, the magnitude of its abrupt increase seems excessive, and the origin of its subsequent almost as sharp decrease is presently not completely understood. Theoretical work along these lines is continuing.

Acknowledgements—I am indebted to C. HERRING and N. F. MOTT for stimulating discussions of this problem.

Bell Telephone Laboratories, Inc. J. F. DEWALD
Murray Hill
New Jersey
U.S.A.

References

1. DEWALD J. F., *Bell Syst. Tech. J.* **39,** 615 (1960).
2. DEWALD J. F., *Second Conference on Semiconductor Surfaces* (1959), *J. Phys. Chem. Solids* **14,** 155 (1960).
3. HERRING C., personal communication.
4. MOTT, N. F., *Nuovo Cim.* **7,** 312 (1958).
5. FRITSCHE H., *J. Phys. Chem. Solids* **6,** 69 (1958).
6. HUTSON A. R., personal communication. See also *Phys. Rev.* **108,** 222 (1957).
7. THOMAS D. G., *J. Phys. Chem. Solids* **9,** 31 (1958).

Observation of oscillatory magnetoresistance in InAs at microwave frequencies

(*Received* 15 *June* 1960)

WE HAVE observed transverse, oscillatory, magnetoresistance in InAs at liquid helium and hydrogen temperatures.

Oscillations in InAs have been previously reported using d.c. techniques.[1,2] The purpose of this letter is to describe observation made with an electron spin resonance spectrometer operating at 24000 mc/sec. These observations have been made accidentally, during a search for plasma resonance absorption in InAs.

The sample was placed on the wall of a TE_{110} cavity in the position of minimum E field. The spectrometer was tuned to absorption and a modulation field of 30 Oe was used. The observed signal was a derivative of the absorption signal with a possibility of some dispersion mixed in. The resistivity of the sample was $5{\cdot}5 \times 10^{-3}$ ohm-cm and the skin depth was about $2{\cdot}5 \times 10^{-3}$ cm, or 0·1 of the total sample thickness.

A typical experiment consisted of sweeping the magnetic field at 24000 mc/sec with the results shown in Fig. 1a. The minima are due to increased power absorption at resistivity maxima whenever a Landau level crosses the Fermi level. The plot of the minima vs. $1/H$ gives agreement with the theory. Ordinary d.c. measurements are exhibited for comparison in Fig. 1b. The sample used in these measurements had a slightly different carrier concentration n.

We do not propose to discuss the results obtained in view of their similarity with those in Refs. (1) and (2). We find our results interesting, however, because the microwave measurements have certain advantages over the d.c. measurements. They can be performed at higher sensitivity with smaller samples without electrodes attached to them. This may be of considerable interest in specific cases. The shape of the oscillatory lines

is not unlike that of plasma resonance absorption, with occasional possibility for confusion.

We have observed similar oscillations in InSb ($n = 5 \times 10^{15}$ cm^{-3}). We have unsuccessfully attempted to find the additional splitting of the individual levels due to two possible orientations

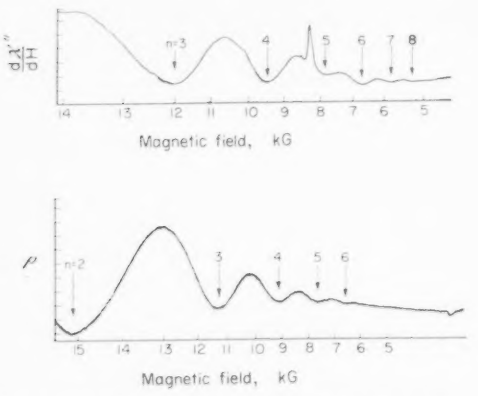

FIG. 1. (a) Microwave absorption at 24000 mc/sec as a function of H field. $T = 1{\cdot}2$°K. Carrier concentration $n = 6{\cdot}5 \times 10^{16}$ cm^{-3}. The extra line at $H = 8200\varphi$ is due to a control sample in the cavity. (b) D.C. resistance as a function of H field. $T = 1{\cdot}2$°K. Carrier concentration $n = 5{\cdot}4 \times 10^{16}$ cm^{-3}.

of electron spin for each Landau level. The spin splitting is to the Landau splitting as

$$\frac{g\mu_B H}{2} \Big/ 2\mu_B H \frac{m}{m^*} = \frac{gm^*}{4m}.$$

In InSb $m^* = 0{\cdot}013\,m$ and $g = 50$. The spin splitting is 0·16 of the Landau level spacing. We have not detected any evidence of such splitting.

Acknowledgement—The authors would like to acknowledge a helpful discussion with W. BOYLE.

Bell Telephone Laboratories
Murray Hill
New Jersey
U.S.A.

G. BEMSKI
B. SZYMANSKI

References

1. FREDERIKSE H. P. R. and HOSLER W. R., *Phys. Rev.* **110,** 880 (1958).
2. SLADEK R. J., *Phys. Rev.* **110,** 817 (1958).

Optical determination of the conduction band structure of GaSb

(*Received* 24 *May* 1960)

OSCILLATORY magneto-absorption measurements in GaSb show that the lowest conduction band minimum is at the center of the Brillouin zone.[1] The energy gap for the direct transitions between valence and conduction band at 4·2°K is $Eg = 0{\cdot}813$ eV,[1] very close to the value found for the direct absorption edge in germanium ($Eg = 0{\cdot}89$ eV[2]). The effective mass at the (000) minimum of the conduction band of GaSb is 0·047 m[1] also close to the value found for the (000) minimum of the conduction band in germanium ($m_e = 0{\cdot}033$ m).[2] The existence of another set of minima in the (111) direction of k space, similar to the lowest conduction band minima of germanium, has been postulated by SAGAR[3] to explain the temperature and pressure dependence of the Hall constant in GaSb. These minima should lie at room temperature 0·08 eV above the lowest (000) conduction band minimum. The large changes with pressure and temperature observed in the Hall constant of highly doped GaSb can be explained as due to changes in the relative population of both sets of minima while the total number of carriers remains constant. In this letter, further experimental evidence for the existence of the (111) set of minima is obtained from the temperature dependence of the free carrier polarizability as determined from infrared reflectivity measurements. The conductivity effective mass at the (111) conduction band minima is shown to be close to the conductivity effective mass at the same minima in germanium. Also the temperature dependence of the energy difference between both sets of conduction band minima is shown to be similar to the temperature dependence of the corresponding difference in germanium.

The reflectivity of highly doped GaSb was measured at 296 and 89°K by comparing it with the reflectivity of an almost intrinsic piece of germanium, using the method described by the author.[4] The Hall coefficient of the sample was measured on a bar cut from the specimen after the optical measurements were finished.

The Hall voltage was measured for magnetic fields up to 18,000 G and showed, within this domain, a linear dependence on magnetic field.

Vol. 17
1960

Figure 1 shows the reflectivity of an n-type GaSb sample at 296 and 89°K. The reflectivity at long wavelengths exhibits a large change with temperature which may be attributed to a change in the free carrier polarizability. The variation in the free carrier polarizability is smaller for all other semiconductors measured (Ge, Si, GaAs, InP)[4, 5] with the exception of PbS.[6] An interpretation of this large change in terms of only one set of equivalent non-parabolic conduction band minima, as was done for Ge, Si, GaAs and InP, is not possible. However, it is possible to explain this change as due to the transfer of carriers from one conduction band set of minima (000) to the higher lying one (111) as the temperature is increased.

The presence of carriers with different mobilities in two different valleys has to be taken into account to calculate the number of free carriers from the measured Hall constant ($R_H = 6{\cdot}88$ cm³/C at 296°K and $R_H = 5{\cdot}95$ at 77°K. The ratio of Hall to conductivity mobility is assumed to be equal to one. While this assumption is justified for the (000) minimum, where the degree of degeneracy is high, this might not be the case for the (111) minimum. However, one can estimate that no large error is introduced by this assumption. The number of carriers N_0 and N_1 in the (000) and (111) minima at room temperature and the position of the Fermi level E_F with respect to the (111) minimum of the band can be obtained by solving the set of equations:

$$R_H = \frac{1}{(N_1+N_0)ec}\left(1+\frac{N_0}{N_1}\right)\frac{1+\left(\frac{\mu_0}{\mu_1}\right)^2\frac{N_0}{N_1}}{\left(1+\frac{\mu_0}{\mu_1}\frac{N_0}{N_1}\right)^2}$$

$$N_0 = \frac{(2kT)^{3/2}m_0^{3/2}}{2\pi^2\hbar^3}F_{1/2}\left(\frac{E_F+\Delta}{kT}\right)$$

$$N_1 = \frac{(2kT)^{3/2}m_{1l}^{1/2}m_{1t}\nu_1}{2\pi^2\hbar^3}F_{1/2}\left(\frac{E_F}{kT}\right) \qquad (1)$$

where:

m_0 is the effective mass at the (000) minimum

m_{1t} is the transverse effective mass at the (111) minimum

m_{1l} is the longitudinal effective mass at the (111) minimum

ν_1 is the number of equivalent minima in the first Brillouin zone.

Δ is the energy difference between the (111) and (000) minima.

$F_{1/2}$ are the Fermi integrals which have been tabulated by BEER *et al.*[7]

μ_0 and μ_1 are the mobilities at the (000) and (111) minima respectively.

In equations (1) $m_0 = 0{\cdot}047$ and $\Delta = 0{\cdot}08$ eV at room temperature.

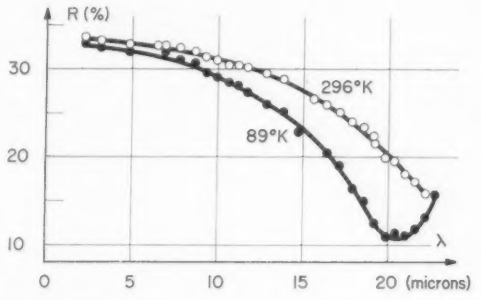

FIG. 1. Reflectivity of an n-type GaSb sample as a function of wavelength.

For the carrier concentrations used in this experiment, one can estimate that m_0 is equal to the effective mass at the bottom of the band.[5] The ratio μ_0/μ_1 in equation (1) is taken equal to 6.[3] Our deductions do not depend critically on the value of μ_0/μ_1.

We further assume that m_{1l}, m_{1t}, and ν_1 have the same values as for germanium. The agreement between the calculated polarizability at room temperature and the observed one will prove the self-consistency of this assumption.

Solving equations (1) we find at 296°K, $N_0 = 3{\cdot}7\times10^{17}$ cm^{-3} and $N_1 = 1{\cdot}26\times10^{18}$ cm^{-3}.

Figure 2 shows the dielectric constant calculated from the reflectivity data of Fig. 1 at 296 and 89°K as a function of the square of the wavelength. The solid line at 296°K is the curve found from the known values of N_1,N_0 and the effective masses m_0,m_{1l}, m_{1t} using the expression:

$$\epsilon = \epsilon_{\text{intrinsic}} - \left[\frac{N_1}{3}\left(\frac{1}{m_{1l}}+\frac{2}{m_{1t}}\right)+\frac{N_0}{m_0}\right]\frac{4\pi e^2}{\omega^2} \qquad (2)$$

The excellent agreement between the experimental and calculated results shows that the (111) minima in GaSb are very similar to the corresponding minima in germanium. From the low temperature dielectric constant, and neglecting the temperature dependence of m_0, m_{1l} and m_{1t}, we can calculate N_0 and N_1 by using equation (2) and the temperature independent value of N_0+N_1

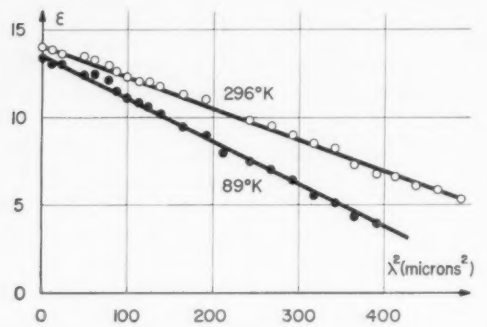

FIG. 2. Dielectric constant of an *n*-type GaSb sample as a function of the square of the wavelength.

determined at room temperature. At 89°K we find $N_1 = 0{\cdot}61 \times 10^{18}$ and $N_0 = 1{\cdot}02 \times 10^{18}$. The same values can be obtained from the first of equations (1) and the low temperature value of R_H if we assume that μ_0/μ_1 is temperature independent. Equations (1) can now be used to calculate E_F and Δ. We find $\Delta = 0{\cdot}057$ eV. Hence this rough calculation indicates that the separation between the (000) and (111) minima increases with increasing temperature at a rate $+10^{-4}$ eV$\times$ (°C)$^{-1}$. The variation of this separation has been measured for germanium[8] and found to be $+5\times10^{-5}$ eV$\times$(°C)$^{-1}$, close to the value determined by us for GaSb. SAGAR[3] found from the temperature dependence of the piezoresistance a coefficient for Δ of -3×10^{-4} eV$\times$(°C)$^{-1}$.

This coefficient disagrees with ours and with the one for germanium even in sign. However, for its derivation, a number of simplifying assumptions about the scattering mechanism had to be made such as the validity of deformation potential theory, implying acoustical mode scattering, and the existence of an energy independent isotropic relaxation time. The presence of ionized impurity and intervalley scattering is likely to affect the piezoresistance while the derivations in this letter do not depend on these assumptions. Since we have postulated a similar behavior for the (000) and (111) minima in germanium and GaSb, it is reasonable to expect that the energy separation between these extrema changes similarly with temperature in both semiconductors, in agreement with our findings.

Laboratories R.C.A. Ltd. M. CARDONA
Zurich
Switzerland

References

1. ZWERDING S., LAX B., BUTTON K. J. and ROTH L. M., *J. Phys. Chem. Solids* **9**, 320 (1959).
2. ZWERDLING S., LAX B. and ROTH L. M., *Phys. Rev.* **108**, 1402 (1957).
3. SAGAR A., *Phys. Rev.* **117**, 93 (1960).
4. CARDONA M., PAUL W. and BROOKS M., *Helv. Phys. Acta* **33**, 329 (1960).
5. CARDONA M., to be published.
6. CARDONA M. and PRAKASH V., unpublished work.
7. BEER A. C., CHASE M. N. and CHOQUARD P. F., *Helv. Phys. Acta* **28**, 529 (1955).
8. MACFARLANE G. G., MCLEAN T. P., QUARRINGTON J. E. and ROBERTS V., *Proc. Phys. Soc. Lond.* **71**, 863 (1958).

Vol. 17
1960

A thermal shutter phenomenon in field-effect measurements

(*Received* 11 *April* 1960)

ONE of the methods widely used in the investigation of the surface properties of semiconductors is the field effect.[1] This method employs capacitatively applied electric fields in order to vary the surface conductance. Where the swing in the electric field is sufficiently large the sample conductance passes through its minimum value. This value depends only on the bulk properties of the sample and the temperature, and its knowledge is essential in the calculation of the surface potential corresponding to any given value of the conductance.[2]

An effect has been observed in this laboratory which can lead to a misinterpretation of field-effect data taken on samples whose temperature

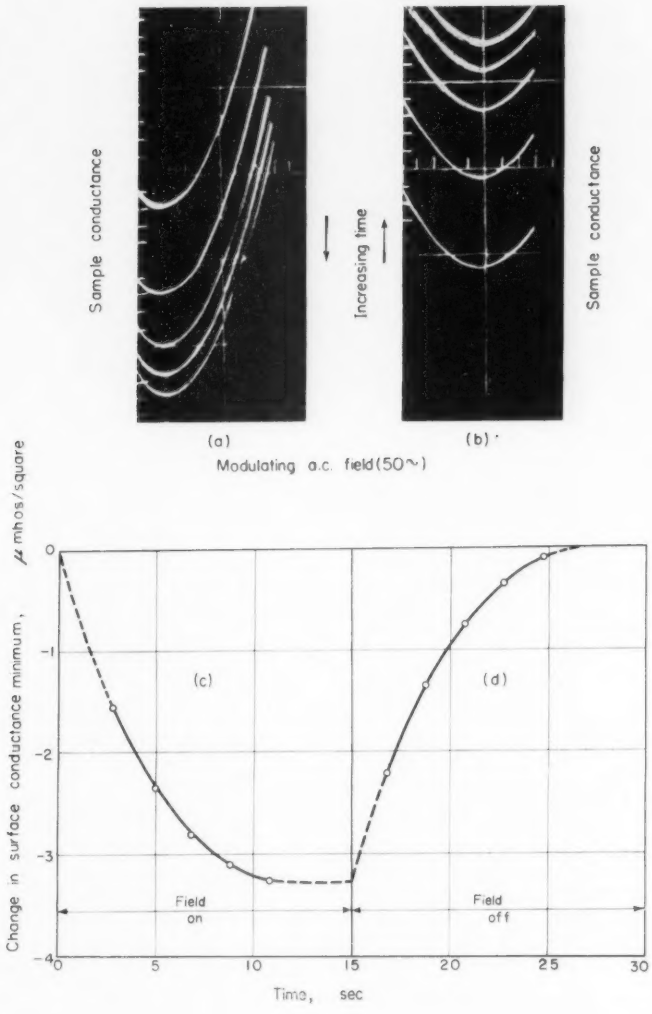

FIG. 1

(a) Oscillogram of field-effect curves of n-type germanium ($N_D - N_A = 3 \times 10^{13}$ cm^{-3}) taken at two-second intervals following application of d.c. field.

(b) Oscillogram of field-effect curves of n-type germanium ($N_D - N_A = 3 \times 10^{13}$ cm^{-3}) taken at two-second intervals following removal of d.c. field.

(c) Replot from (a) above of resulting changes in conductance minimum as a function of time.

(d) Replot from (b) above of resulting changes in conductance minimum as function of time.

Sample temperature 33°C, cryostat in ice bath.

differs from that of their surroundings. When the magnitude of the electric field is changed the value of the conductance minimum undergoes a slow drift. Thus if the minimum is not being displayed on the oscilloscope and is assumed to be constant, as in the point-to-point method of field-effect measurements,[3] an error will be introduced into the calculations of the change in surface conductance due to the applied field. If the minimum is being displayed on the oscilloscope, as in the original a.c. field-effect method,[1] the observed changes in the minimum can give rise to the impression that an additional conduction mechanism is present over and above those of the bulk and space-charge regions. In addition, this effect can be particularly disturbing when studying slow-state relaxation phenomena,[4] due to the similar magnitudes and time constants involved in these two processes.

Figure 1 (a) is an oscillogram of field-effect curves taken at two-second intervals following the application of a d.c. field of 3×10^5 V/cm in series with a modulating a.c. field (50 c.p.s.) of the same order of magnitude. As a result of the application of the d.c. field the conductance minimum together with the entire a.c. field-effect display is seen to descend towards a new equilibrium position. The change in this minimum in $\mu\Omega^{-1}$/square is plotted as a function of time in Fig. 1 (c). After the removal of the d.c. field the field effect curve relaxes back to its original position as shown in Figs. 1 (b) and (d).

The results of various measurements have shown that the changes in the conductance minimum following the application of the electric field are consistent, in both magnitude and direction, with small changes in sample temperature caused by heating or cooling of the sample by its surroundings. Thus, for example, the intrinsic and extrinsic ranges of sample conductance produce effects in opposite directions, and so does the temperature of the sample when it is above and below that of the surroundings. The results of Fig. 1 (a) (filament temperature 33°C, cryostat immersed in ice bath) can thus be interpreted as a decrease of 0·07°C in the temperature of the sample used (*n*-type germanium, $N_D - N_A = 3 \times 10^{13}$ cm^{-3}).

That this effect does not relate to the surface but is entirely thermal in nature was established by measuring directly the sample temperature during the drift of the conductance minimum. For the above sample cooled to liquid air temperature the temperature change amounted to half a degree for a field of the order of 10^5 V/cm. This should result in a change in conductivity of 1 per cent or a change in surface conductance of $60\mu\Omega^{-1}$/square and accounts fully for the magnitude of the drift observed in the sample conductance.

The mechanism seems to be as follows. An increase in the magnitude of the field (d.c. of either polarity, or a.c.) increases the Coulomb forces on the thin dielectric spacer between the plate and the sample, thus improving the thermal contact between the sample and its surroundings. Hence the applied field acts as a thermal shutter, and the presence of any temperature gradient between the sample and its environment will result in a slow heating or cooling of the filament and a corresponding drift in bulk conductance. This is the cause of the drift of the entire a.c. field-effect display shown in Fig. 1.

The characteristics of this temperature drift depend on the method of sample mounting, the nature of the temperature control used and the smoothness of the sample surface. The effect does not appear when the surface is very smooth or the pressure on the plate sufficient so that the thermal contact cannot be further enhanced by the Coulomb forces.

In order to make certain that the nature of this thermal shutter depends only on the mounting of the sample but not on its properties, the germanium was replaced by a metal filament of the same geometry. Under the same experimental conditions similar temperature changes were observed when the electric field was changed.

Department of Physics N. B. GROVER
The Hebrew University Y. GOLDSTEIN
Jerusalem
Israel

Vol. 17
1960

References

1. BROWN W. L., *Phys. Rev.* **100,** 590 (1955).
2. KINGSTON R. H. and NEUSTADTER S. F., *J. Appl. Phys.* **26,** 718 (1955).
3. MANY A. and GERLICH D., *Phys. Rev.* **107,** 404 (1957).
4. KINGSTON R. H., *J. Appl. Phys.* **27,** 101 (1956).

Nuclear magnetic resonance in ferromagnetic Fe^{57}*

IN THIS letter we report the observation of nuclear magnetic resonance in an enriched sample of Fe^{57}. The characteristics of the resonance are very similar to those observed in the nuclear magnetic resonance of ferromagnetic Co^{59}[1] indicating that the iron resonance is driven by domain wall motion.[2]

The resonance frequency with the sample in zero applied field and at room temperature (295°K) is 45·49 Mc/sec. Taking the nuclear magnetic moment of Fe^{57} to be 0·0903 nm as determined by electron-nuclear double resonance[3] we compute a room temperature hyperfine field of 330,500 gauss. This value is in excellent agreement with the value deduced by HANNA *et al.*[4] from polarized Mossbauer studies and confirms their interpretation of the spectrum. On cooling the sample to 77°K the resonance frequency was increased by 2·3 per cent to 46·54 mc/sec. The half-width between half power points is approximately 60 kc/sec at the two temperatures. The spin-lattice relaxation time T_1 was measured by a technique similar to that used for cobalt[1] and was found to be 4 msec at room temperature with no appreciable increase on cooling to 77°K.

The observations were made by placing one gram of finely powdered iron enriched to 76·7 per cent Fe^{57} in the r.f. coil of a marginal oscillator.† Changes in oscillator level resulting from a variation in sample losses through the nuclear resonance were measured by a novel modulation and detection system described below. The resonance as traced onto a strip chart recorder is shown in Fig. 1. The r.f. voltage on the coil was 1V r.m.s. corresponding to a peak r.f. magnetic field of 0·03 Oe. The major source of oscillator losses was associated with eddy currents in the particles. The damping of domain wall motion contributed about 20 per cent of the total losses as determined from a comparison of the losses in zero field with walls present and in high fields with the walls driven out of the particles. The losses associated with the resonance signal were 0·02 per cent of the total sample losses or approximately 0·1 per cent of the wall losses. The observed losses may be compared with a theory of the damping of wall motion by the nuclear spins. The imaginary part of the permeability of a spherical particle in the radio frequency range is given by‡

$$\mu_2 = \frac{3\pi}{4}\frac{\lambda\omega}{(\gamma_e M)}2\frac{a}{\delta}\left[1+(\gamma_e H_n^2/\omega M)(\chi'+\frac{\gamma_e M}{\lambda}\chi'')\right]$$

where λ is the wall damping parameter, a is the domain diameter, δ is the wall thickness, and H_n is the field seen by the nuclear spins. The nuclear dispersion signal relative to the wall losses is given by

$$\rho = (\gamma_e H_n^2/\omega M)\chi_0\omega/\Delta\omega$$

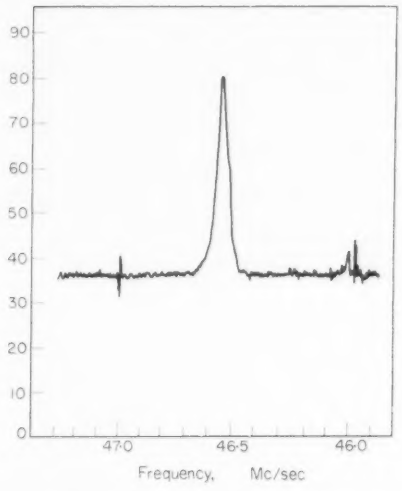

FIG. 1. Nuclear magnetic resonance signal in Fe^{57} at 77°K. The power absorption derivative is displayed, indicating that the absorption is proportional to χ'. The spikes are frequency markers.

* Supported by the United States Atomic Energy Commission.

† The sample used in these experiments was obtained as a metallic powder from the Isotope Sales Division of the Oak Ridge National Laboratory.

‡ A related expression given in Ref. (2) is in error. An expanded version of the present letter will contain the corrected treatment of the problem.

This expression may be put into a simple form by re-expressing the nuclear susceptibility and sample magnetization:

$$\rho = [I(I+1)/3S](\hbar\omega/kT)\omega/\Delta\omega$$

Here I and S are the nuclear and electron spins respectively. Substituting the experimental frequency and line width we obtain a value in reasonable agreement with the observed signal.

Even though the nuclear signal is five orders of magnitude larger than would be expected in a diamagnetic sample of comparable nuclear concentration and field, detection of the resonance still presents some problem. Magnetic field modulation of the resonance is not feasible in the present experiment. A spectrometer in which the frequency is slowly swept and modulated is therefore indicated. The major limitation on a spectrometer of this kind is the large background signal arising from frequency dependent sample losses and from instrumental effects. To overcome this difficulty the following technique was developed. The r.f. oscillator was simultaneously modulated at two frequencies, one above and the other below the nuclear relaxation frequency. The response at the two frequencies was amplified in a common amplifier and then detected separately in a pair of detectors synchronous at the modulation frequencies. Finally the difference in the d.c. output of the two detectors was recorded. In the absence of a nuclear resonance the output of the two channels should cancel. The nuclear resonance signal will be present only in the low frequency channel since the response of the nuclei to the modulation drops off rapidly above the relaxation frequency. Using this technique the frequency dependent background as well as a major part of the low frequency noise was eliminated without distortion of the resonance signal.

Although Fe^{57} with its small magnetic moment yields a considerably smaller resonance signal than does Co^{59} there are a number of features of iron which make it favorable for further resonance study apart from the intrinsic interest in the ferromagnetism of iron. Since the spin of Fe^{57} is $\frac{1}{2}$ there is no electric quadrupole moment and the line broadening is restricted to magnetic effects. The possibility of varying the isotopic enrichment of Fe^{57} should make possible a detailed experimental study of nuclear spin diffusion.[2,5]

Acknowledgement—We are very grateful to Professor W. D. KNIGHT for the design of the marginal oscillator used in these experiments and for a number of conversations on instrumentation.

University of California
Berkeley
California
U.S.A.

A. C. GOSSARD*
A. M. PORTIS
W. J. SANDLE

References

1. GOSSARD A. C. and PORTIS A. M., *Phys. Rev. Letters* **3,** 164 (1959).
2. PORTIS A. M. and GOSSARD A. C., *J. Appl. Phys.* **31,** S205 (1960) (In press).
3. LUDWIG G. W. and WOODBURY H. H., *Phys. Rev.* **117,** 1286 (1930).
4. HANNA S. S., HEBERLE J., LITTLEJOHN C., PERLOW G. J., PRESTON R. S. and VINCENT D. H., *Phys. Rev. Letters* **4,** 177 (1960).
5. SUHL H., *J. Phys. Radium* **20,** 333 (1959).

Vol. 17
1960

Disturbances of carrier concentration in high electric field

(*Received* 20 *June* 1960)

IT IS USUALLY assumed in interpreting experiments where a high electric field is applied to a germanium or silicon sample in the exhaustion region that the observed changes in conductivity are due to mobility changes.[1] Conductivity changes that have been interpreted as arising from changes in carrier concentration have been ascribed to injection or other contact or surface effects. In the present note we shall consider the recombination of hot carriers along the lines used by SHOCKLEY and READ[2] for thermal carriers. It will be seen that this leads to a prediction of changes in carrier concentration occurring as a bulk effect in high fields.

As in the SHOCKLEY–READ model, it is assumed that recombination takes place through the medium of a trap level at energy ϵ_t in the forbidden gap. It is envisioned that the energy transfers required for electron and hole capture or emission

* National Science Foundation Predoctoral Fellow.

take place through a thermal process such as the multi-phonon one, or the cascade process discussed by LAX[3], or a radiative process or some combination of these. Neither the Auger process nor field emission from the traps, which probably requires higher fields than those dealt with here, will be considered. Also, the discussion will be confined to non-degenerate material.

For the processes included here, the average probability per unit time, $c_n(\epsilon)$, for an electron with energy in the range $d\epsilon$ at ϵ to be captured by an empty trap is the average over the states in $d\epsilon$ of v times the capture cross-section A of the trap.* With this, the rate of capture of electrons from the conduction band by traps is*

$$f_p(\epsilon_t)N_t \int_{\epsilon=\epsilon_c}^{\infty} c_n(\epsilon)f(\epsilon)N(\epsilon)\,d\epsilon$$

where $f(\epsilon)$ is the distribution function in an electric field of intensity E rather than the Maxwell–Boltzmann distribution for thermal carriers. This expression can be rewritten $f_p(\epsilon_t)N_t n\langle c_n\rangle^E$, where E indicates that the average is to be taken over the actual distribution in high field.

The rate of emission of electrons from traps for a non-degenerate case is independent of the actual distribution of carriers in the conduction band, and is therefore the same as obtained in Ref. (2), e.g. $N_t f(\epsilon_t)n_1\langle c_n\rangle^0$, where $n_1 = N_c \exp(\epsilon_t-\epsilon_c)/kT$, and the superscript 0 indicates that the average of c_n is to be taken over the zero-field distribution. With the notation $N_t\langle c_n\rangle = C_n$, the resulting net rate of capture of electrons by traps is

$$C_n^E f_p(\epsilon_t)n - C_n^0 f(\epsilon_t)n_1. \tag{1}$$

A similar treatment can be carried out for holes, leading to the net rate of capture of holes by these traps:

$$C_p^E f(\epsilon_t)p - C_p^0 f_p(\epsilon_t)p_1. \tag{2}$$

Consider now what the steady state in high electric field would be if there were no injection or extraction at contacts or surface. From the condition that the net rate of capture of electrons by traps must vanish, we obtain an expression for the degree of filling of the traps in the steady state in a field E:

$$f(\epsilon_t) = \frac{1}{1+(n_1/n)(C_n^0/C_n^E)}, \tag{3}$$

while from the condition that the net rate of capture of holes by traps must vanish we obtain

$$f(\epsilon_t) = \frac{1}{1+(p/p_1)(C_p^E/C_p^0)} \tag{4}$$

Since (3) and (4) are concerned with the same trap level, the two expressions for $f(\epsilon_t)$ must be equal. This leads to

$$np = n_i^2(C_n^0C_p^0/C_n^EC_p^E). \tag{5}$$

According to this relation, in the steady state even when all contact and surface injection and extraction are excluded, the bulk carrier concentrations in high fields will be different from the thermal equilibrium values if either C_n^E or C_p^E is different from its low-field value. Also, if this is the case, it can be seen from (3) or (4) that the degree of filling of the traps in high electric fields will be different from the thermal equilibrium value.

Calculations indicate that the average speed of the carriers in germanium, for example, is increased by a factor of 10 at fields of about 20,000 V/cm at 300°K.[4] If the capture cross-section were independent of v, at such fields np would according to (5) be decreased by a factor of 100. The reason for this is that, with constant cross-section, the heating of the carriers by the field would increase the rate of capture of both electrons and holes by traps. If the trapping cross-section were to decrease with v more rapidly than v^{-1}, as seems to be the case for the mechanism discussed by LAX[3], the effect of high fields would be to increase rather than decrease the carrier concentration. Of course if A were proportional to v^{-1}, no change with field would be expected, but there is no reason to expect this dependence to be generally valid.

It is not likely that effects as large as those suggested by the factor 100 could be seen in practice, because the electric fields that heat the carriers are applied in pulses of a few microseconds

* Except where indicated otherwise, the notation will be that of SHOCKLEY and READ, Ref. (2).

duration at most to avoid heating the sample. For most germanium samples the steady-state carrier concentration would probably not be reached during such a pulse. Despite this, however, it seems that for a near-intrinsic germanium sample, an observable change in carrier concentration should occur during the time of a pulse. Such an effect could be useful for determining the velocity dependence of the trapping cross-section of the various recombination centers. Of course, to utilize it in this way it would be necessary to eliminate or otherwise separate this process from the contact and surface effects that can also cause changes in carrier concentration.

Acknowledgement—It is a pleasure to acknowledge valuable discussions with Dr. A. MANY who suggested this line of investigation.

General Telephone and Electronics E. M. CONWELL
Laboratories, Inc.
Bayside
N.Y.

References

1. See, for example, SHOCKLEY W., *Bell Syst. Tech. J.* **30,** 990 (1951).
2. SHOCKLEY W. and READ T., *Phys. Rev.* **87,** 835 (1952).
3. LAX M., *J. Phys. Chem. Solids* **8,** 66 (1959).
4. CONWELL E. M., *J. Phys. Chem. Solids* **8,** 234 (1959).

Vol. 17
1960